

# The effect of carbon-based additives on the fuel-rich conversion of methane

Von der Fakultät für Ingenieurwissenschaften, Abteilung Maschinenbau und

Verfahrenstechnik der

Universität Duisburg-Essen

zur Erlangung des akademischen Grades

eines

Doktors der Ingenieurwissenschaften

Dr.-Ing.

genehmigte Dissertation

von

Dennis Kaczmarek

aus

Oberhausen

Gutachter: Univ.-Prof. Dr. rer. nat. Tina Kasper  
Univ.-Prof. Dr.-Ing. Francesco Contino

Tag der mündlichen Prüfung: 14.12.2020



*Für meine viel zu  
früh verstorbene Mutter*



---

## Acknowledgments

This thesis was done during my work as a research assistant in the “Mass Spectrometry in Reactive Flows” group of the Department of Thermodynamics at the University of Duisburg-Essen.

At this point, I would like to thank all the people who were involved in the creation of this work and who supported me during my time as a Ph.D. student.

I want to especially thank my supervisor Prof. Tina Kasper for the opportunity to do research on such an exciting topic and participate in such an interesting project. Not only was it possible for me to work on an interesting experiment and constantly develop it further, but I was also able to participate in numerous conferences. I would also like to thank you for sharing your expertise and enthusiasm for science, especially mass spectrometry, which has allowed me to develop both scientifically and personally. You always had – even at late hours – an open ear for questions and problems and stood by me with help and advice. I hope not to have disappointed the trust placed in me and am proud to be one of your Teletubbies :-).

I would like to thank Prof. Burak Atakan for his confidence in my teaching. Especially the transfer of responsibility for the students in the third attempt has enabled me to further develop my thermodynamic understanding. Furthermore, I would like to thank you for the constant scientific exchange and the open ear for questions of all kinds.

I would like to thank Prof. Francesco Contino for kindly reviewing and grading my work. As session chair, you already took away my nervousness during my first international presentation in Belgium, for which I thank you very much.

I thank Dennis Roskosch and Cory Rogers for proofreading parts of the thesis. Cory, it was and still is a pleasure to work with you and I look forward to visiting you in Boulder.

I also want to thank the German Research Foundation for funding the research unit FOR 1993 “Multi-functional conversion of chemical species and energy”. In the context of the research unit, I would like to thank especially Sylvia Porras, Kai Banke, Jürgen Herzler, and the former project member Sebastian Wiemann for their excellent cooperation.

Ulf Bergmann, Stephan Steinbrink, Andreas Görnt, and Erdal Akyldiz always supported me in all technical and IT-problems. Thank you very much! Without Stephan, I would only have built half of the reactors. Ulf, thanks for the unforgettable time at the trotting track!

I would also like to thank my former and current office neighbors Thomas Bierkandt, Robert Hegner, Dominik Schröder, and Shkelqim Shaqiri for the wonderful time. Not only were we able to discuss scientific topics, but we also became very good friends.

Special thanks go to Yasin Karakaya, Sascha Lau, and Charlotte Rudolph, with whom I spent a lot of nice time both at work and privately. Without you, the conferences, including the beer

## Acknowledgments

---

rounds and the gourmet dinners at the “Golden Seagull<sup>1</sup>” would only have been half as nice. We always had a lot of fun together, and you were always by my side. Thank you, guys! Of course, I would like to thank all my colleagues for the always pleasant working atmosphere, the nice coffee rounds, beautiful barbecues, and nice trips. It was a wonderful time! Finally, I would like to thank my family and friends who have supported me in every situation in life. Even in difficult situations, you have given me the strength and perseverance not to lose sight of my goal. Thank you for everything!

---

<sup>1</sup> World’s largest fast-food restaurant, also called McDonalds.

---

## Kurzfassung

Das zukünftige Energiesystem erfordert eine drastische Reduzierung der Treibhausgasemissionen, einerseits durch den Ausbau des erneuerbaren Energiesektors, andererseits durch die Entwicklung CO<sub>2</sub>-neutraler Energieversorgungsketten. Langfristig bedeutet dies den Verzicht auf die Verbrennung fossiler Brennstoffe, die im Wesentlichen für den Klimawandel verantwortlich gemacht wird. Trotz des stark forcierten Ausbaus der erneuerbaren Energien ist mittelfristig nicht mit ihrer ausschließlichen Nutzung zu rechnen, so dass fossile Brennstoffe auch in den kommenden Jahrzehnten noch eine wichtige Rolle spielen werden. Dabei rückt Erdgas immer weiter in den Fokus, da es reichlich vorhanden und vielseitig einsetzbar ist und bei der Verbrennung von Erdgas deutlich weniger CO<sub>2</sub> freigesetzt wird als bei anderen fossilen Brennstoffen. Eine weitere Herausforderung, die mit dem Ausbau erneuerbarer Energien verbunden ist, ist die schwankende Verfügbarkeit der zugrunde liegenden Energiequellen wie Sonne und Wind. Flexible Energieumwandlungssysteme werden daher zunehmend wichtiger.

Eine vielversprechende Technologie ist die Polygeneration in mit Erdgas betriebenen Motoren nach dem Konzept der homogenen Kompressionszündung (engl. Homogeneous Charge Compression Ignition, kurz: HCCI). Dabei bedeutet Polygeneration die bedarfsorientierte Bereitstellung verschiedener Energieformen wie Arbeit, Wärme und Grundchemikalien. HCCI-Motoren sind im Vergleich zu konventionellen Verbrennungsmotoren effizienter und flexibler bezüglich des verwendeten Kraftstoffs. Darüber hinaus sind Verbrennungsmotoren im Allgemeinen industriell erprobt, leicht skalierbar und relativ kostengünstig. Die größte Herausforderung bei HCCI-Motoren ist die Kontrolle des Zündzeitpunktes, der hauptsächlich durch die Reaktionskinetik bestimmt wird. Wird Erdgas oder dessen Hauptkomponente Methan als Brennstoff eingesetzt, sind hohe Eingangstemperaturen oder hohe Kompressionsverhältnisse erforderlich, um die Zündung einzuleiten. Alternativ können dem Gasgemisch kleine Mengen reaktiver Additive wie Dimethylether oder *n*-Heptan zugegeben werden, um die Reaktivität des Gemischs zu erhöhen.

In dieser Arbeit wird der Einfluss von Ethan/Propan/Wasserstoff, *n*-Heptan und Dimethylether auf die partielle Oxidation von Methan bei einem Druck von 6 bar und Temperaturen zwischen 473 und 973 K systematisch untersucht. Dabei kommt ein Strömungsreaktor in Kombination mit einem Molekularstrahl-Flugzeitmassenspektrometer bzw. einem Gaschromatographen zum Einsatz. Der experimentelle Aufbau wurde aus früheren Studien adaptiert und verbessert, um zum Beispiel die Untersuchung von Flüssigkeiten und höheren Kohlenwasserstoffen sowie den Betrieb bei höheren Drücken und Temperaturen zu ermöglichen. Die Untersuchungen werden unter brennstoffreichen Bedingungen ( $2 \leq \phi \leq 20$ ) durchgeführt, um die Produktion von Grundchemikalien wie Synthesegas anstelle der typischen Oxidationsprodukte wie CO<sub>2</sub> und H<sub>2</sub>O unter nahezu stöchiometrischen Bedingungen zu begünstigen. Zusätzlich dazu werden Experimente mit reinem Methan bei Drücken bis zu 20 bar durchgeführt. Die experimentellen

Ergebnisse werden mit Simulationsergebnissen unter Verwendung verschiedener Reaktionsmechanismen aus der Literatur verglichen und mit Hilfe von Reaktionsfluss- und Sensitivitätsanalysen im Detail analysiert. Die Daten werden weiterhin verwendet, um einen in der Forschungsgruppe FOR 1993 entwickelten Reaktionsmechanismus zu validieren und zu modifizieren.

Die Ergebnisse zeigen, dass sowohl *n*-Heptan als auch Dimethylether dazu beitragen können, den Methanumsatz, im Vergleich zu Experimenten mit reinem Methan, bei bis zu 250 K niedrigeren Temperaturen einzuleiten und den Methanumsatz bei hohen Äquivalenzverhältnissen und hohen Temperaturen signifikant zu erhöhen. Die Zugabe von Ethan/Propan/Wasserstoff führt zu keiner Reduzierung der Reaktionsstarttemperatur, erhöht jedoch den Methanumsatz bei höheren Temperaturen in größerem Maße als die beiden anderen Additive. Die Hauptgründe für diese Beobachtung sind der bevorzugte und schnelle Verbrauch von Sauerstoff und Radikalen durch *n*-Heptan und Dimethylether sowie Reaktionswege, die zu einer Methanbildung führen. Zusätzlich zu dem Beginn des Brennstoffumsatzes beeinflussen die Additive auch die Produktzusammensetzung am Ausgang des Reaktors. Insbesondere werden erhöhte Ausbeuten an Synthesegas, oxigenierten Spezies wie Methanol und ungesättigten Kohlenwasserstoffen wie Ethen und Propen beobachtet. Reaktionsflussanalysen zeigen, dass sowohl die Einleitung des Methanumsatzes durch von dem Additiv freigesetzte Radikale als auch Wechselwirkungen zwischen den bei dem Umsatz von Methan und den Additiven gebildeten Intermediaten für die veränderte Produktzusammensetzung verantwortlich sind.

Auch höhere Drücke verlagern den Beginn des Methanumsatzes zu niedrigeren Temperaturen und erhöhen die Ausbeuten an nützlichen Chemikalien, wenn auch in geringerem Maße als die Zugabe von *n*-Heptan oder Dimethylether. Werden hohe Drücke mit brennstoffreichen Bedingungen kombiniert, kann jedoch ein Phänomen beobachtet werden, das bisher nur wenig Beachtung fand, nämlich der Bereich des negativen Temperaturkoeffizienten von Methan. Dieses Verhalten wird bei verschiedenen Drücken und Äquivalenzverhältnissen systematisch untersucht. Dabei zeigt sich, dass die Konkurrenz zwischen Oxidation- und Rekombinationspfaden hauptsächlich für dieses Verhalten verantwortlich ist.

Die Aufklärung des Einflusses von Additiven auf den Brennstoffumsatz und die Interpretation der gewonnenen Daten im Sinne eines modifizierten Reaktionsmechanismus sind wichtige Schritte zur zukünftigen Gestaltung und Steuerung eines Polygenerationsprozesses in HCCI-Motoren.

---

## Abstract

The future energy system requires an enormous reduction in greenhouse gas emissions by increasing the share of renewable energies and developing CO<sub>2</sub>-neutral energy supply chains. In the long term, this will mean abandoning the combustion of fossil fuels, which is essentially held responsible for climate change. Despite the ambitious expansion of renewable energies, their exclusive use is not likely to be achieved in the medium term so that fossil fuels will remain important in the coming decades. In this context, natural gas is attracting increasing attention because it is abundant and versatile and produces significantly less CO<sub>2</sub> per energy unit than other fossil fuels. A second major challenge is the fluctuating nature of renewable energy sources which requires flexible energy conversion technologies.

A promising technology is the polygeneration in homogeneous charge compression ignition (HCCI) engines fueled with natural gas. Polygeneration means the demand-oriented provision of different forms of energy such as work, heat, and base chemicals. Compared to conventional internal combustion (IC) engines, HCCI engines are more efficient and fuel-flexible. In addition, IC engines are industrially proven, easily scalable, and relatively cheap. The main challenge of HCCI engines is the control of the moment of autoignition, which is mainly governed by chemical kinetics. Given the low reactivity of natural gas or its main component methane, high intake temperatures or high compression ratios are required for ignition. Alternatively, small amounts of reactive additives such as dimethyl ether or *n*-heptane can be introduced into the premixed gas mixture to increase the reactivity of the mixture.

In this study, the influence of ethane/propane/hydrogen, *n*-heptane, and dimethyl ether on the partial oxidation of methane is investigated systematically at a pressure of 6 bar and temperatures between 473 and 973 K using a flow reactor in combination with molecular-beam time-of-flight mass spectrometry and gas chromatography. The experimental setup was adapted from previous studies and improved to allow the investigation of liquids and higher hydrocarbons and operation at higher pressures and temperatures, for example. Fuel-rich conditions ranging from  $2 \leq \phi \leq 20$  are selected to favor the production of base chemicals instead of typical oxidation products such as CO<sub>2</sub> and H<sub>2</sub>O at near stoichiometric conditions. Neat methane experiments at pressures up to 20 bar are additionally conducted. The experimental results are compared to predictions of several reaction mechanisms from the literature and analyzed in detail by reaction path and sensitivity analyses. The data are also used to validate and modify a reaction mechanism developed in the research unit FOR 1993.

The results show that both *n*-heptane and dimethyl ether can help to initiate methane conversion at up to 250 K lower temperatures compared to the experiment with neat methane and significantly increase methane conversion at high equivalence ratios and high temperatures. The addition of ethane/propane/hydrogen does not change the conversion onset temperature of

methane but increases methane conversion at higher temperatures to a larger extent than the other two additives. The rapid consumption of oxygen and radicals by *n*-heptane and DME as well as methane producing pathways have been revealed as the main reasons for this observation.

Besides the reaction onset, the additives also influence the product composition at the reactor outlet. In particular, increased yields of synthesis gas, oxygenated species such as methanol, and unsaturated species like ethylene and propene are observed. Reaction path analyses show that both the initiation of methane conversion by released radicals from the additives and interactions of the intermediates formed during the conversion of methane and the additives are responsible for the change in product composition.

Higher pressures also shift the reaction onset of methane to lower temperatures and positively influence yields of useful chemicals although to a lesser extent than the addition of *n*-heptane or dimethyl ether. However, the combination of fuel-rich conditions and high pressures leads to a phenomenon that has received little attention so far, i.e., the negative temperature coefficient region of methane. This behavior is systematically investigated at different pressures and equivalence ratios. It is found that the competition between oxidation and recombination pathways is mainly responsible for this behavior.

Elucidating the influence of additives on the conversion process and interpreting the obtained data in terms of a modified reaction mechanism are important steps towards the design and control of a polygeneration process in HCCI engines.

---

## Table of contents

<b>1</b>	<b>Introduction .....</b>	<b>1</b>
1.1	Task and objective .....	3
<b>2</b>	<b>Theoretical background .....</b>	<b>5</b>
2.1	Mass spectrometry .....	5
2.1.1	Molecular-beam sampling .....	5
2.1.2	Electron ionization .....	8
2.1.3	Time-of-flight mass spectrometer .....	9
2.1.4	Quadrupole mass spectrometer .....	12
2.1.5	Detector .....	13
2.2	Gas chromatography .....	13
2.2.1	Sample introduction .....	13
2.2.2	Species separation .....	14
2.2.3	Detector .....	18
<b>3</b>	<b>Modeling .....</b>	<b>19</b>
3.1	Plug flow .....	19
3.1.1	Conservation equations .....	22
3.2	Boundary-layer flow .....	23
3.2.1	Conservation equations .....	24
3.3	Reaction kinetics .....	25
3.3.1	Chemical reaction rates .....	25
3.3.2	Pressure-dependent reaction rates .....	28
3.3.3	Thermodynamic data .....	30
3.3.4	Transport data .....	31
3.3.5	Reaction pathway and sensitivity analysis .....	32
<b>4</b>	<b>Experimental methodology .....</b>	<b>35</b>
4.1	Flow reactor .....	35
4.1.1	Flow conditions .....	38
4.1.2	Temperature profiles .....	42
4.2	Time-of-flight mass spectrometer (TOF-MS) .....	43
4.2.1	Quantification of TOF-MS data .....	44
4.3	Gaschromatograph/Mass spectrometer (GC/MS) .....	46
4.3.1	Quantification of GC/MS data .....	48

4.4	Uncertainties.....	50
4.4.1	Direct calibration .....	50
4.4.2	Indirect calibration.....	51
4.5	Novelty of the experiment.....	51
<b>5</b>	<b>Introduction to the conversion experiments.....</b>	<b>53</b>
<b>6</b>	<b>Partial oxidation of natural gas/H<sub>2</sub> mixtures.....</b>	<b>55</b>
6.1	Introduction .....	55
6.2	Experimental setup .....	57
6.3	Modeling.....	59
6.4	Results and discussion.....	59
6.4.1	Main species – kinetics and equilibrium .....	59
6.4.2	Major products.....	60
6.5	Conclusion.....	68
<b>7</b>	<b>Partial oxidation of methane/<i>n</i>-heptane mixtures .....</b>	<b>69</b>
7.1	Introduction .....	69
7.2	Experimental methods .....	71
7.3	Simulations.....	74
7.4	Results and discussion.....	75
7.4.1	Reaction onset.....	77
7.4.2	Influence of equivalence ratio and interaction of <i>n</i> -C <sub>7</sub> H <sub>16</sub> with CH <sub>4</sub> .....	81
7.5	Conclusions .....	89
<b>8</b>	<b>Partial oxidation of methane/DME mixtures .....</b>	<b>91</b>
8.1	Introduction .....	92
8.2	Experiments.....	94
8.2.1	Rapid compression machine .....	94
8.2.2	Shock tube .....	96
8.2.3	Flow reactor.....	97
8.2.4	Investigated experimental conditions .....	98
8.3	Modeling of experimental data.....	100
8.3.1	Simulation of RCM and RCEM data.....	100
8.3.2	Simulation of shock-tube data .....	101
8.3.3	Simulation of flow-reactor data.....	101
8.4	Chemical kinetics model .....	102
8.4.1	Sub-mechanism for methane oxidation .....	103
8.4.2	DME sub-mechanism .....	105
8.5	Results and discussion.....	107
8.5.1	Ignition delay times .....	107
8.5.2	Temporal variation of product concentrations.....	111
8.6	Conclusions .....	117

---

<b>9</b>	<b>Partial oxidation of natural gas/DME mixtures .....</b>	<b>119</b>
9.1	Introduction.....	120
9.2	Experimental methods.....	123
9.2.1	Shock tube.....	124
9.2.2	Plug-flow reactor.....	125
9.3	Modeling.....	126
9.3.1	Model improvement.....	126
9.3.2	Shock-tube modeling.....	131
9.3.3	Plug-flow reactor modeling.....	132
9.4	Results and discussion.....	132
9.4.1	Shock tube.....	132
9.4.1.1	Ignition delay times.....	132
9.4.1.2	Product formation.....	135
9.4.2	Plug-flow reactor.....	137
9.4.2.1	Comparison of experimental and modeling results.....	137
9.4.2.2	Maximum yields of major species.....	147
9.5	Conclusions.....	148
<b>10</b>	<b>NTC behavior of methane.....</b>	<b>151</b>
10.1	Introduction.....	152
10.2	Experimental methods.....	153
10.3	Modeling.....	154
10.4	Results.....	155
10.4.1	Comparison between experimental and numerical results.....	156
10.4.2	Reaction path and sensitivity analyses.....	158
10.5	Conclusions.....	161
<b>11</b>	<b>The piston engine as a polygeneration reactor .....</b>	<b>163</b>
11.1	Introduction.....	164
11.2	Thermodynamic and kinetics assessment – <i>a priori</i> .....	167
11.2.1	Thermodynamics.....	167
11.2.2	Kinetics.....	168
11.2.3	Product yield optimization.....	170
11.3	Kinetics: model development and experiments.....	172
11.3.1	Mechanism development and reduction.....	173
11.3.1.1	Detailed mechanism.....	173
11.3.1.2	Mechanism reduction.....	173
11.3.2	Validation experiments.....	177
11.3.2.1	Ignition delay and onset of conversion.....	177
11.3.2.2	Kinetics of product formation.....	179
11.3.3	Energy storage by methane pyrolysis.....	183
11.4	Experiments in engines.....	189
11.4.1	Product formation in the RCM.....	189
11.4.2	Reciprocating engine.....	190

---

11.4.2.1 Operating stability .....	190
11.4.2.2 Outputs and efficiencies .....	192
11.4.2.3 Elevated compression ratios .....	195
11.4.3 Dry reforming: CO <sub>2</sub> conversion with methane.....	196
11.5 Thermodynamic and economic assessment – <i>a posteriori</i> .....	197
11.6 Conclusions and future work.....	200
11.6.1 Approach .....	200
11.6.2 Main results .....	201
11.6.3 Open questions and future directions .....	203
<b>12 Conclusion and Outlook.....</b>	<b>205</b>
12.1 Conclusion.....	205
12.2 Outlook.....	209
<b>Appendix.....</b>	<b>211</b>
A Supplementary material for chapter 8 .....	211
B Supplementary material for chapter 9 .....	217
C Supplementary material for chapter 10 .....	235
<b>References.....</b>	<b>243</b>
<b>Publications .....</b>	<b>265</b>

---

## List of figures

Figure 2-1:	The different regions of a supersonic beam. Inspired by Figure 2.1 in [24].	7
Figure 2-2:	Principle of a linear time-of-flight mass spectrometer.	9
Figure 2-3:	Two-stage reflectron time-of-flight mass spectrometer with two-stage ion extraction and instrument-specific elements described in section 4.2.	11
Figure 2-4:	Principle of a quadrupole mass spectrometer. Adapted from [32].	12
Figure 2-5:	Split/Splitless injector.	14
Figure 2-6:	Principle of adsorption in gas-solid chromatography.	15
Figure 2-7:	Van-Deemter curves for different carrier gases. Adapted from [36].	17
Figure 4-1:	Schematic diagram of the experimental setup. MFC: mass flow controller, V: Valve, T: Temperature sensor, p: pressure sensor, P: pump.	37
Figure 4-2:	Residence time distributions (RTD) according to the dispersion model. Red symbols and line represent experimental values and the associated RTD calculated with the value of $D_{Disp}/uL$ obtained from the experiment, respectively. Blue lines indicate RTDs for calculated values of $D_{Disp}/uL$ and black lines RTDs for $D_{Disp}/uL \leq 0.01$ where they become nonsymmetrical.	39
Figure 4-3:	Axial dispersion ( $D_{Disp}/ud_R$ ) correlated with the Peclet number $Pe$ for selected mixtures and volume flow rates. The minimum ( $Pe = 13.8$ , $D_{Disp}/ud_R = 0.144$ ) represents the point at which the plug-flow assumption is best fulfilled. Inspired by Levenspiel [51,78].	40
Figure 4-4:	Velocity, Temperature, and CO mole fraction distribution as a function of radial and axial distance for a $CH_4/O_2$ mixture at $\phi = 2$ , $p = 6$ bar, and $T = 873$ K.	41
Figure 4-5:	Set of temperature profiles measured in the center of the reactor at an argon flow of 280 sccm and a pressure of 1 bar for the given set temperatures.	42
Figure 4-6:	GC/MS system and reactor sampling interface.	47
Figure 4-7:	Trend of the thermal conductivity of He/H <sub>2</sub> mixtures (adapted from [86]).	48
Figure 6-1:	Plug-flow reactor and time-of-flight mass spectrometer.	58
Figure 6-2:	Mole fractions of CH <sub>4</sub> and CO as a function of temperature and equivalence ratio (Symbols: TOF-MS experiment, solid lines: kinetic simulations based on the reaction mechanism of Burke et al. [117], dashed lines: equilibrium calculations, NG: natural gas).	60
Figure 6-3:	Conversion of alkanes as a function of temperature and equivalence ratio for all investigated mixtures (Symbols: TOF-MS experiment, lines: kinetic simulations based on the reaction mechanism of Burke et al. [117], NG: natural gas).	61

---

Figure 6-4:	Reaction pathway for the NG mixture at $\phi = 2$ and 823 K. The numbers in the diagram show which percentage of carbon flows between educt and product species and the grey scale shows the percentage of carbon flux, related to the highest carbon flux within the reaction path, which is found between CH <sub>4</sub> and CH <sub>3</sub> . .....	63
Figure 6-5:	Yields of synthesis gas as a function of temperature and equivalence ratio (Symbols: TOF-MS experiment, lines: kinetic simulations based on the reaction mechanism of Burke et al. [117], NG: natural gas).....	64
Figure 6-6:	Production rate contribution of important reactions with respect to H <sub>2</sub> formation. ....	65
Figure 6-7:	Yields of unsaturated hydrocarbons as a function of temperature and equivalence ratio (Symbols: TOF-MS experiment, lines: kinetic simulations based on the reaction mechanism of Burke et al. [117], NG: natural gas).....	66
Figure 6-8:	Maximum experimental yields of all major products in case of the NG mixtures for all equivalence ratios. ....	67
Figure 7-1:	Experimental setup: The experimental setup consists of the heated plug-flow reactor, the molecular-beam sampling system made from two differentially pumped stages separated by nozzles and a reflectron time-of-flight mass analyzer with electron ionization. ....	72
Figure 7-2:	Temperature profiles from thermocouple measurements show that typically isothermal zone reaches the set temperature given in the label for each profile. The profiles were measured with an air flow of 280 sccm.....	73
Figure 7-3:	Main areas of formation of detected species at 6 bar in the investigated methane/heptane mixtures. The maximum yields of the respective species within the marked parameter range are given in brackets in the legend. ....	76
Figure 7-4:	Simulated temperature profile for the reactive mixture at $\phi = 20$ and $T = 623$ K. 0 on the y-axis corresponds to the centerline of the reactor. ....	77
Figure 7-5:	Mole fractions of O <sub>2</sub> (a), CH <sub>4</sub> (b) and <i>n</i> -C <sub>7</sub> H <sub>16</sub> (c) for $\phi = 8$ and different mixtures. Symbols: TOF-MS experiment, solid lines: simulations based on the reaction mechanism of Zhang et al. [135]. ....	78
Figure 7-6:	Reaction flow analysis of the neat CH <sub>4</sub> mixture: Important reactions for CH <sub>4</sub> consumption and formation at $\phi = 8$ . ....	78
Figure 7-7:	General formation of OH radicals with respect to CH <sub>4</sub> (left) and <i>n</i> -C <sub>7</sub> H <sub>16</sub> oxidation (right). In the mixture both routes are active. (Black: Most important pathway, Red: High temperature pathway, Blue: Less important pathway). ....	79
Figure 7-8:	Reaction flow analysis of the neat CH <sub>4</sub> mixture: Important reactions for O <sub>2</sub> consumption and formation at $\phi = 8$ . ....	80
Figure 7-9:	O <sub>2</sub> consumption for all investigated methane/heptane mixtures (Experiment: left (GC results), Simulations: middle [135] and right [144]). ....	81
Figure 7-10:	Yield of CO for all investigated methane/heptane mixtures (Experiment: left (GC results), Simulations: middle [135] and right [144]). ....	82

---

Figure 7-11: Mole fractions of CO (a), C <sub>2</sub> H <sub>6</sub> (b) and CH <sub>3</sub> OH (c) for different mixtures at $\phi = 8$ . Symbols: TOF-MS experiment, solid lines: simulations based on the reaction mechanism of Zhang et al. [135]. The gray lines and symbols are always the sum of the results for the two neat fuel experiments or simulations, respectively.....	82
Figure 7-12: Integrated reaction path towards CO and C <sub>2</sub> H <sub>6</sub> for the CH <sub>4</sub> / <i>n</i> -C <sub>7</sub> H <sub>16</sub> -mixture at $\phi = 8$ and 773 K.....	83
Figure 7-13: Yield of C <sub>2</sub> H <sub>6</sub> for all investigated methane/heptane mixtures (Experiment: left (GC results), Simulations: middle [135] and right [144])......	84
Figure 7-14: Important reactions for C <sub>2</sub> H <sub>6</sub> consumption and formation at $\phi = 8$ and 773 K (CH <sub>4</sub> / <i>n</i> -C <sub>7</sub> H <sub>16</sub> ). The reaction flow analysis was performed with the reaction mechanism of Zhang et al. [135]. .....	85
Figure 7-15: Yield of CH <sub>3</sub> OH for all investigated methane/heptane mixtures (Experiment: left (GC results), Simulations: middle [135] and right [144]). ....	85
Figure 7-16: Yield of H <sub>2</sub> for all investigated methane/heptane mixtures (Experiment: left (GC results), Simulations: middle [135] and right [144]). .....	86
Figure 7-17: Yield of CO <sub>2</sub> for all investigated methane/heptane mixtures (Experiment: left (GC results), Simulations: middle [135] and right [144]). .....	87
Figure 7-18: Yield of C <sub>2</sub> H <sub>4</sub> for all investigated methane/heptane mixtures (Experiment: left (GC results), Simulations: middle [135] and right [144]). .....	88
Figure 7-19: Yield of C <sub>3</sub> H <sub>6</sub> for all investigated methane/heptane mixtures (Experiment: left (GC results), Simulations: middle [135] and right [144]). .....	89
Figure 8-1: Rapid compression machine setup.....	95
Figure 8-2: RCEM driving system. (a) Illustration of RCEM operation (b) Experimental pressure traces during ignition and for different $\tau_{\text{hold}}$ . The initial mixture in the reaction chamber (1) is compressed and held in an isochoric state (2) for a controlled hold time, at which the piston is pulled back, expanding the in-cylinder gas (3). The hold time can be varied for obtaining information about the product composition after variable reaction times.....	96
Figure 8-3: Temporal variation of pressure (black) and CH* emission (red) measured in the shock tube with a CH <sub>4</sub> /DME/air mixture ( $\phi = 10$ ) at 28.5 bar and 735 K. ....	97
Figure 8-4: Experimental setup of the plug-flow reactor with TOF-MS.....	98
Figure 8-5: Schematics of the multi-zone model.....	101
Figure 8-6: Low-temperature ignition delay times measured in the RCM (symbols) and simulations based on PolyMech (straight lines) for (a) mixture 3, (b) mixture 4, (c) mixture 5, and (d) mixture 6. Blue lines represent the first-stage ignition and red lines the main ignition. ....	108
Figure 8-7: High-temperature ignition delay times measured in the RCM (symbols) and simulations based on PolyMech (straight lines) for (a) mixture 7, (b) mixture 8, (c) mixture 9, and (d) mixture 10.....	109
Figure 8-8: Comparison of ignition delay times measured in a shock tube (symbols) and simulations with PolyMech (lines) for CH <sub>4</sub> /DME/air mixture at $\phi = 10$ , 30 bar and with 10 mol% DME.....	109

---

Figure 8-9:	Low and high temperatures global OH sensitivity analyses for mixtures at equivalence ratios of $\phi = 6$ and 10. (a) $T_c = 700$ K (mixtures 3 and 5), (b) 950 K (mixtures 7 and 9).....	110
Figure 8-10:	Comparison of reactant's temporal consumption profiles for mixture 15 (left) and 16 (right) measured in an RCEM (symbols) and simulations (lines).....	111
Figure 8-11:	Comparison of the CO, CO <sub>2</sub> and H <sub>2</sub> species profiles as a function of reaction time for mixture 15 (left) and 16 (right) measured in a RCEM (symbols) and simulations (lines). ....	112
Figure 8-12:	Comparison of C <sub>2</sub> species formation time profiles for mixture 15 (left) and 16 (right) measured in an RCEM (symbols) and simulations (lines).....	113
Figure 8-13:	Rate of production analysis on CH <sub>3</sub> for mixtures with equivalence ratios of $\phi = 6$ .....	113
Figure 8-14:	Remaining fractions of reactants as a function of temperature for mixtures 20 (left) and 22 (right). ....	114
Figure 8-15:	Yields of CO, CO <sub>2</sub> and H <sub>2</sub> as a function of temperature for mixtures 20 (left) and 22 (right). ....	115
Figure 8-16:	Yields of C <sub>2</sub> H <sub>4</sub> , C <sub>2</sub> H <sub>6</sub> , C <sub>3</sub> H <sub>6</sub> and C <sub>3</sub> H <sub>8</sub> as a function of temperature for mixtures 20 (left) and 22 (right).....	115
Figure 8-17:	Simulations of time dependent species profiles for shock tube conditions mixture 13 ( $\phi = 10$ ) at 800 K and 30 bar. ....	116
Figure 8-18:	Measured (shock tube, symbols) and simulated (straight lines) product mole fractions after ignition of CH <sub>4</sub> /DME/air mixture (mixture 13) at $\phi = 10$ and 30 bar. ....	116
Figure 9-1:	Sensitivity coefficients of the CO <sub>2</sub> mole fraction for selected plug-flow (left) and shock-tube (right) conditions using the PolyMech1.0 [19]. Coefficients were integrated up to the sampling even of each experiment. ....	128
Figure 9-2:	Sensitivity coefficients of the CH <sub>3</sub> OH (left) and CH <sub>2</sub> O (right) mole fractions for selected plug-flow conditions using the PolyMech1.0 [19]. Coefficients were integrated up to the sampling event of each experiment. ....	129
Figure 9-3:	Sensitivity coefficients of the C <sub>2</sub> H <sub>4</sub> mole fraction for selected plug-flow (left) and shock-tube (right) conditions using the PolyMech1.0 [19]. Coefficients were integrated up to the sampling event of each experiment....	130
Figure 9-4:	Measured and simulated ignition delay times of natural gas/DME/air mixtures at $\phi = 2$ and 30 bar. Symbols: Experiments, full lines: Simulations with PolyMech1.0 [19], dash-dotted lines: Simulations with PolyMech2.0, dashed lines: Simulations with AramcoMech3.0 [124]. ....	133
Figure 9-5:	Measured and simulated ignition delay times of CH <sub>4</sub> and a natural gas/air mixture at $\phi = 10$ and 30 bar. Symbols: Experiments, full lines: Simulations with PolyMech1.0 [19], dash-dotted lines: Simulations with PolyMech2.0, dashed lines: Simulations with AramcoMech3.0 [124], dotted lines: Simulations with the Cai and Pitsch [148] mechanism.....	134

---

- 
- Figure 9-6: Measured and simulated ignition delay times of a natural gas/5 % DME/air mixture at  $\phi = 10$  and 30 bar. Symbols: Experiments, full lines: Simulations with PolyMech1.0 [19], dash-dotted lines: Simulations with PolyMech2.0, dashed lines: Simulations with AramcoMech3.0 [124]. ..... 134
- Figure 9-7: Measured and simulated species mole fractions of a natural gas/air mixture at  $\phi = 10$  and 30 bar after ignition. Symbols: Experiments, full lines: Simulations with PolyMech1.0 [19], dash-dotted lines: Simulations with PolyMech2.0, dashed lines: Simulations with AramcoMech3.0 [124], dotted lines: Simulations with the Cai and Pitsch mechanism [148]. ..... 135
- Figure 9-8: Measured and simulated mole fractions of a natural gas/5 % DME/air mixture at  $\phi = 10$  and 30 bar after ignition. Symbols: Experiments, full lines: Simulations with PolyMech1.0 [19], dash-dotted lines: Simulations with PolyMech2.0, dashed lines: Simulations with AramcoMech3.0 [124]. ..... 136
- Figure 9-9: Mole fractions of reactants and products as a function of temperature for different equivalence ratios for the 95/5 natural gas/DME mixture. Symbols: TOF-MS experiment, lines: Simulations based on the PolyMech1.0 [19] (dotted lines), AramcoMech3.0 [124] (dashed lines), and the PolyMech2.0 (solid lines). Mole fraction uncertainties are displayed by the shaded areas... 138
- Figure 9-10: Mole fractions of reactants and products as a function of temperature for different equivalence ratios for the 90/10 natural gas/DME mixture. Symbols: TOF-MS experiment, lines: Simulations based on the PolyMech1.0 [19] (dotted lines), AramcoMech3.0 [124] (dashed lines), and the PolyMech2.0 (solid lines). Mole fraction uncertainties are displayed by the shaded areas. .... 139
- Figure 9-11: Reaction path analysis using the PolyMech2.0 for the 10 % DME mixture at 973 K and  $\phi = 20$  (calculated at the time corresponding to 25 % DME conversion). The percentages show the relative rate of carbon consumption of the limiting reactant and line darkness represents the percentage of carbon flux, related to the highest carbon flux within the reaction path, which is found between  $\text{CH}_3\text{OCH}_3$  and  $\text{CH}_3\text{OCH}_2$ . Species next to the arrows represent the main reaction partners. .... 141
- Figure 9-12: Reaction path analysis using the PolyMech2.0 for the 5 % DME mixture at 773 K and  $\phi = 10$  (calculated at the time corresponding to 25 % DME conversion). The percentages show the relative rate of carbon consumption of the limiting reactant and line darkness represents the percentage of carbon flux, related to the highest carbon flux within the reaction path, which is found between  $\text{CH}_2\text{O}$  and  $\text{CHO}$ . Species next to the arrows represent the main reaction partner. .... 145

---

Figure 9-13: Excerpt of the reaction path analysis using the PolyMech2.0 for the 10 % DME mixture at 623 K and $\phi = 10$ (calculated at the time corresponding to 25 % DME conversion). The percentages show the relative rate of carbon consumption of the limiting reactant and line darkness represents the percentage of carbon flux, related to the highest carbon flux within the reaction path, which is found between $\text{CH}_3\text{OCH}_3$ and $\text{CH}_3\text{OCH}_2$ . Species next to the arrows represent the main reaction partner. ....	146
Figure 9-14: Maximum yields of products as a function of equivalence ratio and DME amount. Values for neat natural gas (0 % DME) were taken from Ref. [197]. Yields do not add up to 100 % due to unconverted methane. ....	148
Figure 10-1: Simulated ignition delay times (corresponds to a 5 K temperature rise) as a function of the initial temperature at $\phi = 10$ and $p = 10$ bar. ....	155
Figure 10-2: Mole fractions of major species as a function of temperature and equivalence ratio (left: $\phi = 10$ , right: $\phi = 20$ ). Symbols: experiment, lines: simulations based on the Aramco (dashed lines) and modified PolyMech mechanism (solid lines). ....	157
Figure 10-3: Reaction path analysis using the modified PolyMech mechanism for 2 % $\text{CH}_4$ consumption at (a) 823 K, (b) 923 K and (c) 973 K, a pressure of 10 bar and $\phi = 10$ . The percentages show the relative rate of consumption of the limiting reactant and line darkness represents the percentage of carbon flux, related to the highest carbon flux within the reaction path, which is found between $\text{CH}_4$ and $\text{CH}_3$ at 823 K. ....	159
Figure 10-4: Sensitivities of the formation and consumption of $\text{CH}_4$ at (a) 823 K, (b) 923 K and (c) 973 K, $\phi = 10$ and $p = 10$ bar using the modified PolyMech mechanism. ....	160
Figure 11-1: Crank-angle resolved simulation of methane conversion (without additive) for an equivalence ratio of $\phi = 2$ , an engine speed $N = 600$ rpm, a compression ratio $\varepsilon = 18$ and an intake temperature of 428 K. ....	169
Figure 11-2: Major product species as a function of equivalence ratio ( $N = 600$ rpm, $\varepsilon = 18$ ) on the left axis. The intake temperature needed for ignition is plotted on the right axis. ....	170
Figure 11-3: Result of an optimization for $\text{C}_2\text{H}_4$ using PolyMech [19]. Top graph: yields and conversions, bottom graph: optimization variables. The x-axis is the initial temperature $T_0$ that was held constant for each optimization. ....	171
Figure 11-4: Contribution of each timescale (mode) to the total entropy production of the system for $\text{CH}_4/\text{DME}$ mixtures at $\phi = 6$ , $p = 10$ bar, and $T = 600$ K. On the left are the timescales corresponding to the dormant processes ( $\lambda_1 - \lambda_7$ ), in the middle the relevant timescales ( $\lambda_8 - \lambda_{39}$ ), and on the right the fast time scales ( $\lambda_{40} - \lambda_{83}$ ) [338]. ....	174

- 
- Figure 11-5: Comparison of simulation results with the three versions of PolyMech, detailed, skeletal based on local analysis, and based on global analysis. (a) Temporal evolution in the thermochemical state space projected onto the coordinates  $T$ ,  $x_{\text{CH}_2\text{O}}$ , and  $x_{\text{CO}}$  for a  $\text{CH}_4/\text{DME}$  (10 % DME) at  $\phi = 2$ ,  $p = 10$  bar and  $T = 600$  K. (b) Ignition delay times for the same mixture at  $\phi = 6$  and  $p = 10$  bar. .... 175
- Figure 11-6: Comparison of the number of reactions and species in the skeletal models from the global and local analysis with the detailed version of PolyMech [19] for a  $\text{CH}_4/\text{DME}$ -Mixture. .... 176
- Figure 11-7: Comparison of the ignition delay times from the detailed version of PolyMech with the ones from the skeletal mechanism and the implicit form of the global analysis for a  $\text{CH}_4/\text{DME}$  (10 % DME) at  $\phi = 2$  and  $p = 10$  bar. . 176
- Figure 11-8: Measured and simulated ignition delay times of methane/additive mixtures at  $\phi = 2$  and  $p = 30$  bar. Simulations are for 5 % DME addition. Full green line: Simulation with PolyMech [19]. Dashed green line: Simulation with Burke et al. [117]. The measured data were published in Refs. [19,199,297]. .... 177
- Figure 11-9: Ignition delay times of a 10 % DME / 90 %  $\text{CH}_4$  mixture at  $\phi = 10$ . Black circles: Shock tube at  $p = 30$  bar, black line: PolyMech [19] simulation of the shock-tube data, red circles: RCM at  $p = 10$  bar, red line: PolyMech [19] simulation of the RCM data. .... 178
- Figure 11-10: The temperature-dependent methane conversion in mixtures with different additives. All for  $\phi = 2$ ,  $p = 6$  bar and an argon dilution of  $\sim 90$  %. The additive/fuel ratios are 5/95 (*n*-heptane [200] and DME [19]), 10/90 (natural gas [197]) and 20/80 (ethanol). Neat methane data are from Ref. [197]. .... 178
- Figure 11-11: Measured and simulated remaining educts 1- $X$  and yields  $Y$  in the flow reactor at  $p = 6$  bar and  $\phi = 2$ . Inlet mixture: 4.69 %  $\text{CH}_4$ , 0.25 % DME, 5.06 %  $\text{O}_2$ , 90 % Ar. The residence time varies with temperature from 14.5 to 7.6 s at 473 and 973 K, respectively. .... 179
- Figure 11-12: Product mole fractions after ignition of a  $\text{CH}_4/10$  mol% DME/air mixture at  $\phi = 10$ , and 30 bar. Symbols show shock-tube data, full lines show simulations with an updated version of PolyMech [19], dashed lines with the mechanism of Burke et al. [117]. .... 180
- Figure 11-13: Measured and simulated remaining educts 1- $X$  and yields  $Y$  in the RCM compressing an undiluted 90 %  $\text{CH}_4/ 10$  % DME mixture ( $\phi = 10$ ) to 10 bar and temperatures between 714 and 738 K. Simulations with PolyMech [19]. .... 180
- Figure 11-14: Measured and simulated remaining educts 1- $X$  and yields  $Y$  in the flow reactor at  $p = 6$  bar and  $\phi = 10$ . Inlet mixture: 7.44 %  $\text{CH}_4$ , 0.83 % DME, 1.74 %  $\text{O}_2$ , 90 % Ar. The residence time varies with temperature from 14.5 to 7.6 s at 473 and 973 K, respectively. Simulations with PolyMech [19]. .... 181
-

- Figure 11-15: Measured and simulated species conversion and yields from 5 % DME / 95 % CH<sub>4</sub> mixtures for  $p = 6$  bar and  $\phi = 2$  and 10. The residence time varies with temperature from 14.5 to 7.6 s at 473 and 973 K, respectively. The experiments were performed in the flow reactor, PolyMech was used in the simulations. .... 182
- Figure 11-16: Species map of a mixture of 5 % heptane in methane as a function of equivalence ratio and temperature, based on experiments in the flow reactor at 6 bar. The maximum detected yields are listed in the legend, while the regime within about  $\pm 30$  % of this maximum value is indicated in the map. The temperature resolution in the map is 50 K [200]..... 183
- Figure 11-17: Mole fractions and temperature as a function of crank angle for methane at intake conditions of  $T_0 = 423$  K,  $p_0 = 2$  bar, and  $x_{Ar} = 0.96$ .  $\varepsilon = 22$ ,  $N = 3000$  rpm..... 184
- Figure 11-18: CH<sub>4</sub> conversion (colored contours) and top dead center temperature (thick black lines) as a function of the intake temperature and the intake argon mole fraction.  $p_0 = 2$  bar,  $\varepsilon = 22$ ,  $N = 3000$  rpm..... 185
- Figure 11-19: Storage power (solid lines) and efficiency (dashed lines) as a function of intake argon mole fractions for different intake temperatures  $T_0$ .  $p_0 = 2$  bar,  $\varepsilon = 22$ ,  $N = 3000$  rpm,  $\Delta V = 400$  cm<sup>3</sup>. .... 185
- Figure 11-20: Measured species conversion and yields in an RCM for a 5 mol% CH<sub>4</sub> / 90 mol% Ar/ 5 mol% He mixture at 18 bar [341]..... 186
- Figure 11-21: Shock tube: Measured and simulated product species mole fractions of the pyrolysis of a 10 mol% CH<sub>4</sub> / 90 mol% Ar mixture at about 1.5 bar. Symbols: experiment, solid line: simulations with USC mechanism [312], dashed line: simulation with PolyMech [19], dotted line: simulation with the Cai and Pitsch [148] mechanism. .... 187
- Figure 11-22: Measured temperatures during the pyrolysis of a 10 % CH<sub>4</sub>/1 % CO/20 % He mixture in Ar in the shock tube compared with simulations..... 188
- Figure 11-23: Time-resolved CH<sub>4</sub> concentration measurements (solid lines) during the pyrolysis of 10 mol% CH<sub>4</sub> in Ar in a shock tube. Simulations with USC-II ([312] (solid lines), PolyMech [19] (dashed lines), updated PolyMech (dash-dotted lines) and the Cai and Pitsch [148] mechanism (dotted lines). .... 188
- Figure 11-24: Species production in the RCM from CH<sub>4</sub>/DME (90/10)/air mixtures over a wide range of equivalence ratios. (a) Total yields of H<sub>2</sub> and CO, defined as the molar amount of product divided by the initial total molar amount (sum over all species). (b) Carbon yield of the most important products. Compression temperature and pressure:  $T = 756 - 985$  K,  $p = 10$  bar. The error bars indicate the minimum and maximum values in the 6 – 9 repetitions of the experiment at each condition. .... 190
- Figure 11-25: CoV, PRR<sub>max</sub>, CA50, and IMEP for HCCI operation with increasing DME fraction at a constant methane flow, starting from operation without ignition. The white region marks acceptable engine operation. The intake temperature was  $T_{in} = 423$  K and the compression ratio  $\varepsilon = 10$ . .... 192

- 
- Figure 11-26: a) Methane conversion ( $X_{\text{CH}_4}$ ), syngas yield ( $Y_{\text{syngas}}$ ), and product-gas soot concentration (note the logarithmic scale), b) displacement-specific work (IMEP) and heat ( $-Q/\Delta V$ ) output of the engine as well as the coefficient of variation of the net IMEP (CoV), c) exergetic ( $\eta_{\text{ex}}$ ) and thermal efficiencies ( $\eta_{\text{th}}$ ), all as a function of equivalence ratio at  $\varepsilon = 10$ . Spark-ignition experiments with  $T_{\text{in}} = 323$  K, HCCI experiments with  $T_{\text{in}} = 423$  K. Data were not recorded for  $2.5 < \phi < 4$  to avoid excessive soot in the instruments. For  $\phi > 5$ , the methane fraction in the product exceeded the sensor range and therefore,  $Q$ ,  $\eta_{\text{ex}}$ ,  $Y_{\text{syn}}$ , and  $X_{\text{CH}_4}$  could not be determined. For very high CoV some of the performance metrics cannot be evaluated reliably and the corresponding data points have been suppressed. .... 193
- Figure 11-27: DME mole fraction required for stable HCCI engine operation as a function of equivalence ratio for a range of compression ratios  $\varepsilon$  and two different intake temperatures  $T_{\text{in}}$ . .... 195
- Figure 11-28: Simulated temporal evolution of temperature and species during dry reforming in an RCM, with detailed chemistry (solid lines) and equilibrium chemistry (dashed lines). Compression starts at about 20 ms. Note the finer scaling of the time axis between 80 and 82 ms. .... 196
- Figure 11-29: Dry reforming in the RCM. Results of optimization for carbon dioxide conversion as a function of different initial carbon dioxide mole fractions. The predicted conversion is compared with experimental results in the upper part of the figure. The optimal initial compositions are shown in the lower part. Adapted from Ref. [303]. .... 197
- Figure 11-30: Distribution of the hydrogen cost rates and total cost rates in €/h for an uncertainty range of  $\pm 30$  %. The top x-axis translates the hydrogen cost rate into specific hydrogen costs in €/kg [360]. .... 199



---

## List of tables

Table 4-1:	Reynolds numbers.....	38
Table 6-1:	Flow conditions.....	57
Table 7-1:	Flow conditions of the reactants. ....	72
Table 7-2:	Selected reactions from the reaction mechanism of Zhang et al. [135].....	79
Table 8-1:	Investigated mixture compositions (mol%).....	99
Table 9-1:	Recent experimental studies on the ignition delay times of natural gas and DME mixtures with their corresponding experimental conditions (ST: shock tube, RCM: rapid-compression machine, CVB: constant volume bomb). ....	122
Table 9-2:	Reaction conditions (PFR: plug flow reactor, ST: shock tube). ....	123
Table 9-3:	Modified and added reactions of the PolyMech2.0. The rate constants are in the form of $k = AT^n \exp(-E/(RT))$ . Units are mol, cm, K, s and kJ. ....	127
Table 10-1:	Flow conditions.....	153
Table 10-2:	Tested reaction mechanisms from literature. ....	154
Table 11-1:	Gibbs energies ( $G_T$ ) and enthalpies ( $H_T$ ) of methane reactions with different amounts of oxygen or carbon dioxide at 300 K. The stoichiometric coefficients are taken to be positive for the products. The minor entropy changes due to the deviation of each partial pressure from 1 bar were neglected. The table was calculated with the thermodynamics data from the NASA tables for 300 K and 1 bar [331]. ....	168
Table 11-2:	Comparison of separate processes with the engine polygeneration process. (CHP: combined heat and power generation).....	198
Table 11-3:	First-order and total sensitivity indices for the most important input parameters resulting from the sensitivity analysis of the hydrogen costs. (InC=Investment Costs).....	200



---

## List of symbols

### Latin symbols

Symbol	Unit	Description
$A$	—	Constant depending on $\kappa$
$A$	$\text{m}^2$	Cross-sectional area
$A$	—	Instrument factor
$A$	variable	Pre-exponential factor
$A, B, C$	—	Constants in the van-Deemter equation
$A - E$	—	Gas-specific coefficients for the calculation of $\eta$
$CA$	$^\circ$	Crank angle
$CoV$	—	Coefficient of variation
$D$	M	Diameter
$D$	—	Mass discrimination factor
$D_{AB}$	$\text{m}^2 \text{s}^{-1}$	Binary diffusion coefficient
$D_{\text{Disp}}$	$\text{m}^2 \text{s}^{-1}$	Dispersion coefficient
$D^T$	$\text{kg m}^{-1} \text{s}^{-1}$	Thermal diffusion coefficient
$E$	eV	Electron energy
$E$	J	Exergy
$E(\theta)$	—	Residence time distribution
$E_A$	$\text{J mol}^{-1}$	Activation energy
$E_{\text{ad}}$	J	Adsorption Energy
$E_{\text{el}}$	J	Potential energy
$E_{\text{kin}}$	J	Kinetic energy
$F$	—	Broadening factor
$FKT$	—	Sampling function
$F_{\text{cent}}$	—	Parameter for the calculation of $F$ (Troe)
$G$	—	Critical value
$G$	—	Constant depending on $\kappa$
$G$	J	Gibbs free energy
$H$	J	Enthalpy
$H$	m	Plate height
$IE$	eV	Ionization energy
$IMEP$	Pa / bar	Indicated mean effective pressure
$K$	—	Equilibrium constant

List of symbols

---

$L$	m	Length
$M$	kg mol <sup>-1</sup>	Molar mass
$M$	amu	Molecular weight
$Ma$	–	Mach number
$\bar{M}$	kg mol <sup>-1</sup>	Mean molar mass
$N$	–	Number of theoretical plates
$N$	rpm	Rotation speed
$N_R$	–	Number of reactions
$N_{sp}$	–	Number of species
$P$	W	Power
$Pe$	–	Peclet number
$P_r$	–	Reduced pressure
$PRR$	Pa s <sup>-1</sup>	Pressure rise rate
$Q$	J	Heat
$R$	J mol <sup>-1</sup> K <sup>-1</sup>	Universal gas constant (8.3145)
$R$	–	Mass resolution
$Re$	–	Reynolds number
$\overline{ROC}$	–	Relative rate of consumption
$\overline{ROP}$	–	Relative rate of production
$R_c$	–	Chromatographic resolution
$S$	J K <sup>-1</sup>	Entropy
$S$	–	Relative sensitivity
$S$	a.u.	Signal intensity
$S$	–	Selectivity
$SW$	–	Number of summed up spectra
$Sc$	–	Schmidt number
$T$	K	Temperature
$TR$	–	Thermal response factor
$T^*$	–	Reduced temperature
$T^*, T^{**}, T^{***}$	K	Troe-Parameters
$U$	V	Voltage / Potential
$V$	m s <sup>-1</sup>	Multicomponent diffusion velocity
$V$	m <sup>3</sup>	Volume
$V$	V	Voltage
$W$	s	Signal width in the chromatogram
$W$	J	Work
$X$	–	Parameter for the calculation of $F$ (SRI)
$X_k$	–	Conversion of reactant $k$
$Y$	–	Mass fraction
$Y / Yield$	–	Yield
$a$	–	Collision efficiency
$a$	–	SRI-Parameter
$a_1 - a_7$	variable	Coefficients for NASA polynomials

---

$a, b, c$	—	Coefficients for mass calibration (TOF-MS)
$\Delta a, \Delta b, \Delta c$	variable	Single absolute uncertainties
$b$	eV	Distance from $IE$
$b, c$	K	SRI-Parameters
$c$	$\text{m s}^{-1}$	Sonic speed
$c$	$\text{mol m}^{-3}$	Concentration
$c, d, n,$	—	Parameters for the calculation of $F$ (Troe)
$c_p$	$\text{J kg}^{-1} \text{K}^{-1}$	Specific isobaric heat capacity
$c_v$	$\text{J kg}^{-1} \text{K}^{-1}$	Specific isochoric heat capacity
$\bar{c}_p$	$\text{J kg}^{-1} \text{K}^{-1}$	Mean specific heat capacity
$\tilde{c}_p$	$\text{J mol}^{-1} \text{K}^{-1}$	Specific molar isobaric heat capacity
$e$	A s	Elementary charge ( $1.6022 \times 10^{-19}$ )
$e$	$\text{J kg}^{-1}$	Specific chemical exergy
$f(E)$	—	Energy distribution function of the electrons
$\Delta_r \tilde{g}$	$\text{J mol}^{-1}$	Specific molar Gibbs free energy
$h$	$\text{J kg}^{-1}$	Specific enthalpy
$h_L$	$\text{J kg}^{-1}$	Specific lower heating value
$\tilde{h}$	$\text{J mol}^{-1}$	Specific molar enthalpy
$\Delta_r \tilde{h}$	$\text{J mol}^{-1}$	Specific molar reaction enthalpy
$k$	variable	Reaction rate coefficient
$k$	—	Calibration factor
$k_B$	$\text{J K}^{-1}$	Boltzman constant ( $1.38066 \times 10^{-23}$ )
$m$	kg	Mass
$\dot{m}$	$\text{kg s}^{-1}$	Mass flow
$n$	—	Temperature exponent (Arrhenius equation)
$n$	mol	Molar amount
$p$	Pa / bar / atm	Pressure
$q$	C	Electric charge
$q$	$\text{mol m}^{-3} \text{s}^{-1}$	Rate of progress
$r$	m	Radius
$r$	m	Distance
$s$	m	Length
$s$	$\text{J kg}^{-1} \text{K}^{-1}$	Entropy
$\tilde{s}$	$\text{J mol}^{-1} \text{K}^{-1}$	Specific molar entropy
$\Delta_r \tilde{s}$	$\text{J mol}^{-1} \text{K}^{-1}$	Specific molar reaction entropy
$t$	s	Time
$t_r$	s	Retention time
$u$	$\text{m s}^{-1}$	Velocity
$v$	$\text{m s}^{-1}$	Velocity
$w$	—	Mass fraction
$x$	m	Distance
$x$	—	Mole fraction
$x_0$	m	Minimal distance from the nozzle exit

---

## List of symbols

---

$z$	–	Charge
$\Delta z$	variable	Total absolute uncertainty

## Greek symbols

Symbol	Unit	Description
$\phi$	–	Equivalence ratio
$\Phi$	V	Potential
$\Phi$	–	Dimensionless factor
$\Phi$	–	Number of electrons
$\Omega$	–	Lennard-Jones collision integral
$\alpha$	–	Troe-parameter
$\delta^*$	–	Reduced dipole moment
$\varepsilon$	–	Collisional effectiveness parameter
$\varepsilon$	J	Characteristic Lennard-Jones energy
$\varepsilon$	–	Compression ratio
$\eta$	Pa s	Dynamic viscosity
$\eta$	–	Efficiency
$\theta$	–	Dimensionless average residence time
$\kappa$	–	Isentropic exponent
$\lambda$	W K <sup>-1</sup>	Thermal conductivity
$\lambda_0$	m	Mean free path length
$\mu$	D = C m	Dipole moment
$\mu$	variable	Expectation
$\nu$	–	Stoichiometric coefficient
$\pi$	–	Pi (3.14159)
$\rho$	kg m <sup>3</sup>	Density
$\sigma$	Å / m	Lennard-Jones collision diameter
$\sigma$	Å <sup>2</sup> / m <sup>2</sup>	Electron ionization cross section
$\sigma_\theta^2$	variable	Variance
$\tau$	s	Residence time
$\psi$	J	Lennard-Jones potential
$\omega$	s <sup>-1</sup>	Angular frequency
$\dot{\omega}$	mol m <sup>-3</sup> s <sup>-1</sup>	Chemical production rate

## Subscripts

Subscript	Description
$\infty$	High-pressure limit
A	Species A
B	Species B
AB	Between species/molecules A and B
M	Mixture

---

T	Terminal
a	After
avg	Average
b	Background
c	Based on concentration
c	Post compression
cyl	Cylinder
disp	Dispersion
ex	Exergetic
i	Species i
in	Intake
irr	Irreversible
j	Species j
l	Loss
m	Mach disk
max	Maximum
min	Minimum
mix	Mixture
n	Normalized
opt	Optimal
p	Based on pressure
r	Radial
r	Reactive / Reaction
ref	Reference
s	Stable
sur	Surrounding
th	Thermal
0	Initial state / State in front of the nozzle
0	Low-pressure limit
1	State behind the nozzle

### Superscripts

Superscript	Description
'	Forward direction
''	Reverse direction
net	Netto
0	Standard pressure (1 atm)

### Abbreviations

Abbreviation	Description
A/D	<u>A</u> nalog-to- <u>D</u> igital

---

AC	<u>A</u> lternating <u>C</u> urrent
CCU	<u>C</u> arbon <u>C</u> apture <u>U</u> tilization
CFD	<u>C</u> omputational <u>F</u> luid <u>D</u> ynamics
CHP	<u>C</u> ombined <u>H</u> eat and <u>P</u> ower
CI	<u>C</u> ompression <u>I</u> gnition
CPU	<u>C</u> entral <u>P</u> rocessing <u>U</u> nit
CVB	<u>C</u> onstant <u>V</u> olume <u>B</u> omb
DC	<u>D</u> irect <u>C</u> urrent
DFG	<u>D</u> eutsche <u>F</u> orschungsgemeinschaft
DME	<u>D</u> imethylether
EI	<u>E</u> lectron <u>I</u> onization
EICS	<u>E</u> lectron <u>I</u> onization <u>C</u> ross <u>S</u> ection
ESM	<u>E</u> lectronic <u>S</u> upplementary <u>M</u> aterial
FWHM	<u>F</u> ull <u>W</u> idth <u>H</u> alf <u>M</u> aximum
GC	<u>G</u> as <u>C</u> hromatograph / <u>G</u> as <u>C</u> hromatography
GC/MS	<u>G</u> as <u>C</u> hromatography / <u>M</u> ass <u>S</u> pectrometer
GLC	<u>G</u> as- <u>L</u> iquid <u>C</u> hromatography
GQL	<u>G</u> lobal <u>Q</u> uasi- <u>L</u> inearization
GRI	<u>G</u> as <u>R</u> esearch <u>I</u> nstitute
GSC	<u>G</u> as- <u>S</u> olid <u>C</u> hromatography
HCCI	<u>H</u> omogeneous <u>C</u> harge <u>C</u> ompression <u>I</u> gnition
HED	<u>H</u> igh <u>E</u> nergy <u>D</u> ynode
HPLC	<u>H</u> igh- <u>P</u> erformance <u>L</u> iquid <u>C</u> hromatography
IC	<u>I</u> nternal <u>C</u> ombustion
IDT	<u>I</u> gnition <u>D</u> elay <u>T</u> ime
IE	<u>I</u> onization <u>E</u> nergy
MBMS	<u>M</u> olecular- <u>B</u> eam <u>M</u> ass <u>S</u> pectrometry
MCP	<u>M</u> icrochannel <u>P</u> late
MFC	<u>M</u> ass <u>F</u> low <u>C</u> ontroller
MILD	<u>M</u> oderate or <u>I</u> ntense <u>L</u> ow <u>O</u> xygen <u>D</u> ilution
NG	<u>N</u> atural <u>G</u> as
NIST	<u>N</u> ational <u>I</u> nstitute of <u>S</u> tandards and <u>T</u> echnology
NTC	<u>N</u> egative <u>T</u> emperature <u>C</u> oefficient
PAH	<u>P</u> olycyclic <u>A</u> romatic <u>H</u> ydrocarbon
PFR	<u>P</u> lug- <u>f</u> low <u>R</u> eactor
PLOT	<u>P</u> orous <u>L</u> ayer <u>O</u> pen <u>T</u> ubular
QMS	<u>Q</u> uadrupole <u>M</u> ass <u>S</u> pectrometer
RCEM	<u>R</u> apid <u>C</u> ompression <u>E</u> xpansion <u>M</u> achine
RCM	<u>R</u> apid <u>C</u> ompression <u>M</u> achine
RICS	<u>R</u> elative <u>I</u> onization <u>C</u> ross <u>S</u> ection
RRKM	<u>R</u> ice- <u>R</u> amsperger- <u>K</u> assel- <u>M</u> arcus
RTD	<u>R</u> esidence <u>T</u> ime <u>D</u> istribution
SCOT	<u>S</u> upport- <u>C</u> oated <u>O</u> pen <u>T</u> ubular
SEM	<u>S</u> econdary <u>E</u> lectron <u>M</u> ultiplier

SI	<u>S</u> park <u>I</u> gnition
ST	<u>S</u> hock <u>T</u> ube
TCD	<u>T</u> hermal <u>C</u> onductivity <u>D</u> etector
TDC	<u>T</u> op <u>D</u> ead <u>C</u> enter
TOF-MS	<u>T</u> ime- <u>o</u> f- <u>F</u> light <u>M</u> ass <u>S</u> pectrometry / <u>S</u> pectrometer
WCOT	<u>W</u> all- <u>C</u> oated <u>O</u> pen <u>T</u> ubular
aTDC	<u>A</u> fter <u>T</u> op <u>D</u> ead <u>C</u> enter
$m/z$	Mass-to-charge ratio



---

# 1 Introduction

The Paris Agreement, adopted in December 2015, defines the world's global framework to counteract climate change and its consequences. Its goal to limit the global temperature increase to 1.5 °C requires an enormous reduction in greenhouse gas emissions, in particular, from fossil fuels. In the long term, burning fossil fuels must be totally stopped. Effective measures for the transition away from fossil fuels are increasing the share of renewable energy sources and developing CO<sub>2</sub>-neutral energy supply chains. In many sectors, the transition has already successfully been started; examples include the rising share of electricity-driven heat pumps in residential heating or the growing share of electric vehicles [1]. However, there are many sectors where the energy transition leads to several challenges because of the demand for energy carriers with high energy density. Typical examples are the aviation sector and heavy-duty traffic [2,3]. Nevertheless, sustainable transition pathways are also achievable for these sectors. The replacement of fossil fuels by electricity-based synthetic fuels is the most promising approach. The associated processes are known by the synonyms Power-to-Liquid or Power-to-Gas, and are widely discussed in science and the industry [4,5].

Electricity-based synthetic fuels can replace conventional petrol, diesel, or natural gas with similar substances, such as methanol, biodiesel, or synthetic methane. Synthetic fuels can significantly reduce greenhouse gas emissions if electricity from renewable energy sources is used in combination with carbon capture utilization (CCU) methods to use the atmosphere as the carbon source [6,7]. Liquid fuels are usually preferred since they are easier to transport and store than gaseous fuels. They are also less dangerous due to their low vapor pressure. Still, liquid fuels have a higher energy density, which will remain important in aviation and shipping for the coming decades. This insight is also reflected in the World Energy Outlook 2019 [8], indicating crude oil to probably have the highest share in the global primary energy demand until 2040.

Although synthetic fuels produced by renewable energies and CCU are promising in terms of greenhouse gas reduction [6], their exclusive use is not to be expected in the medium term. The main reason is the associated high demand for renewable energy, which cannot be satisfied with the currently installed capacity. In this context, natural gas, both in gaseous and liquefied form, represents a suitable interim solution. Natural gas produces much less CO<sub>2</sub> per energy unit than crude oil or coal and is expected to show the highest growth rate among all fossil fuels [8,9]. It can be utilized in many applications such as heat and electricity generation in residential and industrial sectors, utilization as fuel in the automotive sector, and conversion into base chemicals in the chemical sector.

Today, fuel conversion routes mainly proceed via synthesis gas production from natural gas or methane, as it is still more competitive than the combination of water electrolysis and carbon-

capture processes using only renewable energies [10,11]. The most common method is steam-methane reforming, an energy-intensive endothermic process that is only economically reasonable on a large-scale. Other methods to produce synthesis gas are the partial oxidation of natural gas or its dry reforming with CO<sub>2</sub> [12], separated from the air by carbon capture methods in the best case. Synthesis gas is a typical feedstock chemical and can be converted to various other chemicals such as methanol or dimethyl ether or transportation fuels such as petrol or diesel in a downstream synthesis. Each process is limited in its application purpose and cannot react flexibly to supply and demand in terms of different types of energy. By contrast, most studies agree that a successful energy transition requires highly flexible energy systems that enable smart reactions to the changes in demand and supply.

In terms of flexibility, the most promising are polygeneration processes providing work, heat, and chemicals. A special feature of a polygeneration process is the flexible switch between the provision of work, heat, and chemicals, enabling a demand-oriented supply. Such a process can be realized, for example, by internal combustion (IC) engines driven at special conditions.

A polygeneration process in IC engines using methane or natural gas as feedstock can be a more efficient and flexible alternative to the conventional technologies that are specifically designed and optimized for a single process. For example, the engine could be used to provide electricity and heat if there is not enough solar and wind energy available, or, if there is a sufficient supply of renewable energy, to produce higher-value chemicals. IC engines are expected to be particularly appropriate for polygeneration processes since IC engines are industrially proven, relatively cheap, and easily scalable. They are also flexible in terms of fuel and operating conditions.

Regarding fuel conversion processes, fuel-rich mixtures are required to avoid the complete oxidation of the fuel to CO<sub>2</sub> and H<sub>2</sub>O. Because spark-ignition (SI) engines are flame-speed controlled, fuel-rich mixtures are hard to ignite [13]. In compression ignition (CI) engines, on the other hand, extremely fuel-rich regions in the cylinder due to spray combustion can cause excessive soot formation. An alternative engine concept that is increasingly attracting attention is the homogeneous charge compression ignition (HCCI) engine. In an HCCI engine, the fuel/air mixture is premixed, and the homogeneous mixture auto-ignites at the end of the compression stroke due to the high temperature and pressure. Fuel-rich zones, such as in a CI engine, are avoided because of the simultaneous ignition of the fuel/air mixture in multiple spots. Consequently, less soot or particulate matter is produced while the efficiency of the CI engine is maintained [14]. Also, less nitric oxides are emitted as a result of the lower maximum temperatures.

The main challenge in the design and operation of HCCI engines is to control the time of autoignition, which is mainly governed by chemical kinetics. In addition, natural gas or neat methane, which is the main component of natural gas, is relatively stable, so high temperatures and pressures are required for its conversion. Adding small amounts of more reactive additives to the mixture can significantly lower the reaction onset temperature and, at the same time, be used for controlling the moment of autoignition [15,16]. To gain flexibility in terms of different output quantities and for the control and regulation of the process, quantities like work and heat as well as the exhaust gas composition must be known for various fuels and operating conditions. These quantities can be determined by experiments or simulations. Experiments are time-consuming and expensive, while simulations allow fast and cost-effective predictions of

thermodynamic quantities and product gas compositions. Detailed reaction mechanisms are required for simulations to accurately predict the chemical reactions and the associated exothermal heat release in the cylinder. But, reaction mechanisms from literature are usually not validated for fuel-rich methane/additive mixtures. This gap is addressed here.

## 1.1 Task and objective

The present work was conducted in the framework of the DFG research unit FOR 1993 (multi-functional conversion of chemical species and energy). The research unit investigates whether internal combustion engines, especially HCCI engines, can be used for flexible generation of heat, work, and base chemicals in a polygeneration process. The produced chemicals can either be used in the chemical industry or for energy storage, provided that they are energetically more valuable. To better assess such a process in its entirety, the research unit consists of seven subgroups, covering both theory and experimental verification. In the theoretical groups, a detailed chemical kinetic model is developed, thermodynamic analyses based on an exergo-economic strategy are performed, and mathematical optimization methods are used to determine promising engine operating conditions. For both thermodynamic analysis and optimization, a detailed kinetic model is required to obtain reliable results. The kinetic model is validated by various experiments performed in shock tubes, flow reactors, and a rapid compression expansion machine. The latter, already representing a first step towards the engine, is complemented by experiments in a single-cylinder research engine. Because natural gas mainly consists of methane and is expected to play a significant role in the coming decades, it is used as the primary fuel in all studies. The work of the entire research unit, including work that was performed as part of this thesis, was recently presented in [16] and can be found in chapter eleven.

This thesis concentrates on elucidating the underlying reaction mechanisms of the fuel-rich conversion of methane-based fuels by performing experiments and mechanism optimization. Small amounts of reactive additives are introduced to the mixtures to increase their reactivity. The aim is to understand the influence of different additives on the fuel conversion process. Since not every possible additive can be investigated experimentally, the thesis intends to unravel the general working principles of additives to enable their transfer to other additives. The question is, to what extent the additives can influence the product composition. For this purpose, fuel conversion experiments are performed in a flow reactor coupled with a time-of-flight mass spectrometer. The experimental setup adapted from [17,18] only allowed operation at pressures up to 6 bar and required a long stabilization time after any change in reactor condition during a conversion experiment. Also, only gaseous fuels could be investigated with the setup. This leads to the second aim of the thesis that is to improve the experimental setup to enable less time-consuming experiments at engine-relevant conditions using both gaseous and liquid fuels and increase reproducibility. The main challenges are to extend the operation limits of the reactor to higher pressures and temperatures, to extend the experimental setup by a liquid supply system and evaporator, and to shorten the response time of the reactor. To achieve these goals, additional GC diagnostics will be implemented to enable the investigation of the oxidation of higher hydrocarbons without the problems of fragmentation associated with mass spectrometry.

The final setup is used to investigate the partial oxidation of several methane/additive mixtures at temperatures between 473 and 973 K, pressures of 5 – 20 bar, equivalence ratios of

$\phi = 2 - 20$ , and residence times of several seconds. Long residence times are required to initiate fuel conversion in the investigated temperature range.

Both diagnostic techniques are used to analyze the product gas composition at the reactor outlet. The experimental methodology is described in detail in chapter four. The additives were chosen based on an extended literature research for suitable components and the requirements of the engine processes.

The obtained data are used for the validation of reaction mechanisms from the literature and the development of the PolyMech [19] reaction mechanism of the research unit. On the other hand, the PolyMech and additional reaction mechanisms from the literature are used in simulations to analyze the interaction between reactive additives and methane. The result is a qualitative and quantitative understanding of the reaction processes. The onset of fuel conversion and the formation of valuable products are identified as key targets for the studies. Five different methane/additive mixtures are examined, which are briefly introduced in the following.

In chapter six, the partial oxidation of neat methane is investigated to create a basis for comparison to methane/additive mixtures. Ethane and propane are present in typical natural gas in addition to methane, while hydrogen is likely to be increasingly fed into existing gas pipelines. Thus, the influence of hydrogen on reforming processes based on natural gas is of particular interest. Consequently, the influence of ethane, propane, and hydrogen on the reaction onset temperature and product formation is also investigated

For the third mixture presented in chapter seven, *n*-heptane is selected as an additive because it is a diesel surrogate and expected to be much more reactive than methane. It is also known to have good auto-ignition properties, so it fits into the framework of the research unit. Single fuel experiments are performed to better assess the change in product composition due to the interaction of the two fuels.

Dimethyl ether is expected to be as reactive as *n*-heptane but it has a beneficial lower sooting tendency at high equivalence ratios. Consequently, it is selected as a well-suited additive for methane-fueled HCCI engines. Complementary results from all experimentally oriented sub-projects of the research unit are used to develop a new reaction mechanism optimized for polygeneration-relevant conditions. The results are presented in chapter eight.

The ability of the developed reaction mechanism to predict species profiles with respect to a more complex mixture is assessed by methane/ethane/propane/dimethyl ether mixtures in chapter nine. In this context, the experimental results of two subprojects are used to optimize the previously developed reaction mechanism. The modified mechanism is used for the analysis of the interaction between the reactants at interesting conditions. Special focus is given on unsaturated and oxygenated species.

Chapter ten discusses the influence of pressure on a phenomenon observed in previous neat methane experiments, i.e., the negative temperature coefficient (NTC) behavior of methane. Several reaction mechanisms from literature are evaluated for their ability to predict this behavior, while the most appropriate reaction mechanism is used for analysis.

---

## 2 Theoretical background

This chapter deals with the theoretical foundations relevant to this work. First, the basic principles of a mass spectrometer and a gas chromatograph are outlined, followed by a more detailed description of the specific characteristics of the instruments used in this study.

### 2.1 Mass spectrometry

Mass spectrometry is a versatile tool for the identification and quantification of species in a gas mixture, based on ionization of the species and the subsequent separation of the generated ions according to their mass-to-charge ratio ( $m/z$  ratio). In general, a mass spectrometer consists of an ionization chamber with a specific ionization method, a mass analyzer, in which the ions are separated and a detector to detect the ions. An additional gas inlet is used to introduce the gas sample into the mass spectrometer prior to the analysis. Molecular-beam sampling is used in this study and is briefly described. Subsequently, the electron ionization (EI) process and the time-of-flight (TOF), as well as the quadrupole mass analyzer, are outlined in detail, followed by a short description of the detector.

For information on other ionization techniques, such as electrospray or photoionization, or mass analyzers such as Orbitraps or sector field mass spectrometer, refer to the relevant literature [20,21].

#### 2.1.1 Molecular-beam sampling

A molecular beam is a collimated beam of matter consisting of molecules. A very detailed overview of molecular beams is given in [22,23]. Here, only the supersonic beam, which is found under all experimental conditions using molecular-beam mass spectrometry (MBMS), is explained in more detail.

A supersonic beam is formed when gas at high pressure expands through a nozzle into a vacuum and the mean free path length of the molecules in front of the nozzle is smaller than the diameter of the nozzle opening [24]. During supersonic expansion, molecular collisions still occur even after passing through the nozzle, so that a hydrodynamic continuum flow is formed that can be approximated as isentropic and adiabatic. A part of the enthalpy  $h$  is converted into directed kinetic energy so that the velocity  $v$  of the gas increases. As the enthalpy decreases, the temperature  $T$  also decreases, because the enthalpy only depends on temperature for a perfect gas as shown by equation (2-1) using the first law of thermodynamics and the definition of the isobaric heat capacity  $c_p$ . The indices 0 and 1 represent the states in front of and behind the nozzle, respectively.

$$h_1 - h_0 = \frac{1}{2} \cdot (v_0^2 - v_1^2) = c_p(T_1 - T_0) \quad (2-1)$$

The gas flow can reach sonic speed  $c$  and therefore a Mach number  $Ma = 1$  ( $Ma = v/c$ ) at the nozzle exit if the pressure ratio  $p_0/p_1$  exceeds the critical value given by

$$G = \left(\frac{\kappa + 1}{2}\right)^{\frac{\kappa}{\kappa-1}} \quad (2-2)$$

where  $G$  is lower than 2.1 for all gases [24]. In equation (2-2),  $\kappa$  represents the isentropic exponent that is the ratio between the isobaric and isochoric heat capacity ( $c_p/c_v$ ). In cases of pressure ratios higher than  $G$ , the pressure  $p_a$  of the gas in the molecular beam at the nozzle exit is independent of the background pressure  $p_B$  within the first expansion chamber. This is attributed to the fact that information about the boundary conditions propagates at the speed of sound, whereas the gas moves faster ( $Ma > 1$ ). The pressure  $p_a$  (at  $Ma = 1$ ), calculated as  $p_a = p_0/G$ , is higher than the background pressure  $p_B$  [24]. Consequently, the gas is underexpanded and expands further along radially divergent streamlines to adapt to the boundary condition given by the background pressure  $p_B$ . The Mach number increases beyond one and the flow overexpands. The increasing Mach number is mainly caused by a decreasing speed of sound, which for an ideal gas only depends on temperature (equation (2-3)).

$$c_{\text{ideal gas}} = \sqrt{\kappa \frac{RT}{M}} \quad (2-3)$$

Here,  $R$  represents the universal gas constant and  $M$  the molar mass of the gas. The centerline Mach number as a function of the distance from the nozzle exit can be described by equation (2-4) for a two-dimensional, axial-symmetric flow. It has been calculated numerically by solving the partial differential equations for mass and momentum using the method of characteristics [25,26].

$$Ma(x) = A \left(\frac{x - x_0}{D}\right)^{\kappa-1} - \frac{\frac{1}{2} \left(\frac{\kappa + 1}{\kappa - 1}\right)}{A \left(\frac{x - x_0}{D}\right)^{\kappa-1}} \quad (2-4)$$

The constants  $A$  and  $x_0$  only depend on  $\kappa$ . Values for  $A$  and the minimal distance from the nozzle exit in nozzle diameters ( $x_0/D$ ) are listed in the literature [24,26]. But, the Mach number does not increase continuously because the rapid expansion of the gas leads to a decreasing probability of molecular collisions. As a result, a collisionless (shock-free) free-molecular flow is formed in the so-called zone of silence. The transition region where the continuum flow becomes a free-molecular flow is called quitting or “freezing” surface, since kinetic processes, such as the cooling of the inner degrees of freedom of molecules, gradually come to a standstill. The freezing surface is located only a few nozzle diameters behind the nozzle exit. Here, the

Mach number approaches its maximum value, called the terminal Mach number, and is given by

$$M_T = G \left( \frac{\lambda_0}{D\varepsilon} \right)^{-\frac{(\kappa-1)}{\kappa}} \quad (2-5)$$

in which  $G$  denotes a constant dependent on  $\kappa$ ,  $D$  the diameter of the nozzle opening,  $\lambda_0$  the mean free path length, and  $\varepsilon$  a collisional effectiveness parameter.  $\varepsilon$  represents the fractional change in the mean random velocity of a molecule if a collision occurs [26] and  $G$  is listed in [26] as a function of  $\kappa$ .

The overexpanded flow within the shock-free region must be recompressed and is limited by different shock regions, where the density of the expanding gas reaches the density of the background gas and the Mach number decreases. In these regions, the gas adjusts to the boundary conditions of the expansion chamber. The compression shocks are thin non-isentropic regions that show large density, velocity, and temperature gradients. While the shock regions parallel to the direction of the accelerating jet are called barrel shocks, the vertical shock region, located at a distance  $x_M$  from the nozzle exit is called a Mach disk. At the Mach disk, an immediate transformation from supersonic to subsonic flow takes place. The distance  $x_M$  between the nozzle exit and the Mach disk can be estimated according to equation (2-6) [26].

$$x_M = 0.67D \sqrt{\frac{p_0}{p_1}} \quad (2-6)$$

Figure 2-1 shows the different regions of a supersonic beam.

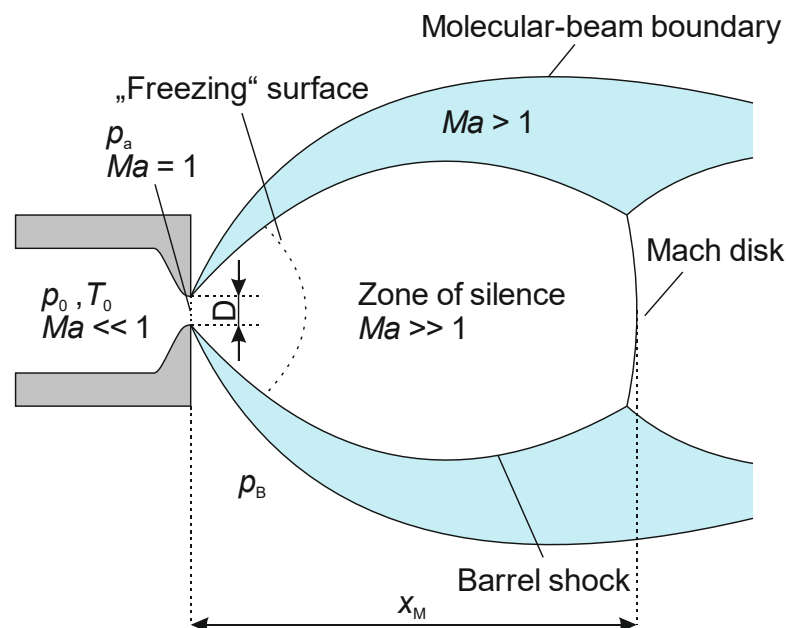


**Figure 2-1:** The different regions of a supersonic beam. Inspired by Figure 2.1 in [24].

To design a molecular beam interface, the mass flow of the gas through the nozzle must be known as it determines the required pump capacity for the expansion chamber. For an isentropic expansion, the mass flow  $\dot{m}$  can be calculated by equation (2-7) [24].

$$\dot{m} = \frac{1}{4} \pi D^2 p_0 \sqrt{\frac{\kappa M}{RT_0} \left( \frac{2}{\kappa + 1} \right)^{\frac{\kappa+1}{2(\kappa-1)}}} \quad (2-7)$$

For MBMS experiments, the pressure in the first expansion chamber is typically in the range of  $10^{-3} - 10^{-4}$  mbar. At such low background pressures, the shock regions expand in the axial direction [27] and become more diffuse [28]. At the same time, the pressure is too high for the ionization chamber of a mass spectrometer. Thus, a second nozzle, also called a skimmer, is used to extract the core of the molecular beam and direct it into the ionization chamber. The skimmer opening should be placed within the zone of silence, outside of the shock regions. The advantage of a second nozzle is the additional collimation of the beam and the extension of the free molecular flow region.

### 2.1.2 Electron ionization

In electron ionization, the molecules entering the ionization chamber are bombarded by energetic electrons. These electrons are generated by a hot cathode, called a filament, which is a thin wire often made of rhenium or tungsten [21]. The emitted electrons are accelerated to the opposite anode and, if an electron and neutral molecule collide, lead to an ejection of an electron from the neutral molecule. As a result, a positive ion is formed (see equation (2-8)). This is due to the transfer of the kinetic energy from the electron to the neutral molecule. But the energy transferred must be higher than the ionization energy (IE) of the respective species, which represents the minimum amount of energy needed for the mentioned ejection of an electron. In addition, the probability for a successful ionization, described by the electron ionization cross section (EICS), is very low at the IE, but rapidly increases with rising energies, reaching a flat maximum near 70 eV. However, energies, which are much higher than the IE of the molecule or atom to be ionized can lead to fragmentation of the species or doubly and even triply charged ions. These events in turn make data analysis more difficult since the signals belonging to the molecular ions can overlap with the signals of the fragments and higher charged ions. So, depending on the application, a compromise between signal strength, averaging time, and degree of fragmentation must be found. In some cases, for example, gas chromatography/mass spectrometry (GC/MS), an ionization at 70 eV can also be advantageous, because the species in the sample to be analyzed are already separated before entering the mass spectrometer (see section 2.2.2). The fragmentation pattern obtained by ionization can then be compared to literature data, usually recorded at 70 eV, enabling the identification of the species.



### 2.1.3 Time-of-flight mass spectrometer

The basic principle of a linear time-of-flight mass spectrometer (TOF-MS) is shown in Figure 2-2.

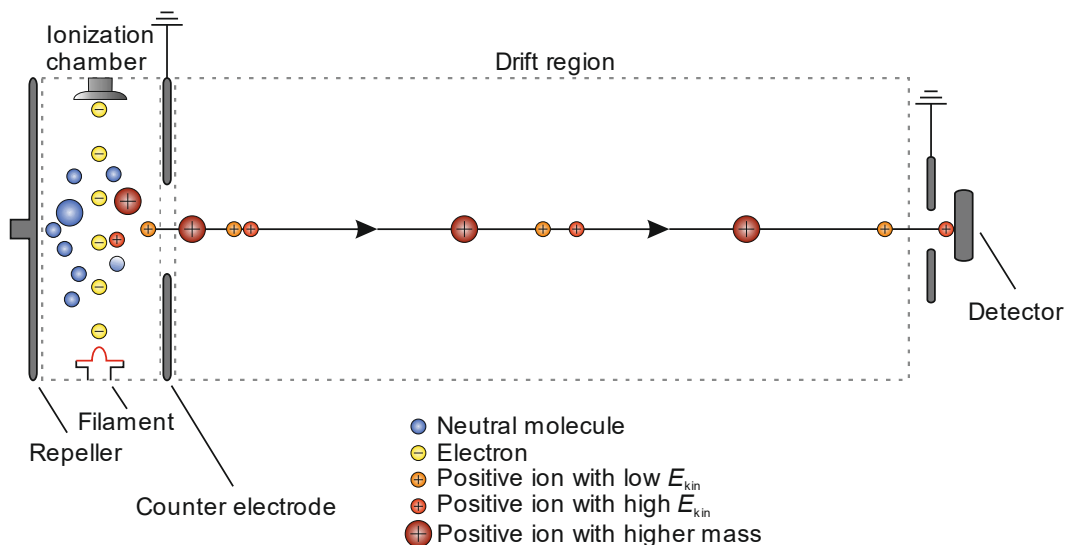


**Figure 2-2:** Principle of a linear time-of-flight mass spectrometer.

Once ionized, the molecules are accelerated towards the detector by an electric field between two electrodes, an energized repulsion electrode called the repeller, and a grounded counter electrode. Assuming all ions have the same starting position between the electrodes and no velocity component in any direction, they uptake the same potential energy, which only depends on the charge  $q$  of the ion and the potential difference  $U$ . The charge of an ion can be described by the product of the number of charges  $z$  and the elementary charge  $e$  (equation (2-9)).

$$E_{el} = q \cdot U = e \cdot z \cdot U \quad (2-9)$$

The potential energy is then transferred to kinetic energy when the ions enter the field-free drift region as shown in equation (2-10). The kinetic energy is the same for all ions.

$$E_{el} = e \cdot z \cdot U = \frac{1}{2} \cdot m_i \cdot v^2 = E_{kin} \quad (2-10)$$

But, the velocity  $v$  of the ions depends on their mass (equation (2-11)), so that ions of lower weight are faster than heavier ions and will reach the detector faster.

$$v = \sqrt{\frac{2 \cdot e \cdot z \cdot U}{m_i}} \quad (2-11)$$

The time  $t$  representing the time required for the ions to pass through the field-free drift region is obtained by the substitution of  $v$  by  $s/t$  and the subsequent changing to  $t$ . Here,  $s$  represents the length of the field-free drift region.

$$t = \frac{s}{\sqrt{2 \cdot e \cdot U}} \cdot \sqrt{\frac{m_i}{z}} \quad (2-12)$$

Equation (2-12) shows that the time is proportional to the square root of  $m/z$  which means that the  $\Delta t$  between two detected ions for a given  $\Delta m/z$  and a constant drift region  $s$  becomes smaller at higher masses. To determine the time accurately, the data acquisition must be adequately fast. In addition, the ion generation or extraction process must be pulsed to avoid overlapping signals from ions with different  $m/z$  ratios.

If different initial positions of the ions in the ionization chamber and different initial velocities or directions of movement are taken into account, it becomes clear that ions with a specific  $m/z$  ratio do not arrive at the detector at the same time, but within a certain time span. Ions with the same  $m/z$  ratio generated near the repeller will have a slightly higher kinetic energy or velocity at the end of acceleration than ions generated near the grounded counter electrode, although having the same  $m/z$  ratio. The point at which the ions with a higher velocity overtake ions with a lower velocity is called space focus (see Figure 2-2). In a linear TOF-MS with a single-stage extraction, this focus point is located near the counter electrode at the beginning of the drift region and only depends on the distance between the electrodes and the applied voltage. The renewed spatial expansion of the ion package behind the space focus due to different velocities of ions leads to broad signals in the mass spectrum. This in turn can lead to overlapping of adjacent signals. Mass resolution  $R$  (see equation (2-13)) is used to evaluate a mass spectrometer's ability to separate adjacent signals.

$$R = \frac{m}{\Delta m} = \frac{m/z}{\Delta(m/z)} = \frac{t}{2 \cdot \Delta t} \quad (2-13)$$

While  $m$  represents the mass of the ion,  $\Delta m$  represents the signal width at a specific signal height. Typically, the full width at half maximum definition (FWHM) is used to calculate the resolution of a TOF-MS. Another definition that is more practical in assessing the ability to separate adjacent ions is the 10 % valley definition ( $R_{10\%}$ ). According to this definition, adjacent signals are assumed to be sufficiently separated if the signals do not overlap more than 10 % of their respective heights [21]. For Gaussian-shaped signals, the ratio between  $R_{10\%}$  and  $R_{FWHM}$  is 1.8. Due to the relationship between  $m/z$  and the flight time  $t$ , the resolution can also be derived for  $t$  (see equation (2-13)).

Linear TOF-MS typically achieve maximum resolutions of only  $R_{FWHM} = 500$  [21]. A two-stage ion extraction, proposed by Wiley and McLaren in 1955 [29], can be utilized to increase the resolution. In contrast to a single-stage extraction, an additional extraction plate is placed between the repeller and the grounded counter electrode, whereas the electric field between both plates can be varied. Thus, the potential gradient between the repeller and the extraction plate differs from that between the extraction plate and the counter electrode, creating two different acceleration regions. Ions that are formed near the repeller will experience a higher fraction of

the extraction voltage in the first extraction stage compared to those formed near the extraction plate and gain a higher kinetic energy or velocity. In the second stage, the potential gradient is the same for all ions. The faster ions will experience a smaller fraction of the extraction voltage in the second extraction stage compared to the slower ones. With optimized extraction voltages, the electric fields in the two stages can be specifically influenced so that the space focus can be shifted further in the direction of the detector. The two-stage extraction approach minimizes the temporal distribution of ions with the same  $m/z$  ratio, originating from different starting positions. Wiley and McLaren also attempted to compensate for the initial energy distribution of ions with the same  $m/z$  ratio by combining pulsed ion generation with a delayed and pulsed ion extraction. This procedure is called time-lag focusing. It transforms the energy distribution of the ions into a spatial distribution, which is then corrected by the space-focusing process discussed above.

A more effective method of energy focusing is a reflectron, invented by Mamyrin in 1966 [30]. A reflectron consists of a single- or multi-stage electric field in which ions are decelerated after the field-free drift region and then reflected towards the detector, usually at a small angle. Ions with a higher kinetic energy dive deeper into the reflectron than slower ions with the same  $m/z$  ratio and stay longer in the reflectron. If the dimensions of the reflectron and the voltages applied to the electrode grids or ring electrodes are properly chosen, ions with the same  $m/z$  ratio but different initial kinetic energies reach the detector at the same time. Figure 2-3 shows a two-stage reflectron. Modern reflectron mass spectrometers easily achieve resolutions  $R_{FWHM}$  of up to 10000-20000.

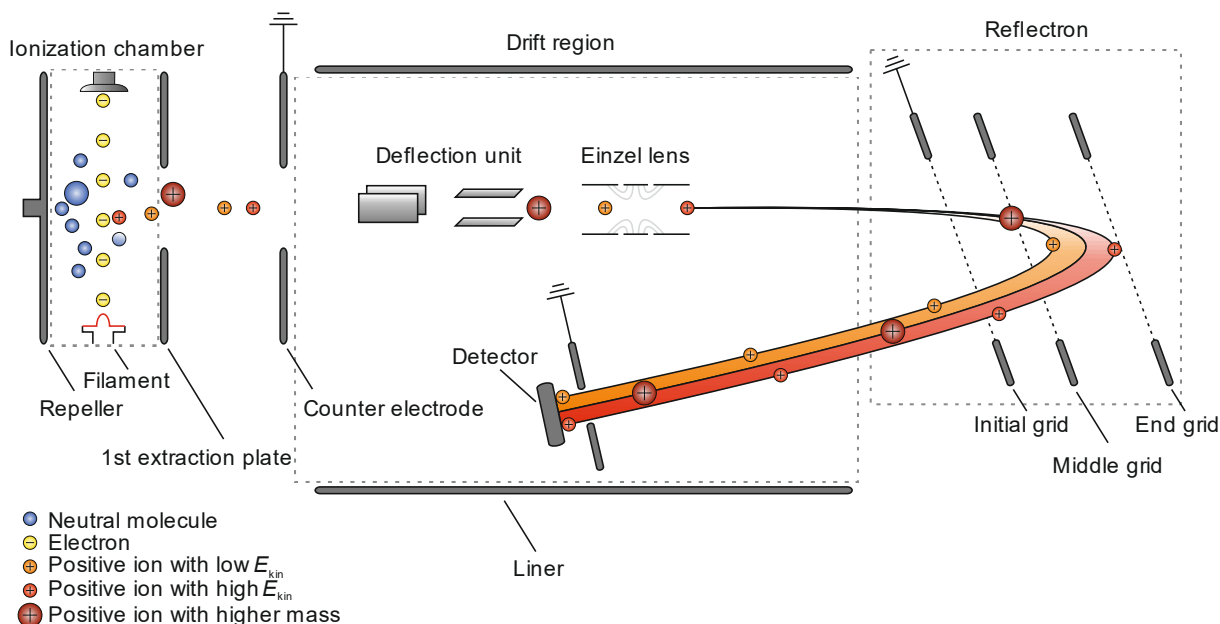


**Figure 2-3:** Two-stage reflectron time-of-flight mass spectrometer with two-stage ion extraction and instrument-specific elements described in section 4.2.

### 2.1.4 Quadrupole mass spectrometer

Inlet and ionizer principles are the same for all types of mass analyzers [21]. Similar to the TOF-MS, the ionized species are accelerated by an extraction plate towards the quadrupole mass analyzer. The analyzer consists of four hyperbolic or cylindrical rod electrodes arranged in a square. The minimal distance between the center and the rod surface corresponds to the radius  $r_0$  of the rods. The respective opposite rods are at the same potential  $\Phi$ , which according to equation (2-14) is composed of a DC voltage  $U$  and a radio-frequency AC voltage  $V$  [21,31].

$$\Phi = \pm(U + V\cos\omega t) \quad (2-14)$$

Here,  $\omega$  represents the angular frequency and  $t$  the time. The periodic voltage causes ions to be alternately attracted and repelled by the rods. With a certain combination of  $U$ ,  $V$ , and  $\omega$ , the total movement of the ions with a specific  $m/z$  ratio or within a specific  $m/z$  ratio range can take place on a stable path through the analyzer. This means that the amplitude of the oscillating ion trajectories will never exceed  $r_0$ . Ions with other  $m/z$  ratios will move on an unstable path and are eliminated by collisions with the rods. This is schematically shown in Figure 2-4. The derivation of the differential equations of ion motion within the electric field is found in [31].

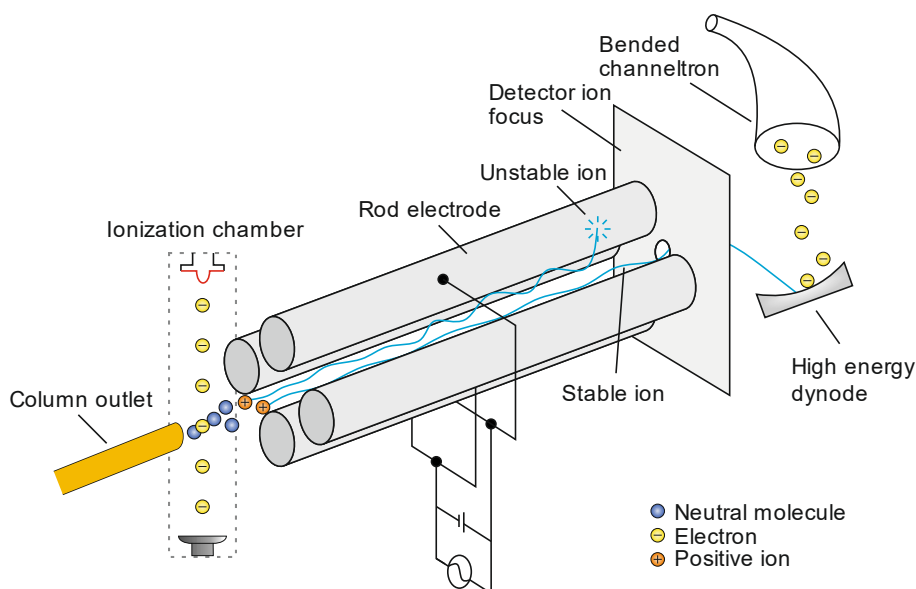


**Figure 2-4:** Principle of a quadrupole mass spectrometer. Adapted from [32].

To obtain a complete mass spectrum within milliseconds, the parameters of the electric field are changed very quickly so that ions with increasing  $m/z$  ratios will hit the detector one after the other. This is done by increasing  $U$  and  $V$  at a constant  $U/V$  ratio. Unit resolution is obtained by adjusting the electric field so that only ions of a certain  $m/z$  ratio  $\pm 0.5$  can pass the analyzer at each  $U/V$  combination [21].

### 2.1.5 Detector

After separation, the ions must be detected. The most common detectors are secondary electron multiplier detectors (SEM) [21]. These make use of the fact that electrons are emitted from a metal or semiconductor surface when it is hit by a charged particle or ion. There are different versions of SEMs, for example with discrete dynodes or as continuous dynodes in channeltrons or microchannel plates (MCP). The detection of the ions in the TOF-MS and quadrupole mass spectrometer (QMS) used in this study is carried out by a bent channeltron (QMS) and an MCP (TOF-MS). An MCP is typically made of glass and consists of many linear channeltrons, i.e., very thin electron multiplier tubes, coated with a high-resistance semiconducting material. If an ion enters a channel and hits its surface, a secondary electron is emitted and accelerated towards the back of the plate due to an applied potential difference. The channels are angled with respect to the surface of the plates to ensure that the ions do not fly through and released secondary electrons trigger further secondary electrons by wall collisions as they pass through the channels. Because the number of emitted electrons also depends on the energy of the colliding particles, the ions are often accelerated again in front of the detector. This mitigates the lower sensitivity of the MCP to slower ions, i.e., ions with higher  $m/z$  ratios.

Stacking two MCPs, the so-called chevron plate, leads to gains of  $10^6 - 10^7$  [21]. The current of the huge number of exiting electrons can be measured and converted into a voltage. The voltage is then converted into a digital signal by an analog-digital converter. In the TOF-MS instrument used in this study, a threshold-digital converter is used. The data acquisition card allows the setting of a threshold voltage to reduce the detected ions per mass spectrum to one ion. Ion counting increases the dynamic range of the measurements by decreasing the noise level but requires larger averaging times.

## 2.2 Gas chromatography

In gas chromatography, a gas mixture or liquid that can evaporate without decomposition is introduced into a mobile carrier gas which flows through a packed or coated column. The separation of the gas mixture is based on differently pronounced interactions of the individual species within the mixture with the packing or coating of the column. In general, a gas chromatograph consists of an injector, one or more separating columns placed in an oven, and one or more detectors. In the following, the different components are described in more detail.

### 2.2.1 Sample introduction

The liquid or gaseous sample is usually introduced into an injector with a syringe. In the injector, the sample – if not already gaseous – is vaporized in an inlet liner, mixed with the carrier gas, and transferred to the packed or capillary column. The most common injector in combination with capillary columns is the split/splitless injector shown in Figure 2-5. It is also used in this study.

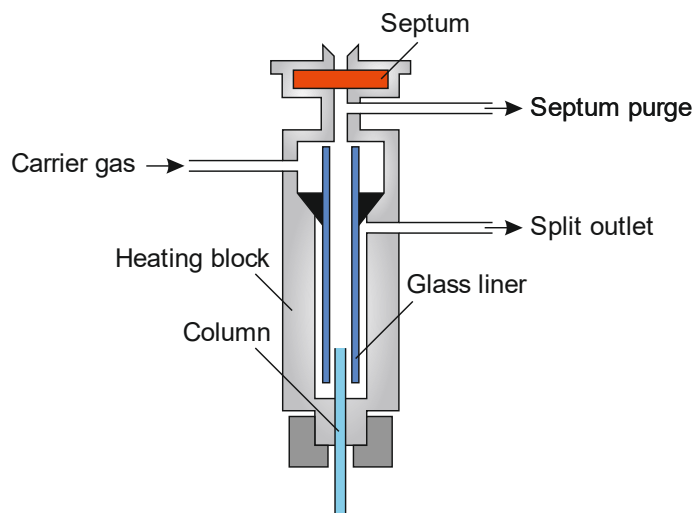


**Figure 2-5:** Split/Splitless injector.

After the sample is vaporized in the inert glass liner, it is diluted with the carrier gas to control the amount of sample that is introduced into the connected column. Dilution is required because of the limited sample capacity of the column. The dilution given as a split ratio (sample to carrier gas) can be adjusted depending on the injected sample volume and the column capacity. Typical values are 1:10 – 1:100 or more [33]. Only a small amount of the sample is introduced into the column, while the major part leaves the injector via the split outlet. Another advantage of the splitting technique, besides the minimized amount of sample, is the fast vaporization of liquid samples and the increased velocity of the carrier gas. The faster sample transfer to the column and the resulting narrower signals in the chromatogram lead to a higher chromatographic resolution.

The injector is sealed by a septum made of silicon rubber. The physical interaction with the syringe and the high temperatures of the injector can lead to the release of particles and volatiles from the septum, respectively. While released particles could clog the column, volatiles lead to “ghost signals” in the chromatogram. This is counteracted by a small flow of carrier gas that purges the septum and leaves the injector via the septum purge outlet. In the case of splitless injection, e.g., for trace analysis, the split valve is closed, and the sample is introduced undiluted into the column.

To achieve a low standard deviation of the measurement results, an automated injection via an auto-sampler is preferred to a manual injection.

## 2.2.2 Species separation

After vaporization, the carrier gas, also called the mobile phase, guides the sample into a separating column. A distinction is made between capillary and packed columns. Packed columns are filled with an adsorbent or support material, also called the stationary phase, while in capillary columns the stationary phase is applied to the inner wall in liquid or solid form. Because only capillary columns are used in this study, these are explained in more detail.

Capillary columns usually consist of fused silica that is coated with a polyimide layer for greater flexibility and stability. Capillary columns have an inner diameter of 0.1 – 0.53 mm and a length of 10 – 100 m [34]. The stationary phase on the inside of the column can be solid (gas-solid

chromatography, GSC) or liquid (gas-liquid chromatography, GLC). In the case of a solid stationary phase, the column is called a porous layer open tubular (PLOT) column, whereas it is called a wall-coated open tubular (WCOT) column for a liquid stationary phase. In addition, support-coated open tubular (SCOT) columns exist, where the liquid stationary phase is coated on a thin layer of support material, e.g., diatomaceous earth, attached to the inside of the column. In this study, only solid stationary phases are used so that only GSC will be described. Details regarding WCOT and SCOT columns can be found in [34,35]. In GSC, the dominant physical process with respect to the separation of the gas mixture is adsorption and desorption. During adsorption, gases or dissolved substances are reversibly deposited on the surface of a solid. For non-polar stationary phases, only dispersion interactions, e.g., Van-der-Waals interactions, occur. In contrast, polar stationary phases can also involve polar interactions like hydrogen bonds or dipole-dipole interactions [34,36]. The binding energy resulting from these forces is called adsorption energy  $E_{ad}$ . Adsorption occurs when a molecule can release its kinetic energy and the adsorption energy  $E_{ad}$  [37]. This is an exothermal process. To desorb the molecule, activation energy equal to the adsorption energy  $E_{ad}$  is required. This energy can be provided either by the moving mobile phase or by heat. Adsorption can be regarded as a kind of equilibrium reaction whose position depends on the properties of the surface and the substance to be adsorbed as well as on pressure and temperature.

A special type of PLOT columns are molecular sieves. Molecular sieves are artificially prepared alkali metal aluminosilicates with a well-defined porous structure whose dimensions are similar to those of small molecules [38]. Molecules smaller than the pore size diffuse into them and undergo several adsorption/desorption processes on the large surface area. Thus, there is a second retention mechanism on molecular sieves based on molecular size. Molecular sieves can only be used for molecules that are smaller than the pore size.  $\text{CO}_2$  and water are strongly adsorbed and, in some cases, can no longer be removed from the column, which greatly shortens its lifetime [39]. In the case of the most common molecular sieve with a pore size of 0.5 nm this also applies to high boiling species from  $\text{C}_2$  upwards [38]. Molecular sieves with a larger pore size exist to enable the separation of paraffins and naphthalenes. Molecular sieves are the best choice for the separation of the permanent gases  $\text{H}_2$ ,  $\text{O}_2$ ,  $\text{N}_2$ , Ar, CO, and  $\text{CH}_4$  [38].

Because the columns are placed within an oven, the repetitive adsorption/desorption process can be controlled so that in the best case all species in the sample are retained for different lengths of time in the stationary phase as schematically shown in Figure 2-6.

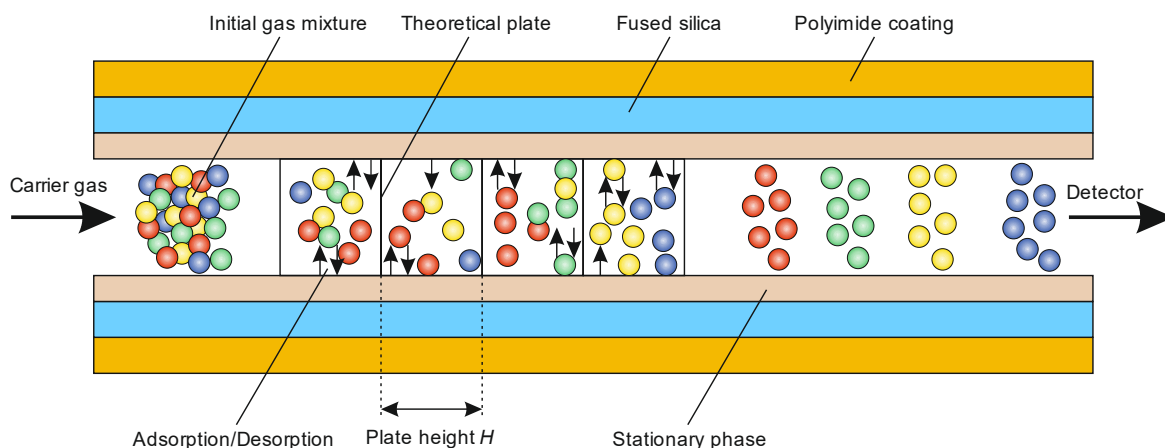


**Figure 2-6:** Principle of adsorption in gas-solid chromatography.

The duration after which a specific species leaves or elutes from the column and is detected is called retention time  $t_R$ . The retention time can be used to identify the respective species.

The chromatographic resolution or the possibility of a baseline separation of two subsequently eluting species depends on the column dimensions, the extent of the interaction between the species and the stationary phase, and the type of carrier gas and its velocity. The model of theoretical plates is often used to assess the efficiency of a column. In this model, the column of length  $L$  is divided into theoretical plates  $N$  of a plate height  $H$  (equation (2-15)). The plate height corresponds to the theoretical height, where an equilibrium between the concentration of molecules in the mobile phase and the mean concentration of molecules in the stationary phase is established once [34,40]. The higher the theoretical plates  $N$  the higher the efficiency of the column.

$$N = \frac{L}{H} \quad (2-15)$$

Considering the properties of Gaussian-shaped signals, equation (2-16) can be derived, in which  $t_R$  is the retention time and  $W$  is the signal width at the baseline, determined as the distance between the points of intersections of the inflection tangents of the Gaussian-shaped signal.

$$N = 16 \left( \frac{t_R}{W} \right)^2 \quad (2-16)$$

The complete derivation of equation (2-16) can be found in [35]. As shown in equation (2-16), an efficient column, indicated by a high number of theoretical plates, results in sharp signals and long retention times. Both  $H$  and  $N$  are given by column manufacturers. To compare different columns with respect to their efficiency the values should be determined using the same substance.

The effect of different carrier gases and the gas velocity on the efficiency of a column can be visualized by the van-Deemter equation [36]:

$$H = A + \frac{B}{u} + C \cdot u \quad (2-17)$$

In equation (2-17)  $u$  is the linear velocity of the carrier gas and  $A$ ,  $B$ ,  $C$  are constants for a given combination of column and carrier gas. The constants describe the extent of a contribution to signal broadening due to eddy-diffusion ( $A$ ), longitudinal diffusion ( $B$ ), and mass transport effects ( $C$ ) [36]. The eddy-diffusion term describes the effect that molecules of the same type can pass through a layer of adsorbent particles on different pathways. This effect only occurs for packed columns and can be neglected for capillary columns ( $A = 0$ ).  $B$  represents the effect of the diffusion of molecules from the high-concentration region of the initially introduced narrow-banded gas mixture to regions of a lower concentration in front of and behind it. Due to different binary diffusion coefficients for different combinations of analyte and carrier gas and a velocity-dependent residence time of the analyte in the column,  $B$  depends both on the type and the velocity of the carrier gas. Lastly, the mass transport effect, indicated by  $C$ , is attributed

to the time required by the analyte to reach equilibrium between the stationary and mobile phase. It depends on the column dimensions, the thickness of the stationary phase, and the diffusion coefficients of the analyte in both the stationary and mobile phase.

Figure 2-7 shows the van-Deemter curves for different carrier gases and a given column.

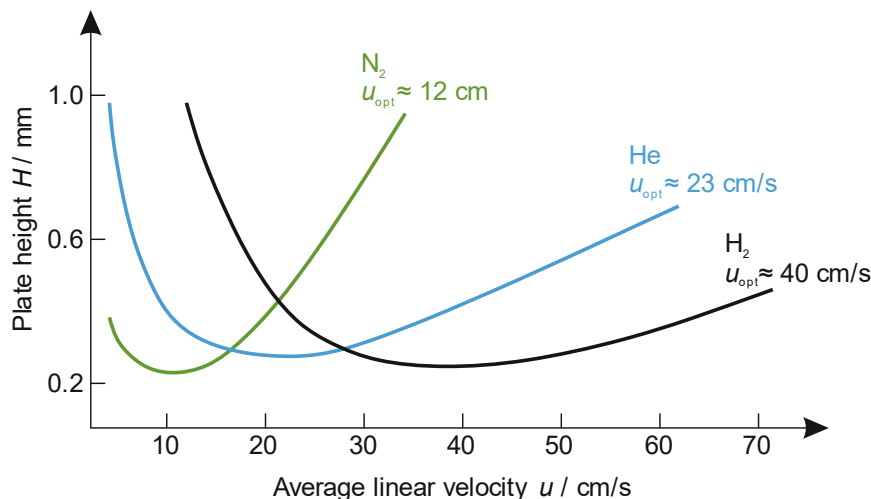


**Figure 2-7:** Van-Deemter curves for different carrier gases. Adapted from [36].

It is seen that the lowest plate height  $H$ , i.e., highest column efficiency, is similar for the carrier gases  $N_2$ ,  $He$ , and  $H_2$ , but is reached at different average velocities. Compared to  $He$  and  $H_2$ , which show a very broad minimum at higher average velocities,  $N_2$  exhibits a narrow minimum at low average velocities.  $He$  and  $H_2$  are preferred as carrier gases because they allow lower analysis times and a higher resolution for a broader range of carrier gas velocities. Although the shortest analysis time can be achieved with  $H_2$ ,  $He$  is mainly used as a carrier gas, because of its non-flammability in contrast to  $H_2$ . In addition,  $H_2$  cannot be used if it is also a target species in the gas mixture to be separated, because its presence as a carrier gas would obscure its detection in the gas sample.

A resolution of 1.5 is required for a baseline separation of two consecutively eluting species A and B [36]. The resolution is expressed as the ratio of the difference in retention times  $(t_R)_A$  and  $(t_R)_B$  of species A and B and the sum of half the signal widths  $W_A/2$  and  $W_B/2$  at the baseline, as shown in equation (2-18).

$$R_c = \frac{(t_R)_B - (t_R)_A}{\frac{W_A}{2} + \frac{W_B}{2}} \quad (2-18)$$

Combining equations (2-16) and (2-18) the resolution can also be expressed as a function of the theoretical plates  $N$ . The resulting equation (2-19) shows that the resolution is proportional to  $\sqrt{N}$ , so that a high number of theoretical plates or a small plate height  $H$  (equation (2-15)) is desired. This effect can be achieved for example by longer and thinner columns, a thicker and more effective stationary phase, an optimal carrier gas velocity according to the van-Deemter equation, and a temperature program tailored to the specific application.

$$R_c = \frac{(t_R)_B - (t_R)_A}{(t_R)_B} \cdot \frac{\sqrt{N}}{4} \quad (2-19)$$

### 2.2.3 Detector

In gas chromatography, many different types of detectors are used for different types of applications. In this study, a QMS and a thermal conductivity detector (TCD) are used for the detection of the separated species. Because the QMS is described in section 2.1.4, only the TCD and the benefits from using a QMS in combination with a GC are briefly outlined here. Details of other common detectors such as the flame ionization detector or the electron capture detector are given in [35,36].

A TCD is a non-selective concentration-dependent detector, based on the different thermal conductivities of the gas eluting from the column compared to the thermal conductivity of the pure carrier gas. In a TCD, the eluting gas mixture is guided through a small cell that contains a heated filament. The filament is heated either to a constant temperature or by a constant heating current or voltage. The analytes cause a change in thermal conductivity of the gas that leads to a temperature change of the filament due to different heat losses to the surrounding block or change in required power to keep the temperature of the filament constant [36,41]. The changed resistance of the filament due to the temperature change or the change in required power is measured and translated into a signal intensity.

In early TCDs, the two gas streams (carrier gas + analyte and pure carrier gas) were passed through two different cells (reference and measuring cell) with the filaments incorporated in a Wheatstone bridge circuit. If the thermal conductivities of the two flows differ, the difference in filament resistance leads to an unbalanced bridge and a voltage can be measured. To increase sensitivity and stability, four cells, i.e., two reference and two measuring cells, can be used. Today, usually only one cell with alternating (5 – 10 Hz) flow of reference and measurement gas is used [35]. The amplitude of the electrical output signal depends on the difference in thermal conductivities of the two flows. The reference flow minimizes the effect of variations in flow rate, pressure, temperature, and applied power on the obtained signal.

The most commonly used carrier gases in combination with TCDs are H<sub>2</sub> and He as they provide the highest detector sensitivity due to much higher thermal conductivities compared to other gases.

In contrast to the TCD, the QMS can also be used to identify eluting species. For this purpose, the obtained fragmentation pattern of the eluting species is compared with fragmentation patterns from the literature, e.g., from the mass spectral library of the National Institute of Standards and Technology (NIST) [42].

---

## 3 Modeling

In this study, the experimental results are compared with simulation results using a one-dimensional plug-flow approach. In addition, to verify the pug-flow assumption, two-dimensional simulations are performed for selected conditions using the cylindrical shear-flow approach of Chemkin Pro 19.0 [43]. The plug-flow assumptions and a method for their validation are outlined in detail and the underlying conservation equations are presented. The shear-flow model including its conservation equations is briefly outlined. Subsequently, the fundamentals of the reaction kinetics of homogeneous gas-phase reactions are given. In this section, the approaches of calculating thermodynamic and transport properties used in the simulation software, i.e., Chemical Workbench 4.1 [44] and Chemkin Pro 19.0 [43], are briefly described.

### 3.1 Plug flow

Plug flow is an ideal flow pattern in tubular flow reactors in which the fluid is perfectly mixed in the radial direction, i.e., there are no radial gradients in velocity, temperature, or concentration. Also, there is no mixing in the axial direction so that each plug or each volume element has the same residence time in the reactor. Axial concentration and temperature gradients occur only due to chemical reactions and non-isothermal conditions, respectively [45].

A plug-flow pattern reduces the mathematical problem of the flow simulation from a two-dimensional to a one-dimensional one, which greatly simplifies modeling and is computationally efficient.

In a real flow reactor, a distinction is made between laminar and turbulent flow, characterized by the Reynolds number  $Re$ :

$$Re = \frac{\rho u d_R}{\eta} \quad (3-1)$$

The Reynolds number shows the ratio of inertia to viscous forces. In equation (3-1),  $\rho$  is the density of the fluid,  $u$  the fluid velocity,  $d_R$  the diameter of the tube, and  $\eta$  the dynamic viscosity. The dynamic viscosity of a gas mixture  $\eta_{\text{mix}}$  is given by equation (3-2), in which  $\eta_i$  is the dynamic viscosity of species  $i$ ,  $x_i$  and  $x_j$  the mole fractions of the species  $i$  and  $j$ , and  $\Phi_{ij}$  a dimensionless factor given by equation (3-3) [46]. Here,  $M_i$  and  $M_j$  represent the molar masses of the species  $i$  and  $j$ , respectively.

$$\eta_{\text{mix}} = \sum_{i=1}^n \frac{\eta_i}{1 + \frac{1}{x_i} \sum_{j=1}^n x_j \Phi_{ij}} \quad (3-2)$$

$$\Phi_{ij} = \frac{\left[ 1 + \left( \frac{\eta_i}{\eta_j} \right)^{1/2} \left( \frac{M_i}{M_j} \right)^{1/4} \right]^2}{\sqrt{8} \left[ 1 + \frac{M_i}{M_j} \right]^{1/2}} \quad (3-3)$$

The dynamic viscosities of each component in the gas mixture at a given temperature can be calculated by the polynomial shown in (3-4) [47].

$$\frac{\eta}{\text{Pas}} = A + B \frac{T}{\text{K}} + C \left( \frac{T}{\text{K}} \right)^2 + D \left( \frac{T}{\text{K}} \right)^3 + E \left( \frac{T}{\text{K}} \right)^4 \quad (3-4)$$

The coefficients  $A$ - $E$  are listed in the literature for different gases [47]. The influence of pressure on viscosity can be neglected at temperatures above 1.5 times the critical temperature of a gas and pressures below half the critical pressure [48].

For  $Re < 2300$ , the pipe flow can be considered laminar and for higher values, the transition to turbulent flow occurs [49]. The laminar flow is characterized by a parabolic velocity distribution with the highest velocity in the middle of the tube and the lowest velocity at the walls due to friction. The fluid acts in layers and no radial mixing occurs. In contrast, the turbulent flow is characterized by a flow swirled in space and time that leads to a continuous mixing of the fluid. Because of the mixing process, the velocity distribution of a turbulent flow is flatter and more uniform compared to the laminar flow [49] so that a turbulent flow can be regarded as a flow with small deviations from plug flow. The same applies to laminar flows in long tubes, where the molecular diffusion in radial direction has enough time to smooth or eliminate the radial concentration gradients [50].

A useful model to check whether a flow can be regarded as plug flow is the dispersion model of Levenspiel [51]. Dispersion means the broadening of a fluid element due to velocity gradients and molecular diffusion. It is characterized by the dimensionless expression shown in equation (3-5) and called vessel dispersion number, in which  $D_{\text{Disp}}$  represents the dispersion coefficient,  $u$  the fluid velocity, and  $L$  the tube length.

$$\frac{D_{\text{Disp}}}{uL} \quad (3-5)$$

For  $D_{\text{Disp}}/uL = 0$ , the flow can be regarded as ideal plug flow and for values lower than 0.01 only small deviations from plug flow exist. The dispersion coefficient can be determined from the residence time distribution  $E(\theta)$  of a tracer injected at the tube inlet using equation (3-6). In this equation,  $\theta$  indicates the dimensionless average residence time ( $\theta = \tau/\tau_{\text{avg}}$ ). The equation was derived for open tubes and  $D_{\text{Disp}}/uL > 0.01$  so that it also covers flows with larger deviations from plug flow. In this case, the residence time distribution curves become nonsymmetrical due to the broadening of the injected tracer. But, for values of  $D_{\text{Disp}}/uL < 0.01$ , the resulting curves are close to symmetrical and a small deviation from plug flow can be assumed.

$$E(\theta) = \frac{1}{2} \frac{1}{\sqrt{\pi\theta \left(\frac{D_{\text{Disp}}}{uL}\right)}} \exp\left[-\frac{(1-\theta)^2}{4\theta \left(\frac{D_{\text{Disp}}}{uL}\right)}\right] \quad (3-6)$$

Fast data acquisition is required to experimentally determine the time-dependent concentration of the tracer at the reactor outlet under the specific operating conditions. Alternatively, a correlation (equation (3-7)) derived from Taylor [52,53] and Aris [54] can be used to calculate  $D_{\text{Disp}}$  from the binary diffusion coefficient  $D_{\text{AB}}$ , the fluid velocity  $u$ , and the diameter  $d_{\text{R}}$  of the tube.

$$D_{\text{Disp}} = D_{\text{AB}} + \frac{u^2 d_{\text{R}}^2}{192 D_{\text{AB}}} \quad (3-7)$$

While dispersion is promoted by molecular diffusion at low velocity, it is promoted by axial convection and radial diffusion at higher velocities. As a result, an optimum is found for a specific combination of  $u$ ,  $d_{\text{R}}$ , and  $D_{\text{AB}}$ . If the dispersion number (equation (3-5)) is correlated with the Peclet number  $Pe$  (equation (3-8)), a curve is formed showing a minimum for low axial dispersion in laminar pipe flow. This minimum corresponds to the conditions at which the flow can best be regarded as plug flow. The Peclet number  $Pe$  is the product of Reynolds  $Re$  and Schmidt number  $Sc$  and expresses the ratio between the mass transfer by convection and diffusion. Because the characteristic length  $d_{\text{R}}$  is used instead of  $L$ ,  $L$  is also replaced by  $d_{\text{R}}$  in the dispersion number. Consequently, the dispersion intensity is independent of the geometry factor  $L/d$  so that the resulting diagram only applies to pipe flows with  $L \gg d_{\text{R}}$  [51].

$$Pe = Re \times Sc = \frac{\rho u d_{\text{R}}}{\eta} \frac{\eta}{\rho D_{\text{AB}}} = \frac{u d_{\text{R}}}{D_{\text{AB}}} \quad (3-8)$$

According to Hirschfelder et al. [55], the binary diffusion coefficient  $D_{\text{AB}}$  [cm<sup>2</sup>/s] can be calculated using equation (3-9). Here,  $p$  indicates the pressure in atm,  $M_{\text{A}}$  and  $M_{\text{B}}$  the molecular weights of the species A and B,  $\sigma_{12}$  a reduced collision diameter in Angstroms, and  $\Omega_{\text{AB}}^{(1,1)}$  the collision integral.

$$D_{\text{AB}} = \frac{1.86 \cdot 10^{-3} \sqrt{T^3 \left(\frac{1}{M_{\text{A}}} + \frac{1}{M_{\text{B}}}\right)}}{p \sigma_{12}^2 \Omega_{\text{AB}}^{(1,1)}} \quad (3-9)$$

The collision integral is a function of the reduced temperature  $T^*$  given in equation (3-10). In this equation,  $\epsilon_{\text{AB}}$  indicates the characteristic energy of the intermolecular forces between the molecules A and B and  $k_{\text{B}}$  the Boltzmann constant ( $k_{\text{B}} = 1.38066 \times 10^{-23} \text{ J K}^{-1}$ ).

$$T^* = \frac{k_{\text{B}} T}{\epsilon_{\text{AB}}} \quad (3-10)$$

Usually, the Lennard-Jones (12-6) potential  $\psi$  is used to describe the intermolecular forces between two non-polar spherical particles, e.g., atoms or molecules, at a distance  $r$  [56,57].

$$\psi = 4\varepsilon \left[ \left( \frac{\sigma}{r} \right)^{12} - \left( \frac{\sigma}{r} \right)^6 \right] \quad (3-11)$$

The Lennard-Jones (12-6) potential parameters  $\varepsilon$  and  $\sigma$  in equation (3-11) correspond to the characteristic Lennard-Jones energy that quantifies the depth of the potential well and the distance at which the potential approaches zero, respectively. The parameters are listed in [58] for some common species. To relate the Lennard-Jones (12-6) potential parameters between two species A and B to the parameters of the individual species, equations (3-12) and (3-13) are used [59], as data are only available for a few gas pairs in the literature.

$$\varepsilon_{AB} = \sqrt{\varepsilon_A \varepsilon_B} \quad (3-12)$$

$$\sigma_{AB} = \frac{1}{2}(\sigma_A + \sigma_B) \quad (3-13)$$

The collision integral  $\Omega_{AB}^{(1,1)}$  is tabulated as a function of  $T^*$  for the Lennard-Jones (12-6) potential in [60]. Kim and Monroe [61] derived empirical equations from high-accuracy calculations of 16 collision integrals for the Lennard-Jones (12-6) potential. Equation (3-14) presents the equation for the collision integral  $\Omega_{AB}^{(1,1)}$  that is required for equation (3-9).

$$\Omega_{AB}^{(1,1)} = A^{(1,1)} + \sum_{i=1}^6 \left[ \frac{B_i^{(1,1)}}{(T^*)^i} + C_i^{(1,1)} (\ln T^*)^i \right] \quad (3-14)$$

The coefficients for equation (3-14) are listed in [61]. The authors indicate that the collision integrals can be predicted within 0.007 % in the range of  $0.3 \leq T^* \leq 400$ .

With equations (3-7) – (3-14), the plug flow approximation can be validated for given operating conditions.

### 3.1.1 Conservation equations

The general equations for the conservation of mass, energy, and momentum for pipe flows are described in [62]. Here, only the simplified versions with respect to steady-state plug flow are presented. This includes the assumptions that there are no gradients in the radial direction and that diffusion in the axial direction can be neglected. In addition, the cross-sectional area  $A$  is assumed to be constant and surface reactions are not considered. Consequently, only variations of fluid properties, e.g., velocity and temperature, in the flow direction  $x$  are considered.

Taking these assumptions into account, the mass conservation equation, also known as the continuity equation, is described by equation (3-15)

$$\frac{\partial(\rho u)}{\partial x} = 0 \quad (3-15)$$

where  $\rho$  and  $u$  represent the density and axial velocity, respectively. The density is calculated via the ideal gas equation of state as shown in equation (3-16).

$$\rho = \frac{p\bar{M}}{RT} \quad (3-16)$$

Here,  $p$  denotes the pressure,  $\bar{M}$  the mean molar mass,  $R$  the universal gas constant ( $R = 8.3145 \text{ J/molK}$ ), and  $T$  the temperature.

Although the total mass is constant, the mass fractions of species in a gas mixture can change due to chemical reactions. The species conservation equation is presented in equation (3-17).

$$\rho u \frac{\partial Y_i}{\partial x} = M_i \dot{\omega}_i \quad (3-17)$$

In this equation,  $Y_i$  and  $M_i$  indicate the mass fraction and the molar mass of species  $i$ , respectively and  $\dot{\omega}_i$  the chemical production rate of species  $i$  due to gas-phase reactions. The production rate  $\dot{\omega}_i$  is described in detail in section 3.3.1.

There is no need to solve the momentum equation if the pressure can be assumed to be constant and friction can be neglected. The same applies to the energy equation for systems with constrained temperature. For an adiabatic reactor, the energy equation is as follows:

$$\rho u \bar{c}_p \frac{\partial T}{\partial x} = - \sum_{i=1}^{N_{\text{sp}}} h_i \dot{\omega}_i M_i \quad (3-18)$$

where  $N_{\text{sp}}$  represents the number of species,  $h_i$  the specific enthalpy of species  $i$ , and  $\bar{c}_p$  the mean specific heat capacity at constant pressure per unit mass of gas. The calculation of  $h_i$  and  $\bar{c}_p$  is described in section 3.3.3.

Because the residence time  $\tau$  is often a quantity of interest, equation (3-19) can additionally be solved.

$$\frac{\partial \tau}{\partial x} = \frac{1}{u} \quad (3-19)$$

## 3.2 Boundary-layer flow

In boundary-layer or shear flow, it is assumed that axial diffusion can be neglected compared to radial diffusion and axial convective transport. Gravitational influences are also neglected [63,64]. This simplifies the required system of equations considerably, e.g., by eliminating the momentum in the radial direction and the angle dependence which reduces the problem to two dimensions. Consequently, the boundary-layer flow model allows the calculation of two-

dimensional concentration, velocity, and temperature fields by coupling hydrodynamics with gas-phase chemistry. It can be applied if  $ReSc \frac{d}{L} \gg 1$  [65].

### 3.2.1 Conservation equations

The required system of equations is shown below (equations (3-20)-(3-23)) [64].

Compared to plug flow, the mass conservation equation is extended by the mass transfer in the radial direction as shown in equation (3-20).

$$\frac{\partial(\rho u)}{\partial x} + \frac{1}{r} \frac{\partial(r \rho v)}{\partial r} = 0 \quad (3-20)$$

Here,  $u$  and  $v$  represent the velocity components in axial ( $x$ ) and radial ( $r$ ) directions, respectively. Regarding the conservation of species, radial diffusion must be considered along with the convective mass transfer of a specific species in the radial direction. The species conservation equation can be written as

$$\rho \left( u \frac{\partial Y_i}{\partial x} + v \frac{\partial Y_i}{\partial r} \right) = - \frac{1}{r} \frac{\partial(r \rho Y_i V_{i,r})}{\partial r} + \dot{\omega}_i M_i \quad (3-21)$$

where  $V_{i,r}$  indicates the multicomponent diffusion velocity in the radial direction. Because in boundary-layer flow the development of a parabolic velocity profile is considered, viscous forces directed in the radial direction lead to convective acceleration or deceleration of the fluid. This is shown by the momentum conservation equation in axial direction:

$$\rho \left( u \frac{\partial u}{\partial x} + v \frac{\partial u}{\partial r} \right) = \frac{1}{r} \frac{\partial}{\partial r} \left( \eta r \frac{\partial u}{\partial r} \right) \quad (3-22)$$

where  $\eta$  describes the dynamic viscosity of the gas mixture. Equation (3-23) presents the energy conservation equation. Compared to the energy equation (3-18) for plug flow, it is extended by the radial components of the convective energy transfer as well as thermal conduction and diffusion in the radial direction.

$$\rho \bar{c}_p \left( u \frac{\partial T}{\partial x} + v \frac{\partial T}{\partial r} \right) = \frac{1}{r} \frac{\partial}{\partial r} \left( r \lambda \frac{\partial T}{\partial r} \right) - \sum_{i=1}^{N_{sp}} \rho c_{p,i} Y_i V_{i,r} \frac{\partial T}{\partial r} - \sum_{i=1}^{N_{sp}} h_i \dot{\omega}_i M_i \quad (3-23)$$

In equation (3-23)  $\lambda$  represents the thermal conductivity of the gas mixture.

As can be seen from the equations, transport properties are required whose calculation is described in section 3.3.4.

A more detailed description of the boundary-layer flow model is found in [63,64].

### 3.3 Reaction kinetics

To solve the conservation equations for plug flow, the rate of production of chemical species  $\dot{\omega}$  and the thermodynamic properties, e.g., the specific heat capacity  $c_p$ , enthalpy  $h$ , and entropy  $s$  must be calculated. For the boundary-layer flow, transport properties like thermal conductivity, diffusion, and viscosity must also be known.

With the help of thermodynamics, only equilibrium states of chemical reactions can be described. No information about the reaction path and the reaction rate can be given. The reaction kinetics, on the other hand, describe chemical reactions qualitatively and quantitatively, including the pathways of species formed or consumed and the time scales of the reactions.

The fundamentals of kinetic modeling including the calculation of thermodynamic and transport data are described in this chapter. First, chemical reaction rates are introduced, followed by the treatment of pressure-dependent reactions. Subsequently, the approach for calculating thermodynamic and transport data in kinetic modeling is outlined. Reaction path and sensitivity analysis are introduced in the last section.

#### 3.3.1 Chemical reaction rates

Reaction mechanisms used in kinetic modeling consist of hundreds to thousands of reactions. Usually, these reactions are reversible elementary reactions, i.e., reactions that occur at the molecular level exactly as they are formulated. An elementary reaction  $j$  can be expressed as



where  $A_i$  represents the species  $i$  and  $v'_{ij}$  and  $v''_{ij}$  the stoichiometric coefficients of the species in the forward (‘) and reverse (‘’) direction, respectively. The number of species is denoted by  $N_{\text{sp}}$ . The molar rate of production of a chemical species is equal to the temporal change of its molar concentration  $c_i$  as shown in equation (3-25).

$$\dot{\omega}_i = \frac{dc_i}{dt} = \sum_{j=1}^{N_{\text{R}}} (v''_{ij} - v'_{ij}) q_j \quad (3-25)$$

On the right-hand side of equation (3-25)  $q_j$  is the net rate of reaction, also called the rate of progress and  $N_{\text{R}}$  denotes the number of reactions in which species  $i$  is involved. The net rate of reaction is calculated by the difference of the forward and reverse rates as follows:

$$q_j = k'_j \prod_{i=1}^{N_{\text{sp}}} c_i^{v'_{ij}} - k''_j \prod_{i=1}^{N_{\text{sp}}} c_i^{v''_{ij}} \quad (3-26)$$

Here,  $k_j'$  and  $k_j''$  are the so-called rate coefficients of the forward and reverse reaction, respectively. Equation (3-26) shows that the unit of the rate coefficient of an elementary reaction  $j$  depends on the order of reaction given by the sum of the stoichiometric coefficients of all reactants involved in the reaction.

The most common types of reactions are unimolecular and bimolecular reactions, i.e., reactions involving only one and two reactants, respectively. The reaction rate of a unimolecular reaction is of first order and only depends on the concentration of one reactant. Typical examples of unimolecular reactions are decomposition or isomerization reactions. Bimolecular reactions are of second order so that their reaction rates are proportional to the product of the concentrations of two reactants or the squared concentration of one reactant. Examples are hydrogenation or dimerization reactions. Termolecular reactions, which are of third order, are rare because they require the simultaneous collision of three reactants.

For some reactions, a “third body”, usually denoted as  $M$ , is required for the reaction to occur. These reactions are typically decomposition or recombination reactions, i.e., reactions with a single reactant or product. For a recombination reaction, the collision of the involved reactants leads to a huge amount of energy transferred to the product due to the conservation of momentum. This excess energy must be transferred to the third body by collision to stabilize the product. In this process, some species act more efficiently than others so that a collision efficiency  $a_{ji}$  must be considered in relation to these species. For reactions involving a third body the rate of progress changes to:

$$q_j = \left( \sum_{i=1}^{N_{sp}} a_{ji} c_i \right) \left( k_j' \prod_{i=1}^{N_{sp}} c_i^{v'_{ij}} - k_j'' \prod_{i=1}^{N_{sp}} c_i^{v''_{ij}} \right) \quad (3-27)$$

If all species contribute equally as a third body,  $a_{ji}$  is 1 for all species. In the case of more efficient collisions,  $a_{ji}$  can be higher than one. This results in an effective concentration of the third body that is higher than its real concentration. Third-body reactions are of third order.

The reaction rate coefficient of the forward reaction is usually expressed by a modified Arrhenius form equation:

$$k_j' = AT^n \exp \left( \frac{-E_A}{RT} \right) \quad (3-28)$$

with the pre-exponential factor  $A$ , the activation energy  $E_A$ , the universal gas constant  $R$ , and the temperature exponent  $n$ . The pre-exponential factor  $A$  is related to the frequency of collisions and the probability that these collisions lead to a chemical reaction. Its temperature dependence is expressed by the temperature exponent  $n$ . The activation energy  $E_A$  is the energy barrier that must be overcome for the reaction to proceed. The fraction of particles (atoms or molecules) with an energy of at least  $E_A$  is represented by the exponential expression in equation (3-28).

The reaction rate coefficient of the reverse reaction can either be expressed in the same way or calculated from the forward reaction rate using thermodynamic relationships. When a reversible

reaction is in equilibrium, the rate of progress approaches zero because the forward and reverse reaction rates are equal. This gives equation (3-29):

$$k'_j \prod_{i=1}^{N_{sp}} c_i^{v'_{ij}} = k''_j \prod_{i=1}^{N_{sp}} c_i^{v''_{ij}} \quad (3-29)$$

The relation between the forward and reverse reaction rates is described by the equilibrium constant  $K_{c,j}$  based on concentrations, as shown in equation (3-30).

$$K_{c,j} = \frac{k''_j}{k'_j} = \prod_{i=1}^{N_{sp}} c_i^{(v''_{ij}-v'_{ij})} \quad (3-30)$$

The equilibrium constant can also be expressed based on pressure using the partial pressures of species  $i$  and the standard pressure  $p^0$  ( $p^0 = 1$  atm). The equilibrium constant based on pressure is indicated by  $K_{p,j}$  and calculated from equation (3-31).

$$K_{p,j} = \prod_{i=1}^{N_{sp}} \left( \frac{p_i}{p^0} \right)^{(v''_{ij}-v'_{ij})} \quad (3-31)$$

Using the ideal gas law ( $c = n/V = p/RT$ ), equation (3-30) can be expressed as a function of pressure:

$$K_{c,j} = \prod_{i=1}^{N_{sp}} \left( \frac{p_i}{RT} \right)^{(v''_{ij}-v'_{ij})} \quad (3-32)$$

Comparing equations (3-31) and (3-32) leads to equation (3-33):

$$K_{c,j} = K_{p,j} \prod_{i=1}^{N_{sp}} \left( \frac{p^0}{RT} \right)^{(v''_{ij}-v'_{ij})} = K_{p,j} \left( \frac{p^0}{RT} \right)^{v_{net}} \quad (3-33)$$

with  $v_{net}$  representing the net change in the number of gas-phase species in the reaction  $j$ .  $K_{p,j}$  can also be expressed as:

$$K_{p,j} = \exp \left( \frac{-\Delta_r \tilde{g}_j^0}{RT} \right) \quad (3-34)$$

with the molar Gibbs free energy  $\Delta_r \tilde{g}_j^0$  at standard pressure, calculated from the specific reaction enthalpy  $\Delta_r \tilde{h}_j^0$  and entropy  $\Delta_r \tilde{s}_j^0$  as outlined in equation (3-35).

$$\Delta_r \tilde{g}_j^0 = \Delta_r \tilde{h}_j^0 - T \Delta_r \tilde{s}_j^0 \quad (3-35)$$

Substituting equations (3-34) and (3-35) in equation (3-33) results in the final expression of  $K_{c,j}$ .

$$K_{c,j} = \exp \left( \frac{-\Delta_r \tilde{s}_j^0}{R} - \frac{-\Delta_r \tilde{h}_j^0}{RT} \right) \left( \frac{p^0}{RT} \right)^{v_{\text{net}}} \quad (3-36)$$

Equations (3-30) and (3-36) show that the reaction rate coefficient of the reverse reaction can be calculated from thermodynamic data. The calculation of the required quantities like enthalpy and entropy is described in section 3.3.3.

### 3.3.2 Pressure-dependent reaction rates

Under certain conditions, a reaction rate can show pressure-dependent behavior in addition to temperature dependence. This effect is mostly found for unimolecular/recombination reactions. Lindemann [66] proposed that unimolecular decomposition only occurs when the decomposing reactant is in an activated state due to a non-reactive collision with another molecule M. The activated species can be deactivated by another collision or decompose to form the products. This formulation also applies to recombination reactions, e.g., the recombination of methyl ( $\text{CH}_3$ ) radicals shown below:



At a specific high-pressure limit, no additional collision partner is required, and the recombination occurs according to reaction (R 3-1). In contrast, at a low-pressure limit a third body (see section 3.3.1) is required so that the reaction can be expressed as:



The reaction rate coefficients for the high-pressure and low-pressure limit, denoted by the subscripts 0 and  $\infty$ , respectively, can still be expressed in their respective Arrhenius form and are independent of pressure:

$$k_0 = A_0 T^{n_0} \exp \left( \frac{-E_{A,0}}{RT} \right) \quad (3-37)$$

$$k_\infty = A_\infty T^{n_\infty} \exp \left( \frac{-E_{A,\infty}}{RT} \right) \quad (3-38)$$

But in the transition region, the so-called fall-off region, a more complex, pressure-dependent reaction rate coefficient is necessary. In this case, the third body is usually enclosed in parentheses in the reaction equation. The rate coefficient at any given pressure is then calculated by equation (3-39):

$$k = k_{\infty} \left( \frac{P_r}{1 + P_r} \right) F \quad (3-39)$$

where  $F$  is the broadening factor and  $P_r$  the reduced pressure, defined as follows:

$$P_r = \frac{k_0 c_M}{k_{\infty}} \quad (3-40)$$

Here,  $c_M$  is the total concentration of the gas mixture in mole per unit volume, including possibly enhanced third-body efficiencies (see section 3.3.1). The concentration of the mixture finally depends on pressure.

For the Lindemann expression [66] the broadening factor  $F$  equals one, however, a comparison of experiments and theory showed large disagreements in the fall-off region [67]. The reason for this is that Lindemann assumed that the required activation energy would be provided by a simple collision. Lindemann did not consider that the internal degrees of freedom of the reactant can also contribute to the provision of the required energy.

A more complex expression of the broadening factor is given by Troe [68] and Gilbert et al. [69]:

$$\log F = \left[ 1 + \left[ \frac{\log P_r + c}{n - d \log(P_r + c)} \right]^2 \right]^{-1} \log F_{\text{cent}} \quad (3-41)$$

in which the parameters  $c$ ,  $n$ , and  $d$  are defined as:

$$c = -0.4 - 0.67 \log F_{\text{cent}} \quad (3-42)$$

$$n = 0.75 - 1.27 \log F_{\text{cent}} \quad (3-43)$$

$$d = 0.14 \quad (3-44)$$

The parameter  $F_{\text{cent}}$  depends on temperature and the reaction-specific constants  $\alpha$ ,  $T^*$ ,  $T^{**}$ , and  $T^{***}$  that must be specified in the reaction mechanism. It is calculated according to equation (3-45).

$$F_{\text{cent}} = (1 - \alpha) \exp\left(\frac{-T}{T^{***}}\right) + \alpha \exp\left(\frac{-T}{T^*}\right) + \exp\left(\frac{-T^{**}}{T}\right) \quad (3-45)$$

A similar approach to that of Troe and Gilbert was proposed by Stewart et al. [70], who used a different broadening factor  $F$  given by equation (3-46).

$$F = a \exp\left(\frac{-b}{T}\right) + \exp\left(\frac{-T}{c}\right)^x \quad (3-46)$$

with

$$X = \frac{1}{1 + (\log P_r)^2} \quad (3-47)$$

The method is called the SRI method. The parameters  $a$ ,  $b$ , and  $c$  in the  $F$  expression must be supplied in the reaction mechanism. Both the Troe and SRI methods can accurately predict the fall-off behavior of single-well reactions, but they do not adequately predict multi-well and multi-product reactions [71]. A method capable of accurately predicting the temperature and pressure dependence of these types of reactions is the Chebyshev method proposed by Venkatesh et al. [71]. The Chebyshev method is much more complex than the previous methods and needs much more parameters to be specified in the reaction mechanism. Because this method was not used in any of the reaction mechanisms used in this study, it is not described here. Refer to the literature [71] for more information.

Another common method to describe pressure-dependent reaction rate coefficients is the PLOG fit [72]. This method is based on logarithmic interpolation between two rate coefficients given for discrete pressures  $p_i$  and  $p_{i+1}$  below and above the current pressure  $p$ .

$$\ln(k) = \ln(k_i) + (\ln(k_{i+1}) - \ln(k_i)) \frac{\ln(p) - \ln(p_i)}{\ln(p_{i+1}) - \ln(p_i)} \quad (3-48)$$

The reaction rate coefficients for each pressure are described in terms of the standard modified Arrhenius form equation (see equation (3-28)). At pressures lower or higher than any of those provided in the reaction mechanism, the rate coefficient for the lowest or highest pressure is used.

### 3.3.3 Thermodynamic data

To solve the energy equations (3-18) and (3-23), the values of  $h_i^0$ ,  $c_{p,i}^0$ , and  $\bar{c}_p$  must be known for every temperature. In addition, the specific molar reaction enthalpy  $\Delta_r \tilde{h}_j^0$  and entropy  $\Delta_r \tilde{s}_j^0$  are required to calculate the equilibrium constant  $K_c$  and the reverse rate coefficient for any reaction (see section 3.3.1). Note that the superscript 0 denotes the standard state of 1 atm pressure.

In general, the species-specific specific molar enthalpy and entropy at a given temperature for an ideal gas are calculated by equations (3-49) and (3-50), respectively.

$$\tilde{h}_i^0(T) = \tilde{h}_{i,\text{ref}}^0 + \int_{T_{\text{ref}}}^T \tilde{c}_{p,i}^0 dT \quad (3-49)$$

$$\tilde{s}_i^0(T) = \tilde{s}_{i,\text{ref}}^0 + \int_{T_{\text{ref}}}^T \tilde{c}_{p,i}^0 d \ln T \quad (3-50)$$

Here, the subscript “ref” denotes the standard conditions of usually 298 K of temperature so that the reference values represent the enthalpy and entropy of formation. Usually, the heat capacity is given as a polynomial, with the most common polynomials being the NASA

polynomials [73]. Based on these polynomials, the specific molar heat capacity is calculated by equation (3-51).

$$\frac{\tilde{c}_{p,i}^0}{R} = a_{1,i} + a_{2,i}T + a_{3,i}T^2 + a_{4,i}T^3 + a_{5,i}T^4 \quad (3-51)$$

Substituting equation (3-51) into equations (3-49) and (3-50), equations (3-52) and (3-53) are obtained to calculate the specific molar enthalpy and entropy at a given temperature, respectively.

$$\frac{\tilde{h}_i^0}{RT} = a_{1,i} + \frac{a_{2,i}}{2}T + \frac{a_{3,i}}{3}T^2 + \frac{a_{4,i}}{4}T^3 + \frac{a_{5,i}}{5}T^4 + \frac{a_{6,i}}{T} \quad (3-52)$$

$$\frac{\tilde{s}_i^0}{R} = a_{1,i} \ln(T) + a_{2,i}T + \frac{a_{3,i}}{2}T^2 + \frac{a_{4,i}}{3}T^3 + \frac{a_{5,i}}{4}T^4 + a_{7,i} \quad (3-53)$$

The constants  $a_{6,i} \times R$  and  $a_{7,i} \times R$  represent the enthalpy and entropy of formation of species  $i$ , respectively. As can be seen from the equations, seven coefficients ( $a_1$ - $a_7$ ) are required for each species. The NASA polynomials consist of two sets of coefficients, i.e., a total of 14 coefficients, with one set covering the low- (300 – 1000 K) and one set covering the high-temperature range (1000 – 5000 K).

The specific reaction enthalpy and entropy are then calculated according to equations (3-54) and (3-55), respectively.

$$\Delta_r \tilde{h}_j^0 = \sum_{i=1}^{N_{sp}} (v''_{ij} - v'_{ij}) \tilde{h}_i^0 \quad (3-54)$$

$$\Delta_r \tilde{s}_j^0 = \sum_{i=1}^{N_{sp}} (v''_{ij} - v'_{ij}) \tilde{s}_i^0 \quad (3-55)$$

To convert the molar enthalpy and heat capacity to the values per unit mass required for the conservation equations, the values must be divided by the molar mass. The mean specific heat capacity for a mixture of ideal gases is calculated by equation (3-56).

$$\bar{c}_p = \sum_{i=1}^{N_{sp}} Y_i c_{p,i} \quad (3-56)$$

### 3.3.4 Transport data

In addition to thermodynamic properties, transport properties like dynamic viscosity, thermal conductivity, and diffusion coefficients must be calculated to solve the conservation equations related to the boundary-layer flow model.

The dynamic viscosity  $\eta$  of the mixture is calculated according to equation (3-2) with the species-specific dynamic viscosity given as [55]:

$$\eta_i = \frac{5}{16} \frac{\sqrt{\pi M_i k_B T}}{\pi \sigma_i^2 \Omega^{(2,2)}} \quad (3-57)$$

where  $\sigma_i$  is the Lennard-Jones collision diameter (see section 3.1) and  $\Omega^{(2,2)}$  a collision integral that depends on the reduced temperature (equation (3-10)) and the reduced dipole moment  $\delta_i^*$ . The dipole moment is given by:

$$\delta_i = \frac{1}{2} \frac{\mu_i^2}{\epsilon_i \sigma_i^3} \quad (3-58)$$

with  $\mu_i$  and  $\epsilon_i$  representing the dipole moment and the Lennard-Jones potential well depth (see section 3.1), respectively. The values of  $\epsilon$  as  $\epsilon/k_B$ ,  $\sigma_i$ , and  $\mu_i$  must be specified in the transport file of the respective reaction mechanism. The collision integral  $\Omega^{(2,2)}$  is determined by interpolation of the tabulated values based on the Stockmayer potential given by Monchick and Mason [74].

The multicomponent diffusion velocity in the radial direction for species  $i$  and the thermal conductivity of the mixture are calculated by equations (3-59) [64] and (3-60) [75], respectively.

$$V_{i,r} = \frac{1}{x_i \bar{M}} \sum_{j \neq i}^{N_{sp}} M_j D_{ij} \frac{\partial x_j}{\partial r} - \frac{D_i^T}{\rho Y_i T} \frac{\partial T}{\partial r} \quad (3-59)$$

$$\lambda = \frac{1}{2} \sum_{i=1}^{N_{sp}} x_i \lambda_i + \frac{1}{\sum_{i=1}^{N_{sp}} \frac{x_i}{\lambda_i}} \quad (3-60)$$

Here,  $\bar{M}$  is the mean molar mass,  $D_{ij}$  the binary diffusion coefficient,  $D_i^T$  the thermal diffusion coefficient, and  $\lambda_i$  the thermal conductivity of species  $i$ . The mean molar mass can be calculated similarly to the mean specific heat capacity (see equation (3-56)), whereby the mole fraction must be used instead of the mass fraction. The diffusion coefficients are calculated from the solution of a system of equations defined by the so-called L matrix, whose components are given by Dixon-Lewis [76]. All required quantities such as the Lennard-Jones potential well depth and collision diameter or the dipole moment must be specified in the transport file of the reaction mechanism.

The thermal conductivities of pure species are calculated by the approach given by Warnatz [77] taking translational, rotational, and vibrational contributions into account.

### 3.3.5 Reaction pathway and sensitivity analysis

Reaction mechanisms can be used in combination with numerical models to perform reaction pathway and sensitivity analyses. Reaction pathway analyses are performed to unravel the formation and consumption pathways of products or reactants, respectively. In addition, comparative reaction pathway analyses with different reaction mechanisms can contribute to their

improvement, e.g., by adapting reactions of a mechanism that shows a better agreement with the experiments. Regarding the reaction pathway analysis, a distinction is made between integral (over the entire reactor length) and local analysis (at a specific position in the reactor). For a local analysis, the relative rates of production (ROP) and consumption (ROC) are calculated by equations (3-61) and (3-62), respectively.

$$\overline{ROP}_{ij} = \frac{\max(v''_{ij} - v'_{ij}, 0)q_i}{\sum_{j=1}^{N_R} \max(v''_{ij} - v'_{ij}, 0)q_i} \quad (3-61)$$

$$\overline{ROC}_{ij} = \frac{\min(v''_{ij} - v'_{ij}, 0)q_i}{\sum_{j=1}^{N_R} \min(v''_{ij} - v'_{ij}, 0)q_i} \quad (3-62)$$

The relative rates of production and consumption indicate the relative contribution of a reaction  $j$  to the net formation or consumption of a target species  $i$ , respectively. When studying the combustion or partial oxidation of hydrocarbons, usually only the pathway of carbon is considered in a reaction path analysis, e.g., along which reaction path a carbon atom of the fuel arrives in the products CO or CO<sub>2</sub>.

For an integrated reaction path analysis, the absolute rates of production or consumption are integrated over the total residence time in the reactor and divided by the integrated rates of production or consumption for all reactions in which the species of interest is involved (see equations (3-63) and (3-64)).

$$ROP_{ij} = \frac{\int \max(v''_{ij} - v'_{ij}, 0)q_i}{\sum_{j=1}^{N_R} \int \max(v''_{ij} - v'_{ij}, 0)q_i} \quad (3-63)$$

$$ROC_{ij} = \frac{\int \min(v''_{ij} - v'_{ij}, 0)q_i}{\sum_{j=1}^{N_R} \int \min(v''_{ij} - v'_{ij}, 0)q_i} \quad (3-64)$$

Consequently, the integral reaction path analysis considers the total formation and depletion of a species  $i$  during the reaction process. When comparing reaction mechanisms, local reaction path analyses are often preferred because they can be performed for a specific position in the reactor where, for example, the same fuel conversion is found.

A sensitivity analysis with respect to the reaction rate coefficients is performed to identify important, rate-limiting reactions within the reaction mechanism regarding a global parameter like ignition delay time or the formation or consumption of a target species. The latter is done by separately varying the  $A$ -factor of each reaction in the mechanism and evaluating its effect on the mole fraction of the respective species. The relative sensitivity is calculated by equation (3-65)

$$S_{ij} = \frac{\partial x_i}{\partial k_j} \frac{k_j}{x_i} \quad (3-65)$$

with  $x_i$  and  $k_j$  representing the mole fraction and rate coefficient of the specific species and reaction, respectively. A high positive sensitivity  $S_{ij}$  indicates a reaction that is important for

the formation of the species, whereas a high negative sensitivity indicates a reaction that is important for its consumption. The sensitivity coefficients can be integrated in time to obtain coefficients for a specific position in the reactor. This is done to identify reactions that have a direct influence on the mole fraction of a target species at this position.

---

## 4 Experimental methodology

In this chapter, the experimental setup and the methods for evaluating the experimental results are presented. First, the flow reactor and its periphery used in this study are described, followed by an analytical and numerical validation of the plug-flow assumption. Second, the specifications of the analytical instruments, i.e., TOF-MS and GC/MS, are outlined. In this context, the quantification methods for each instrument are described. Finally, an uncertainty analysis of the experimental results is presented.

### 4.1 Flow reactor

Figure 4-1 shows a schematic diagram of the flow reactor and its periphery. Note that this diagram represents the most recent version of the experimental setup. The setup was modified continuously and the status at the time of the respective study is mentioned in the corresponding chapter.

The flow reactor consists of a 65 cm long quartz tube ( $8 \times 1$  mm) that is embedded in a silicon-coated Inconel tube ( $12 \times 1$  mm). Quartz was chosen as the reactor material because of its chemical inertness and Inconel as the pressure shell because of its high mechanical stability and oxidation resistance. The gap between both tubes is sealed with Teflon tape at both ends to guide the gas through the quartz tube. The silicon coating ensures that no catalytic reactions take place between the Inconel wall and gas entering the gap. The Inconel tube is enclosed by a 50 cm long copper shell ( $32 \times 8$  mm) for uniform heating, while the heat is provided by two 6 m long heating tapes wrapped around the copper shell. The temperature is controlled by two type-K thermocouples placed in 5 mm deep drill holes in the copper shell and temperature controllers. An isothermal zone of 40 cm length is established (see section 4.1.2). Heat losses are minimized by insulation with high-temperature-resistant fabric tape and fleece. For reactor operation at temperatures above 1000 K, the copper shells can be removed and an oven can be used for heating. This design allows temperatures of up to 1400 K.

Gases are metered by Coriolis mass flow controllers pressurized from the feed gas cylinders. Liquid reactants are introduced to a home-made evaporator by a calibrated high-performance liquid chromatography (HPLC) or syringe pump. In the most recent setup, the liquid feeding system was modified to overcome the pulsing nature of both pumps and to allow lower amounts of liquids to be introduced to the evaporator. This is done by a stainless-steel syringe filled with the liquid and pressurized from an argon gas cylinder. A Coriolis mass flow controller downstream of the syringe is used to meter the liquid up to very low mass flows of 0.1 g/h, which corresponds to a volume flow rate of less than 0.5 sccm in the example of *n*-heptane.

The evaporator consists of a 1 m long bent stainless-steel tube placed in a temperature-controlled oil bath. The vapor is entrained in the diluent gas used in the respective study and mixed with oxygen and other remaining reactants downstream of the evaporator and well before entering the reactor. The reactor pressure is controlled by a needle valve downstream of the reactor and then reduced to the sampling pressure of the instrument used for product analysis (see sections 4.2 and 4.3). Pressure fluctuations were always lower than 0.5 %. All lines made of stainless steel downstream of the reactor are heated to at least 373 K to prevent condensation of products. If liquid reactants are used, also the lines between the evaporator and the reactor are heated. This is indicated by the sinusoidal curves in the schematic diagram. In case of an unexpected pressure increase, the reactor is equipped with a safety valve that opens at a pre-defined pressure and releases the gas to the exhaust.

The final setup is designed for reactor operation at temperatures of up to 1000 K (copper shells) or 1400 K (oven) and pressures from 0.1 to 40 bar.

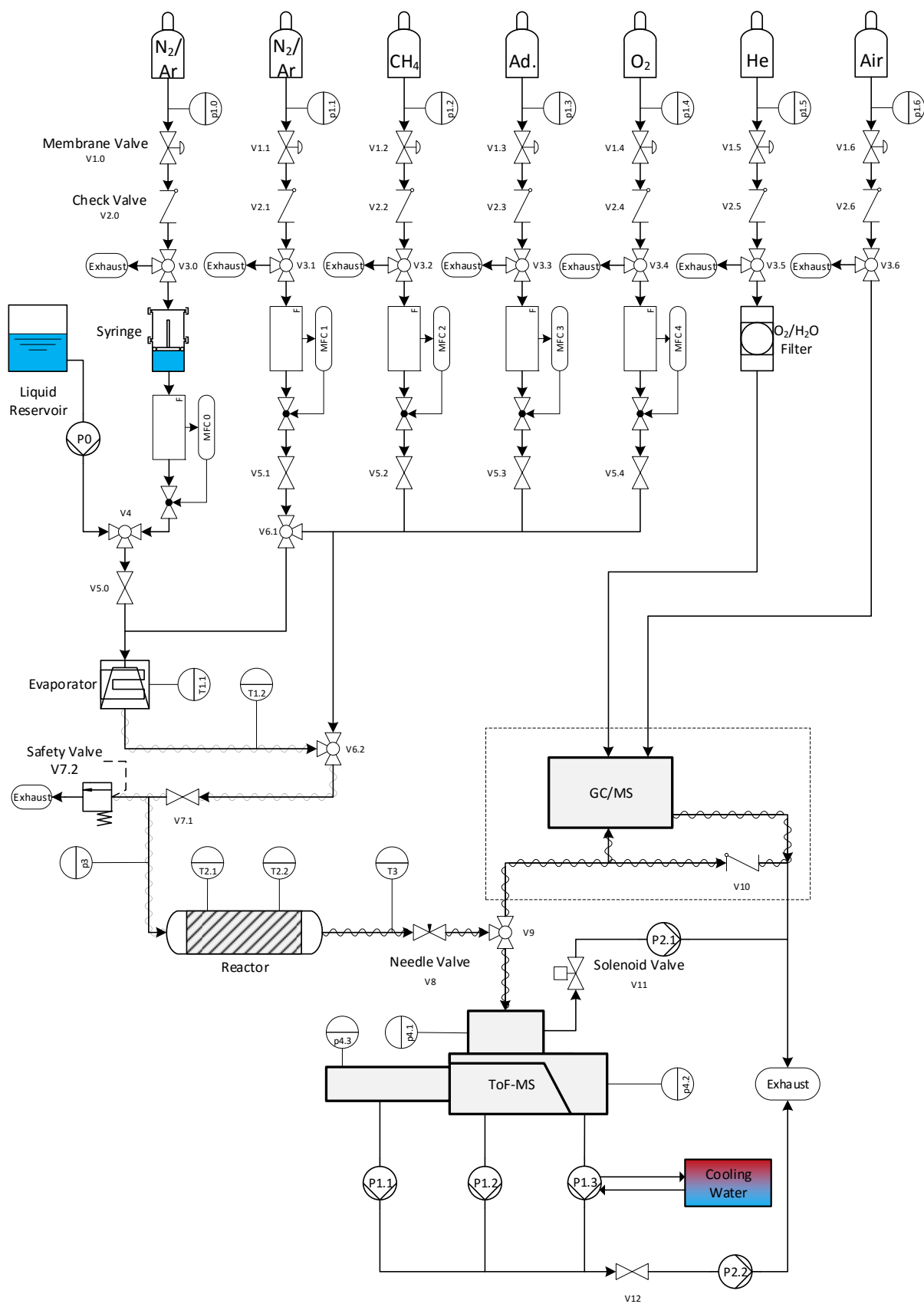


**Figure 4-1:** Schematic diagram of the experimental setup. MFC: mass flow controller, V: Valve, T: Temperature sensor, p: pressure sensor, P: pump.

### 4.1.1 Flow conditions

All experiments are performed at a constant volume flow rate of 280 sccm (standard conditions:  $p = 1$  atm,  $T = 273.15$  K) to approximate plug flow. This approximation was validated by the dispersion model described in section 3.1 and by two-dimensional simulations using the boundary-layer flow model described in section 3.2. The results of both approaches are presented here.

First, the flow regime in the reactor is characterized by calculating the Reynolds number using equations (3-1) – (3-4). The axial velocity is calculated by dividing the reactor volume by the volume flow rate at the investigated conditions. The ideal gas law is used to convert the volume flow rate at standard conditions to the volume flow rate at the investigated conditions and to calculate the density of the gas mixture. The dynamic viscosity is calculated for a mixture of methane, oxygen, and argon or nitrogen with mole fractions of 0.05, 0.05, and 0.9, respectively. This mixture is representative of all mixtures investigated in this study, except for the methane/*n*-heptane mixtures, where a lower dilution was used (see Table 7-1). To cover these mixtures, Reynolds numbers for the two mixtures that deviated the most are additionally calculated. The very small fractions of additives used in the studies are neglected as they do not significantly influence the results. Table 4-1 shows the Reynolds numbers calculated for the mixtures at temperatures of 373 and 973 K.

**Table 4-1:** Reynolds numbers.

Mixture / mol%				$Re$	$Re$
Ar	N <sub>2</sub>	CH <sub>4</sub>	O <sub>2</sub>	(373 K)	(973 K)
90	0	5	5	65.51	32.49
0	90	5	5	58.76	30.56
0	78	10	12	58.94	30.54
0	64	32	4	59.60	30.04

As seen in Table 4-1, the Reynolds numbers are well below the critical value of 2300 so that the flow is laminar at all conditions.

To check whether the dispersion model can be used, the residence time distribution (RTD) of an injected tracer was determined experimentally. A small amount of propane was injected via a syringe 25 cm upstream of the reactor. The propane was entrained in an argon flow of 280 sccm at a reactor temperature of 293 K. The TOF-MS was used to measure the propane signal at the reactor outlet. Because the data acquisition of the used TOF-MS is not fast enough to record several mass spectra in the short time period of the outflowing propane, only one mass spectrum with a long averaging time was taken. The increasing signal of propane was recorded by a camera with 60 frames per second and the signal height was noted for every frame until the signal stopped increasing. The RTD was then obtained by plotting the signal height increase over the reduced residence time (see section 3.1). The obtained distribution was in good agreement with a Gaussian shape so that the variance was determined and used in equation (4-1) [51] to calculate  $D_{\text{Disp}}/uL$ .

$$\sigma_{\theta}^2 = 2 \frac{D}{uL} + 8 \left( \frac{D}{uL} \right)^2 \quad (4-1)$$

The result of  $D_{\text{Disp}}/uL=0.0031$  shows that the plug-flow assumption is justified. Figure 4-2 shows the RTD corresponding to the value of  $D_{\text{Disp}}/uL=0.0031$  (red line) and the measured values (symbols) scaled to the curve using a constant factor for all values. A very good agreement between the measurements and the calculated RTD is seen so that the dispersion model is applicable. It is interesting to note that the calculated RTD for a propane/argon mixture at 293 K (red, dashed line) is broader than the experimental curve. This effect could be caused by experimental uncertainties or the calculation of binary diffusion coefficients without considering its dependence on mixture composition. But, because the calculated RTD is broader, it can be assumed that the plug-flow assumption is valid if the calculations indicate this. To cover all investigation parameters, RTDs for different values of  $D_{\text{Disp}}/uL$  were calculated for mixtures of Ar/O<sub>2</sub>, Ar/CH<sub>4</sub>, N<sub>2</sub>/O<sub>2</sub>, and N<sub>2</sub>/CH<sub>4</sub>, temperatures between 373 K and 973 K, and a volume flow rate of 280 sccm using equations (3-6) – (3-14). Because the RTDs of the nitrogen and the argon mixtures are very similar only the RTDs for the argon mixtures with the highest values of  $D_{\text{Disp}}/uL$  are shown in Figure 4-2 (blue lines). While the solid line represents the RTD for an Ar/O<sub>2</sub> mixture at 373 K, the dashed line represents the RTD for the same mixture at 973 K. RTDs for  $D_{\text{Disp}}/uL = 0.01$  and 0.1 are also plotted to show the limit at which the plug-flow approximation is acceptable and the broadening of the RTDs at lower values, respectively.

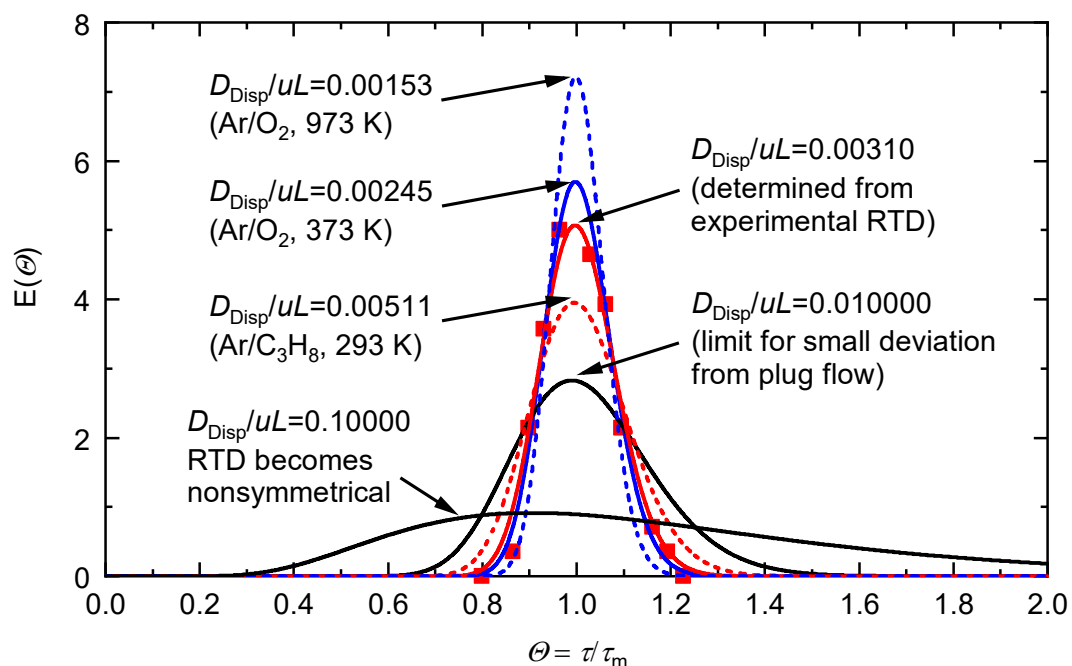


**Figure 4-2:** Residence time distributions (RTD) according to the dispersion model. Red symbols and line represent experimental values and the associated RTD calculated with the value of  $D_{\text{Disp}}/uL$  obtained from the experiment, respectively. Blue lines indicate RTDs for calculated values of  $D_{\text{Disp}}/uL$  and black lines RTDs for  $D_{\text{Disp}}/uL \leq 0.01$  where they become nonsymmetrical.

Figure 4-2 shows that the RTD becomes narrower at higher temperatures. The much larger binary diffusion coefficient at 973 K compared to 373 K nearly compensates for the higher

velocity at this temperature so that the dispersion coefficient increases only slightly compared to the velocity. This compensation results in a lower value of  $D_{\text{Disp}}/uL$ .

In addition to the RTDs, calculated values of  $D_{\text{Disp}}/ud_R$  are correlated with the Peclet number (see section 3.1) in Figure 4-3 considering the Ar/O<sub>2</sub> and N<sub>2</sub>/O<sub>2</sub> mixtures and three different volume flow rates (50, 280, 1000 sccm).

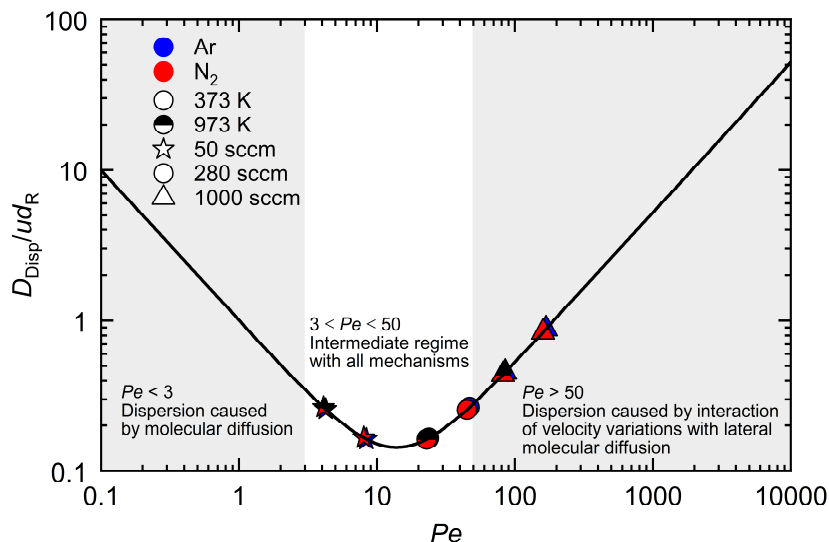


**Figure 4-3:** Axial dispersion ( $D_{\text{Disp}}/ud_R$ ) correlated with the Peclet number  $Pe$  for selected mixtures and volume flow rates. The minimum ( $Pe = 13.8$ ,  $D_{\text{Disp}}/ud_R = 0.144$ ) represents the point at which the plug-flow assumption is best fulfilled. Inspired by Levenspiel [51,78].

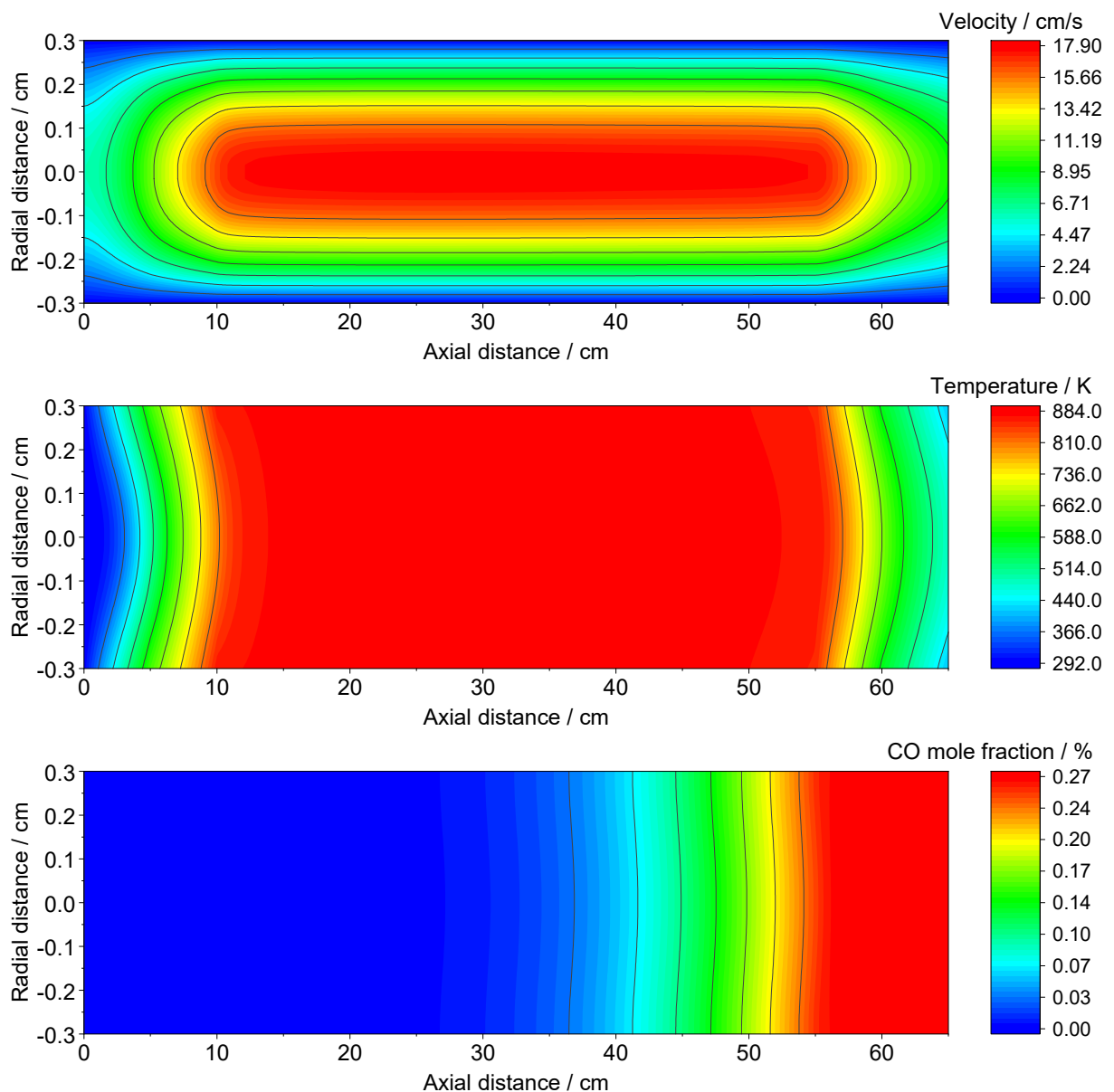
Figure 4-3 shows that the calculated values with respect to the volume flow rate of 280 sccm are very close to the minimum, especially at higher temperatures. At higher flow rates the values are shifted to the right so that the deviation from plug flow increases. In contrast, at lower flow rates (here 50 sccm) the points are shifted to the left and the deviation from plug flow is as small as for 280 sccm. But, the lower the flow rate, the higher the residence time of the gases in the reactor. This would in turn lead to an increased stabilization time after a change of reactor conditions and would also require a reactor length of less than 65 cm because the reactions would only occur in the first cm of the reactor. A shorter reactor would again raise the question to what extent the plug-flow assumption is justified. Also, it becomes increasingly difficult to meter the required gas volumes, as the total flow rate decreases. In summary, the volume flow rate of 280 sccm is a very good compromise between residence time and practicability, while providing a good approximation to plug flow.

The plug-flow approximation was further validated by boundary-layer flow simulations described in section 3.2. Schwarz et al. [79] showed that the results of these simulations are in excellent agreement with the results of CFD calculations considering the complete set of steady-state, laminar Navier-Stokes equations, especially regarding the mole fractions at the reactor outlet.

For the boundary-layer flow model, the inlet velocity profile must be given as input. After entering a tube, a certain distance is required for the fluid to build up to a fully developed parabolic flow. This distance can be calculated by equation (4-2) [58].

$$L_e = 0.035D_R Re \quad (4-2)$$

$L_e$  is 1.38 cm for the highest Reynolds number shown in Table 4-1. Because the transfer line to the reactor after the mixing section of the reactants is much longer, a fully developed parabolic flow is chosen in the simulations. Figure 4-4 shows the calculated velocity, temperature, and CO mole fraction distribution using the example of a  $\text{CH}_4/\text{O}_2$  mixture at 873 K, 6 bar, and  $\phi = 2$ . The recently published reaction mechanism of Kaczmarek et al. [80] was used for the simulations. The measured temperature profile for the set temperature of 873 K (see section 4.1.2) was used for the wall temperature of the reactor and the inlet temperature was set to 293 K.



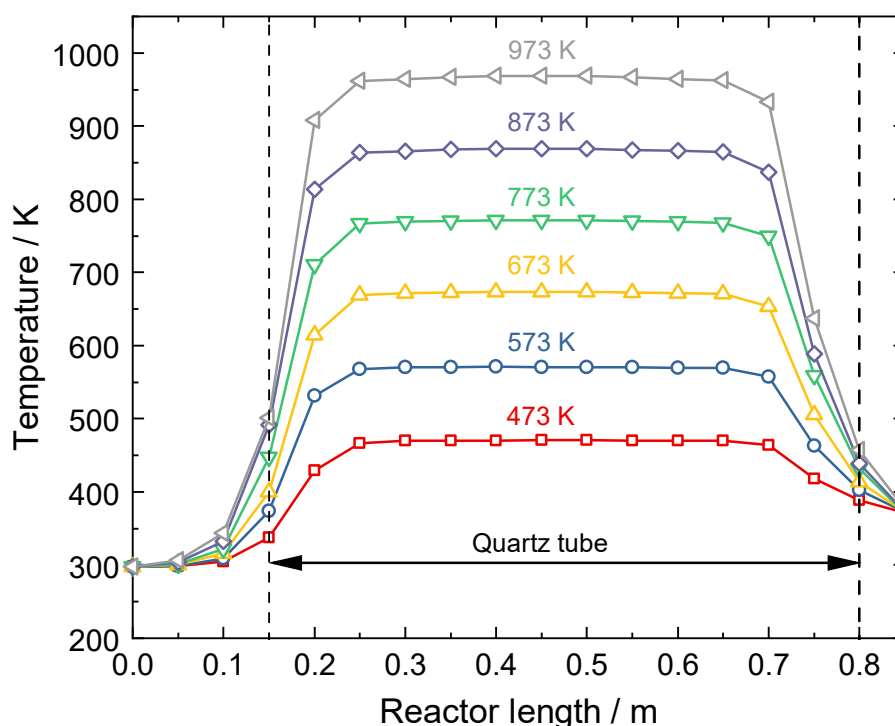
**Figure 4-4:** Velocity, Temperature, and CO mole fraction distribution as a function of radial and axial distance for a  $\text{CH}_4/\text{O}_2$  mixture at  $\phi = 2$ ,  $p = 6$  bar, and  $T = 873$  K.

Figure 4-4 clearly shows the parabolic velocity profile with the highest velocity in the center of the tube. But, the temperature and the CO mole fraction exhibit much smaller radial gradients.

That means that the heat transfer and diffusion in the radial direction are fast enough to overcome the velocity gradients so that the flow can be regarded as plug flow. A comparison between the mole fractions at the reactor outlet of boundary-layer flow and plug-flow simulations also showed no significant difference. Because the two-dimensional simulations need much more computational time (factor 10 – 100), only plug-flow simulations were performed in most cases.

### 4.1.2 Temperature profiles

The temperature profiles are required to assign the set temperature of the temperature controller to a gas temperature inside the reactor. In addition, they are required as input for the simulations. Figure 4-5 shows an example of temperature sets, measured inside of the reactor at a pressure of 1 bar and an argon flow of 280 sccm. The temperatures were measured by a type-K thermocouple, starting at 15 cm upstream of the reactor and ending at the needle valve. In this case, the lines downstream of the reactor were heated to 373 K. As can be seen from the figure, there is a steep rise and fall in temperature before and after the heating zone, which has an isothermal zone ( $\pm 5$  K) of at least 40 cm. The reactor (quartz tube embedded in the silicon-coated Inconel tube) was positioned in such a way that the temperature in front of and behind the reactor always remains below 500 K to avoid catalytic reactions with the stainless-steel tubes. The influence of pressure on the temperature profile was examined up to a pressure of 5 bar and was found negligible. It is assumed that this also applies to pressures up to 20 bar.



**Figure 4-5:** Set of temperature profiles measured in the center of the reactor at an argon flow of 280 sccm and a pressure of 1 bar for the given set temperatures.

Using nitrogen instead of argon for the temperature measurements only resulted in slightly different heating and cooling zones. This did not affect the simulation results significantly.

Additionally, it was found that computational time can be saved by using reduced temperature profiles without considering the post-heating zone as well as the first 15 cm upstream of the reactor without influencing the simulation results. In contrast, neglecting the steep increase and decrease of the temperature led to slightly different predictions, especially for mixtures that contained reactants with low-temperature chemistry.

## 4.2 Time-of-flight mass spectrometer (TOF-MS)

A time-of-flight mass spectrometer with a two-stage ion extraction and a two-stage reflectron from Kaesdorf was used for the detection of species during the partial oxidation of several fuels. The basic principle of a TOF-MS is outlined in section 2.1.3. Here, only the specifications of the used instrument including the sampling process are shown.

The product species are transferred to the ionization chamber of the TOF-MS by a two-stage molecular-beam extraction described in section 2.1.1. For this purpose, the reactor pressure is throttled down to  $\sim 200 - 500$  mbar (depending on the exact nozzle diameter) and the product mixture is transferred to the intermediate chamber via a nozzle with an opening of  $60 \mu\text{m}$ . The pressure in the intermediate chamber is typically in the range of  $10^{-4}$  mbar. A second nozzle, called a skimmer, extracts the isentropic core of the molecular beam into the ionization chamber, kept at  $\sim 10^{-7}$  mbar, where the product gas is ionized by electron ionization. A kinetic energy of the electrons of 17 eV was used to ionize all products including argon and minimize fragmentation as much as possible. But fragmentation could not be avoided completely as the energy of 17 eV is much higher than the ionization energies of most species so it had to be considered in the data reduction (see section 4.2.1). The electron beam is guided by a magnetic field generated by two permanent magnets. Both the ionization and the following extraction are pulsed to avoid the detection of ions with the same  $m/z$  ratio at different times. The extraction is done in two stages to compensate for the different starting positions of the ions. To ensure that the drift region is field-free, it is shielded by the liner against the housing of the mass spectrometer as shown in Figure 2-3. The liner potential equals the potential of the grounded counter electrode and the initial grid of the reflectron. A deflection unit is located between the counter electrode and the initial grid to compensate for uniform transverse velocities of the ions. In addition, an electrostatic Einzel lens is used to compensate for the diverging ion beam due to fragmentation and space charge effects. Entering the reflectron, consisting of the initial, middle, and end grid, the ions are decelerated by an increasing potential and reflected at a small angle towards the detector. A post-acceleration zone between the reflectron and detector ensures that even very heavy ions can be detected. A chevron plate was used as a detector in conjunction with a pre-amplifier to amplify the voltage signal which is then registered by a multichannel analyzer (FAST P7887) with a time resolution of 250 ps. For data acquisition, a threshold can be defined from which voltage pulses are counted as signals. If the threshold is correctly adjusted, only one ion per mass spectrum arrives at the detector.

The voltages can be adjusted manually with potentiometers on the control unit of the spectrometer. They are transferred to a computer via an A/D converter and displayed in the software TOF5.0. In this software, the heating current of the filament, the pulsation and delay times of ionization and extraction, the kinetic energy of the electrons, and the threshold for data acquisition can be set. In addition, the repetition rate (number of spectra per time) and the averaging

time or number of summed up spectra for a measurement can be adjusted. In this study, a repetition rate of 20 kHz was used in combination with 5 to 10 million sweeps to achieve a good signal-to-noise ratio.

### 4.2.1 Quantification of TOF-MS data

To assign a species to a signal, the time-of-flight spectra must be transformed into mass spectra. This is done by equation (4-3):

$$m/z = at^2 + bt + c \quad (4-3)$$

The coefficients  $a$ ,  $b$ , and  $c$  can be determined by assigning at least three signals to their corresponding  $m/z$  ratio. The more signals are known and used, the more accurate the fitting becomes. For the highest accuracy, the signals used for the fitting should cover the whole mass range of the spectrum if possible. The signal of each species is proportional to its mole fraction in the gas mixture. Consequently, the signals must be integrated prior to quantification. If all voltages of the TOF-MS are set correctly, the signals can be approximated by a Gaussian distribution. In this study, both OriginPro 2019b and Flammen-Fit4.4 were used for the integration of the Gaussian-shaped signals. Flammen-Fit4.4 was developed by Vietmeyer [81] within his diploma thesis at Bielefeld University. The software allows the integration of overlapped signals by fitting the Gaussian curves to the raw signal so that the sum curve of all Gaussian curves corresponds to the raw signal. To achieve the most accurate deconvolution of the signals, the mass resolution of the mass spectrometer defined by the user is considered. After importing a species list that contains all species of interest with their respective molecular mass and input of the coefficients for the mass calibration, Flammen-Fit4.4 automatically integrates all signals. Adjustments can be made by individual specifications of the mass resolution or tolerance of the signal position. The peak analyzer tool of OriginPro 2019b was used when integration with Flammen-Fit4.4 was not possible, e.g., due to a very large overlap of adjacent signals.

To convert the measured signal intensities of product species to mole fractions, the relationship between the two quantities must be known. In general, the signal intensity  $S$  of a species  $i$  in the mass spectrum at given kinetic energy of the electrons is described by the convolution of the electron-ionization cross section (EICS)  $\sigma_i$  and the energy distribution function  $f(E)$  of the ionizing electrons. This is shown in equation (4-4) [82]

$$S_i(E) = x_i \cdot A \cdot SW \cdot \Phi \cdot FKT \cdot D_i \cdot \int \sigma_i(E) \cdot f(E) dE \quad (4-4)$$

where  $x_i$  represents the mole fraction of species  $i$ ,  $A$  an energy-specific instrument factor,  $SW$  the number of summed up spectra,  $\Phi$  the number of electrons,  $FKT$  a temperature-dependent sampling function, and  $D_i$  a mass discrimination factor that depends on the molecular mass of the species. The mass discrimination factor considers the detection efficiency of ions of different masses, for example, because of the enrichment of heavy ions in the ionization chamber or the dependency of the detector sensitivity to slow and fast ions. The equation is simplified by

referring the signal of species  $i$  to the signal of a reference species “ref” as all quantities related to the sampling process or the used instrument are equal for both signals.

$$\frac{S_i}{S_{\text{ref}}} = \frac{x_i}{x_{\text{ref}}} \frac{D_i}{D_{\text{ref}}} \frac{\int \sigma_i(E) f(E) dE}{\int \sigma_{\text{ref}}(E) f(E) dE} \quad (4-5)$$

Because of the post-acceleration region before the detector and the relatively narrow range of molecular masses of the species relevant in this study, the mass discrimination factors can also be neglected. The remaining unknown quantities can be determined either by direct or indirect calibrations.

For direct calibration, all unknown quantities on the right-hand side of equation (4-5) except the mole fractions are combined to a species-specific calibration factor  $k_i$ . This simplifies the equation to:

$$\frac{S_i}{S_{\text{ref}}} = \frac{x_i}{x_{\text{ref}}} k_i \quad (4-6)$$

The calibration factor  $k_i$  can be determined by measurements with cold gas mixtures of known composition using the same instrument settings as for the experiments. Usually, only one species to be calibrated is mixed with the dilution gas to prevent fragments of other species to contribute to the signal. The mixtures can either be prepared manually using mass flow controllers or bought from a gas supplier. Three to five measurements are typically performed for each binary gas mixture. The ratios of the signal intensities are then plotted over the mole fraction ratios in a diagram. The calibration factor  $k_i$  corresponds to the slope of the regression line that runs through the plotted points. Once calculated,  $k_i$  can be used to calculate the unknown mole fraction of the species  $i$  detected in the product gas mixture. To apply this method, the mole fraction of the reference gas must be known. Here, argon is used as the reference, because it is used as a dilution gas in large excess and its mole fraction is expected to remain constant during the experiment. Argon was used as a dilution gas in all experiments involving the TOF-MS because its signal does not overlap with signals of interest.

The calibration measurements are also used to determine the fragmentation patterns and the ratios of each fragment signal and the signal of the molecular ion for all calibrated species. This allows the signals in the product gas measurements to be corrected for the contribution of the fragments.

Not all species can be calibrated directly, e.g., because they are radicals, extremely poisonous species, or species that cannot be easily transferred to the gas phase. In this case, only indirect calibrations can be done using the EICS of the species at a given energy. Usually, EICS at some low electron energy are only available for a few species in the literature [83] so that the “Relative Ionization Cross Section” (RICS) method developed by Biordi [84] must be used. Here, it is assumed that the EICS of a stable reference species S shows a similar dependence on the ionization energy as a chemically and structurally similar reactive species R. In that case the ratio of the EICS of the two species at an electron energy differing from their respective ionization energies by the same amount is equal to the ratio of the EICS at 70 eV (equation (4-7)).

$$\frac{\sigma_S(IE_S + b)}{\sigma_R(IE_S + b)} = \frac{\sigma_S(70 \text{ eV})}{\sigma_R(70 \text{ eV})} \quad (4-7)$$

Using equation (4-7), the EICS for a reactive species at a given electron energy  $E$  can be derived from the EICS of the reactive and stable species at 70 eV and the trend of the EICS of the stable species. The latter can be determined from an energy scan of the stable species, where the electron energy is increased stepwise from a value below the ionization energy of the species up to a much higher electron energy. The resulting curve (signal intensity plotted over electron energy) is called the ionization efficiency curve. EICS at 70 eV are known from measurements or can be calculated by an empirically-derived addition theorem for organic molecules proposed by Fitch and Sauter [85]. The EICS or the calibration factor  $k$  of the indirect calibrated species can then be derived from the ionization efficiency curve of the stable species and equations (4-5)-(4-7). The required energy distribution function can be approximated by a Gaussian distribution:

$$f(E) = \frac{1}{\sqrt{2\pi\sigma^2}} \exp\left(-\frac{(E - \mu)^2}{2\sigma^2}\right) \quad (4-8)$$

In equation (4-8)  $\sigma$  represents the standard deviation and  $\mu$  the expectation of the distribution. The standard deviation can also be expressed by the width at half maximum of the energy distribution, which is approximately 2.4 (exact:  $2\sqrt{2\ln 2}$ ) times  $\sigma$ . The expectation  $\mu$  corresponds to the position of the maximum of the energy distribution.

It must be noted that total ionization cross sections are required for the RICS method, which are the sum of the ionization cross sections of the molecular ion and its fragments. Therefore, the calibration factors of the respective reference species, which are typically only determined for the molecular ion, must be corrected by the proportion of their fragments.

In this study, nearly all species of interest are calibrated directly. The binary mixtures are prepared with the mass flow controllers or the HPLC pump in case of liquid species.

### 4.3 Gaschromatograph/Mass spectrometer (GC/MS)

In addition to the TOF-MS, a GC/MS system was used to analyze the reaction products during the partial oxidation of several mixtures. The system consists of a 7890 Agilent gas chromatograph coupled to a 5977 Agilent quadrupole mass spectrometer. For sample introduction, the GC is equipped with a GERSTEL auto-sampler. Figure 4-6 schematically shows the GC/MS system and the reactor sampling interface. In early studies, a heated sampling container was used so that the product gas had to be extracted manually from the reactor. In the current configuration, the product gas can be taken directly from the reactor via the auto-sampler. For this purpose, a T-piece is installed downstream of the needle valve, which is closed with a septum to allow the auto-sampler syringe to extract the product gas and introduce it to the split/spitless injector. A split ratio of 1:3 – 1:15 was used depending on the dilution of the mixture in the reactor. Both the lines downstream of the reactor and the syringe are heated to avoid condensation of low-volatility components.

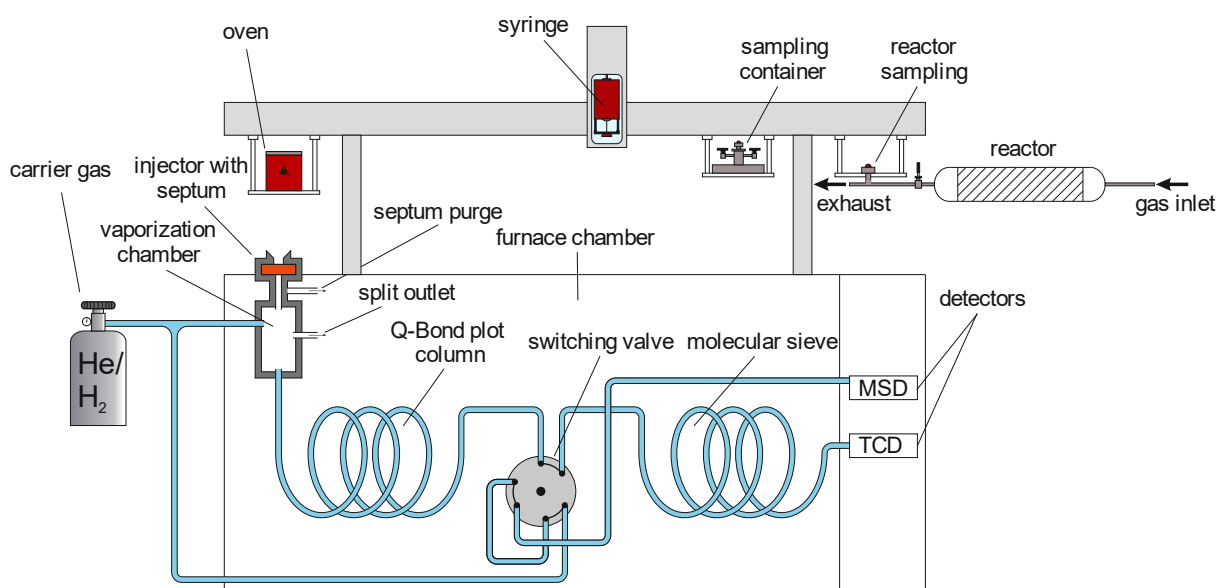


**Figure 4-6:** GC/MS system and reactor sampling interface.

The product gas mixture is separated by two different sequential columns. The first column that is connected to the injector is a Rt-Q-Bond PLOT column. Divinylbenzene is used as the stationary phase which makes the column suitable for the separation of  $C_1$  to  $C_3$  hydrocarbons as well as isomers and alkanes up to  $C_{10}$ . It is also used for the separation of carbon dioxide and water. Permanent gases (Ar,  $N_2$ ,  $O_2$ ,  $H_2$ , CO,  $CH_4$ ) are not separated and they would elute together at the end of the column leading to a broad signal in the chromatogram. This coelution is counteracted by a switching valve which directs the permanent gases into the second column, a molecular sieve 5A, where they are separated. Both columns are 30 m long and have an inner diameter of 0.32 mm. The permanent gases are detected by a single-cell TCD (see section 2.2.3), while the remaining products are detected by a QMS (see section 2.1.4). To increase the detector sensitivity for ions with higher mass or lower kinetic energy, the QMS is equipped with a high-energy dynode (HED) located in front of the detector (see Figure 2-4). A very high negative potential is applied to the HED to attract the positive ions with great force. When the ions hit the HED, a huge number of secondary electrons are emitted and attracted to the more positive channeltron. This detector design significantly increases the signals of the ions being detected.

A mixture of 12.5 %  $H_2$  and 87.5 % He is used as a carrier gas to allow the detection of hydrogen. Using pure He as carrier gas would result in a signal inversion and nonlinear dependence of the  $H_2$  signal on the amount of  $H_2$  in the mixture. This is caused by a decrease of the thermal conductivity of a He/ $H_2$  mixture with an increasing amount of  $H_2$  up to a local minimum at  $\sim 6.5$  %  $H_2$  before it increases again up to the thermal conductivity of pure  $H_2$  [86,87] as shown in Figure 4-7. The carrier gas mixture ensures that the  $H_2$  concentration is always higher than that at the minimum of the curve in Figure 4-7. A quadratic relationship between the  $H_2$  signal and the  $H_2$  amount in the mixture is observed while maintaining the same sensitivity to other species.

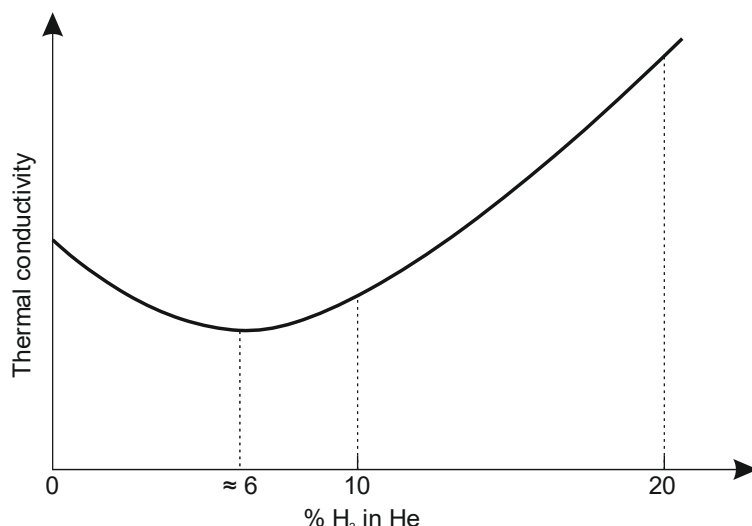


**Figure 4-7:** Trend of the thermal conductivity of He/H<sub>2</sub> mixtures (adapted from [86]).

The GC was operated in a constant volume flow mode. The volume flow was chosen so that the average carrier gas velocity was close to the minimum of the van-Deemter curve (see section 2.2.2.).

### 4.3.1 Quantification of GC/MS data

Similar to the quantification procedure of TOF-MS data, the signals in the chromatogram must first be assigned to the corresponding species. The retention times of the permanent gases were determined by separate injections of the respective species. The remaining species, all detected by the QMS, can be identified by comparing their fragmentation patterns to fragmentation patterns from a NIST library implemented in the Agilent Qualitative Analysis 6.0 software. This software was also used for numerical integration of the signals in the chromatogram. Only for signals that could not be completely separated, OriginPro 2019b's peak analyzer tool was used for integration, assuming Gaussian-shaped signals.

The calibration procedure is based on the procedures mentioned in section 4.2.1. But, in contrast to the procedure used for TOF-MS measurements, most species were calibrated using certified calibration mixtures containing the species of interest. This is possible because most species are completely separated and fragmentation of one eluting species has no effect on another. Three to five measurements with different dilutions of the gas mixtures were performed to obtain the species calibration factors according to equation (4-6). At low split ratios, the high dilution used in the experiments led to "peak tailing" with respect to the dilution gas, indicating column oversaturation. In that case, the method of the external standard was additionally used for the direct calibration of the product species. The calibration factor is then calculated according to equation (4-9).

$$\frac{S_i}{x_i} = k_i \quad (4-9)$$

Using this method, the calibration measurements must be performed under the same conditions as the measurements of the product gases, since pressure and temperature deviations are not compensated by a reference species.

For species whose calibration standard is not available or stable, indirect calibrations need to be done to obtain a calibration factor. The species detected by the QMS can be calibrated using the RICS method described in section 4.2.1. Because the QMS is typically operated at 70 eV and the signals of every species contain the contributions from fragments, no corrections are required for the calibration factors of the reference species calibrated directly. In addition, the influence of the energy distribution on the signal of a species can be neglected as the trend of the EICS in the region near 70 eV is similar for all species and the deviation of the energy relative to 70 eV is small. The calibration factor of a species can then be determined from the calibration factor of the reference species and the EICS at 70 eV as follows:

$$k_i = k_{\text{ref}} \frac{\sigma_i}{\sigma_{\text{ref}}} \quad (4-10)$$

This approach was tested for direct calibrated species like ethane and ethylene and found to be accurate within 20 %.

For species detected by the TCD, mole fractions can be calculated from thermal response factors from the literature. These response factors correlate the signal intensity with the amount of the species in the mixture. If no internal standard is used, the mole fractions can be calculated according to equation (4-11)

$$x_i = \frac{S_i \cdot TR_i}{\sum_{j=1}^{N_{\text{sp}}} S_j \cdot TR_j} \cdot \left( 1 - \sum_{j=1}^{N_{\text{sp(MSD)}}} x_j \right) \quad (4-11)$$

with  $TR_i$  indicating the thermal response of species  $i$ . As shown by equation (4-11) the mole fraction of a species  $i$  can be obtained by normalizing the response value of a species  $i$ , given by the product of signal intensity and thermal response, by the sum of the response values of all species. The normalization has the same effect as an internal standard since pressure and temperature changes are assumed to affect the signals of all species equally. Because in this study only a few species are detected with the TCD and the rest with the MSD, the mole fractions of species detected with the TCD can only add up to 1 if no species are detected with the MSD. If this is not the case, the mole fractions obtained by the left part of the equation (4-11) must be multiplied by the maximum possible sum of mole fractions. This factor is obtained by subtracting the sum of the mole fractions of all species detected by the MSD ( $N_{\text{sp(MSD)}}$ ) from one. Thermal response factors for many species can be found in [88]. Dietz [88] notes that the thermal response factors are independent of the used detector, carrier gas, temperature, and flow rate. Gislason and Wharry [89] determined response factors of several species using six different TCDs and compared the results to the values given by Dietz [88]. They showed that the response factors differ between -19 % to +29 % from the reported values, which clearly showed the dependence of the response factors on the instrument.

In this study, direct calibrations are always done for all permanent gases.

## 4.4 Uncertainties

The content of this chapter is based on the supplementary material of the paper presented in chapter 10 of this study [90].

### 4.4.1 Direct calibration

General uncertainties are estimated using the error propagation law, considering the uncertainties of all used instruments.

Some errors such as slight pressure fluctuations in the reactor can be observed during the measurements. Other measurement uncertainties can be determined by repeated measurements. Error sources are mass flow controller (MFC), time-of-flight mass spectrometer, gas chromatograph, and HPLC or syringe pump. The errors that emanate from the slight temperature fluctuations of the evaporator can be neglected due to insignificance. The MFCs from MKS and Bronkhorst are factory-provided with tolerances. This causes measurement uncertainties, which are quantified by the manufacturer with a total of 1 % and 0.5 % of the mass flow rate for the MKS and Bronkhorst MFCs, respectively. Unlike the MFCs, there is no quoted measurement uncertainty for the used HPLC and syringe pump. One reason for this is that components such as capillaries or syringes can be individually exchanged or adapted. Calibration measurements were made to keep the error between the set and the delivered flow rate as small as possible. Since the calibration is also accompanied by uncertainties, it was checked for reproducibility. This procedure resulted in a mean deviation of the calibrations of 0.3 %.

Pressure fluctuations were less than 0.5 % during the experiments.

Reproducibility measurements have been made for the TOF-MS and GC/MS. These gave a standard deviation of  $\leq 5$  %. This value considers the uncertainties of the instruments and the integration of the signals.

When calculating a total uncertainty, the influence of the HPLC or syringe pump and pressure fluctuations are neglected. Only the measurement uncertainties of the TOF-MS or GC/MS and the MFCs are included in the calculation. The Gaussian error propagation law (see equation (4-12)) is used to determine an overall uncertainty in the calculated mole fractions.

$$\Delta z = \sqrt{\left(\frac{\partial f}{\partial a} \Delta a\right)^2 + \left(\frac{\partial f}{\partial b} \Delta b\right)^2 + \left(\frac{\partial f}{\partial c} \Delta c\right)^2 + \dots} \quad (4-12)$$

Here,  $z$  represents a function of measured mole fractions and  $\Delta z$  the absolute uncertainty in these mole fractions. The single uncertainties are described with  $\Delta a$ ,  $\Delta b$ , and  $\Delta c$  and can represent estimated values, calculated uncertainties, or manufacturer information.

To determine the total uncertainty, the absolute uncertainty for the mole fractions used in the calibration measurements is first calculated. Since all calibration measurements are carried out using two mass flow controllers, the corresponding uncertainties of 1 % or 0.5 % (see above) each must be considered. The resulting absolute uncertainties in the mole fractions of the species  $i$  to be calibrated and the dilution or reference gas have an influence on the determined calibration factor of the species  $i$ . Since the respective samples are analyzed with the GC/MS or TOF-MS, their measurement uncertainty of 5 % must be included. Each calibration curve

consists of several measurement points, so the calculations must be performed for each point. Subsequently, the mean value of the absolute uncertainties of the calibration measurements is determined. Using this average value, the relative uncertainty of the species calibration factor is calculated.

To calculate the absolute uncertainty in the final mole fraction of a reactant, the uncertainty in the mole fraction of the dilution gas must first be determined, considering all MFCs used in the experiment. The absolute uncertainty in the mole fraction of the reactant can then be calculated by equations (4-6) and (4-12). Usually, the relative uncertainties in the mole fractions of the reactants are in the range of 5 – 8 % so that a general uncertainty of 10 % is estimated for reactants and products. For some species like liquids or species showing a low signal-to-noise ratio, higher uncertainties are assumed. This is mentioned in the respective study.

#### **4.4.2 Indirect calibration**

Species that were not available for direct calibration are quantified according to a relative ionization cross section method described by Biordi [84] along with calculated electron-ionization cross sections from empirically-derived addition theorems described by Fitch and Sauter [85] (see section 4.2.1). The resulting uncertainties are estimated to be of a factor of 2 – 4 [82,91].

### **4.5 Novelty of the experiment**

The modification of the experimental setup was a central part of the present work and the most recent setup was described in the previous sections. The setup consists of the flow reactor and its periphery and the two analytical devices used in this study, i.e., TOF-MS and GC/MS.

The flow reactor was designed to approximate plug flow to simplify its modeling and allow a better interpretation of the kinetic results. The plug-flow assumption was validated by the dispersion model developed by Levenspiel [51] both experimentally and analytically, and by two-dimensional simulations. The detailed characterizations substantially extend the knowledge and reliable reactor operation compared to previous work [17,18].

The reactor is made of quartz and embedded in an Inconel housing that enables operation at temperatures of up to 1000 K or 1400 K depending on the heating method (see section 4.1). The operating pressure ranges from sub-atmospheric pressures up to 40 bar. Compared to the older reactor designs [17,18] much higher pressures can be reached. In the literature, only a few high-pressure flow reactors exist [92]. In addition, the product analysis at the reactor outlet is usually limited to stable species. Here, molecular-beam TOF-MS can be used for product analysis allowing the detection of unstable species such as hydroperoxides, which can be crucial for understanding reaction pathways. Also, product analysis is much faster compared to GC/MS enabling rapid screening of interesting conditions by real online detection. High-pressure flow reactor experiments with directly coupled TOF-MS are rare in the literature.

In contrast, the GC/MS provides quantitative results with lower uncertainties and allows the separation of isomers. Consequently, the complementary use of both techniques can significantly improve the analysis of reaction pathways during partial oxidation processes.



---

## 5 Introduction to the conversion experiments

The experimental setup presented in the previous chapter is used to investigate the partial oxidation of several methane/additive mixtures. The obtained data is used to validate reaction mechanisms from the literature and, in particular, to optimize the PolyMech reaction mechanism developed in the research unit FOR 1993. The research unit is investigating the question to what extent engines can be used for polygeneration of work, heat, and chemicals and how efficient or economical such a process is compared to conventional processes. For this purpose and to find interesting conditions by using optimization methods, a detailed reaction mechanism, which is as compact as possible, is required. Thus, providing validation data with respect to polygeneration-relevant conditions is of great importance. The scientific connections within the FOR 1993 and how they contributed to the investigation of polygeneration processes have recently been summarized by Atakan et al. [16].

Methane, the main component of natural gas, is selected as the primary fuel because natural gas has a better CO<sub>2</sub>-balance than other fossil fuels and is expected to play a significant role in the energy system in the coming decades. Because methane requires high temperatures to be converted, small amounts of reactive additives are added to the gas mixture to initiate conversion at lower temperatures. In this study, five different methane/additive mixtures are investigated systematically and the interaction between methane and the additives is analyzed with the help of simulations. Reaction path and sensitivity analyses with respect to interesting products are performed using reaction mechanisms that can reasonably predict the experimental data. All experiments are performed under the same conditions to allow the comparison of the different mixtures.

First, the partial oxidation of neat methane is investigated to create a basis for comparison, followed by methane/ethane/propane and methane/ethane/propane/hydrogen mixtures. Ethane and propane are selected as the first additives as they are found in natural gas in significant amounts. The natural gas surrogate used here consists of 90 % methane, 9 % ethane, and 1 % propane, representing a typical natural gas composition without further contamination by nitrogen, carbon dioxide, or hydrogen sulfide, for example. Electricity-based hydrogen is expected to be increasingly fed into existing natural gas pipelines with an allowed percentage between 1 – 10 %. Here, 2 % of the fuel is replaced by hydrogen to investigate its influence on the partial oxidation of natural gas mixtures, which can be of interest for reforming processes.

Crude oil is also expected to play a major role in the transition period to a sustainable energy system, because the transport sector, in particular aviation, shipping, and heavy trucks, relies on energy-dense fuels and will struggle with electrification in the near future. One interesting additive that can be obtained from the distillation of crude oil is *n*-heptane. Due to its good auto-ignition properties, *n*-heptane serves as a diesel surrogate and was shown to be a suitable

additive by other authors, e.g. [17,93]. Its influence on the partial oxidation of methane is investigated in chapter seven. Special emphasis is placed on the interaction between *n*-heptane and methane to reveal the contribution of methane to the formation of interesting products.

A similar reactive additive, which can additionally be produced from biomass, is dimethyl ether (DME). Methane/DME and natural gas/DME mixtures are investigated in chapters eight and nine, respectively, focusing on the development and improvement of the PolyMech reaction mechanism. This is done in cooperation with several subgroups of the research unit, providing a huge set of validation data. The challenge was to develop a compact reaction mechanism that could still provide accurate predictions of potential products. At very high equivalence ratios there is a risk of soot formation in the engine so that the reaction mechanism was extended by a benzene and PAH sub-mechanism (chapter nine) allowing the prediction of important soot precursors. The modified reaction mechanism is then used to analyze the interaction of DME and the natural gas surrogate with respect to fuel conversion and product formation.

In several experiments, a distinct change in the reactivity of methane was observed in a specific temperature range which is usually only seen for higher alkanes. Such a behavior can be important for fuel conversion processes operated at conditions where this behavior is observed. Chapter ten deals with this so-called negative temperature coefficient behavior of methane. In addition, the influence of pressure and equivalence ratio on this behavior is systematically analyzed.

Chapter eleven presents a review of the systematic approach to polygeneration in piston engines that the research unit FOR 1993 is pursuing.

Following the detailed presentations of the studies in chapters 6 – 11, the results will be summarized and common features will be discussed in chapter 12.

---

## 6 Partial oxidation of natural gas/H<sub>2</sub> mixtures

The content of this chapter was published in *Combustion Science and Technology*:

D. Kaczmarek, B. Atakan, T. Kasper, Plug-Flow Reactor Study of the Partial Oxidation of Methane and Natural Gas at Ultra-Rich Conditions, *Combustion Science and Technology* 191, pp. 1571-1584 (2019).

© 2019 Taylor & Francis Group, LLC. Reprinted with permission.

My own contribution included setting up the experiment, performing the experiments, analyzing and visualizing the results, and writing the manuscript. Burak Atakan and Tina Kasper supported me in the conceptual design of the study and contributed to the interpretation of the results and the manuscript.

### Abstract

The homogeneous partial oxidation of fuel-rich CH<sub>4</sub>/O<sub>2</sub>, CH<sub>4</sub>/C<sub>2</sub>H<sub>6</sub>/C<sub>3</sub>H<sub>8</sub>/O<sub>2</sub> as well as CH<sub>4</sub>/C<sub>2</sub>H<sub>6</sub>/C<sub>3</sub>H<sub>8</sub>/H<sub>2</sub>/O<sub>2</sub> mixtures is investigated in a plug-flow reactor at intermediate temperatures ( $473 \leq T \leq 973$  K) and a pressure of 6 bar. Experiments are carried out at equivalence ratios ( $\phi$ ) of 2, 10, and 20. Product species are analyzed using time-of-flight molecular-beam mass spectrometry. The experimental results are further compared with kinetic simulations. It was found that under the investigated conditions, the onset temperature for CH<sub>4</sub> oxidation is above 773 K. The highest methane conversion at equivalence ratios of 10 and 20 was between 0 – 3 % for neat methane as fuel and 10 – 13 % for natural gas as fuel. The conversions yield useful chemicals like synthesis gas (H<sub>2</sub>/CO), C<sub>2</sub>H<sub>4</sub>, C<sub>2</sub>H<sub>6</sub>, or C<sub>3</sub>H<sub>6</sub>. Higher CH<sub>4</sub> conversion in the natural gas mixtures results in much higher yields of all products. The natural gas components ethane and propane do not influence the reaction onset temperature.

### 6.1 Introduction

Homogeneous partial oxidation in internal combustion engines could be an exergetically viable alternative to normal combustion, because useful chemicals, work, and heat can be provided at the same time. This process can be considered a polygeneration process. A well-suited fuel could be methane (CH<sub>4</sub>), a major component of natural gas (NG), or NG itself, since it will continue to play a major role in the energy sector in the near future and will also be sufficiently available. In addition, the growth of renewable energies requires an expansion of the power grid and new options for storing fluctuating electricity from renewable sources. Power-to-gas, i.e., the storage of renewable electrical energy as chemical energy in hydrogen (H<sub>2</sub>) and the direct seasonal storage capacity and distribution in existing natural gas infrastructure, can make an important contribution to the transformation of the energy system. Atakan [94] showed that gas

turbines are suitable for the polygeneration of synthesis gas (H<sub>2</sub>, CO) and mechanical power and that the combined generation had excellent exergetic efficiency. Hegner et al. and Wiemann et al. [93,95,96] presented the possibility to use a homogeneous charge compression ignition (HCCI) engine as a polygenerator to provide heat, work, and useful chemicals simultaneously. Gossler et al. [97] showed that a HCCI engine could theoretically be used to produce H<sub>2</sub> with yields of up to 90 %. In all of these studies, CH<sub>4</sub> or NG was used as the fuel at very fuel-rich conditions. For the HCCI of methane high initial temperatures or compression ratios are needed, because methane is relatively inert. Other small alkanes present in natural gas have higher reactivity. They can reduce the initial temperature or the compression ratio required. To analyze the governing reaction paths during the partial oxidation process, kinetic simulations using elementary reaction mechanisms have to be performed. At these uncommon reaction conditions reaction mechanisms for CH<sub>4</sub> and NG are rarely validated. The homogeneous partial oxidation of CH<sub>4</sub> has already been extensively studied by different groups in high-pressure flow reactors [98–104] and jet-stirred reactors [105], covering pressures from 1 – 100 bar, temperatures from 600 – 1800 K and equivalence ratios from 0.06 to 100. With respect to natural gas mixtures fewer studies have been published. One of the most comprehensive studies has been performed by Healy et al. [106], presenting ignition delay times for a wide range of parameters ( $1 \leq p \leq 50$  atm,  $0.5 \leq \phi \leq 2$  and  $770 \leq T \leq 1580$  K) measured in a rapid compression machine and high-pressure shock tube. In this study, an improved chemical kinetic mechanism was also developed, which predicted the experimental data well. But, Zhou et al. [107] selected a subset of the experimental data obtained by Healy et al. [106] and compared the results with simulations, conducted with three different reaction mechanisms from the literature. They concluded that no mechanism is able to predict the experimental results for all temperatures and pressures, which corroborate the need for better kinetic models, even for well-studied fuels like CH<sub>4</sub> or NG. El Bakali et al. [108] investigated the oxidation of natural gas in a premixed flame at low pressure and a jet-stirred reactor at 1 atm, equivalence ratios between 0.75 and 1.5, and temperatures between 1100 and 1500 K, and also proposed a detailed reaction mechanism. Further modeling studies, together with experiments in shock tubes [109,110] and jet-stirred reactors [111] revealed that higher hydrocarbons in the NG mixtures like ethane (C<sub>2</sub>H<sub>6</sub>) or propane (C<sub>3</sub>H<sub>8</sub>) react before CH<sub>4</sub>. They initiate CH<sub>4</sub> conversion at lower temperatures, compared to a neat CH<sub>4</sub> case. According to Tan et al. [111] this is due to an enhanced formation of OH, H and O radicals in case of NG mixtures. The shock-tube experiments were performed at  $1 \leq p \leq 31$  atm,  $0.5 \leq \phi \leq 3$  and  $1042 \leq T \leq 2248$  K, whereas the reactor experiments were done at  $1 \leq p \leq 10$  atm,  $0.1 \leq \phi \leq 1.5$  and  $800 \leq T \leq 1240$  K.

For H<sub>2</sub> addition to NG mixtures, only a few studies have been reported in the literature. They have mainly investigated the effect of H<sub>2</sub> addition on the flame speed of NG mixtures [112–114]. It is reported that the flame speed increases with increasing H<sub>2</sub> amount. NG/H<sub>2</sub> mixtures were investigated by Dagaut et al. [115,116], using a jet-stirred reactor. The investigated parameter range covers pressures of 1 and 10 atm, equivalence ratios between 0.3 and 2 and temperatures between 900 and 1450 K. In both studies it was shown that the formation of hydroperoxyl radicals (HO<sub>2</sub>) is boosted if H<sub>2</sub> is added to the mixtures and that the reaction  $H + HO_2 = OH + OH$  becomes more important. As a result of these kinetic processes, the reactivity of the investigated mixtures is increased. Finally, there is a lack of data for NG and NG/H<sub>2</sub> mixtures at high equivalence ratios ( $\phi > 2$ ) which are interesting for partial oxidation processes

in the chemical industry. No studies of the partial oxidation of these mixtures in flow reactors have been published to our knowledge. This gap will be addressed in the work presented here. To extend the experimental dataset of NG oxidation and to investigate the impact of H<sub>2</sub> addition to NG, fuel-rich ( $2 \leq \phi \leq 20$ ) diluted CH<sub>4</sub>/O<sub>2</sub> as well as CH<sub>4</sub>/C<sub>2</sub>H<sub>6</sub>/C<sub>3</sub>H<sub>8</sub> and CH<sub>4</sub>/C<sub>2</sub>H<sub>6</sub>/C<sub>3</sub>H<sub>8</sub>/H<sub>2</sub> mixtures are investigated at 6 bar and temperatures between 573 and 973 K in a plug-flow reactor. Product species are analyzed by time-of-flight molecular-beam mass spectrometry. The data are compared to model results with the intention to assess the performance of the reaction mechanism of Burke et al. [117], a well-cited and prominently used reaction mechanism, for such uncommon reaction conditions with future application potential.

## 6.2 Experimental setup

The investigated flow conditions are shown in Table 1. A low volume flow of 280 sccm (standard conditions: 273.15 K, 1 atm) is used to ensure compliance with a plug-flow assumption and a high dilution is used to avoid or reduce temperature changes due to exothermal reactions. Details of the experimental setup can be found in [17].

**Table 6-1:** Flow conditions.

CH <sub>4</sub>	O <sub>2</sub>	C <sub>2</sub> H <sub>6</sub>	C <sub>3</sub> H <sub>8</sub>	H <sub>2</sub>	Ar	$\phi$
[mol%]						[-]
5.00	5.00	0	0	0	90	2
4.32	5.20	0.43	0.048	0	90	2
4.27	5.16	0.43	0.047	0.095	90	2
8.33	1.67	0	0	0	90	10
7.40	1.78	0.74	0.082	0	90	10
7.27	1.76	0.73	0.081	0.162	90	10
9.09	0.91	0	0	0	90	20
8.12	0.98	0.81	0.090	0	90	20
7.97	0.96	0.80	0.089	0.177	90	20

Important features of the current setup and deviations from the previous experiments are summarized in Figure 6-1.

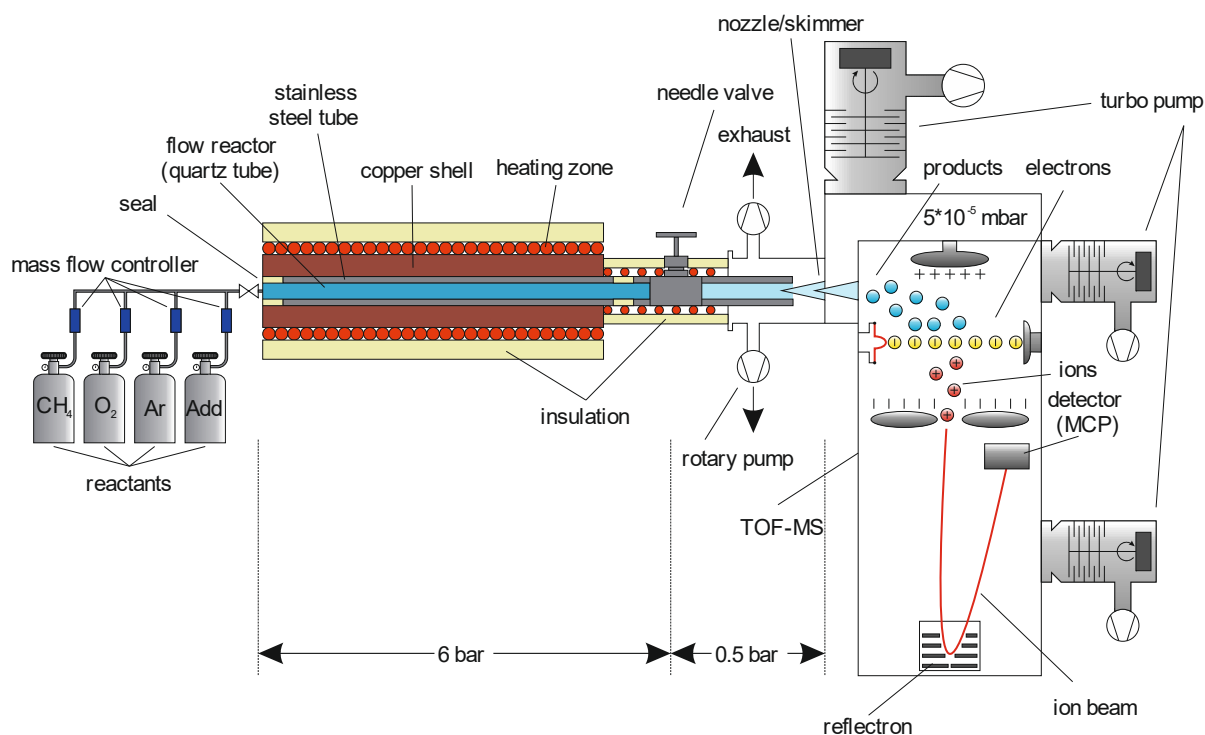


**Figure 6-1:** Plug-flow reactor and time-of-flight mass spectrometer.

The flow reactor is made of quartz and has an inner diameter of 6 mm. Quartz was used, because of its inertness and high temperature stability. Although stainless steel would be the better choice for high pressure applications, earlier studies showed that a stainless-steel tube leads to the total oxidation of the intermediates [118,119]. The quartz tube is embedded in a stainless-steel tube, which acts as a pressure shell. To prevent catalytic reactions with the stainless steel, the gap between the quartz and the stainless-steel tube is sealed with teflon tape at both ends. The gases and the tube are heated by two temperature-regulated heating tapes, wrapped around two copper shells, which in turn enclose the stainless-steel tube. This structure produces a homogeneous temperature profile with deviations below  $\Delta T = \pm 5$  K, and an isothermal reaction zone of 45 cm at an overall reactor length of 65 cm. The temperature profiles were determined along the center axis of the reactor tube by a moving type-K thermocouple in an inert gas flow of argon. The temperature profiles can be found in the electronic supplementary material (ESM). Gas flows are metered by calibrated mass flow controllers. The reactor pressure is regulated manually with a heated needle valve at the reactor outlet. The reactor is coupled to a time-of-flight mass spectrometer (TOF-MS) for online measurements. In contrast to our previous work [17], the gas samples are now extracted in the form of a molecular beam in a differentially pumped three-stage extraction. The TOF-MS has a mass resolution of  $m/\Delta m = 2000$ . The pressure in the ionization chamber is near  $10^{-7}$  mbar. The gases are ionized by electron ionization at 18 eV kinetic energy to avoid excessive fragmentation. Uncertainties in the mole fractions of the detected species have been calculated by means of the Gaussian error propagation law, taking all main error sources into account. They are estimated to be around 10 % for all major species.

## 6.3 Modeling

The reaction mechanism of Burke et al. [117], developed at the combustion chemistry centre at NUI Galway, is used for simulations in the Chemical Workbench Ver. 4.1 [44]. It covers H<sub>2</sub> as well as C<sub>1</sub> – C<sub>3</sub> chemistry, including oxygenated species like methanol, acetaldehyde or dimethyl ether. The mechanism has also been validated against a huge dataset of experiments, including shock tubes, rapid compression machines, flames, jet-stirred and plug-flow reactors and is well-suited for the simulation of the mixtures investigated in this study. For the reactor simulations, the plug-flow model of the Chemical Workbench software is used with the measured temperature profiles as input. The mole fractions of all species at the end of the reactor are evaluated and compared to the experimental results.

An equilibrium model with constant pressure and temperature is used for additional equilibrium calculations.

## 6.4 Results and discussion

Mole fractions of all detected species and the corresponding simulation results, can be found in the ESM. The most interesting product species profiles are shown and discussed here, namely CO, H<sub>2</sub>, ethylene (C<sub>2</sub>H<sub>4</sub>) and propene (C<sub>3</sub>H<sub>6</sub>). In addition, the conversions of all reactants are presented. Because the flow reactor is relatively long and the residence times of the reacting mixture vary between 6 and 15 seconds, the mixture may reach their equilibrium composition. To verify that the kinetics are investigated in these experiments, equilibrium calculations are presented first and compared to kinetic simulations and experimental results. Subsequently the experimental yields are compared to kinetic simulations to determine how well the reaction mechanism can predict the experimental data.

### 6.4.1 Main species – kinetics and equilibrium

Figure 6-2 shows the experimentally determined mole fractions of CH<sub>4</sub> and CO (symbols) in comparison to the mole fractions, obtained from equilibrium calculations (dashed lines) and kinetic simulations (solid lines), all for the same initial composition. For the conversion of neat CH<sub>4</sub> at  $\phi = 2$ , it can be noticed that the mole fractions of CH<sub>4</sub> are much lower in equilibrium compared to the experimental results and the kinetic simulations and that they are nearly equal for the neat CH<sub>4</sub> and NG mixture. At higher  $\phi$  the same behavior can be found for the neat CH<sub>4</sub> mixtures. For the NG mixtures, however, the predicted equilibrium mole fraction of CH<sub>4</sub> even becomes slightly higher than the initial experimental mole fraction of CH<sub>4</sub> at temperatures below 750 K. This is due to methane producing pathways from reactions of C<sub>2</sub>H<sub>6</sub>, dominating at infinitely long reaction times. Only at higher temperatures, a positive conversion of CH<sub>4</sub> is observed for the NG mixtures. In contrast, the kinetic simulations predict the trend of the CH<sub>4</sub> mole fractions well in all cases. Comparing the equilibria with the observed mole fractions, it can be concluded that the product composition is far from reaching the equilibrium composition. This deviation from equilibrium is even more pronounced for the CO mole fractions; at least for  $\phi \geq 10$  the calculated mole fractions are much higher than the experimental ones and the mole fractions obtained from kinetic simulations.

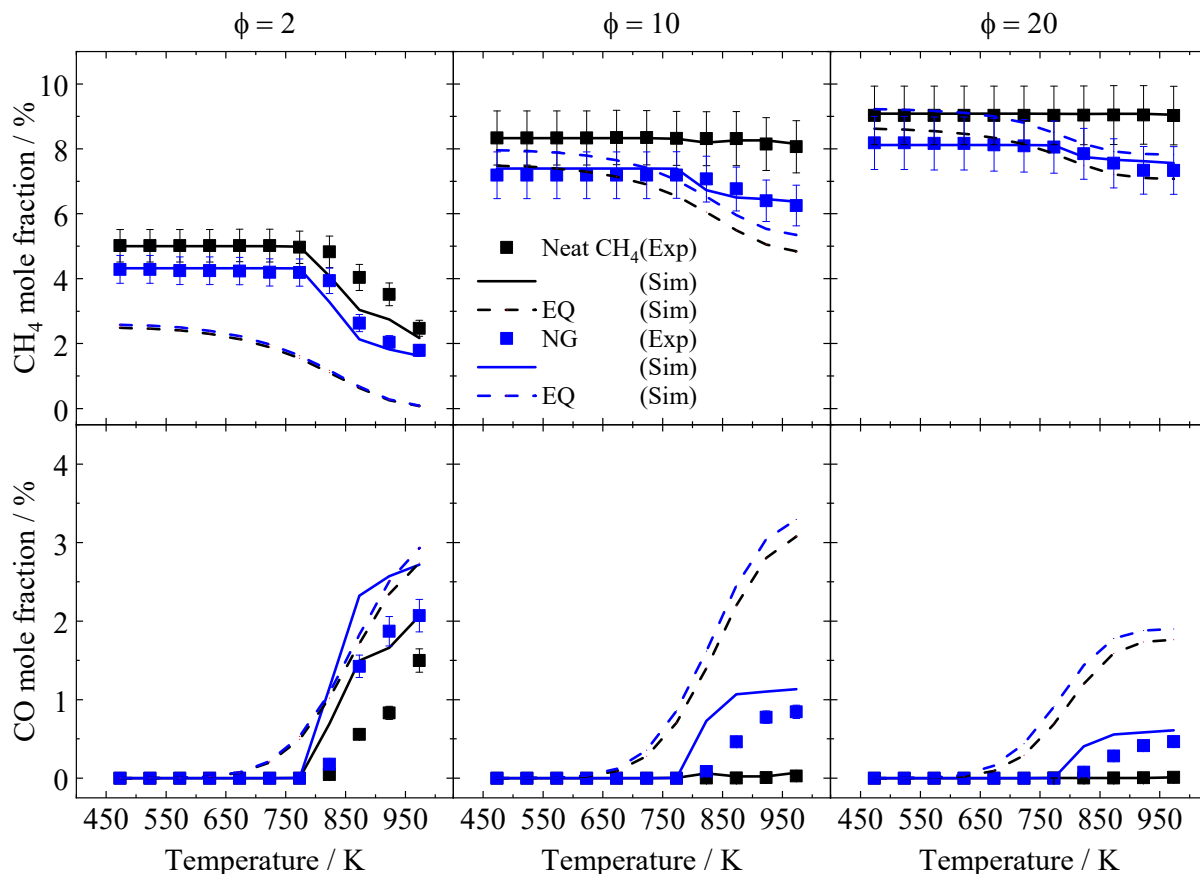


**Figure 6-2:** Mole fractions of CH<sub>4</sub> and CO as a function of temperature and equivalence ratio (Symbols: TOF-MS experiment, solid lines: kinetic simulations based on the reaction mechanism of Burke et al. [117], dashed lines: equilibrium calculations, NG: natural gas).

### 6.4.2 Major products

In order to compare different results, yields were used instead of mole fractions. Yields are easier to compare because they take into account differences in initial mixture and stoichiometry, which result in different mole fractions. The following figures show the conversion of the hydrocarbons within the mixture (Figure 6-3), yields of CO and H<sub>2</sub> (Figure 6-5) as well as C<sub>2</sub>H<sub>4</sub> and C<sub>3</sub>H<sub>6</sub> (Figure 6-7) as a function of temperature and equivalence ratio. Symbols represent experimental data and lines simulation results. The different mixtures are marked by different colors. Yields ( $Y$ ) are calculated according to equation (6-1), using the number of C atoms for all hydrocarbons and the number of H atoms for water (H<sub>2</sub>O) and H<sub>2</sub>.

$$Y_i = \frac{x_i \cdot \text{number of C/H atoms in product species } i}{\sum_{\text{Reactants}} x_j \cdot \text{number of C/H atoms in reactant species } j} \quad (6-1)$$

From Figure 6-3 it is obvious that the fuel conversion starts around 750 K for all mixtures. But, if  $\phi$  is increased from 2 to 20 the conversion of CH<sub>4</sub> decreases rapidly from 50 % to nearly 0 % in case of the CH<sub>4</sub> mixture. At  $\phi = 10$  the conversion is very low (< 4 %).

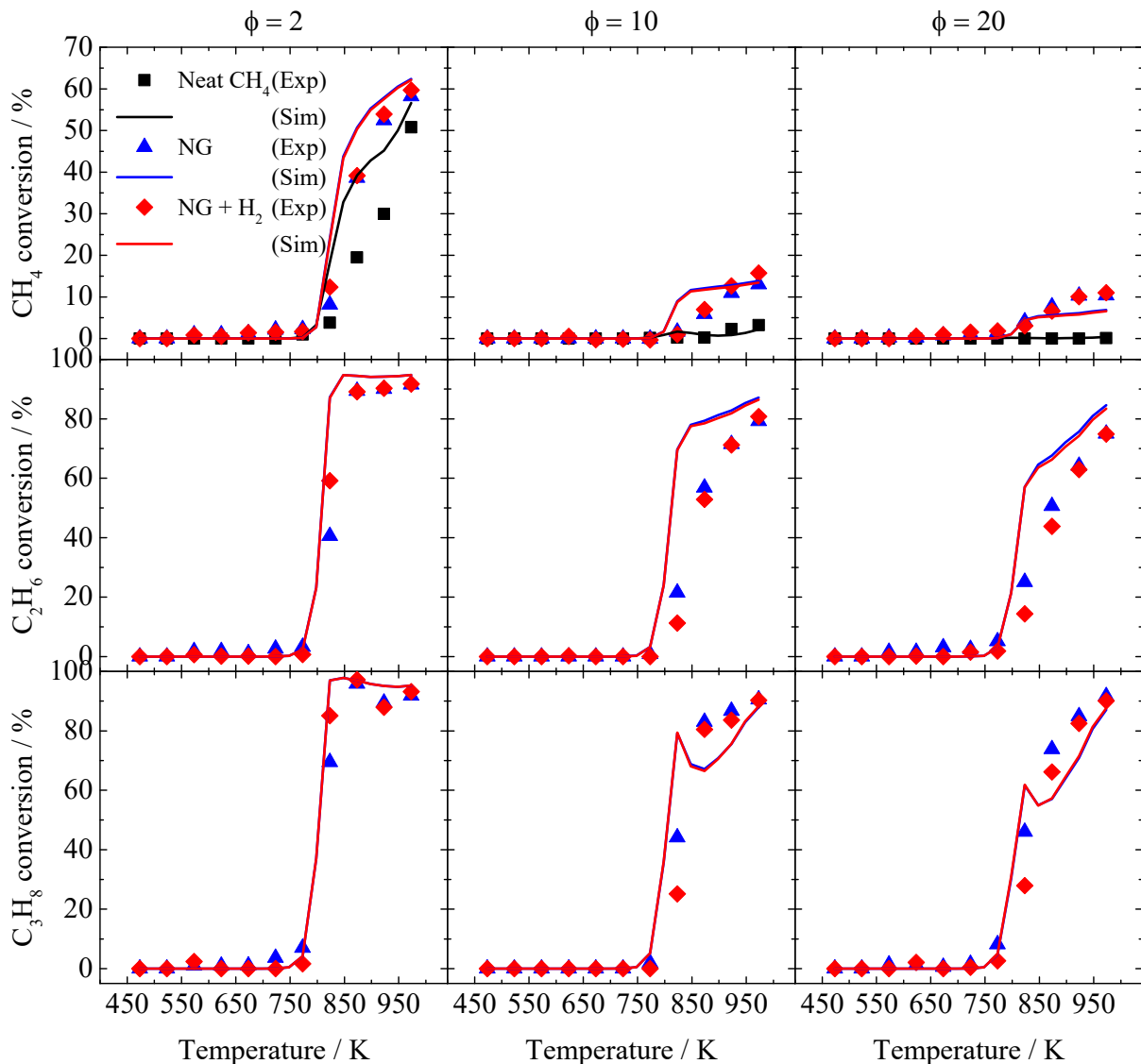


**Figure 6-3:** Conversion of alkanes as a function of temperature and equivalence ratio for all investigated mixtures (Symbols: TOF-MS experiment, lines: kinetic simulations based on the reaction mechanism of Burke et al. [117], NG: natural gas).

Methane conversion in the experiments fueled by NG is higher than in the experiments with neat CH<sub>4</sub> fuel. So even at  $\phi = 20$ , 10 % CH<sub>4</sub> is converted at temperatures above 873 K in natural gas mixtures, while the conversion of C<sub>2</sub>H<sub>6</sub> reaches more than 80 % and C<sub>3</sub>H<sub>8</sub> conversion more than 90 % at the highest investigated temperature of 973 K. This was expected due to the higher reactivity of these molecules, compared to CH<sub>4</sub>.

For C<sub>3</sub>H<sub>8</sub> conversion a NTC (negative temperature coefficient) region is predicted by the model in the expected temperature range between 800 and 900 K [120,121]. At  $\phi = 2$  this behavior is much less pronounced and barely visible at slightly higher temperatures (850 – 950 K) in the model. In the experiments, a slightly decreasing conversion of C<sub>3</sub>H<sub>8</sub> is also observed at 923 K, compared to 873 K, followed by an increasing conversion at 973 K. This could be interpreted as experimental evidence for the NTC region in this temperature range, but the two points, which seem to show NTC behavior, are within the error bars of the neighboring points. To proof such a NTC behavior, the temperature resolution of the experiment would have to be increased

and the uncertainty reduced. A possible explanation, why this behavior is missed in the experiments at  $\phi \geq 10$  could be that not sufficient temperature steps are taken to resolve the narrow predicted NTC temperature range of around 100 K. Additionally, the investigated mixtures are highly diluted in argon and the mole fraction of C<sub>3</sub>H<sub>8</sub> is very low, which makes it more difficult to notice the NTC region [122]. As described in [123] the NTC phenomenon is attributed to the competition of peroxide chemistry and reactions leading to less reactive products like olefins. Unfortunately, the reaction mechanism used in this study does not contain C<sub>3</sub> peroxides and hydroperoxides so that a kinetic analysis at these conditions would not be conclusive. To ensure that the simulation results are not unique to this mechanism, some simulations were repeated with the reaction mechanism Aramco 3.0 [124]. This mechanism also contains higher hydrocarbons and the before mentioned peroxides and hydroperoxides. No significant differences between the results of the two sets of simulations were observed. As the analysis of the NTC phenomenon of propane is not the primary aim of this study and the simulations using the Aramco 3.0 mechanism require much more CPU time, the use of the mechanism of Burke et al. [117] seems to be justified.

The general trends are predicted well by the model. The CH<sub>4</sub> conversion is slightly overestimated for all mixtures at  $\phi = 2$  and 10 in the temperature range between 773 K and 923 K and underestimated at  $\phi = 20$  at temperatures higher than 873 K. Also, the C<sub>2</sub>H<sub>6</sub> conversion at  $\phi \geq 10$  is overestimated by the model. To identify the reason for the higher CH<sub>4</sub> conversion in natural gas mixtures, the global reaction flow was analyzed for specific mixtures. As an example, the main reaction pathway of the NG mixture for  $\phi = 2$  at  $T = 873$  K is shown in Figure 6-4. The darker the lines are, the higher is the carbon flux along an indicated path. On the left side of the figure, the reaction pathway of CH<sub>4</sub> can be seen, which is now connected to the oxidation pathways of the higher alkanes. It is observed that CH<sub>4</sub> is also produced from C<sub>2</sub>H<sub>6</sub> oxidation and that CH<sub>3</sub> radicals are also formed in the oxidation of C<sub>3</sub>H<sub>8</sub>. Regarding C<sub>2</sub>H<sub>6</sub> and C<sub>3</sub>H<sub>8</sub> oxidation, nearly direct pathways to the unsaturated hydrocarbons C<sub>2</sub>H<sub>4</sub> and C<sub>3</sub>H<sub>6</sub> are important, so that considerable yields of these species are expected in the product gas. The main oxidation pathway of each fuel is fuel + OH forming the corresponding alkyl radical and H<sub>2</sub>O. The OH radicals are needed to induce significant fuel conversion, so it is important to know where the OH radicals come from. According to the reaction mechanism of Burke et al. [117] the initiation reaction in case of the NG mixtures is the reaction of C<sub>2</sub>H<sub>6</sub> with O<sub>2</sub> forming an ethyl radical (C<sub>2</sub>H<sub>5</sub>) and a hydroperoxyl radical (HO<sub>2</sub>). HO<sub>2</sub> reacts with CH<sub>4</sub>, C<sub>2</sub>H<sub>6</sub> and C<sub>3</sub>H<sub>8</sub> forming the respective alkyl radical and hydrogen peroxide (H<sub>2</sub>O<sub>2</sub>). H<sub>2</sub>O<sub>2</sub> finally decomposes into two OH radicals. The most important reaction with respect to CH<sub>4</sub> conversion is the H-abstraction by OH radicals to yield methyl radicals (CH<sub>3</sub>) and water (H<sub>2</sub>O), as shown above in Figure 6-4 and by Dagaut et al. [105]. Consequently, higher OH concentrations enhance the consumption of CH<sub>4</sub>.

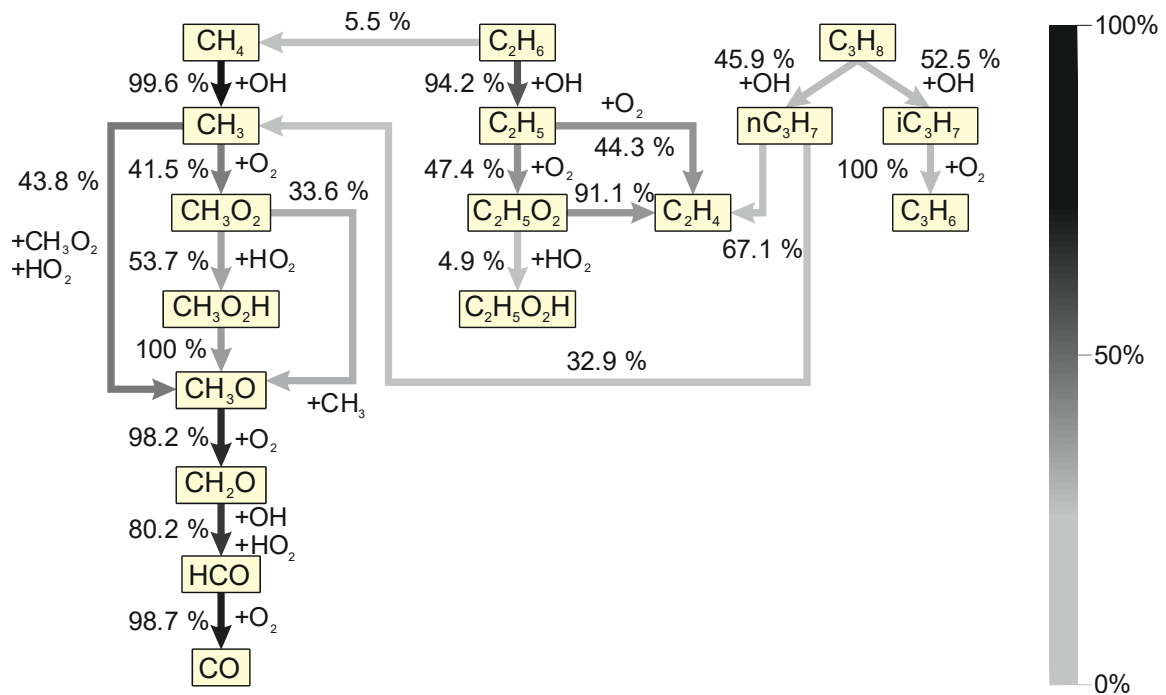


**Figure 6-4:** Reaction pathway for the NG mixture at  $\phi = 2$  and 823 K. The numbers in the diagram show which percentage of carbon flows between educt and product species and the grey scale shows the percentage of carbon flux, related to the highest carbon flux within the reaction path, which is found between  $\text{CH}_4$  and  $\text{CH}_3$ .

With respect to the  $\text{H}_2$  addition into the NG mixtures no significant influence onto the oxidation process is detected.

Two of the main products of all conversion experiments are  $\text{CO}$  and  $\text{H}_2$ , both presented in Figure 6-5. In this figure, the  $\text{CO}$  yield was multiplied by a factor of 4 and 9 for the  $\phi = 10$  and 20 cases, respectively.

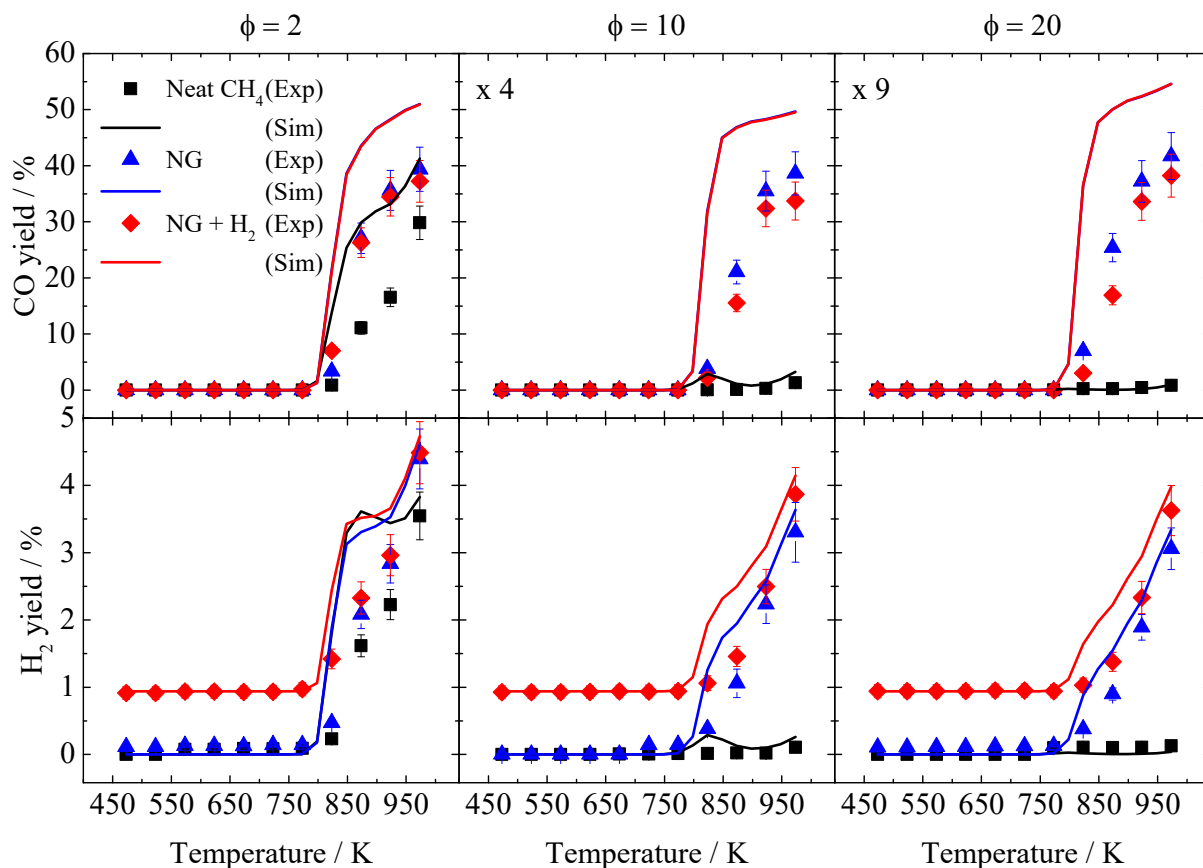


**Figure 6-5:** Yields of synthesis gas as a function of temperature and equivalence ratio (Symbols: TOF-MS experiment, lines: kinetic simulations based on the reaction mechanism of Burke et al. [117], NG: natural gas).

Figure 6-5 shows that for all mixtures the yields of CO and H<sub>2</sub> increases with temperature and that the highest CO yield is found for  $\phi = 2$ . For H<sub>2</sub>, yields of 4 – 5 % can be observed at 973 K for all NG mixtures as well as the CH<sub>4</sub> mixture at  $\phi = 2$ . Since less CH<sub>4</sub> is converted at  $\phi = 10$  and 20, compared to  $\phi = 2$ , and more than 80 % of ethane and propane are converted at 973 K, it can be presumed that most H<sub>2</sub> is formed by C<sub>2</sub>H<sub>6</sub> and C<sub>3</sub>H<sub>8</sub> oxidation. To check this assumption, the production rate contributions of important reactions for H<sub>2</sub> formation were calculated at  $T = 973$  K and all equivalence ratios and are presented in Figure 6-6. In contrast to the initial assumption, CH<sub>4</sub> plays an important role in H<sub>2</sub> formation. The reaction of CH<sub>4</sub> with hydrogen atoms contributes up to 19 % of the hydrogen at  $\phi = 20$ . In addition, this reaction becomes more important at higher equivalence ratios, while the contributions of reactions involving C<sub>2</sub>H<sub>6</sub> and C<sub>3</sub>H<sub>8</sub> increase only slightly. The most important pathway towards H<sub>2</sub> is via the reaction of formaldehyde (CH<sub>2</sub>O) with H atoms to HCO and H<sub>2</sub>. CH<sub>2</sub>O, in turn, mainly arises from CH<sub>4</sub> oxidation (Figure 6-4), so it can be concluded that the contribution of CH<sub>4</sub> to H<sub>2</sub> formation is very high.

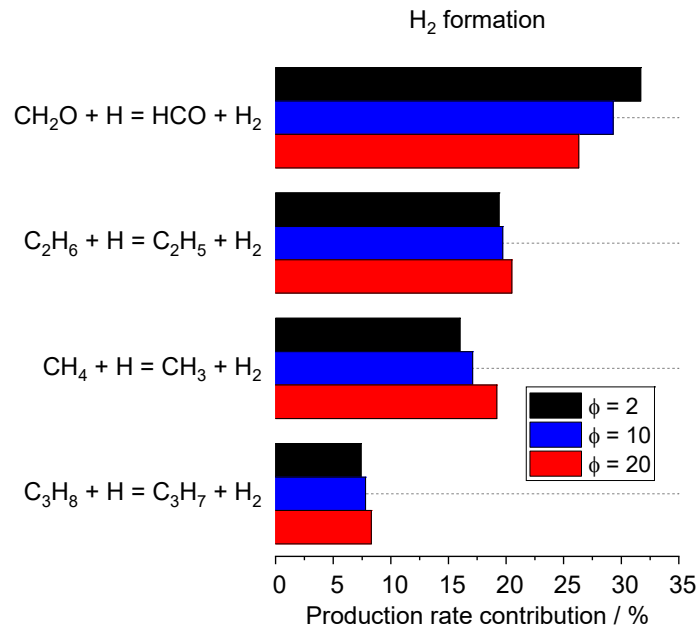


**Figure 6-6:** Production rate contribution of important reactions with respect to H<sub>2</sub> formation.

All H<sub>2</sub> containing NG mixtures show the same behavior as neat NG mixtures with the difference that the H<sub>2</sub> yields start at 1 %, which is the initial H<sub>2</sub> amount in the mixture. At temperatures above 773 K, the H<sub>2</sub> yields are similar, independent of the initial H<sub>2</sub> content in the mixture. The experimental data for most other species do not differ significantly for mixtures with and without hydrogen addition to the fuel so that it can be concluded that the oxidation pathways are not influenced significantly by the presence of H<sub>2</sub>.

The predicted yields of CO and H<sub>2</sub> exceed experimental yields indicating that the model overpredicts the reactivity for the investigated conditions.

C<sub>2</sub>H<sub>4</sub> and C<sub>3</sub>H<sub>6</sub> are produced in all NG experiments mainly at high  $\phi$  (see Figure 6-7).

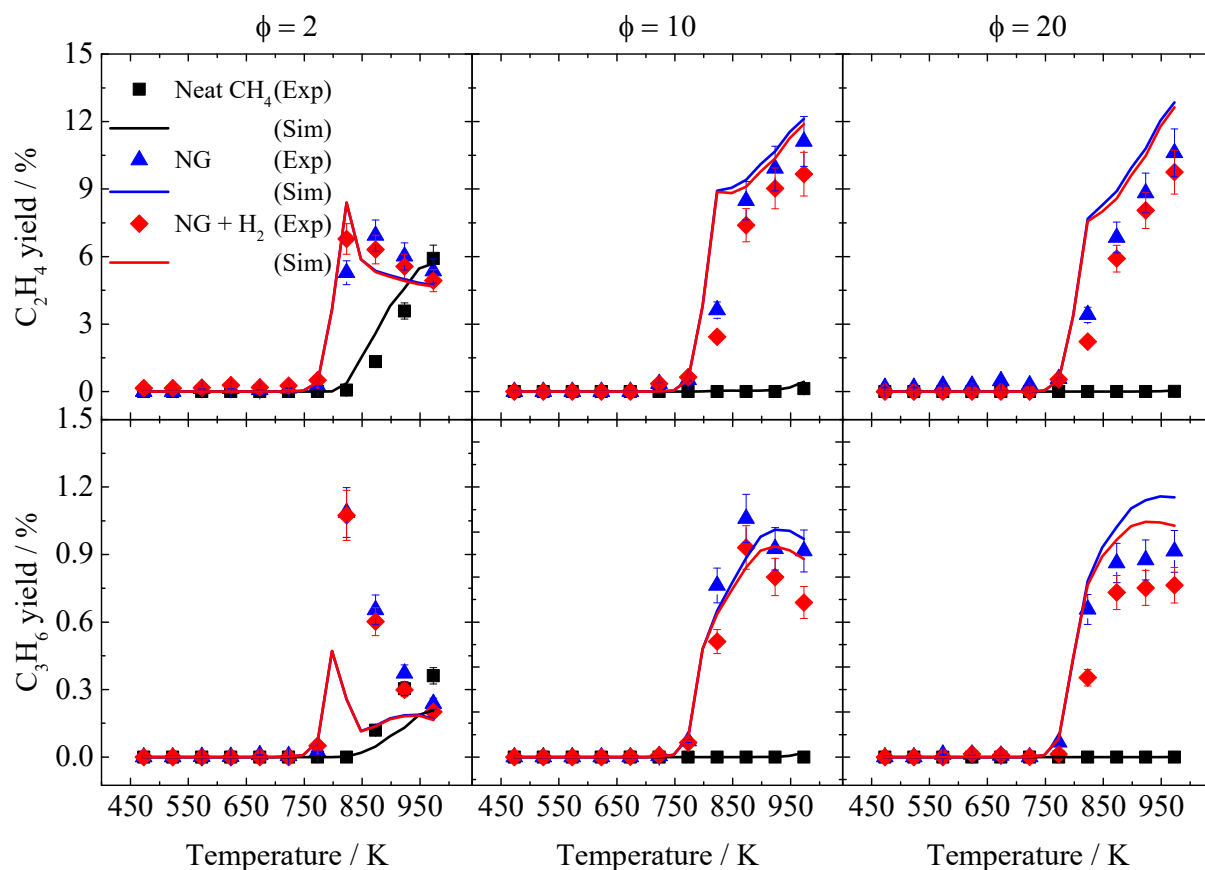


**Figure 6-7:** Yields of unsaturated hydrocarbons as a function of temperature and equivalence ratio (Symbols: TOF-MS experiment, lines: kinetic simulations based on the reaction mechanism of Burke et al. [117], NG: natural gas).

Using neat methane as fuel,  $C_2H_4$  is only formed at  $\phi = 2$ , because of the negligible conversion of  $CH_4$  at higher  $\phi$ . For the conversions at  $\phi = 10$  and 20, maximum yields of  $C_2H_4$  of up to 12 % are observed at the highest investigated temperature (973 K).  $C_2H_4$  must be produced from  $C_2H_6$  and  $C_3H_8$  because of the  $CH_4$  conversion at these conditions (see Figure 6-4). At  $\phi = 2$  the maximum ethylene yields are about 7 and 6 % for the NG and  $CH_4$  mixtures, respectively. For the NG mixture, the maximum is found at 773 K with slightly decreasing yields at higher temperatures, whereas in the neat  $CH_4$  case, a linear increase of the yield with temperature can be noticed from 773 K to 973 K. The reason for the higher yields at lower temperatures is the direct route towards  $C_2H_4$  in the reaction network of the NG mixtures. As shown before, the initiation reaction in the NG mixtures forms  $C_2H_5$ . This radical reacts with  $O_2$ , finally forming  $C_2H_4$  and  $HO_2$ . In the  $CH_4$  mixture, first of all  $C_2H_6$  is formed by the recombination of two  $CH_3$  radicals.  $C_2H_5$  is then formed by H-abstraction from  $C_2H_6$  by  $CH_3$ ,  $OH$  or  $HO_2$  radicals. Finally,  $C_2H_4$  is formed by the same reaction as in the NG mixture. The number of additional steps needed to produce  $C_2H_4$  from neat  $CH_4$  explains the higher yields in the NG experiments. The decrease in the  $C_2H_4$  yields at temperatures above 773 K is due to the reaction of  $C_2H_4$  with  $OH$  radicals forming an ethenyl radical ( $C_2H_3$ ) and  $H_2O$ . With respect to the reaction flow analysis, this reaction becomes more important at higher temperatures at  $\phi = 2$ . Multiple reaction steps are needed to form  $C_3H_6$  from methane, while only two steps are needed in the NG mixtures. In the mixtures investigated here, the most important reaction sequence forming  $C_3H_6$  is

by H-abstraction from  $C_3H_8$  by different radicals forming propyl radicals ( $C_3H_7$ ), which decompose to  $C_3H_6$  (see Figure 6-4). The maximum yield of  $C_3H_6$  is around 1 % for all mixtures. The maximum slightly shifts towards higher temperatures with rising  $\phi$ . The small yields of  $C_2H_4$  and  $C_3H_6$  are caused by the small initial concentrations of  $C_2H_6$  and  $C_3H_8$ . Assuming that 100 % of both unsaturated hydrocarbons are formed due to the oxidation of the related saturated hydrocarbon  $C_2H_6$  and  $C_3H_8$ , yields would nearly reach 80 % for  $C_2H_4$  and 50 % for  $C_3H_6$  at  $\phi = 10$  and 973 K and 873 K, respectively. This observation emphasizes again the small amount of the methane conversion. Both the trends and the yields are in good agreement with the model predictions, except for the yield of  $C_3H_6$  at  $\phi = 2$  in the NG mixtures. In this case, the model underpredicts the yield by a factor of 2. As the enthalpies of formation of unsaturated hydrocarbons are much higher than the enthalpies of their related saturated hydrocarbons, such a partial oxidation process could be used in order to store excess energy, coming from volatile energy sources like wind or solar power plants.

Other common products like carbon dioxide ( $CO_2$ ) and  $H_2O$ , but also oxygenated species like methanol ( $CH_3OH$ ) and formaldehyde ( $CH_2O$ ) as well as hydrocarbons up to  $C_4$ - and  $C_5$ -species are also formed and detected experimentally. The  $C_4$ - and  $C_5$ -species are not included in the evaluation, because their mole fractions are negligibly small. For the purpose of comparison, the maximum yields of the major products of the NG mixtures are shown in Figure 6-8. The highest  $CH_3OH$  yields of around 0.3 % are found at  $\phi = 2$  and a temperature of 823 K. For  $CH_2O$ , yields of up to 2 % ( $\phi = 2$ ) are observed, whereas the maximum of the oxygenated species is located at intermediate temperatures around 823 K.

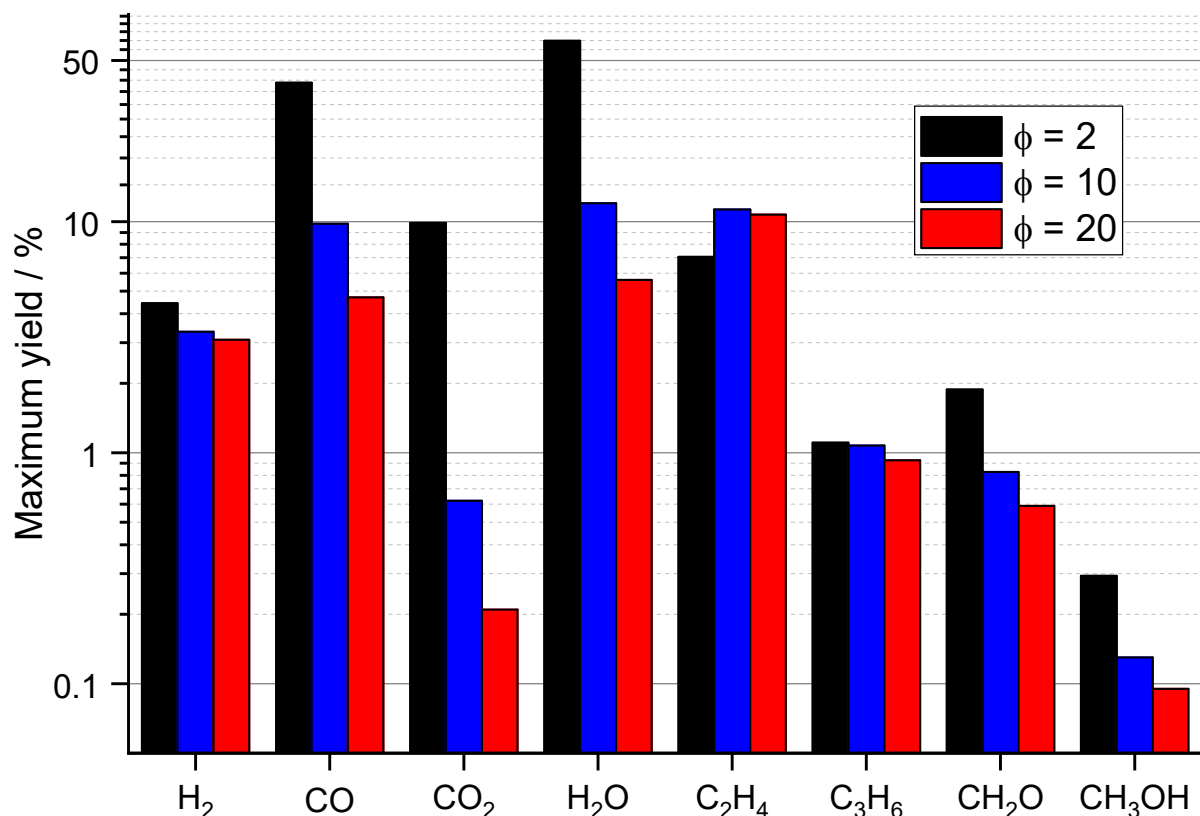


**Figure 6-8:** Maximum experimental yields of all major products in case of the NG mixtures for all equivalence ratios.

## 6.5 Conclusion

The homogeneous partial oxidation of CH<sub>4</sub> and NG mixtures, as well as H<sub>2</sub> doped NG mixtures, was investigated in a plug-flow reactor at temperatures between 473 and 973 K and a pressure of 6 bar. It is observed that the CH<sub>4</sub> conversion can be significantly enhanced if reactive species like C<sub>2</sub>H<sub>6</sub> and C<sub>3</sub>H<sub>8</sub> are present in the mixture. At very high equivalence ratios (10 and 20), CH<sub>4</sub> conversion was negligibly small in neat CH<sub>4</sub> experiments but increased to more than 10 % in experiments using NG mixtures. Because of that, much higher product yields of synthesis gas, C<sub>2</sub>H<sub>4</sub>, C<sub>3</sub>H<sub>6</sub>, or CH<sub>3</sub>OH for example, can be obtained with NG at these equivalence ratios, compared to neat CH<sub>4</sub>. The addition of small amounts of H<sub>2</sub> into the NG mixture, as it may be practiced in the future from regenerative sources, did not alter the product composition in any case. The initiation reactions, as well as the reaction pathway towards the major products have been analyzed by performing global reaction flow analyses with the reaction mechanism of Burke et al. [117]. It is found that CH<sub>4</sub> plays an important role in H<sub>2</sub> formation and that unsaturated hydrocarbons like C<sub>2</sub>H<sub>4</sub> and C<sub>3</sub>H<sub>6</sub> are mainly formed from C<sub>2</sub>H<sub>6</sub> and C<sub>3</sub>H<sub>8</sub>, respectively. In general, simulations, conducted with this mechanism, showed reasonable quantitative agreements with the experimental yields. Some discrepancies could be observed as well, which corroborate the need for experimental data that can help to improve models for these uncommon reaction conditions.

---

## 7 Partial oxidation of methane/*n*-heptane mixtures

The content of this chapter was published in Combustion and Flame:

D. Kaczmarek, B. Atakan, T. Kasper, Investigation of the partial oxidation of methane/*n*-heptane mixtures and the interaction of methane and *n*-heptane under ultra-rich conditions, Combustion and Flame 205, pp. 348-357 (2019).

© 2019 The Combustion Institute. Published by Elsevier. Reprinted with permission.

My own contribution included setting up the experiment, performing the experiments, analyzing and visualizing the results, and writing the manuscript. Burak Atakan and Tina Kasper supported me in the conceptual design of the study and contributed to the interpretation of the results and the manuscript.

### Abstract

The homogeneous partial oxidation of methane is an interesting approach to obtain useful chemicals like synthesis gas, higher hydrocarbons, aldehydes or alcohols. Because of the low reactivity of methane, the homogeneous conversion needs high temperatures to proceed at reasonable reaction rates. Additives like *n*-heptane form reactive intermediates at comparatively low temperatures and initiate the conversion. To study the kinetics of doped conversion reactions, fuel-rich diluted methane/*n*-heptane/oxygen/argon-mixtures ( $2 \leq \phi \leq 20$ ) were investigated in a plug-flow reactor at a pressure of 6 bar, at intermediate temperatures between 423 and 973 K and at relatively long residence times ( $7 \leq \tau \leq 14$  s). The product composition at the reactor outlet is analyzed by gas chromatography and mass spectrometry. Species profiles as a function of equivalence ratio and temperature are compared with simulations, and serve as validation data for different reaction mechanisms. Rates of production and reaction paths are analyzed to investigate the interaction of methane and *n*-heptane during the oxidation process. They show that the chemical interaction of the oxidation products of both fuels has a promoting effect on the formation of different useful products like carbon monoxide, methanol or ethane. To prove this observation, mole fraction profiles as a function of temperature were compared between experiments with an equivalence ratio of  $\phi = 8$  using neat methane, neat *n*-heptane and methane/*n*-heptane mixtures as fuels. The results show that the yields of these species are much higher in case of the methane/*n*-heptane mixture compared to the yields obtained in the neat methane and neat *n*-heptane conversions or the sum of both.

### 7.1 Introduction

To reduce carbon dioxide emissions, major efforts are undertaken to increase the use of renewable energy. Fluctuating electricity generation, particularly by wind and solar power plants,

leads to a discrepancy between supply and demand and drives the development of processes that can store excess energy. Fossil fuels, mostly natural gas, are used to cover the energy requirements at all times. High transportation costs to the places of use can be reduced if the natural gas is converted into liquid fuels.

A conceivable way to overcome some of these challenges could be a polygeneration process with the ability to provide work, heat and useful chemicals simultaneously depending on the respective demand.

For example, Atakan [94] showed by thermodynamic calculations that a fuel-rich gas turbine process is suitable for the polygeneration of work as well as hydrogen (H<sub>2</sub>) and carbon monoxide (CO), using methane (CH<sub>4</sub>) as fuel. In this study, the separation of the product gases and the utilization of the turbine exhaust stream were not considered, but Hegner and Atakan [95] conducted a modeling study of such a process in a homogeneous charge compression ignition (HCCI) engine and considered the separation of H<sub>2</sub> from the product gases and the utilization of the process heat. The polygeneration process was found to be much more efficient than the “separated production of power, heat and hydrogen”. Another modeling study of a fuel-rich operated HCCI engine can be found in [97]. Besides optimal engine conditions for high H<sub>2</sub> yields, the authors identified some promising hydrocarbon H<sub>2</sub> precursors. Polygeneration processes in ignition compression engines are advantageous because engines are much cheaper, easily scalable, and can be operated on shorter time scales than gas turbines.

In order to obtain syngas (H<sub>2</sub>, CO), methanol (CH<sub>3</sub>OH) or higher hydrocarbons using CH<sub>4</sub> as fuel, CH<sub>4</sub> has to be oxidized partially in fuel-rich mixtures, at moderate temperatures and high pressures. Reaction mechanisms are rarely validated experimentally in the required regime. The kinetics of the homogeneous partial oxidation of CH<sub>4</sub> have been studied before, e.g. by Glarborg et al. and Rytz et al. in tubular high-pressure flow reactors [98–102,125] and by Dagaut et al. in jet-stirred reactors [105]. It was observed that the higher the CH<sub>4</sub> conversion is, the smaller is the selectivity and yield of partially oxidized products; e.g. Rytz and Baiker [98] found that the CH<sub>3</sub>OH yield decreases at high CH<sub>4</sub> conversion.

High initial temperatures are needed to obtain autoignition of methane after compression. The initial temperature may be reduced with the help of additives with a higher reactivity than methane [17,100,125,126]. Concerning HCCI engines, especially dimethyl ether (DME) and *n*-heptane (*n*-C<sub>7</sub>H<sub>16</sub>) promote the ignition of CH<sub>4</sub> [93,96,127]. A high pressure shock-tube study of CH<sub>4</sub> ignition [128] showed that *n*-C<sub>7</sub>H<sub>16</sub> is even more effective than DME. Both DME/CH<sub>4</sub>/O<sub>2</sub> and *n*-C<sub>7</sub>H<sub>16</sub>/CH<sub>4</sub>/O<sub>2</sub>-mixtures were investigated in [17] at an equivalence ratio of 2, using a shock-tube and a flow reactor. The oxidation of *n*-C<sub>7</sub>H<sub>16</sub> has also been extensively studied in jet-stirred reactors [129–136] covering pressures from 1 to 40 atm, temperatures from 490 to 1200 K and equivalence ratios from 0.25 to 4. High-pressure flow reactor studies [137–139] cover equivalence ratios from 0.5 to 2.22. Several pyrolysis studies have also been performed [138,140,141]. More recently, Li et al. [142] investigated the effect of CH<sub>4</sub> substitution on the ignition of *n*-heptane/air mixtures at engine relevant conditions. They concluded that CH<sub>4</sub> substitution leads to a prolonged ignition delay and a slower conversion of *n*-C<sub>7</sub>H<sub>16</sub> compared to *n*-C<sub>7</sub>H<sub>16</sub> conversion in the neat *n*-heptane mixture. Liang et al. [143] also determined ignition delay times of CH<sub>4</sub>/*n*-C<sub>7</sub>H<sub>16</sub> mixtures with different CH<sub>4</sub> contents and found that even small amounts of *n*-C<sub>7</sub>H<sub>16</sub> within the CH<sub>4</sub>/*n*-C<sub>7</sub>H<sub>16</sub> mixture can help to decrease the ignition delay significantly. This result is in agreement with the work of Li. These studies document

that *n*-heptane is a promising additive to increase the conversion of methane at lower temperatures, but, to our knowledge, no studies of the partial oxidation of neat CH<sub>4</sub>, *n*-C<sub>7</sub>H<sub>16</sub>, or their mixtures at equivalence ratios between 4 and 20 have been published. The present work provides experimental flow reactor data for *n*-C<sub>7</sub>H<sub>16</sub> doped CH<sub>4</sub>/O<sub>2</sub>-mixtures at ultra-rich conditions ( $2 \leq \phi \leq 20$ ) to provide validation data for reaction mechanisms, used for simulations at conditions which are relevant for polygeneration systems. Mole fraction profiles of all detected species are determined as a function of temperature and equivalence ratio to identify suitable products during the partial oxidation process. Suitable products must be produced with acceptable yields and can be oxygenated compounds such as ethers, aldehydes, ketones, or alcohols or hydrocarbons formed by C-C-coupling reactions from methane, e.g., ethane, ethylene, acetylene. The preferred formation of these species under fuel-rich conditions justifies the studied range of equivalence ratios. In addition, the reaction onset temperature of CH<sub>4</sub>/*n*-C<sub>7</sub>H<sub>16</sub> mixtures is compared with the reaction onset temperature of a neat CH<sub>4</sub> mixture to assess the change in reactivity due to the presence of *n*-C<sub>7</sub>H<sub>16</sub>. As all mixtures are highly diluted in argon or nitrogen a transfer of the results of this study to engine conditions is only possible with the help of models and suitable reaction mechanisms. The results presented here can serve as validation data for the optimization of such reaction mechanisms. But, the comparison of experimental and modeling results, using literature reaction mechanisms, in combination with an integrated reaction flow analysis at  $\phi = 8$ , also helps to understand the reasons for the activation of the reactions, which in turn can help to find other suitable additives.

## 7.2 Experimental methods

The investigated flow conditions are shown in Table 7-1. A neat CH<sub>4</sub> and a neat *n*-C<sub>7</sub>H<sub>16</sub> conversion at an equivalence ratio of  $\phi = 8$  as well as conversion of CH<sub>4</sub>/*n*-C<sub>7</sub>H<sub>16</sub> mixtures in the ratio 19 to 1 with  $\phi = 2 - 20$  have been investigated in detail. All experiments were performed at a pressure of 6 bar, covering a temperature range of 473 – 973 K. Because of a constant volume flow, the residence times vary between 7 and 14 s, depending on the temperature. Because of technical limitations of the HPLC pump, the *n*-C<sub>7</sub>H<sub>16</sub> flow could not be reduced sufficiently for the mixtures at  $\phi = 2$  and 4 and the oxygen flow had to be increased to keep the CH<sub>4</sub>/*n*-C<sub>7</sub>H<sub>16</sub> ratio as well as the total volume flow constant. For the (neat) single fuel experiments with an equivalence ratio of  $\phi = 8$ , the mole fractions of each fuel were the same as in the CH<sub>4</sub>/*n*-heptane mixture, and oxygen (O<sub>2</sub>) and the buffer gas were adjusted to obtain the equivalence ratio. As an unavoidable consequence the C/O and C/H ratio is slightly lower for the neat CH<sub>4</sub> mixture and it is higher for the neat *n*-C<sub>7</sub>H<sub>16</sub> mixture, than in the CH<sub>4</sub>/*n*-heptane mixture. The benefit of these conditions is that the sum of the initial mole fractions in the inlet flow leads to the same amount of oxygen and of each fuel as for the *n*-heptane/methane mixture. In this way it is possible to identify effects related to fuel interaction by comparing product mole fractions in the doped mixture to the sum of the product mole fractions of each individual conversion reaction. The low flow velocity ensures compliance with a plug-flow assumption according to the dispersion model as outlined by Levenspiel [51]. The high dilution with inert gas renders the heat release from exothermal reactions negligible in comparison with the external heating.

**Table 7-1:** Flow conditions of the reactants.

CH <sub>4</sub>	O <sub>2</sub>	n-C <sub>7</sub> H <sub>16</sub>	Ar/ N <sub>2</sub>	$\phi$
[mol%]				[-]
9.41	12	0.47	78.12	2
9.41	6	0.47	84.12	4
9.41	4	0.47	86.12	6
12.55	4	0.63	82.82	8
12.55	3.13	0	84.31	8
0	0.86	0.63	98.51	8
15.68	4	0.78	79.53	10
18.82	4	0.94	76.24	12
21.96	4	1.1	72.94	14
25.1	4	1.25	69.65	16
28.24	4	1.41	66.35	18
31.37	4	1.57	63.06	20

Details of the experimental setup (see Figure 7-1) are given in [17,18].

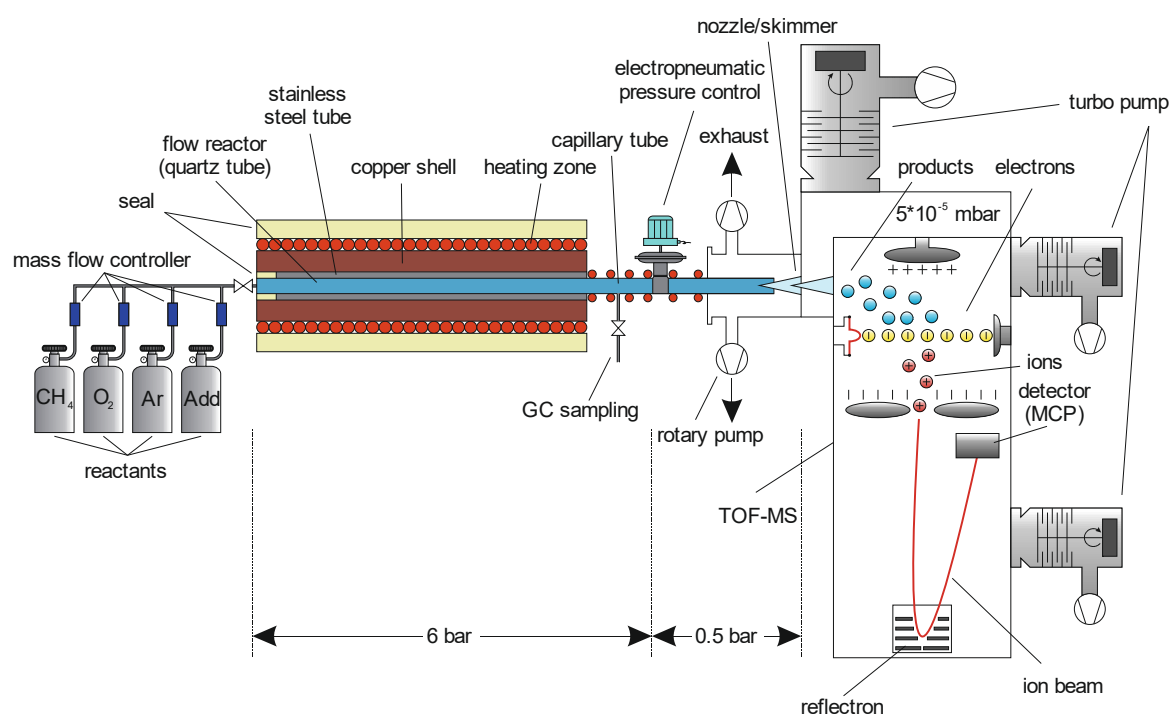


**Figure 7-1:** Experimental setup: The experimental setup consists of the heated plug-flow reactor, the molecular-beam sampling system made from two differentially pumped stages separated by nozzles and a reflectron time-of-flight mass analyzer with electron ionization.

Compared to our previous work [17], the pressure control and product analysis were improved. Important features of the current setup are summarized below. The flow reactor consists of an inert quartz tube with an inner diameter of 6 mm. It is surrounded by a stainless-steel tube for safety reasons. The reactor is heated by temperature controlled heating tape. A homogeneous temperature profile with deviations below  $\Delta T = \pm 5$  K, and an isothermal reaction zone of 45 cm at an overall reactor length of 65 cm with similar gas flows is confirmed prior to the experiments

as a function of the set temperature of the heating tape (see Figure 7-2). These profiles were measured with type-K thermocouples.

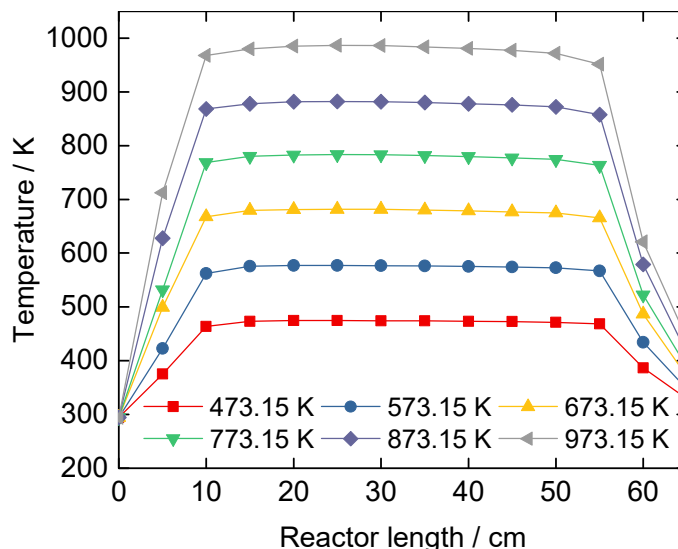


**Figure 7-2:** Temperature profiles from thermocouple measurements show that typically isothermal zone reaches the set temperature given in the label for each profile. The profiles were measured with an air flow of 280 sccm.

Gases are metered by calibrated mass flow controllers. *n*-Heptane was introduced with a calibrated HPLC pump and mixed with nitrogen or argon at the inlet of a home-made vaporizer. Right in front of the reactor inlet the Ar/*n*-C<sub>7</sub>H<sub>16</sub> or N<sub>2</sub>/*n*-C<sub>7</sub>H<sub>16</sub>-mixture is mixed with CH<sub>4</sub> and O<sub>2</sub>. The total flow rate is 280 sccm in all experiments. The reactor is coupled to a time-of-flight mass spectrometer (TOF-MS) for online measurements and to a sample valve for offline gas chromatographic measurements. For the online measurements, a pressure controller regulates the mass flow of the gas into the TOF-MS so that a pressure of 500 mbar is established in the first expansion chamber, while the rest of the gases are exhausted by a rotary pump. The gases in the first expansion stage are sampled by a nozzle with an orifice diameter of 40 μm into a vacuum chamber kept at 10<sup>-5</sup> mbar. A skimmer with a diameter of 1 mm extracts the core of the molecular beam formed in the nozzle expansion and directs it into the ion optics of the TOF-MS with a mass resolution of  $m/\Delta m=2000$ . The gases are ionized with electrons at 17 eV kinetic energy to avoid excessive fragmentation. To transfer gas from the reactor to the gas chromatograph (GC), samples are extracted into a heated sampling platform (373 K); this avoids condensation of low-volatility components. In the GC, the gas mixture is separated by two different columns. For permanent gases, a Rt-Msieve 5A column and a thermal conductivity detector are used, whereas hydrocarbons are separated within a Rt-Q-Bond PLOT column and detected by a mass-selective detector. A mixture of 8.5 % H<sub>2</sub> and 91.5 % helium (He) was used as carrier gas for GC analyses. The reason for this is that the thermal conductivity of a H<sub>2</sub>/He mixture is not a simple monotonically increasing function of the H<sub>2</sub> concentration. Instead, the thermal conductivity passes through a local minimum at low H<sub>2</sub> concentrations before rising up to the value of pure H<sub>2</sub> [86,87]. The minimum is located at approximately 6 % H<sub>2</sub> and 94 % He. Utilizing pure He as carrier gas would provide an ambiguous, non-linear response between the H<sub>2</sub> signal and the amount of H<sub>2</sub> in the mixture. The mixture, mentioned above, however, leads

to a simple quadratic response between the signal and the amount of H<sub>2</sub> and allows the quantification of hydrogen. Quantification is done by comparing the resulting signals with calibration measurements, done with self-mixed binary cold gas mixtures. Generally, mole fraction uncertainties with respect to both analytical techniques are estimated using the error propagation law, considering uncertainties of all instruments, resulting in around 10 % for species, calibrated by the cold gas mixtures. For H<sub>2</sub> mole fraction measurements by GC/MS, higher uncertainties of around 50 % are estimated due to very small signals at small mole fractions (< 0.5 mol%). In addition, signals of species which could not be calibrated directly, are quantified according to a relative ionization cross section method described by Biordi et al. [84] along with calculated electron-ionization cross sections from empirically-derived addition theorems described by Fitch and Sauter [85]. The resulting uncertainties are estimated to be of a factor of 2 – 4 [82,91]. Mole fractions are used to calculate yields of all species, which allows a better comparison between the investigated mixtures. The yields are calculated according to equation (7-1). C atoms were used as reference for all hydrocarbons and H atoms are the reference for H<sub>2</sub>O and H<sub>2</sub>.

$$Yield_i = \frac{x_i \cdot \text{number of C/H atoms in product species } i}{\sum_{\text{Reactants}} x_j \cdot \text{number of C/H atoms in reactant species } j} \quad (7-1)$$

While N<sub>2</sub> was used as a diluent for GC/MS measurements, Ar was used for TOF-MS measurements to avoid convolutions of signals in both cases. To ensure that the different heat capacities of the diluents do not influence the results, some temperature profiles were remeasured with an argon flow of 280 sccm. The profiles deviate in the heating and cooling zone, but do not change the temperature or length of the isothermal zone (see supplementary material). Simulations of the mole fractions at the reactor outlet with both profiles do not differ significantly.

### 7.3 Simulations

In order to validate reaction mechanisms for the atypical reaction conditions of polygeneration processes, the experimental results are compared with simulations. A plug flow reactor model is used with a fixed temperature profile, including the temperature rise and drop at the reactor in- and outlet, and constant pressure for simulations in the Chemical Workbench Ver. 4.1 [44]. Reaction mechanisms of Zhang et al. [135] and Ranzi et al. [144] are used for the simulations with which the experiments are compared. Zhang et al. [135] developed a reaction mechanism for *n*-C<sub>7</sub>H<sub>16</sub>, based on sub-mechanisms for C<sub>0</sub>-C<sub>4</sub> fuels, pentane isomers and *n*-hexane. The sub-mechanism for C<sub>0</sub> – C<sub>4</sub> was taken from AramcoMech 2.0 [145] which has been widely validated for several fuels. The sub-mechanism for *n*-C<sub>7</sub>H<sub>16</sub> has been validated against shock-tube and jet-stirred reactor experiments, covering pressures from 1 to 38 bar, temperatures from 500 to 1412 K and equivalence ratios from 0.25 to 4. The reaction mechanism of Ranzi et al. [144] has been developed for pyrolysis, partial oxidation and combustion of hydrocarbon and oxygenated fuels up to C<sub>16</sub> and validated against a huge set of experimental data. Using these mechanisms, the product composition at the reactor outlet is evaluated and compared to the experimental results. For several reaction conditions an integrated reaction flow analysis was performed [146]. In addition to the mentioned reaction mechanisms, also the reaction

mechanisms of Hakka et al. [134], Seidel et al. [147] and Cai and Pitsch [148] are used for further simulations to assess their ability to predict the product spectra of the investigated mixtures. As these mechanisms turned out to perform worse, compared to the mechanisms of Ranzi and Zhang et al. the results are included in the supplementary material. Selected reactions, which are mentioned in the text, are listed in Table 7-2.

## 7.4 Results and discussion

Here, only some products ( $H_2$ ,  $CO$ ,  $CO_2$ ,  $C_2H_4$ ,  $C_2H_6$ ,  $C_3H_6$ ,  $CH_3OH$ ) are discussed in detail, because they were considered to be most interesting and they were formed in considerable amounts. At an equivalence ratio of  $\phi = 8$  the interaction of  $n\text{-}C_7H_{16}$  with  $CH_4$  is analyzed with respect to the reactants and selected products. The mole fraction profiles of the reactants and the yields of all experimentally detected intermediates can be found in the electronic supplementary material (ESM). Intermediates include  $H_2$  and  $C_1 - C_6$  species, covering alkanes, alkenes,  $CH_3OH$ , benzene ( $C_6H_6$ ), aldehydes and ketones. To summarize the general findings: Synthesis gas is mainly formed at low  $\phi$ , whereas alkanes, alkenes and  $C_6H_6$  are preferentially produced at higher  $\phi$  and high temperatures. Aldehydes and ketones are formed at all  $\phi$ , but the temperature range of their formation is extended at higher  $\phi$ . Although ketones are also interesting products and formed in considerable amounts according to the experiments, the uncertainties with respect to these species are much higher than the uncertainties of the species mentioned above. For this reason, the yields of ketones are not compared to simulations in this study, but are available in the electronic supplementary material. Figure 7-3 shows the main areas of formation of detected species within the investigated parameter range to give an overview of the formed species and their obtainable yields (see equation (7-1)). The maximum yields of the specific products within the marked parameter ranges are given in brackets in the legend.

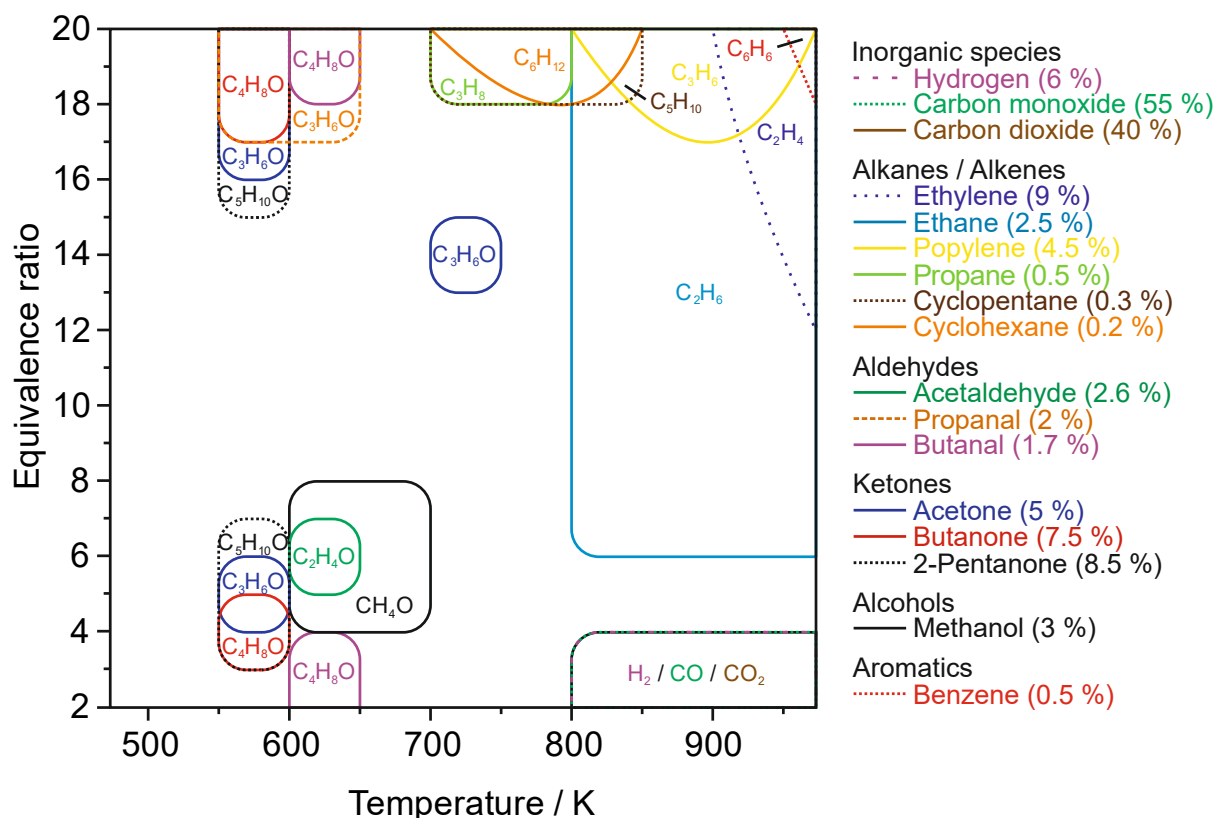


**Figure 7-3:** Main areas of formation of detected species at 6 bar in the investigated methane/heptane mixtures. The maximum yields of the respective species within the marked parameter range are given in brackets in the legend.

To check the justification of using a plug-flow model for the simulations, some simulations were also carried out using the cylindrical shear flow model of ChemKin Pro 19.0 [43] before interpreting the results. The simulations enable a rotation symmetric 2D simulation of the reactor, including heat transfer from the wall to the gas as well as the heat release due to exothermal reactions. For these simulations, the Zhang et al. [135] mechanism was used and the experimental temperature profile of the wall was fixed as boundary condition. The results show heat release due to the rapid conversion of *n*-heptane in a small area of the reactor as can be seen in Figure 7-4, which shows the temperature as a function of axial and radial distance of the reactor. The simulations were performed for  $\phi = 20$  and  $T = 623$  K as nominal value in the isothermal region. Consequently, the temperature increases by less than  $\Delta T = 100$  K above the temperature within the isothermal zone of the reactor. The largest temperature increase was found for the example shown in Figure 7-4. Even at these conditions, the trends of the mole fractions as a function of temperature do not differ significantly from the results obtained with the plug-flow model with predefined temperature profile. Typically the mole fractions at the reactor outlet, where the sampling takes place in the experiment, differ by less than 10 %. For CO the difference is typically less than 5 %. As the CPU time needed for these simulations is more than 10 times higher than for the simulations mentioned in the modeling section, and the results do not change the conclusions drawn in this paper, plug-flow simulations are considered adequate and accurate enough. Simulations, performed with the shear flow model are included in the ESM for  $\phi = 2, 4, 8$  and 20.

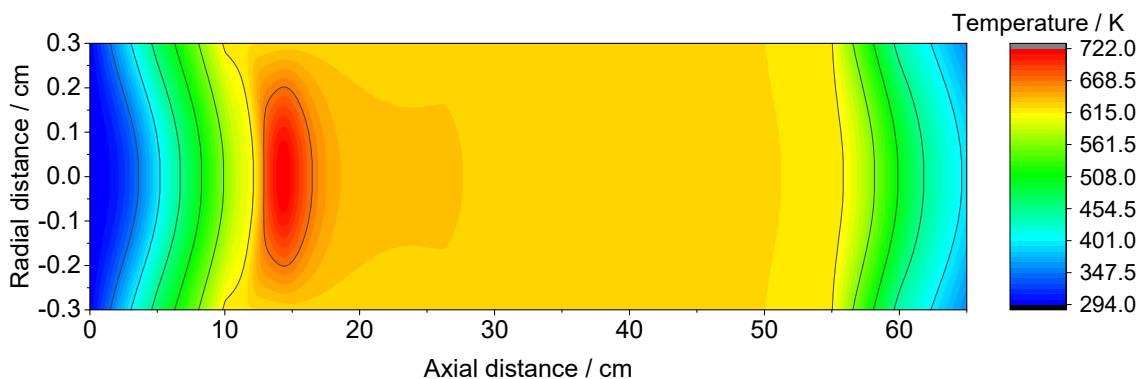
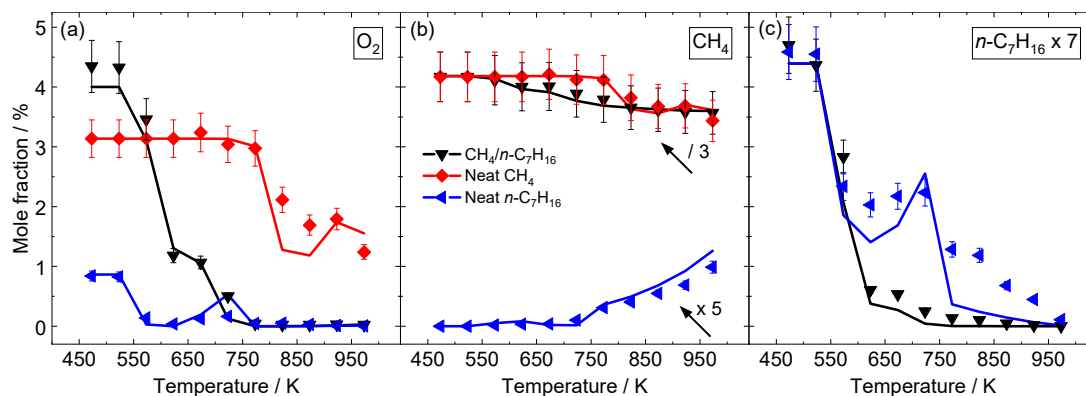


**Figure 7-4:** Simulated temperature profile for the reactive mixture at  $\phi = 20$  and  $T = 623$  K. 0 on the y-axis corresponds to the centerline of the reactor.

The carbon balance for every methane/heptane sample was within  $\pm 10$  % of the expected value. One exception occurs at 573 K where ketones and aldehydes are formed and up to 25 % more carbon is found than expected. The most probable reason for this observation is the higher uncertainty in the mole fractions of ketones and aldehydes, resulting from the calibration procedure used for these species. In addition, the carbon balance at  $\phi = 2$  is slightly worse at high temperatures.

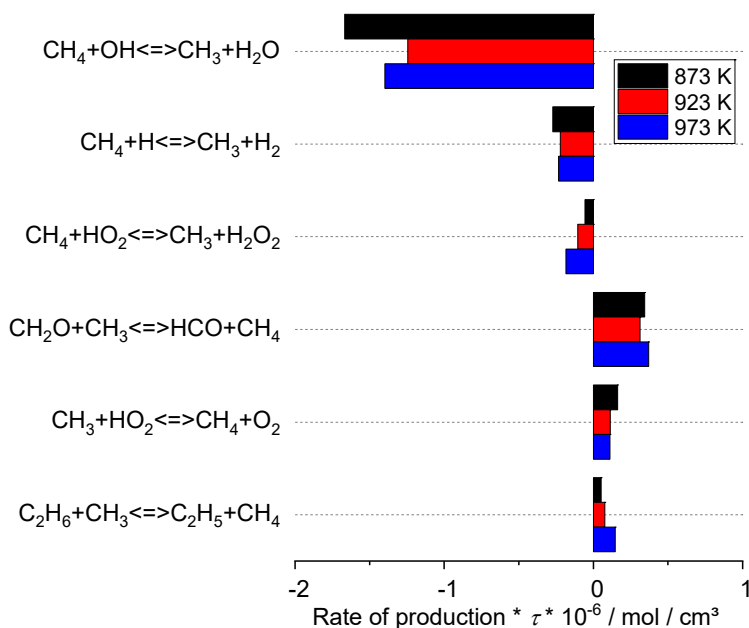
### 7.4.1 Reaction onset

Figure 7-5 shows the mole fractions of  $O_2$  (a),  $CH_4$  (b) and  $n-C_7H_{16}$  (c) as a function of temperature for  $\phi = 8$  for the  $CH_4/n-C_7H_{16}$ -mixture and the neat  $CH_4$ - and  $n-C_7H_{16}$ -mixtures, respectively. Symbols represent experimental data, obtained with the TOF-MS, and lines simulations using the reaction mechanism of Zhang et al. [135], as it showed the best performance in comparison to the experiments. The progress of the overall oxidation is visualized by the decrease in the  $O_2$  mole fraction, because oxygen is the limiting reactant under such rich conditions. The differences in the initial  $O_2$  mole fractions are caused by the different dilution of the mixtures. The conversion of oxygen can be detected starting at a temperature of 823 K for neat  $CH_4$  and at 573 K for  $n-C_7H_{16}$  containing mixtures.  $CH_4$  starts to react at 573 K in the mixture with  $n-C_7H_{16}$  whereas in the experiments with neat  $CH_4$  the conversion begins between 773 and 823 K, indicating that the initiation temperature was lowered by 200 – 250 K due to the additive. The experimentally observed mole fractions are predicted quite well by the model.



**Figure 7-5:** Mole fractions of  $\text{O}_2$  (a),  $\text{CH}_4$  (b) and  $n\text{-C}_7\text{H}_{16}$  (c) for  $\phi = 8$  and different mixtures. Symbols: TOF-MS experiment, solid lines: simulations based on the reaction mechanism of Zhang et al. [135].

Since not only the oxygen conversion but also the methane conversion is influenced by  $n$ -heptane addition to methane, the question arises how the intermediates of these two fuels interact. In order to analyze this interaction, a reaction path analysis was performed for all reactants and specific products using the reaction mechanism of Zhang et al. [135]. The most important reaction for  $\text{CH}_4$  conversion is the H-abstraction by hydroxyl radicals ( $\text{OH}$ ) yielding methyl radicals ( $\text{CH}_3$ ) and water ( $\text{H}_2\text{O}$ ) (see reaction R2 and Figure 7-6) as also reported in [105].



**Figure 7-6:** Reaction flow analysis of the neat  $\text{CH}_4$  mixture: Important reactions for  $\text{CH}_4$  consumption and formation at  $\phi = 8$ .

In the absence of  $n\text{-C}_7\text{H}_{16}$  the  $\text{OH}$  radicals are mainly formed by the dissociations of either methylhydroperoxide ( $\text{CH}_3\text{O}_2\text{H}$ ) below 800 K or hydrogen peroxide ( $\text{H}_2\text{O}_2$ ) at higher temperatures.  $\text{CH}_3\text{O}_2\text{H}$  is formed by H-abstraction from  $\text{CH}_4$  by methyl peroxy radicals ( $\text{CH}_3\text{O}_2$ ), which in turn are formed by the addition of  $\text{O}_2$  to  $\text{CH}_3$  (see Figure 7-7).

**Table 7-2:** Selected reactions from the reaction mechanism of Zhang et al. [135].

Nr.	Reaction
R1	$\text{CH}_4 + \text{O}_2 \rightleftharpoons \text{CH}_3 + \text{HO}_2$
R2	$\text{CH}_4 + \text{OH} \rightleftharpoons \text{CH}_3 + \text{H}_2\text{O}$
R3	$\text{C}_2\text{H}_6 + \text{CH}_3 \rightleftharpoons \text{C}_2\text{H}_5 + \text{CH}_4$
R4	$\text{CH}_3 + \text{O}_2 \rightleftharpoons \text{CH}_3\text{O}_2$
R5	$\text{C}_2\text{H}_5 + \text{O}_2 \rightleftharpoons \text{C}_2\text{H}_4 + \text{HO}_2$
R6	$2 \text{HO}_2 \rightleftharpoons \text{H}_2\text{O}_2 + \text{O}_2$
R7	$\text{HCO} + \text{M} = \text{H} + \text{CO} + \text{M}$
R8	$\text{CH}_3\text{CO} (+\text{M}) \rightleftharpoons \text{CH}_3 + \text{CO} (+\text{M})$
R9	$\text{C}_2\text{H}_5\text{O} \rightleftharpoons \text{CH}_3 + \text{CH}_2\text{O}$
R10	$\text{CH}_3\text{O} + \text{HO}_2 \rightleftharpoons \text{CH}_3\text{OH} + \text{O}_2$
R11	$\text{CH}_3 + \text{CH}_3 (+\text{M}) \rightleftharpoons \text{C}_2\text{H}_6$

$\text{CH}_3$  finally arises from the initiation reaction (R1). In contrast,  $\text{H}_2\text{O}_2$  is produced in a bimolecular reaction of two hydroperoxyl radicals ( $\text{HO}_2$ ) (reaction R6). In the presence of  $n\text{-C}_7\text{H}_{16}$  the most important route of OH formation is the intramolecular isomerization of  $\text{C}_7\text{H}_{15}\text{O}_2$  to  $\text{C}_7\text{H}_{14}\text{OOH}$ , subsequent  $\text{O}_2$  addition ( $\text{C}_7\text{H}_{14}\text{OOH} + \text{O}_2 \rightleftharpoons \text{C}_7\text{H}_{14}\text{OOH-O}_2$ ) and the formation of ketohydroperoxides ( $\text{C}_7\text{H}_{14}\text{OOH-O}_2 \rightleftharpoons \text{C}_7\text{H}_{14}\text{O}_3 + \text{OH}$ ), also shown by the black route of the  $n\text{-C}_7\text{H}_{16}$  pathway, presented in Figure 7-7. Both the formation of ketohydroperoxides and their decomposition produces OH radicals. The importance of these reactions was also pointed out by Li et al. [142]. In addition, two further pathways towards OH can be found in Figure 7-7, which are comparable to the pathways, described for  $\text{CH}_4$  oxidation. But, it must be noted that four isomeric heptyl radicals ( $\text{C}_7\text{H}_{15}$ ) can be formed due to hydrogen abstraction from  $n\text{-C}_7\text{H}_{16}$  by  $\text{O}_2$ , leading to many more pathways towards OH, compared to neat  $\text{CH}_4$  oxidation. The reaction path from  $n\text{-C}_7\text{H}_{16}$  towards OH via heptyl hydroperoxides ( $\text{C}_7\text{H}_{15}\text{OOH}$ ) is also described by Dagaut et al. [132].

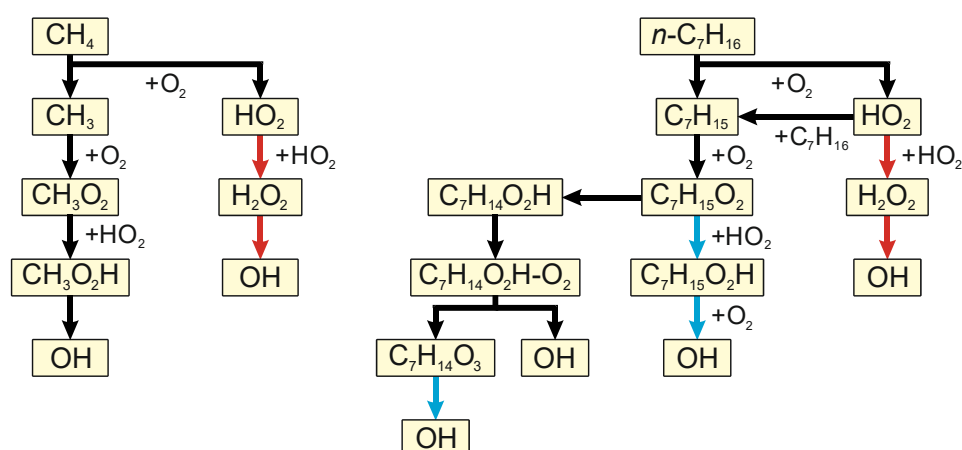


**Figure 7-7:** General formation of OH radicals with respect to  $\text{CH}_4$  (left) and  $n\text{-C}_7\text{H}_{16}$  oxidation (right). In the mixture both routes are active. (Black: Most important pathway, Red: High temperature pathway, Blue: Less important pathway).

To summarize the findings, the conversion of  $n\text{-C}_7\text{H}_{16}$  at relatively low temperatures leads to an increased formation of OH radicals, reacting with  $\text{CH}_4$  and lowering the temperature of reaction onset, compared to neat  $\text{CH}_4$ .

In the oxidation of neat  $n\text{-C}_7\text{H}_{16}$ ,  $\text{CH}_4$  is detected at temperatures above 673 K as one of the main intermediates. The formation of  $\text{CH}_4$  from larger hydrocarbon intermediates is a possible reason for the decreased conversion of  $\text{CH}_4$  (14.4 % vs. 17.9 %) observed in  $\text{CH}_4/n\text{-C}_7\text{H}_{16}$ -experiments at 973 K (see Figure 7-5b). The negative temperature coefficient region of  $n\text{-C}_7\text{H}_{16}$  is clearly present in the expected temperature range for  $n\text{-C}_7\text{H}_{16}$  containing mixtures [132], as seen by the increase in  $n\text{-C}_7\text{H}_{16}$  mole fractions from 600 to 800 K. The resulting s-shape is more pronounced in the model prediction in case of the neat  $n\text{-C}_7\text{H}_{16}$ -mixture. For neat  $\text{CH}_4$ , a similar behavior between 800 and 1000 K is observed, both, in the experiments and the model prediction in the  $\text{O}_2$  and  $\text{CH}_4$  profiles. Although the different  $\text{CH}_4$  mole fractions are within the error limits of the experiment, the apparent NTC behavior was reproducible, as checked several times by repeated measurements and simulations with different mechanisms. The results always indicate a negative temperature coefficient around 850 – 950 K. A reaction flow analysis indicates that less  $\text{CH}_4$  is consumed by OH at 923 K compared to 873 and 973 K (see Figure 7-6). The reaction (R2) is the most important reaction for  $\text{CH}_4$  consumption. In addition, H-abstraction from  $\text{C}_2\text{H}_6$  by  $\text{CH}_3$  radicals leads to an enhanced formation of  $\text{CH}_4$  (reaction R3) with increasing temperatures, resulting in a lower consumption of  $\text{O}_2$  by  $\text{CH}_3$  to methyl peroxide (reaction R4) at 923 K (see Figure 7-8). At 973 K,  $\text{O}_2$  consumption is accelerated again due to the reaction with ethyl radicals ( $\text{C}_2\text{H}_5$ ) to  $\text{C}_2\text{H}_4$  and  $\text{HO}_2$  (reaction R5), and the reaction (R6) towards  $\text{O}_2$  becomes less important at higher temperatures.

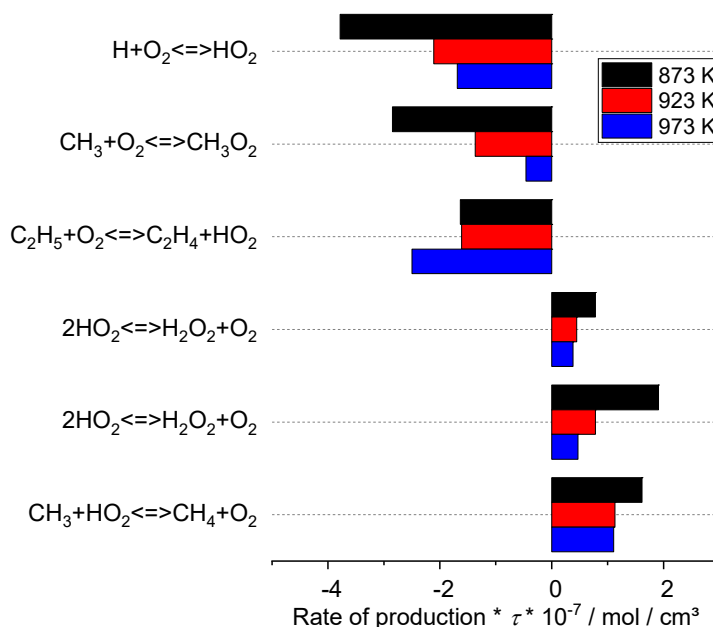


**Figure 7-8:** Reaction flow analysis of the neat  $\text{CH}_4$  mixture: Important reactions for  $\text{O}_2$  consumption and formation at  $\phi = 8$ .

Apart from the mentioned discrepancies, the experimental results are in good agreement with model predictions and show that  $n\text{-C}_7\text{H}_{16}$  is a suitable additive to activate  $\text{CH}_4$  conversion.

## 7.4.2 Influence of equivalence ratio and interaction of $n\text{-C}_7\text{H}_{16}$ with $\text{CH}_4$

Experiments at  $\phi = 2 - 20$  were carried out to investigate how the additive influences the mole fractions of different products, and to test the model predictions further. The discussion, emphasizing the interaction of  $n\text{-C}_7\text{H}_{16}$  with  $\text{CH}_4$  focuses on three representative major products:  $\text{CO}$ ,  $\text{C}_2\text{H}_6$  and  $\text{CH}_3\text{OH}$ . In addition, trends of the yields of  $\text{H}_2$ ,  $\text{CO}_2$ ,  $\text{C}_2\text{H}_4$  and  $\text{C}_3\text{H}_6$  are also presented and described.

Oxygen is the compound limiting the conversion in the fuel-rich regime; Figure 7-9 shows its conversion, whereas Figure 7-10, Figure 7-13 and Figure 7-15 show the yields (see equation (7-1)) of  $\text{CO}$ ,  $\text{C}_2\text{H}_6$  and  $\text{CH}_3\text{OH}$  as a function of temperature and equivalence ratio in false color diagrams.  $\text{CO}$  represents a main product under fuel-rich conditions, whereas  $\text{C}_2\text{H}_6$  represents a C-C-coupling and  $\text{CH}_3\text{OH}$  an oxygenated product. The experimental results (left), all obtained by GC/MS, are compared to kinetic simulations, using the reaction mechanisms of Zhang et al. [135] (middle) and Ranzi et al. [144] (right). The results of simulations with the reaction mechanism of Ranzi et al. [144] were included in the comparison because it has been validated against many experimental measurements and is suitable for different reaction conditions.

From Figure 7-9 it is evident that at all equivalence ratios more than 50 % of  $\text{O}_2$  is converted below 600 K.

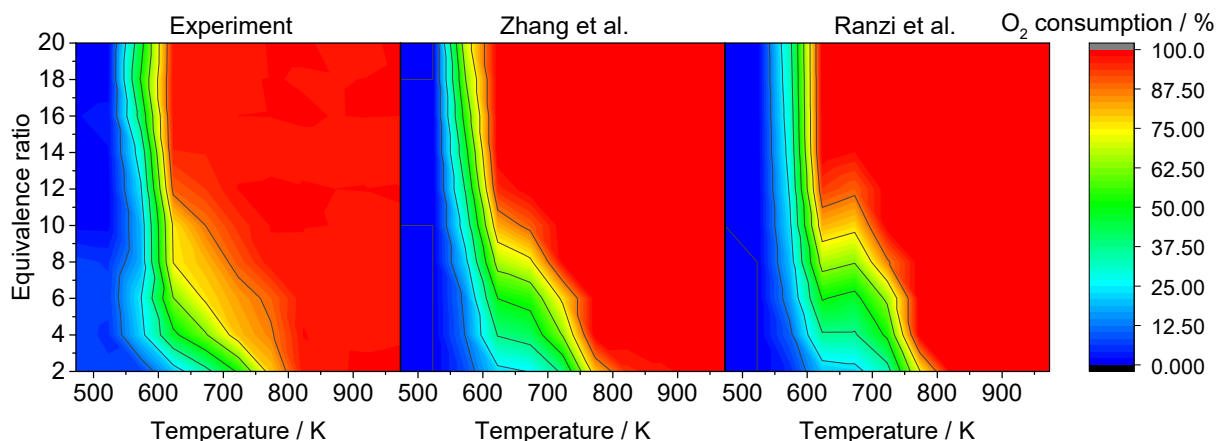


**Figure 7-9:**  $\text{O}_2$  consumption for all investigated methane/heptane mixtures (Experiment: left (GC results), Simulations: middle [135] and right [144]).

The low  $\text{CH}_4$  conversion at these temperatures (Figure 7-5b) leads to the conclusion that  $\text{O}_2$  is mainly consumed by the additive. This observation agrees with the complete conversion of  $n\text{-C}_7\text{H}_{16}$  at all equivalence ratios at high temperatures (as shown in the ESM). The general trends in the consumption of reactants predicted in the simulations are in good agreement with the experimental data, even though both models underpredict the  $\text{CH}_4$  conversion at  $\phi \geq 6$  slightly (see Figure 7-5b and ESM). In addition, the model of Ranzi et al. [144] overestimates the NTC behavior of  $n$ -heptane so that less  $\text{O}_2$  is consumed by  $n$ -heptane at 673 K, compared to the experimental results and the results, obtained with the model of Zhang et al. [135].

One of the main products in all experiments is  $\text{CO}$  (Figure 7-10).

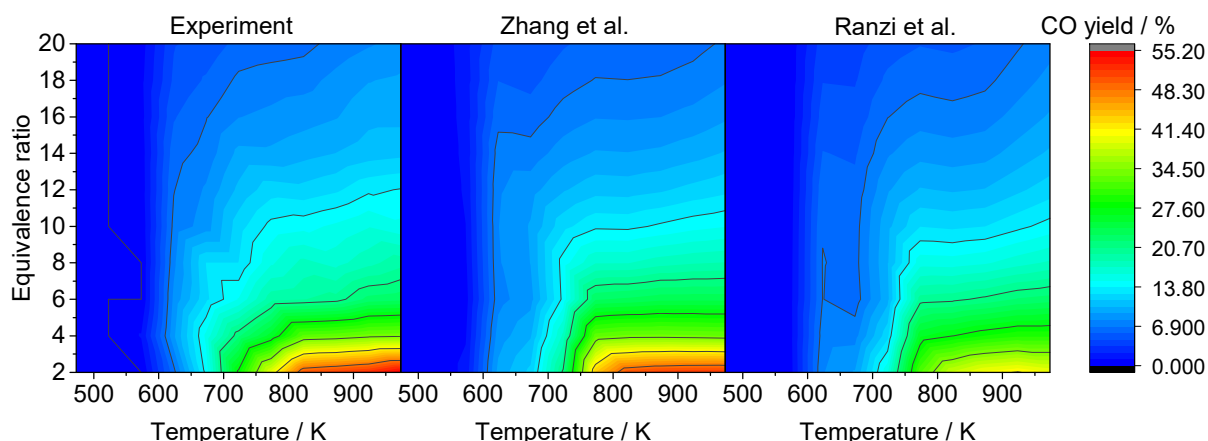


**Figure 7-10:** Yield of CO for all investigated methane/heptane mixtures (Experiment: left (GC results), Simulations: middle [135] and right [144]).

The formation of CO starts at 573 K at all equivalence ratios and increases rapidly with rising temperature. The maximum CO yield of 55.1 % is observed at 973 K and  $\phi = 2$ , which is the condition with the highest CH<sub>4</sub> conversion. Above 823 K, the CO yield rises only slightly with increasing temperature. The simulations, with the reaction mechanism of Zhang et al. [135], are in good agreement with the experimental data, regarding general trends and yields. Simulations with the reaction mechanism of Ranzi et al. [144] underestimate the maximum CO yield by around 30 %. An interesting observation is the following: Nearly no CO is formed in the neat CH<sub>4</sub>-experiment and only 0.4 % CO in the neat *n*-C<sub>7</sub>H<sub>16</sub>-experiment, in contrast to 2.8 % in the *n*-C<sub>7</sub>H<sub>16</sub>/CH<sub>4</sub>-experiments, indicating some interaction between the species pools resulting from *n*-heptane and methane conversion. This is shown by the TOF-MS results, presented in Figure 7-11a.

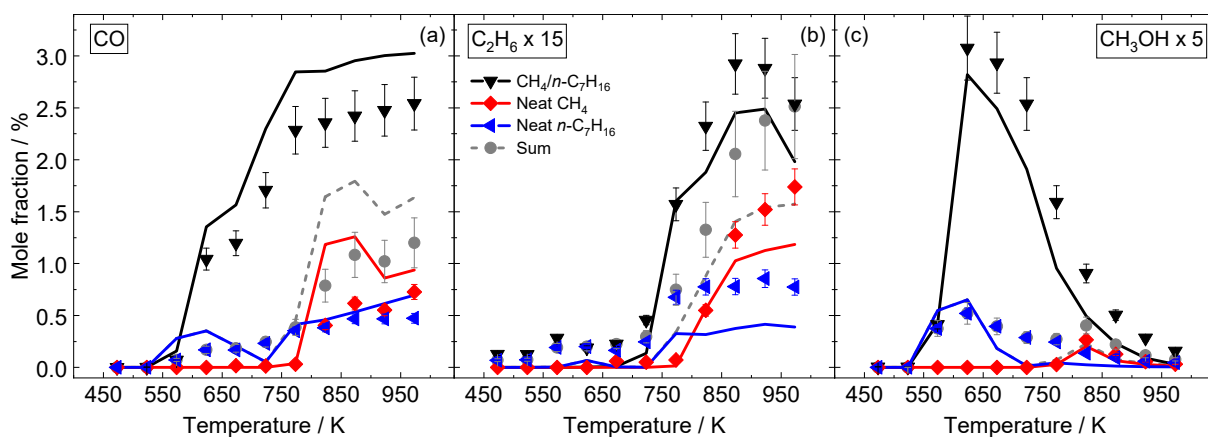


**Figure 7-11:** Mole fractions of CO (a), C<sub>2</sub>H<sub>6</sub> (b) and CH<sub>3</sub>OH (c) for different mixtures at  $\phi = 8$ . Symbols: TOF-MS experiment, solid lines: simulations based on the reaction mechanism of Zhang et al. [135]. The gray lines and symbols are always the sum of the results for the two neat fuel experiments or simulations, respectively.

Here, mole fractions are presented instead of yields to determine a possible interaction between methane and heptane oxidation pathways. An interaction is assumed if the sum of mole fractions of specific products (shown in gray) observed in the single fuel experiments differs from those obtained by the methane/heptane mixture. Using yields, such a comparison would not be



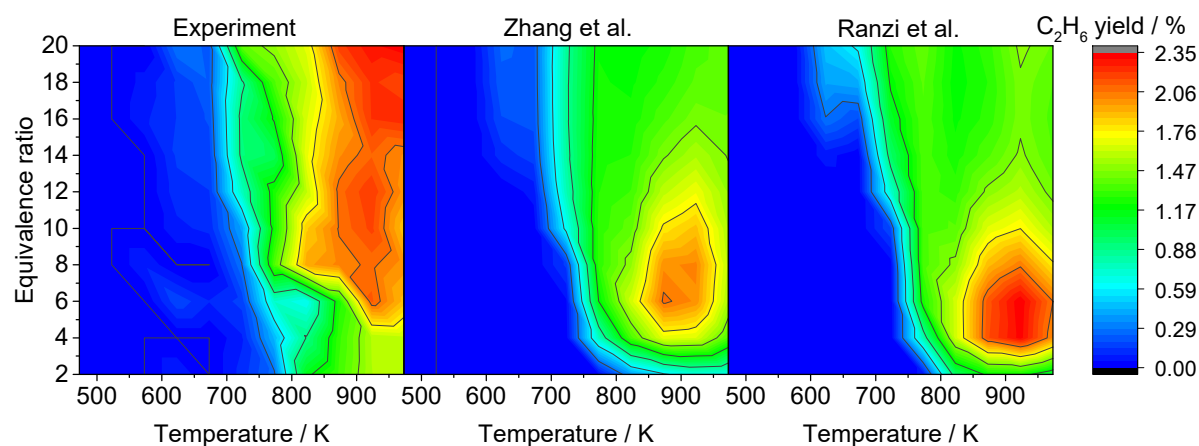


**Figure 7-13:** Yield of  $C_2H_6$  for all investigated methane/heptane mixtures (Experiment: left (GC results), Simulations: middle [135] and right [144]).

The maximum yield of  $C_2H_6$  is observed at the highest investigated equivalence ratio ( $\phi = 20$ ) and temperature ( $T = 973$  K). At equivalence ratios below 16,  $C_2H_6$  decomposes to  $C_2H_4$  and  $H_2$  and the ethane yield decreases at temperatures above 923 K. Experiments are in good quantitative agreement with the simulations for ethane up to  $\phi = 8$  and all investigated temperatures as well as for higher  $\phi$  and temperatures up to 773 K. But, the agreement with the simulations performed with the reaction mechanism of Zhang et al. [135] is slightly better than those performed with the mechanism of Ranzi et al. [144]. For equivalence ratios above 8 and temperatures higher than 773 K, both models predict a decreasing yield, contrary to a slightly increasing yield in the experiments. Only the reaction mechanism of Cai et al. [148] is able to predict the  $C_2H_6$  yields within the uncertainty limits. Using this mechanism, a very good agreement with respect to the  $C_2H_6$  yields at temperatures higher than 773 K is found. The yields at lower temperatures are overpredicted by the model (see ESM). At temperatures lower than 773 K, a reaction flow analysis reveals that most of the  $C_2H_6$  is formed by *n*-heptane oxidation. Based on these observations, it can be concluded that the *n*-heptane sub-scheme within the mechanism of Zhang et al. [135] performs better than the *n*-heptane sub-scheme of the Cai and Pitsch mechanism [148]. However, the rate constants for reactions, which are responsible for  $C_2H_6$  formation at higher temperatures seem to be more suitable in case of the mechanism of Cai and Pitsch [148]. A reaction path analysis explains the increase in  $C_2H_6$  yields in the doped mixtures. The recombination of two  $CH_3$  radicals to  $C_2H_6$  (R11) is by far the most important reaction for  $C_2H_6$  formation with  $CH_4$  as a fuel. For *n*- $C_7H_{16}$  this reaction is less important, since  $C_2$  compounds are formed in the oxidation of heptane, and the governing pathway to produce  $C_2H_6$  is the reaction of  $C_2H_5$  and  $H_2O_2$  to  $C_2H_6$  and  $HO_2$  (see Figure 7-12).  $C_2H_5$  is formed in several reaction steps directly from *n*- $C_7H_{16}$ . Again, in the *n*- $C_7H_{16}/CH_4$ -mixture both routes are active, but the recombination of  $CH_3$  is the dominant reaction, since  $CH_3$  formation is enhanced by *n*- $C_7H_{16}$  oxidation (see Figure 7-14). In addition, a new reaction appears in the reaction network forming  $C_2H_6$  by reaction of  $C_2H_5$  with  $CH_4$ . These observations explain the increased  $C_2H_6$  production in the *n*- $C_7H_{16}/CH_4$ -mixture in Figure 7-11b for  $\phi = 8$ . For a better quantitative agreement between the predictions by Zhang et al. [135] and the experimental data, the rate constants of the Cai and Pitsch [148] mechanism with respect to reaction R11 should be considered.

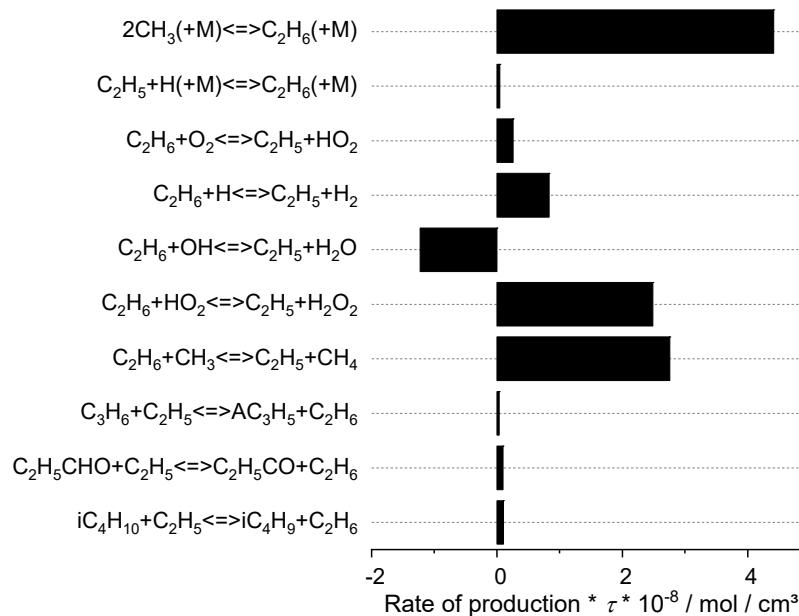


**Figure 7-14:** Important reactions for  $\text{C}_2\text{H}_6$  consumption and formation at  $\phi = 8$  and 773 K ( $\text{CH}_4/n\text{-C}_7\text{H}_{16}$ ). The reaction flow analysis was performed with the reaction mechanism of Zhang et al. [135].

$\text{CH}_3\text{OH}$  is mainly formed at intermediate temperatures between 523 and 823 K at all  $\phi$  (Figure 7-15) in all investigated methane/heptane mixtures.

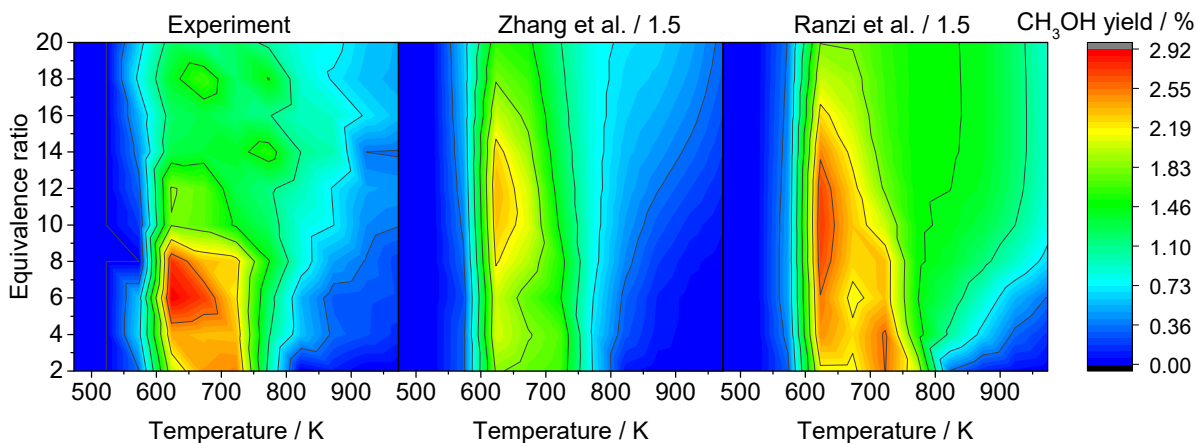


**Figure 7-15:** Yield of  $\text{CH}_3\text{OH}$  for all investigated methane/heptane mixtures (Experiment: left (GC results), Simulations: middle [135] and right [144]).

The  $\text{CH}_3\text{OH}$  yield reaches its maximum at 623 K ( $4 \leq \phi \leq 20$ ) and at 723 K ( $\phi = 2$ ), respectively. The overall maximum yield of 2.9 % is located between  $6 \leq \phi \leq 8$ . With rising  $\phi$ , the formation of  $\text{CH}_3\text{OH}$  occurs in a wider temperature range. Similar trends are observed in the simulations. Generally, the model predictions, obtained with the reaction mechanism of Zhang et al. [135] are in better agreement with the experimental results than the ones with the reaction mechanism of Ranzi et al. [144]. While the latter predicts 1.5 – 4 times higher yields of  $\text{CH}_3\text{OH}$ , compared to the experimental results, the mechanism of Zhang et al. [135] predicts yields which are close to the experimental uncertainty limits up to  $\phi = 8$ . Independent yield measurements at

$\phi = 8$ , obtained with the directly coupled time-of-flight mass spectrometer, also agree with model predictions by the mechanism of Zhang et al. [135] within the error limits, as shown in Figure 7-11c. At  $\phi \geq 10$ , the predicted  $\text{CH}_3\text{OH}$  yields are two to three times larger than the experimental results. The overall maximum yield at 623 K also extends between  $6 \leq \phi \leq 14$  with respect to the simulations. In summary, the predicted consumption of methanol due to reactions towards formaldehyde and finally CO is too high under these conditions. Accordingly, further validation data are needed to improve reaction kinetics schemes for ultra-rich conditions. The reaction flow was analyzed at 623 K, since maximum  $\text{CH}_3\text{OH}$  yields were observed at this temperature for both  $n\text{-C}_7\text{H}_{16}$  containing mixtures.  $\text{CH}_3\text{OH}$  was not detected in the neat  $\text{CH}_4$ -mixture. The most important reaction for  $\text{CH}_3\text{OH}$  formation is (R10), in which  $\text{CH}_3\text{O}$  is produced from  $\text{CH}_3$  via peroxide intermediates. Consequently,  $\text{CH}_3$  is the key component for  $\text{CH}_3\text{OH}$  formation. In agreement with the observation at 773 K, the  $\text{CH}_3$  production is enhanced significantly at 623 K if  $\text{CH}_4$  and  $n\text{-C}_7\text{H}_{16}$  are both present, because the oxidation of the latter provides the OH radicals that are needed for the H-abstraction from  $\text{CH}_4$ . As a result, the  $\text{CH}_3\text{OH}$  yields are much higher in case of the  $n\text{-C}_7\text{H}_{16}/\text{CH}_4$ -mixture compared to both neat fuels. Another interesting feature of the mixtures is that the production of  $\text{CH}_3\text{OH}$  occurs in the complete investigated temperature range, compared to the very limited temperature range observed for the neat fuels (see Figure 7-11c).

Figure 7-16-Figure 7-19 show the yields of  $\text{H}_2$ ,  $\text{CO}_2$ ,  $\text{C}_2\text{H}_4$  and  $\text{C}_3\text{H}_6$  as a function of equivalence ratio and temperature in false color diagrams. Except for  $\text{CO}_2$ , which represents a fully oxidized product, these species could be interesting in terms of applications in chemical industry or even energy storage. The yields are calculated as mentioned before (see equation (7-1)). Again the experimental results (left) are compared to kinetic simulations, using the reaction mechanisms of Zhang et al. [135] and Ranzi et al. [144].

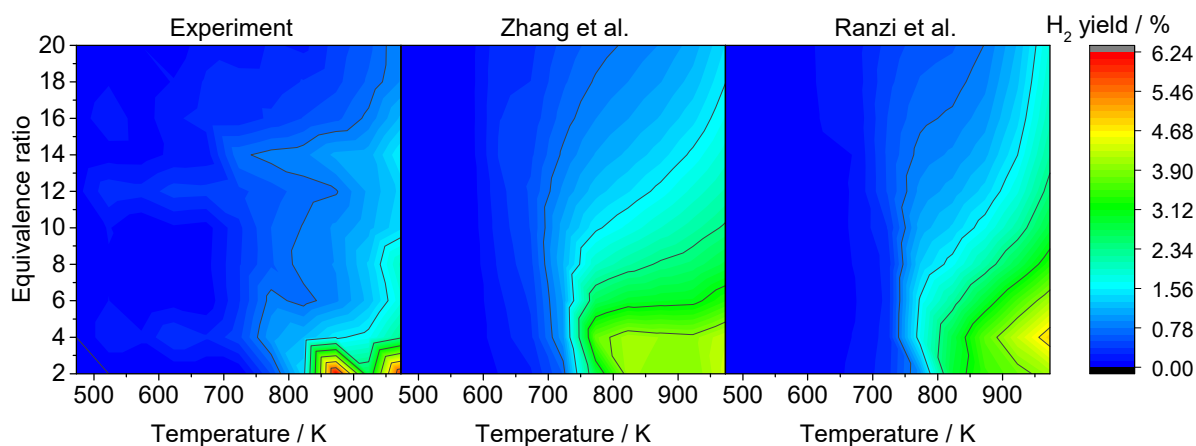


**Figure 7-16:** Yield of  $\text{H}_2$  for all investigated methane/heptane mixtures (Experiment: left (GC results), Simulations: middle [135] and right [144]).

The highest  $\text{H}_2$  yields of up to 6 % are observed at 873 K and 973 K at  $\phi = 2$  (Figure 7-16). At higher equivalence ratio, the maximum yield is always found at the highest investigated temperature of 973 K and it decreases with increasing  $\phi$ . The experimental yields are up to 80 % lower than the yields predicted by both models at  $\phi \geq 4$  for temperatures above 800 K, but at  $\phi = 2$  the experimental yields are 60 and 30 % higher at 873 K and 973 K, respectively. The

predictions using the Zhang et al. [135] mechanism also show two local maxima at these temperatures. In contrast, the predictions using the mechanism of Ranzi et al. [144] show a continuously increasing H<sub>2</sub> yield with rising temperature. Also, the maximum H<sub>2</sub> yield at  $\phi = 4$  predicted by the mechanism of Ranzi, slightly differs from the experimental results and model predictions using the mechanism of Zhang et al. [135], where the global maximum can be found at  $\phi = 2$ . One possible reason for the large deviations between experimental results and model predictions may be caused by higher uncertainties in the H<sub>2</sub> mole fraction, resulting from the detection procedure mentioned above. This suggestion is confirmed by the fact that the TOF-MS data for H<sub>2</sub> at  $\phi = 8$  are in better agreement with the simulation results, compared to the GC data. GC/MS and TOF-MS measurements for other species are in good agreement with each other. If only the general trends of the predicted and experimental H<sub>2</sub> yields are compared reasonable agreement is observed.

For the CO<sub>2</sub> yields (see Figure 7-17), the trends are comparable to the trends of the CO yields (see Figure 7-10), as CO<sub>2</sub> is mainly formed by CO and HO<sub>2</sub> or OH. The highest yield of nearly 40 % can be found at 873 K at  $\phi = 2$ . In general, the qualitative agreement between experimental results and model predictions is very good, but the yields, obtained in the experiments, are much higher than the yields, predicted by both reaction mechanisms. This becomes obvious by the fact that the predicted yields are multiplied by 1.5 and 2 for the mechanisms of Zhang et al. [135] and Ranzi et al. [144], respectively.

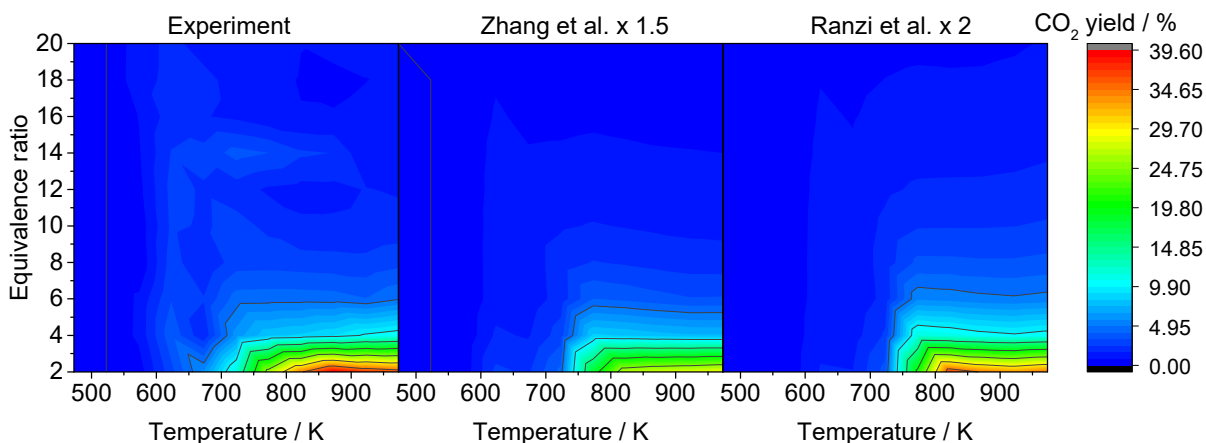


**Figure 7-17:** Yield of CO<sub>2</sub> for all investigated methane/heptane mixtures (Experiment: left (GC results), Simulations: middle [135] and right [144]).

The formation of C<sub>2</sub>H<sub>4</sub> starts at 623 K at all investigated equivalence ratios (see Figure 7-18). However, the yield only reaches 0.6 % on average at this temperature. Because the CH<sub>4</sub> conversion is less than 3 % (see ESM) at these conditions, it can be concluded that C<sub>2</sub>H<sub>4</sub> is mainly formed from *n*-C<sub>7</sub>H<sub>16</sub>.

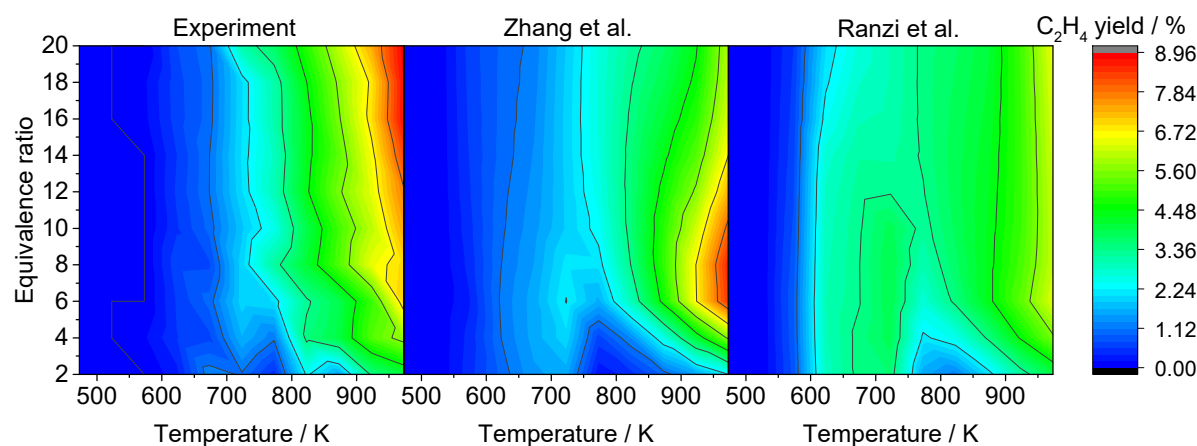


**Figure 7-18:** Yield of  $C_2H_4$  for all investigated methane/heptane mixtures (Experiment: left (GC results), Simulations: middle [135] and right [144]).

According to the reaction path analysis, performed with the mechanism of Zhang et al. [135] at  $\phi = 8$  and 623 K, the most important reaction for  $C_2H_4$  formation is the decomposition of an ethyl peroxy radical ( $C_2H_5O_2$ ), which in turn is formed by  $O_2$  addition to  $C_2H_5$ . Ethyl is formed by the decomposition of the propionyl radical ( $C_2H_5CO$ ), originating from the reaction of propanal ( $C_2H_5CHO$ ) and different radicals, or the reaction of acetaldehyde and OH. Both  $CH_3CHO$  and  $C_2H_5CHO$  are typical products of  $n$ - $C_7H_{16}$  oxidation [132,134,135] and have also been detected by gas chromatography in this study (see ESM) at this temperature. At temperatures higher than 723 K, where  $CH_4$  conversion starts to increase significantly, the  $C_2H_4$  yield also increases rapidly. In this temperature range the most important reaction for  $C_2H_4$  formation is the H-abstraction from  $C_2H_5$  by  $O_2$ , forming  $C_2H_4$  and  $HO_2$ , where  $C_2H_5$  is produced by the reaction of  $C_2H_6$  and  $CH_3$ . As shown before,  $C_2H_6$  originates by the recombination of two  $CH_3$  radicals. Finally, it can be concluded that most  $C_2H_4$  is formed in the oxidation of methane at temperatures above 723 K. With increasing equivalence ratio, the  $C_2H_4$  yield also increases, reaching around 9 % at  $\phi = 20$  and 973 K. As for  $C_2H_6$ , experiments are in good agreement with the simulations, performed with the reaction mechanism of Zhang et al. [135]. Only at temperatures higher than 823 K and  $\phi > 10$  the predicted yields are 20 ( $\phi = 10$ ) – 60 % ( $\phi = 20$ ) lower as expected because of the lower predicted  $C_2H_6$  yields. As the deviations rise with increasing  $\phi$ , the model has to be optimized mainly for these conditions in order to improve the model predictions. With respect to the model by Ranzi et al. [144], the predicted yields are much higher in the low temperature regime ( $573 \text{ K} \leq T \leq 723 \text{ K}$ ) and slightly lower at higher temperatures. Comparing the model predictions by Cai et al. [148] with the experimental results, a better agreement is observed due to the better prediction of the  $C_2H_6$  yields (see ESM). Propene ( $C_3H_6$ ) is preferentially formed at high temperatures and high equivalence ratios (see Figure 7-19).

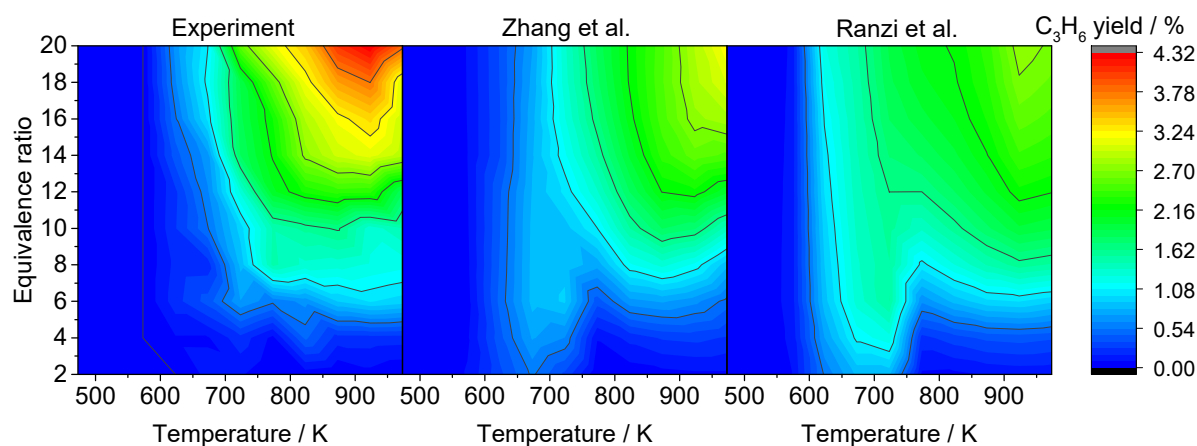


**Figure 7-19:** Yield of  $C_3H_6$  for all investigated methane/heptane mixtures (Experiment: left (GC results), Simulations: middle [135] and right [144]).

Similar to  $C_2H_4$  the formation starts at 623 K, and the yield increases rapidly at temperatures higher than 723 K with a maximum of 4.3 % at 923 K and  $\phi = 20$ . Based on this observation, the same conclusion is drawn as before: at low temperature  $C_3H_6$  is formed by  $n-C_7H_{16}$  oxidation, while the combined formation of  $C_3H_6$  from  $CH_4$  and  $n-C_7H_{16}$  oxidation gets important at higher temperatures. Comparing experimental results to the simulations, generally good agreement is found, especially regarding the trends of the yields. But, the models of Zhang et al. [135] and Ranzi et al. [144] predict lower maximum yields of 3 % and 2 % within the investigated parameter range, respectively. In addition, higher yields of  $C_3H_6$  are predicted in the temperature range between 623 K and 773 K at  $\phi < 6$  by both models, compared to the experimental results. With respect to the reaction path towards  $C_3H_6$  at  $\phi = 20$  and 923 K, one key species is  $C_3H_8$ , formed from  $CH_3$  and  $C_2H_5$ . The contribution of  $CH_4$  to the production rate of  $CH_3$  and  $C_2H_5$  is  $\approx 71$  and  $\approx 14$  %, respectively.  $C_3H_8$  can react with different radicals to the isopropyl radical ( $iC_3H_7$ ), which finally undergoes an  $O_2$  addition, so that the isopropyl peroxy radical ( $iC_3H_7O_2$ ) is formed.  $iC_3H_7O_2$  will finally decompose to propene and  $HO_2$ . The last reaction is the most important reaction with respect to  $C_3H_6$  formation with a production rate contribution of  $\approx 30$  %.

## 7.5 Conclusions

The homogeneous partial oxidation of  $n-C_7H_{16}/CH_4/O_2$ -mixtures was investigated in a plug-flow reactor in a wide parameter range. The product gases were analyzed by gas chromatography and mass spectrometry. An additional set of experiments was performed at  $\phi = 8$ , consisting of neat  $n-C_7H_{16}$ , neat  $CH_4$  and  $n-C_7H_{16}/CH_4$ -mixtures to analyze the influence of  $n-C_7H_{16}$  and its decomposition products on the partial oxidation of  $CH_4$ . Reaction path analyses were carried out after modeling the experiments, using the elementary reaction mechanisms of Zhang et al. [135] and Ranzi et al. [144]. In general, the model predictions are in reasonable agreement with the experimental data, but the model of Zhang et al. [135], which has been developed for fuel-rich  $n-C_7H_{16}$  oxidation, in general shows a better performance. Larger deviations in the predicted amounts of some species, e.g.  $CH_3OH$ , compared to experimental data are observed and indicate the need for model improvement at fuel-rich conditions.

The addition of heptane to methane shifted also the reaction onset of CH<sub>4</sub> by 200 – 250 K towards lower temperatures due to the enhanced production of OH radicals, which in turn initiate CH<sub>4</sub> conversion. In addition to the main products like CO, CO<sub>2</sub>, H<sub>2</sub>O and H<sub>2</sub>, also oxygenated species like CH<sub>3</sub>OH and useful hydrocarbons up to C<sub>6</sub> were detected. For CH<sub>3</sub>OH, maximum yields of almost 3 % can be found at temperatures between 523 K and 823 K at  $4 \leq \phi \leq 8$  under these dilute conditions. According to the reaction flow analysis, CH<sub>3</sub>OH formation is enhanced significantly in the presence of *n*-C<sub>7</sub>H<sub>16</sub> due to an enhanced formation of CH<sub>3</sub> and CH<sub>3</sub>O radicals, which are precursors of CH<sub>3</sub>OH. So the high reactivity of *n*-heptane has a positive effect on the consumption of methane at low temperatures and favors the reaction pathways from methane to methanol. CO was formed in high amounts of up to 55 % at  $\phi = 2$  and  $T \geq 923$  K. Comparing experiments with the mixture of both fuels with neat CH<sub>4</sub> and *n*-C<sub>7</sub>H<sub>16</sub> as fuels, it is observed that the CO and C<sub>2</sub>H<sub>6</sub> production was also enhanced in the mixture, due to the increased formation of CH<sub>3</sub> radicals. Also for the unsaturated hydrocarbons, e.g. C<sub>2</sub>H<sub>4</sub> and C<sub>3</sub>H<sub>6</sub>, a reaction path analyses revealed that CH<sub>4</sub> plays an important role in their formation during the oxidation of CH<sub>4</sub>/*n*-C<sub>7</sub>H<sub>16</sub> mixtures. These routes could be interesting in the matter of storing excess energy, coming from renewables, as the enthalpies of formation of these species are much higher than the enthalpy of formation of methane. In general, hydrocarbons, like C<sub>2</sub>H<sub>4</sub>, C<sub>2</sub>H<sub>6</sub>, C<sub>3</sub>H<sub>6</sub>, C<sub>3</sub>H<sub>8</sub> and C<sub>6</sub>H<sub>6</sub> are preferentially formed at higher  $\phi$ . Referring to polygeneration processes this means that high equivalence ratios are the most interesting conditions for the formation of useful chemicals. Because of the reduced fuel conversion and lower heat release due to less exothermal reactions the maximum temperature in the engine would decrease. So, even species, preferentially formed at temperatures below 1000 K, could probably be formed in an engine. But, first of all it has to be tested, which equivalence ratio represents a reasonable limit with respect to the simultaneous supply of chemicals, work and heat by performing experiments in a real piston engine.

The results show that the addition of small amounts of *n*-C<sub>7</sub>H<sub>16</sub> into CH<sub>4</sub>/O<sub>2</sub>-mixtures can initiate CH<sub>4</sub> conversion at much lower temperatures and increase mole fractions of specific species significantly. The comparison between experimental and modeling results and the observed differences corroborate the need for better kinetics models for these uncommon reaction conditions. Especially at  $\phi \geq 10$  larger deviations between experimental data and model predictions are observed. It could also be demonstrated that the comparison of experimental results and model predictions of different reactions mechanisms can help to identify reaction rates that require reassessment and optimization for better quantitative agreement, as it was shown for C<sub>2</sub>H<sub>6</sub>.

---

## 8 Partial oxidation of methane/DME mixtures

The content of this chapter was published in *Combustion and Flame*:

S. Porras, D. Kaczmarek, J. Herzler, S. Drost, M. Werler, T. Kasper, M. Fikri, R. Schießl, B. Atakan, C. Schulz, U. Maas, An experimental and modeling study on the reactivity of extremely fuel-rich methane/dimethyl ether mixtures, *Combustion and Flame* 212, pp. 107-122 (2020).

© 2019 The Authors. Published by Elsevier. Reprinted with permission.

For this paper, Sylvia Porras developed the reaction mechanism, coordinated the assembling of the manuscript, and wrote most of the results and the introductory part of the manuscript as well as the sub-chapter concerning the description of the chemical kinetics model. Jürgen Herzler provided the shock-tube results and wrote the corresponding part in the manuscript. Simon Drost and Marc Werler performed the rapid compression machine experiments and contributed by writing the associated part. As for myself, I carried out the flow reactor experiments, which included the preparation of the experimental setup, the execution of the experiments as well as the analysis and evaluation of the obtained experimental data. I was also responsible for writing the corresponding part of the manuscript. Tina Kasper, Mustapha Fikri, Robert Schießl, Burak Atakan, Christoph Schulz, and Ulrich Maas contributed to the development of the constructed numerical and experimental data, and to their interpretation. All authors were engaged in the correction and later proof-reading of the manuscript.

### Abstract

Chemical reactions in stoichiometric to fuel-rich methane /dimethyl ether /air mixtures (fuel air equivalence ratio  $\phi = 1 - 20$ ) were investigated by experiment and simulation with the focus on the conversion of methane to chemically more valuable species through partial oxidation. Experimental data from different facilities were measured and collected to provide a large database for developing and validating a reaction mechanism for extended equivalence ratio ranges. Rapid Compression Machine ignition delay times and species profiles were collected in the temperature range between 660 and 1052 K at 10 bar and equivalence ratios of  $\phi = 1 - 15$ . Ignition delay times and product compositions were measured in a shock tube at temperatures of 630 to 1500 K, pressures of 20 – 30 bar and equivalence ratios of  $\phi = 2$  and 10. Additionally, species concentration profiles were measured in a flow reactor at temperatures between 473 and 973 K, a pressure of 6 bar and equivalence ratios of  $\phi = 2, 10,$  and 20. The extended equivalence ratio range towards extremely fuel-rich mixtures as well as the reaction-enhancing effect of dimethyl ether were studied because of their usefulness for the conversion of methane into chemically valuable species through partial oxidation at these conditions. Since existing reaction models focus only on equivalence ratios in the range of  $\phi = 0.3 - 2.5$ , an extended chemical

kinetics mechanism was developed that also covers extremely fuel-rich conditions of methane/dimethyl ether mixtures. The measured ignition delay times and species concentration profiles were compared with the predictions of the new mechanism, which is shown to predict well the ignition delay time and species concentration evolution measurements presented in this work. Sensitivity and reaction pathway analyses were used to identify the key reactions governing the ignition and oxidation kinetics at extremely fuel-rich conditions.

## 8.1 Introduction

Recently, interest in co-generation and polygeneration processes for flexible conversion between different forms of energy and coupled production of valuable chemical species like syngas, acetylene ( $C_2H_2$ ), and ethylene ( $C_2H_4$ ) from cheap substances (especially methane) has increased [94,95,97,149]. The production of such chemicals is usually most efficient at very high equivalence ratios (typically exceeding  $\phi = 6$ ), which are not used in conventional combustion processes. There is a lack of studies providing empirical data and validated chemical kinetics models for the ultra-rich regime.

The reaction kinetics of methane ( $CH_4$ ), a suitable resource for polygeneration processes, have been extensively investigated in the last few decades by several authors. Hughes et al [150] developed a comprehensive chemical mechanism to describe the oxidation of methane. The mechanism also accounts for the oxidation kinetics of other species as hydrogen, carbon monoxide, ethane, and ethene in flames as well as the autoignition problem in homogeneous mixtures. Petersen et al [151], on the other hand, conducted an analytical study of  $CH_4/O_2$  mixtures over a large range of conditions. A reaction mechanism was developed to supplement the high-pressure shock tube experiments on autoignition delay times [151]. Ignition delay times of similar mixtures have been reported by Brett et al [152] and Gersen [153] using a RCM and by Shukov et al [154], who measured IDTs behind reflected shock waves at elevated pressures between 3 and 450 bar and high initial temperatures. Measurements of species profiles describing the homogeneous partial oxidation of  $CH_4$  have also been studied by different groups in high pressure flow reactors [101,102,104,155] and jet-stirred reactors [156], for a large range of reaction conditions covering pressures from 1 – 100 bar and temperatures between 600 and 1800 K. Most of the studies on methane combustion and oxidation have been focused on stoichiometric to slightly fuel-rich mixtures [106,150,151,156]. The thermodynamics and kinetics underlying methane pyrolysis at high temperatures have also been a point of interest for many research groups [157,158]. Some of them also studied the possibility of increasing the fuel conversion [159] or the yield of desired products [160,161] by investigating methane pyrolysis at temperatures higher than 1300K.

Because the reactivity at ultra-rich conditions is generally lower compared to that of stoichiometric fuel/air mixtures, reaction enhancers are often used to initiate the reaction under practically accessible pressures and temperatures [155]. DME (dimethyl ether,  $CH_3OCH_3$ ) having a high cetane number, low sooting tendency, and good availability is a suitable ignition enhancer [162–165]. DME is also used in gas turbines as an additive or alternative to natural gas [166,167]. Several experimental [163–165,168–174] and theoretical [175–177] studies have described the reaction of pure DME under a wide range of conditions: Curran et al. investigated the pyrolysis and oxidation of DME experimentally under highly diluted conditions for

equivalence ratios between 0.7 and 4.2 [23, 27]. Zhao et al. [178] performed a theoretical and experimental analysis of the unimolecular decomposition of DME applying a hierarchical methodology to develop a high-temperature model describing pyrolysis and oxidation of DME at  $\phi \leq 2.5$ . Dagaut et al. [163,169] studied the oxidation of DME by measuring concentration profiles of reactants, intermediates, and products in a jet-stirred reactor at 10 atm,  $0.2 \leq \phi \leq 1$  and in a temperature range of 550 – 1100 K as well as ignition delay times in a shock tube at 1200 to 1600K, 3.5 atm of pressure and equivalence ratios between  $\phi = 0.5 - 2$ . They also proposed a reaction mechanism. Shock tube measurements have also been performed to study the self-ignition of DME/air mixtures under engine relevant conditions [171] as well as its thermal dissociation [179] and pyrolysis [180]. Zheng et al. [172] determined experimentally the ignition temperature of DME/N<sub>2</sub> mixtures in counterflow diffusion flames; experiments were carried out varying the DME concentration from 5.9 to 30 % in a pressure range of 1.5 – 3 atm. Other experiments including measurements of DME flame speeds have been published by de Vries et al. [181] and Daly et al. [173]. On the other hand, Amano et al. [104] studied the ignition enhancing effect of DME in CH<sub>4</sub>/air-mixtures by adding small amounts of DME to the gas mixture. They found that a small amount of DME had a stimulating effect on autoignition of CH<sub>4</sub>/air-mixtures [104]. Similar conclusions were made by Chen et al. [182] and Tang et al. [183], who measured the effect of DME on methane mixtures at high temperatures [182] and mole fractions of DME in the mixture from 1 to 50 % [183]. The effect of adding dimethyl ether to methane with respect to the laminar flame speed was studied experimentally and numerically by Lowry et al [184] over a range of initial pressures from 1 to 10 atm, different fuel blends ranging from 60 % CH<sub>4</sub>/40 % DME to 80 % CH<sub>4</sub>/20% DME in volume. The influence of DME in the formation of soot and polycyclic aromatic hydrocarbons (PAH) on methane fuel mixtures was also a topic studied by Yoon et al. [185]. They found, that the formation of soot and PAH significantly decreases for the mixtures of DME with methane, ethane and propane, while a higher presence of these compounds was observed in DME/ethylene mixtures compared to mixtures of the fuel without additive [185].

Detailed and validated chemical kinetics models describing CH<sub>4</sub>/DME mixtures are readily available for stoichiometric or near-stoichiometric conditions. It is unclear whether they are also suitable as predictive tools in the ultra-rich regime. Burke et al. [117] developed a reaction mechanism for methane, DME, and their mixtures which has been validated for mixtures in a wide range of temperatures and pressures at  $\phi = 0.3 - 2.5$ . Hashemi et al. [186], on the other hand, presented a chemical kinetic model to describe the pyrolysis and oxidation of DME and its mixtures with methane at high pressures (50 – 100 bar), intermediate temperatures (450 – 900 K) and equivalence ratios of  $\phi = 0.06, 1$  and 20 studied in a laminar flow reactor. Other mechanisms, like the DME mechanisms of Zhao et al. [178] or Fischer et al. [164] were not developed to describe methane oxidation.

To provide a reaction mechanism tailored for polygeneration-relevant conditions, a new detailed kinetics mechanism including CH<sub>4</sub>/DME was developed based on existing mechanisms for methane pyrolysis [187] and oxidation [188], and the DME mechanism of Zhao et al. [178]. Hidaka et al [180] developed a chemical kinetic model able to predict accurately the pyrolysis and oxidation of methane at elevated temperatures, which are needed to initiate the reaction of methane without aditivation at lower presence of oxygen in the initial mixtures. On the other hand, Heghes [188] presented a C<sub>1</sub> – C<sub>4</sub> elementary reaction mechanism, which accurately

describes stoichiometric to slightly fuel-rich mixtures ( $\phi < 2$ ) of CH<sub>4</sub> and air. The combination of these should be able to describe the oxidation of methane at extremely fuel-rich conditions without missing any significant reaction pathway. The DME sub-mechanism of Zhao et al. [178] was included, as DME is used as reaction enhancer in this study in order to perform experiments at engine relevant conditions.

Experimental results of the oxidation of CH<sub>4</sub>/DME mixtures were carried out in a rapid compression machine, a high-pressure shock tube and in a flow reactor. The three experimental setups present different timescales and operational characteristics providing valuable experimental data in a large range of initial conditions, namely temperature and pressure, that complements each other. The information about the reactivity of the mixtures through ignition delay times and species profiles is of great importance for mechanism validation and a comprehensive study of the kinetics taking place at low and high temperatures.

In the following, experimental results of the oxidation of CH<sub>4</sub>/DME mixtures are described. Then, the development of the new kinetics model is outlined. Finally, comparisons of experimental data with model predictions based on the new reaction mechanism are presented.

## 8.2 Experiments

### 8.2.1 Rapid compression machine

Measurements of ignition delay times and species concentration profiles were carried out in a Rapid Compression Machine (RCM) and in a Rapid Compression-Expansion Machine (RCEM), respectively. The RCM facility has been described previously by Werler et al. [189]. It consists of a temperature-controlled cylinder-piston device in which the piston compresses the cylinder load, before being locked at top dead center (TDC). A creviced piston was used which can swallow the boundary layer peeling off the cylinder wall [189], providing more homogeneous in-cylinder thermal conditions compared to a standard piston. Pre-compression pressures were measured using a capacitance manometer (MKS Baratron 121A). This, combined with a pressure transducer (Kistler 6061 B) attached to the cylinder head, enables the determination of time-resolved absolute pressure traces. Pre-compression temperatures were measured with a type-K thermocouple. The cylinder head was equipped with an optical access via a quartz glass fiber. A photomultiplier (Hamamatsu H10722-210) equipped with a short pass filter (450 nm) was used for time-resolved chemiluminescence detection. During the measurement, a potentiometric position sensor (Burster type 7812) recorded the piston position. A mixing vessel was connected to the RCM, in which a homogeneous mixture of the test gas was created and stored. A scheme of the RCM is shown in Figure 8-1.

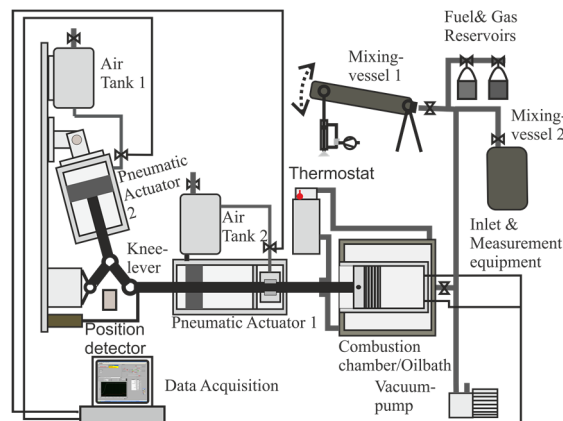


**Figure 8-1:** Rapid compression machine setup.

In RCM ignition delay time measurements, the time span between the moment where the piston reaches TDC and the inflection point of the pressure trace (point at which the pressure gradient reaches a maximum) due to first-stage ignition as well as main (second-stage) ignition were defined as the first and main ignition delay time, respectively. Values of temperature and pressure immediately after compression were assigned to the measured IDT. The post-compression pressure  $p_c$  was measured and the corresponding temperature  $T_c$  was calculated from  $p_c$  and pre-compression values  $p_0$  and  $T_0$  using the isentropic-core assumption [190,191].

To obtain a desired combination of temperature and pressure at TDC in an RCM experiment, the initial temperature, compression ratio, and composition of the inert gas in the mixture were varied. The accumulated uncertainties of the measurement equipment caused maximum uncertainties of  $\pm 1.4\%$  and  $\pm 0.71\%$  in the determination of  $T_c$  and  $p_c$ , respectively

The RCEM is an extension of the RCM, which adds a controlled expansion phase to the conventional RCM process [190,192,193]. The driving system of the experimental setup is shown in Figure 8-2. After compression, the gas mixture is held in an isochoric state for a controllable hold time  $\tau_{\text{hold}}$ . After this, the piston is retracted, resulting in a rapid expansion of the trapped gas. The quick decrease of temperature and pressure during expansion largely freezes the ongoing chemical reactions, allowing convenient subsequent sampling and *ex situ* analysis of the expanded gas, without requiring high-speed measurement devices. The species measurement system attached to the facility features a micro gas chromatograph (Agilent 490 Micro GC) with three chromatography columns, namely MS5A, PPU, and a CP-Sil 5CB, with their respective thermal conductivity detector, allowing the analysis of permanent gases as well as many hydrocarbons up to  $C_{10}$  species. The compression-expansion cycle comprised in the RCEM, combined with the adjustable hold time and post-compression probe sampling capability, allows monitoring the evolution of species concentrations during reaction as a function of hold time.

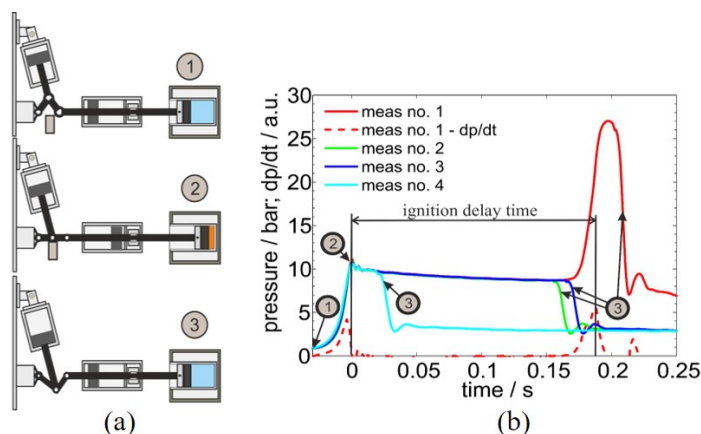


**Figure 8-2:** RCEM driving system. (a) Illustration of RCEM operation (b) Experimental pressure traces during ignition and for different  $\tau_{\text{hold}}$ . The initial mixture in the reaction chamber (1) is compressed and held in an isochoric state (2) for a controlled hold time, at which the piston is pulled back, expanding the in-cylinder gas (3). The hold time can be varied for obtaining information about the product composition after variable reaction times.

Figure 8-2 highlights the RCEM operation; in particular, Figure 8-2b depicts some pressure profiles which were taken from subsequent experiments with identical initial conditions, but with different hold times.

In these measurements, uncertainties related to species profiles are caused mainly by the GC calibration gas and the measurement equipment, obtaining relative uncertainties of 3.8–9.3 % for the inlet fuel and main products (e.g., CO, H<sub>2</sub>) and between 14.3 – 15.5 % for the C<sub>2</sub>-products [194].

## 8.2.2 Shock tube

Measurements of ignition delay times and end products were carried out in a high-pressure shock-tube with a constant inner diameter of 90 mm and lengths of the driver and driven sections of 6.4 and 6.1 m, respectively. Allowable post-ignition peak pressures are 500 bar and the maximum test time is extended up to 12 – 15 ms by driver-gas tailoring. Helium was used as the main driver gas component and argon was added to match the acoustic impedance of the driver gas with the one of the test gas. The driver gas was mixed *in situ* by using two high-pressure mass flow controllers. The driver gas composition depends on the test gas mixture composition and the Mach number was calculated prior to the experiment. For the calculation, formulas by Oertel [195] and Palmer and Knox [196] were used.

Test gas mixtures were prepared manometrically in a mixing vessel and stirred for one hour to ensure homogeneity. DME was purified before use by freezing with liquid nitrogen and removing remaining gases (e.g., N<sub>2</sub>) by pumping.

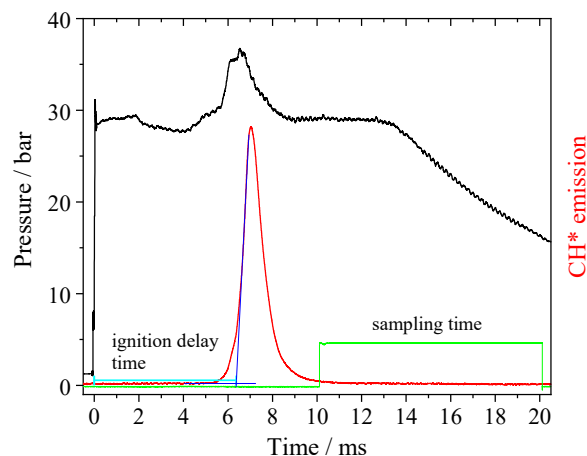


**Figure 8-3:** Temporal variation of pressure (black) and  $\text{CH}^*$  emission (red) measured in the shock tube with a  $\text{CH}_4/\text{DME}/\text{air}$  mixture ( $\phi = 10$ ) at 28.5 bar and 735 K.

The temperature and pressure behind the reflected shock waves were computed from the incident shock velocity using a one-dimensional shock model with an estimated temperature uncertainty of  $T < 15$  K. The shock velocity was measured over two intervals using three piezoelectric pressure transducers at different distances from the end flange. Band pass-filtered ( $413 \pm 5$  nm) emission from  $\text{CH}^*$  chemiluminescence was monitored through a window in the sidewall 15 mm from the end flange with Hamamatsu 1P28 photomultiplier tubes. The pressure was recorded at the same position using a piezoelectric pressure transducer. Ignition delay times were defined as the interval between the rise in pressure due to the arrival of the reflected shock wave at the measurement port and the extrapolation of the steepest increase in  $\text{CH}^*$  emission to its zero level on the time axis (Figure 8-3).

Gas samples were taken with a fast opening valve integrated in the end wall (Parker Hannifin Pulse Valve Series 9) connected to a 50 ml vessel. The valve was operated with a Parker Hannifin Iota One driver. The valve was opened 10 ms after the arrival of the reflected shock wave for 10 ms. The samples were analyzed with gas chromatography and mass spectrometric analysis (GC/MS, Agilent Technologies GC System 7890 A, MSD 5975C with a J&W HP-PLOT Q column). Each mixture used in the experiments contained 2 % Ne as internal concentration standard and all concentrations were determined relative to the internal standard. Mixtures of the expected products and the internal standard were prepared manometrically in a mixing vessel and used for calibration of the GC/MS system.

### 8.2.3 Flow reactor

Species concentration profiles were measured in a plug-flow reactor displayed in Figure 8-4. It consists of a 65 cm quartz tube embedded in a stainless-steel tube. The stainless-steel tube, which in turn is surrounded by two copper shells for improving temperature homogeneity, acts as a pressure shell. The gap between the quartz and the stainless-steel tube is sealed with teflon tape to prevent reactants from entering the gap. Heating tapes are wrapped around the copper shells and used to provide the heat that is necessary to initiate the reaction. Due to this arrangement, the temperature profile along the reactor consists of a 45 cm long isothermal zone and very steep temperature increases and decreases at the inlet and the outlet of the reactor. To

ensure that no condensation of product species takes place at the reactor outlet, the path behind the reactor is also heated by heating tapes to 393 K. Individual reactant flows are regulated by mass flow controllers (MKS) and mixed before entering the reactor. For the analysis of the species at the outlet, the reactor is coupled with a molecular-beam time-of-flight mass spectrometer (TOF-MS) via a heated needle valve and three pressure stages. The mass resolution of the TOF-MS is  $m/\Delta m = 2000$ . After entering the ionization chamber of the TOF-MS, the product gas is ionized by electron ionization (17 eV kinetic energy) to avoid excessive fragmentation.

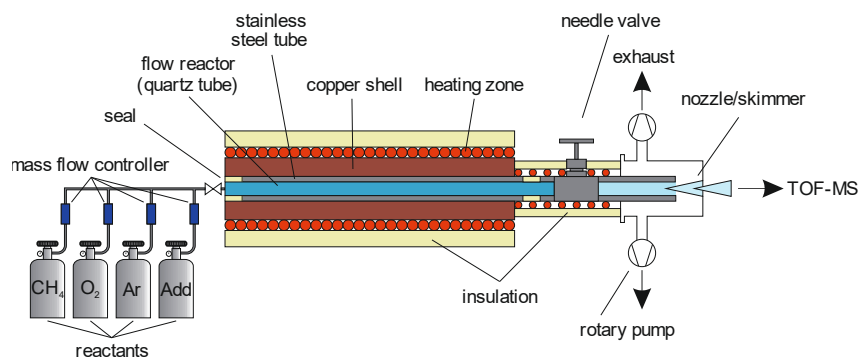


**Figure 8-4:** Experimental setup of the plug-flow reactor with TOF-MS.

Species mole fractions in the reacting argon-diluted  $\text{CH}_4/\text{DME}/\text{O}_2$  mixture were measured at the exit of the plug-flow reactor at various temperatures and equivalence ratios. Prior to the experiments, calibration measurements using self-mixed binary cold gas mixtures were carried out. The resulting relative uncertainties in calculated mole fractions of calibrated and detected species are 10 %. The uncertainties were evaluated based on a Gaussian error propagation law taking all relevant sources of error into account. A detailed description of the experimental setup can be found in [17,197].

#### 8.2.4 Investigated experimental conditions

All investigated mixtures in this study are listed in Table 8-1. IDTs of  $\text{CH}_4/\text{DME}/\text{air}$  mixtures were measured in the RCM at equivalence ratios of  $\phi = 1, 2, 6, 7, 10,$  and  $15$ , for  $T_c = 600 - 1050$  K and  $p_c = 10$  bar using DME as additive with a concentration of 10 mol% in the fuel. The equivalence ratio was defined treating  $\text{CH}_4$  and DME as fuels and  $\text{O}_2$  as oxidizer, i.e., assigning the O-atom in DME to the fuel, not to the oxidizer. For investigations in the  $\phi = 6 - 15$  range, two sets of IDT measurements were conducted for: (i) mixtures with air: 79:21 Ar/ $\text{O}_2$ , and (ii) mixtures with high Ar dilution: 95:5 Ar/ $\text{O}_2$  to reach high post-compression temperatures corresponding to mixtures 3 – 6 and 7 – 10 in Table 8-1, respectively.

IDTs were also measured in a shock tube for  $\text{CH}_4/\text{DME}/\text{air}$  mixtures at  $\phi = 2$  and  $10$  at 20 bar (mixtures 11 – 12 in Table 8-1) and 30 bar (mixture 11 and 13) and temperatures between 630 and 1500 K (mixtures 11 – 13). The DME concentration was varied from 5 to 20 mol% with respect to the fuel. End products were determined only for mixture 13 ( $\phi = 10$ ) at 30 bar. For this case, 2 mol% neon was added to the mixture as indicated in the section above.

Product species concentrations after variable reaction times were measured in the RCEM for the mixtures 14, 15, and 16 (Table 8-1). These mixtures represent the equivalence ratios  $\phi = 2$ , 6, and 10, respectively; mixture 15 and 16 feature identical amounts of fuel and oxygen as mixtures 3 and 5 with the difference that 10 % of argon was replaced by nitrogen. This provided a GC-detectable inert gas, thus the reaction-induced change of moles in the mixture could be monitored for further comparison with simulations. No significant chemical conversion could be observed in our experiments at  $\phi = 15$  so that the data for these conditions are not presented here.

**Table 8-1:** Investigated mixture compositions (mol%).

	No.	%CH <sub>4</sub>	%DME	%O <sub>2</sub>	%Ar	%N <sub>2</sub>	%Ne	$\phi$
RCM	1	8.18	0.91	19.09	0	71.82	0	1.0
	2	15.00	1.67	17.50	0	65.83	0	2.0
	3	33.75	3.75	13.13	49.38	0	0	6.0
	4	37.06	4.12	12.35	46.47	0	0	7.0
	5	45.00	5.00	10.50	39.50	0	0	10.0
	6	54.00	6.00	8.40	31.60	0	0	15.0
	7	13.54	1.52	5.30	79.55	0	0	6.0
	8	13.43	1.49	4.47	80.60	0	0	7.0
	9	14.90	1.66	3.48	79.97	0	0	10.0
	10	16.85	1.87	2.62	78.65	0	0	15.0
Shock tube	11	15.83	0.83	17.08	0	66.25	0	2.0
	12	12.57	3.14	17.28	0	67.01	0	2.0
	13	44.40	4.94	10.38	0	38.23	2.00	10.0
RCEM	14	15.00	1.67	17.50	0	65.83	0	2.0
	15	33.75	3.75	13.13	44.44	4.94	0	6.0
	16	45.00	5.00	10.50	35.55	3.95	0	10.0
Flow reactor	17	4.69	0.25	5.06	90.00	0	0	2.0
	18	4.39	0.49	5.12	90.00	0	0	2.0
	19	7.89	0.41	1.70	90.00	0	0	10.0
	20	7.44	0.83	1.74	90.00	0	0	10.0
	21	8.62	0.45	0.93	90.00	0	0	20.0
	22	8.14	0.90	0.95	90.00	0	0	20.0

In the plug-flow reactor, species mole fractions as function of temperature in the isothermal zone were measured for the reacting CH<sub>4</sub>/DME/O<sub>2</sub> mixtures at  $\phi = 2$ , 10, and 20 for 473 – 973 K

and 6 bar. A high dilution of argon (90 %) in the mixtures was needed to minimize the temperature increase due to exothermal reactions. Simulations of the system using the shear flow model of ChemKin Pro 19.2 to include heat transfer from the wall to the gas as well as the heat release due to exothermal reactions show that typically the temperature increase by reactions is a very localized phenomenon and limited to less than 60 K, if the dilution is  $\geq 90$  %. Therefore, the effect on the mole fractions at the outlet of the reactor can be neglected. The amount of DME was varied between 5 mol% (mixtures 17, 19, and 21) and 10 mol% (mixtures 18, 20, and 22) related to the fuel for each equivalence ratio.

## 8.3 Modeling of experimental data

### 8.3.1 Simulation of RCM and RCEM data

Simulations of IDTs were performed using a homogeneous reactor model based on an adiabatic-core hypothesis for all mixtures [190]. A volume trace describing the compression and expansion of the core gas was used as an input for the simulations to account for the compression phase and the heat loss. For each mixture, this volume trace was derived from the pressure trace of RCM experiments without reaction, as described in Mittal et al. [190]. For these non-reacting measurements, O<sub>2</sub> was replaced by the same molar amount of N<sub>2</sub>, yielding an inert mixture with similar isentropic exponents and thermal diffusivities as the corresponding reacting mixture [198].

The adiabatic-core model is suitable for the reproduction of IDTs since it can describe the reactions taking place in the core of the reaction chamber between compression and ignition, typically a time span in the range of a few to 100 ms. The reaction core represents a small portion of the total reaction volume only. It can reach temperatures that are significantly higher than in the rest of the reaction chamber. In the course of reaction, this thermal inhomogeneity causes a compositional inhomogeneity through the strongly temperature-dependent reaction rates.

A realistic description of the temporal evolution of the product species requires consideration of the entire reaction volume as well as the heat transfer from the core to the rest of the reaction chamber [198]. A multi-zone model was used to account for this effect. This model assumes that the reaction chamber consists of multiple zones that are arranged in an onion-like fashion. Within every zone, all scalar fields are assumed to be spatially uniform but may differ from zone to zone. The zones have the same instantaneous (but temporally variable) pressure and can exchange heat and expansion work, but not mass. A scheme of the model is shown in Figure 8-5.

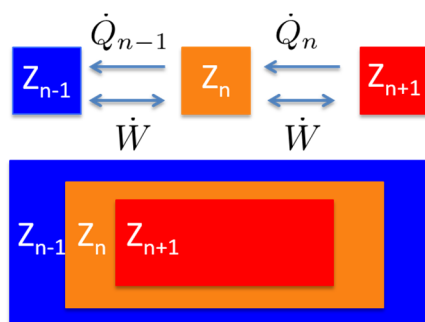


**Figure 8-5:** Schematics of the multi-zone model.

The heat exchanged between adjacent zones or the outermost zone and the wall is calculated from their temporally varying contact surface, the temperature difference between adjacent zones, and two heat-transfer coefficients. The heat-transfer coefficients between the zones are assumed to be equal while a second one is calculated for the heat flow taking place between the outermost zone and the wall. These values are calibrated by pressure traces measured in non-reactive RCEM experiments. The multi-zone model can then treat transient cylinder volume traces and therefore also the compression-expansion phases of the RCEM, allowing the zones to develop different chemical progress according to the thermodynamic conditions in each zone. The measured overall composition in the RCEM is modeled by the mass-averaged composition over all zones.

The number of zones required for a realistic description of the heat transfer was determined by comparing experiment and simulation: Pressure profiles of unreactive experiments were compared to pressure profiles predicted by multi-zone simulations which received the experimental cylinder volume trace  $V_{\text{cyl}}(t)$  as an input. Simulations using 13 zones were found to be sufficient to match the experimental data well. A more detailed description of the multi-zone model and its respective validation can be found in [194,198].

### 8.3.2 Simulation of shock-tube data

The simulations of the shock-tube data are based on the observed pressure increase of 1 %/ms ( $\phi = 10$ ) or 5 %/ms ( $\phi = 2$ ) for the first 2.8 ms to account for the facility effect [199]. This pressure increase was determined by measurements with inert gas mixtures that exhibit no heat release during the measurement time. After the first 2.8 ms, when the reflected shock wave passed through the contact surface, no further pressure increase was typically observed (Figure 8-3). The simulations were performed with a constant-pressure assumption considering a temperature increase by the gas dynamic adiabatic and isentropic compression measured in inert mixtures. For the simulation of the product formation the cooling after the measurement time was also considered based on the measured pressure profiles and adiabatic and isentropic expansion [199].

### 8.3.3 Simulation of flow-reactor data

The measured flow-reactor data was simulated via a plug-flow model [200] that assumes invariant gas composition and velocity in radial direction, reducing the problem to a one-dimensional approach without the influence of heat transfer. The plug-flow is an efficient model for flow-

reactor simulations where the gas temperature and pressure along the reactor can be assumed to remain constant during the reactions process. Simulations were performed using the geometric specifications of the flow reactor as well as the gas temperature profiles measured inside of the reactor prior to the experiments with similar gas flows as inputs. The simulations used the complete temperature profile along the center line of the axis including the isothermal zone as well as the zones of temperature rise and decrease at the reactor inlet and outlet; the resulting mole fractions at the outlet were compared between simulation and experiment.

## 8.4 Chemical kinetics model

Modeling of extremely fuel-rich conditions relevant in polygeneration processes requires reaction mechanisms developed especially for the prediction of the reaction kinetics for these mixture compositions. Unfortunately, chemical kinetics models found in the literature describing the combustion and oxidation of CH<sub>4</sub>/DME mixtures have been developed and validated to predict the kinetics of mixtures up to  $\phi < 2.5$  [117,168,178]. No dedicated mechanism describing very high equivalence ratios was found in the literature, motivating the development of a new chemical kinetics model. Another motivation for the development of a dedicated reaction mechanism for polygeneration applications is that the mechanism can be comparatively small so that it is well suited to further manipulation, e.g. reduction procedures. Polygeneration conditions have not been investigated in detail yet and an optimization of reaction conditions using efficient simulation and optimization procedures [97] is needed to obtain reasonable product yields in technical polygeneration reactors, e.g. piston engines [95].

The new assembled model is based on existing detailed mechanisms describing stoichiometric to slightly fuel-rich ( $\phi = 1 - 2$ ) combustion and pyrolysis of methane as well as the oxidation of DME/air mixtures. The new model aims at predicting IDTs and species concentration–time profiles of CH<sub>4</sub>/DME/air mixtures at  $\phi \geq 6$ .

Sensitivity and reaction flow-rate analyses were carried out for different temperatures and mixture compositions in order to identify the rate-limiting reactions in the range covered by the experimental data. Reaction rate constants of some of these reactions were modified based on either previous publications by other authors [168,178,201,202] or a chemical kinetic database found in the literature [203]. Physical soundness of these modifications was a concern, so all changes were performed only within the documented experimental uncertainty range. A detailed description of the mechanism construction is given in the subsections below.

The resulting polygeneration mechanism (PolyMech) consists of 558 elementary reactions among 83 species. A description of the key reactions and reaction pathways needed for the prediction of the regimes studied in this work as well as the mechanism validation against ignition delay times and species profiles measured in the experimental setups mentioned above are presented in the following section. The mechanism with its corresponding thermodynamic data file is attached to this paper as supplement.

### 8.4.1 Sub-mechanism for methane oxidation

Due to the lack of reaction mechanisms available in the literature for the description of methane oxidation at very high equivalence ratios ( $\phi \geq 6$ ) and the temperature ranges covered in this work, a new model was assembled based on existing mechanisms developed for combustion and high temperature pyrolysis of  $\text{CH}_4$ . The reaction model published by Heghes [188,204] describing stoichiometric to slightly fuel-rich mixtures ( $\phi < 2$ ) was merged with the pyrolysis mechanism of Hidaka et al. [187] for this purpose. Both were constructed for predictions of  $\text{CH}_4$ /air mixtures in a wide temperature range. The combination of these were carried out primarily by taking the pyrolysis and non- $\text{O}_2$  reactions from Hidaka's mechanism [187] as well as the oxidation steps from Heghes [188] avoiding the duplication of reactions. The resulting kinetics model was complemented with reactions not included in the previous mechanisms describing pyrolysis and oxidation of acetylene [205], vinylacetylene [206], propyne and allene [207], as well as the ethanol sub-mechanism presented by Marinov [208].

Rates of methane reactions were modified to allow the prediction at extremely fuel-rich conditions. Rates for the H-abstraction from methane by hydroperoxyl ( $\text{HO}_2$ ) used in this work were derived by Scott and Walker [209] which proposed a non-Arrhenius form for the expression of reaction rate constant using a temperature exponent of 2.5, based on calculations applying the method of Chen et al. [210]. The expression for the reaction rates was obtained implementing the experimental values measured by Baldwin et al. [211] together with an  $A$  factor per C-H bond identical to the one measured for the reaction between  $\text{HO}_2$  and ethane. The authors reported an uncertainty of the reaction rate of 1.41 between 600-800 K rising up to 5 at 2000 K. For the H-abstraction reaction from  $\text{CH}_4$  by H atoms, the recommended values presented by Baulch et al. [201] were implemented. These are shown to be in good agreement with the expression presented by Cohen [212] and Sutherland et al. [213]. Sutherland et al derived their rate expression by combining their own measurements with the one performed by other authors [201]. The pre-exponential factor of these reactions were reduced by 30 % and 50 %, respectively, which is within the uncertainty limits reported by the authors [211,213] and are in accordance with the expressions presented by Metcalfe et al [214] and Burke et al [117]. Heghes [188] and Baulch et al. [201] proposed the same reaction rates for the reaction of methane with oxygen, which were estimated based on the H-abstraction reaction from  $\text{HCHO}$  by  $\text{O}_2$ . Calculations of the reverse reaction using ab initio molecular orbital theory and variational RRKM theory performed by Zhu and Lin [215] are consistent with the expression presented by Heghes [188]. The combination of the theoretical values of Zhu and Lin [215] together with thermodynamic data were implemented, giving reaction rate values with an uncertainty of 3 to 5 over the range of 500-2000 K [201]. The pre-exponential factor of the latter reaction was modified by a factor of 1.65, resulting in reaction rates similar to the values published by Burke et al [117], Hidaka et al [187] and Reid et al [216], who performed simulations of ignition delay times for methane/air mixtures.

Methyl radicals ( $\text{CH}_3$ ) are mostly produced by H-abstraction from methane. These radicals recombine quickly to produce ethane ( $\text{C}_2\text{H}_6$ ) triggering a sequence of H-abstraction reactions to stable species such as ethylene ( $\text{C}_2\text{H}_4$ ) and acetylene ( $\text{C}_2\text{H}_2$ ). The rates of the methyl recombination reaction was replaced by the values recommended by Baulch et al [201] based on the experimental data of Glänzer et al. [217], Hippler et al. [218], Slagle et al [219] and Macpherson

et al. [220] at high temperatures and the measurements of Walter et al. [221] for the low temperature range. While the expression for the low-pressure limit presented by Baulch et al is in accordance with the values published by Blitz et al [222], the pre-exponential factor of the high-pressure limit was lowered by a factor of 1.5 to meet the recently proposed rates presented by Blitz et al [222], who performed an analysis of the reaction rates using revised cross sections and second order master equation to determine their proposed values. Rates of  $C_2H_5$  dissociation to  $C_2H_4$  and H were replaced by the coefficients included in Heghes' reaction mechanism [188], presenting reaction rates, being a factor of 2.56 higher for the high-pressure limit and a factor of 0.57 lower for the low-pressure limit compared to the values from Hidaka's reaction mechanism [187]. The reaction rates presented by Heghes [188] are the same as the ones proposed in the analysis performed by Baulch et al. [201], which are based on a large library of experimental data regarding the temperature range of 200-1100 K.

Formaldehyde ( $CH_2O$ ) has been identified as an important intermediate in the oxidation and combustion of methane [117,187]. Reactions comprising the H-abstraction from  $CH_2O$  by several radicals have shown to be very important for the accurate predictions of IDTs and of CO concentration-time profiles. Rates of the H-abstraction reaction from formaldehyde by H radicals were taken originally from the mechanism of Heghes [188]. The reaction rate coefficients presented by Heghes are the result of a least squares 3 parameter fit of low and high temperature measurements carried out by other authors [223–225]. The resulting expression has a reported uncertainty factor of 1.25 at 290K increasing up to 3.2 with increasing temperature. Expressions derived by other authors [201,226] have shown to be in a good agreement with the rates included in Heghes' mechanism [188] at ambient temperatures. Nevertheless, these have shown some discrepancies with increasing temperature. The pre-exponential factor of this reaction was modified within their reported reliability. At high temperatures,  $HO_2$  radicals are able to abstract an H atom from formaldehyde, while at temperatures near 298 K,  $HO_2$  molecules tend to be added forming  $HOCH_2OO$ . Rates for the H-abstraction were taken from the values reported by Eiteneer et al. [227], who derived the expression fitting a complex mechanism and considering measurements presented by other studies. The derived values were modified within their uncertainties, resulting in similar rates as the ones published in the mechanism of Burke et al. [117]. The rates for the formation of methane molecules from the H-abstraction reaction from  $CH_2O$  by methyl radicals were selected from the recommended values of Baulch et al. [201]. These represent the best fit of several rate coefficient measurements [228–230] together with reviews and evaluations carried out by Kerr and Parsonage [231]. A modification of the  $A$  factor of this reaction was made, giving similar values as the reported ones by Burke et al. [117]. Finally, the reaction rates of the reaction of  $CH_2O$  with OH were obtained from the reported values by Warnatz [232]. These were increased in order to meet the values presented by other authors [233] at low temperatures.

Reactions comprising the oxidation and thermal dissociation of ethanol were substituted by the sub-mechanism of Marinov's mechanism [208] that was specifically developed to describe the reaction of ethanol. Ethanol reacts to form three isomeric radicals by losing an hydrogen atom, with 1-hydroxyethyl ( $CH_3CHOH$ ) being the primary product [234]. Rates of ethanol reactions with  $CH_3$ , OH, and  $HO_2$  radicals were modified following the preferred values presented by Baulch et al. [201].  $CH_3CHOH$ , the main product of ethanol decomposition and also formed by isomerization of  $CH_3CH_2O$  through an H shift, produces  $CH_3CO$  and  $CH_2CHO$  by several H-

abstractions. The pathway towards  $\text{CH}_3\text{CO}$  has been considered more important in contrast to the one towards  $\text{CH}_2\text{CHO}$  in several studies [222]. Reactions of acetaldehyde with  $\text{CH}_3$  and  $\text{H}$  radicals forming  $\text{CH}_3\text{CO}$  were adapted according to the recommendation by Baulch et al. [201]. The formation of hydroxyl from  $\text{H} + \text{O}_2$  and  $\text{H}_2 + \text{O}$  reactions are extremely important in the hydrogen sub-mechanism (especially the first one), since these dominate and determine the reaction velocity of hydrocarbon fuel undergoing oxidation at temperatures higher than 1000 K. For temperatures lower than 1000 K (also depending on the system pressure) the formation of OH-radicals competes with the production of  $\text{HO}_2$  from the reaction of  $\text{H} + \text{O}_2$ . Reaction rates for the formation of hydroxyl radicals presented in the methane mechanism of Hidaka et al. [187] were reduced by 20 % to meet the newly published values from the hydrogen mechanism of K eromn es [202] et al. They adopted the measured rate constants from Hong et al. [235] and Sutherland et al. [236] respectively. The first author combined their  $\text{H}_2\text{O}$  absorption measurements behind reflected shock waves with those reported by Masten et al. [237], while the second one combined a flash photolysis-shock tube technique with an atomic resonance absorption spectroscopy to obtain their expression for the reaction rates. On the other hand, the reaction rates of  $\text{H} + \text{O}_2$  to hydroperoxyl radicals, important for the low temperature oxidation were adopted from the reaction mechanism of K eromn es et al. [202], who combined the low pressure rate limit constant from Bates et al. [238] with the high pressure limit from Fernandes et al. [239] to match their RCM and shock tube measurements. The pre-exponential factor of the low-pressure limit was increased in order to obtain better prediction of the presented low temperature RCM experimental data for equivalence ratios between  $\phi = 6 - 15$ . The formation and consumption of hydrogen peroxide ( $\text{H}_2\text{O}_2$ ) also play an important role in the determination of IDTs and species concentration–time profiles. The thermal dissociation of  $\text{H}_2\text{O}_2$  is one of the main production sources of OH radicals and a highly sensitive reaction. Dissociation rates of  $\text{H}_2\text{O}_2$  were obtained from the theoretical analysis carried out by Troe [240], who reviewed experimental data to obtain a pressure dependent rate constant expression for this reaction. The rates presented by Troe have been implemented by other authors showing good results in the prediction of ignition delay times at different pressures [202]. The formation rates of  $\text{H}_2\text{O}_2$  by recombination of two  $\text{HO}_2$  radicals were adopted from the studies carried out by Hippler et al. [241]. Hippler et al. investigated the reaction rates of this reaction experimentally and obtained a rate constant expression by combining their high pressure measurements with evaluated low temperature data. The set of rate constants recommended by Hippler et al. [241] was slightly increased within their experimental uncertainties. The recombination reaction of  $\text{HO}_2$  concur in the intermediate temperature oxidation range with the reaction of  $\text{HO}_2$  with  $\text{H}_2$  to produce one hydrogen peroxide molecule and a hydrogen atom. Rates of the latter reaction were adopted from Ellingson et al. [242], who performed canonical variational transition state theory calculations with multidimensional tunneling for obtaining the proposed reaction rate expression.

### 8.4.2 DME sub-mechanism

As mentioned before, a small amount of DME was added to the fuel mixtures to enable methane conversion at low temperatures. Methane is relatively inert at low temperatures, which is more pronounced at high equivalence ratios because of the lack of oxygen (and thus heat release) in the mixture. DME was also added to PolyMech as a reaction enhancer. Its sub-mechanism

represents a key element in the kinetics description of the mixtures covered in this study. DME reacts easily with  $O_2$  at low temperatures providing the conditions (formation of radicals and increasing the temperature of the gas mixture) needed for methane to react. Zhao's DME sub-mechanism [178] was selected for the description of DME decomposition and oxidation. However, several reaction rates were modified or substituted by the ones presented in other studies. The DME sub-mechanism from Zhao [178] was complemented with other reactions presented in Burke [117] and Curran's kinetics models [168], which were not included in Zhao's mechanism [178].

DME reacts with several radicals to form  $CH_3OCH_2$  through the abstraction of an H atom. Burke et al. [117] found that Zhao's reaction mechanism did not include the H-abstraction reaction from DME by  $CH_3O_2$  radicals, which may be the reason for the high rates reported by Zhao et al. [178]. Rates for the reaction of DME with  $HO_2$  were adopted from the quantum chemical calculations performed by Mendes et al. [243], which are the same implemented in the chemical kinetic model proposed by Burke et al. [117], while the rate coefficient expression for the reaction of DME with methylperoxyl radicals was estimated based on the calculations done by Carstensen and Dean [244].  $CH_3OCH_2$ , on the other hand, reacts with  $O_2$  at temperatures below 800 K [244]. The path leading to the formation of  $CH_2O$  and  $CH_3$  from  $CH_3OCH_2$  decomposition is only significant at very high temperature, according to Curran et al. [168]. The pre-exponential factor of Zhao's reaction rates for the dissociation of  $CH_3OCH_2$  was decreased by a factor of 2, which is in accordance with the expression obtained by Li et al. [245] from their direct ab initio and density-functional theory dynamics study. The resulting rates are similar to the presented rates by Burke et al. for the pressure range of interest in this study. The pressure dependent rates for the oxidation of  $CH_3OCH_2$  to  $CH_3CH_2OO$  were adopted from the studies of Burke et al. [117]. These are in accordance with the temperature independent expression proposed by Curran et al., at low temperatures, while higher discrepancies were observed with increasing temperature.  $CH_3OCH_2OO$  product of  $CH_3OCH_2$  oxidation, rearranges through a H-shift to  $CH_2OCH_2OOH$ . The subsequent reaction paths of  $CH_2OCH_2OOH$  show a high dependence on the gas temperature, dissociating at intermediate temperatures and reacting with  $O_2$  at lower ones [168,175]. The rate coefficients of  $CH_3OCH_2OO$  isomerization reaction to  $CH_2OCH_2OOH$  as well as the dissociation reaction of the latter species into one OH radical and two  $CH_2O$  molecules and the  $O_2$  addition reaction to  $CH_2OCH_2OOH$  presented in the mechanisms of Zhao et al. are the same as the rate expressions presented by Curran et al. in his analysis with regard to the low temperature chemistry of DME [168]. Rate expressions of both reactions comprising  $CH_2OCH_2OOH$  were found to be too fast compared to the pressure dependence data from the study by Burke et al. Therefore, reactions comprising the dissociation of  $CH_2OCH_2OOH$  into  $CH_2O$  and OH as well as the formation of  $OOCH_2OCH_2OOH$  were modified by lowering their pre-exponential factors by a factor of 2.5 and 2, respectively. The pre-exponential factor of the  $CH_3OCH_2OO$  H-shift reaction to  $CH_2OCH_2OOH$  was also modified within their reported uncertainties.

## 8.5 Results and discussion

Experimental data of ignition delay times and species profiles measured in a rapid compression machine, a high-pressure shock tube and in a flow reactor for CH<sub>4</sub>/DME/oxidizer mixtures are compared in the following sections to simulation results. Simulations were performed implementing the polygeneration mechanism (PolyMech) and other reaction mechanisms from the literature, whose presentation is omitted since the experimental condition range presented in this work is out of their validation range.

### 8.5.1 Ignition delay times

Ignition delay times of CH<sub>4</sub>/DME mixtures measured in a RCM for equivalence ratios of  $\phi = 6, 7, 10,$  and  $15, p_c = 10$  bar and at low and high temperatures (mixtures 3 – 6 and 7 – 10 in Table 1) are presented below. Shock-tube IDT data for mixtures at  $\phi = 10$  (mixture 13) measured at 630–1500 K and 30 bar are also presented and compared to the predictions of the PolyMech (chapter 8.4).

Measurements and simulations carried out for mixtures with  $\phi = 1 - 2$  are attached to this work as supplementary material (see appendix A), since these are not essential in the context of poly-generation but serve as additional validation targets for the mechanism.

For low-temperature measurements in the RCM, initial temperatures were increased to achieve higher temperatures at the end of compression while avoiding a possible ignition of the mixture during this process. Post-compression temperatures of  $T_c = 660 - 740$  K were obtained from experiments keeping the same initial pressure and mixture composition. Measurements at higher temperatures were not possible without ignition occurring already during compression, complicating the later data evaluation and calculation of the corresponding  $T_c$ . The oxidizer for the fuel mixtures in this section is a combination of argon and oxygen in air (ratio 79:21 Ar/O<sub>2</sub>) as mentioned in 8.2.4.

Simulations of the experimental IDTs were carried out implementing the adiabatic-core model mentioned in chapter 8.3. The results for mixtures 3 – 6 are displayed in Figure 8-6. This figure shows IDTs as a function of the temperature reached at the end of compression for mixtures with equivalence ratios of  $\phi = 6, 7, 10,$  and  $15$ . Two-stage ignition was observed for this set of experiments due to the presence of DME in the mixtures. In general, the predictions by PolyMech are in good agreement with the experimental data. PolyMech slightly under predicts the first-stage ignition delay times for  $\phi = 7$  (Figure 8-6b) at temperatures above 770 K while the main ignition is well predicted in the entire temperature range. A similar behavior can be seen for  $\phi = 6$  (Figure 8-6a) at temperatures above 700 K. Figure 8-6c shows a good agreement of the first stage of ignition between predictions of PolyMech and the data measured in the RCM, while the main ignition is slightly under predicted by the model at temperatures around 715 K. The two-stage ignition behavior observed in the experiments was also reproduced in the simulations with PolyMech, showing that the developed mechanism is able to reproduce the partial oxidation process accurately.

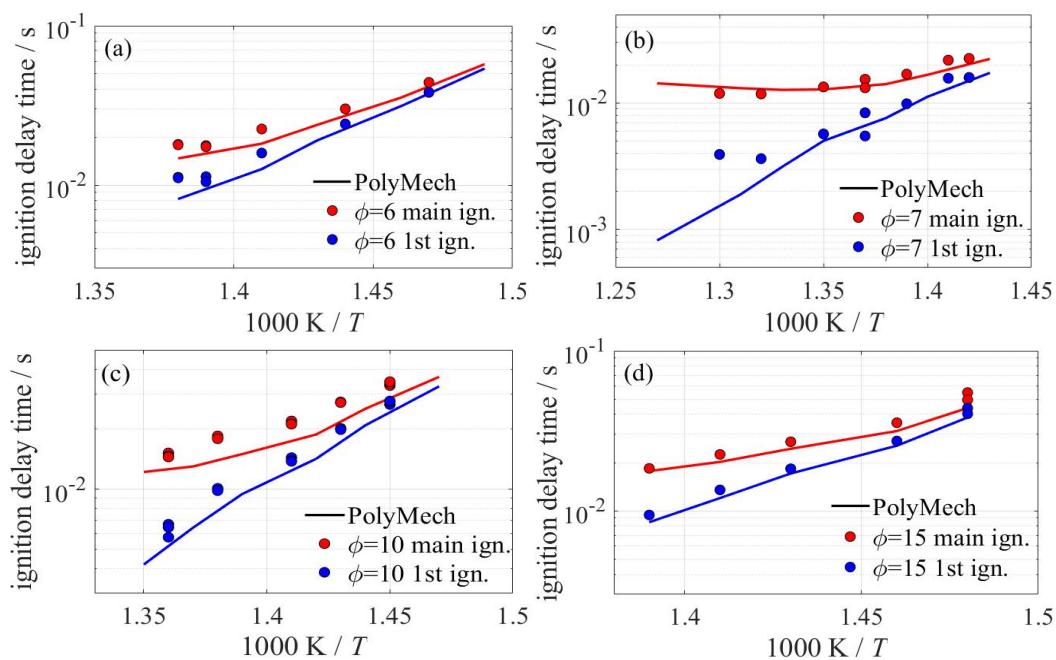


**Figure 8-6:** Low-temperature ignition delay times measured in the RCM (symbols) and simulations based on PolyMech (straight lines) for (a) mixture 3, (b) mixture 4, (c) mixture 5, and (d) mixture 6. Blue lines represent the first-stage ignition and red lines the main ignition.

In order to avoid ignition of the mixture during compression and to achieve higher post-compression temperatures, ignition delay time measurements in the RCM were carried out with mixtures having high contents of argon. The mixtures 7 – 10 (Table 8-1) present the same fuel/oxidizer ratio as the mixtures 3 – 6 with the difference that for the first case the argon/oxygen ratio was set to 95:5 Ar/O<sub>2</sub> instead of the conventional air ratio applied for the low-temperature measurements. This made it possible to reach post-compression temperatures of 870 – 1052 K. Comparison of simulations applying PolyMech with experimental data measured in the RCM for mixtures at  $\phi = 6, 7, 10,$  and  $15$  are presented in Figure 8-7.

For this case, the simulations were carried out implementing the multi-zone model instead of the adiabatic-core model since the reaction core remains adiabatic for a time span shorter than the measured IDTs, which makes the latter model inappropriate for the high temperature IDT computations.

For the high-temperature set of mixtures, only the main ignition was observed in the experiments while the simulations predict two-stage ignition. Species concentration profiles of DME and CH<sub>4</sub> for the conditions presented in Figure 8-7 illustrate the two fuel components igniting separately from each other, corresponding to the first observable ignition to DME and the second one to methane. Figure 8-7 displays the results for the main ignition. It can be seen that predictions of PolyMech are generally in good agreement with experimental data. PolyMech slightly under predicts IDTs for mixtures at  $\phi = 6$  and temperatures below 960 K (Figure 8-7a) as well as for mixtures at  $\phi = 7$  and temperatures between 960–1000 K (Figure 8-7b). For higher equivalence ratios ( $\phi > 10$ , see Figure 8-7c and d), the simulation results are in accordance with the measurements. In this set of mixtures, a slight temperature dependence was observed in experiments and simulations, resulting in almost flat curves especially for mixtures at  $\phi > 10$ .

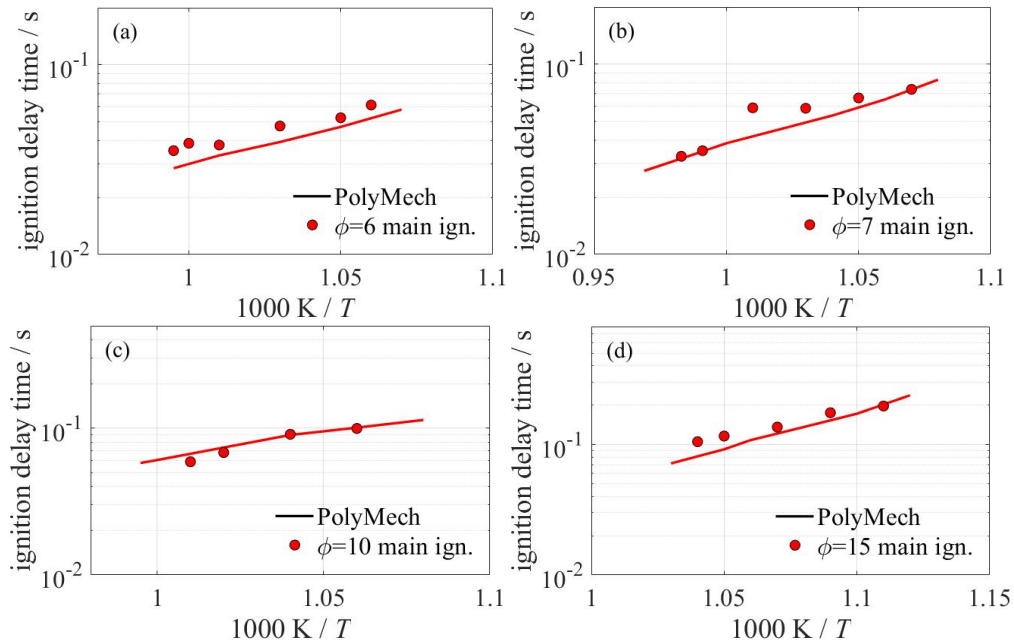


**Figure 8-7:** High-temperature ignition delay times measured in the RCM (symbols) and simulations based on PolyMech (straight lines) for (a) mixture 7, (b) mixture 8, (c) mixture 9, and (d) mixture 10.

Ignition delay times for fuel-rich  $\text{CH}_4/\text{DME}$  mixtures were also measured in a shock tube but this time at higher initial pressures than the pressures obtained after compression in the RCM and for temperatures up to 1500 K. Comparison of experimental data with the predictions of PolyMech for  $\phi = 10$  mixtures and additive concentration of 10 mol% are presented in Figure 8-8.

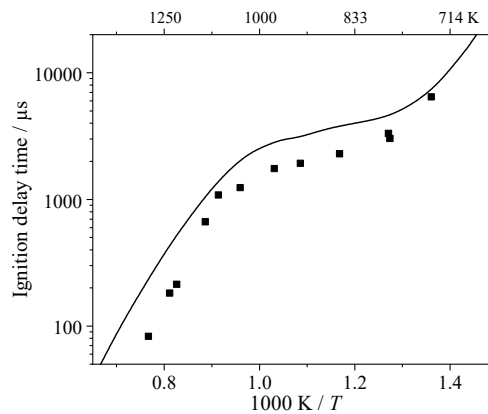


**Figure 8-8:** Comparison of ignition delay times measured in a shock tube (symbols) and simulations with PolyMech (lines) for  $\text{CH}_4/\text{DME}/\text{air}$  mixture at  $\phi = 10$ , 30 bar and with 10 mol% DME.

Figure 8-8 shows that the temperature dependence of the measurements is very well predicted by PolyMech. However, IDTs are over predicted by simulations for the entire temperature range. Similar deviations as presented in Figure 8-8 were also observed for mixtures 11 and 12 with equivalence ratios of  $\phi = 2$  (see appendix A), indicating that the observed trends do not depend on the mixture composition.

Sensitivity analyses were carried out to determine the rate-limiting reaction steps as well as to identify the key reactions important for the kinetic description at the conditions studied in this work. Figure 8-9 shows OH global sensitivities for  $\phi = 6$  and 10 at high and low temperatures. Figure 8-9a shows that at low temperatures, the rate-limiting reaction steps are dominated by DME decomposition and subsequently chain-branching reactions of DME's sub-products, explaining the importance of the DME sub-mechanism for the kinetic description and the prediction of the first ignition stages observed in Figure 8-6. At low temperatures and an equivalence ratio of  $\phi = 6$  (Figure 8-9a), the most strongly inhibiting reaction is the H-abstraction from DME by OH while the most promoting reaction is the H-abstraction from methane. As the equivalence ratio increases, the sensitivities on DME sub-mechanism reactions are also increased, probably because of the lack of oxygen in the mixtures and the lowered temperatures reached in the gas-phase, causing lower methane conversion at higher equivalence ratios ( $\phi > 10$ ). Figure 8-9b displays OH global sensitivity analysis for high initial temperatures. It is shown that the sensitivity of H-abstraction reactions from CH<sub>4</sub> and DME by H, CH<sub>3</sub>, and HO<sub>2</sub> increased notably compared to the results in Figure 8-9a. The recombination of methyl radicals to C<sub>2</sub>H<sub>6</sub> is the most strongly inhibiting reaction for both equivalence ratios while the most promoting reactions are the H-abstraction from DME as well as reactions comprising the dissociation of H<sub>2</sub>O<sub>2</sub> and formation of CHO from CH<sub>2</sub>O with CH<sub>3</sub>. Furthermore, an increase in the sensitivity of reactions involving H<sub>2</sub>O<sub>2</sub> and HO<sub>2</sub> radicals can be seen in Figure 8-9b.

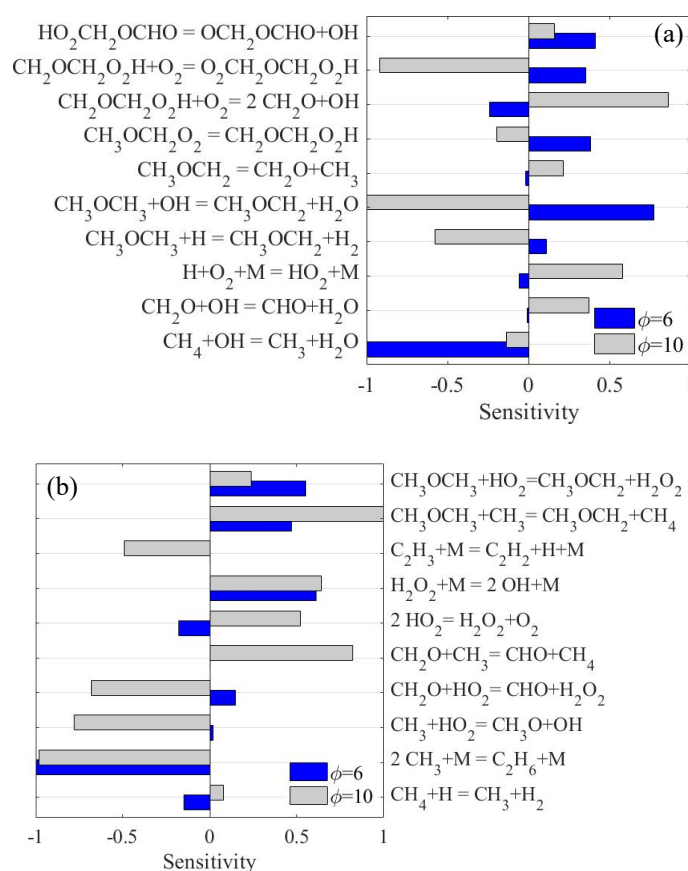


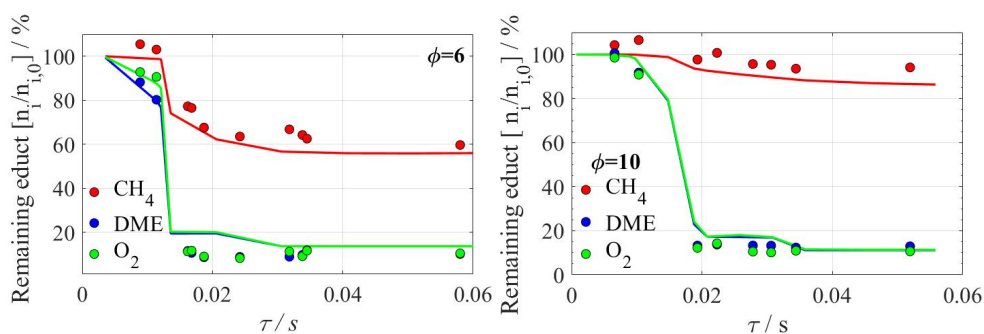
**Figure 8-9:** Low and high temperatures global OH sensitivity analyses for mixtures at equivalence ratios of  $\phi = 6$  and 10. (a)  $T_c = 700$  K (mixtures 3 and 5), (b) 950 K (mixtures 7 and 9).

## 8.5.2 Temporal variation of product concentrations

The temporal variation of the product composition of reacting CH<sub>4</sub>/DME mixtures was measured in a RCEM for  $\phi = 2, 6,$  and  $10$  (mixtures 14–16 in Table 8-1) at 714–738 K and 10 bar. In a flow reactor, species mole fractions were measured at the end of the reactor (Figure 8-4) for mixtures at equivalence ratios of  $\phi = 2, 10,$  and  $20$  (mixtures 17–22 in Table 8-1), 473 – 973 K and 6 bar. Shock-tube experimental data on species concentration after the ignition were also collected for mixtures at  $\phi = 10$  (mixture 13) at 730 – 1310 K and 30 bar.

Comparisons between experimental data and simulations with PolyMech (chapter 8.4) are presented below. Results for mixtures with equivalence ratios of  $\phi = 2$  and for mixtures 16 and 18 are attached to this work as supplementary material (see appendix A). Although very high pressures (above 30 bar) are not in the focus of our study, we compared also results of simulations using PolyMech with experimental data from the literature at  $\phi = 20$  and 100 bar [102] (presented in the supplementary material (appendix A)).

The temporal consumption of reactants (CH<sub>4</sub>, DME, O<sub>2</sub>) and the evolution of stable intermediates (CH<sub>2</sub>O, C<sub>2</sub>H<sub>6</sub>, C<sub>2</sub>H<sub>4</sub>, C<sub>2</sub>H<sub>2</sub>, CH<sub>3</sub>OH) and products (CO<sub>2</sub>, CO, H<sub>2</sub>) during the ignition period were investigated in the RCEM. Simulations were performed applying the multi-zone model described in chapter 8.3. It is important to note that some species are not completely frozen by the fast expansion of the piston but continue to react during this process. For this reason, simulations were carried out using the experimental volume curve which includes not only the compression but also the expansion phase, resulting in a detailed description of the experiments. Species mole fractions at the end of the expansion phase for each  $\tau_{\text{hold}}$  were taken, as it was done for the experiments in order to avoid discrepancies between both of them in respect of further reactions of some species.



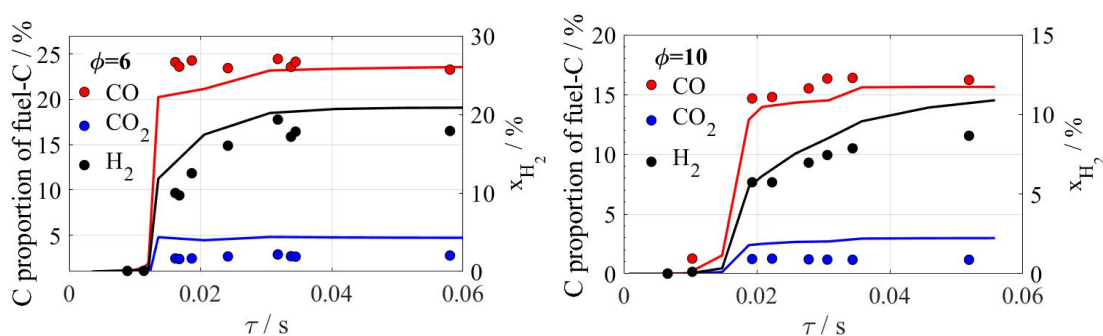
**Figure 8-10:** Comparison of reactant's temporal consumption profiles for mixture 15 (left) and 16 (right) measured in an RCEM (symbols) and simulations (lines).

Figure 8-10 shows the remaining fraction of methane, DME, and oxygen plotted against the reaction time. A small initial increase in methane (values exceeding 100 %) was observed in experiments for mixtures 15 and 16. A possible reason for this is the formation of CH<sub>4</sub> from DME at the first stages of reaction combined with the measurement uncertainties. This effect was also observed in simulations but in a smaller proportion, predicting an increase of less than 0.5 % in the remaining fraction of methane. DME rapidly decreases at the initial steps of

reaction while methane remains constant, explaining the strong dependence of ignition delay times on the DME sub-mechanism as observed in Figure 8-9.

In Figure 8-10 (left), complete consumption of DME and oxygen is observed while 60 % of the initial mole fraction of methane still remains in the gas mixture. DME reacts with  $O_2$  enabling methane conversion through radical formation and increasing the temperature of the mixture. Simulations at  $\phi = 10$  in Figure 8-10 (right) show a slightly lower consumption of  $CH_4$  compared to experimental data while oxygen and DME concentration time profiles were predicted quite well. No change in the remaining amount of methane is observed after 30 ms in both cases, possibly due to the low gas temperatures insufficient to dissociate methane thermally and the unavailability of oxygen. Methane conversion decreases considerably with the increase of  $\phi$ , with only negligible conversion (2 % and less) at  $\phi > 15$ .

Results concerning the formation of major products like  $CO$ ,  $CO_2$ , and  $H_2$  as well as temporal concentration profiles of stable  $C_2$  species are displayed in Figure 8-11 and Figure 8-12, respectively. Figure 8-11 shows the proportion of C atoms to the initial amount of C atoms in the fuel of  $CO$  and  $CO_2$  as well as the mole fraction of  $H_2$  as a function of time. The main product for the mixtures at equivalence ratios of  $\phi = 6$  (left) and  $\phi = 10$  (right) is  $CO$  followed by  $H_2$ . The comparison of simulated and experimental species profiles shows an overall good agreement. PolyMech under predicts the amount of  $CO$  in both cases, with a difference that it is more pronounced for mixture 15 ( $\phi = 6$ ) at times around 0.015 s. Mole fractions of  $H_2$  are slightly over predicted by simulations for both mixtures. Higher discrepancies were found for mixture 16 after 30 ms of reaction. The concentration profiles of  $CO_2$  shown in Figure 8-11 are over predicted by PolyMech.  $CO_2$  is produced shortly after  $CO$ , reaching quickly constant values. This behavior is observed both in the simulations and the experiments. The amount of products observed in Figure 8-11 decreases with increasing equivalence ratio. A possible explanation for this behavior is the strong decrease of methane conversion between  $\phi = 6$  and  $\phi = 10$  observed in Figure 8-10 (the conversion of DME is nearly the same for both equivalence ratios), influencing the amount of C-atoms available for products.



**Figure 8-11:** Comparison of the  $CO$ ,  $CO_2$  and  $H_2$  species profiles as a function of reaction time for mixture 15 (left) and 16 (right) measured in a RCEM (symbols) and simulations (lines).

Figure 8-12 displays the formation of  $C_2H_4$  and  $C_2H_6$  in C-atom proportions as a function of reaction time. The production of  $C_2H_4$  is slightly over predicted for mixture 15 (Figure 8-12 left) shortly after ignition, whereas the deviation rises with increasing time. For mixture 16, the

ethylene concentration profile is predicted well. Simulations of ethane are in good agreement with the measurements at  $\phi = 6$  up to 30 ms. At longer reaction times, the yield is slightly over predicted by the model. Experimental data of ethane are under predicted by simulations for all reaction times at  $\phi = 10$ .

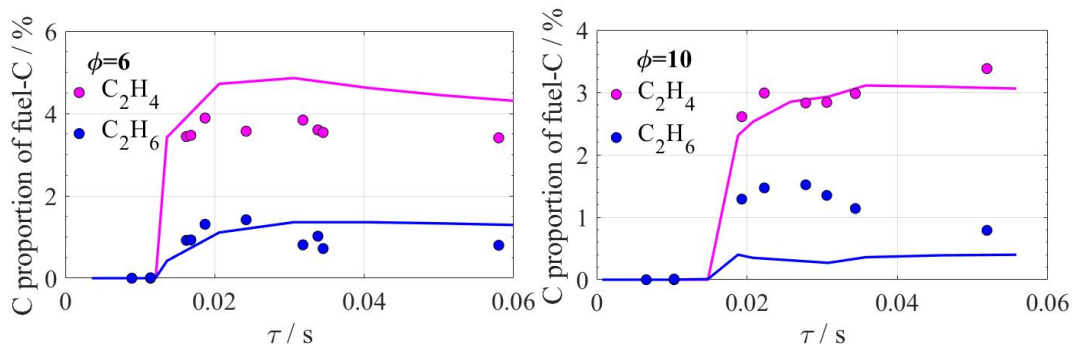


**Figure 8-12:** Comparison of  $C_2$  species formation time profiles for mixture 15 (left) and 16 (right) measured in an RCEM (symbols) and simulations (lines).

Figure 8-12 indicates that the amount of products does not change as much with varying equivalence ratio, as it was observed for  $CO$ ,  $CO_2$ , and  $H_2$  in Figure 8-11. Unsaturated  $C_2$  species are mostly formed by a sequential H-abstraction from  $C_2H_6$  to produce  $C_2H_2$ . Methyl recombination to ethane is a primary termination reaction and is the major sink for  $CH_3$  radicals (Figure 8-13), which are formed either from  $CH_4$  or DME and can be oxidized to formaldehyde, subsequently producing  $CO$ , or recombine to ethane. The path followed by these radicals is strongly influenced by the lack of oxygen in the mixtures, which is the reason why the second path prevails over the first one for mixtures at extremely high equivalence ratios as can be seen in Figure 8-13. Ethane reacts to  $C_2H_4$ ; ethylene, on the other hand, reacts to more than 90 % to form acetylene while the other 10 % are consumed to produce propene. The subsequent reactions of  $C_2H_2$  are very complex. When formed, propyne and allyl will produce  $C_3H_3$  at high temperatures, which mostly recombines and goes on to form benzene (main soot precursor).

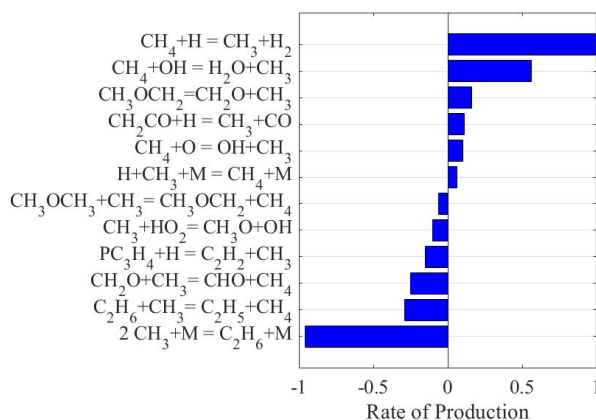
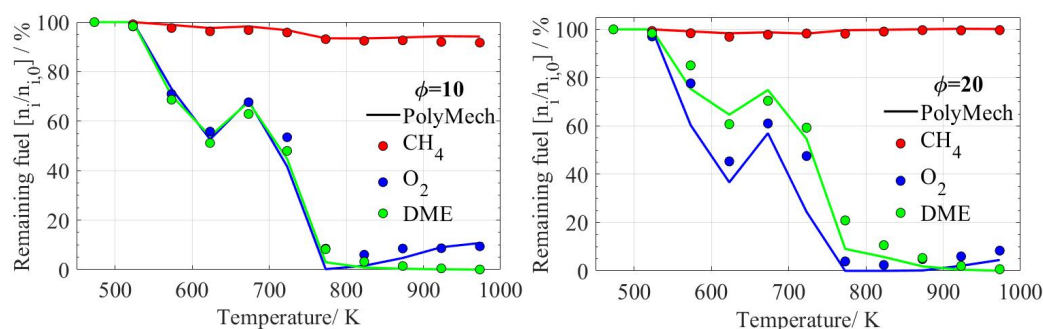


**Figure 8-13:** Rate of production analysis on  $CH_3$  for mixtures with equivalence ratios of  $\phi = 6$ .

The decrease of the reactants and the formation of stable products as a function of temperature was investigated in the plug-flow reactor. In this case, gas mixture compositions at the end of

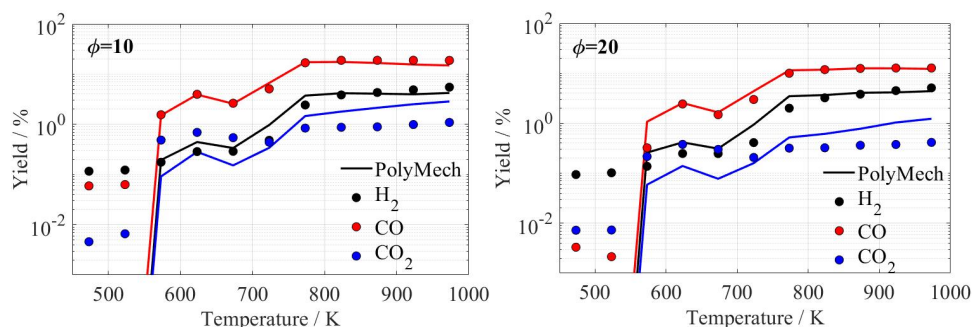
the reactor were computed implementing the plug-flow simulation model mentioned in chapter 8.3 and compared to experimental data.

Figure 8-14 shows the remaining fractions of CH<sub>4</sub>, O<sub>2</sub> and DME as a function of temperature and equivalence ratio. The first consumption of the fuel takes place at temperatures higher than 523 K. This is shown by the decreasing fuel fraction of DME and CH<sub>4</sub> as well as by the consumption of O<sub>2</sub>. DME decreases much faster than CH<sub>4</sub>, which is caused by the higher reactivity of DME, as already shown in Figure 8-10 for the species time profile measurements in the RCEM. Even at the highest investigated temperature of 973 K and  $\phi = 10$ , more than 90 % of the CH<sub>4</sub> remains in the mixture, whereas DME is completely consumed at temperatures above 823 K. With increasing equivalence ratio, the fraction of remaining CH<sub>4</sub> also increases, reaching values higher than 100 % at  $\phi = 20$  and  $T > 823$  K (mixture 22). This effect is caused by methane formation under these conditions. The trends and absolute values of the remaining fraction of methane and DME are predicted very well by the model, including the observed NTC region in the 623–773 K range. The remaining amount of O<sub>2</sub> is also in good agreement with the model predictions up to 773 K. At higher temperatures, higher O<sub>2</sub> consumption was observed for the mixtures with 5 % DME (see supplementary materials (appendix A)) in the experiments. These deviations become smaller with increasing temperatures.



**Figure 8-14:** Remaining fractions of reactants as a function of temperature for mixtures 20 (left) and 22 (right).

Yields of major products (CO, CO<sub>2</sub> and H<sub>2</sub>) as well as higher hydrocarbons (C<sub>2</sub> and C<sub>3</sub> species) as a function of temperature and equivalence ratio are presented in Figure 8-15 and Figure 8-16. Figure 8-15 shows that CO is the main product in all experiments and that the yields of CO and CO<sub>2</sub> decrease with increasing  $\phi$  from nearly 19 % and 1 % at  $\phi = 10$  to 13 % and less than 0.5 % at  $\phi = 20$  for CO and CO<sub>2</sub>, respectively. The reason for this behavior is the lack of oxygen, decreasing the reactivity of the mixtures. The lower conversion of methane and gas temperatures obtained at higher equivalence ratios are also a consequence of the low oxygen concentration. For H<sub>2</sub>, on the other hand, yields nearly remain constant from  $\phi = 10$  (5.5 %) to 20 (5.1 %). This suggests that most H<sub>2</sub> is formed by oxidation of DME, as DME is fully oxidized at temperatures higher than 823 K (Figure 8-14). Additionally, the yields rise with increasing DME amount, whereas this effect is much more pronounced at  $\phi \geq 10$ , compared to  $\phi = 2$  (see supplementary material (appendix A)).



**Figure 8-15:** Yields of CO, CO<sub>2</sub> and H<sub>2</sub> as a function of temperature for mixtures 20 (left) and 22 (right).

In general, good agreement between simulations and experiments is found, especially regarding the trends of the product yields. Only for CO<sub>2</sub>, the model predicts much higher yields in comparison to the experiments. This observation is similar to that in case of the RCEM experiments. Also, for H<sub>2</sub>, the model slightly under predicts the yields in the 573 – 773 K range. The experimental data at 473 – 523 K can be neglected as they arise from the fluctuating background in the spectra of the TOF-MS.

C<sub>2</sub> and C<sub>3</sub> species are formed at temperatures higher than 723 K. The maximum yields of C<sub>2</sub>H<sub>4</sub> were found at  $\phi = 2$  (see supplementary material (appendix A)). The yields of C<sub>2</sub>H<sub>6</sub>, C<sub>3</sub>H<sub>6</sub>, and C<sub>3</sub>H<sub>8</sub> show a local maximum at  $\phi = 10$  within the investigated parameter range. Except for C<sub>2</sub>H<sub>4</sub> at  $\phi \geq 10$ , the yields of these hydrocarbons decrease with increasing DME amount. Additionally, it can be noticed that the unsaturated hydrocarbons C<sub>2</sub>H<sub>4</sub> and C<sub>3</sub>H<sub>6</sub> are formed by H-abstraction from C<sub>2</sub>H<sub>6</sub> and C<sub>3</sub>H<sub>8</sub> at higher temperatures, as the yields of the alkanes are exceeded by the alkene ones. As the temperatures are relatively low, no formation of C<sub>2</sub>H<sub>2</sub> was observed. With respect to the simulations, an overall good agreement of the experimental and simulated data is found. For C<sub>2</sub>H<sub>4</sub> and C<sub>3</sub>H<sub>6</sub>, the model under predicts the experimental data.

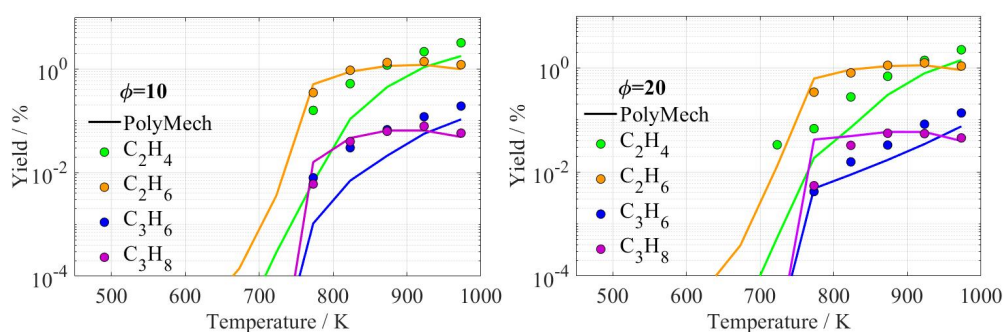


**Figure 8-16:** Yields of C<sub>2</sub>H<sub>4</sub>, C<sub>2</sub>H<sub>6</sub>, C<sub>3</sub>H<sub>6</sub> and C<sub>3</sub>H<sub>8</sub> as a function of temperature for mixtures 20 (left) and 22 (right).

Species concentrations of several hydrocarbons including benzene, were measured after the ignition in a shock tube. The shock-tube data were simulated for mixture 13 ( $\phi = 10$ ) at 30 bar and 800 K (Figure 8-17).

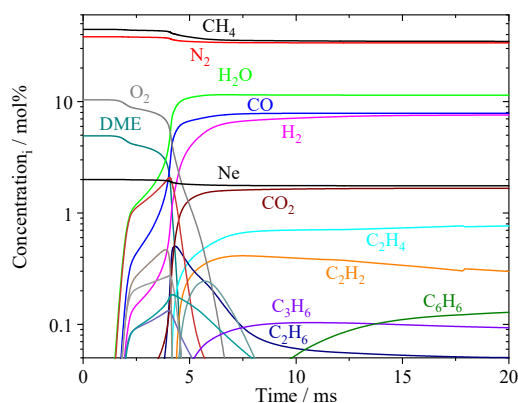


**Figure 8-17:** Simulations of time dependent species profiles for shock tube conditions mixture 13 ( $\phi = 10$ ) at 800 K and 30 bar.

The results in Figure 8-17 show that the main reaction products at these conditions are  $\text{H}_2$ ,  $\text{CO}$ ,  $\text{H}_2\text{O}$ ,  $\text{CO}_2$ ,  $\text{C}_2\text{H}_4$ ,  $\text{C}_2\text{H}_2$ ,  $\text{C}_3\text{H}_6$ ,  $\text{C}_2\text{H}_6$ , and  $\text{C}_6\text{H}_6$ . The mole fractions of most species (except  $\text{H}_2$ ,  $\text{C}_2\text{H}_6$ , and  $\text{C}_6\text{H}_6$ ) reach nearly constant values about 2 ms after ignition while a temperature decrease is observable after the measurement time of 12 ms. The gas temperature decrease due to rarefaction waves is caused by the high heat capacity of the mixture that is not sufficient to stop radical reactions so that the benzene concentration steadily increases over time while the ethane concentration decreases. These radical reactions are stopped by the strong temperature decrease during sampling in the evacuated 50 ml vessel. In order to compare simulation results with the experimental data measured in a shock tube (Figure 8-18), an average reaction time of 15 ms was assumed.

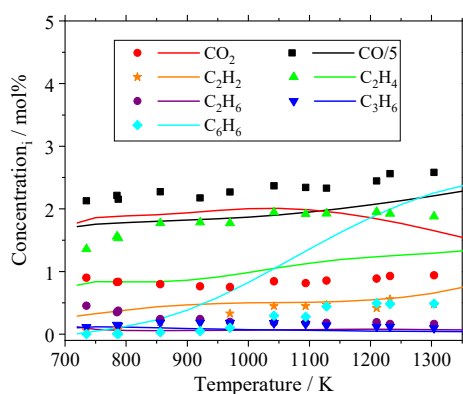


**Figure 8-18:** Measured (shock tube, symbols) and simulated (straight lines) product mole fractions after ignition of  $\text{CH}_4/\text{DME}/\text{air}$  mixture (mixture 13) at  $\phi = 10$  and 30 bar.

Figure 8-18 shows the results of the product measurements and simulations with PolyMech as a function of the initial temperatures. The product yields of the species displayed in Figure 8-18, with the exception of benzene, show low dependence on the initial temperature. This is predicted well by the simulations. The absolute concentrations of  $\text{C}_2\text{H}_2$  and  $\text{CO}$  are in good agreement with the simulations whereas for benzene much higher concentrations are predicted due to the lack of reactions in the mechanism describing the consumption of benzene. Benzene is considered to be a soot precursor and its further reactions lead to the formation of PAHs [148]. In this case, no further aromatic species or soot were detected during experiments. Although, it

was not possible to measure benzene in the RCM and no benzene was detected in the flow reactor experiments, a carbon balance of all measured species in the RCM and the flow reactor does not suggest the presence of benzene or any other larger hydrocarbon molecule.

## 8.6 Conclusions

In this work, the oxidation of CH<sub>4</sub>/DME mixtures under extremely fuel-rich conditions was investigated by measuring ignition delay times (IDTs) in a rapid compression machine (RCM) and in a shock tube as well as quasi-time resolved histories of stable species during the reaction in a rapid compression–expansion machine (RCEM), a shock tube, and a flow reactor. The measurements cover an extended range of equivalence ratios ( $\phi = 1 - 20$ ) to provide data that are of special interest for partial oxidation and polygeneration processes. The variation of product concentrations as a function of reaction time revealed syngas (CO and H<sub>2</sub>) as a main product of the reaction of the studied mixtures; promising yields of valuable species like C<sub>2</sub>H<sub>4</sub> and C<sub>2</sub>H<sub>2</sub> were also observed.

Even though the formation of soot and PAHs is reported to be enhanced at low temperatures, none of these were observed in the experiments presented in this study, probably because of the presence of DME in the fuel mixtures. Small concentrations of benzene (considered as a soot precursor) were detected in shock tube experiments, showing a composition increase of the species with increasing temperatures above 1000 K. These high initial temperatures could not be achieved in the RCM and flow reactor measurements.

A reaction mechanism (PolyMech) was developed with a special focus on the description of the ultra-rich reaction conditions important for polygeneration processes, since most of the chemical kinetics models found in the literature are validated only for the conventional combustion regime ( $\phi = 0.5 - 2$ ). The PolyMech is based on existing mechanisms describing the oxidation and pyrolysis of methane as well as the reaction of DME, which was included in the fuel mixture as auto-ignition and reaction promoter. Sensitivities and reaction pathways analyses were carried out at different conditions in order to identify the rate-limiting reactions at the conditions covered in this study. It was found that at low temperatures, the sub-mechanism of DME plays an important role on the kinetics of the mixtures, as it provides radicals and increases the gas temperature promoting the further reaction of methane. At low temperatures, a two stage ignition was observed in experiments as well as in simulations. At higher temperatures, only one main ignition was observed; reaction analyses on these conditions showed an increase in the sensitivity of reactions including CH<sub>2</sub>O and hydrogen sub-mechanisms.

With increasing equivalence ratios, a notoriously decrease of the methane conversion was observed, while DME and oxygen were completely consumed in all cases. An influence of the decreasing methane conversion was also observed in the formation of some species like C<sub>2</sub>H<sub>4</sub> and C<sub>2</sub>H<sub>6</sub>, which displayed smaller concentrations in the mixtures at higher equivalence ratios. An increase in the sensitivities of reactions including radicals like H and CH<sub>3</sub> with rising equivalence ratios was also observed. This was expected due to the lack of oxygen present in the initial mixtures at these conditions.

In order to improve the simulation predictions of experimental data in a wide range of conditions, rates of some limiting reactions were modified within their uncertainties as described in the chapter 8.4 of this study. The identification of these reactions was carried out by applying

sensitivity analyses at different temperatures and mixture compositions. The presented polygeneration mechanism (PolyMech) is shown to predict the measured ignition delay times and species concentration variations very well. But, it has to be noticed that further reactions describing the formation and reaction of benzene should be included in order to obtain better predictions of C<sub>2</sub> species profiles. Consequently, the PolyMech is a valuable tool for describing reactions in the ultra-rich regime, which is relevant for several future combustion applications.

---

## 9 Partial oxidation of natural gas/DME mixtures

The content of this chapter will be published in Proceedings of the Combustion Institute:

D. Kaczmarek, J. Herzler, S. Porras, S. Shaqiri, M. Fikri, C. Schulz, B. Atakan, U. Maas, T. Kasper, Plug-flow reactor and shock-tube study of the oxidation of very fuel-rich natural gas/DME/O<sub>2</sub> mixtures, *Combustion and Flame* 38, accepted (2020).

© 2019 The Combustion Institute. Published by Elsevier. Reprinted with permission.

My own contribution included setting up the plug-flow experiment, performing the experiments, analyzing and visualizing the results, coordinating the assembling of the manuscript, and writing the introductory and modeling part as well as all plug-flow related parts of the manuscript. I also coordinated the assembling of the manuscript. Jürgen Herzler provided the shock-tube results, was involved in the development of the PolyMech2.0 mechanism, and wrote the shock-tube related part in the manuscript. Sylvia Porras developed the original PolyMech mechanism and contributed to the development of the modified mechanism. Shkelqim Shaqiri helped to build the experimental setup and conduct the experiments. Mustapha Fikri, Christof Schulz, Ulrich Maas, Burak Atakan, and Tina Kasper contributed to the interpretation of the results and the manuscript. Tina Kasper also supported me in the conceptual design of the study. All authors were engaged in the correction and later proof-reading of the manuscript

### Abstract

A polygeneration process with the ability to provide work, heat, and useful chemicals according to the specific demand is a promising alternative to traditional energy conversion systems. By implementing such a process in an internal combustion engine, products like synthesis gas or unsaturated hydrocarbons and very high exergetic efficiencies can be obtained through partial oxidation of natural gas, in addition to the already high flexibility with respect to the required type of energy. To enable compression ignition with natural gas as input, additives such as dimethyl ether are needed to increase the reactivity at low temperatures. In this study, the reaction of fuel-rich natural gas/dimethyl ether (DME) mixtures is investigated to support the further development of reaction mechanisms for these little studied reaction conditions. Temperature-resolved species concentration profiles are obtained by mass spectrometry in a plug-flow reactor at equivalence ratios  $\phi = 2, 10,$  and  $20,$  at temperatures between  $473$  and  $973$  K and at a pressure of  $6$  bar. Ignition delay times and product-gas analyses are obtained from shock-tube experiments, for  $\phi = 2$  and  $10,$  at  $710 - 1639$  K and  $30$  bar. The experimental results are compared to kinetic simulations using two literature reaction mechanisms. Good agreement is found for most species. Reaction pathways are analyzed to investigate the interaction of alkanes and DME. It is found that DME forms radicals at comparatively low temperatures and initiates the conversion of the alkanes. Additionally, according to the reaction pathways, the interaction of

the alkanes and DME promotes the formation of useful products such as synthesis gas, unsaturated hydrocarbons and oxygenated species.

## 9.1 Introduction

The increasing use of fluctuating renewable energy requires the development of flexible energy conversion systems. One possible concept is polygeneration that can provide different types of energy depending on demand. Atakan [94] and Hegner et al. [95] performed modeling studies of a fuel-rich operated gas turbine and a homogenous-charge compression-ignition (HCCI) engine and found that the simultaneous – but variable – provision of work and chemicals as well as heat in a thermochemical process can lead to very high exergetic efficiencies. They compared the polygeneration process with combined individual processes to provide work, heat, and hydrogen and highlighted the higher efficiency of the polygeneration process. In both studies, methane ( $\text{CH}_4$ ) was used as fuel. Gossler and Deutschmann [97] showed that  $\text{H}_2$  yields of more than 90 % can be achieved theoretically using fuel-rich HCCI conditions with a fuel mixture of 99 %  $\text{CH}_4$  and 1 % propane ( $\text{C}_3\text{H}_8$ ). More recently, such processes were investigated experimentally in a rapid-compression machine (RCM) [96] and an HCCI engine [93,246]. In these studies, it was shown that, besides providing a considerable amount of work, high yields of synthesis gas are produced under slightly fuel-rich conditions ( $\phi \sim 2$ ). The product mix of work and chemicals resulted in high exergetic efficiencies of the investigated processes.

The above-mentioned conversion of methane towards valuable chemicals preferentially takes place at high equivalence ratios (typically  $\phi \gg 2$ ), moderate temperatures, and high pressures. At these conditions, the fuel (e.g.  $\text{CH}_4$  or natural gas) is partially oxidized such that synthesis gas, oxygenated hydrocarbons, or larger hydrocarbons compared to the reactants are formed. As HCCI engines are based on autoignition and  $\text{CH}_4$  is relatively inert, more reactive species like *n*-heptane [93] or dimethyl ether (DME) [96,127] can be added to the fuel to reach autoignition conditions at the end of the compression stroke. Validated reaction mechanisms for such mixtures that could support the development of reaction concepts under these uncommon conditions are only slowly becoming available and require further improvement. The development requires experiments under well-controlled boundary conditions.

For  $\text{CH}_4$ , the homogeneous partial oxidation has been investigated in flow reactors [17,18,98–104] or jet-stirred reactors [105]. The investigated conditions cover pressures from 1 – 100 bar, temperatures between 600 and 1800 K and equivalence ratios ranging from 0.06 to 100. Most of these studies focus on the development of reaction mechanisms for fuel-rich combustion, whereas the work of Rytz and Baiker [98] specifically focused on the optimization of the generation of methanol. They found that the selectivity towards methanol increases with increasing pressure and decreases with increasing temperature or increasing oxygen concentration.

Ignition delay times of homogeneous fuel/air mixtures were measured for fuel-rich methane and natural gas in shock tubes or rapid-compression machines, as summarized in Table 9-1; species concentration profiles were measured less frequently. El Bakali et al. [108], Tan et al. [111], and Kaczmarek et al. [197] measured species concentration profiles as a function of temperature for various natural gas mixtures in jet-stirred and flow reactors. The experiments cover a range of  $\phi = 0.5 - 20$ ,  $p = 1 - 10$  bar and  $T = 473 - 1240$  K. In addition, El Bakali et al. [108]

also investigated the oxidation of natural gas in a stoichiometric premixed flame at low pressure (10.6 kPa).

The kinetics of DME have been investigated extensively in the last two decades. In addition to ignition delay time measurements in different experimental configurations (Table 9-1), several reactor studies have been performed. Dagaut et al. [163,169] investigated the oxidation of DME in a jet-stirred reactor at  $\phi = 0.25 - 2$ ,  $p = 1 - 10$  bar and  $T = 550 - 1300$  K and proposed one of the first reaction mechanisms, using also shock-tube ignition delay times (IDTs) from Pfahl et al. [171]. Curran et al. [166] improved this reaction mechanism by adjusting the rate constants for unimolecular fuel decomposition and methoxy–methyl radical  $\beta$ -scission and adding a new low-temperature oxidation scheme. Further modifications on the reaction mechanism were done by Fischer et al. [164] and Curran et al. [168]. They used additional data, obtained in jet-stirred and flow reactor experiments under oxidizing ( $\phi = 0.2 - 4.2$ ,  $p = 1 - 18$  bar,  $T = 800 - 1300$  K) and pyrolyzing (2.5 bar, 1060 K) conditions as well as IDTs from shock-tube experiments [171]. They observed formic acid as a major intermediate of DME oxidation and added reaction pathways leading to formic acid for better predictions of the experimental data [168].

Zhao et al. [178] proposed a model after revising the rate constant of the unimolecular decomposition reaction of DME and considering flow reactor experiments under pyrolyzing conditions. More recently, Burke et al. [117] incorporated measured rate constants and high-level calculations for the reactions of DME and applied a pressure-dependent treatment to the low-temperature chemistry of DME within their detailed kinetics mechanism. They also used new IDTs with respect to CH<sub>4</sub>, DME and their mixtures [117] for validation. More reactor experiments with respect to the oxidation of DME can be found in [19,186,247–251]. Except the studies of Hashemi et al. [186] and Porras et al. [19], all of these studies have been performed at atmospheric pressure. Hashemi et al. [186] extended the available database regarding the oxidation of DME to pressures up to 100 bar and equivalence ratios up to 20. Additionally, they performed pyrolysis experiments and experiments with CH<sub>4</sub>/DME blends. They also proposed a kinetics model for DME/CH<sub>4</sub> oxidation and concluded that the addition of DME to the CH<sub>4</sub> fuel has a promoting effect on the reaction onset temperature of CH<sub>4</sub> and that the effect is more pronounced in extremely fuel-rich conditions ( $\phi = 20$ ). Similar results can be found in Refs. [17,104], where the addition of DME was also found to be more effective than the addition of C<sub>2</sub>H<sub>6</sub>. Porras et al. [19] extended the experimental database with respect to fuel-rich oxidation ( $\phi = 2 - 10$ ) of CH<sub>4</sub>/DME mixtures to the intermediate pressure range (6 – 30 bar) with flow-reactor, rapid-compression machine, and shock-tube experiments with special emphasis on polygeneration processes. The authors also proposed a new kinetics model for the description of the reaction of these mixtures

DME can accelerate ignition [121,182,183,252] if it is added to methane or propane and it increases the flame speed of methane/air mixtures [182,184]. But, with respect to ethane, it was shown that the DME blending ratio shows a nonlinear effect on the IDTs due to interactions between DME and the radical pool provided by ethane oxidation [253]. More fundamental experiments regarding the oxidation of natural gas/DME mixtures showing such interactions are rare. The present work is intended to fill this gap by extending the study of these mixtures to high equivalence ratios.

**Table 9-1:** Recent experimental studies on the ignition delay times of natural gas and DME mixtures with their corresponding experimental conditions (ST: shock tube, RCM: rapid-compression machine, CVB: constant volume bomb).

Mixtures	$p$ / bar	$T$ / K	$\phi$	Facility	Ref.
CH <sub>4</sub> /C <sub>2</sub> -C <sub>5</sub>	0.2	1400-2000	1	ST	[254]
CH <sub>4</sub>	3-300	1200-2100	0.2-2	ST	[255]
CH <sub>4</sub> /C <sub>2</sub> -C <sub>4</sub>	4	1200-1850	0.2-0.4	ST	[256]
CH <sub>4</sub> /C <sub>2</sub> -C <sub>4</sub>	3	1400-2000	0.2	ST	[257]
CH <sub>4</sub> /C <sub>3</sub>	2.5	1300-1600	1	ST	[258]
CH <sub>4</sub> /C <sub>2</sub> -C <sub>4</sub>	3-15	1300-2000	0.45-1.25	ST	[259]
CH <sub>4</sub>	9-480	1410-2040	0.5-4	ST	[260]
DME	13-40	650-1300	1	ST	[171]
DME	3.5	1200-1600	0.5-2	ST	[169]
CH <sub>4</sub>	40-260	1040-1500	0.4-6	ST	[151]
CH <sub>4</sub>	35-260	1040-1600	0.4-6	ST	[261]
DME	0.83-2.9	900-1900	Pyrolysis	ST	[180]
CH <sub>4</sub> /C <sub>2</sub> -C <sub>3</sub>	5-20	900-1700	0.5-1	ST	[262]
CH <sub>4</sub> /C <sub>2</sub> -C <sub>3</sub>	3-13	1485-1900	0.5-2	ST	[263]
CH <sub>4</sub>	3-450	1200-1700	0.5	ST	[154]
CH <sub>4</sub>	16-40	1000-1350	0.7-1.3	ST	[264]
CH <sub>4</sub> /C <sub>2</sub> -C <sub>3</sub>	16-40	900-1400	1	ST	[265]
CH <sub>4</sub> /C <sub>2</sub> -C <sub>3</sub> , H <sub>2</sub>	0.54-30	1091-2001	0.5	ST	[110]
CH <sub>4</sub> /C <sub>2</sub> -C <sub>5</sub>	15.5-27.5	786-1107	0.5	ST	[266]
CH <sub>4</sub> /C <sub>3</sub> H <sub>8</sub>	10-30	740-1550	0.3-3	ST, RCM	[267]
CH <sub>4</sub> /C <sub>2</sub> H <sub>6</sub> /C <sub>3</sub> H <sub>8</sub>	1-50	770-1580	0.5-2	ST, RCM	[106]
CH <sub>4</sub> /C <sub>2</sub> /C <sub>3</sub>	13-21	850-925	0.6-1	RCM	[268]
CH <sub>4</sub> /H <sub>2</sub>	15-70	950-1060	0.5-1	RCM	[125]
DME	10-20	615-735	0.43-1.5	RCM	[269]
CH <sub>4</sub> /C <sub>2</sub> H <sub>6</sub> /H <sub>2</sub>	1-16	900-1800	0.5-1	ST	[270]
DME	1.6-6.6	1175-1900	0.5-3	ST	[271]
CH <sub>4</sub> /DME	1-10	1134-2105	1	ST	[183]
CH <sub>4</sub> /C <sub>2</sub> H <sub>6</sub>	1-31	1154-2250	0.5-2	ST	[109]
DME/C <sub>3</sub> H <sub>8</sub>	20	1100-1500	0.5-2	ST	[252]
C <sub>2</sub> H <sub>6</sub> /DME	2-20	1100-1500	0.5-2	ST	[253]
CH <sub>4</sub>	1-10	1350-1950	0.5-2	ST, CVB	[272]
CH <sub>4</sub> /DME	7-41	600-1600	0.3-2	ST, RCM	[117]
CH <sub>4</sub> /DME	1-1.6	1650-2050	2	ST	[17]
DME	0.55-1.2	1075-1860	0.5-1	ST	[273]

This study presents ignition delay times and species profiles as a function of temperature for different natural gas (90 % CH<sub>4</sub>, 9 % C<sub>2</sub>H<sub>6</sub>, 1 % C<sub>3</sub>H<sub>8</sub>)/DME blends at equivalence ratios of 2, 10, and 20 by combining complementary results of shock-tube ( $\phi = 2$  and 10,  $p = 30$  bar,

$T = 710 - 1630$  K) and flow-reactor measurements ( $\phi = 2, 10, \text{ and } 20, p = 6$  bar,  $T = 473 - 973$  K). The results are compared to predictions of two reaction mechanisms from literature [19,124] and a modified mechanism to assess their ability of describing the interaction between DME and natural gas under uncommon reaction conditions.

The experimental, modeling, and results part of the paper is divided into three chapters. In section 9.2, the experimental methods are presented and relevant details of the individual experimental arrangements are given. Section 9.3 deals with modeling. In section 9.3.1, sensitivity analyses are shown that form the basis for the modification of the mechanism of Porras et al. [19]. The most sensitive reactions at different conditions are evaluated and the modifications to the mechanism are described. Sections 9.3.2 and 9.3.3 briefly outline the simulation methods used.

Section 9.4 discusses the results, starting with the shock-tube measurements. While section 9.4.1.1 presents ignition delay times for  $\text{CH}_4/\text{air}$ , natural gas/air, and natural gas/DME/air mixtures at  $\phi = 2$  and 10 and 30 bar, section 9.4.1.2 shows the products formed after ignition for natural gas/air and natural gas/DME/air mixtures at  $\phi = 10$  and 30 bar. In section 9.4.2, the results of the reactor experiments are presented with a focus on the influence of DME on the fuel conversion and product composition. In section 9.4.2.1, figures presenting all experimental results compared to the predictions of the different mechanisms are shown. These results are further discussed in the following sub-sections. The first section examines the fuel conversion and the formation of three selected types of product species: synthesis gas ( $\text{H}_2, \text{CO}$ ), unsaturated hydrocarbons ( $\text{C}_2\text{H}_4, \text{C}_3\text{H}_6$ ), and oxygenated species ( $\text{CH}_3\text{OH}, \text{CH}_2\text{O}$ ). The reaction pathways towards the individual products are analyzed in detail and possible reasons for deviations of the model predictions are discussed. The individual sections are briefly summarized at the end of each chapter to highlight the core statements. In the last result chapter, the maximum yields of the main species are compared for all mixtures in a single diagram and the overall findings are discussed without further analysis. Together with the species profiles at the beginning of the chapter, readers who are primarily interested in the product composition can view the main results without having to go into further details.

## 9.2 Experimental methods

The investigated reaction conditions are shown in Table 2. Details of both experimental arrangements are given below.

**Table 9-2:** Reaction conditions (PFR: plug flow reactor, ST: shock tube).

$\text{CH}_4$	$\text{C}_2\text{H}_6$	$\text{C}_3\text{H}_8$	DME	$\text{O}_2$	Ar	$\text{N}_2$	Ne	$p$	$T$	$\phi$	Exp.
			mol%					bar	K	-	-
4.065	0.406	0.045	0.238	5.246	90	0	0	6	473-973	2	PFR
3.813	0.381	0.042	0.471	5.292	90	0	0	6	473-973	2	PFR
7.004	0.700	0.078	0.410	1.808	90	0	0	6	473-973	10	PFR
6.613	0.661	0.073	0.816	1.836	90	0	0	6	473-973	10	PFR
7.700	0.770	0.086	0.450	0.994	90	0	0	6	473-973	20	PFR
7.281	0.728	0.081	0.899	1.011	90	0	0	6	473-973	20	PFR

CH <sub>4</sub>	C <sub>2</sub> H <sub>6</sub>	C <sub>3</sub> H <sub>8</sub>	DME	O <sub>2</sub>	Ar	N <sub>2</sub>	Ne	$p$	$T$	$\phi$	Exp.
			mol%					bar	K	-	-
14.330	1.433	0.159	0	17.236	0	66.842	0	30	950-1630	2	ST
13.396	1.340	0.149	0.783	17.288	0	67.044	0	30	850-1450	2	ST
12.492	1.249	0.139	1.542	17.338	0	67.240	0	30	710-1480	2	ST
44.245	4.425	0.492	0	10.422	0	38.416	2.000	30	930-1540	10	ST
41.176	4.118	0.458	2.408	10.627	0	39.213	2.000	30	860-1500	10	ST

### 9.2.1 Shock tube

A high-pressure shock tube for post-ignition peak pressures up to 500 bar with a constant inner diameter of 90 mm and lengths of the driver and driven sections of 6.4 and 6.1 m, respectively, was used for ignition delay time (IDT) and product composition measurements. The maximum test time is extended up to 15 ms by driver-gas tailoring with helium as the main driver gas component and Ar addition to match the acoustic impedance of the driver gas with the one of the test gas. The driver gas was mixed *in situ* by using two high-pressure mass flow controllers (Bronkhorst Hi-Tec flowmeter F-136AI-FZD-55-V and F-123MI-FZD-55-V). The driver gas composition depends on the test gas mixture and the Mach number and was calculated prior to the experiment using formulas by Oertel [195] and Palmer and Knox [196]. Test gas mixtures were prepared manometrically in a mixing vessel and stirred for at least one hour to ensure homogeneity. The experiment is described in more detail in Ref. [274].

The temperature  $T_5$  and pressure  $p_5$  behind the reflected shock waves were computed from the incident shock velocity using a one-dimensional shock-wave model. The shock-wave velocity was measured over three intervals using four piezoelectric pressure transducers (PCB 112-B05) and the related temperature uncertainty of  $\pm 15$  K was determined by the method of Petersen et al. [275] that considers the uncertainty of the position of the pressure transducer, the time when the incident shock wave passes the pressure transducer, and the error caused by the interpolation of the incident shock-wave speed to that at the end flange. The determined error represents an average value for the temperature range of our measurements. Band-pass-filtered ( $308 \pm 5$ ,  $431 \pm 5$  nm) emission from OH\* and CH\* chemiluminescence was monitored through windows in the sidewall 15 mm from the end flange with fiber-coupled Hamamatsu 1P28 photomultipliers. The pressure was recorded at the same position using a piezoelectric pressure transducer (PCB-112B05) that was shielded with a thin high-temperature silicone layer. Ignition delay times were defined as the interval between the rise in pressure due to the arrival of the reflected shock wave at the measurement port and the extrapolation of the steepest increase in emission to its zero level on the time axis. The uncertainty of the determination of ignition delay times from the chemiluminescence profiles is about  $\pm 10$   $\mu$ s for IDTs  $< 100$   $\mu$ s,  $\pm 30$   $\mu$ s for IDTs of about 1000  $\mu$ s and  $\pm 100$   $\mu$ s for IDTs around 10 ms. These values were determined considering the uncertainties of the extrapolation of the steepest increase of the measured chemiluminescence intensity and the uncertainties of the blast-wave correction [261].

Gas samples were taken from the shock tube with a fast-acting valve (Parker Hannifin Pulse Valve Series 9 with IOTA ONE® driver) that was integrated in the end flange and connected to a 50-ml sample vessel. The valve was opened 14 ms after the arrival of the reflected shock wave for 10 ms. The samples were analyzed with GC/MS (Agilent Technologies GC System

7890 A, MSD 5975C) using an Agilent J&W HP-PLOT Q column. Each mixture used in the experiments at  $\phi = 10$  contained 2 % Ne as internal standard. All mole fractions were determined relative to this internal standard so that the measured species mole fractions are independent on the inlet pressure in the sample and the accuracy is limited by the errors in calibration, the preparation of the fuel/air mixture, and by the uncertainty of the GC measurement. Calibration mixtures with various mole fraction levels were prepared in a 50-L mixing vessel using very precise pressure transducers. We estimate that the error of the calibration factor caused by the mixture preparation and the GC measurement uncertainty is below 5 %. For all substances, linear behavior with no offset between signal and mole fraction was observed. Another 5 % error is related to uncertainties in the Ne mole fraction in the fuel/air mixture. The low uncertainty ( $< 10$  % in total) was confirmed by measurements of the fuel/air mixtures at temperatures where no oxidation occurs and by calculating the carbon balance, which was found to be  $1 \pm 0.05$  at low temperatures, where oxidation but no formation of larger PAHs occurred.

### 9.2.2 Plug-flow reactor

In this study, a flow reactor coupled to a time-of-flight mass spectrometer (see supplemental material (appendix B) or [197]) is used to investigate the partial oxidation of natural gas/DME mixtures at a pressure of 6 bar and temperatures between 473 and 973 K. A constant volumetric flow rate of 280 sccm (standard conditions:  $T = 273.15$  K,  $p = 1$  bar) was used to approximate plug-flow conditions according to the model of Levenspiel [51]. The residence time varied between 14.5 s at 473 K and 7.6 s at 973 K, considering the complete reactor length. Details of the experimental setup are given elsewhere [17,200] and only a brief description is provided here.

The reactor consists of a 65 cm long quartz tube, surrounded by a stainless-steel tube for safety. A 40-cm long isothermal reaction zone ( $\pm 10$  K) is established by temperature-controlled heating tapes, wrapped around a copper shell that encloses the stainless-steel tube. The gap between the stainless-steel and the quartz tube is sealed at the in- and outlet of the reactor to prevent gases from entering this gap and reacting with the steel wall. The reactants are metered by calibrated mass flow controllers and premixed at room temperature before entering the reactor, while the pressure is regulated manually by a heated needle valve downstream of the reactor. Pressure fluctuations, measured by a pressure transducer upstream of the reactor, are less than 20 mbar. A high argon dilution is used to minimize the temperature rise due to exothermal reactions.

After passing the reaction zone, the product gases are guided through the needle valve into a time-of-flight mass spectrometer (TOF-MS, Kaesdorf) via molecular beam extraction for product analysis. The products are ionized by electron ionization at 17 eV to minimize fragmentation. Because fragmentation could not be avoided completely, it was considered for all directly calibrated species in data analysis. The mass resolution of the spectrometer is  $m/\Delta m \sim 2000$ . The TOF-MS enabled the detection of stable species, formed in the partial oxidation process. The mole fractions of the reactants ( $\text{CH}_4$ ,  $\text{C}_2\text{H}_6$ ,  $\text{C}_3\text{H}_8$ , DME,  $\text{O}_2$ ) as well as those of  $\text{CO}$ ,  $\text{CO}_2$ ,  $\text{C}_2\text{H}_4$ ,  $\text{C}_3\text{H}_6$ ,  $\text{CH}_2\text{O}$  and  $\text{CH}_3\text{OH}$  were measured. The uncertainties with respect to mole fractions of gaseous and liquid species are estimated to be around 10 and 20 %, respectively.

### 9.3 Modeling

Reaction mechanisms of Porras et al. [19] and Zhou et al. [124] were used for the simulation of the shock-tube and flow-reactor experiments. The reaction mechanism of Porras et al., called PolyMech (in the following PolyMech1.0), was developed for the prediction of very fuel-rich CH<sub>4</sub> and CH<sub>4</sub>/additive mixtures, by combining literature mechanisms developed for the pyrolysis and combustion of CH<sub>4</sub>, as well as an ethanol and a DME sub-mechanism (by Zhao et al. [178]). Also, several rate constants were adjusted within their documented uncertainty range for a better prediction of ignition delay times and species profiles as a function of temperature, obtained by shock-tube, RCM and flow-reactor experiments at high equivalence ratios. It covers the oxidation of H<sub>2</sub>, C<sub>2</sub>H<sub>2</sub>, C<sub>1</sub> – C<sub>3</sub> alkanes, and alkenes as well as oxygenated C<sub>1</sub>–C<sub>2</sub> species.

The reaction mechanism of Zhou et al. [124], also known as AramcoMech3.0, was developed at NUI Galway and covers C<sub>1</sub> – C<sub>4</sub>-chemistry, including oxygenated species and peroxide chemistry. The included DME mechanism is that of Burke et al. [117]. Similar to the mechanism of Porras et al. [19], the AramcoMech3.0 [124] shows a hierarchical structure, ranging from an H<sub>2</sub>, to butene and butadiene mechanisms. It was validated by a large experimental dataset, comprising data from shock tubes, RCMs, flames, and various types of reactors making it well-suited for the simulations of the mixtures investigated in this study.

#### 9.3.1 Model improvement

To improve the PolyMech predictions of experimental data, especially with species profiles of CO, CO<sub>2</sub>, H<sub>2</sub>, C<sub>2</sub>H<sub>2</sub>, C<sub>2</sub>H<sub>4</sub>, C<sub>3</sub>H<sub>8</sub>, and C<sub>6</sub>H<sub>6</sub>, some rate constant expressions were updated by more recent ones and missing pathways were added to the mechanism. The reactions were identified by integrated sensitivity analyses and comparative reaction path analyses using the PolyMech1.0 and AramcoMech3.0. Here, only the analyses performed with the PolyMech1.0 are shown. Sensitivity analyses performed with the updated PolyMech (PolyMech2.0) and the AramcoMech3.0 can be found in the supplemental material (appendix B). The AramcoMech3.0 was used for comparison because its predictions showed a good agreement with the experimental data, it contains current rate constants, and is one of the most detailed mechanisms with respect to C<sub>1</sub> – C<sub>4</sub>-chemistry. This is also the reason why the mechanism was not modified in contrast to the PolyMech1.0, which is an in-house mechanism with a very limited number of species and reactions and specifically made for the polygeneration conditions investigated here. Modified or added reactions are listed in Table 9-3. Sensitivity coefficients ( $S_{ij}$ ) are defined as

$$S_{ij} = \frac{\partial x_i}{\partial k_j} \frac{k_j}{x_i} \quad (9-1)$$

with  $x_i$  and  $k_i$  representing the mole fraction and rate constant of the specific species and reaction, respectively.

**Table 9-3:** Modified and added reactions of the PolyMech2.0. The rate constants are in the form of  $k = AT^n \exp(-E/(RT))$ . Units are mol, cm, K, s and kJ.

	Reaction	$A$	$n$	$E_A$	Ref.
1	$\text{CO} + \text{HO}_2 = \text{CO}_2 + \text{OH}$	$1.57 \times 10^5$	2.18	75.061	[276]
2	$\text{CH}_3 + \text{HO}_2 = \text{CH}_3\text{O} + \text{OH}$	$1 \times 10^{12}$	0.269	-2.8765	[277]
3	$\text{CO} + \text{OH} = \text{CO}_2 + \text{H}$	$7.046 \times 10^4$	2.053	-1.489	[278]
4	$\text{CO} + \text{OH} = \text{CO}_2 + \text{H}$	$5.757 \times 10^{12}$	-0.664	1.389	[278]
5	$\text{HCCO} + \text{O}_2 = \text{CO} + \text{CO}_2 + \text{H}$	$4.78 \times 10^{12}$	-0.142	4.812	[279]
6	$\text{HCCO} + \text{O}_2 = \text{CO} + \text{CO} + \text{OH}$	$1.91 \times 10^{11}$	-0.020	4.268	[279]
7	$\text{CH}_3\text{O} + \text{CH}_2\text{O} = \text{CHO} + \text{CH}_3\text{OH}$	$6.62 \times 10^{11}$	0	9.5981	[280]
8	$\text{CH}_3\text{OH} + \text{HO}_2 = \text{CH}_3\text{O} + \text{H}_2\text{O}_2$	$1.22 \times 10^{12}$	0	83.976	[281]
9	$\text{CH}_3\text{OH} + \text{O}_2 = \text{CH}_3\text{O} + \text{HO}_2$	$3.58 \times 10^4$	2.27	178.927	[282]
10	$\text{CH}_2\text{O} + \text{OH} = \text{CHO} + \text{H}_2\text{O}$	$7.82 \times 10^7$	1.63	-4.414	[283]
11	$\text{CH}_2\text{O} + \text{CH}_3 = \text{CHO} + \text{CH}_4$	$3.83 \times 10^1$	3.36	18.041	[201]
12	$\text{CH}_2\text{O} + \text{H} = \text{CHO} + \text{H}_2$	$5.860 \times 10^3$	3.13	6.3353	[284]
13	$\text{C}_2\text{H}_4(+\text{M}) = \text{C}_2\text{H}_2 + \text{H}_2(+\text{M})$	$8.0 \times 10^{12}$	0.44	371.414	[285] <sup>a</sup>
14	$\text{C}_2\text{H}_4 + \text{OH} = \text{C}_2\text{H}_3 + \text{H}_2\text{O}$	$1.30 \times 10^{-1}$	4.2	-3.598	[286]
15	$\text{C}_2\text{H}_5 + \text{HO}_2 = \text{CH}_3\text{CH}_2\text{O} + \text{OH}$	$3.00 \times 10^{13}$	0	0	[287]
16	$\text{C}_2\text{H}_4 + \text{H} = \text{C}_2\text{H}_3 + \text{H}_2$	$1.266 \times 10^5$	2.752	48.739	[288]
17	$\text{CH}_3 + \text{CH}_3 (+\text{M}) = \text{C}_2\text{H}_6 (+\text{M})$	$9.455 \times 10^{14}$	-0.538	0.5654	[289,290] <sup>a</sup>
18	$\text{C}_3\text{H}_8 + \text{OH} = \text{N-C}_3\text{H}_7 + \text{H}_2\text{O}$	$2.732 \times 10^7$	1.811	3.633	[291]
19	$\text{C}_3\text{H}_8 + \text{OH} = \text{I-C}_3\text{H}_7 + \text{H}_2\text{O}$	$1.975 \times 10^7$	1.751	0.266	[291]
20	$\text{PC}_3\text{H}_4 + \text{H} = \text{C}_2\text{H}_2 + \text{CH}_3$	$2.830 \times 10^{08}$	1.74	32.202	[292]
21	$\text{CH}_4 (+\text{M}) = \text{CH}_3 + \text{H} + (\text{M})$	$2.105 \times 10^{16}$	0	439.00	[293] <sup>a</sup>

<sup>a</sup> See electronic supplemental material for low-pressure limits and Troe parameters

Figure 9-1 shows the results of the sensitivity analysis for CO<sub>2</sub>. It is found that the reaction of CO and hydroperoxyl radicals (HO<sub>2</sub>) is the most sensitive one with an increasing sensitivity at higher equivalence ratios and a decreasing sensitivity at higher temperatures. Its rate constant expression was replaced by the expression implemented in the AramcoMech3.0 and proposed by You et al. [276], showing much lower rates at temperatures higher than 800 K. The reaction of methyl (CH<sub>3</sub>) and HO<sub>2</sub> radicals, showing the second highest sensitivity under the investigated conditions, was updated to the values given by Jasper et al. [277]. These modifications resulted in a very good prediction of the measured CO and CO<sub>2</sub> mole fractions in the plug-flow reactor. To further improve the predictions for the shock-tube conditions, the rate expression for the reaction of CO and hydroxyl radicals (OH) was adapted from Joshi and Wang [278]. Only the low-pressure-limit rate coefficient, which was fitted by a sum of two modified Arrhenius equations (reactions 2 and 3), was implemented in PolyMech1.0, as the authors stated that it is applicable for most combustion applications. The rate constants for reactions of HCCO and O<sub>2</sub> (reactions 5 and 6) were updated to the values proposed by Klippenstein et al. [279].

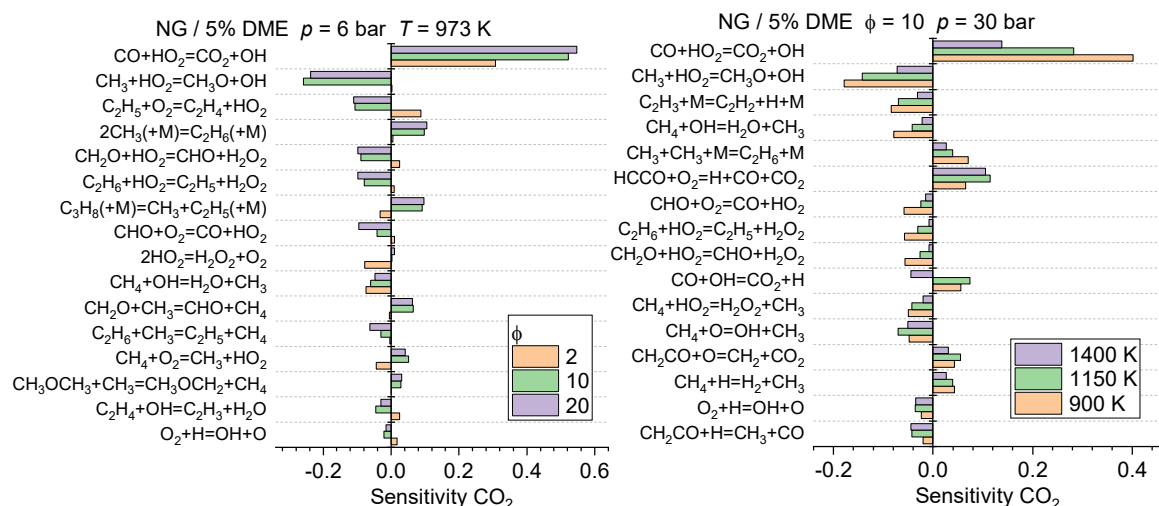


**Figure 9-1:** Sensitivity coefficients of the  $\text{CO}_2$  mole fraction for selected plug-flow (left) and shock-tube (right) conditions using the PolyMech1.0 [19]. Coefficients were integrated up to the sampling even of each experiment.

With respect to  $\text{CH}_3\text{OH}$ , the sensitivity analysis was performed for 623 and 773 K, two different DME amounts and  $\phi = 2$  (Figure 9-2), at which the largest deviation between experiment and simulation was found. The modeling predictions are most sensitive to reactions involving DME at 623 K, because of its low-temperature chemistry. The sensitivities are much higher for the 5 % DME mixture compared to the 10 % DME mixture. Because of a very good prediction of DME mole fractions at all conditions, the DME chemistry set was not modified. The  $\text{CH}_3\text{OH}$  mole fraction is also sensitive to H-abstraction from  $\text{CH}_4$  and  $\text{C}_2\text{H}_6$  by OH radicals, especially at low temperature. The rate constant expression for  $\text{CH}_4+\text{OH}$ , implemented in the PolyMech1.0, was adapted from Baulch et al. [201] with a reliability given by  $\Delta \log k = \pm 0.1$  over the range 250–350 K, rising to  $\pm 0.2$  at 800 K and  $\pm 0.3$  at 2400 K. Taking these error limits into account, the expression is in very good agreement to the more recent one proposed by Srinivasan et al. [294] and was congruously not modified. The same applies to the expression for  $\text{C}_2\text{H}_6+\text{OH}$  that only shows a maximum deviation of 9.78 % at 570 K, compared to the expression proposed by Krasnoperov et al. [295]. This rate expression was obtained by new shock-tube studies and shows an excellent agreement to literature data. The rate expression for the reaction of methoxy ( $\text{CH}_3\text{O}$ ) radicals and formaldehyde ( $\text{CH}_2\text{O}$ ), however, was changed to the one implemented in the AramcoMech3.0 and originally proposed by Fittschen et al. [280] because it improved the model predictions by 1.5 to 3 times higher rates at the relevant temperatures. As the results obtained by the AramcoMech3.0 still showed a better agreement to the experiments, a reaction pathway analysis was performed to identify important pathways yielding  $\text{CH}_3\text{OH}$ . The two most important reactions were added to the PolyMech as reactions 8 and 9 (see Table 9-3).

For  $\text{CH}_2\text{O}$ , the PolyMech1.0 slightly underpredicts the mole fractions at temperatures between 600 and 800 K at all equivalence ratios. In Figure 9-2, the sensitivity analysis performed at 773 K for all 5 % DME mixtures, identifies only three reactions with high sensitivities at all  $\phi$ . These reactions are the already discussed H-abstraction from  $\text{CH}_4$  by OH and H-abstractions from  $\text{CH}_2\text{O}$  by OH (reaction 10) and  $\text{CH}_3$  (reaction 11). The rate expression of reaction 10, originally adapted from Warnatz [232], was replaced by the more recent rate expression

proposed by Vasudevan et al. [283]. They combined new high-temperature shock-tube measurements with low-temperature measurements by Sivakumaran et al. [296]. The three-parameter fit covers the temperature range between 200 and 1670 K and shows good agreement to experimental data at intermediate temperatures [283]. Comparing both rate expressions, more than two times lower rates are found for the new expression throughout the investigated temperature range, yielding higher CH<sub>2</sub>O mole fractions. Regarding the rate expression of reaction 11, only the *A* factor was reduced by 20 % and thus changed to its original value, recommended by Baulch et al. [201]. Lastly, reaction 12 was updated to the values proposed by Wang et al. [284]. The same three rate expressions are also implemented in the AramcoMech3.0.

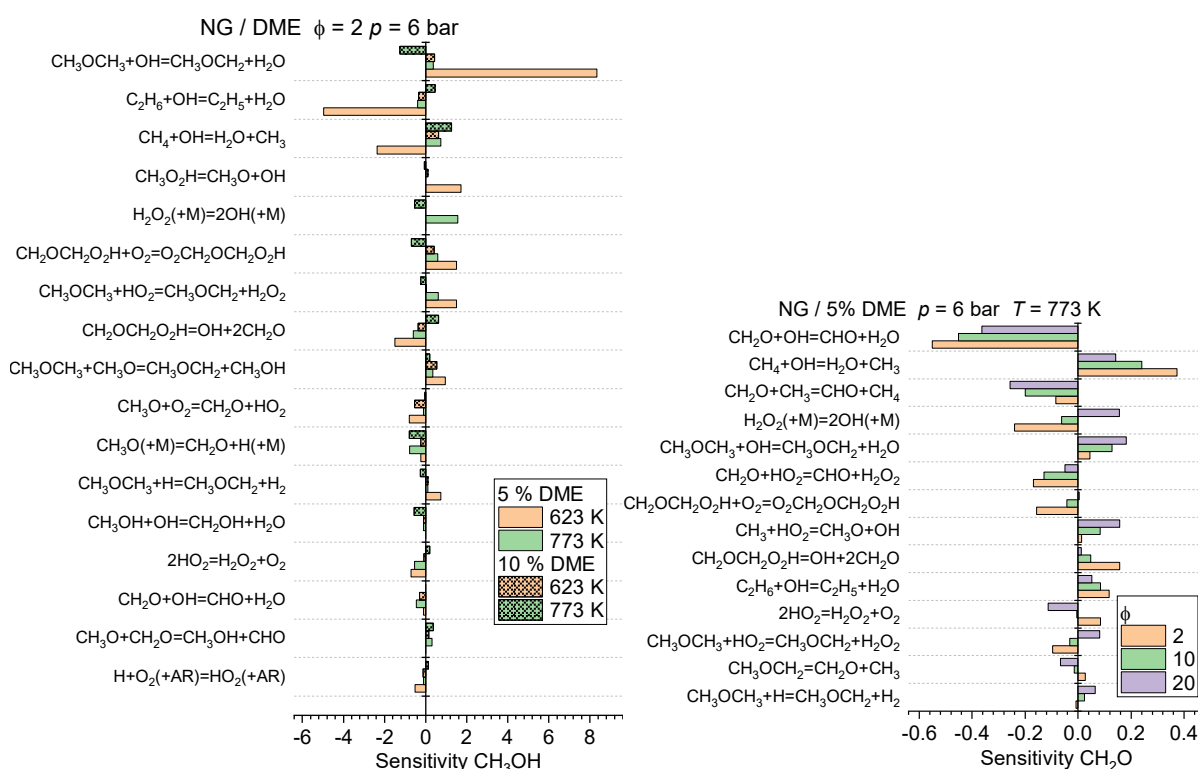


**Figure 9-2:** Sensitivity coefficients of the CH<sub>3</sub>OH (left) and CH<sub>2</sub>O (right) mole fractions for selected plug-flow conditions using the PolyMech1.0 [19]. Coefficients were integrated up to the sampling event of each experiment.

The sensitivity analysis for C<sub>2</sub>H<sub>4</sub> (Figure 9-3) reveals that, besides reaction 2 (only plug flow), the recombination of CH<sub>3</sub> radicals (reaction 17) is the most sensitive reaction for the selected plug-flow and shock-tube conditions. The rates of the recombination reaction were replaced by the values proposed by Wang et al. [290] and Klippenstein et al. [289], using the high-pressure limit of Klippenstein et al. and the low-pressure limit as well as the Troe parameters of Wang et al. Implementing the high-pressure limit of Klippenstein et al. [289] resulted in 1.2 times higher rates at 700 K rising to 1.4 times higher rates at 1400 K in the investigated pressure range compared to the rates obtained by the expression of Wang et al. [290], which is implemented in the AramcoMech3.0. In addition, the reactions of C<sub>2</sub>H<sub>4</sub> with OH (reaction 14) and H (reaction 16) were updated to the values proposed by Senosiain et al. [286] and Huynh et al. [288], especially to improve the model predictions at the investigated plug-flow conditions. The new rate constant expressions lead to slightly lower and up to five times lower rates, respectively,

compared to the rate expressions integrated in the PolyMech1.0. To slightly improve model predictions at lower temperatures, the rate expression for the reaction of  $C_2H_5$  and  $HO_2$  was taken from Bozzelli et al. [287].

With respect to the shock-tube analysis, reactions of acetylene ( $C_2H_2$ ) and propargyl radicals ( $C_3H_3$ ) are also shown to be very sensitive to the prediction of  $C_2H_4$ . Both species are precursors of benzene ( $C_6H_6$ ), which is found in the shock-tube experiments in considerable amounts. As the PolyMech1.0 contains only three reactions describing the formation of  $C_6H_6$  and none for its consumption, much higher mole fractions of  $C_6H_6$  are predicted compared to the experiments. To improve this, the complete  $C_6H_6$  sub-mechanism of the reaction mechanism of Cai and Pitsch [148] including the formation of some higher polycyclic aromatic hydrocarbons (PAHs) was adapted and added to the PolyMech. The benzene/PAH sub-mechanism of Cai and Pitsch predicts  $C_6H_6$  mole fractions with very good agreement for experimental shock-tube data for  $CH_4$ ,  $CH_4$ /diethyl ether,  $CH_4$ /*n*-heptane, and  $CH_4$ /dimethoxymethane [199,297] mixtures. The added reactions can be found in the electronic supplemental material. The mechanism of Cai and Pitsch was developed for describing the combustion behavior of gasoline surrogate fuel. It contains no DME chemistry and a lot of species which are not interesting for our conditions. Therefore, only its benzene and PAH chemistry was considered here. This chemistry up to 4-ring PAHs contains only 67 species and 162 reactions so that the PolyMech2.0 is still short but can now describe well acetylene and benzene concentrations and contains also pyrene which can be used as indication for soot formation. The prediction of soot formation trends by using the square of the pyrene concentration [298] is very important for the use of the mechanism for simulating technical polygeneration processes.

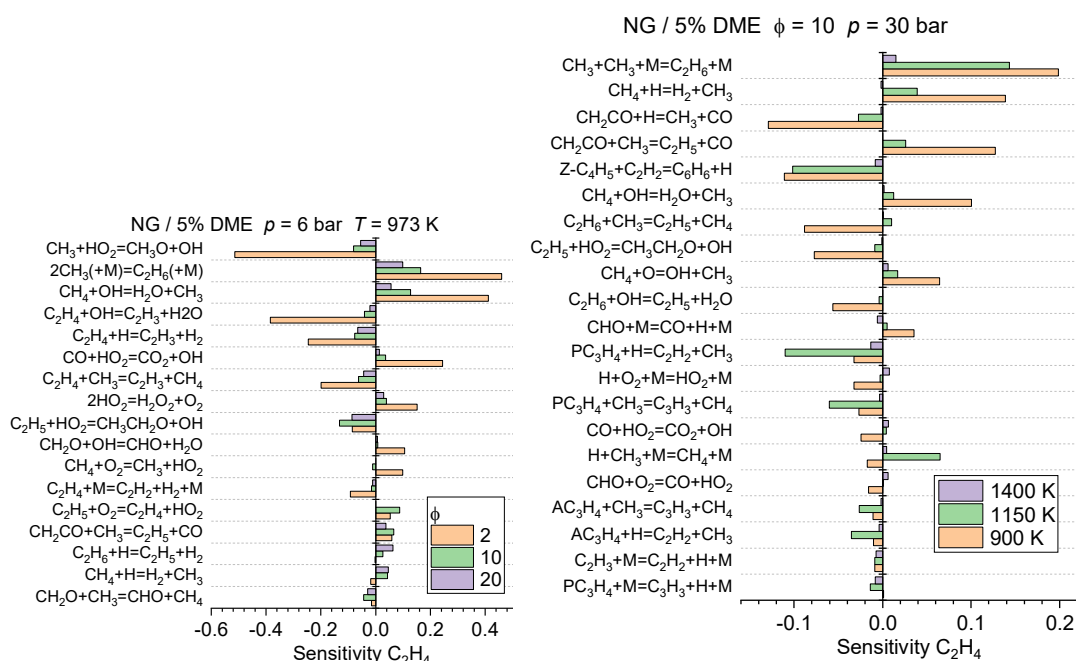


**Figure 9-3:** Sensitivity coefficients of the  $C_2H_4$  mole fraction for selected plug-flow (left) and shock-tube (right) conditions using the PolyMech1.0 [19]. Coefficients were integrated up to the sampling event of each experiment.

In addition, the rate constant for the sensitive reaction of propyne and H radicals to  $C_2H_2$  and  $CH_3$  was adapted from Wang et al. [292]. Besides the reactions indicated by the sensitivity

analyses, the rate constant for the thermal decomposition of  $C_2H_4$  to  $C_2H_2$  and  $H_2$  (reaction 13) was changed to the values integrated in the GRI 3.0 mechanism [285]. This change was required, because the rates obtained by the PolyMech1.0 expression were too high at temperatures higher than 1000 K, compared to literature values, and led to a different temperature dependence of the  $C_2H_4$  mole fractions compared to the shock-tube experiments. The rate expression is also used in the AramcoMech3.0 yielding  $H_2CC$  instead of  $C_2H_2$  directly. But the rates for the isomerization of  $H_2CC$  to  $C_2H_2$  are very high, thus the addition of this reaction did not change model predictions and was therefore omitted.

Using the PolyMech1.0, a much lower propane ( $C_3H_8$ ) conversion was observed compared to the plug-flow reactor experiments, especially at  $\phi \geq 10$ . The sensitivity analysis revealed the H-abstraction by OH forming *iso*- and *n*- $C_3H_7$  as two of the most sensitive reactions. These rate expressions were updated by the more recent ones proposed by Sivaramakrishnan et al. [291]. The addition of several reactions describing the oxidation of  $C_2H_6$  and  $C_3H_8$  did not significantly improve the model predictions and was not considered in order to keep the final modified version of the PolyMech as small as possible. The new rate coefficient of the methane decomposition to methyl and H atoms of Wang et al. [293] has also almost no influence on the present results but the old rate coefficient was replaced because the new value improves the simulation of methane pyrolysis at high temperatures significantly [299].

### 9.3.2 Shock-tube modeling

Ignition delay times and species mole fractions were simulated with Chemical Workbench® [44] using the conP approach (adiabatic isentropic compression or expansion) based on predefined pressure profiles that are derived from experiments with non-reactive test-gas mixtures. Default values (relative tolerance:  $10^{-5}$ , absolute tolerance:  $10^{-16}$ ) were used for the tolerances. For measurements at  $\phi = 2$ , a pressure increase of 2 %/ms was considered for the initial 2.8 ms followed by a constant pressure. At  $\phi = 10$ , no pressure increase was observed, thus the simulations were performed with the initial pressure  $p_5$ . For the simulations of the species mole fraction profiles at  $\phi = 10$ , a constant pressure was used for the initial 12 ms followed by a pressure decrease of 12 % of  $p_5$ /ms (caused by the cooling due to rarefaction waves) for 7 ms (based on an averaged sampling time) and a very fast pressure decrease to 50 mbar (by expansion into the evacuated sampling vessel). The simulation is continued at this low pressure/temperature for 6 ms. The calculated species mole fractions are then normalized relative to the calculated Ne mole fraction at this time ( $x_{i,n} = x_i \times 2\%/x_{Ne}$ , 2 % Ne as internal standard in the initial mixture) to compare them to the standard-normalized measured values. Sensitivity analyses were performed with the conP approach and a constant pressure for 15 ms. The calculated product mole fractions for this reaction time are very similar to the ones calculated with cooling. The times chosen for the simulation of the products were selected for the following reasons: The concentrations of almost all species reach a quasi-constant level at about 2 ms after ignition (see Ref. [19] for a similar mixture). Only the concentrations of acetylene and especially benzene vary after these 2 ms. The increase of the benzene concentration could not be stopped in the cooling phase by rarefaction waves because the temperature decrease is too low due to the high heat capacity of the mixture and the radical chain reactions are continued. The reactions are then stopped by the expansion into the sampling vessel. The amount of gas in the reaction

vessel is small compared to the amount in the shock tube so that the pressure and temperature in the shock tube are not influenced by the sampling. Simulating the reactions also in the cooling phase until 7 ms after the opening of the sampling valve gives a good approximation of the sampling, considering that the pressure is strongly decreasing during the sampling time of 10 ms. More details, such as calculated species concentrations and an experimental pressure profile are given in Ref. [19]. The ignition delay times at  $\phi = 2$  are determined by Chemical Workbench from the time when CH reaches its maximum value, which is identical to the occurrence of the CH\* chemiluminescence peak. Both peaks are so narrow that it makes no difference if the peak position or the interpolation of the steepest increase of the signal intensities to the zero line are used as indicator for the ignition delay time. The simulations at  $\phi = 10$  show very broad CH\* and OH\* peaks. For this reason, ignition delay times were determined by extrapolating the steepest increase of the simulated CH\* mole fraction to the zero line.

### 9.3.3 Plug-flow reactor modeling

For the flow reactor simulations, the plug-flow model with fixed temperature profile of ChemKin Pro 19.0 [43] was used. Besides the geometric specification of the reactor, the complete temperature profiles, including the heating and cooling zone at the in- and outlet are used for the simulations. The temperature profiles were measured prior to the experiments using a moving type-K thermocouple along the center axis of the reactor in an inert gas flow of argon. Temperature profiles, inlet conditions and measured mole fractions are provided as electronic supplementary material.

To estimate the temperature rise of the gas mixture due to exothermal reactions, additional simulations were performed for the mixture with the highest heat release ( $\phi = 2$ , 10 % DME). For this simulation, the shear-flow model of ChemKin Pro 19.0 was used, taking radial diffusion, the heat transfer from the wall to the gas and the exothermal heat release into account. It is a two-dimensional approach, predicting temperature, velocity and species concentration fields within the reactor.

## 9.4 Results and discussion

### 9.4.1 Shock tube

Ignition delay times ( $\phi = 2$  and 10) and product composition ( $\phi = 10$ ) of natural gas and natural gas/DME mixtures were determined in a high-pressure shock tube and compared to predictions using the AramcoMech3.0 [124], PolyMech1.0 [19], and PolyMech2.0 (see section 9.3.1).

#### 9.4.1.1 Ignition delay times

Measured and simulated IDTs at  $\phi = 2$  are presented in Figure 9-4. The data with natural gas as fuel show shorter IDTs compared to neat methane data [199]. A further reduction of the IDTs is achieved by the addition of DME. The AramcoMech3.0 [124] predicts all measured IDTs very well. Only for the experiments with 10 % DME addition at temperatures  $< 900$  K about 50 % longer IDTs are predicted. The simulations with the PolyMech1.0 [19] and the measured IDTs for natural gas and natural gas/DME mixtures agree very well for temperatures above

1200 K. For lower temperatures, 50–90 % too long ignition delay times are predicted. The PolyMech2.0 predicts about 25 % longer IDTs at higher temperatures compared to the original version whereas at the lower temperature end the predictions are almost identical.

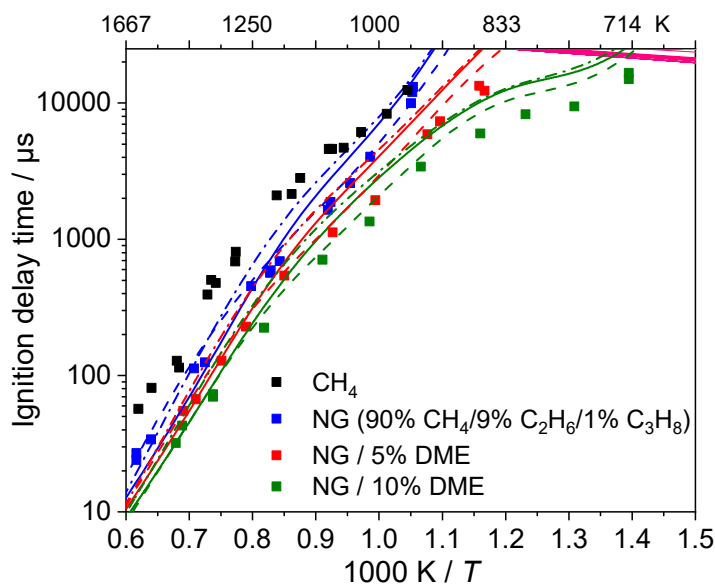


**Figure 9-4:** Measured and simulated ignition delay times of natural gas/DME/air mixtures at  $\phi = 2$  and 30 bar. Symbols: Experiments, full lines: Simulations with PolyMech1.0 [19], dash-dotted lines: Simulations with PolyMech2.0, dashed lines: Simulations with AramcoMech3.0 [124].

Measured and simulated IDTs of natural gas/air mixtures at  $\phi = 10$  are shown in Figure 9-5. For temperatures above 1200 K it was very difficult to determine the IDTs because the OH\* and CH\* peaks exhibit two distinct steep increases and very broad peaks. This behavior has not been observed before for CH<sub>4</sub>, CH<sub>4</sub>/additive and natural gas/DMM mixtures at  $\phi = 10$  [199,297] and is also not predicted by the simulations. The measured OH\* and CH\* chemiluminescence signals and the corresponding simulations using the AramcoMech3.0 can be found in the supplemental material (appendix B) at temperatures of 974, 1204, and 1427 K. A pressure increase by the ignition could not be observed. We assume that the first increase is caused by ethane/propane oxidation and the second by methane oxidation. The IDTs of natural gas are much shorter compared to methane and are similar to the values at  $\phi = 2$ . The measured IDTs are very well predicted by the AramcoMech3.0 [124] and the Cai and Pitsch [148] mechanism. For lower temperatures, about 50 % too long IDTs are predicted by the PolyMech1.0 [19]. Especially at higher temperatures the modifications of the PolyMech1.0 cause longer ignition delay times. The same effect was observed for the natural gas/5 % DME mixture at  $\phi = 10$  (Figure 9-6). It is mainly caused by the lower rate coefficient for reaction 13 ( $C_2H_4(+M) = C_2H_2 + H_2(+M)$ ), so that less H<sub>2</sub>, which accelerates the ignition, is produced.

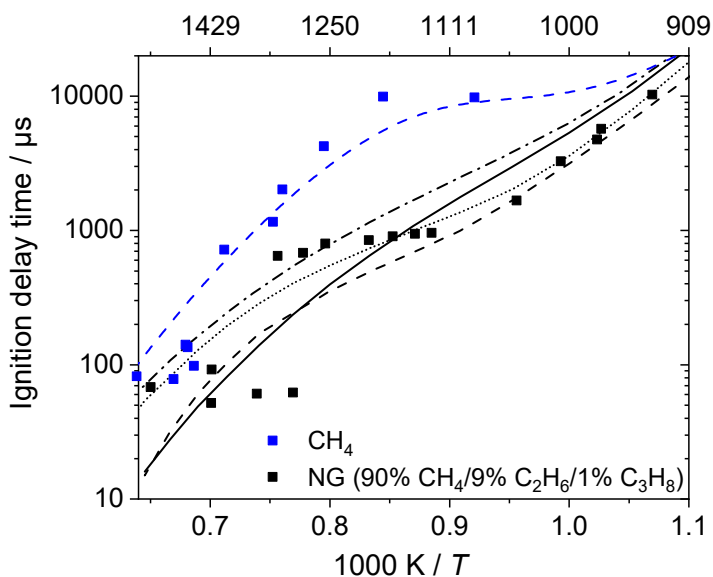


**Figure 9-5:** Measured and simulated ignition delay times of  $\text{CH}_4$  and a natural gas/air mixture at  $\phi = 10$  and 30 bar. Symbols: Experiments, full lines: Simulations with PolyMech1.0 [19], dash-dotted lines: Simulations with PolyMech2.0, dashed lines: Simulations with AramcoMech3.0 [124], dotted lines: Simulations with the Cai and Pitsch [148] mechanism.

Measured and simulated IDTs of a natural gas/5 % DME/air mixture at  $\phi = 10$  are shown in Figure 9-6. The IDTs are reduced by the DME addition. Measurements and simulations with the AramcoMech3.0 [124] agree very well whereas the PolyMech1.0 [19] predicts about 50 % too long IDTs.

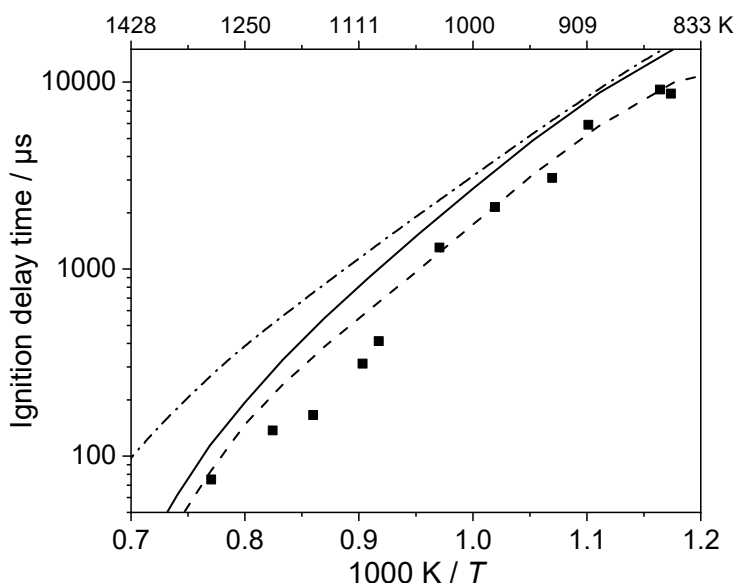


**Figure 9-6:** Measured and simulated ignition delay times of a natural gas/5 % DME/air mixture at  $\phi = 10$  and 30 bar. Symbols: Experiments, full lines: Simulations with PolyMech1.0 [19], dash-dotted lines: Simulations with PolyMech2.0, dashed lines: Simulations with AramcoMech3.0 [124].

### 9.4.1.2 Product formation

The product composition of a natural gas/air mixture at  $\phi = 10$  after ignition, which is very similar to experiments with  $\text{CH}_4$ ,  $\text{CH}_4/n\text{-C}_7\text{H}_{16}$ ,  $\text{CH}_4/\text{diethyl ether}$  [199],  $\text{CH}_4/\text{DME}$  [19] and  $\text{CH}_4/\text{dimethoxymethane}$  [297] as fuel, is shown in Figure 9-7.

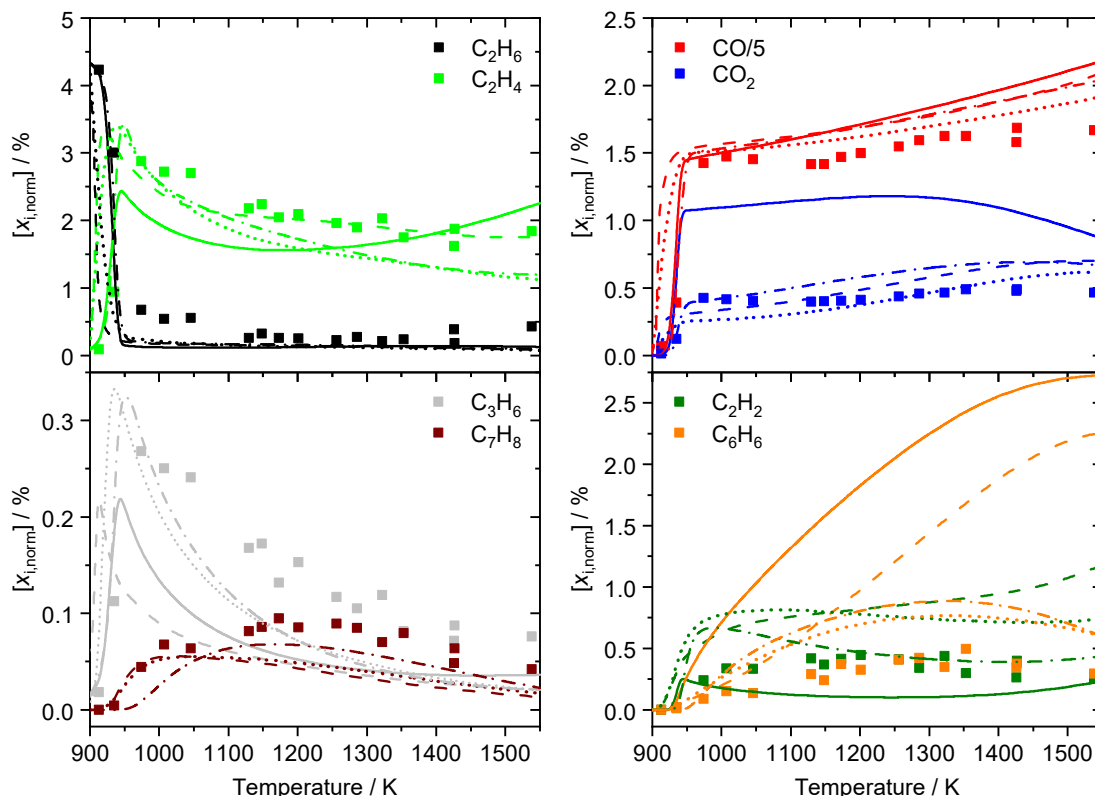


**Figure 9-7:** Measured and simulated species mole fractions of a natural gas/air mixture at  $\phi = 10$  and 30 bar after ignition. Symbols: Experiments, full lines: Simulations with PolyMech1.0 [19], dash-dotted lines: Simulations with PolyMech2.0, dashed lines: Simulations with AramcoMech3.0 [124], dotted lines: Simulations with the Cai and Pitsch mechanism [148].

Main products are  $\text{CO}$ ,  $\text{H}_2$  (not quantified),  $\text{CO}_2$ ,  $\text{H}_2\text{O}$  (not quantified),  $\text{C}_2\text{H}_2$ ,  $\text{C}_2\text{H}_4$ ,  $\text{C}_2\text{H}_6$ ,  $\text{C}_3\text{H}_6$ , benzene and toluene. About half of the consumed fuel is converted to  $\text{CO}$ , the other half to hydrocarbons. The experimental results were compared to the predictions of four mechanisms: Cai and Pitsch [148], AramcoMech3.0 [124], PolyMech1.0 [19], and the PolyMech2.0 (section 9.3.1). The simulations with the Cai and Pitsch mechanism [148] agree very well for all products with the exception of  $\text{C}_2\text{H}_2$ , benzene (temperature dependence is very well predicted but measured values are 40 % lower than the simulated ones) and  $\text{C}_2\text{H}_4$  (measured values are 30 % higher than the simulated ones except at low temperatures). The AramcoMech3.0 [124] predicts all product mole fractions very well with the exception of much too high mole fractions of acetylene and benzene (up to a factor of eight). Contrary to the Cai and Pitsch [148] mechanism, the benzene mole fraction constantly increases with higher temperatures in the experiments. The benzene consumption reactions to form higher PAHs contained in the mechanism are obviously too slow. The original PolyMech1.0 [19] predicts only the  $\text{CO}$  and  $\text{C}_3\text{H}_6$  mole fractions well. Much too high mole fractions for  $\text{CO}_2$  (about a factor of two) and benzene (up to a factor

of ten) and much too low mole fractions for  $C_2H_2$  (about a factor of four) are predicted. At low temperatures, too low  $C_2H_4$  mole fractions are predicted whereas at high temperatures a good agreement for  $C_2H_4$  is observed. With the PolyMech2.0, the predictions of all these species mole fractions are significantly improved, the simulations for benzene and  $C_2H_4$  are now very similar to the ones of the Cai and Pitsch mechanism [148], the predicted  $CO_2$  mole fractions are reduced, and  $C_2H_2$  is now predicted very well. Toluene is now included in the mechanism and is also predicted very well. The integration of the benzene and PAH chemistry of the Cai and Pitsch mechanism [148] was successful, the slight differences in the predicted benzene mole fractions are caused by different mole fractions of species forming benzene. With the PolyMech2.0, a mechanism with relative few species and reactions is now available which can predict all observed product species well.

The product composition of a natural gas/5 % DME/air mixture at  $\phi = 10$  after ignition is shown in Figure 9-8. The measured and simulated product composition is almost identical to the experiments without DME as additive but is shifted to about 100 K lower temperatures due to the shorter ignition delay times. The results for the comparison of the simulations with the different mechanisms and the experiments are identical to the ones without DME but simulations with the Cai and Pitsch mechanism [148] were not possible because it contains no DME submechanism.

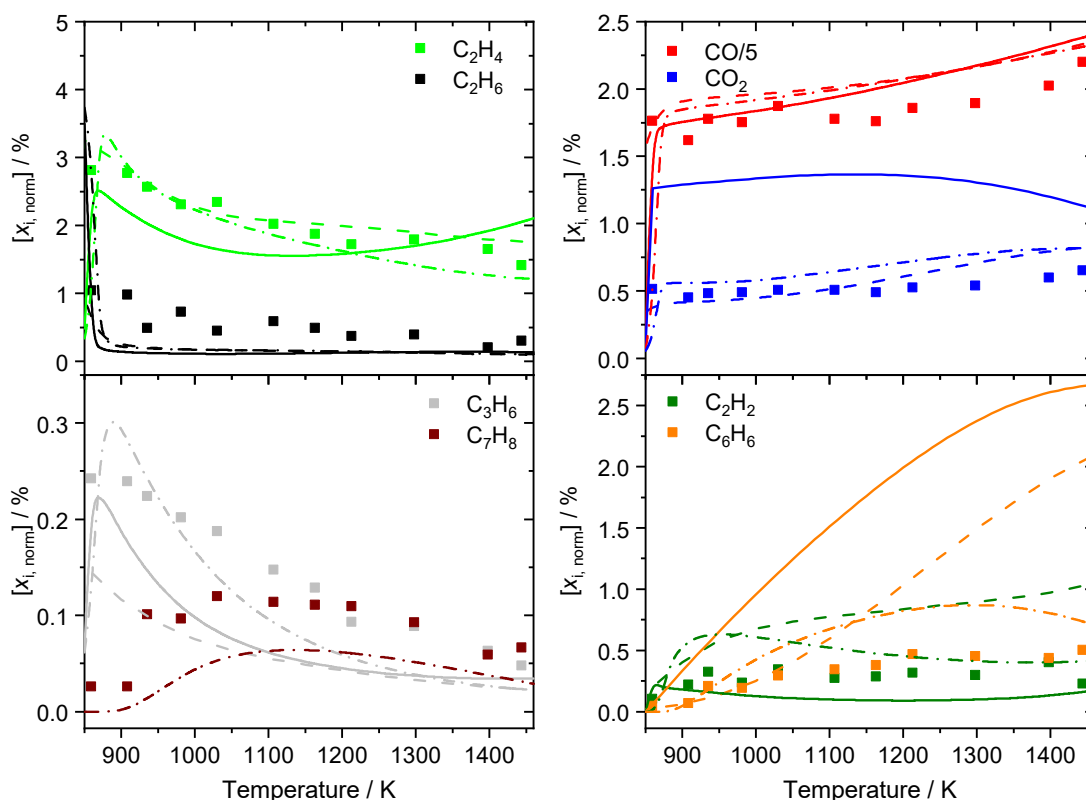


**Figure 9-8:** Measured and simulated mole fractions of a natural gas/5 % DME/air mixture at  $\phi = 10$  and 30 bar after ignition. Symbols: Experiments, full lines: Simulations with PolyMech1.0 [19], dash-dotted lines: Simulations with PolyMech2.0, dashed lines: Simulations with AramcoMech3.0 [124].

## 9.4.2 Plug-flow reactor

In this section, experimental species profiles of the fuel and major products as a function of temperature and equivalence ratio will be presented and compared to model predictions and results of neat natural gas/O<sub>2</sub> experiments published earlier [197]. In addition, reaction pathways towards interesting products are analyzed to assess the influence of DME on the partial oxidation process.

The TOF-MS signals of other detected species relative to the argon signal can be found in the ESM. Although these species mole fractions were not quantified, the trends as a function of temperature can be used for validation purposes. The results of the shear-flow simulation mentioned in section 9.3.3 showed a maximum temperature rise of  $\approx 84$  K at a nominal temperature of 873 K within the isothermal zone. Nevertheless, the difference between the calculated mole fractions of the shear-flow and plug-flow simulations at the end of the reactor was less than 10 % (see appendix B). A negligible difference in calculated mole fractions was observed for lower and higher temperatures so that it seems justified to present only the results of plug-flow simulations in this section.

### 9.4.2.1 Comparison of experimental and modeling results

Figure 9-9 and Figure 9-10 show the mole fractions of major species as a function of temperature and equivalence ratio for the 5 and 10 % DME mixtures, respectively. Experimental results (symbols) are compared to simulations (lines).

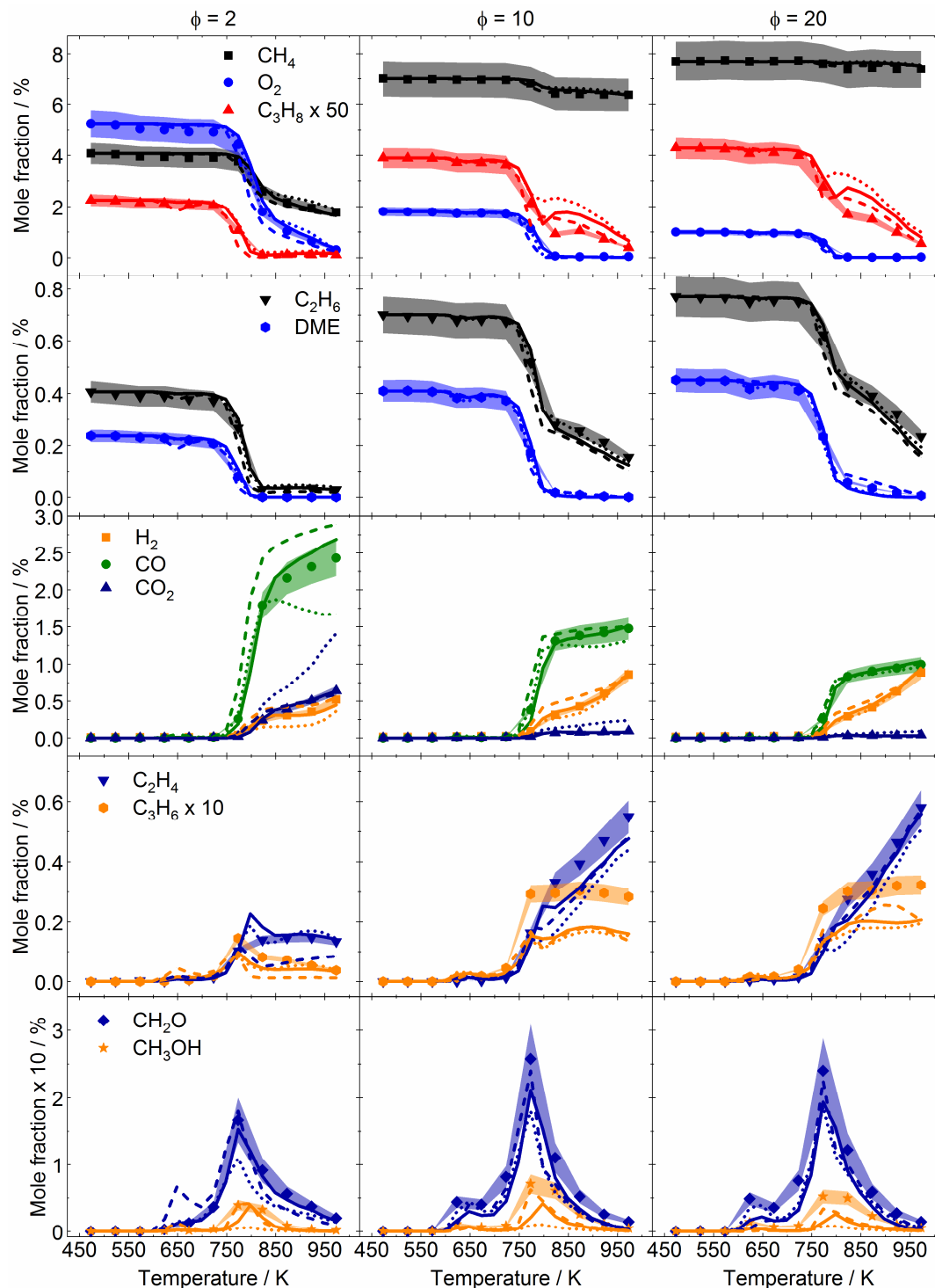


**Figure 9-9:** Mole fractions of reactants and products as a function of temperature for different equivalence ratios for the 95/5 natural gas/DME mixture. Symbols: TOF-MS experiment, lines: Simulations based on the PolyMech1.0 [19] (dotted lines), AramcoMech3.0 [124] (dashed lines), and the PolyMech2.0 (solid lines). Mole fraction uncertainties are displayed by the shaded areas.

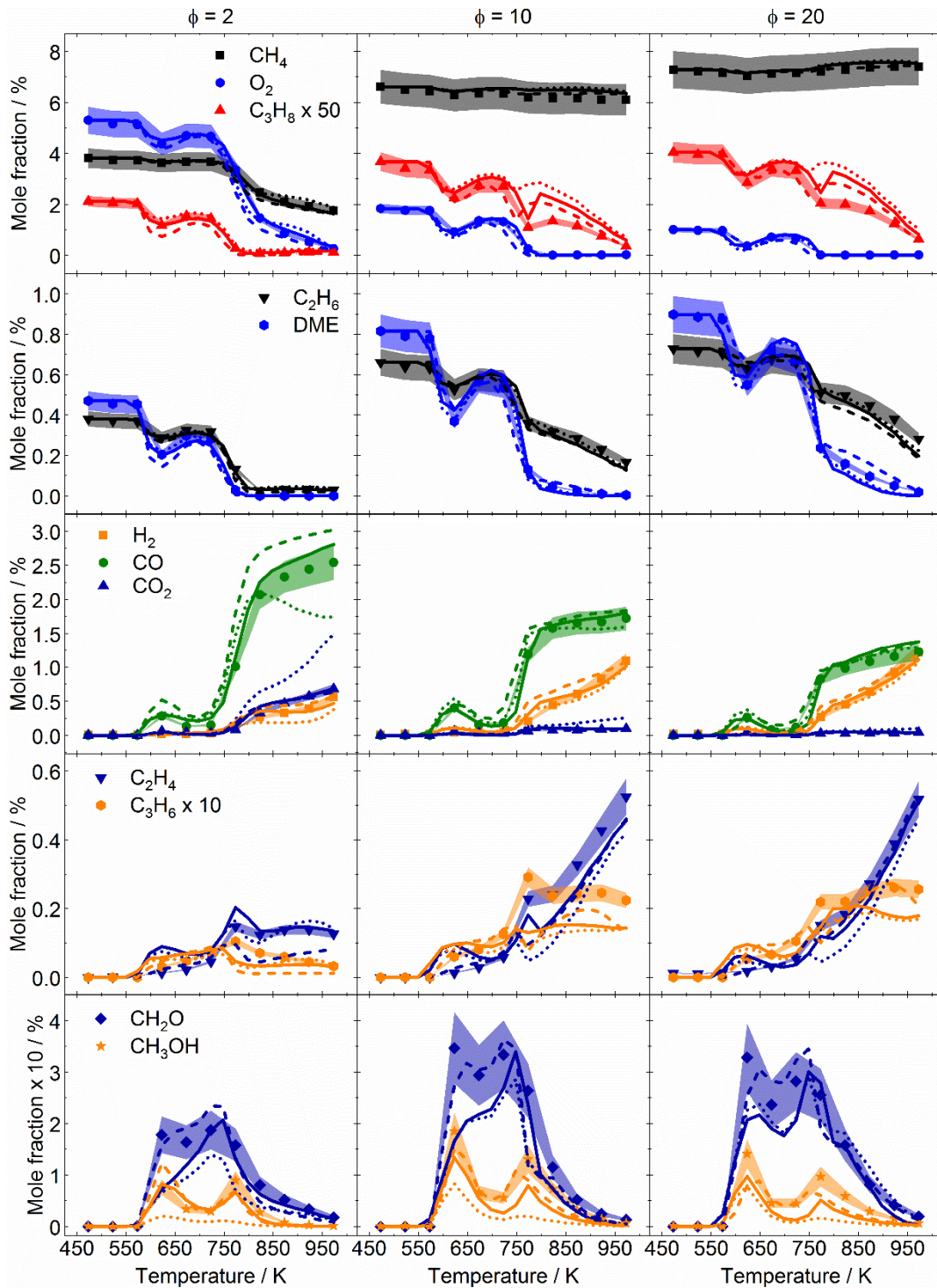


**Figure 9-10:** Mole fractions of reactants and products as a function of temperature for different equivalence ratios for the 90/10 natural gas/DME mixture. Symbols: TOF-MS experiment, lines: Simulations based on the PolyMech1.0 [19] (dotted lines), AramcoMech3.0 [124] (dashed lines), and the PolyMech2.0 (solid lines). Mole fraction uncertainties are displayed by the shaded areas.

## 9.4.2.1.1 Influence of DME on fuel conversion

As seen in Figure 9-9 and Figure 9-10, the conversion of DME starts between 523 and 573 K in all natural gas/DME experiments, reaching a local maximum at 623 K, followed by a local minimum between 673 and 723 K. For the 5 % DME mixture at  $\phi = 2$ , only a relatively slow conversion up to a temperature of 723 K is observed. At higher temperatures, the conversion of DME increases for all mixtures until total depletion is reached at temperatures between 773 and 973 K, depending on the equivalence ratio. This behavior, which is more pronounced at high equivalence ratios as well as for fuel mixtures with a natural gas/DME ratio of 9/1, can be attributed to the negative temperature coefficient (NTC) behavior of DME: Similar results can be found for CH<sub>4</sub>/DME mixtures presented in Refs. [19,186]. In Ref. [186] the NTC region is slightly shifted towards lower temperatures because of higher reactor pressures. The high reactivity of DME and the associated formation of radicals at low temperatures initiate the conversion of all alkanes at 200 K lower temperatures compared to the single fuel experiments (neat natural gas) presented in Ref. [197]. The conversion of CH<sub>4</sub> stays low (< 5 %) at temperatures up to 773 K, whereas more than 20 and 40 % C<sub>2</sub>H<sub>6</sub> and C<sub>3</sub>H<sub>8</sub>, respectively, are converted at the first NTC inflection point (623 K). It must be noted that CH<sub>4</sub> contains around 75 and 68 % of the total amount of carbon in the 5 and 10 % DME mixtures, respectively. This means that even if less CH<sub>4</sub> than C<sub>2</sub>H<sub>6</sub> or C<sub>3</sub>H<sub>8</sub> is converted it can contribute more carbon to the products. The conversion of CH<sub>4</sub> is counteracted by methane producing pathways from DME, C<sub>2</sub>H<sub>6</sub>, and C<sub>3</sub>H<sub>8</sub>. This effect is apparent in the reaction pathway analysis for the 10 % DME mixture at 973 K and  $\phi = 20$  at the time corresponding to 25 % DME conversion in Figure 9-11. It is clearly seen that the reactions of all reactants, mainly with CH<sub>3</sub> radicals, lead to the formation of CH<sub>4</sub>. Also, the reaction of CH<sub>2</sub>O with CH<sub>3</sub> contributes largely to CH<sub>4</sub> production. Although most of CH<sub>3</sub> is produced via H-abstraction from CH<sub>4</sub> by OH, the net carbon flux between these two species is towards CH<sub>4</sub>. The formation of CH<sub>4</sub> exceeds its consumption under these conditions. The reaction onset temperature in natural gas mixtures is lowered which is desirable in polygeneration processes with auto-ignition at realistic compression ratios.



and propane lead to CH<sub>4</sub> production and even higher CH<sub>4</sub> mole fractions at  $\phi = 10$  compared to the initial amount in the mixture. The PolyMech2.0 shows better predictions of the mole fractions of all reactants compared to the unmodified mechanism. All three reaction mechanisms show a good agreement to the experimental data.

Regarding product formation, synthesis gas (H<sub>2</sub>/CO), unsaturated hydrocarbons (C<sub>2</sub>H<sub>4</sub>, C<sub>3</sub>H<sub>6</sub>), oxygenated species (CH<sub>2</sub>O, CH<sub>3</sub>OH), CO<sub>2</sub> and H<sub>2</sub>O (not shown here, see ESM) are found as major products and will be discussed in the following.

#### 9.4.2.1.2 Synthesis gas and CO<sub>2</sub>

CO and CO<sub>2</sub> are preferentially formed at low  $\phi$  and high temperatures with the CO<sub>2</sub> mole fractions becoming negligibly small at  $\phi \geq 10$ . In contrast, CO remains the main product throughout the investigated mixtures with maximum mole fractions of  $\approx 2.5\%$  and  $\approx 1\%$ , going from  $\phi = 2$  to  $\phi = 20$ , independent of the DME amount in the mixture. The mole fraction of H<sub>2</sub> increases with increasing temperature, equivalence ratio and DME amount, reaching 0.5% at  $\phi = 2$  (natural gas/DME = 95/5) and 1.2% at  $\phi = 20$  (natural gas/DME = 90/10) and the highest investigated temperature of 973 K, respectively. In addition, the NTC region of DME leads to a local maximum in the species mole fractions at 623 K, especially visible for CO and the 10% DME mixtures (Figure 9-10). With respect to these species, the PolyMech2.0 shows the best agreement with the experiments. While the AramcoMech3.0 overpredicts the synthesis gas mole fractions at  $\phi = 2$ , the PolyMech1.0 underpredicts synthesis gas at  $\phi = 2$  and  $T > 800$  K and extremely overpredicts CO<sub>2</sub> for all mixtures at  $T > 800$  K.

#### 9.4.2.1.3 Unsaturated hydrocarbons

The formation of the unsaturated hydrocarbons C<sub>2</sub>H<sub>4</sub> and C<sub>3</sub>H<sub>6</sub> is favored at high equivalence ratios and high temperatures, as it is shown in Figure 9-9 and Figure 9-10. At  $\phi = 2$  the mole fraction of C<sub>2</sub>H<sub>4</sub> nearly remains constant at about 0.2% at temperatures higher than 800 K. It increases with increasing temperature for the mixtures at  $\phi = 10$  and 20 to more than 0.5%. Figure 9-11 (10% DME mixture at  $\phi = 20$  and 973 K) and Figure 9-12 (5% DME mixture at  $\phi = 10$  and 773 K) reveal that most C<sub>2</sub>H<sub>4</sub> is formed from C<sub>2</sub>H<sub>6</sub> and C<sub>3</sub>H<sub>8</sub>. At  $\phi = 2$ , the higher amount of oxygen and the associated higher reactivity of the mixture lead to a depletion of C<sub>2</sub>H<sub>6</sub> and C<sub>3</sub>H<sub>8</sub> for  $T > 800$  K, explaining the observed temperature dependence of the C<sub>2</sub>H<sub>4</sub> mole fraction. The lack of oxygen plays a key role in the formation of the unsaturated hydrocarbons. Reaction path analyses performed for the mixtures at  $\phi \geq 10$  and temperatures above 900 K with the PolyMech2.0 reveal a slow but steady increase in the importance of pyrolysis reactions. For example, at temperatures higher than 800 K the long reaction times after the consumption of oxygen in the first 20 cm of the reactor, can lead to the pyrolysis of C<sub>2</sub>H<sub>6</sub> and C<sub>3</sub>H<sub>8</sub> as well as C<sub>3</sub>H<sub>6</sub>. Typical products are C<sub>3</sub>H<sub>6</sub>, C<sub>2</sub>H<sub>4</sub>, H<sub>2</sub> and CH<sub>4</sub> [300,301] in the  $\phi \geq 10$  mixtures.

The simulations using the PolyMech2.0 show the best agreement with the experiments for the 5% DME mixtures at all temperatures and the 10% DME mixtures at temperatures above 700 K, both qualitatively and quantitatively. The unmodified version predicts slightly lower mole fractions at  $\phi \geq 10$ . The AramcoMech3.0, however, underpredicts C<sub>2</sub>H<sub>4</sub> mole fractions at  $\phi = 2$  and  $T > 800$  K and at the same time overpredicts CO at these conditions. This is partly due to lower reaction rates for the recombination of CH<sub>3</sub> radicals to C<sub>2</sub>H<sub>6</sub> in the AramcoMech3.0

compared to the PolyMech2.0, so that the oxidation pathway ( $\text{CH}_3 \rightarrow \text{CO}$ ) is favored compared to the recombination pathway yielding  $\text{C}_2\text{H}_6$  and subsequently  $\text{C}_2\text{H}_4$ . At higher  $\phi$ , the oxidation pathway becomes less important (see Figure 9-11 and Figure 9-12), which leads to a better agreement with the experiments.

In contrast to  $\text{C}_2\text{H}_4$ , the  $\text{C}_3\text{H}_6$  mole fractions start to decrease at temperatures above 800 K for the  $\phi = 2$  mixtures.  $\text{C}_3\text{H}_8$  is completely consumed at these conditions and  $\text{O}_2$  is still available for the reaction to proceed so there are two options for  $\text{C}_3\text{H}_6$  to be consumed and expected to occur simultaneously: The pyrolysis of  $\text{C}_3\text{H}_6$  and, since  $\text{C}_3\text{H}_6$  is more reactive than  $\text{C}_2\text{H}_4$ , the scavenging of available radicals. At higher equivalence ratios, oxygen is depleted at  $T > 800$  K so that fewer radicals are available. The missing radicals and probably the competition between pyrolysis of  $\text{C}_3\text{H}_6$  and  $\text{C}_3\text{H}_8$ , which is still available at  $\phi > 2$ , contribute to nearly constant mole fractions of  $\text{C}_3\text{H}_6$ . According to literature,  $\text{C}_3\text{H}_6$  is not the main product during the pyrolysis of  $\text{C}_3\text{H}_8$ , but  $\text{C}_2\text{H}_4$  and  $\text{CH}_4$  [300]. Nevertheless, a small part of  $\text{C}_3\text{H}_8$  will undergo H-abstraction by H radicals yielding propyl radicals and finally form  $\text{C}_3\text{H}_6$ . The dominant channel of  $\text{C}_3\text{H}_6$  decomposition is the pyrolysis to allyl ( $\text{C}_3\text{H}_5$ ) and H radicals [302]. While H radicals can react with  $\text{C}_3\text{H}_6$  to form  $\text{H}_2 + \text{C}_3\text{H}_5$ ,  $\text{CH}_3 + \text{C}_2\text{H}_4$  or  $\text{C}_3\text{H}_5 + \text{CH}_4$ , for example, the allyl radicals can also lead to the formation of higher hydrocarbons like 1,3-butadiene ( $\text{C}_4\text{H}_6$ ), cyclopentadiene ( $\text{C}_5\text{H}_6$ ) or benzene ( $\text{C}_6\text{H}_6$ ). These species were observed in flow reactor experiments, presented by Wang et al. [301]. All of these hydrocarbons were detected in the TOF-MS experiments at  $\phi > 2$  in small quantities. Signals of fragments formed during the ionization of these  $\text{C}_4$  and  $\text{C}_5$  species overlap with the signal of  $\text{C}_3\text{H}_6$  and can contribute to the discrepancy between simulation and measured mole fraction in the experiments with  $\phi > 2$  above 700 K. But this experimental uncertainty alone cannot explain the large differences. This conclusion is supported by the fact that a reasonable agreement between experimental and simulation results, obtained with the AramcoMech3.0, is found for the  $\phi = 20$  mixtures, at which the highest signals for the higher hydrocarbon species were detected. Missing reactions or outdated rate expressions need to be considered with respect to the competition between oxidation and pyrolysis of  $\text{C}_3\text{H}_8$  and  $\text{C}_3\text{H}_6$ . In summary, the unsaturated hydrocarbons  $\text{C}_2\text{H}_4$  and  $\text{C}_3\text{H}_6$  are preferentially formed at large equivalence ratios and high temperatures. The main reaction pathways to these species are found to be reactions of different radicals with the respective alkane ( $\text{C}_2\text{H}_6$  and  $\text{C}_3\text{H}_8$ ) and at high temperatures ( $T > 800$  K) also their pyrolysis. The modified reaction mechanism predicts the mole fractions of  $\text{C}_2\text{H}_4$  well, but missing reactions are suggested to be the reason for poor predictions of  $\text{C}_3\text{H}_6$  mole fractions compared to the very detailed AramcoMech3.0.

#### 9.4.2.1.4 Oxygenated species

The mole fraction profiles of  $\text{CH}_2\text{O}$  and  $\text{CH}_3\text{OH}$  show two local maxima at 623 K and 723 – 773 K (Figure 9-9 and Figure 9-10). In general, the formation of both species is favored at high equivalence ratios with maximum mole fractions of 0.26 % ( $\text{CH}_2\text{O}$ ) and 0.07 % ( $\text{CH}_3\text{OH}$ ) for the 5 % DME mixture and 0.35 % ( $\text{CH}_2\text{O}$ ) and 0.18 % ( $\text{CH}_3\text{OH}$ ) for the 10 % DME mixture at  $\phi = 10$ . Because the mole fractions are much higher compared to the neat natural gas experiments, presented in Ref. [197] (0.07 %  $\text{CH}_2\text{O}$  and 0.01 %  $\text{CH}_3\text{OH}$ ), both species are suggested to be formed mainly from DME oxidation. The maximum of both species is shifted to 100 K lower temperatures, compared to the neat natural gas mixtures [197].

With respect to  $\text{CH}_2\text{O}$ , both the AramcoMech3.0 and the PolyMech2.0 predict the mole fractions of both species in good agreement with the experiments. Deviations occur for the first maximum between 623 K and 723 K for the 5 % DME mixture at  $\phi = 2$  where the AramcoMech3.0 overpredicts the mole fractions and between 573 K and 723 K for all 10 % DME mixtures where the PolyMech2.0 underpredicts the mole fractions. This overprediction of the mole fraction of  $\text{CH}_2\text{O}$  by the AramcoMech3.0 coincides with a much higher conversion of DME as well as  $\text{C}_2\text{H}_6$  and  $\text{C}_3\text{H}_8$  and overprediction of the mole fractions of  $\text{C}_2\text{H}_4$ ,  $\text{C}_3\text{H}_6$ , and  $\text{CH}_3\text{OH}$ , compared to the PolyMech2.0. In case of the AramcoMech3.0 the reactivity of DME is predicted to be too high, leading to the formation of radicals, the subsequent conversion of  $\text{C}_2\text{H}_6$  and  $\text{C}_3\text{H}_8$ , and finally the production of  $\text{CH}_2\text{O}$ . Regarding the PolyMech2.0, the predicted lower  $\text{CH}_2\text{O}$  mole fractions correspond to higher mole fractions of  $\text{C}_2\text{H}_4$ , compared to the experiment and the predicted mole fractions using the AramcoMech3.0. A reaction path analysis with the AramcoMech3.0 at  $\phi = 2$  and 623 K for the 10 % DME mixture reveals three different pathways for  $\text{CH}_2\text{O}$  formation: 1) via the  $\text{C}_2$ -peroxide pathway and the sequence:  $\text{C}_2\text{H}_6 \rightarrow \text{C}_2\text{H}_5 \rightarrow \text{C}_2\text{H}_5\text{O}_2 \rightarrow \text{C}_2\text{H}_5\text{O}_2\text{H} \rightarrow \text{C}_2\text{H}_5\text{O} \rightarrow \text{CH}_2\text{O}$ , 2) via the  $\text{C}_1$ -peroxide pathway and the same sequence as before starting with  $\text{CH}_4$  and 3) via decomposition of  $\text{CH}_3\text{OCH}_2\text{O}_2$  and  $\text{CH}_2\text{OCH}_2\text{O}_2\text{H}$ . Both the  $\text{C}_2$ -peroxide pathway, in which the decomposition of  $\text{C}_2\text{H}_5\text{O}_2\text{H}$  releases OH radicals, and the decomposition of  $\text{CH}_3\text{OCH}_2\text{O}_2$  yielding two  $\text{CH}_2\text{O}$  molecules and an OH radical, are not included in the PolyMech. The extra OH radicals further enhances  $\text{CH}_4$  consumption and thus promotes pathway 2, also increasing the formation of  $\text{CH}_2\text{O}$ . In addition, the  $\text{C}_2$ -peroxide pathway leads to smaller  $\text{C}_2\text{H}_4$  mole fractions, as the rate of the reaction  $\text{C}_2\text{H}_5 + \text{O}_2 = \text{C}_2\text{H}_5\text{O}_2$  is much higher (two orders of magnitude) compared to the rate of the reaction  $\text{C}_2\text{H}_5 + \text{O}_2 = \text{C}_2\text{H}_4 + \text{HO}_2$ , which is the main pathway of  $\text{C}_2\text{H}_5$  consumption in case of the PolyMech under these conditions. These differences explain the deviations in the predicted  $\text{C}_2\text{H}_4$  and  $\text{CH}_2\text{O}$  mole fractions by both mechanisms. The rather complex  $\text{C}_2$ -peroxide chemistry and further DME reactions were not added to the PolyMech. This would have made the mechanism much larger and would only lead to a slightly better agreement in a small temperature range in the best case. The possibility of adding  $\text{C}_2$ - and  $\text{C}_3$ - peroxide chemistry in a reduced form without neglecting important pathways will be investigated in the future.

$\text{CH}_3\text{OH}$  is also predicted well by the AramcoMech3.0 and PolyMech2.0, especially regarding the trend as a function of temperature. The remaining discrepancies show that the interaction between the natural gas components and DME has not yet been fully understood. But it can be suggested that the DME subset is responsible for the deviations at low temperatures, since it was shown by sensitivity analyses that the  $\text{CH}_3\text{OH}$  mole fractions are very sensitive to DME involved reactions (see Figure 9-2).

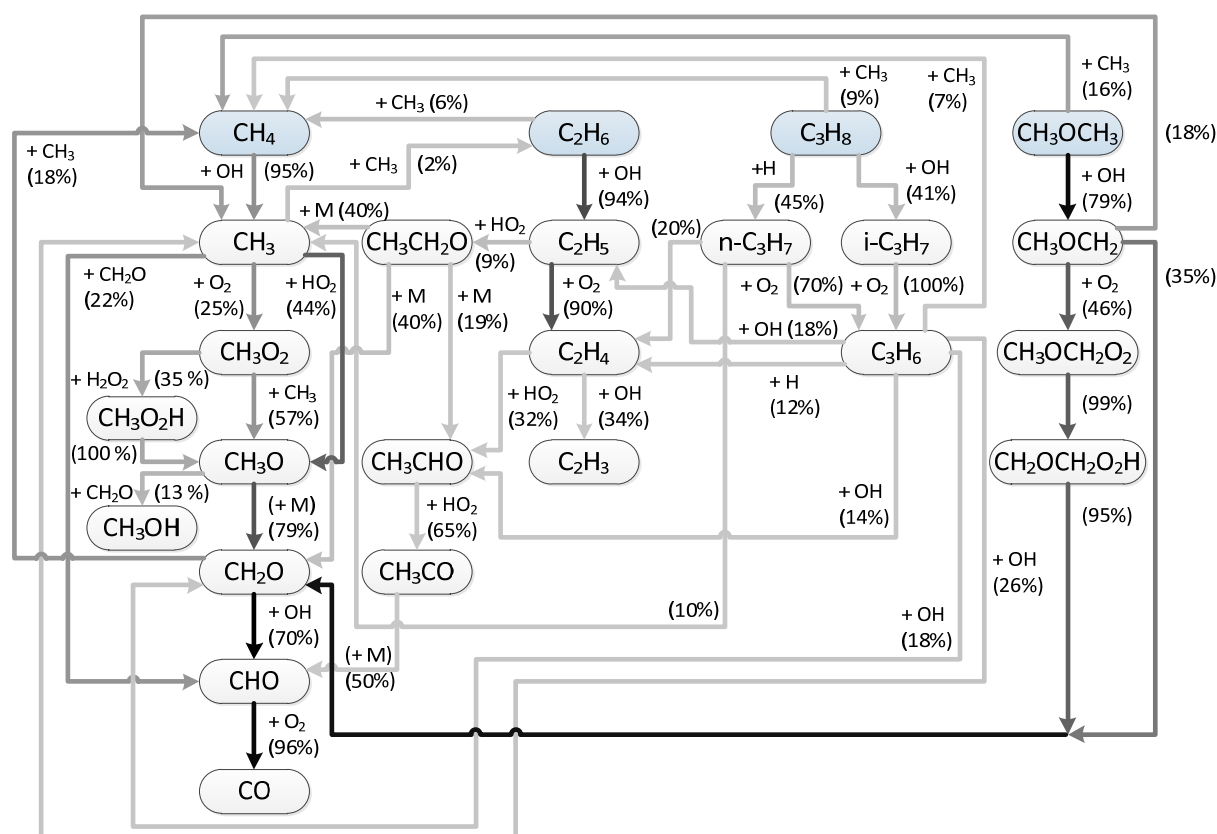


**Figure 9-12:** Reaction path analysis using the PolyMech2.0 for the 5 % DME mixture at 773 K and  $\phi = 10$  (calculated at the time corresponding to 25 % DME conversion). The percentages show the relative rate of carbon consumption of the limiting reactant and line darkness represents the percentage of carbon flux, related to the highest carbon flux within the reaction path, which is found between  $\text{CH}_2\text{O}$  and  $\text{CHO}$ . Species next to the arrows represent the main reaction partner.

To unravel the influence of DME on the production of both oxygenated species, a reaction pathway analysis was performed with the PolyMech2.0 at  $\phi = 10$  and 773 K for the 5 % DME mixture, see Figure 9-12.

A large part of  $\text{CH}_2\text{O}$  is formed by DME oxidation, more specifically the dissociation of  $\text{CH}_3\text{OCH}_2$  and  $\text{CH}_2\text{OCH}_2\text{O}_2\text{H}$ . While the first species is formed by H-abstraction from DME, the second species is formed by isomerization of  $\text{CH}_3\text{OCH}_2\text{O}_2$ , produced by  $\text{O}_2$  addition to  $\text{CH}_3\text{OCH}_2$ . Under these conditions, DME contributes to more than 58 % to the production of  $\text{CH}_2\text{O}$  by these two reactions. The remaining  $\text{CH}_2\text{O}$  is formed by the dissociation of  $\text{CH}_3\text{O}$  radicals, which in turn are nearly exclusively formed by reactions involving  $\text{CH}_3$  radicals and the methyl peroxy radical. The highest carbon flux to  $\text{CH}_3$  comes from  $\text{CH}_4$ , followed by  $\text{CH}_3\text{OCH}_2$ . In addition, pathways from  $\text{CH}_2\text{O}$ ,  $\text{C}_2\text{H}_6$ ,  $\text{C}_3\text{H}_8$ , and DME to  $\text{CH}_4$  are found under these conditions. Finally, indirect reaction pathways from DME,  $\text{C}_2\text{H}_6$ , and  $\text{C}_3\text{H}_8$  also lead to the formation of  $\text{CH}_2\text{O}$ , decreasing the contribution of  $\text{CH}_4$ .

For  $\text{CH}_3\text{OH}$ , a slightly different situation is observed, as it is nearly exclusively formed by reactions involving  $\text{CH}_3\text{O}$  radicals with a contribution of about 60 %. Although  $\text{CH}_3\text{O}$  contains carbon that comes from DME and the other educts via the reaction sequence (Educt  $\rightarrow \text{CH}_4 \rightarrow \text{CH}_3 \rightarrow \text{CH}_3\text{O}$ ), no important direct pathways to  $\text{CH}_3\text{O}$  and  $\text{CH}_3\text{OH}$  are observed under these conditions. So, the contribution of  $\text{CH}_4$  to the formation of  $\text{CH}_3\text{OH}$  is expected to be higher

compared to the formation of  $\text{CH}_2\text{O}$ .  $\text{C}_2\text{H}_6$  and  $\text{C}_3\text{H}_8$  contribute slightly to methanol production, which is seen by the light grey arrows, connecting their oxidation pathways with the one of  $\text{CH}_4$ .

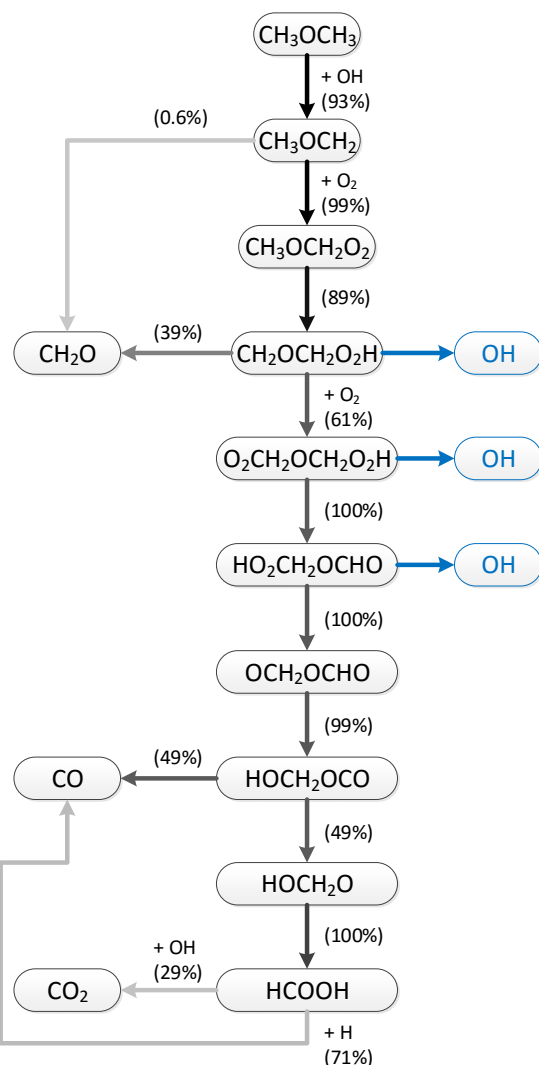


**Figure 9-13:** Excerpt of the reaction path analysis using the PolyMech2.0 for the 10 % DME mixture at 623 K and  $\phi = 10$  (calculated at the time corresponding to 25 % DME conversion). The percentages show the relative rate of carbon consumption of the limiting reactant and line darkness represents the percentage of carbon flux, related to the highest carbon flux within the reaction path, which is found between  $\text{CH}_3\text{OCH}_3$  and  $\text{CH}_3\text{OCH}_2$ . Species next to the arrows represent the main reaction partner.

With increasing DME amount in the mixture, the contribution of DME to the formation of both oxygenated species increases, as the direct pathways towards  $\text{CH}_2\text{O}$  (decomposition of  $\text{CH}_3\text{OCH}_2$  and  $\text{CH}_2\text{OCH}_2\text{O}_2\text{H}$ ) and  $\text{CH}_3\text{OH}$  (the reaction of DME and  $\text{CH}_3\text{O}$  radicals) are favored. Additionally, a larger part of  $\text{CH}_3$  radicals is produced from the decomposition of  $\text{CH}_3\text{OCH}_2$ , further increasing the contribution of DME to  $\text{CH}_2\text{O}$  and  $\text{CH}_3\text{OH}$  production. Surprisingly, for the 10 % DME mixtures at  $T = 623$  K, at which the first maximum in the  $\text{CH}_2\text{O}$  and  $\text{CH}_3\text{OH}$  mole fractions is observed, the contribution of DME with respect to  $\text{CH}_2\text{O}$  and  $\text{CH}_3\text{OH}$  production is much lower compared to the product contribution at higher temperature.

This is because a large amount of oxygen is still available, favoring the  $\text{CH}_3\text{OCH}_2 \rightarrow \text{CH}_3\text{OCH}_2\text{O}_2$  pathway compared to the  $\text{CH}_3\text{OCH}_2 \rightarrow \text{CH}_3$  and  $\text{CH}_3\text{OCH}_2 \rightarrow \text{CH}_2\text{O}$  pathways. Also,  $\text{CH}_2\text{OCH}_2\text{O}_2\text{H}$  does not decompose to  $\text{CH}_2\text{O}$  to the same extent as shown in Figure 9-12 for the 5 % DME mixture at 773 K. Instead,  $\text{O}_2$  is added to the species yielding  $\text{O}_2\text{CH}_2\text{OCH}_2\text{O}_2\text{H}$ , which decomposes to  $\text{HO}_2\text{CH}_2\text{OCHO}$  and OH radicals. An excerpt of the reaction pathway including subsequent steps is shown in Figure 9-13. It can be observed that the main products from DME oxidation at this temperature are CO and  $\text{CO}_2$  instead of  $\text{CH}_2\text{O}$  and  $\text{CH}_3$  or  $\text{CH}_4$ . Moreover, the higher amount of released OH radicals (shown in blue) lead to a  $\text{CH}_4$  conversion of  $\approx 5\%$  and thus favor the pathways towards  $\text{CH}_3\text{OH}$  and  $\text{CH}_2\text{O}$ . Finally, a higher DME amount in the mixture enhances the formation of oxygenated species from  $\text{CH}_4$  at low temperatures.

Summarizing the main findings, the conversion of DME leads to an enhanced production of  $\text{CH}_2\text{O}$  and  $\text{CH}_3\text{OH}$  via direct and indirect reaction pathways. The major fraction of this species is formed from DME. With increasing DME amount in the mixture, the contribution of  $\text{CH}_4$  with respect to  $\text{CH}_2\text{O}$  and  $\text{CH}_3\text{OH}$  formation also increases, initiated by reactions of  $\text{CH}_4$  with radicals formed during DME conversion. This increase of  $\text{CH}_4$  reactivity only applies to low temperatures. At these conditions, the decomposition of intermediate species of the DME oxidation leading to the formation of  $\text{CH}_2\text{O}$  and  $\text{CH}_3\text{OH}$  is rather slow and enough oxygen is available to favor  $\text{O}_2$  addition reactions. These addition products form CO and  $\text{CO}_2$  and not  $\text{CH}_2\text{O}$  and  $\text{CH}_3\text{OH}$ . The formed radicals convert  $\text{CH}_4$  to  $\text{CH}_3$  so that  $\text{CH}_2\text{O}$  and  $\text{CH}_3\text{OH}$  are produced mainly from  $\text{CH}_4$  at these conditions. Both the AramcoMech3.0 and the PolyMech2.0 shows a much better agreement to the experimental data than the PolyMech1.0.

#### 9.4.2.2 Maximum yields of major species

In order to compare the product spectra of all mixtures with each other, yields are calculated according to equation (9-2) and shown in Figure 9-14. In addition to the results of the natural gas/DME mixtures, the results of the neat natural gas/ $\text{O}_2$  mixtures are shown for comparison.

$$\text{Yield}_i = \frac{x_i \times \text{number of C/H atoms in product species } i}{\sum_{\text{Reactants}} x_j \times \text{number of C/H atoms in reactant species } j} \quad (9-2)$$

As expected, the maximum yields of the common combustion products  $\text{CO}_2$  and  $\text{H}_2\text{O}$  decrease rapidly with increasing equivalence ratio and slightly increase with the addition of DME. Higher yields of both  $\text{H}_2$  and CO can be observed, if DME is added to the natural gas/ $\text{O}_2$  mixture. While the yields of  $\text{H}_2$  are nearly independent of the equivalence ratio, the maximum yields of CO decrease with increasing equivalence ratio due to the lower amount of oxygen. This results in an increasing  $\text{H}_2/\text{CO}$  ratio, making it more interesting for subsequent processes such as the Fischer-Tropsch synthesis. Despite lower yields compared to the DME mixtures, the highest  $\text{H}_2/\text{CO}$  ratio of  $\approx 1.3$  is obtained for the neat natural gas/ $\text{O}_2$  mixture at  $\phi = 20$ .

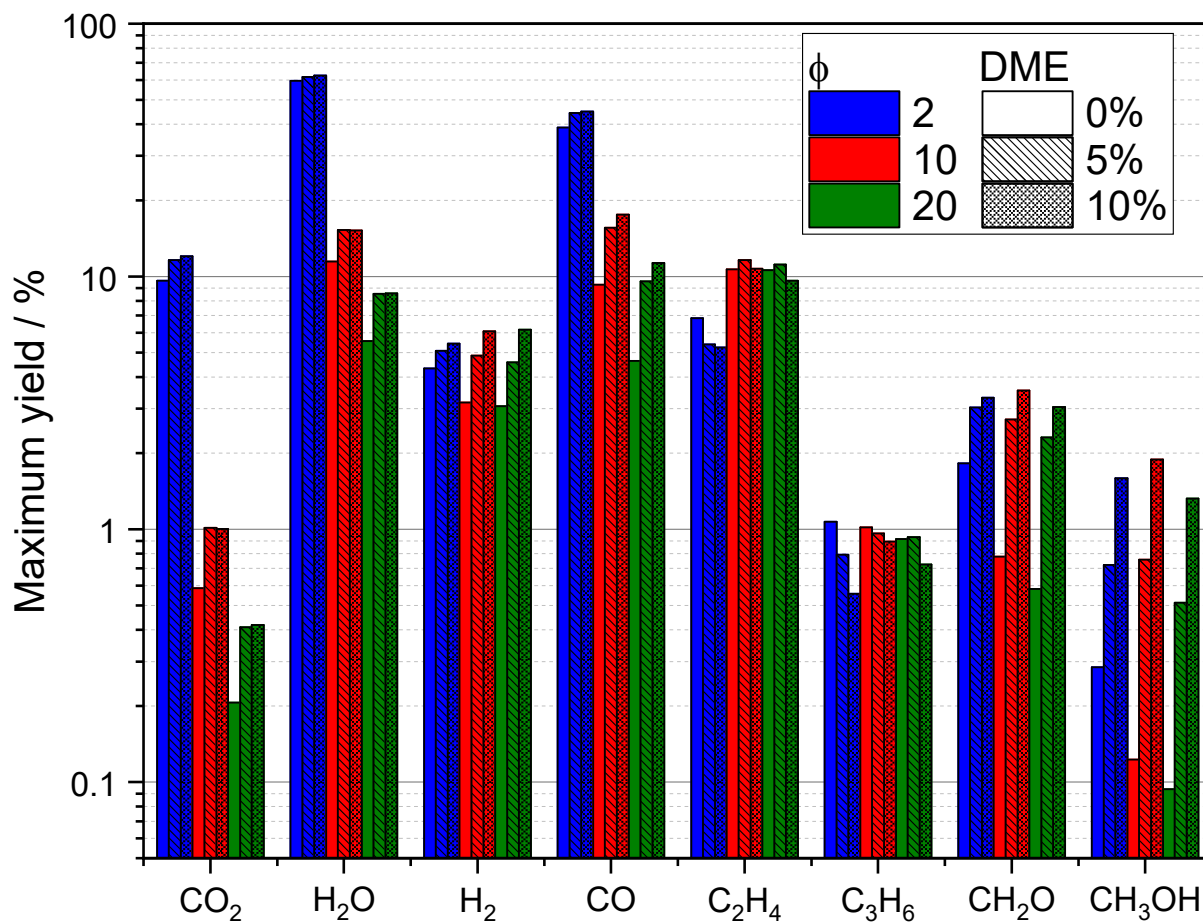


**Figure 9-14:** Maximum yields of products as a function of equivalence ratio and DME amount. Values for neat natural gas (0 % DME) were taken from Ref. [197]. Yields do not add up to 100 % due to unconverted methane.

C<sub>2</sub>H<sub>4</sub>, mainly formed from C<sub>2</sub>H<sub>6</sub> and C<sub>3</sub>H<sub>8</sub> (see Figure 9-11 and Figure 9-12), is preferentially produced at high  $\phi$ , because further reactions are prevented, if less O<sub>2</sub> is present in the mixture and fewer radicals are produced. In addition, no significant influence of DME on the formation of C<sub>2</sub>H<sub>4</sub> is observed. The same is true for the yields of C<sub>3</sub>H<sub>6</sub>, except for  $\phi = 2$ , at which the higher reactivity of the DME mixtures is responsible for an enhanced C<sub>3</sub>H<sub>6</sub> consumption, resulting in lower yields. The equivalence ratio does also not influence the C<sub>3</sub>H<sub>6</sub> yields noticeably. The last group of useful chemicals shown here are the oxygenated species represented by CH<sub>2</sub>O and CH<sub>3</sub>OH. While CH<sub>2</sub>O and CH<sub>3</sub>OH are important precursors for the production of several chemicals, CH<sub>3</sub>OH is also an alternative transportation fuel. The formation of both species is significantly enhanced, if DME is added to the natural gas/O<sub>2</sub> mixtures, as seen in Figure 9-14. Both species are easy to liquify so that they could be separated from the product gas at low cost.

## 9.5 Conclusions

The homogeneous partial oxidation of natural gas/DME mixtures was investigated experimentally using a plug-flow reactor and a high-pressure shock tube at relevant conditions for polygeneration processes. The experiments cover equivalence ratios of 2, 10, and 20, temperatures between 473 and 1400 K, and pressures of 6 and 30 bar. In addition, the amount of DME was

varied to assess its influence on the oxidation process. The addition of DME effectively reduces the reaction onset temperature of the natural gas/O<sub>2</sub> mixture by 200 K compared to neat natural gas/O<sub>2</sub> and promotes the formation of several useful products like synthesis gas and the oxygenated species CH<sub>2</sub>O and CH<sub>3</sub>OH. At the highest investigated equivalence ratio of 20, the replacement of 10 % fuel by DME lead to CH<sub>4</sub> production instead of consumption due to additional CH<sub>4</sub>-producing pathways from DME. This observation was discussed by reaction path analyses, using PolyMech2.0, a modified version of the mechanism of Porras et al. [19]. To overcome this challenge, ozone could be a viable alternative additive to DME to initiate CH<sub>4</sub> conversion at low temperatures [15]. It was also found that CH<sub>2</sub>O is nearly exclusively formed from DME, whereas CH<sub>3</sub>OH is partly produced from CH<sub>4</sub> at temperatures around 800 K. At a temperature of 623 K, at which the maxima of CH<sub>2</sub>O and CH<sub>3</sub>OH mole fractions were observed in the 10 % DME mixtures, CH<sub>4</sub> contributes greatly to the production of both species. The reason for this behavior is that more OH radicals are produced due to the oxidation of DME, which react with CH<sub>4</sub> and, in connection with a low temperature, favor the production of both oxygenated species. In contrast, at higher temperatures pathways from DME to CH<sub>2</sub>O, CH<sub>3</sub>OH and its precursors are favored, decreasing the product contribution of CH<sub>4</sub>. Unsaturated hydrocarbons like C<sub>2</sub>H<sub>4</sub> and C<sub>3</sub>H<sub>6</sub> were found to be mainly produced from C<sub>2</sub>H<sub>6</sub> and C<sub>3</sub>H<sub>8</sub>, respectively. Considerable yields (related to the total amount of carbon in the mixture) of  $\approx 10\%$  (C<sub>2</sub>H<sub>4</sub>) and  $\approx 1\%$  (C<sub>3</sub>H<sub>6</sub>) were found with respect to these species, considering the low initial mole fractions of C<sub>2</sub>H<sub>6</sub> and C<sub>3</sub>H<sub>8</sub>.

Model predictions of the modified reaction mechanism and another state-of-the-art reaction mechanism are in good agreement with the experimental data and have proven useful to identify suitable conditions for the formation of useful chemicals. Some disagreement between simulation and experiments corroborate the need for further improvement of both mechanisms. This need is reinforced by high-pressure shock tube measurements. The mole fractions of benzene could only be predicted well by PolyMech2.0 and in the case of pure natural gas by the Cai and Pitsch mechanism [148]. At these high-pressure conditions and higher temperatures compared to the flow reactor the influence of the natural gas components on the product composition was much less pronounced. The product composition is almost identical to experiments with methane or methane/additive (*n*-heptane, diethyl ether, dimethoxymethane) mixtures [199,297] as fuel. Ignition delay time measurements showed that the reactivity of the natural gas/air mixture is significantly increased by DME addition and that natural gas is much more reactive compared to methane also at these very fuel-rich conditions. The AramcoMech3.0 [124] predicts the measured IDTs very well whereas the PolyMech2.0 predicts slightly too long IDTs. Regarding the prediction capabilities for ignition delay times and product formation and its low number of species and reactions the PolyMech2.0 is currently the best choice for simulating and optimizing polygeneration processes with natural gas/DME as fuel at very fuel-rich conditions in IC engines.



---

## 10 NTC behavior of methane

The content of this chapter was published in Proceedings of the Combustion Institute:

D. Kaczmarek, S. Shaqiri, B. Atakan, T. Kasper, The Influence of Pressure and Equivalence Ratio on the NTC Behavior of Methane, Proceedings of the Combustion Institute 38, accepted (2021).

© 2019 The Combustion Institute. Published by Elsevier. Reprinted with permission.

My own contribution included setting up the experiment, performing the experiments, analyzing and visualizing the results, and writing the manuscript. Shkelqim Shaqiri helped to build the experimental setup and conduct the experiments. Burak Atakan and Tina Kasper supported me in the conceptual design of the study and contributed to the interpretation of the results and the manuscript.

### Abstract

Methane based polygeneration processes in piston engines offer the possibility of a controllable and flexible conversion of energy, to up-convert low value chemicals and to store energy. These processes preferably take place under fuel-rich conditions and at high pressures. Under fuel-rich conditions, there was one experimental report that a distinctive negative temperature coefficient (NTC) behavior occurs in methane oxidation (Petersen et al., 1999). To design a polygeneration process, reliable kinetic models are required to capture the impact of pressure and equivalence ratio variations on reactivity of the gas mixtures. Here, the experimental basis for methane oxidation is expanded to high pressures and very fuel-rich conditions and compared to literature models, both with special emphasis on the NTC behavior. The oxidation of methane/oxygen mixtures at  $2 \leq \phi \leq 20$  and pressures ranging from 1 to 20 bar is investigated. The literature reaction mechanisms are assessed with respect to their ability to predict this phenomenon and used to identify reaction pathways. It is found that NTC behavior occurs in a temperature range between 700 and 1000 K and at pressures higher than 5 bar. The lower temperature limit is slightly shifted towards higher temperatures with decreasing equivalence ratio. In addition, the higher the equivalence ratio, the broader the pressure range, in which the NTC behavior is observed. In general, predictions of some models are in good agreement with the experimental data. Reaction path analyses reveal that the competition between oxidation and recombination pathways are responsible for the NTC region in methane oxidation.

## 10.1 Introduction

Natural gas is an important fuel for a wide variety of applications like electricity generation, production of chemicals or heating purposes. In view of the ongoing transition of the energy system towards mainly renewable energies, the demand for flexible energy conversion systems increases. Flexible processes should be adaptable to transient loads and different fuels, as well as be able to store or deliver electricity as needed. In this respect, different innovative technologies gain importance, e.g. polygeneration and MILD combustion. A polygeneration process could be a flexible way to provide one or more types of energy simultaneously depending on demand. Examples include gas turbines [94] and engines [13,93,95,96,246] operated under fuel-rich conditions. In these studies, the authors have shown that the simultaneous supply of work, heat and useful chemicals is possible in combination with very high exergetic efficiencies. Lim et al. [13] presented a concept for using an engine in tandem with a liquid synthesis reactor to produce methanol. The concept makes it possible to operate the plant profitably on a much smaller scale due to the lower cost of engines compared to conventional chemical reactors. Hegner and Atakan [95] performed a modeling study of a fuel-rich operated HCCI engine and claimed higher exergetic efficiencies compared to those of the separated processes to provide power, heat and hydrogen. Their study was extended by rapid compression machine [96] and HCCI engine [93,246] experiments. Besides synthesis gas, small amounts of ethylene were found in the product gas. Other concepts, also using IC engines, are the almost exclusive production of hydrogen with yields of up to 90 % [97] and the dry reforming of CO<sub>2</sub> into synthesis gas with a CO<sub>2</sub> conversion of up to 50 % [303]. In addition, the Sun Oil Co. describes a method to produce liquid chemicals like formaldehyde, methanol or acetic acid using a methane fueled engine operated at compression ratios higher than 20 and an equivalence ratio of  $\phi = 18$  [304]. In contrast, MILD combustion is characterized by the conversion of highly diluted reactant mixtures outside flammability limits that are pre-heated to temperatures higher than the auto-ignition temperature of the mixture [305]. The technology combines a high energetic efficiency with the potential to reduce CO, CO<sub>2</sub>, and NO<sub>x</sub> emissions and can be used in gas turbines or HCCI engines [305]. Studies on methane auto-ignition delay times with respect to MILD combustion applications have shown different combustion regimes in CH<sub>4</sub> oxidation [306]. Sabia et al. [307] performed a modeling study on auto-ignition delay times of methane and showed that only a few reaction mechanisms can predict an NTC behavior of methane. They explained that the competition of oxidation and recombination pathways is responsible for this phenomenon. More precisely, CH<sub>3</sub> radicals recombine to C<sub>2</sub>H<sub>6</sub> at intermediate temperatures instead of favoring the oxidation pathway towards CO by forming methyl peroxide. As C<sub>2</sub>H<sub>6</sub> is relatively stable at intermediate temperatures and stores CH<sub>3</sub> radicals, the net reaction rate decreases. A similar behavior was found by Tao et al. [308], who measured the ignition delay times of acetaldehyde in a rapid compression machine at 10 atm. They observed an NTC region of acetaldehyde around 1000 K and showed that the concurrence of oxidation and recombination pathways with CH<sub>3</sub> as a key component are responsible for this behavior. Apart from that, only a few experiments provide evidence of the NTC region of methane [151,261,264,309], although its oxidation has been studied extensively by many groups in flow reactors, e.g. [17,98,100–102,197], and jet-stirred reactors [105].

A systematic investigation of the NTC behavior of methane regarding the influence of pressure and equivalence ratio is missing in the literature. As methane is an important fuel for future applications, reliable kinetic models are needed to describe the occurrence of the NTC region of methane to design and dimension such processes.

In the present study, we used a plug-flow reactor to investigate the partial oxidation of methane at temperatures between 673 and 973 K, pressures between 1 and 20 bar and equivalence ratios of 2, 10 and 20. The work explores the influence of pressure and equivalence ratio on the NTC regime of methane. Different reaction mechanisms from literature were used to verify their ability to predict the change in reactivity for these fuel-rich mixtures. Additionally, reaction path and sensitivity analyses are performed to explain the NTC phenomenon and identify the most important reactions.

## 10.2 Experimental methods

The experiments were performed in a plug-flow reactor at  $1 \leq p \leq 20$  bar,  $673 \leq T \leq 973$  K and very high equivalence ratios (Table 10-1). A low volume flow rate of 280 sccm was used to approximate plug-flow, according to the dispersion model of Levenspiel [51]. A temperature rise due to exothermal heat release was dampened by a relatively high dilution with nitrogen. The residence time varied between 1.77–1.28 s at 1 bar and 35.41 – 25.39 s at 20 bar in the temperature range between 673 and 973 K, respectively, considering the complete reactor length.

**Table 10-1:** Flow conditions.

CH <sub>4</sub>	O <sub>2</sub>	N <sub>2</sub>	$\phi$
[mol%]			[-]
5	5	90	2
8.33	1.67	90	10
9.09	0.91	90	20

Details of the experimental setup can be found in [18,200]; a brief description is given here. The reactions take place in a 65 cm long quartz tube with an inner diameter of 6 mm. Compared to our previous work [200], the quartz tube is embedded in a silicon dioxide coated Inconel tube instead of stainless-steel, as it features a higher thermal and mechanical stability. In addition, catalytic reactions of gases, entering the gap between the quartz reactor and the Inconel tube are prevented. The tube is heated by heating tapes, wrapped around copper shells, which finally enclose the Inconel tube. An extended isothermal zone ( $\pm 10$  K) of 40 cm length with a steep temperature in- and decrease at the in- and outlet of the reactor is confirmed by temperature measurements along the centerline of the reactor prior to the experiments for different set temperatures with a flow of 280 sccm nitrogen at atmospheric pressure. The residence time inside the isothermal zone can be described by  $\tau[s] = 653 \cdot p[\text{bar}] / T[\text{K}]$ . Gases are metered by Coriolis mass flow controllers and the pressure is regulated by a heated needle valve downstream of the reactor. The complete pathway behind the reactor up to the exhaust downstream of the sampling point is heated to 450 K to prevent condensation of liquid products. The product gas is expanded to atmospheric pressure before it is analyzed by gas chromatography. Samples are taken

automatically by an auto-sampler, which guarantees excellent reproducibility. No contaminations from previous measurements were observed. The GC is equipped with a MSieve 5A and a Q-Bond PLOT column for the separation of permanent gases and CO<sub>2</sub>, H<sub>2</sub>O as well as hydrocarbons, respectively. Permanent gases are detected by a thermal conductivity detector and all other species by a mass spectrometer. A mixture of 12.5 % H<sub>2</sub> and 87.5 % He was used as carrier gas to allow the detection of hydrogen [86,87]. Gases were calibrated using certified calibration mixtures, and liquids (Methanol, formaldehyde and water) were calibrated by self-mixed mixtures. The uncertainties in calculated mole fractions are estimated to be around 10 % for all gaseous and around 20 % for liquid species. For H<sub>2</sub>, a higher uncertainty of 50 % is estimated due to very small signals in the low-percentage range (< 1 %).

### 10.3 Modeling

The plug-flow module of ChemKin Pro 19.2 [310] is used for the simulations, using the complete temperature profiles, including the temperature ramps at the in- and outlet of the reactor. The plug-flow assumption, the influence of species diffusion, and heat release were assessed by shear-flow simulations for the most reactive mixture ( $\phi = 2$ ,  $p = 20$  bar). The highest temperature increase of  $\Delta T = 150$  K, localized in a very small part of the reactor, was found for a set temperature of  $T = 773$  K. Even in this extreme case, the mole fractions of the most important species at the reactor outlet do not differ more than 10 % from the plug-flow calculations. At  $\phi = 10$  and  $p = 20$  bar the temperature increase was less than  $\Delta T = 40$  K for a set temperature of  $T = 773$  K. A comparison of temperature profiles for  $\phi = 2$  and  $\phi = 10$  as well as mole fractions as a function of temperature for  $\phi = 2$ , obtained by plug-flow and shear-flow simulations, is found in the supplementary material (appendix C). Axial and radial mole fraction distributions further confirmed the plug-flow assumption, because nearly no radial gradient was observed (see appendix C). Consequently, only plug-flow simulations are presented in the results section.

To identify reaction mechanisms from literature, which can predict NTC behavior, nine reaction mechanisms (Table 10-2) were chosen and compared with respect to the prediction of homogeneous, adiabatic, and isobaric auto-ignition delay times of a fuel-rich CH<sub>4</sub>/O<sub>2</sub> mixture ( $\phi = 10$ ), at a pressure of  $p = 10$  bar and diluted in N<sub>2</sub> (90 %).

**Table 10-2:** Tested reaction mechanisms from literature.

Model	Ref.	No. of species	No. of reactions
Polimi	[144]	107	2642
GRI-Mech 3.0	[311]	53	325
USC-Mech II	[312]	111	784
San Diego	[313]	58	270
LLNL	[314]	1163	4714
Aramco 3.0	[124]	581	3037
PolyMech	[19]	83	558
Zhukov	[154]	23	51
Hashemi	[102]	68	631

The auto-ignition delay times shown in Figure 10-1 represent the point, where the temperature of the mixture is 5 K higher than the initial temperature at a pressure of 10 bar. It is obvious that only four reaction mechanisms (Aramco 3.0, LLNL, Polimi and PolyMech) predict a large change in CH<sub>4</sub> reactivity as a function of inlet temperature, as shown by the S-shape in the ignition delay times. These mechanisms were selected for the plug-flow simulations.

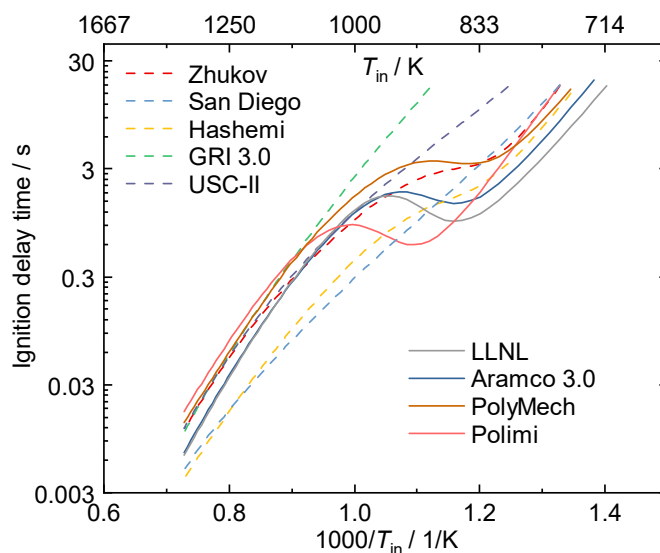


**Figure 10-1:** Simulated ignition delay times (corresponds to a 5 K temperature rise) as a function of the initial temperature at  $\phi = 10$  and  $p = 10$  bar.

The Aramco 3.0 mechanism covers C<sub>1</sub> – C<sub>4</sub>-chemistry, including oxygenated species and peroxide chemistry. The Polimi mechanism has been developed for pyrolysis, partial oxidation and combustion of hydrocarbon and oxygenated fuels up to C<sub>16</sub>. The reaction mechanism of Sarathy et al. (LLNL) contains chemistry of 2-methyl alkanes up to C<sub>20</sub> and alkanes up to C<sub>16</sub>. Regarding these two mechanisms only reduced versions (up to C<sub>3</sub> and C<sub>8</sub>, respectively) were used here. The PolyMech mechanism represents the smallest mechanism and was developed for the description of polygeneration processes in internal combustion engines. It covers chemistry up to C<sub>3</sub> and was validated against very fuel-rich CH<sub>4</sub>/dimethyl ether mixtures.

## 10.4 Results

Many species were detected experimentally at the reactor outlet as a function of temperature, pressure and equivalence ratio. All mole fractions of detected species are found in the electronic supplementary material (ESM). The detected product species cover synthesis gas (H<sub>2</sub>/CO), CO<sub>2</sub>, H<sub>2</sub>O as well as CH<sub>2</sub>O and CH<sub>3</sub>OH, and alkanes and alkenes up to C<sub>3</sub>. While synthesis gas and CH<sub>2</sub>O are preferentially formed at lower  $\phi$ , CH<sub>3</sub>OH and higher hydrocarbons show a local mole fraction maximum at  $\phi = 10$  within the investigated range of equivalence ratios. Higher pressures shift the reaction onset towards lower temperatures and they lead to an increased CH<sub>4</sub> conversion at higher temperatures. As mentioned in the experimental section, higher pressures lead to substantially larger residence times of the gases in the reactor and as a result also favor the conversion of CH<sub>4</sub> and the formation of useful products like synthesis gas. To check, whether the observed NTC behavior is more sensitive to pressure or to residence time,

simulations were performed for all mixtures at pressures of 5 and 10 bar and the same residence times as in the 10 and 20 bar simulations (see ESM). As expected, higher residence times lead to higher conversions of the reactants and to higher product mole fractions. The results obtained with the longer residence times clearly differed from those obtained at the initial residence time at twice the pressure. More important for this study, the NTC behavior was only present for the same  $\phi/p$  combinations as obtained in the simulations with the residence time equivalent to 280 sccm gas flow rate in the experiments. The observations suggest that the pressure is more important with respect to the occurrence of this phenomenon than the residence time.

As this study focuses on the occurrence of an NTC like behavior in CH<sub>4</sub> oxidation, predominantly observed at high equivalence ratios, only the  $\phi=10$  and 20 mixtures are presented here. The measurements at 5 bar are not included in the paper but as electronic supplementary material, because of negligible CH<sub>4</sub> conversion at higher  $\phi$ .

After comparing numerical predictions with experimental results, reaction path analyses are shown to understand the NTC phenomenon in CH<sub>4</sub> oxidation. Subsequently, sensitivity analyses are performed and presented, followed by a short discussion on model improvement.

### 10.4.1 Comparison between experimental and numerical results

Figure 2 shows the mole fractions of the reactants CH<sub>4</sub> and O<sub>2</sub> and the products CO and C<sub>2</sub>H<sub>6</sub> as a function of temperature and pressure for the  $\phi = 10$  (left) and 20 (right) mixtures. Experimental results are represented by symbols and simulations by lines. Only simulations using the Aramco and the PolyMech mechanism are presented, because they showed better agreement with the experimental data. The comparison between experimental and numerical results obtained by the other two mechanisms is provided as supplementary material (see appendix C). Simulations with the PolyMech mechanism predict much lower CO and higher CO<sub>2</sub> mole fractions at temperatures higher than 700 K as found experimentally. Sensitivity analyses revealed reaction (R 10-1) to be the most important one for CO<sub>2</sub> formation. If its rate constant expression, given as  $k(\text{cm}^3/\text{mol}\cdot\text{s})=1.5\times 10^{14}e^{-11879\text{K}/T}$  was replaced by the expression  $k(\text{cm}^3/\text{mol}\cdot\text{s})=1.57\times 10^5T^{2.18}e^{-9030\text{K}/T}$  proposed by You et al. [276] and implemented in the Aramco mechanism, a better agreement between model predictions and experimental data was obtained both for CO and CO<sub>2</sub>. All results shown here are obtained with the modified version of the PolyMech.



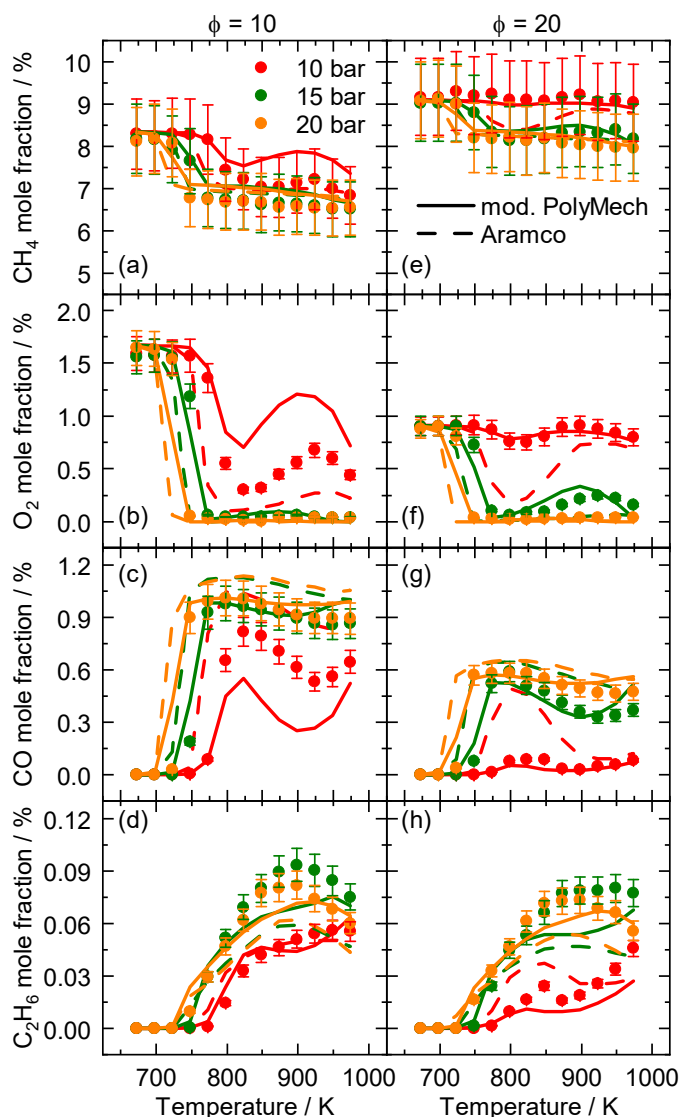


**Figure 10-2:** Mole fractions of major species as a function of temperature and equivalence ratio (left:  $\phi = 10$ , right:  $\phi = 20$ ). Symbols: experiment, lines: simulations based on the Aramco (dashed lines) and modified PolyMech mechanism (solid lines).

Depending on pressure,  $\text{CH}_4$  conversion starts at temperatures between 723 K and 773 K, as seen in figure 2. A 5 bar pressure increase and the simultaneous increase in residence time by approximately 33 % leads to a 25 K shift of the reaction onset towards lower temperatures. The maximum conversion increases with pressure and residence time. This effect is more pronounced at  $\phi = 20$ , especially going from 10 to 15 bar. Following the trend of the mole fractions as a function of temperature, a change in reactivity is clearly seen between 773 K and 973 K. In the measurements with an equivalence ratio of  $\phi = 10$ , the temperature dependence of the mole fractions shows similar trends at 15 bar and 20 bar, while the measurements at 10 bar differ. The experimental temperature dependence of the  $\phi = 20$  mixture at 10 bar and 20 bar differs significantly and the curves obtained at 15 bar show an intermediate behavior. In detail, the mole fractions of  $\text{CH}_4$  and  $\text{O}_2$  decrease continuously with temperature for  $\phi = 10$  at 15 bar and 20 bar, and for  $\phi = 20$  at 20 bar. For all other conditions, the mole fractions of  $\text{CH}_4$  and  $\text{O}_2$  decrease up to a local minimum at around 823 K, increase up to a local maximum at 923 K and

decrease again at higher temperatures. An inverse dependence of mole fraction on temperature is observed for CO. For C<sub>2</sub>H<sub>6</sub>, only at  $\phi = 20$  and  $p = 10$  bar a decrease of mole fraction with increasing temperature is observed below 900 K. At all other conditions, the mole fractions of C<sub>2</sub>H<sub>6</sub> start to increase 25 K after the reaction onset and rise with temperature up to a local maximum at temperatures around 900 K, followed by an accelerated consumption at higher temperatures. The temperatures for C<sub>2</sub>H<sub>6</sub> formation correspond to the temperatures, at which formaldehyde (CH<sub>2</sub>O) and methanol (CH<sub>3</sub>OH), formed at lower temperatures, are consumed (see ESM). Both, the formation of C<sub>2</sub>H<sub>6</sub> via reaction (R 10-2) and the consumption of the oxygenated species should be responsible for the decreased reactivity between 773 K and 973 K.

For  $\phi = 10$ , the simulations are in good agreement with the experimental results at pressures higher than 10 bar. At 10 bar, both models are not able to predict the mole fractions correctly. While the PolyMech mechanism underpredicts the reactivity of the mixture, shown by higher mole fractions of CH<sub>4</sub> and O<sub>2</sub>, compared to the experiment, the Aramco mechanism predicts a much higher reactivity, resulting in an almost complete consumption of O<sub>2</sub> at temperatures above 800 K. Also, the NTC behavior is not predicted by the Aramco mechanism to the same extent as observed in the experiments and predictions using the PolyMech mechanism. The difference between both predictions is even more pronounced at  $\phi = 20$ . Here, the PolyMech simulations, are in very good agreement with the experimental results, whereas the Aramco simulations fail to predict the mole fractions qualitatively for the mixtures investigated at pressures of 10 and 15 bar.

#### 10.4.2 Reaction path and sensitivity analyses

Because the modified PolyMech mechanism captures the trends in the experimental results better, it was chosen for reaction path analyses, which aim to understand the reason for the reactivity changes observed in the mixtures. Subsequently, to identify specific differences in the model that lead to the observed disagreement between experiment and simulations in Figure 10-2, the reaction pathways obtained with the modified PolyMech and the Aramco mechanism are compared and lead to suggestions for model improvement. Although the mechanism underpredicts the reactivity for the  $\phi = 10$  mixture at 10 bar, this condition was selected for the analysis, because the simulated trends of the mole fractions are in very good agreement with the experiment and the NTC phenomenon is particularly pronounced. The reaction pathways were analyzed at temperatures of 823 K, 923 K and 973 K, representing conditions before, in the middle of, and after the NTC regime. All analyses were performed at the position in the reactor where 2 % of CH<sub>4</sub> is consumed in terms of comparability. The values given in brackets indicate the relative rate of the consumption of the limiting reactant. In addition, the darker the lines the higher the absolute rate of production along the indicated pathway. The consumption of CH<sub>4</sub> mainly proceeds via H-abstraction by OH radicals for all temperatures, yielding methyl (CH<sub>3</sub>) radicals. The CH<sub>3</sub> radicals have four main consumption pathways: the oxidation initiated by hydroperoxyl (HO<sub>2</sub>) radicals to methoxy radicals (CH<sub>3</sub>O), the reaction with O<sub>2</sub> producing CH<sub>2</sub>O, the reaction with CH<sub>2</sub>O forming CHO, and the self-recombination yielding C<sub>2</sub>H<sub>6</sub>. At 823 K, an additional pathway towards methyl peroxide (CH<sub>3</sub>O<sub>2</sub>) is active via O<sub>2</sub> addition. Because of the fuel-rich mixtures and the associated low amount of oxygen in the mixture, this

pathway becomes unimportant at higher temperatures, where most of the oxygen is consumed by the  $C_2H_6$  oxidation pathway.

Comparing the reaction pathways at 823 K and 923 K, it is obvious that the importance of the pathways leading to  $CH_3O$  decreases with increasing temperature, while the importance of the recombination pathways increases. This shift results in a decreased production of  $HO_2$  radicals (for example via  $CHO+O_2=CO+HO_2$ ), while the remaining  $CH_3$  radicals are stored in  $C_2H_6$ , which is relatively stable at these temperatures. Two of the main sources for  $OH$  radicals, which are the most important radicals for  $CH_4$  consumption, are the reactions (R 10-3) and (R 10-4). Because  $H_2O_2$  is mainly formed by the reactions (R 10-5) and the formation of  $HO_2$  is suppressed, the net production of  $OH$  decreases. In addition, pathways forming  $CH_4$  become more important at higher temperatures like the reactions of  $CH_2O$  or  $C_2H_6$  and  $C_2H_4$  with  $CH_3$  radicals, seen in Figure 10-3. This effect further decreases the net consumption of  $CH_4$ .

At higher temperatures, the oxidation of  $C_2H_6$  becomes more significant and the reactivity of the mixture increases. This change is shown by the decreasing  $C_2H_6$  mole fractions at high temperatures in Figure 10-2 and the slightly darker lines between  $C_2H_6$  and  $C_2H_5$  in the reaction pathway for  $T = 973$  K in Figure 10-3. In fact, the absolute carbon flux between  $C_2H_6$  and  $C_2H_5$  is two and five times higher compared to  $T = 823$  K and  $T = 923$  K, respectively. Besides an enhanced consumption of  $C_2H_6$ , additional pathways appear due to the oxidation of  $C_2H_4$  and lead to the formation of more  $CO$ , for example. Increasing  $CO$  mole fractions at higher temperatures outside of the NTC regime (see Figure 10-2c), confirm the plausibility of the reaction pathways.

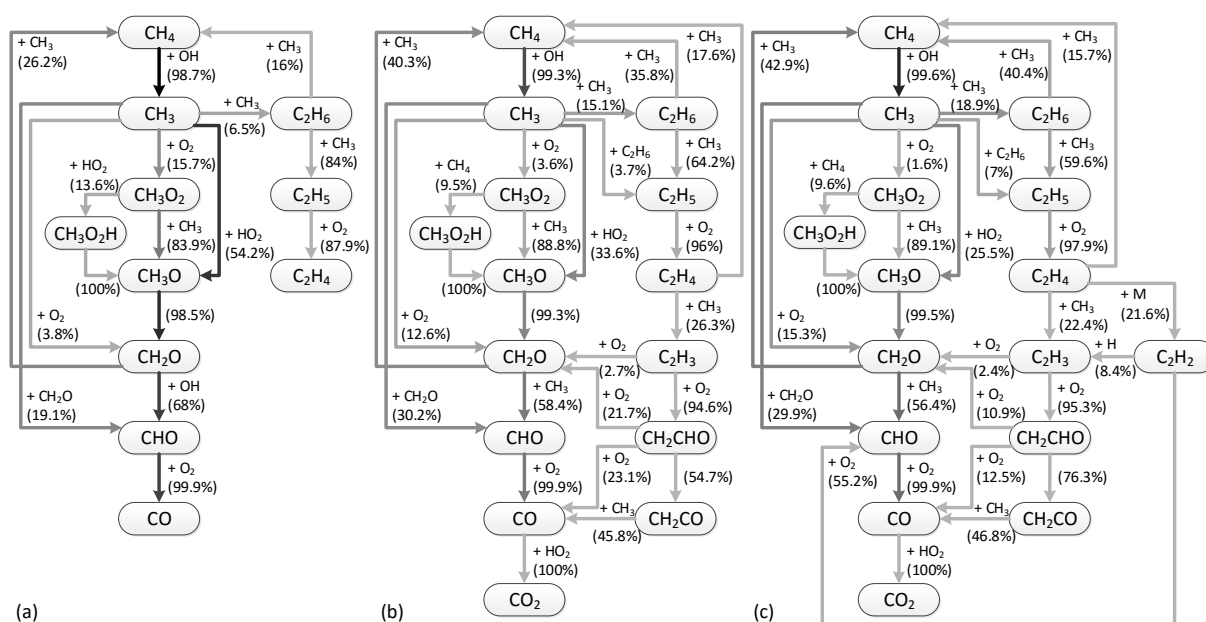


**Figure 10-3:** Reaction path analysis using the modified PolyMech mechanism for 2 %  $CH_4$  consumption at (a) 823 K, (b) 923 K and (c) 973 K, a pressure of 10 bar and  $\phi = 10$ . The percentages show the relative rate of consumption of the limiting reactant and line darkness represents the percentage of carbon flux, related to the highest carbon flux within the reaction path, which is found between  $CH_4$  and  $CH_3$  at 823 K.

Besides reaction path analyses, sensitivity analyses were performed for 823 K, 923 K and 973 K, to unravel key reactions with a strong influence on the prediction of CH<sub>4</sub> consumption (see Figure 10-4). The sensitivity coefficient ( $S_i$ ) is defined as

$$S_i = \frac{(\Delta x_{\text{CH}_4} / x_{\text{CH}_4})}{(\Delta k_i / k_i)} \quad (10-1)$$

where  $x_i$  represents the mole fraction and  $k_i$  the rate constant of the specific reaction. Figure 10-4 shows that the consumption of CH<sub>4</sub> is mainly sensitive to reactions forming H<sub>2</sub>O<sub>2</sub> or, finally, OH. But, at 823 K, reactions related to CH<sub>3</sub>O<sub>2</sub> are also important for the prediction of CH<sub>4</sub> conversion, as still enough oxygen is present in the mixture for the reaction to proceed along the peroxide pathway (see Figure 10-3a). The formation of CH<sub>4</sub> is mainly sensitive to the recombination pathway to C<sub>2</sub>H<sub>6</sub> (reaction (R 10-2))(R 10-2) at all temperatures. The reason for the already high sensitivity of reaction (R 10-2) at 823 K is the beginning of the NTC regime at only slightly higher temperatures, so the influence of C<sub>2</sub>H<sub>6</sub> formation and the associated storage of radicals can already be present. Performing the sensitivity analysis for 773 K affirms this statement, as the sensitivity of reaction (R 10-2) is much lower (0.016) than at 823 K. The sensitivity of reaction (R 10-2) does not significantly change at 923 K, whereas reaction (R 10-4) and the reaction of CH<sub>3</sub>O<sub>2</sub> and CH<sub>3</sub> to CH<sub>3</sub>O become much less sensitive for CH<sub>4</sub> formation and consumption. At 973 K, both OH formation reactions and the recombination pathway gain importance. That is because the temperature is high enough for C<sub>2</sub>H<sub>6</sub> oxidation to proceed to a larger extent compared to lower temperatures, so more radicals are formed in total and the oxidation pathway is favored.

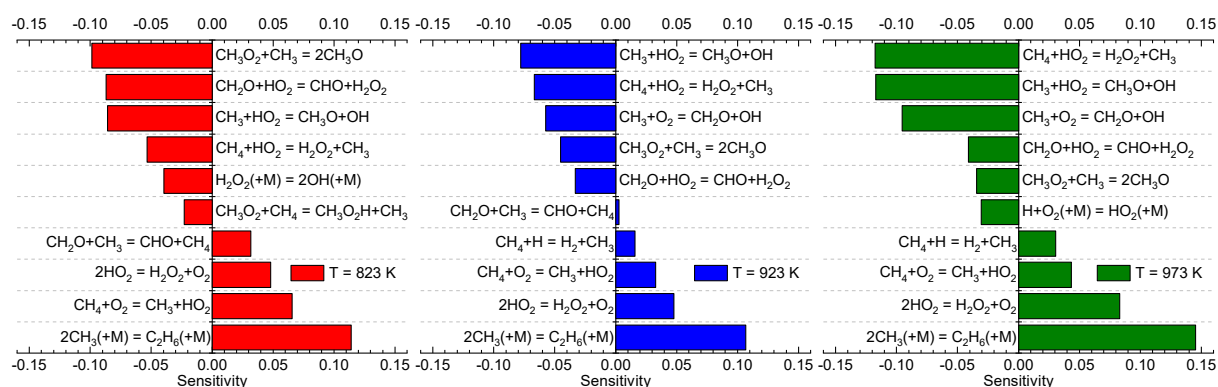


**Figure 10-4:** Sensitivities of the formation and consumption of CH<sub>4</sub> at (a) 823 K, (b) 923 K and (c) 973 K,  $\phi = 10$  and  $p = 10$  bar using the modified PolyMech mechanism.

To identify specific differences between the used models, the reaction pathway predicted by the Aramco mechanism was compared to the reaction pathway predicted by the modified PolyMech mechanism shown in Figure 10-3a at the same conditions (see ESM). A significantly higher carbon flux and an additional reaction path from C<sub>2</sub>H<sub>5</sub> to C<sub>2</sub>H<sub>5</sub>O<sub>2</sub> via O<sub>2</sub> addition was obtained for the Aramco mechanism. The dissociation of C<sub>2</sub>H<sub>5</sub>O<sub>2</sub> and of the subsequently formed species C<sub>2</sub>H<sub>5</sub>O<sub>2</sub>H leads to OH and HO<sub>2</sub> radicals, increasing the reactivity of the mixture. In addition, the rate constant expression for reaction (R 10-2) leads to lower reaction rates so the oxidation pathway is favored compared to the PolyMech mechanism. The oxidation

produces HO<sub>2</sub> and OH radicals via reactions (R 10-4) – (R 10-7) and the dissociation of CH<sub>3</sub>O<sub>2</sub>H. Significantly higher reaction rates for reaction (R 10-6), together with the much higher reaction rates for the reaction of CH<sub>3</sub>O<sub>2</sub> and CH<sub>2</sub>O yielding CH<sub>3</sub>O<sub>2</sub>H and 5 % higher reaction rates for its dissociation lead to a higher reactivity of the mixture and an increased oxidation of CH<sub>4</sub> in the Aramco simulations. As a result, the importance of the C<sub>2</sub>-peroxide pathway and the mentioned reactions should be reassessed to improve reaction mechanisms for the very fuel-rich mixtures.

## 10.5 Conclusions

In this work, the partial oxidation of CH<sub>4</sub> was investigated experimentally at very high equivalence ratios, temperatures between 673 and 973 K and pressures between 1 and 20 bar in a plug-flow reactor. Special emphasis was placed on the NTC behavior in CH<sub>4</sub> oxidation, which was so far only observed in a few experimental studies. In the present work, NTC behavior for methane was also observed at  $\phi = 10$  and  $p = 10$  as well as  $\phi = 20$  and  $p = 10$  bar and  $p = 15$  bar in a temperature range between 823 K and 973 K. Accompanying simulations showed that only the Aramco 3.0 and the PolyMech mechanism predicted the kinetics well for these conditions. At  $\phi = 20$ , only the PolyMech mechanism, as the only reaction mechanism developed for and validated against such conditions, was able to predict the change in reactivity correctly. However, in the PolyMech the rate coefficient expression for the reaction of CO and HO<sub>2</sub> had to be exchanged to the one proposed by You et al. [276] in order to predict the experimental data well. Only at  $p = 10$  bar and  $\phi = 10$ , the model underpredicts the reactivity of the mixture, but can predict the trends of mole fractions as a function of temperature accurately. The NTC behavior in methane oxidation is due to the competition between oxidation and recombination pathways, as revealed by reaction path analyses. In addition, CH<sub>4</sub> producing pathways at low temperatures intensify this competition by reducing the net conversion of CH<sub>4</sub>. The most sensitive reactions for a correct prediction of CH<sub>4</sub> consumption and formation are found to be reactions forming OH radicals and C<sub>2</sub>H<sub>6</sub>, respectively. A comparative reaction path analysis using another state-of-the-art reaction mechanism helped to provide directions in improving reaction mechanisms for these extremely fuel-rich mixtures.

Future applications like polygeneration processes or MILD combustion are based on uncommon reaction conditions, emphasizing the need for experimental results for the development of suitable reaction mechanisms, which can help to design such processes.



---

## 11 The piston engine as a polygeneration reactor

The content of this chapter was published in *Renewable and Sustainable Energy Reviews*

B. Atakan, S. A. Kaiser, J. Herzler, S. Porras, K. Banke, O. Deutschmann, T. Kasper, M. Fikri, R. Schießl, D. Schröder, C. Rudolph, D. Kaczmarek, H. Gossler, S. Drost, V. Bykov, U. Maas, C. Schulz, Flexible energy conversion and storage via high-temperature gas-phase reactions: The piston engine as a polygeneration reactor, *Renewable and Sustainable Energy Reviews* 133, 110264 (2020).

© 2019 The Combustion Institute. Published by Elsevier. Reprinted with permission.

Burak Atakan is the corresponding author, coordinated the assembling of the manuscript, and wrote most parts of the manuscript. Burak Atakan, Sebastian Kaiser, Olaf Deutschmann, Tina Kasper, Ulrich Maas, and Christof Schulz were responsible for the conceptual design of the study and funding acquisition and administrated the respective studies together with Robert Schießl and Mustapha Fikri. Sebastian Kaiser and Christof Schulz were also involved in the writing of the original draft. Tina Kasper and Robert Schießl reviewed and edited the manuscript. Sylvia Porras, Dominik Schröder, Hendrik Gossler, Jürgen Herzler, Simon Drost, Kai Banke, and Charlotte Rudolph were responsible for the investigations related to the reaction mechanism, thermodynamic and economic assessment of the process, optimization procedures, shock-tube experiments, rapid compression machine experiments, HCCI engine experiments, and energy storage part, respectively. They also wrote the corresponding part in the manuscript. My own contribution included setting up the plug-flow experiment, performing the experiments, analyzing and visualizing the results, and writing the corresponding part in the manuscript. This was done under the supervision of Burak Atakan and Tina Kasper.

### Abstract

Piston engines are typically considered devices converting chemical energy into mechanical power via internal combustion. But more generally, their ability to provide high-pressure and high-temperature conditions for a limited time means they can be used as chemical reactors where reactions are initiated by compression heating and subsequently quenched by gas expansion. Thus, piston engines could be “polygeneration” reactors that can flexibly change from power generation to chemical synthesis, and even to chemical-energy storage. This may help mitigating one of the main challenges of future energy systems – accommodating fluctuations in electricity supply and demand. Investments in devices for grid stabilization could be more economical if they have a second use.

This paper presents a systematic approach to polygeneration in piston engines, combining thermodynamics, kinetics, numerical optimization, engineering, and thermo-economics. A focus is on the fuel-rich conversion of methane as a fuel that is considered important for the foreseeable

future. Starting from thermodynamic theory and kinetic modeling, promising systems are selected. Mathematical optimization and an array of experimental kinetic investigations are used for model improvement and development. To evaluate technical feasibility, experiments are then performed in both a single-stroke rapid compression machine and a reciprocating engine. In both cases, chemical conversion is initiated by homogeneous-charge compression-ignition. A thermodynamic and thermo-economic assessment of the results is positive. Examples that illustrate how the piston engine can be used in polygeneration processes to convert methane to higher-value chemicals or to take up carbon dioxide are presented. Open issues for future research are addressed.

### 11.1 Introduction

In the transformation of the energy system towards sustainable sources of primary energy, like wind, solar, and biomass, several approaches for the conversion and storage of energy are discussed. A large part of the primary energy from such sources will be available in the form of electricity, and large fluctuations in generation and demand on various timescales will have to be handled. Storing energy in electrochemical devices like batteries seems an obvious solution since it has the advantage of high conversion efficiencies. However, this is counterbalanced by the low volumetric and specific energy densities and the high costs per unit stored energy. Thus, energy storage in batteries will remain limited in capacity. For the large-scale energy storage that is required to bridge longer time spans and to enable long-distance mobility, chemical storage in bulk materials is important.

A considerable amount of the sustainable primary energy is expected to come from biogenic sources, including biogas consisting to a large part of methane. In addition, in several CO<sub>2</sub>-reduction scenarios, it appears that natural gas will continue to be converted at least on an extended intermediate time scale, until the CO<sub>2</sub> reduction surpasses 90 % [315]. Currently, 95 % of the global use of methane (or natural gas) is for energy conversion, while only about 5 % are used in chemical industry, mainly via conversion to synthesis gas (H<sub>2</sub>/CO mixtures, also abbreviated “syngas”) and then towards different useful chemicals like alcohols, alkenes, and others. Syngas production can go along different paths, such as steam reforming or partial oxidation. Exergetic efficiencies near 63 % are reached for these processes [316]. The energetic use of methane takes place in combustion processes, either in stand-alone piston engines and gas turbines, or in combined-cycle power plants. The exergetic efficiency of the latter is good (> 60 %), while the efficiencies of the former two are much lower, often below 35 %. One may ask whether a combined process producing work, heat, and useful chemicals may have a better efficiency than two separate processes. For several polygeneration systems this advantage has been demonstrated. However, the literature examples mostly concern otherwise unchanged processes that are combined into polygeneration systems by coupling heat flows or by re-using otherwise unused exhaust streams, e.g. Ref. [317–321]. Additionally, such a polygeneration process that can be shifted between different input and output targets could dampen the fluctuating availability and demand of electrical energy.

The combustion community traditionally aims to describe, predict, and design combustion systems in which the chemical reactions are coupled to various, often turbulent flow fields to achieve high conversion efficiencies with low amounts of pollutant formation. Since

mechanical work (or sometimes kinetic energy, as in aerospace engines) is the typical target output of such processes, stoichiometric or fuel-lean combustion has been in the center of interest. Complex chemical reaction mechanisms were developed to predict the pollutant formation and thus control the processes to minimize pollutant concentrations in the exhaust gases. The main pollutants addressed are nitric oxides, particles including soot, and unburned or partially oxidized hydrocarbons.

Such partially oxidized species are pollutants when exhausted to the environment but are actually useful when produced in the chemical industry. For them to be synthesized in high-temperature reactions, the equivalence ratio must be fuel-rich, which is unusual for traditional combustion. The question then is if and how the approaches and mechanisms used for traditional combustion can also be employed or extended towards fuel-rich combustion to understand and create operating conditions in piston engines that maximize the output of useful chemicals. Several issues arise. One of them is the feasibility of initiating reactions on a time scale that is characteristic for typical engine processes. Another one is the competition of the formation of the wanted small (oxygenated) hydrocarbon species with the formation of unwanted by-products like soot. Other important questions include the challenges of gas separation and the overall thermodynamics and economics.

The compression-expansion process in an internal combustion (IC) piston engine has direct influence on the reacting gas mixture. Compression leads to a temperature rise initiating high-temperature reactions, while the expansion stroke leads to a temperature decrease that can be useful to slow down (freeze) the reactions and prevent the conversion of valuable metastable intermediates, so that they can be harvested from the product stream. One may ask how to choose a time-temperature profile that leads to high yields of wanted products and reduces the formation of unwanted products. Some of the primary issues are related to the potential products that can be expected from thermodynamics and chemical reaction kinetics: Besides syngas, is it possible to produce significant amounts of unsaturated or partially oxidized hydrocarbons? Can the formation of large amounts of soot be prevented? Is the flame-speed-controlled spark-ignition process preferable or a kinetically controlled homogeneous-charge compression-ignition (HCCI) process, where the premixed mixture is ignited due to compression? Methane and natural gas are comparably inert, and high temperatures are needed for ignition. This property may lead to problems in the HCCI process. Ignition-enhancing additives might be of interest to increase reaction rates already at moderate temperatures.

Methane reforming in IC engines has been investigated in the past. Since a recent extensive review on fuel reforming in IC engines by Tartakovsky and Steintuch is available [322], only a few papers are mentioned here. Very recently Eyal and Tartakovsky analyzed the entropy production in HCCI engines with external reforming and found efficiencies improved by 7–9 % [323]. In a dual-fuel approach with thermochemical recovery, Chuahy and Kokjohn improved the second-law efficiency by 20 % [324]. Reforming in HCCI engines was also investigated with the respect to reducing the pressure rise rate, but turned out to be of minor importance [325]. But fuel reforming with the heat from the exhaust gas may help in HCCI control [326]. However, in these works the fuel was reformed outside of the engine itself, and the main purpose of the overall process was to produce mechanical power.

Also true in-cylinder reforming has been investigated. Already in 1956, Szeszich produced syngas in a spark-ignition (SI) engine via partial oxidation of methane/oxygen mixtures [327].

Equivalence ratios between  $\phi = 2.58$  and  $2.86$  yielded up to 95 vol% syngas in the dry exhaust (product) gas. McMillian and Lawson investigated the combustion of fuel-rich natural-gas mixtures in SI engines in experiment and simulation [328]. At a compression ratio of  $\varepsilon = 13.3$  and equivalence ratios from  $\phi = 1.3$  to  $1.6$ ,  $H_2$  fractions of up to 11 vol% in the dry exhaust were found. Lim et al. [13] preheated the intake mixture up to 723 K to achieve stable SI operation at equivalence ratios between 1.8 and 2.8. at  $\varepsilon = 13.8$ . They added  $H_2$  and  $C_2H_6$  to the mixture and found that especially  $H_2$  addition reduced the required intake temperature. Karim et al. investigated partial oxidation in a Diesel engine. Fuel-rich mixtures of methane and oxygen-enriched air were ignited by a very short diesel fuel injection [329]. This enabled operation up to about  $\phi = 2.4$  and yielded a maximum syngas fraction of 80 % in the dry exhaust. While the chemical conversion was investigated in some depth, the thermodynamic and economic assessment is often lacking, even though it is crucial for large-scale and wide-spread implementation. Reaction mechanisms for the fuel-rich regime exist, but generally they are not well-validated for high equivalence ratios. Therefore, their evaluation and improvement are necessary, which includes validation experiments with respect to ignition kinetics and product species predictions. Several mechanism describing the oxidation of DME or  $CH_4$ /DME mixtures are published, e.g. Fischer et al. (79 species / 683 reactions, up to  $C_2$ -species) [164], Zhao et al. (55 species / 290 reactions, up to  $C_2$ -species) [178], Prince and Williams (63 species / 284 reactions, up to  $C_4$ -species) [330], Burke et al. (113 species / 710 reactions, up to  $C_3$ -species) [117], AramcoMech2.0 (493 species / 2716 reactions, up to benzene) [145], AramcoMech3.0 (581 species / 3037 reactions, up to  $C_4$  and PAH) [124]. Our own mechanism, “PolyMech”, has 83 species and 558 reactions up to benzene. To describe the oxidation and product formation at very fuel-rich conditions, a mechanism must contain benzene, which was identified as one of the main products at  $\phi = 10$  in high-pressure shock-tube experiments [19]. Other than PolyMech, only AramcoMech2.0 [145] and AramcoMech3.0 [124] fulfill this requirement, but the former is much smaller than the latter two, making it much more suitable for complex simulations and optimizations.

It is imaginable that polygeneration processes can even be used for chemical storage of mechanical work in endothermic and endergonic processes. That may involve even more unusual thermo-chemical states. Experiments for the development and improvements of reaction mechanism can take place in flow reactors, shock tubes, or rapid-compression machines (RCM), the latter being already a first step towards a reciprocating piston engine.

While conditions are easily varied in an RCM, there are more complexities in real engines. Intake preheating or variations in compression ratio and reactant compositions may entail significant hardware modification. In particular in HCCI mode, excessive cycle-to-cycle variations and high pressure rise rates limit useful engine operation. Therefore, engine experiments are crucial for identifying practical issues and determining realistic efficiencies and yields. The number of process parameters can become quite large, i.e., intake temperature and pressure, compression ratio, equivalence ratio, engine speed, additive concentrations, etc. Here, mathematical optimization, even with less-than-perfect reaction mechanisms, can help the experimentalists to choose promising sets of conditions. For this optimization, but also for future multi-dimensional modeling of complex turbulent flows with fuel-rich chemistry, a reduction of the newly developed and optimized reaction mechanisms is necessary.

In addition to the processes in the IC engine itself, a polygeneration process may require upstream conditioning of the reactants, like preheating, compression, or mixing, and then downstream separation and after-treatment of the products. The associated thermodynamic losses (or gains) cannot be neglected in an accurate evaluation of the overall efficiency. Beyond thermodynamics, the economics of the process need to be assessed, again in comparison with separate processes with the same products. Since large uncertainties are present in such an analysis, a global sensitivity analysis helps finding the most important parameters and possible price ranges for the products, and their uncertainty.

This overview indicates that the cooperation of several scientific disciplines is required, including contributions from combustion science. In the following, the reasoning, procedures, and most important results will be presented from such an inter-disciplinary collaboration. The article follows the collaborative research procedure. It is structured along the initial (*a priori*) selection and evaluation of promising parameters and processes, followed by the discussion of kinetics studies and model development and reduction. The implementation in an RCM and a reciprocating IC engine follows, before the thermodynamics and thermo-economics of the complete process including gas separation are discussed for a selected example. In all parts, the main example process is partial oxidation with positive work output from the system, but energy storage systems, where work is transferred into the system, are also considered.

## 11.2 Thermodynamic and kinetics assessment – a priori

### 11.2.1 Thermodynamics

The combustion of methane (or any other hydrocarbon) at an equivalence ratio  $\phi = 1$  can be complete with the products of lowest chemical potential formed, water and carbon dioxide:



This reaction is strongly exothermic and exergonic, with Gibbs energies ( $G_r$ ) and enthalpies ( $H_r$ ) of about  $-800$  kJ/mol, as seen in the first row of Table 11-1. If the amount of  $\text{O}_2$  is reduced, as seen in the next lines of the table, the reaction becomes less exothermic and exergonic, but it remains exergonic even at an equivalence ratio  $\phi = 4$  (row/reaction (3)). The change in Gibbs energy gives the amount of work which could potentially be transferred from the system. Thus, even for reactions carried out at  $\phi = 2$  (row/reaction (2)), significant work ( $-315$  kJ/mol<sup>1</sup>) could be transferred from the system along a reversible path, while syngas with an  $\text{H}_2 / \text{CO}$  ratio of unity is produced.

Instead of evaluating the material and energetic outputs separately, a holistic concept is preferable. From thermodynamics, the concept of exergy (or available energy) is available for that purpose. Exergy is conserved in reversible processes, while it is (in part) destroyed in irreversible processes. Lean combustion generally leads to much exergy destruction, limiting the efficiency of such processes. The exergetic analysis of fuel-rich combustion in gas-turbine cycles [94] shows that the exergy is conserved to more than 85 % at equivalence ratios above 2, while

<sup>1</sup> The so-called “European” thermodynamics sign convention is used throughout this work. Energy flows into the system are positive, out of it negative.

it was below 70 % in the fuel-lean regime. Thus, fuel-rich combustion with work transfer from the system seem to be promising. As opposed to that previous work, the current investigation focuses on piston engines rather than gas turbines, mostly because the experimental effort is much lower, but that preliminary conclusion from theory should still hold.

Table 11-1 also shows that if  $O_2$  is not added (row/reaction (4)), endergonic and endothermal conversion can take place, e.g., to form acetylene ( $C_2H_2$ ). This would be a possible way to store mechanical energy by increasing the Gibbs energy of the gas mixture. The products could either be used later in combustion reactions making use of their increased combustion enthalpy, or preferably, they could be used directly in the chemical industry. One could even combine the endothermal-endergonic conversion of methane with the carbon dioxide conversion to form syngas via dry reforming (row (5)). This could be one step within a carbon capture and utilization (CCU) processes. Again, the syngas produced this way could be burned or used, e.g., in a Fischer-Tropsch synthesis.

**Table 11-1:** Gibbs energies ( $G_r$ ) and enthalpies ( $H_r$ ) of methane reactions with different amounts of oxygen or carbon dioxide at 300 K. The stoichiometric coefficients are taken to be positive for the products. The minor entropy changes due to the deviation of each partial pressure from 1 bar were neglected. The table was calculated with the thermodynamics data from the NASA tables for 300 K and 1 bar [331].

CH <sub>4</sub>	O <sub>2</sub>	CO <sub>2</sub>	CO	H <sub>2</sub>	C <sub>2</sub> H <sub>2</sub>	H <sub>2</sub> O	$\phi$	$G_r$	$H_r$	
Stoichiometric coefficients								kJ/mol	kJ/mol	
-1	-2	1	0	0	0	2	1	-800.99	-802.54	(1)
-1	-1	0	1	1	0	1	2	-315.45	-277.71	(2)
-1	-0.5	0	1	2	0	0	4	-86.95	-35.86	(3)
-1	0	0	0	1.5	0.5	0	$\infty$	155.67	188.75	(4)
-1	0	-1	2	2	0	0	-	170.09	247.13	(5)

### 11.2.2 Kinetics

Although the thermodynamic analysis promises small exergy losses if methane is converted in a polygeneration process, such a process may not be technically feasible because of the low reactivity of methane. For HCCI, ignition of the gas mixture must take place as a result of the temperature rise after compression and initiate the radical chemistry responsible for both pyrolytic and oxidative processes. Ignition delay times (IDTs) in a piston engine mainly depend on the initial temperature of the gas mixture, the compression ratio, and the heat capacity ratio. The available time is related to the engine speed. At speeds between 600 and 3000 rpm (revolutions per minute), the entire cycle takes place on a time scale of some tens of milliseconds. Maybe one-tenth of the cycle is available if ignition and the bulk of the reactions are to complete near or shortly after top dead center (TDC), which is thermodynamically most favorable. Methane ignition generally has IDTs of less than 1 ms for temperatures above 1300 K. The heat capacity ratio increases with the equivalence ratio, reducing the temperature reached at TDC. This can be counterbalanced by higher intake temperatures or higher compression ratios. If conventional IC engines are to be used, the intake temperature should remain below 430–470 K, although some researchers modified the engine such that 753 K were possible [13]. Typical compression ratios  $\varepsilon = V_{\max} / V_{\min}$  are in the range of 8–25.

Additives that ignite at lower temperatures can reduce the required intake temperature. Several additives are possible candidates as ignition enhancers for methane, e.g., *n*-heptane [199], dimethyl ether (DME) [19], or other ethers [155,182,189,332]. Hegner et al. [96] performed a simulation-based pre-selection of process parameters and additives. Using a detailed chemical mechanism, but without soot formation, the engine cylinder was modeled as a homogeneous adiabatic single-zone reactor. A series of consecutive strokes was simulated, including the effect of mixing the remaining reacted gas mixture with the unreacted fresh gases at the start of each compression. Selecting a base case with an engine speed of 3000 and a compression ratio of 16.5 with methane and air as reactants, the influence of several parameters on the required intake temperature and on several output parameters was investigated. At an equivalence ratio of 2, an intake temperature of 635 K was needed to ignite methane. Increasing the compression ratio to 22 reduced that to 555 K. Reducing the engine speed to 600/min instead had a comparable effect (560 K), while replacing 10 mol% of the methane by DME reduced the intake temperature to 455 K. The work output per cycle (but not per mass of fuel) did not vary much when increasing the equivalence ratio from 0.5 to 2, but the exergetic efficiency of this idealized system increased by 12 %-points. Thus, DME addition appears to be a promising approach for enabling an HCCI polygeneration process and its influence on ignition kinetics and engine operation was investigated in more detail, as discussed below.

The residual gas from the previous cycle – depending on the compression ratio 5 – 10 vol% of the fresh charge – influences the current cycle. Since this gas has a higher temperature than the intake, it is expected to reduce the required intake temperature. Figure 11-1 shows a typical example of a crank-angle resolved simulation result for methane conversion at an equivalence ratio of 2, calculated with the mechanism of Burke [117].

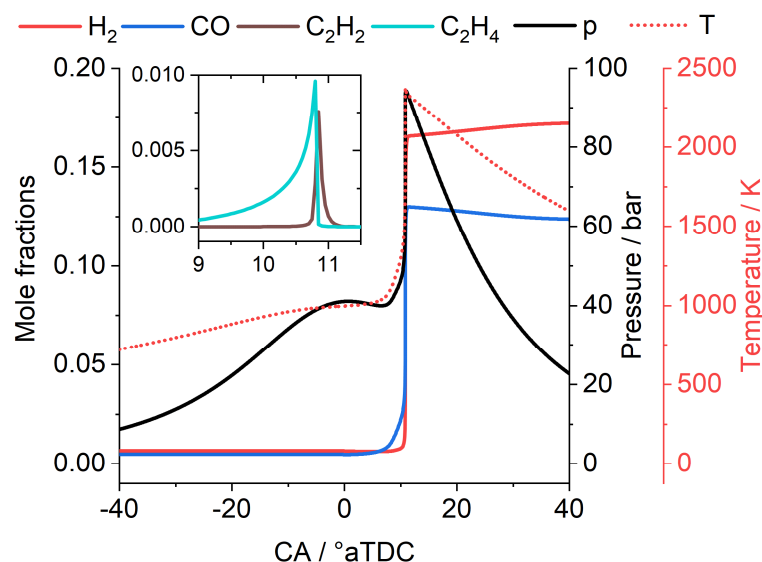


**Figure 11-1:** Crank-angle resolved simulation of methane conversion (without additive) for an equivalence ratio of  $\phi = 2$ , an engine speed  $N = 600$  rpm, a compression ratio  $\varepsilon = 18$  and an intake temperature of 428 K.

The simulation is converged on a cycle basis, i.e., each cycle does not differ from the previous one. The intake temperature needed for ignition of pure methane at an engine speed of 600 rpm

and  $\varepsilon = 18$  is 428 K, while it is 560 K if the residual gas is excluded. From the figure it is seen that relatively large fractions of  $H_2$  and  $CO$  are formed at  $11^\circ CA$  after top dead center (aTDC). These species also survive until the end of the cycle. This is different for ethylene and acetylene. Both are produced in low concentrations between 10 and  $11^\circ CA$ , and both are converted quickly at these conditions.

The final mole fractions near  $180^\circ CA$  describe the potential composition of the product gas of a polygeneration process. They are shown in Figure 11-2 as a function of equivalence ratio for methane as fuel with a compression ratio of 18 and an engine speed of 600 rpm.  $H_2$  and  $CO$  are predicted to be produced in considerable mole fractions, generally with an  $H_2 / CO$  ratio above 1. Unsaturated hydrocarbons like acetylene and ethylene are predicted to be formed at lower concentrations at very fuel-rich conditions. Since air is the oxidizer here, large fractions of  $N_2$  are present in the mixture, thus the product mole fractions are in part limited by the inert-gas mole fraction. The separation of the product-gas mixture will need to be addressed later. It is also seen that at these conditions the methane conversion is incomplete at higher equivalence ratios.

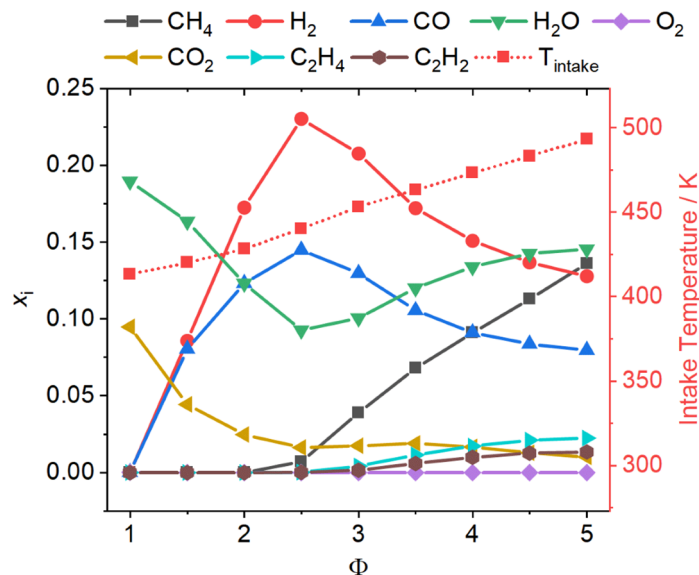


**Figure 11-2:** Major product species as a function of equivalence ratio ( $N = 600$  rpm,  $\varepsilon = 18$ ) on the left axis. The intake temperature needed for ignition is plotted on the right axis.

### 11.2.3 Product yield optimization

Ethylene is an important industrial chemical and the precursor for polyethylene. A catalytic polygeneration process for its production has been mathematically optimized [321]. It is interesting to explore a potentially simpler non-catalytic process in an engine. However, the mole fractions of ethylene shown in the previous section are in the range of 0 to 2.5 % and are thus relatively low. Numerical optimization was employed to potentially find operating conditions leading to higher product yields. For ethylene production, a suitable objective function to be maximized in such optimization is the mole fraction of ethylene at the end of the expansion stroke. The optimization variables here are the engine speed  $N$ , and the fresh gas composition  $n(t_0)$ , where the considered reactants are  $CH_4$ , DME,  $O_2$ , and  $N_2$ . The initial temperature  $T_0$  is kept constant for each optimization run. Two linear constraints are formulated: One to ensure

that the initial pressure  $p_0$  is equal to 1.0 bar, by using the ideal gas equation. The second linear constraint ensures that the  $N_2/O_2$  ratio corresponds to that of air. An inequality constraint is in place to make sure that the amount of additive is at most 10 % of the fuel. This avoids potential situations in which the additive is the main fuel component instead of methane. Bounds for the engine speed were set to 60 – 6000 rpm. As for the work discussed in the section above, a simple single-zone model was used [97] with the chemical mechanism “PolyMech” [19] including detailed chemistry without soot, as will be discussed in Section 11.3.1.

Figure 11-3 shows the results of the optimization for  $C_2H_4$  as a function of the fresh gas temperature. The bottom graph shows the optimal conditions at a given temperature that lead to the yields  $Y$  and conversion  $X$  (i.e., the outcome) shown in the top graph. The top graph also shows the conversion of methane on the right axis at the corresponding conditions shown in the bottom. DME is fully converted at all shown conditions; for clarity, this is not shown in the figure. Although the  $C_2H_4$  mole fraction at the end of the expansion stroke was maximized in the optimization, the top graph shows the yield (left axis) as this represents a better metric to assess the outcome of the process. Except for  $H_2$ , the yield was calculated on the basis of C atoms according to the formula

$$Y_{i,j}(t) = \frac{a_{j,i}n_i(t) - a_{j,i}n_i(t_0)}{\sum_{\ell \in I} (a_{j,\ell}n_{\ell}(t_0))_{\ell \neq i}} \quad (11-1)$$

where  $a_{j,i}$  is the number of atoms of type  $j$  (i.e., element) in species  $i$ ,  $I$  denotes the set of species indices, and  $n$  is the amount of substance. Equation (11-1) effectively states how many of the initially available atoms of type  $j$  (given by the sum in the denominator) are bound in product  $i$ .

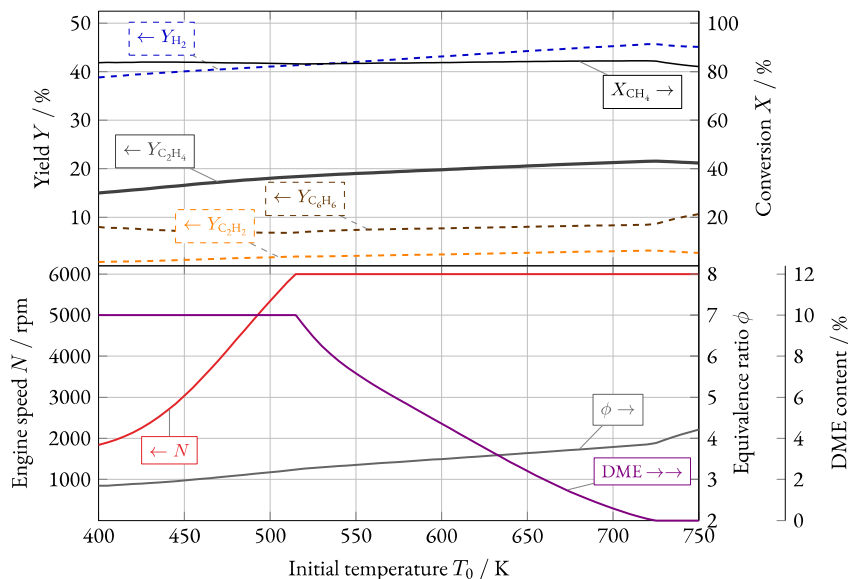


**Figure 11-3:** Result of an optimization for  $C_2H_4$  using PolyMech [19]. Top graph: yields and conversions, bottom graph: optimization variables. The x-axis is the initial temperature  $T_0$  that was held constant for each optimization.

The engine speed (optimization variable) is plotted directly, while the gas composition is represented by the equivalence ratio  $\phi$  and the molar fraction of DME in the fuel. For example, at  $T_0 = 600$  K, the optimal remaining operating parameters are  $\phi = 3.5$ , a fuel composition of 4.7 % DME and 95.3 % CH<sub>4</sub>, and an engine speed of 6000 rpm. Operating the engine with those parameters is predicted to result in a C<sub>2</sub>H<sub>4</sub> yield of 19.8 %.

In the considered temperature range, the predicted C<sub>2</sub>H<sub>4</sub> yields are between 15 % at 400 K and over 21 % at 750 K. At intake temperatures above about 520 K, the optimum engine speed is always at the maximum set limit of 6000 rpm, indicating that higher yields could be obtained at higher speeds. Optimum equivalence ratios are between 2.8 at the lowest temperature and 4.2 at the highest. A similar relation between temperature and equivalence ratio was observed for the H<sub>2</sub> optimization ( $\phi = 2.5 - 3$ ). High temperatures permit richer mixtures, i.e., higher  $\phi$  values. The predicted DME content in the fuel spans the complete range of permissible values. At lower intake temperatures, the optimization predicts a DME content of 10 %, corresponding to the set bound. This value decreases almost linearly to nearly 0 % at 725 K. Over the entire range of considered inlet temperatures, DME was fully converted (not shown in the figure), whereas CH<sub>4</sub> showed conversions of approx. 80 %.

Figure 11-3 also shows the yields of other species as dashed lines. It can be seen that although the optimization was carried out for C<sub>2</sub>H<sub>4</sub>, other valuable species are also produced with significant yields. H<sub>2</sub> yields of around 40 %, C<sub>6</sub>H<sub>6</sub> yields of 8 – 10 %, but also small fractions of C<sub>2</sub>H<sub>2</sub> (yields of 0.7 – 3.1 %) were obtained. A production of formaldehyde and methanol was not predicted under these conditions. Such optimizations can also be carried out for other valuable chemicals. Since most of them are not stable at high temperatures, the optimized parameters will lead probably to high-speed engine operation.

The results and reasoning so far rely on theory and on models that were in general not developed for such fuel-rich conditions. Thus, the development of validated models using kinetics experiments is discussed next.

### 11.3 Kinetics: model development and experiments

Generally, kinetic models in combustion are optimized to predict ignition delay times and flame speeds correctly, while the prediction of product species is of minor importance, except when pollutants are addressed. Much work has been published for fuel-lean to slightly fuel-rich combustion, but not for higher equivalence ratios. Many mechanistic investigations were carried out at reduced or ambient pressure, while in engines, conditions between near-ambient and pressures of more than 30 bar prevail. In order to assess the predictions of established models, well-characterized kinetics experiments are needed. For example, the existing models (e.g. [117,148]) predict a strong influence of additives like DME or *n*-heptane on the methane conversion at lower temperatures. A question is whether some of the additives are more effective than others, also the interaction between additive and methane is important, because it is not the goal to convert only the additive. These questions were addressed in experiments in shock tubes, flow reactors, and a rapid-compression machine (RCM). Shock tubes are well suited to study IDTs and reactions at intermediate and high temperatures and short times, while the residence times in RCMs and flow reactors are generally longer and the temperatures lower.

Compared to shock tubes and RCMs that require measurements with high time resolution, steady-state flow reactors offer an easier approach to gas-phase diagnostics.

Validation experiments were performed in three different ranges in equivalence ratio: At moderately fuel-rich conditions ( $\phi = 2$ ) with synthesis gas as the main product, at very fuel-rich conditions ( $\phi = 6 - 20$ ), resulting in the additional formation of higher hydrocarbons, and without oxygen ( $\phi = \infty$ ), representing methane and natural-gas pyrolysis for energy storage. Additives were mixed with methane to reduce the reaction temperature. Details of the experimental methods are given in Refs. [17,19].

### 11.3.1 Mechanism development and reduction

#### 11.3.1.1 Detailed mechanism

The chemical mechanism developed here specifically for use in simulations of polygeneration processes is termed “PolyMech” [19]. It is a comparatively small mechanism, based on existing detailed mechanisms describing stoichiometric to slightly fuel-rich ( $\phi = 1 - 2$ ) combustion and pyrolysis of methane as well as the oxidation of DME/air mixtures. The oxidation model of Heghes et al. [188] was combined with the methane pyrolysis mechanism of Hidaka et al. [187] to characterize the oxidation of methane. Both mechanisms were developed for describing the oxidation and pyrolysis behavior of methane over a wide temperature range. Duplicate reactions contained in both mechanisms were avoided. For better characterization of the product formation at oxidative fuel-rich conditions, reactions describing the pyrolysis and oxidation of acetylene [205], vinylacetylene [206], propyne and allene [207], and the benzene sub-mechanism of Pitz et al. [333] were added. Reactions from the ethanol mechanism of Marinov [208] and the DME mechanism of Zhao et al. [178] are used to model the oxidations and pyrolysis of both additives. For a better description of DME oxidation, further reactions from the mechanism of Burke et. al. [117] were added.

The newly assembled mechanism was then further developed and improved. The first step was the validation of the mechanism with the IDTs and the species concentrations determined in shock tube, RCM, and flow reactor. The comparison of simulation and experiment allows identifying parameter regions where the predictions should be improved. Analyses of the mechanism, including sensitivity and reaction pathway analysis, were carried out to identify the key reactions for a wide range of temperatures and mixture compositions. The reaction rates of some of these reactions were modified based on previous publications, but only within the documented experimental uncertainty range. The resulting mechanism can well predict IDTs and species concentrations for CH<sub>4</sub>/additive mixtures over a very wide range in temperature, pressure, and equivalence ratio ( $\phi = 1 - 20$ ), while the validation was only carried out for fuel-rich conditions. It can also model the pyrolysis of methane and natural gas very well.

#### 11.3.1.2 Mechanism reduction

PolyMech contains 93 species and 575 reactions. This number is moderate in size compared to other mechanisms (e.g., Burke et al, 113 species and 708 reactions [117]) considering that PolyMech describes also product formation of higher hydrocarbons like benzene. But it is still too large for parametric studies with more complex models (e.g., multizone) or CFD simulations

that may be needed for the further development of polygeneration processes in reciprocating engines [334]. This motivated the development of reduced-model concepts able to describe combustion processes within an acceptable level of accuracy, but with a significant reduction in computational costs [335]. Therefore, reduced versions of PolyMech were developed. The reduction method is based on the decomposition of the system into low-dimensional subsystems describing relatively slow and fast dynamics. Timescales and entropy-production analysis are used to decompose the system and to formulate reduced subsystems [336]. Two types of characteristic time scales – global and local – are determined, based on corresponding linear approximations of a vector field of a detailed model of chemical kinetics [337]. The time scales are obtained by using the Jacobian matrix (local analysis) or the global quasi-linearization (GQL) matrix (global analysis) [338]. The identification of low-dimensional sub-systems is carried out by decoupling the relevant timescales. To investigate the relevance of a certain time scale (i.e., mode of chemical reaction process), the concept of relative entropy production is implemented. The entropy produced in each characteristic time scale is calculated using the invariant subspaces of either local or global approximations. The relevance of the time scale is accessed by comparison with the total entropy produced by the system (Figure 11-4) [336,338,339]. Thereby, sub-groups of timescales describing the dynamics of dormant, relatively slow, and fast processes are identified [336].

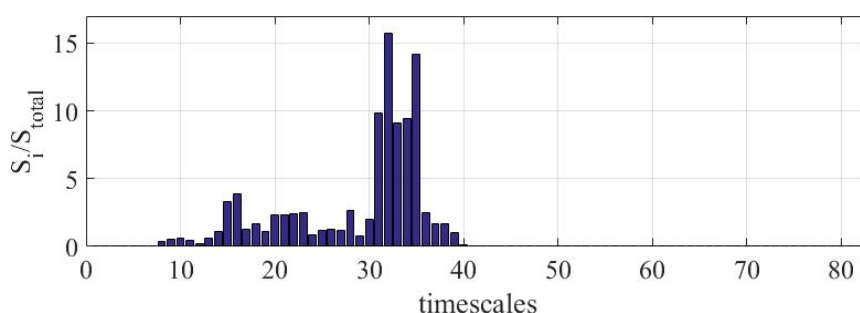


**Figure 11-4:** Contribution of each timescale (mode) to the total entropy production of the system for  $\text{CH}_4/\text{DME}$  mixtures at  $\phi = 6$ ,  $p = 10$  bar, and  $T = 600$  K. On the left are the timescales corresponding to the dormant processes ( $\lambda_1 - \lambda_7$ ), in the middle the relevant timescales ( $\lambda_8 - \lambda_{39}$ ), and on the right the fast time scales ( $\lambda_{40} - \lambda_{83}$ ) [338].

Chemical reaction processes can be decomposed into: (i) Fast processes governed by quick relaxation of the system dynamics that in most cases remain stationary or quasi-stationary and in Figure 11-4 no significant contribution to entropy production is seen, (ii) very slow (dormant) processes that can be considered as quasi-conserved and again in Figure 11-4 no significant contribution to entropy production is seen, and finally (iii) processes with characteristic time scales in between, which describe and govern the progress of chemical reactions, and therefore are the only reactions modes that need to be accounted for. As seen in Figure 11-4, the latter contribute strongly to entropy production. The processes with fast and dormant timescales can be approximated by established implicit algebraic relations. Namely, the quasi-steady-state approximation for the fast subsystem and a conservation assumption for the dormant one. Once the fast and dormant reactions are decoupled, the only processes that have to be integrated are those of the relatively slow subsystem [336].

A local characteristic timescale analysis delivers precise information on the development of the system with time but requires higher computational effort because the Jacobian matrix must be calculated and decoupled for each thermo-kinetic state. A global analysis offers a rougher approximation of the timescales, but it nevertheless allows to describe the fast relaxation processes needed to constrain the system dynamics as described above with sufficient accuracy. The GQL matrix also provides a constant approximation for the invariant subspaces. This means, once obtained it can be used for implementations over a wide range of initial conditions ( $p$ ,  $T$ ,  $\phi$ ) [338]. The number of relevant characteristic time-scales corresponds to the dimension of the reduced model [336].

The results of the local analysis can be incorporated in the form of a skeletal mechanism, while the results from the GQL method are implemented as a differential-algebraic system of equations (DAE) or in the form of a skeletal mechanism. Skeletal mechanisms are obtained by further implementation of entropy-production analysis. Key reactions contained in the skeletal mechanism are identified by evaluating the entropy produced by each reaction on each relevant time scale. This process is repeated for several sets of parameters ( $p$ ,  $T$ ,  $\phi$ ), so that the obtained skeletal mechanism will be valid for a wide range of initial conditions.

The detailed version of PolyMech was reduced to two skeletal mechanisms, one from the local analysis and one from the global analysis [336,339]. For a CH<sub>4</sub>/DME mixture, Figure 11-5 compares results obtained with the two skeletal mechanisms with predictions with the detailed version of PolyMech. Since almost no difference is observed when the species mole fractions are plotted over the reaction time, Figure 11-5a presents the temperature as a function of mole fractions of other chemical species like CO and CH<sub>2</sub>O. Figure 11-5b shows that IDTs from the simulations with both reduced models are very similar (the discrepancy is around 1 %). Compared to the detailed mechanism, IDTs obtained with the skeletal mechanism from the local analysis have an average error of 4.5 %, while from the global analysis the error is slightly greater (5.4 %). The temporal evolution of the state space represented in Figure 11-5a shows that the skeletal mechanisms predict the final (equilibrium) state of the mixture very well, while compared to the detailed model their time traces show discrepancies of up to 3 % for the local analysis and up to 26 % for the global analysis.

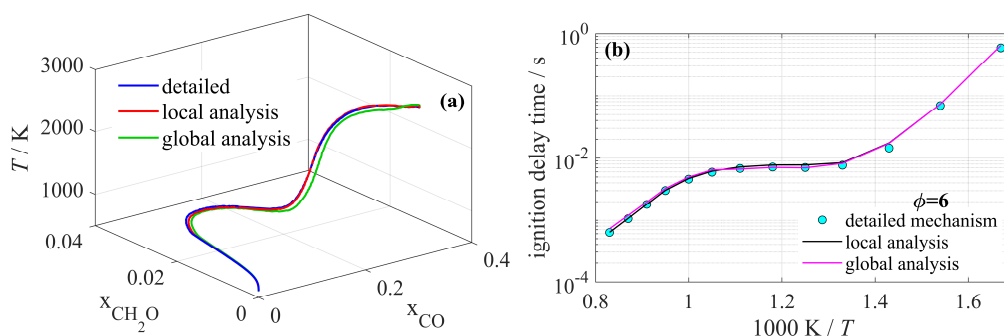


**Figure 11-5:** Comparison of simulation results with the three versions of PolyMech, detailed, skeletal based on local analysis, and based on global analysis. (a) Temporal evolution in the thermochemical state space projected onto the coordinates  $T$ ,  $x_{\text{CH}_2\text{O}}$ , and  $x_{\text{CO}}$  for a CH<sub>4</sub>/DME (10 % DME) at  $\phi = 2$ ,  $p = 10$  bar and  $T = 600$  K. (b) Ignition delay times for the same mixture at  $\phi = 6$  and  $p = 10$  bar.

With local analysis, a dimension of 32 was found to be sufficient to describe the ignition process with an acceptable accuracy, while with global analysis a dimension of 38 remains. This represents a reduction in dimensionality of about 60 % with respect to the detailed mechanism. Figure 11-6 graphically represents the number of reactions and species in the three versions of PolyMech.

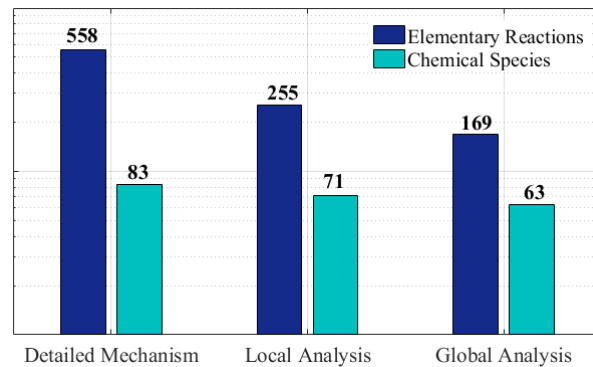


**Figure 11-6:** Comparison of the number of reactions and species in the skeletal models from the global and local analysis with the detailed version of PolyMech [19] for a CH<sub>4</sub>/DME-Mixture.

A representation of the reduced model as a DAE in implicit form is only possible in the case of the global analysis, in which an optimal GQL matrix is obtained. The GQL matrix is used to find the sub-space of slow processes and to formulate the slow sub-system that needs to be integrated. The integration of the slow sub-system is carried out in HOMREA [340] such that other sub-systems governing fast and dormant processes are approximated automatically by quasi-steady-state and quasi-conservation assumptions. The dimension of the reduced model is in this case equal to the dimension of the slow invariant subspaces of the GQL matrix. For IDTs an error of 1.5 % is obtained. IDTs obtained using the skeletal mechanism and the implicit form of the global analysis are compared in Figure 11-7. Good agreement of both results with each other and with the results of the detailed simulation is observed, even though better predictions are obtained using the implicit form of the reduced model.

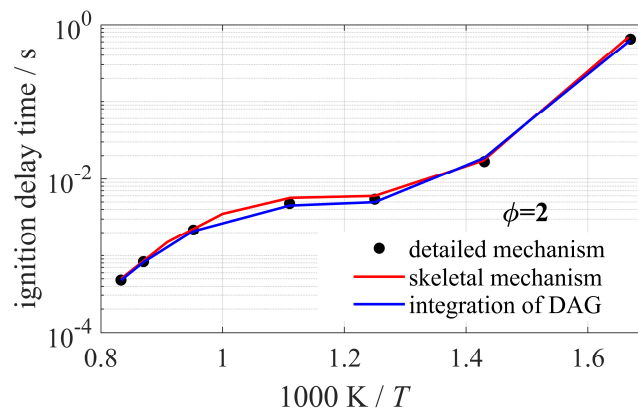


**Figure 11-7:** Comparison of the ignition delay times from the detailed version of PolyMech with the ones from the skeletal mechanism and the implicit form of the global analysis for a CH<sub>4</sub>/DME (10 % DME) at  $\phi = 2$  and  $p = 10$  bar.

## 11.3.2 Validation experiments

### 11.3.2.1 Ignition delay and onset of conversion

Ignition delay times are valuable validation targets for reaction mechanisms describing the combustion in engines. Figure 11-8 shows experimental results obtained in shock tubes at  $\phi = 2$  for methane with selected additives (DME, DEE, DMM, and *n*-heptane). All additives lead to a broadly similar reduction of the IDT at a given temperature, except that *n*-heptane shows a pronounced negative temperature coefficient (NTC) behavior. Conversely, any of the additives reduces the temperature required for an IDT of 2 ms from 1250 K to about 1000 K. While the molar concentration of *n*-heptane is lower than for the ethers, the fraction of added carbon atoms is comparable. These data enable validating reaction mechanisms at engine-typical conditions. Experiments at 20 bar with 20 % DME showed very good agreement with simulations using the mechanism of Burke et al. [117]. Measured IDTs in the RCM show very good agreement with shock-tube data in the small overlapping temperature range near 850 K and allow extending the validation range to lower temperatures [19]. Overall, a preliminary conclusion is that the additives investigated here are to some extent interchangeable in their effect on global kinetics at  $\phi = 2$  and can be selected due to other criteria, such as thermodynamics, practical handling, sustainability, or simply cost. However, the influence of the additive at different equivalence ratios and on product formation is not clear yet.

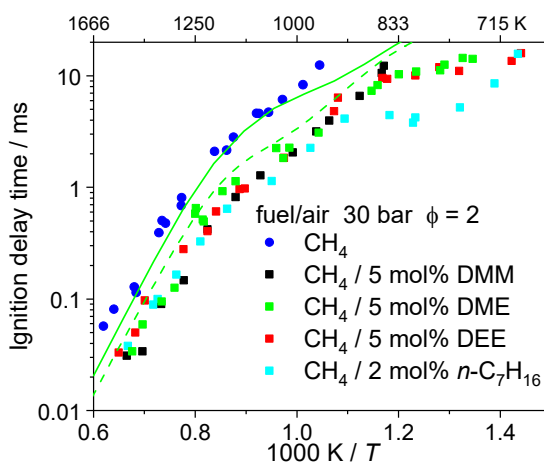


**Figure 11-8:** Measured and simulated ignition delay times of methane/additive mixtures at  $\phi = 2$  and  $p = 30$  bar. Simulations are for 5 % DME addition. Full green line: Simulation with PolyMech [19]. Dashed green line: Simulation with Burke et al. [117]. The measured data were published in Refs. [19,199,297].

Next, very fuel-rich conditions with  $\phi = 10$  are considered. Compared to  $\phi = 2$ , these conditions may offer the advantage of greater exergy storage by the formation of higher hydrocarbons. For this purpose, very fuel-rich mixtures must be used to minimize the heat production so that the final temperature after ignition remains too low for significant soot formation. IDTs measured in a high-pressure shock tube and an RCM are shown in Figure 11-9. The simulations with PolyMech [19] agree well with the experiments.

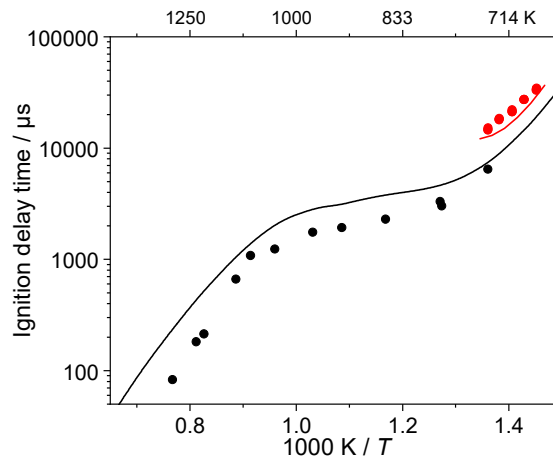


**Figure 11-9:** Ignition delay times of a 10 % DME / 90 % CH<sub>4</sub> mixture at  $\phi = 10$ . Black circles: Shock tube at  $p = 30$  bar, black line: PolyMech [19] simulation of the shock-tube data, red circles: RCM at  $p = 10$  bar, red line: PolyMech [19] simulation of the RCM data.

The effect of different additives is seen in the flow reactor, as shown in Figure 11-10. If methane in a mixture with an additive is converted at lower temperatures than without additive, the additive has activated the methane conversion. For 5 % *n*-heptane or DME addition, Figure 11-10 shows that the methane conversion is already increased at temperatures between 523 and 673 K. If 9 % ethane and 1 % propane are added to methane to represent the composition of typical natural gas, compared to the reaction of neat methane the effect is minor. Ethane and propane are converted at slightly lower temperatures than methane (not shown here), but without noticeable chemical interaction with methane. The addition of 20 % ethanol increases the methane conversion only at temperatures of 773 K and above. These results fit well with the findings in shock tubes and RCMs but cover the lower temperature range that is important for low-temperature conversion of the fuel before ignition in the compression stroke of an engine. It could be shown, for example, that methane exhibits a region of weak NTC behavior at low temperatures and high pressures that may influence its ignition in the engine [90].

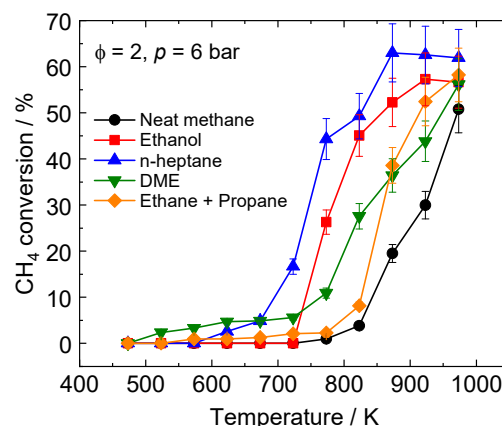


**Figure 11-10:** The temperature-dependent methane conversion in mixtures with different additives. All for  $\phi = 2$ ,  $p = 6$  bar and an argon dilution of  $\sim 90$  %. The additive/fuel ratios are 5/95 (*n*-heptane [200] and DME [19]), 10/90 (natural gas [197]) and 20/80 (ethanol). Neat methane data are from Ref. [197].

### 11.3.2.2 Kinetics of product formation

Product formation and composition is especially important in the context of polygeneration. The product formation was studied with four complementary techniques: Time-resolved infrared diode-laser absorption measurements of CO concentrations in a shock tube [17] gas-chromatography of time-resolved samples from a RCM [19], GC/MS (gas chromatography/mass spectrometry) in fast-drawn samples from a high-pressure shock tube (in the cooling phase after the reflected shock wave) [19], and time-of-flight mass spectrometry (TOF-MS) in a high-pressure flow reactor [19]. All techniques confirmed that syngas (CO and H<sub>2</sub>) is the main product at  $\phi = 2$ . Simulations with PolyMech predicted the product formation very well. Figure 11-11 shows fuel consumption and product formation measured in a flow reactor. The fuel consumption and the product formation show an NTC behavior, which was also observed in the IDT measurements.

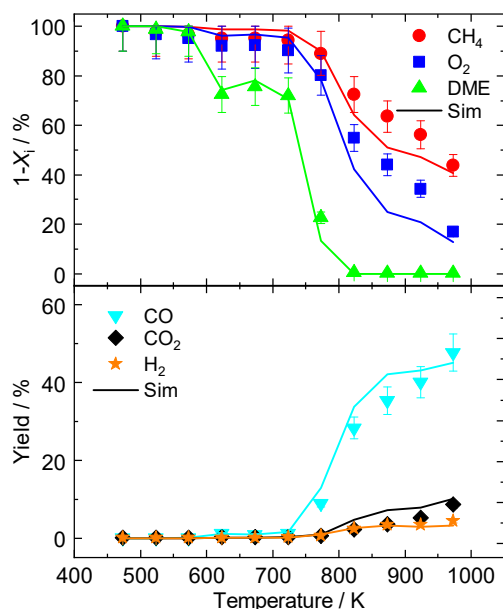


**Figure 11-11:** Measured and simulated remaining educts  $1-X$  and yields  $Y$  in the flow reactor at  $p = 6$  bar and  $\phi = 2$ . Inlet mixture: 4.69 % CH<sub>4</sub>, 0.25 % DME, 5.06 % O<sub>2</sub>, 90 % Ar. The residence time varies with temperature from 14.5 to 7.6 s at 473 and 973 K, respectively.

Also for ultra-rich mixtures, product composition measurements were performed in the high-pressure shock tube, the RCM [341], and the flow reactor. The shock-tube results at  $\phi = 10$  are shown in Figure 11-12. They were obtained by GC/MS analysis after fast sampling in the cooling phase and are relative to neon as an internal standard. H<sub>2</sub> could not be detected by the GC/MS system. Here, 10 % DME were used as an ignition promoter, but with other additives (DEE, DMM, and *n*-heptane) the product composition was almost the same [199]. About half of the consumed carbon is converted to CO, the other half to higher hydrocarbons. Simulations show that almost constant product concentrations are reached about 2 ms after ignition except for benzene (still increasing) and acetylene (still decreasing). Comparing the experimental results with CH<sub>4</sub>/DME mixtures with different mechanisms from the literature [117,164,178], it is found that most show large deviations from the corresponding experimental results,

especially for acetylene and benzene. This is not surprising because the mechanisms were not developed for these fuel-rich conditions and often do not contain benzene formation chemistry.

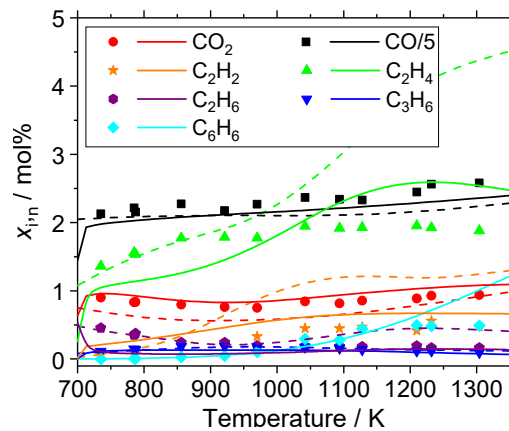


**Figure 11-12:** Product mole fractions after ignition of a  $\text{CH}_4/10$  mol% DME/air mixture at  $\phi = 10$ , and 30 bar. Symbols show shock-tube data, full lines show simulations with an updated version of PolyMech [19], dashed lines with the mechanism of Burke et al. [117].

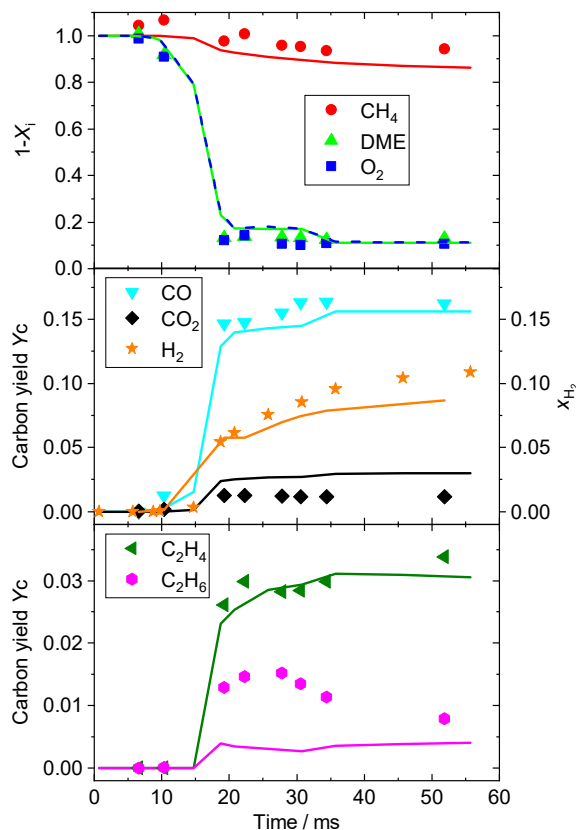


**Figure 11-13:** Measured and simulated remaining educts  $1-X$  and yields  $Y$  in the RCM compressing an undiluted 90 %  $\text{CH}_4/10$  % DME mixture ( $\phi = 10$ ) to 10 bar and temperatures between 714 and 738 K. Simulations with PolyMech [19].

For other additives, only the mechanism of Cai and Pitsch [148] can predict the observed product composition of  $\text{CH}_4/\text{additive}$  mixtures well [199] (for  $\text{CH}_4/n$ -heptane). With PolyMech, the predictions of  $\text{CO}_2$  and benzene concentrations initially did not agree well with shock tube measurements [19]. This was greatly improved by replacing the rate coefficient of

$\text{CO} + \text{HO}_2 = \text{CO}_2 + \text{OH}$  with a recent value of You et al. [276] and by adding benzene consumption reactions (see Figure 11-12). The mechanism of Burke et al. [117] overpredicts the concentrations of  $\text{C}_2$  species because it contains only species up to  $\text{C}_3$  and no benzene formation chemistry.

Figure 11-13 shows time-resolved RCM results for an undiluted 90 %  $\text{CH}_4$ / 10 % DME mixture at 10 bar and temperatures between 714 and 738 K. Simulations were performed with a multi-zone model and PolyMech [19]. The fuel consumption and the product formation are well predicted [198]. The additive is consumed faster than methane and initiates methane consumption. The main products are  $\text{H}_2$  and  $\text{CO}$ , but higher hydrocarbons are also detected.

The results from the flow reactor, shown in Figure 11-14, confirm those from shock tube and RCM: There is an NTC region, the additive is consumed faster and more completely than methane, the main products is syngas but  $\text{C}_2$  and  $\text{C}_3$  hydrocarbons are also found. Simulations with the PolyMech [19] predict the temperature-dependent fuel consumption and product formation very well.

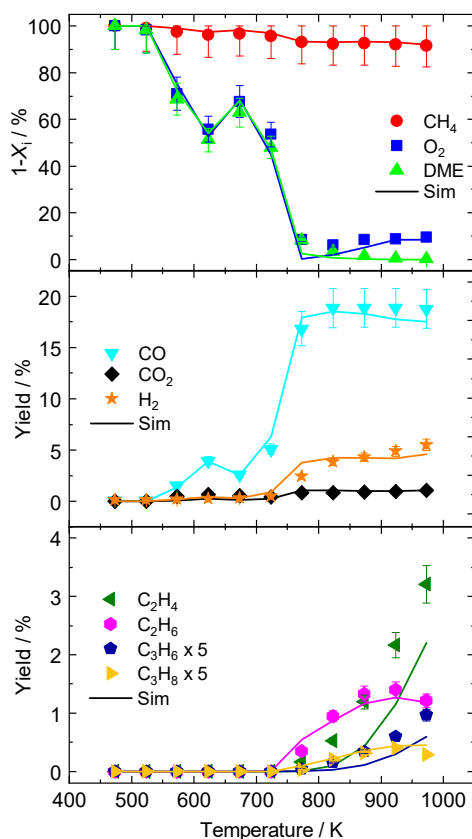


**Figure 11-14:** Measured and simulated remaining educts  $1-X$  and yields  $Y$  in the flow reactor at  $p = 6$  bar and  $\phi = 10$ . Inlet mixture: 7.44 %  $\text{CH}_4$ , 0.83 % DME, 1.74 %  $\text{O}_2$ , 90 % Ar. The residence time varies with temperature from 14.5 to 7.6 s at 473 and 973 K, respectively. Simulations with PolyMech [19].

A comparison of experimental results from the flow reactor with simulations using PolyMech is shown in Figure 11-15 for mixtures of 5 % DME in methane at 6 bar and  $\phi = 2$  and 10. The shaded area represents the confidence interval of the experiments. Overall, the agreement between experimental and simulation is very good for  $\phi = 10$ , but not as good for  $\phi = 2$ .

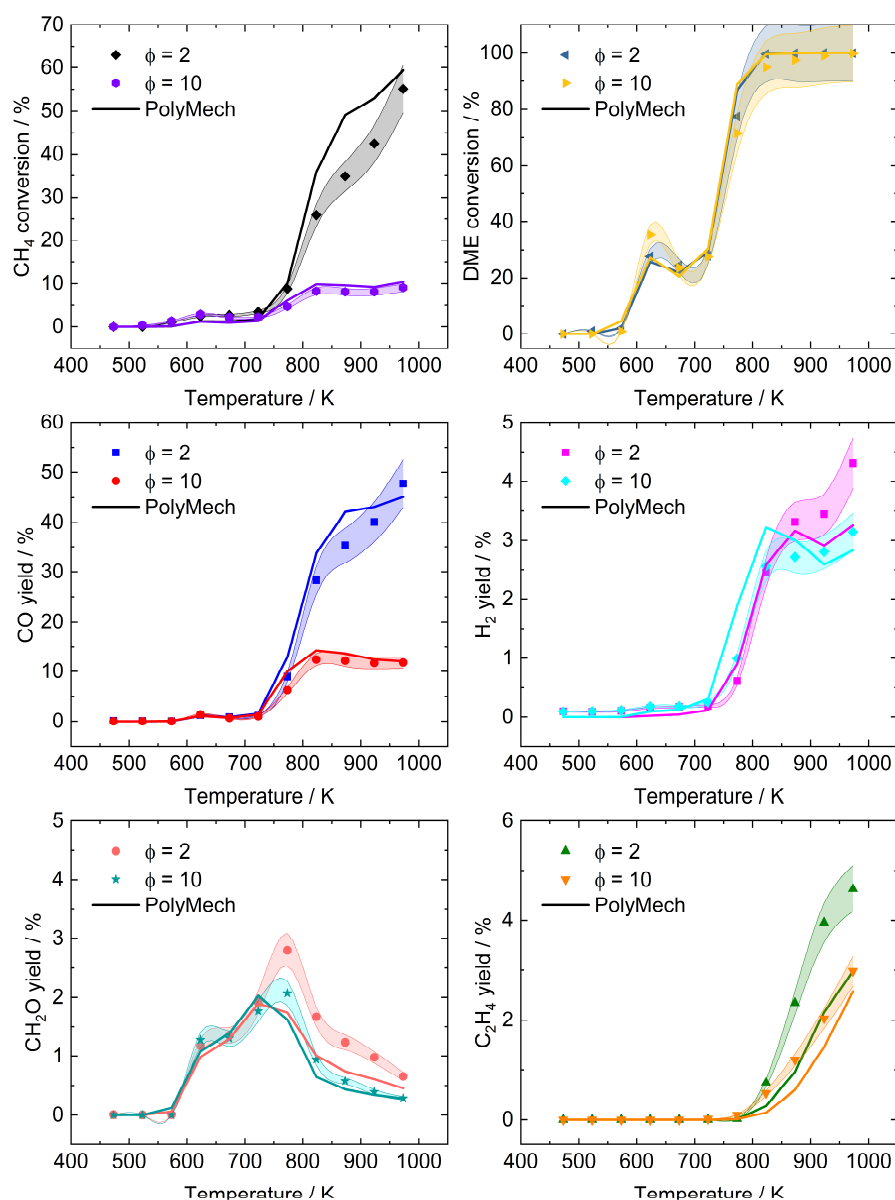


**Figure 11-15:** Measured and simulated species conversion and yields from 5 % DME / 95 % CH<sub>4</sub> mixtures for  $p = 6$  bar and  $\phi = 2$  and 10. The residence time varies with temperature from 14.5 to 7.6 s at 473 and 973 K, respectively. The experiments were performed in the flow reactor, PolyMech was used in the simulations.

In the flow reactor, numerous species concentrations were quantitatively detected at the reactor outlet with GC/MS as a function of equivalence ratio and temperature. The results for a 5 % heptane / 95 % CH<sub>4</sub> mixture are condensed into the semi-quantitative map shown in Figure 11-16. Such maps can be useful to find operating conditions for the production or avoidance of specific species. For example, Figure 11-16 shows that moderately high equivalence ratios and high temperatures are favorable for the formation of synthesis gas, while high temperatures and high equivalence ratios lead to high ethylene yields. The yields of oxygenated species like ketones can be considerable, but this is limited to low temperatures with relatively low methane conversion. Benzene starts to form at temperatures around 900 K and peaks at  $\phi = 20$  in the investigated temperature range. Its yield could be increased by increasing the temperature, but with the risk of further conversion towards PAHs and soot.

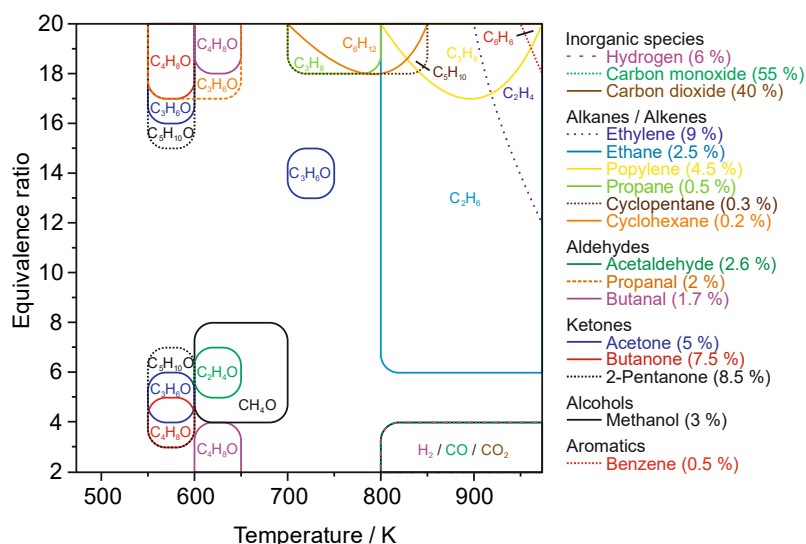


**Figure 11-16:** Species map of a mixture of 5 % heptane in methane as a function of equivalence ratio and temperature, based on experiments in the flow reactor at 6 bar. The maximum detected yields are listed in the legend, while the regime within about  $\pm 30$  % of this maximum value is indicated in the map. The temperature resolution in the map is 50 K [200].

Overall, PolyMech is a very good mechanism for these unusual conditions and often predicts species profiles better than, or at least as good, as the discussed alternative mechanisms, most of which include considerably more species.

### 11.3.3 Energy storage by methane pyrolysis

The conversion of mechanical to chemical energy is also of interest to store energy. It could be carried out in engines, which then mainly act as compressors. If electrical energy is available, an electric motor would convert that into mechanical work, which would then be used in a compression–expansion cycle in a piston engine. Simple hydrocarbons could then be converted endothermically to higher-enthalpy hydrocarbons and  $H_2$ . The energy input for the endothermal reaction would be provided through the work supplied in the compression stroke. At first sight, it may seem preferable to use pure hydrocarbons like methane. For methane conversion, temperatures between 1300 and 2000 K are needed, according to equilibrium calculations and experiments [293,342,343], with  $H_2$ , ethylene, benzene, and acetylene being the main products. However, the heat capacities of pure hydrocarbons are very high. Thus, at engine-typical initial temperatures and compression ratios, the TDC temperatures are far too low to obtain a measurable conversion [342]. At a compression ratio of 25, an initial temperature of 720 K would be needed in an adiabatic system to obtain temperatures high enough for high conversion. Alternatively, sufficiently high temperatures for pyrolysis can be reached by dilution with an atomic inert gas (most readily available is argon), decreasing the heat capacity of the gas mixture. The kinetics of the process can again be investigated as described above, with engine parameters modified in favor of the pyrolysis process. Mainly, a compression ratio of  $\varepsilon = 22$  and an engine speed  $N = 3000$  rpm were chosen. The reactions were simulated using the Polimi mechanism [144], an elementary reaction mechanism that includes 484 species up to  $C_{20}$  and 19341 reactions. These high-molecular-weight species are not yet included in PolyMech. A thermodynamic analysis was included, in particular a calculation of the chemical and physical exergy

of the gas mixture according to Ref. [342]. The storable energy is then calculated as the difference of the exergy between reactant and product gas. The storage efficiency is the storable energy divided by the supplied work. To find engine parameters that favor the pyrolysis process, the process can be kinetically investigated as described in Section 11.2.2.

The results of a typical simulation are shown in Figure 11-17 for an intake temperature of 423 K, an intake pressure of 2 bar, and an intake argon mole fraction of 96 %. The consumption of methane at temperatures above 1300 K and the formation of the main products as a function of the crank angle are seen. The main products are hydrogen and higher hydrocarbons like acetylene, ethylene, and benzene. The model also shows that acetylene reacts between 180 and 200 °CA to soot precursors like C<sub>20</sub>H<sub>10</sub> and C<sub>20</sub>H<sub>16</sub>, and methane is formed again. After 200°CA, the mixture composition is “frozen” by the decreasing temperatures in the expansion stroke. Overall, for these intake parameters, a CH<sub>4</sub> conversion of 90 % is predicted together with yields for acetylene, ethylene, and benzene of 24, 9, and 3 %, respectively. The exergy of the mixture was increased by about 6 %.

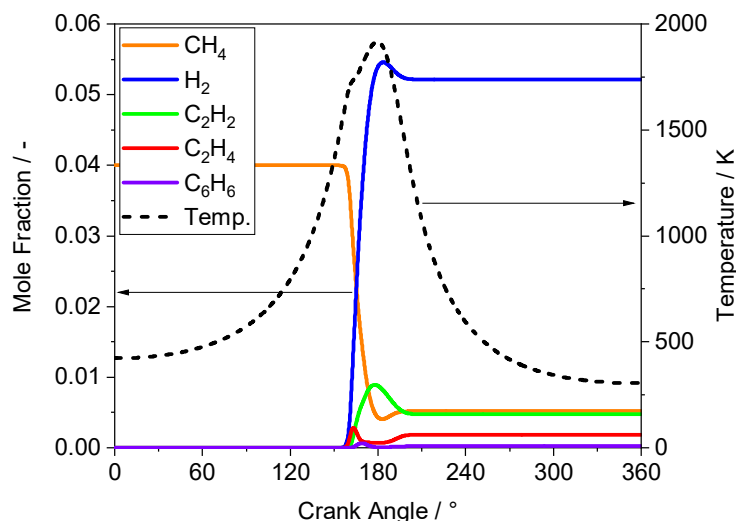


**Figure 11-17:** Mole fractions and temperature as a function of crank angle for methane at intake conditions of  $T_0 = 423$  K,  $p_0 = 2$  bar, and  $x_{Ar} = 0.96$ .  $\varepsilon = 22$ ,  $N = 3000$  rpm.

The pyrolysis reaction, and thus the methane conversion strongly depends on temperature. From literature, it is known that the pyrolysis of methane starts at temperatures of 1300 K [344]. Methane conversion in this process is mainly controlled by the temperatures at the end of the compression stroke. Figure 11-18 shows the methane conversion as a function of intake temperature and intake argon mole fraction (the remainder of the mixture is methane). The graph also includes isothermal curves of the TDC temperature. It can be seen that higher argon mole fractions with lower intake temperatures lead to the same TDC temperature and the same conversion as lower argon mole fractions and higher intake temperatures. The isothermal curves of the TDC temperatures are parallel to the CH<sub>4</sub> conversion. For a TDC temperature of 1600 K 15 % of methane are converted. This is significantly less than what would be expected in chemical equilibrium at that temperature, i.e., conversion is kinetically limited by the short reaction times in the engine (but most stationary engines actually run slower than 3000 rpm). A methane conversion of 80 % can be reached at TDC temperatures of 1800 K. This is reached for example

by an intake parameter combination of 97 % argon and 323 K, but also for 89 % argon and 723 K.

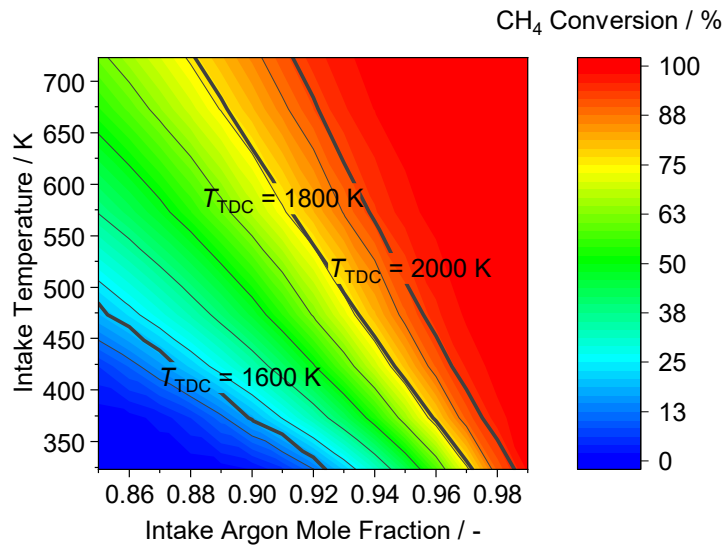


**Figure 11-18:** CH<sub>4</sub> conversion (colored contours) and top dead center temperature (thick black lines) as a function of the intake temperature and the intake argon mole fraction.  $p_0 = 2$  bar,  $\varepsilon = 22$ ,  $N = 3000$  rpm.

The storage power depends on the methane conversion, but also on the intake dilution. In order to examine whether high argon dilutions or high intake temperatures are more favorable for the process, the storage power and the storage efficiency are compared as a function of intake argon mole fraction for three different intake temperatures of 323, 423, and 523 K at an intake pressure of 2 bar. Figure 11-19 shows that for all intake temperatures storage power and efficiency decrease for both the lowest and the highest argon dilutions. This is caused by the low conversion with lower argon dilution and by the small fraction of methane in the mixture when the argon dilution is too high. With increasing intake temperatures, the effect is less pronounced, and the maximum storage power and efficiency shift to lower argon dilutions.

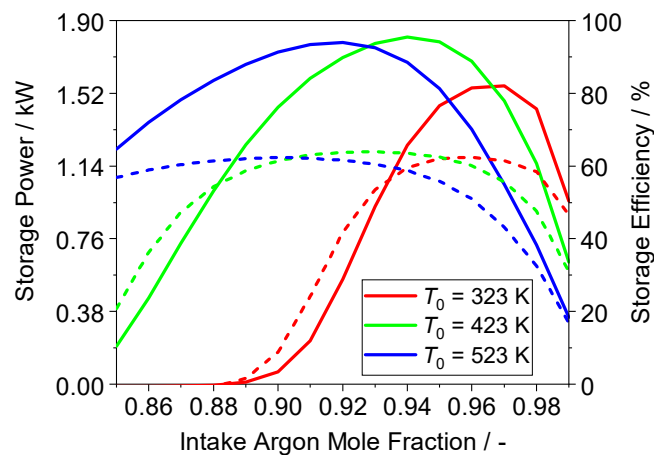


**Figure 11-19:** Storage power (solid lines) and efficiency (dashed lines) as a function of intake argon mole fractions for different intake temperatures  $T_0$ .  $p_0 = 2$  bar,  $\varepsilon = 22$ ,  $N = 3000$  rpm,  $\Delta V = 400$  cm<sup>3</sup>.

The storage power has a local maximum at  $T_0 = 423$  K and  $x_{\text{Ar}} = 0.94$  of 1.8 kW for  $N = 3000$  rpm and  $\Delta V = 400$  cm<sup>3</sup> in this four-stroke engine. Unexpectedly, the maximum storage power decreases for intake temperatures higher than 423 K. This is due to the formation of soot precursors and re-formation of CH<sub>4</sub>. The maximum efficiencies are between 60 and 63 %, which is promising.

Experiments were performed to validate the simulation results. The pyrolysis of methane (1 and 5 mol% CH<sub>4</sub> in Ar/He mixture,  $p = 12 - 26$  bar,  $T = 1350 - 1750$  K, [341]) and natural gas (5 % NG surrogate, with the composition described in section 11.3.2.2) in Ar/He,  $p = 21 - 31$  bar,  $T = 1380 - 1690$  K [345]) was studied in the RCM. After expansion by rapid retraction of the piston [198], the products were analyzed with a GC. The temperature dependency of the methane pyrolysis and product formation are shown in Figure 11-20. H<sub>2</sub>, C<sub>2</sub>H<sub>2</sub>, and C<sub>2</sub>H<sub>4</sub> are the main products. The GC used here cannot detect benzene. In the temperature range investigated here, the conversion of methane and the formation of products slightly decreases with increasing pressure [345]. The conversion decreases also with increasing methane concentration due to the higher temperature decrease (higher endothermicity) with higher concentrations [345]. The trends for pressure and temperature dependency observed for methane pyrolysis were found also for natural-gas pyrolysis. As found in the kinetics investigations, ethane and propane decompose much faster than methane.

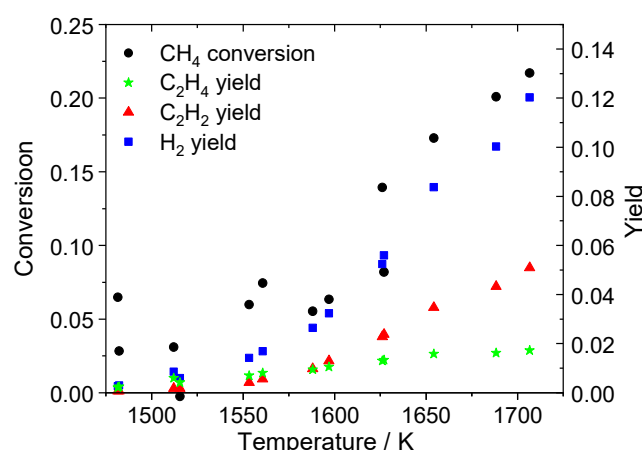


**Figure 11-20:** Measured species conversion and yields in an RCM for a 5 mol% CH<sub>4</sub> / 90 mol% Ar / 5 mol% He mixture at 18 bar [341].

Simulations show that high conversions can be achieved for concentrations of up to 10 % methane in argon. These CH<sub>4</sub>/Ar mixtures were studied in shock tubes [299] and an RCM [341]. In adiabatic systems, a characteristic feature of this methane pyrolysis is a fast decrease in the temperature due to the formation of products with a higher enthalpy (energy storage process), which leads to a quasi-equilibrium at a relatively low temperature with negligible further methane consumption. An end-product analysis alone is not sufficient for the validation of different mechanisms because it cannot distinguish how fast the quasi-equilibrium is reached. Therefore, we also performed time-resolved temperature and methane infrared absorption measurements. Species concentration measurements with GC/MS were performed in shock tubes at about 1.5 bar (single-pulse shock tube) and at 30 bar (with fast sampling). The results at 1.5 bar are shown in Figure 11-21. The main detected product is C<sub>2</sub>H<sub>2</sub>, while other C<sub>2</sub> as well as C<sub>3</sub>, C<sub>4</sub>

species, and benzene are formed in smaller amounts. The other main product,  $H_2$ , could not be detected with our GC/MS system. The methane consumption and the product formation were well-predicted in simulations using PolyMech [19]. At 30 bar, similar results were observed, but the methane consumption curve shifted by about 300 K towards lower temperatures. The product composition shifted towards benzene such that about equal amounts of  $C_2H_2$ ,  $C_2H_4$ , and benzene were observed. At the upper temperature end of the high-pressure measurements soot formation was observed. Species concentration measurements at about 1.5 and 30 bar were also performed in shock tubes for a natural-gas surrogate (90 mol%  $CH_4$ , 9 mol%  $C_2H_6$ , 1 mol%  $C_3H_8$ ). The results were very similar to the methane pyrolysis. The products and the methane consumption were almost identical, but ethane and propane decomposed at significantly lower temperatures [346].

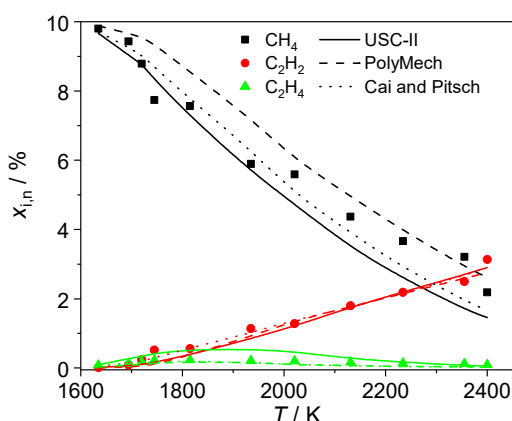


**Figure 11-21:** Shock tube: Measured and simulated product species mole fractions of the pyrolysis of a 10 mol%  $CH_4$  / 90 mol% Ar mixture at about 1.5 bar. Symbols: experiment, solid line: simulations with USC mechanism [312], dashed line: simulation with PolyMech [19], dotted line: simulation with the Cai and Pitsch [148] mechanism.

Mid-IR diode lasers were used for the time-resolved temperature and methane concentration measurements in a shock tube. 1 % CO was added to the mixture for temperature measurements with CO thermometry [299]. Typical temperature traces are shown in Figure 11-22. A very fast temperature decrease can be observed for high initial temperatures, whereas at lower initial temperatures the temperature decreases more slowly. The temperature decrease is higher with higher methane consumption, as seen in Figure 11-23. PolyMech predicts too slow a methane pyrolysis at lower temperatures. The predictions can be significantly improved by using a recently published rate coefficient for the  $CH_4 (+M) = CH_3 + H$  reaction [293] (orange lines in Figure 11-23). A general result of the pyrolysis experiments is that the experiments can be well reproduced by oxidation mechanisms.

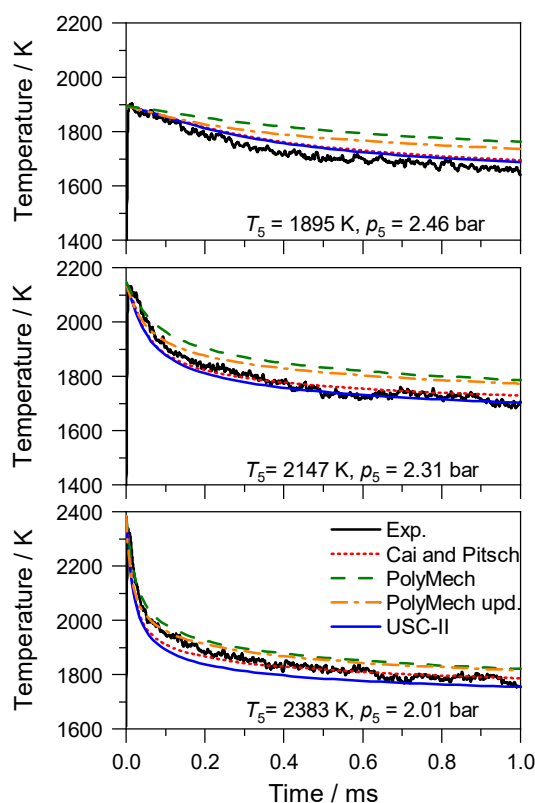


**Figure 11-22:** Measured temperatures during the pyrolysis of a 10 % CH<sub>4</sub>/1 % CO/20 % He mixture in Ar in the shock tube compared with simulations.

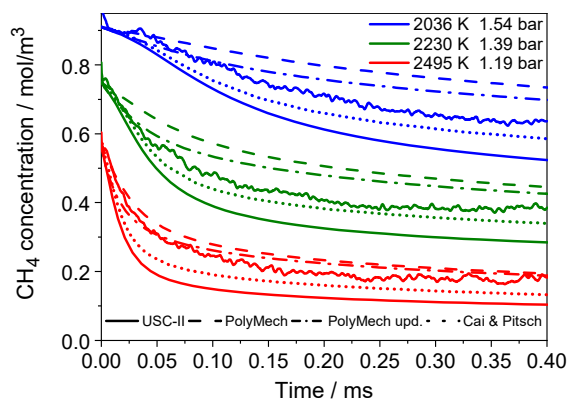


**Figure 11-23:** Time-resolved CH<sub>4</sub> concentration measurements (solid lines) during the pyrolysis of 10 mol% CH<sub>4</sub> in Ar in a shock tube. Simulations with USC-II ([312]) (solid lines), PolyMech [19] (dashed lines), updated PolyMech (dash-dotted lines) and the Cai and Pitsch [148] mechanism (dotted lines).

In summary, energy can be stored via methane pyrolysis in piston engines, but because methane is very inert, high temperatures are needed. Due to the high heat capacity of methane these temperatures could only be established with unusual conditions, like high Ar dilution. This could in part be overcome with higher pre-heating combined with higher compression ratios. Other, less inert energy storage molecules like ethane may be an alternative worth investigating. The product-gas composition can be influenced by selecting suitable initial conditions and process parameters, which may make this approach interesting for the chemical industry.

## 11.4 Experiments in engines

### 11.4.1 Product formation in the RCM

In both the RCM and a single-cylinder research engine, experiments with mixtures of CH<sub>4</sub> and DME were conducted over a wide range of equivalence ratios.

Because the RCM avoids some of the complexities of a reciprocating engine, results from these experiments are discussed first. Figure 11-24 shows the product-gas species. At stoichiometric conditions ( $\phi = 1$ ), the fuel components methane and DME are found only in small amounts in the product mixture. Since stoichiometric mixtures would be expected to undergo complete combustion, the CH<sub>4</sub> and DME found in the product gas can be interpreted as residuals from wall quenching e.g., near the cylinder and piston top or in crevices. Only small amounts of H<sub>2</sub> and CO are produced (Figure 11-24a). CO<sub>2</sub> is the main carbon-containing product (Figure 11-24b), as seen from a carbon yield of nearly 100 % for CO<sub>2</sub>. This is the “classical”, nearly complete combustion process.

At  $\phi = 2$ , the picture changes. Here, only 18 % of the fuel carbon end up in CO<sub>2</sub>, but 70 % in CO. This strongly increased CO formation relative to  $\phi = 1$  is simply due to the fact that for a fuel-rich mixture complete combustion – in the sense of conversion to H<sub>2</sub>O and CO<sub>2</sub> – is not possible anymore. The lack of oxygen at  $\phi = 2$  favors the formation of CO. All other investigated species combined contain less than 2 % of the fuel carbon. Similarly, the H<sub>2</sub> yield increases relative to  $\phi = 1$ . Note that also the fraction of CH<sub>4</sub> in the product gas is now considerably higher than for  $\phi = 1$ . The carbon yield of CH<sub>4</sub> increases from about 3 % at  $\phi = 1$  to about 10 % at  $\phi = 2$ , i.e., by a factor of 3. This is consistent with the notion that in addition to the wall quenching also observed at  $\phi = 1$ , some fraction of the methane in the product gas is actually a genuine product of chemical reactions in the bulk gas. This is corroborated by the fact that the equilibrium composition of a CH<sub>4</sub>/DME/air mixture at  $\phi = 2$  contains several percent of CH<sub>4</sub>. Figure 11-24a shows that the molar H<sub>2</sub>/CO ratio for  $\phi = 2$  is about 1.2.

At  $\phi = 6$  and  $\phi = 7$ , the product still contains more H<sub>2</sub> than CO. The latter now captures about 25 % of the fuel carbon. There is also significant conversion into higher hydrocarbons, with C<sub>2</sub>H<sub>4</sub> and C<sub>2</sub>H<sub>6</sub> yields of almost 2 % and about 0.75 %, respectively. When the equivalence ratio is increased further, the yields of C<sub>2</sub>H<sub>4</sub>, C<sub>2</sub>H<sub>2</sub>, and H<sub>2</sub> decrease again. Of all investigated product species, only the methanol (CH<sub>3</sub>OH) yield increases for even richer mixtures. However, at  $\phi = 15$ , only 0.3 % of the fuel carbon is converted to CH<sub>3</sub>OH carbon, with that species presumably mainly originating from DME. More importantly, the formation of C<sub>2</sub> species is at least in the percent regime. Similar studies on dry reforming of methane described in Section 11.4.3 suggest that by systematic optimization (supported by numerical simulations), much higher yields should be possible. Figure 11-24 also shows that by tuning the equivalence ratio the H<sub>2</sub>/CO ratio can be varied, which may be of interest for further processing of syngas.

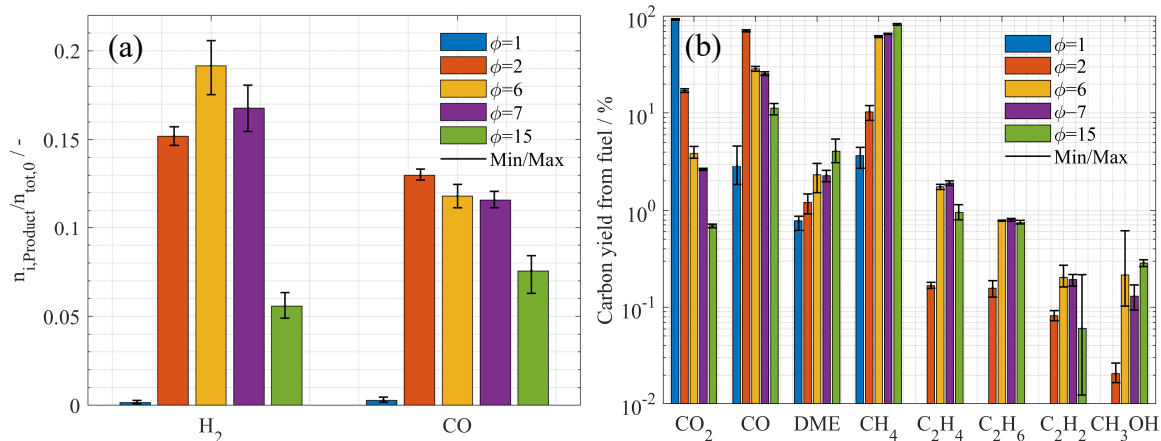


**Figure 11-24:** Species production in the RCM from CH<sub>4</sub>/DME (90/10)/air mixtures over a wide range of equivalence ratios. (a) Total yields of H<sub>2</sub> and CO, defined as the molar amount of product divided by the initial total molar amount (sum over all species). (b) Carbon yield of the most important products. Compression temperature and pressure:  $T = 756 - 985$  K,  $p = 10$  bar. The error bars indicate the minimum and maximum values in the 6 – 9 repetitions of the experiment at each condition.

For basic research, the RCM allows much experimental freedom and control over the thermochemical conditions with well-defined initial and boundary conditions. However, in a reciprocating engine, further complexity arises, e.g., the coupling between successive cycles via the residual gas that remains in the cylinder after the exhaust stroke. Thus, experiments in an engine are reported next.

## 11.4.2 Reciprocating engine

The experiments were conducted in a single-cylinder engine that was originally designed for octane number testing of liquid fuels at compressions ratios between 4 and 10. It has 337 cm<sup>3</sup> displacement volume and was run here at a speed of 600 rpm. The engine was modified to operate also with gaseous fuels and to reach compression ratios of up to 20. Gaseous and liquid fuels were metered into the (also metered) intake air and the mixture was preheated before it enters the intake. The crank-angle resolved cylinder pressure was recorded, and in the product-gas stream the mole fractions of O<sub>2</sub>, CH<sub>4</sub>, C<sub>2</sub>H<sub>4</sub>, CO, and H<sub>2</sub> were measured by gas analyzers (ABB) in continuous on-line sampling. The soot content was measured as a filter smoke number by an AVL smoke meter and converted to a mass fraction. The product gases are poisonous and combustible, and since in the laboratory context there is no downstream processing, they were burned. More experimental details can be found in Refs. [93,246].

### 11.4.2.1 Operating stability

Given the unusual intake compositions targeted here, the first concern was how HCCI operation could be achieved. Among other considerations, “good” engine operation requires that ignition occurs in every cycle, and that combustion is timed appropriately with respect to the kinematics of compression and expansion – if it is too early, the cylinder pressure increases very quickly,

which can damage the engine, and if it is too late, the high-temperature chemistry is frozen before the desired chemical conversion can take place.

As expected, due to the low reactivity of methane, at compression ratios typical for spark-ignition engines (about 9 – 14), autoignition did not occur for any equivalence ratio. Adding a few percent ethane or propane to the methane – to yield a surrogate more representative of pipeline natural gas – did not change this situation. However, as discussed above, with more reactive additives like DME or DEE, HCCI operation is possible within a certain window of additive content in the fuel.

The basic procedure applied here for determining this operating window is a scan, in which the additive flow is systematically increased for a constant methane flow [246]. Two criteria for acceptable operation were chosen. The first criterion is a low coefficient of variation (CoV), a metric of cycle repeatability.

$$\text{CoV} = \frac{\sigma(\text{IMEP}_{\text{net}})}{\text{IMEP}_{\text{net}}} \quad (11-2)$$

where IMEP<sub>net</sub> is the net indicated mean effective pressure defined as

$$\text{IMEP}_{\text{net}} = \text{IMEP} - \text{IMEP}_{\text{mot}} \quad (11-3)$$

That is, at each operating point the indicated mean effective pressure (IMEP) was calculated from the pressure traces of 140 cycles, the IMEP<sub>mot</sub> from a motored cycle was then subtracted from each, and the standard deviation  $\sigma$  was also estimated from that the resulting IMEP<sub>net</sub>. The IMEP is directly linked to the indicated work  $W$  per cycle and the swept volume  $\Delta V$ :

$$W = \text{IMEP} \times \Delta V \quad (11-4)$$

A CoV value of 10 % was chosen as an upper limit for stable operation. The second criterion is the maximum pressure-rise rate (PRR<sub>max</sub>), a metric for mechanical stress on piston, cylinder, and related components. It was measured with the in-cylinder pressure transducer and an upper limit of 10 bar/°CA was deemed acceptable.

Figure 11-25 shows a scan for a constant methane flow with the DME flow varied. Across the scan, the overall equivalence ratio slightly changes, from  $\phi = 2.0$  at the lowest to 2.2 at the highest DME fraction. In addition to the CoV and PRR<sub>max</sub>, IMEP and CA50 are plotted. CA50 is the crank angle at which 50 % of the heat release has taken place, a metric of combustion phasing, that is, how the chemical reactions are timed with respect to the kinematics of the engine cycle.

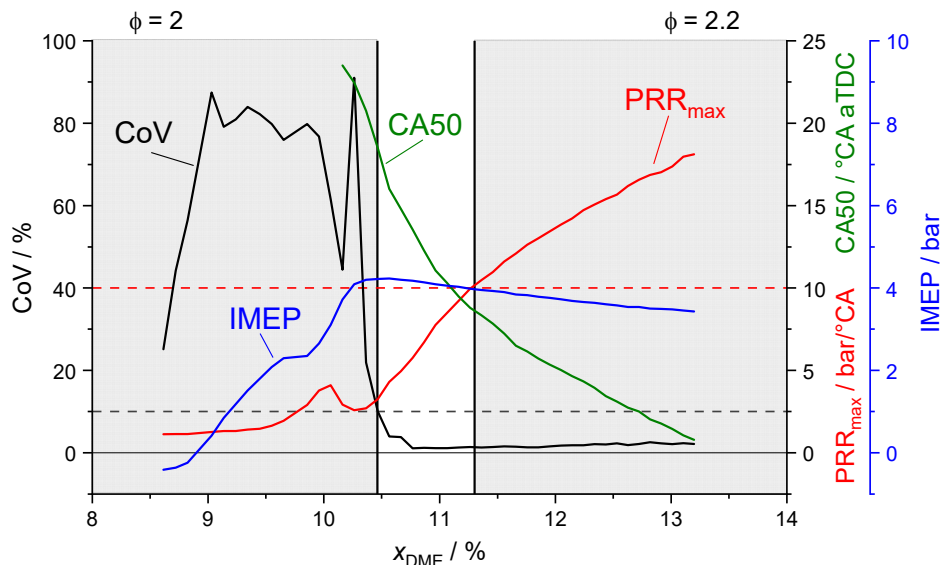


**Figure 11-25:** CoV,  $PRR_{max}$ , CA50, and IMEP for HCCI operation with increasing DME fraction at a constant methane flow, starting from operation without ignition. The white region marks acceptable engine operation. The intake temperature was  $T_{in} = 423$  K and the compression ratio  $\varepsilon = 10$ .

At low DME mole fractions, the mixture does not ignite, resulting in negative IMEP values. Adding more DME first leads to irregular firing and consequently to a high CoV. With increasing additive concentration, more cycles fire, and the CoV decreases while IMEP and  $PRR_{max}$  increase. The non-monotonic behavior in these metrics at  $x_{DME} = 10 - 10.4$  % is associated with alternating firing and misfiring cycles due to the residual gas transferring unreacted or reacted mixture, respectively, from one cycle to the next. Increasing the intake additive fraction further induces stable engine operation at 10.5 % DME. With more additive, CA50 shifts early. This results in increasing  $PRR_{max}$  because the heat is released at a smaller cylinder volume. The maximum IMEP is reached for the latest CA50 with stable engine operation, 16°CA after TDC. In modern engines with a more compact shape of the combustion chamber than this octane-number testing engine, the specific heat losses are lower and (for stoichiometric operation) typical CA50 at maximum IMEP are 3–8°CA after TDC. At 11.3 % DME the  $PRR_{max}$  reaches the 10 bar/°CA limit. Once the operating window was established, further experiments were performed with the lowest amount of additive that yielded stable operation – here, 10.5 % DME.

#### 11.4.2.2 Outputs and efficiencies

Figure 11-26 shows the species and energetic outputs from the engine as well as efficiencies over a wide range of equivalence ratios, from 0.5 to 12. The figure contains three groups of data points: spark ignition (SI) at lean, stoichiometric, and rich equivalence ratios, rich HCCI (with DME as an additive), and ultra-rich HCCI (with DEE). For  $0.5 < \phi < 2.1$  the engine was operated in SI mode without any additive. Figure 11-26 includes some SI operating points with a CoV exceeding the 10 % limit. In HCCI mode, DME was used as additive for  $1.5 < \phi < 2.5$ , but DEE for higher equivalence ratios, because the mass flow controller for (gaseous) DME did not allow sufficient flow rates, while the liquid DEE could be injected in higher quantities by a commercial port fuel injector.

As Figure 11-26a shows, the highest methane conversions  $X_{\text{CH}_4}$  are achieved with SI for lean to stoichiometric equivalence ratios. For very lean equivalence ratios, operation is unstable and conversion decreases because of increasing numbers of misfires. The yield  $Y$  of syngas is nearly zero. This is the conventional regime of engine operation. For  $\phi > 1$ , the methane conversion is lower, and a significant amount of syngas is produced, with the maximum in yield in SI mode at  $\phi = 1.5$ . For higher equivalence ratios, the yield is lower because of frequent misfires.

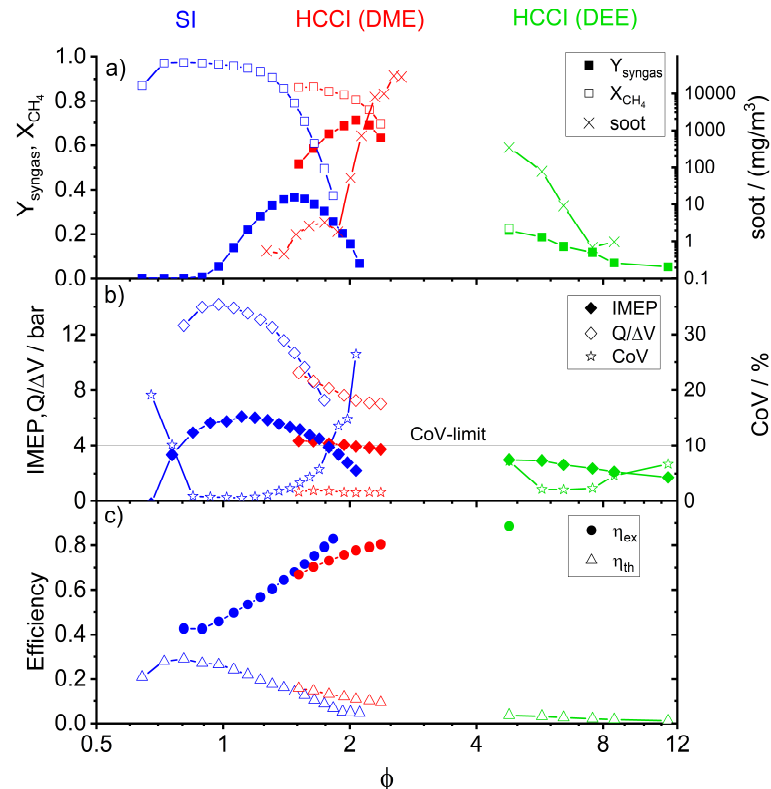


**Figure 11-26:** a) Methane conversion ( $X_{\text{CH}_4}$ ), syngas yield ( $Y_{\text{syngas}}$ ), and product-gas soot concentration (note the logarithmic scale), b) displacement-specific work (IMEP) and heat ( $-Q/\Delta V$ ) output of the engine as well as the coefficient of variation of the net IMEP (CoV), c) exergetic ( $\eta_{\text{ex}}$ ) and thermal efficiencies ( $\eta_{\text{th}}$ ), all as a function of equivalence ratio at  $\varepsilon = 10$ . Spark-ignition experiments with  $T_{\text{in}} = 323$  K, HCCI experiments with  $T_{\text{in}} = 423$  K. Data were not recorded for  $2.5 < \phi < 4$  to avoid excessive soot in the instruments. For  $\phi > 5$ , the methane fraction in the product exceeded the sensor range and therefore,  $Q$ ,  $\eta_{\text{ex}}$ ,  $Y_{\text{syn}}$ , and  $X_{\text{CH}_4}$  could not be determined. For very high CoV some of the performance metrics cannot be evaluated reliably and the corresponding data points have been suppressed.

Operating the engine in HCCI mode with additives allowed for stable operation at all equivalence ratios greater than 1.5 (see CoV in Figure 11-26b). Towards stoichiometric conditions, operation is limited by high  $\text{PRR}_{\text{max}}$ . The methane conversion is again decreasing with increasing equivalence ratio, but in this case mostly due to a lack of oxygen. For  $\phi > 1.5$  it is significantly higher than in SI mode because misfires do not occur with HCCI. In the latter mode, the maximum syngas yield is at about  $\phi = 2.1$ . Increasing the equivalence ratio further decreases the syngas yield, even though the partial oxidation of methane to syngas is stoichiometric at more fuel-rich conditions ( $\phi = 4$ , reaction (3) in Table 11-1). Like in SI mode (not shown here),

the soot concentration in the product gas is very low ( $< 10 \text{ mg/m}^3$ ) for equivalence ratios below  $\phi = 2$  but increases strongly for richer mixtures. In the range of  $2.4 < \phi < 4$  no experiments were carried out to prevent damage to the instruments, and generally operation was limited to  $\phi < 2.1$ . As the equivalence ratio increases beyond  $\phi > 4$ , decreasing soot concentrations were measured, and beyond  $\phi = 7$  soot formation becomes again insignificant. This is likely because due the high heat capacity of these ultra-rich mixtures and the low heat release, the in-cylinder temperatures are too low for soot formation. The ultra-rich regime with  $\phi > 4$  is not interesting for syngas production, because the yield is low, but at  $\phi = 7$  the product gas contains about 1.5 vol% ethylene.

Figure 11-26b shows heat and work production of the process. The maximum work and heat outputs are, as expected, at  $\phi = 1$ . As with the syngas yield (Figure 11-26a), HCCI yields better results at  $\phi > 1.5$  than SI because misfiring is avoided. The work output is positive at all investigated equivalence ratios. At  $\phi = 11.5$ , with 2 bar IMEP it is still about 30 % of the maximum at stoichiometric.

In Figure 11-26c, the thermal and exergetic efficiencies are shown. The two metrics were calculated as

$$\eta_{\text{th}} = \frac{W}{\sum_i m_i \times h_{L,i}} \quad (11-5)$$

$$\eta_{\text{ex}} = 1 - \frac{E_l}{\sum_i m_i \times e_i} \quad \text{with } E_l = T_{\text{sur}} \times S_{\text{irr}} \quad (11-6)$$

where  $h_{L,i}$  is the (specific) lower heating value and  $e_i$  is the specific chemical exergy of each hydrocarbon species  $i$  at the engine inlet. The exergy loss  $E_l$  is the product of the surrounding temperature  $T_{\text{sur}}$  and the irreversible entropy generation  $S_{\text{irr}}$ . The latter is determined from a first law and second law analysis as described in Ref. [93].

While the thermal efficiency counts only work as a useful output, the exergetic efficiency considers all outputs, in this case work, heat, and product gas. With 29 %, the thermal efficiency has its maximum at  $\phi = 0.8$  and decreases with increasing equivalence ratio. In contrast, the exergetic efficiency has its minimum value of 40 % at lean equivalence ratios and increases to over 70 % at  $\phi > 1.5$ . However, when the methane conversion is low, as it is for unstable SI operation with frequent misfires and ultra-rich HCCI, the value of the exergetic efficiency as a figure of merit of the process is limited.

Overall, if syngas is the target chemical output, a good operating strategy would be HCCI at  $\phi = 1.9$ . The syngas yield would be higher in slightly richer operation, but this is just lean enough to keep engine-out soot concentrations low. The engine runs very stably, the (indicated) work that could be used by other machinery in the plant is still half of its maximum, and the exergetic efficiency is 75 %. To put the latter number in context, [316] gives the exergetic efficiency of the commonly used methane steam reforming as 63 %. Polygeneration based on solar collectors, providing electricity, heat, cooling, and desalinated water yields exergetic efficiencies up to 32 % [347]. Other systems combining power cycles with methanol production or desalination reach efficiencies up to 60 % [348].

### 11.4.2.3 Elevated compression ratios

For a compression ratio of  $\varepsilon = 10$ , relatively large quantities of additive (over 20 mass%) are needed for stable fuel-rich HCCI operation. Higher temperatures towards the end of compression are one way of increasing the mixture reactivity with less additive. This could be achieved by increasing the compression ratio or the intake temperature, but the latter also increases heat losses and potentially the hardware costs, e.g., because more temperature-resistant materials are needed in the engine design. Figure 11-27 shows the DME mole fraction required for stable engine operation (i.e., at the CoV limit) for compression ratios from  $\varepsilon = 10$  to 19 at intake temperatures of 423 and 323 K and equivalence ratios from  $\phi = 1.2$  to 2.

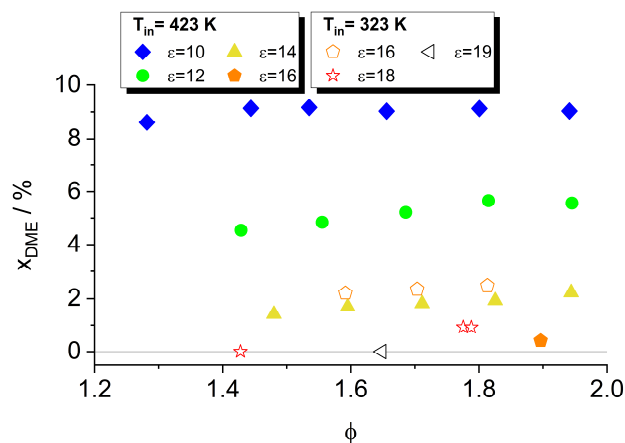


**Figure 11-27:** DME mole fraction required for stable HCCI engine operation as a function of equivalence ratio for a range of compression ratios  $\varepsilon$  and two different intake temperatures  $T_{in}$ .

Towards high equivalence ratios, excessive sooting above  $\phi = 2$  limits useful operation at all compression ratios, while high pressure-rise rates determine the limits towards lower equivalence ratios. For higher compression ratios this limit shifts to higher equivalence ratios because the cylinder volume during the reaction is smaller. There is only a weak dependency of the required DME mole fraction on equivalence ratio, but a strong one on compression ratio. For an intake temperature of 423 K, the required DME fraction decreases to less than 2 vol% at  $\varepsilon = 14$ . At  $\varepsilon = 16$  just 0.5 % DME are needed, but only at  $\phi = 1.9$  stable, low-sooting operation without excessive pressure-rise rates could be established. Lowering the intake temperature to 323 K increases the additive demand but broadens the operating envelope in terms of  $\phi$ . Increasing the compression ratio to 18 and 19 enables acceptable operation without any DME addition at  $\phi = 1.42$  and 1.64, respectively. However, without additive, the remaining control parameters are intake temperature and equivalence ratio. Adjusting the former is slow, and the latter has little authority – both are known issues in “classic” lean HCCI. It may therefore be desirable to retain combustion control via a small fraction of an effective additive. For this purpose, ozone may be a promising candidate, as work on lean HCCI [349–352] has shown.

### 11.4.3 Dry reforming: CO<sub>2</sub> conversion with methane

As a prospective application of chemical conversion in piston compressor devices, the dry reforming of methane with CO<sub>2</sub> was investigated in an RCM [303]. The dry reforming process converts a CO<sub>2</sub>/CH<sub>4</sub> mixture into syngas, according to the overall reaction (see Table 11-1)



This process offers a double benefit by both consuming CO<sub>2</sub> and creating valuable chemical species.

As in the previous applications, conversion requires high temperatures due to the low reactivity of CH<sub>4</sub> and CO<sub>2</sub>. With pure CH<sub>4</sub>/CO<sub>2</sub> mixtures, it proves difficult to reach sufficiently high temperatures by compression, as discussed in Section 11.3.3. In addition to the measures discussed above – ignition promotors, dilution by monatomic gases – adding small amounts of oxygen to allow partially exothermal reactions may be considered here. A suitable combination of these strategies allows reaching good conversion levels.

Figure 11-28 depicts simulated time histories of temperature and species during dry reforming of CH<sub>4</sub> in an RCM. Two simulation approaches were taken. One is based on detailed chemistry, the other one is assuming that the system is always in chemical equilibrium at given (time-dependent) volume and internal energy. The initial mixture contains CO<sub>2</sub>, CH<sub>4</sub>, DME as reaction promoter, and also some oxygen.

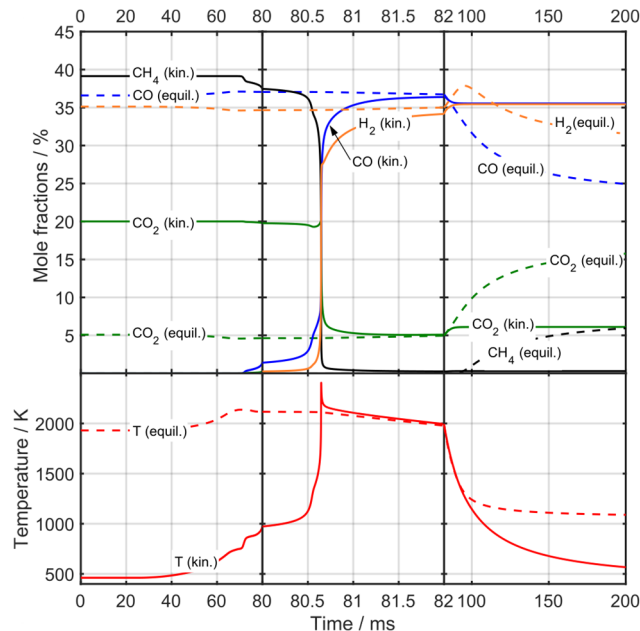


**Figure 11-28:** Simulated temporal evolution of temperature and species during dry reforming in an RCM, with detailed chemistry (solid lines) and equilibrium chemistry (dashed lines). Compression starts at about 20 ms. Note the finer scaling of the time axis between 80 and 82 ms.

Compression starts after about 20 ms, causing the initial temperature rise. Later, at about 70 ms, chemical reactions commence, and one observes an additional temperature rise due to exothermal reactions. CO<sub>2</sub> is reduced from 20 mol% to 5 mol% between 80 and 81 ms. At about

82 ms, the reactions have brought the system close to its equilibrium. If the reactions during the cool-down in the RCM were fast enough to keep the system in equilibrium, undesirable formation of  $\text{CO}_2$  would result (i.e., the rise of equilibrium  $\text{CO}_2$  after about 82 ms). Finite-rate chemistry combined with a temperature drop due to heat losses and expansion helps keeping the system in a state of high  $\text{CO}_2$  conversion.

Mathematical optimization was used to identify a suitable initial composition [303], varying the gas composition among the species Ar,  $\text{CH}_4$ , DME,  $\text{O}_2$ , and  $\text{CO}_2$ . For this, detailed chemistry simulations were carried out using an experimental volume profile from the RCM as a temporal constraint. The result is shown in Figure 11-29. For initial  $\text{CO}_2$  mole fractions between 20 and 40 %, a conversion between 40 and 50 % is predicted and is also found experimentally in the experiments. In the RCM, some argon was added to increase the temperature after compression. This could be avoided with higher starting temperatures. The optimization approach was particularly helpful here in finding conditions that would have been substantially more difficult to find empirically. This kind of conversion could be a possible approach for carbon capture and use, e.g., if the energy required for compression can be taken from surplus work from renewable energies.

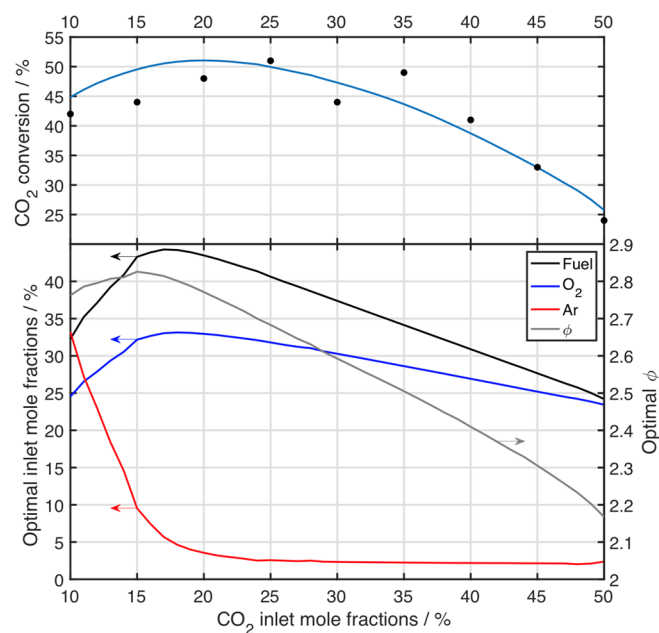


**Figure 11-29:** Dry reforming in the RCM. Results of optimization for carbon dioxide conversion as a function of different initial carbon dioxide mole fractions. The predicted conversion is compared with experimental results in the upper part of the figure. The optimal initial compositions are shown in the lower part. Adapted from Ref. [303].

## 11.5 Thermodynamic and economic assessment – a posteriori

From the previous sections it is clear that a polygeneration process in a reciprocating IC engine is feasible, and that the exergetic efficiency considering only the engine with syngas, work, and heat as outputs is good. But at least two further issues must be addressed, the influence of all additional resources needed besides the engine on the efficiency of the process, and an overall economic assessment. A combination of thermodynamic and economic analysis is often performed with methods that are summarized e.g. in Refs. [353–356]. The exergoeconomic

methods and values used here for the analysis of the polygeneration system are described in more detail in Ref. [357]. Such exergoeconomic analysis mainly facilitates comparing the economic importance of investment costs and exergy destruction and finding those parts of the process that are most crucial for cost reductions. Such an analysis was also carried out for this system, but first the thermodynamic assessment has to be favorable.

For the thermodynamic assessment, the polygeneration system is compared with separate devices producing the same output of chemicals and work. The comparison from Ref. [95] is given in Table 11-2. It shows that a polygeneration HCCI engine with a displacement of 22.6 L reaches an exergetic efficiency of 79.2 %, which is higher than that of two separate processes selected according to the best values found in literature. Considering the engine only, exergy destruction mainly is due to the irreversibilities of the chemical reaction, and due to the heat flux through the wall. But in a complete system there may be other significant exergy losses. The product, although having a high exergy, consists of a mixture, including large amounts of N<sub>2</sub>. Thus, downstream product-gas separation must also be considered, as well as upstream conditioning of the reactants. As an example, a polygeneration system producing pure H<sub>2</sub> as one of the material outputs was investigated [95]. In the model, the H<sub>2</sub> separation was obtained with a noble-metal membrane, and the heat flows as well as the energy required for the compressors were integrated into the system. Downstream of the engine, the H<sub>2</sub> yield was increased in a water-gas shift reactor with heat integration. These additional process steps reduce the exergetic efficiency by 20 %-points to a more realistic exergetic efficiency of 59.4 %. This is similar to steam methane reforming but much higher than combined heat and power generation (CHP).

**Table 11-2:** Comparison of separate processes with the engine polygeneration process. (CHP: combined heat and power generation).

Value	IC engine CHP	Steam methane reforming	HCCI engine polygeneration, engine only	HCCI engine polygeneration, whole process
Output	Work, heat	H <sub>2</sub>	Work, heat, product gas	Work, heat, H <sub>2</sub>
$\phi$	< 1	0.97	2	2
$E$	≤ 47.3 %	62.7 %	79.2 %	59.4 %
Costs	Work: 3 ct/kWh	-	-	Work: 3.4 ct/kWh
	-	H <sub>2</sub> : 1.74 €/kg	-	H <sub>2</sub> : 1.75 €/kg
Ref.	[358]	[316,359]	[360]	[360]

From an engineering point of view the process is favorable when the efficiency is high, while in practice the economics plays a crucial role: will the prices of the products be lower or at least similar to market prices? As part of an exergoeconomic analysis [357], the costs of the products were estimated using the investment costs via scaling laws, prices for methane, interest rates, lifetime of the unit, and other parameters. The resulting prices are also included in Table 11-2. The estimated prices for work are 13 % higher than from a combined heat and power (CHP) plant, while the H<sub>2</sub> costs are similar to large-scale steam methane reforming with an H<sub>2</sub> output of 9000 kg/h, even though the output of the polygeneration system is much lower with 20.4 kg/h.

The resulting prices depend on the engine size and the economic parameters. The latter, for example unit lifetime, operating hours per year, prices for fuel and electricity, as well as the investment and installation costs of the 15 main components (engine, heat exchangers, compressors, membrane, etc.) are uncertain. Many are estimated based on current market prices that fluctuate considerably. Investments costs are interpolations from earlier compilations, as discussed in Ref. [357]. To evaluate the influence of these parameters on the costs of hydrogen, electricity, steam, and heat, a global sensitivity analysis was conducted [361] with an estimated relative uncertainty of  $\pm 30\%$  [362]. A complete list of the parameters that were varied can be found in Ref. [357] (Tables 3 and A3), but in the current work the capital investment values differ, because the engine size is different. From several ten thousands of calculations with a Monte-Carlo based design, where the costs and further parameters are varied according to a probability distribution within their uncertainty ranges, a distribution of hydrogen costs is obtained. The resulting cost distributions for hydrogen and total cost rates are shown in Figure 11-30. The cost rate, which includes all outputs (hydrogen, work, and heat) shows that the hydrogen costs are about 70 % of the total costs. Thus, all outputs are important from an economic point of view. Due to nonlinear relations between the economic parameters and the resulting prices, the most probable  $H_2$  price (the mean value) is 1.9 €/kg, which is higher than the price calculated with the initially estimated prices without variation, while the price distribution ranges from 1.2 to 2.9 €/kg.

Such a sensitivity analysis with a probability distribution gives a good impression of the influence of each parameter and its uncertainties on the outcome. The first-order sensitivity coefficients agree well with the total sensitivities, indicating that higher-order sensitivities are negligible. The six highest sensitivity coefficients are listed in Table 11-3 for two different engine sizes. All other parameters influence the  $H_2$  price only to a minor degree. For the smaller engine size, the hydrogen cost is mainly sensitive to the operating hours per year, the noble-metal membrane costs, and the lifetime, while the fuel costs are less important. This changes with engines size and the higher throughput. Now the methane costs are crucial for the  $H_2$  price, followed by the membrane costs. This also indicates that to reduce the hydrogen costs, in future work alternatives to membrane separation should be considered, such as pressure-swing adsorption or membranes from lower-cost materials.

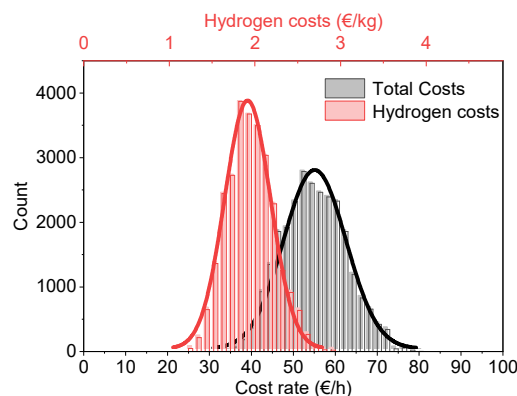


**Figure 11-30:** Distribution of the hydrogen cost rates and total cost rates in €/h for an uncertainty range of  $\pm 30\%$ . The top x-axis translates the hydrogen cost rate into specific hydrogen costs in €/kg [360].

**Table 11-3:** First-order and total sensitivity indices for the most important input parameters resulting from the sensitivity analysis of the hydrogen costs. (InC=Investment Costs).

Engine displacement	1.6 L		22.6 L	
	$S_I$	$S_T$	$S_I$	$S_T$
Fuel costs	0.076	0.072	<b>0.419</b>	<b>0.412</b>
Operating hours	<b>0.306</b>	<b>0.327</b>	0.196	0.209
InC membrane	0.249	0.252	0.162	0.164
Interest rate	0.193	0.192	0.123	0.123
Lifetime	0.124	0.128	0.079	0.082
InC engine	0.030	0.035	0.010	0.015

Also, the engine size could be further increased towards the size of large stationary engines or maritime diesel engines (sizes of 150–2000 L/cylinder are in operation today), which would probably reduce the sensitivity of the H<sub>2</sub> cost on the investments and lifetimes further. However, for some of the engines the process would have to be modified due to the lower engine speeds.

## 11.6 Conclusions and future work

### 11.6.1 Approach

The methods and knowledge of combustion science can be used successfully towards the co-generation of useful chemicals in piston engines. The coordinated interplay of thermodynamic pre-assessment followed by a preliminary kinetic investigation with known but not yet validated models gives good and relatively fast insight into whether a certain system is worth further efforts and helps identifying the challenges. Here, it was helpful to start with simple and idealized models, for example assuming an adiabatic process with a homogeneous charge, initially neglecting the effects of residual gases. Thereby it was learned that the process could in fact be thermodynamically favorable, and which initial temperatures, compression ratios, and additive concentrations should be used as an experimental starting point. But caution is warranted because of the idealizations and lack of validation for some of the models. Therefore, in a next step the kinetics on various time scales were explored and product distributions were determined. Many reaction mechanisms were mainly developed and optimized to predict ignition delay times and flame speeds, while the product formation is only relevant for certain pollutants, but not for many major species that might be useful chemicals. Thus, the mechanisms had to be expanded using the established models as basis. This new mechanism then needs to be validated and improved. Here, three experimental facilities complemented each other to provide data over a large range of temperatures and thus time scales. The flow reactor covers the longest time scales and the lowest temperatures, while the shock tube is limited in its longest reaction time but can reach any practically useful temperature. The RCM is in between. RCMs can also be considered the next step in complexity towards the application. These machines, while emulating the transient pressure and temperature of a reciprocating engine, retain certain idealizations. For instance, it is relatively easy to do RCM experiments with well-defined initial conditions with respect to mixture composition, temperature, and pressure. RCMs can therefore bridge the gap between chemical kinetics studies and reciprocating engines. In addition, these experiments can identify promising additives or operating conditions for the

production of specific species. Also, conditions with strong soot formation were identified, which in general should be avoided in reciprocating engines. However, the time until the mixture is analyzed in an RCM is relatively long and reactions continue on this timescale. In particular the slow reactions leading to soot formation may be overemphasized. Finally, even though they are much effort and, in some respect, provide less details, experiments in reciprocating engines must be performed, because many practical limitations are only seen in such experiments. Nevertheless, with the insight from the other methods, the engine experiments lead to faster success, and they can be understood in much more detail. The limits with respect to pressure rise rates, stable ignition (COV), and soot formation are best evaluated in the engine itself. This provides data not only on realistic product yields, but also on exergetic efficiency. From there, the process assessment needs to be expanded by including product separation and an overall thermodynamic and economic analysis with realistic error estimates from a global sensitivity analysis. Here, this was done via exergoeconomic modeling, since experiments on a systems level were beyond the scope of the investigation.

### 11.6.2 Main results

The initial gas composition, in particular the equivalence ratio  $\phi$ , is the most important influence on the product-gas composition. The yields of the target species, i.e.,  $\text{H}_2/\text{CO}$ ,  $\text{C}_2\text{H}_4$ , also showed a pronounced temperature dependence. Hence, favorable conditions for the production of chemicals in engines requires significant preheating. If preheating is not an option, then fuel additives can be used to promote ignition. To this end, DME (dimethylether, up to 10 % of the fuel) was used. However, to reduce the additive fraction, finding alternatives to DME as a fuel additive seems essential for the production of useful products in an engine. A promising candidate is ozone, since it does not compete with the  $\text{CH}_4$  as a carbon source and can be produced from air with relatively low energy input [15].

The conversion of methane to synthesis gas with work and heat output can be established at equivalence ratios below 2, with an engine running stably in HCCI mode without significant soot formation. The yields of small hydrocarbons are low at these conditions. Better yields of higher hydrocarbons can be achieved at higher equivalence ratios, but soot formation is a problem at equivalence ratios between 2 and 4, while increasing the equivalence ratio further restricts the methane conversion. But this could perhaps be optimized.

A comparison of experiments and simulations with different literature oxidation mechanisms for fuel-rich mixtures (from  $\phi = 2$  to  $\infty$ ) showed that these mechanisms can often predict the measured ignition delay times well, even for  $\phi = 10$ . The product formation at  $\phi = 2$  (mostly syngas) can also be predicted well by several mechanisms, but most cannot predict the product formation at  $\phi = 10$  correctly for methane and natural-gas pyrolysis. This is not surprising, because these mechanisms were developed and validated for oxidation at lean and stoichiometric conditions, and therefore often do not contain benzene and PAH formation chemistry. Thus, especially acetylene and benzene mole fractions cannot be predicted well. An exception is the mechanism of Cai and Pitsch [148] that contains sufficiently detailed benzene and PAH chemistry.

However, this mechanism can be used only for *n*-heptane as the additive because it does not contain the chemistry of ethers like DME and DEE. Therefore, the development of a mechanism

for CH<sub>4</sub>/DME mixtures (“PolyMech”) was necessary to be able to predict both IDT and product concentrations. The experimental results obtained here were used as validation targets during the development. Deficiencies of PolyMech were detected and corrected by comparisons of experimental results and simulations. After including improved rate coefficients for CH<sub>4</sub> + M = CH<sub>3</sub> + H [293] and CO + HO<sub>2</sub> = CO<sub>2</sub> + OH [276], PolyMech now seems to be useful over a wide range of equivalence ratios, including reactant mixtures with oxygenates, but is yet to be validated at stoichiometric and lean conditions. Benzene consumption reactions have to be added in the future.

A mathematical model based on timescales and entropy-production analysis was proposed for the reduction of high-dimensional reaction mechanisms. The results of local and global time scale analysis for PolyMech were used to find an optimal reduced-model dimension. Invariant sub-spaces of the linearization matrices allowed formulating the reduced model in the decomposed form (as a DEA), while entropy production was further employed to identify key reactions and to construct reliable skeletal mechanisms

Experiments in the RCM and single-zone simulations of endothermal methane pyrolysis and dry reformation of CO<sub>2</sub> with methane (forming syngas) showed that work can efficiently be used for chemical conversion. However, the efficiency strongly and nonlinearly depends on the initial and boundary conditions. This, together with the large number of relevant conditions (initial temperature, pressure, mixture composition, compression parameters like compression ratio and speed and expansion) makes finding good operation conditions difficult. A combination of experiments with numerical simulations was demonstrated that allows a systematic optimization of the process.

The exergetic efficiency of polygeneration in the IC engine reaches values of up to 79.2 %, which is very high. With upstream reactant conditioning and downstream product separation considered, the efficiency of the polygeneration decreases to a still reasonable 59.4 % and is thus similar to steam reforming and much better than heat-power cogeneration. Work and hydrogen can be provided at competitive costs if larger engines are used.

In experiments in a single-cylinder engine with a compression ratio  $\varepsilon = 10$ , stable HCCI operation with acceptable pressure-rise rates could be established for equivalence ratios in the range of  $1.5 < \phi < 12$ . Soot formation can be avoided for  $\phi < 2$  and  $\phi > 7$ . The maximum syngas yield in the soot-free regime is 69 % at  $\phi = 1.9$ . Operation at  $\phi = 7$  yielded 1.5 % ethylene in the product gas. However, energetically significant fractions of ignition-promoters like DME or DEE had to be added to the methane fuel. Increasing the compression ratio enables stable operation with much decreased additive demand. At  $\varepsilon = 18$  and 19 operation without any additive could be achieved.

Finally, an economic assessment was performed for one exemplary system. It turns out that a global sensitivity analysis is most helpful for at least two reasons: First, the most critical parameters for cost reduction are easily found. In the investigated example, besides parameters like operating hours or fuel costs, in terms of plant design it was the gas separation for which alternative methods should be investigated. Second, it is found that the most probable costs are not the same as the costs calculated with the most probable parameters, due to the nonlinear dependence between input parameters and product costs.

### 11.6.3 Open questions and future directions

Having found that this process is promising in general, future directions can be considered. On one hand, more specific questions have to be addressed that were not part of the initial investigation. On the other, a further generalization towards different gas-phase conversions seems interesting.

For example, the inhomogeneity in the engine is neglected so far, including the flow field. This can be addressed to obtain information about better engine geometries and higher yields for some conditions. Also, more complex valve timings, multiple fuel injections, or different additives appear promising. In-cylinder catalysts, e.g. porous materials in part of the combustion chamber, may reduce conversion temperatures, but would probably be transport-limited and may increase wall heat losses. Nevertheless, a more systematic investigation would be interesting. Any increase in complexity will benefit from mathematical optimizations.

The initial motivation of the work presented here on dry reforming of  $\text{CH}_4$  with  $\text{CO}_2$  was to find a process that allows storing energy via an endothermal reaction. However, since oxygen burns part of the fuel, energy is not as effectively stored as possible, despite the net conversion of  $\text{CO}_2$ . Oxygen was used in the experiments to attain higher temperatures during compression, since the RCM had a maximum compression ratio of approximately 10, and the maximum initial temperature was 462 K. These two aspects limit the maximum temperature attainable by compression work alone. For an energy storage process, future work will need to focus on whether dry reforming can be carried out without associated combustion. This probably requires more preheating or different additives.

For industrial applications upscaling will be needed. A good medium-size target may be wastewater treatment plants, where off-gases containing mostly methane and  $\text{CO}_2$  are produced and syngas products like methanol are needed for feeding the microorganisms. Also, an engine polygeneration process has been investigated for converting flare gases from off-grid oil wells into more easily transportable liquids [13]. On a larger scale, industrial syngas plants produce on the order of 100 000 standard cubic meters per hour ( $\text{ms}^3/\text{h}$ ) of dry syngas. The experimental results in Section 11.4.2 showed a syngas ( $\text{CO} + \text{H}_2$ ) output of  $1.24 \text{ ms}^3/\text{h}$  for an engine with 0.337 L displacement operating at 1 bar intake pressure and 600 rpm, while the IMEP was 4.4 bar. A more common operating condition for a large four-stroke engine would be 1500 rpm with turbocharging to an intake pressure of 3 bar. Assuming that the output of the HCCI process scales up linearly in engine speed and intake pressure, this kind of engine would produce  $27.6 \text{ ms}^3/\text{h}$  per liter of engine displacement, and 13.2 bar IMEP. Large commercially available combined heat-power plants have displacements on the order of 100 L. Thus, about 37 of such plants would be needed for 100 000  $\text{ms}^3/\text{h}$  of syngas. Some of the mechanical power output could be used for downstream gas separation, as discussed in Ref. [95]. Among the issues that will need to be addressed before practical implementation is long-term durability of the engine under such unusual operating conditions.

Beyond the conversion of hydrocarbons including biofuels, there are very different energy storage systems including nitrogen or sulfur oxides. It may be worth studying whether polygeneration in a piston engine may be favorable for some of these processes from a thermodynamic, kinetic, and finally an economic point of view.



---

## 12 Conclusion and Outlook

### 12.1 Conclusion

The starting point of this work was the question of the research group FOR 1993, whether a polygeneration process can be realized in an internal combustion engine. A polygeneration process can be a suitable method to provide work, heat, and different types of chemicals as needed. Such flexible energy conversion processes become increasingly important in the transition period to a sustainable energy system associated with an increasing use of renewable energies. Because several energy-intensive applications will struggle with electrification in the coming decades, natural gas seems to be a reasonable alternative to petroleum-based fuels. The combustion of natural gas releases much less CO<sub>2</sub> per energy unit than other fossil fuels such as coal or petroleum.

If an internal combustion engine is used to convert natural gas to base chemicals, usually high equivalence ratios, i.e., fuel-rich mixtures, are required. Consequently, the homogeneous charge compression ignition (HCCI) engine was the engine of choice for investigation. This is because spark-ignition engines are flame-speed controlled, making fuel-rich mixtures hard to ignite. Compression ignition or diesel engines, on the other hand, are usually operated in a diffusion combustion mode, which would cause excessive soot. In contrast, HCCI engines are controlled by chemical kinetics. The premixed air/fuel mixture ignites simultaneously in multiple spots at the end of the compression stroke, avoiding large composition gradients in the gas mixture. To achieve auto-ignition of natural gas or its main component methane, high temperatures are required which can lower the lifetime of the engine. This challenge can be counteracted by small amounts of more reactive additives in the natural gas mixture.

For the required flexibility of the engine, the work and heat output, as well as the exhaust gas composition, must be predictable for different operating conditions. The same applies to the prediction of the moment of auto-ignition, which is responsible for stable engine operation. The predictions can only be achieved by fast simulations, which require detailed reaction mechanisms. Reaction mechanisms from the literature are usually not validated for the uncommon conditions and fuel/additive mixtures required for the proposed polygeneration process. The systematic approach of the FOR 1993 to polygeneration in internal combustion engines was presented in chapter eleven.

In this thesis, the partial oxidation of several methane/additive mixtures was investigated experimentally to assess the general working principles of the additives with respect to the reaction onset temperature and product gas composition. The additives were selected as representatives for natural gas components, diesel surrogates, and biofuels. Experiments were performed

in a plug-flow reactor covering a wide parameter range. The experimental results were compared to simulation results using reaction mechanisms from the literature.

The modification of the plug-flow reactor was an essential part of the study and further improvements are ongoing work. The most recent reactor is designed to be operated at temperatures of up to 1400 K and pressures from 0.1 to 40 bar. To achieve such conditions, the reactor consists of a quartz tube embedded in a silicon-coated Inconel tube. The reactor is equipped with a gaseous and liquid fuel delivery system allowing the investigation of fuel mixtures with several components. High-precision Coriolis mass flow controllers are used to obtain results with relatively low uncertainties. Consequently, the reactor design allows the investigation of several fuels at engine-relevant conditions. The product gas was analyzed by time-of-flight mass spectrometry with a sample introduction via a molecular-beam sampling interface to perform fast online measurements. The new interface significantly improved the response time of the reactor. In addition to the TOF-MS, a GC/MS system was successfully implemented as a second diagnostic technique to enable a more accurate investigation of the oxidation of higher hydrocarbons. The higher accuracy is related to the ability of isomer separation and the generally different separation method compared to the TOF-MS, which does not lead to overlapping signals due to fragmentation. Fragmentation can become excessively large for higher hydrocarbons, which considerably complicates the evaluation of TOF-MS data. The repetition of experiments with both diagnostic techniques leads to similar results which adds confidence to the data, data analysis, and enables their use for the validation of reaction mechanisms.

Prior to the conversion experiments, the plug-flow assumption was validated by the dispersion model of Levenspiel [51] both experimentally and analytically. For further proof, Chemkin Pro 19.0 [43] was used to perform two-dimensional simulations including radial diffusion and heat transfer. The results did not show significant deviations from the results of plug-flow simulations. They rather showed that radial diffusion and heat conduction are fast enough to overcome the radial velocity gradients of the laminar flow, resulting in “plug flow” in terms of temperature and species mole fractions. These studies were part of a systematic characterization of the reactor and the results are used to quantify uncertainties. Unknown experimental uncertainties present a major challenge to reaction mechanism development because of the ambiguity in assigning discrepancies between experiments and simulations to the reaction mechanism or the experimental uncertainty.

To allow the comparison across all fuel/additive mixtures, experiments were performed at a pressure of 6 bar, temperatures between 473 and 973 K, and equivalence ratios of  $\phi = 2 - 20$  for all mixtures. Additional neat methane experiments were carried out at pressures up to 20 bar, which made it possible to compare the influence of pressure with the influence of additives on the conversion process. Simulations were performed and compared to the experimental results to identify suitable reaction mechanisms for specific mixtures and to analyze the chemical interaction between methane and the additives.

In the neat methane experiments, methane conversion started at temperatures of 823 K at all equivalence ratios and decreased with increasing equivalence ratio, becoming negligibly small at  $\phi \geq 10$ . At  $\phi = 2$ , the main products were synthesis gas, ethylene, and ethane with yields of up to 30 % (CO), 3.6 % (H<sub>2</sub>), 6 % (C<sub>2</sub>H<sub>4</sub>), and 2.2 % (C<sub>2</sub>H<sub>6</sub>). The highest observed H<sub>2</sub>/CO ratio was 0.3. Only very small yields of oxygenated species and propene were found. Also, considerable yields of CO<sub>2</sub> and H<sub>2</sub>O were found in the product. This observation emphasizes that

reaction enhancers are required to shift the onset of methane conversion to lower temperatures and to increase the reactivity of the mixture at higher equivalence ratios.

A common feature of all methane/additive mixtures investigated was that they significantly increased the reactivity of the mixtures but to varying degrees. While the addition of ethane and propane mainly increased the reactivity at higher temperatures and had no effect on the reaction onset temperature, the addition of dimethyl ether or *n*-heptane shifted the start of methane conversion to 200 – 250 K lower temperatures. The latter is caused by the pronounced low-temperature chemistry of both fuels. It was shown by reaction pathway analyses that low temperatures favor the formation of several hydroperoxides whose formation and decomposition leads to the release of OH radicals. In particular, *n*-heptane undergoes H-abstraction to form heptyl radicals ( $C_7H_{15} = R$ ) which either react with oxygen to form heptylperoxy radicals (ROO) or react with small radicals to form heptyl hydroperoxides (ROOH) at relatively low temperature. While ROOH's easily decompose and release OH radicals, the ROO radicals isomerize to hydroperoxyheptyl (QOOH) radicals. A second addition to  $O_2$  yields hydroperoxy-heptylperoxy radicals (OOQOOH) which either decompose to several products or react to C<sub>7</sub>-ketohydroperoxides (C<sub>7</sub>-KET). Both the formation and decomposition of ketohydroperoxides release OH radicals, significantly increasing the reactivity of the mixture and initiating methane conversion via  $CH_4 + OH = CH_3 + H_2O$ . The oxidation of DME was shown to occur via the same working principle as for *n*-heptane, i.e.:  $Fuel \rightarrow R \rightarrow ROO \rightarrow QOOH \rightarrow OOQOOH \rightarrow C_2-KET$ . Consequently, it can be assumed that this reaction sequence is similar for fuels with a pronounced low-temperature chemistry and responsible for the reaction onset of methane at lower temperatures. Although propane, present in the natural gas mixture, also has a low-temperature chemistry, such behavior was not found under the conditions investigated in this study. This is due to a much lower reactivity compared to large *n*-alkanes so that high fuel concentrations would be required to observe low-temperature oxidation of propane [363]. Nevertheless, the addition of ethane and propane was most effective in increasing methane conversion at high equivalence ratios. For example, a conversion of more than 10 % could be achieved at  $\phi = 20$  and 973 K if 10 % of methane were replaced by ethane and propane (9 % ethane, 1 % propane) compared to  $\leq 6$  % conversion in the case of 5 % fuel replacement by DME or *n*-heptane. A higher amount of DME (10 % of the fuel) even resulted in negative methane conversion at  $\phi = 20$  and  $T \geq 873$  K. Reaction path analyses revealed methane producing pathways and a rapid consumption of oxygen by the more reactive additive to be the major reasons for the decreased methane conversion. Similar behavior was found for the methane/*n*-heptane mixtures.

Regarding the influence of the additives on product formation, it was shown by reaction path analyses and single fuel experiments that it mainly depends on the extent of released radicals and the chemical interaction between the intermediates formed during the oxidation of methane and the respective additive. In general, there are two major mechanisms of a positive interaction: First, the conversion of the additive releases many OH radicals at low temperature initiating methane conversion while the reactivity of the mixture is still too low to favor the oxidation pathways towards CO and CO<sub>2</sub>. For example, for the 10 % natural gas/DME mixture at  $\phi = 10$  and  $T = 623$  K or the *n*-heptane mixtures at  $2 \leq \phi \leq 8$  and  $T = 623$  K, the contribution of methane to the formation of oxygenated species such as methanol and formaldehyde can be significantly high. Maximum yields of up to 2.9 % and 3.5 % were observed for methanol and formaldehyde, respectively. Second, the additive releases radicals initiating methane

conversion while the temperature is high and the remaining amount of oxygen low so that oxidation pathways towards CO and CO<sub>2</sub> are suppressed and C-C coupling reactions are favored, e.g., the recombination of CH<sub>3</sub> radicals to ethane. This was shown for the methane/*n*-heptane mixtures at high equivalence ratios ( $\phi \geq 10$ ) and high temperatures ( $T > 800$  K) by an enhanced formation of C<sub>2</sub> and C<sub>3</sub> species. In addition to these rules of thumb, the degree and type of interaction always depend on the intermediates formed during the oxidation of the additive. In the methane/*n*-heptane mixture, for example, the C<sub>2</sub>H<sub>5</sub> radical, which was shown to be mainly produced during *n*-heptane oxidation, leads to the increased formation of C<sub>3</sub> species by reaction with CH<sub>3</sub> radicals from methane oxidation.

In contrast, it was also shown that some products were nearly exclusively produced from the additive, e.g., ethylene and propene in natural gas mixtures. However, considerable yields of both species were observed in these mixtures. Assuming the sole formation of these species from their respective alkane, maximum yields of up to 80 % for ethylene and 50 % for propene were found at  $\phi = 10$ . Regarding synthesis gas, it could be shown that the additive can help to increase the H<sub>2</sub>/CO ratio to some extent with the largest range of 0.1 – 1.3 being found in natural gas mixtures.

Comparing the influence of the additives with the influence of pressure there are two main conclusions. On the one hand, the pressure increase to 20 bar resulted in a similar increase of methane conversion at high equivalence ratios as found for the natural gas mixture. On the other hand, the pressure increase is less effective in increasing the yields of interesting products other than synthesis gas, especially CO, and lowering the reaction onset temperature of methane. In particular, the reaction onset temperature could be lowered by  $\sim 150$  K if the pressure is increased to 20 bar compared to the 6 bar measurements.

The results show that it is still a challenge to derive general rules for suitable conditions for the formation of target species for specific methane/additive mixtures. Thus, reaction mechanisms validated for polygeneration-relevant conditions are of special interest as they can be used in simulations to predict promising conditions. A new reaction mechanism, called PolyMech [19], was developed by Sylvia Porras based on the input of several groups of the research unit covering C<sub>1</sub> – C<sub>3</sub> chemistry including DME and ethanol. The detailed flow reactor data obtained in this thesis have contributed significantly to its development. The reaction mechanism was shown to predict ignition delay times of CH<sub>4</sub>/DME mixtures obtained by rapid-compression-machine (RCM) and shock-tube (ST) experiments, and species profiles obtained by RCM, ST, and flow reactor experiments in good agreement with the experiments. But, deviations were observed for benzene and C<sub>2</sub> species for the shock-tube conditions. Consequently, the reaction mechanism was further modified based on experimental results obtained for methane/ethane/propane/DME mixtures by complementary shock-tube and flow-reactor experiments and sensitivity analyses using the original version. The reaction mechanism was also extended by a benzene and small PAH sub-mechanism to allow the prediction of soot precursors. The accurate prediction of soot precursors is essential for later applications in an HCCI engine to avoid probable sooting conditions. The modified mechanism predicted the experimental data well including species such as benzene, acetylene, and naphthalene observed in the shock-tube experiments.

During the conversion experiments, evidence of a negative temperature coefficient (NTC) region of methane under fuel-rich ( $\phi \geq 8$ ) conditions was observed. This phenomenon has rarely

been observed experimentally, even in the literature, and has never been systematically investigated. This was done as part of this thesis focusing on the influence of pressure and equivalence ratio on this behavior, usually observed for higher alkanes. It was shown that methane exhibits a distinct NTC behavior at  $\phi = 10$  and  $p = 10$  bar and  $\phi = 20$  and pressures from 10 to 15 bar. While these conditions seem of little practical relevance at first glance, they do occur in HCCI engines if the ignition timing is controlled by intermediate compressions or sequential fuel injections. Under these conditions, reduced methane conversion in its NTC region influences the ignition behavior of the main ignition. Utilizing several reaction mechanisms from the literature in addition to the PolyMech showed that only a few reaction mechanisms can predict this phenomenon. The PolyMech, which was explicitly validated for these conditions, showed the best agreement. Reaction path analyses performed with the PolyMech revealed the competition between recombination and oxidation pathways of  $\text{CH}_3$  radicals to be the major reason for this phenomenon. A second contributor are  $\text{CH}_3$ -consuming pathways at intermediate temperatures producing methane.

In summary, this thesis presents a first approach to elucidate general working principles of additives which are of special interest in terms of polygeneration processes in HCCI engines. The influence of different additives on the conversion process was investigated and analyzed by experiments and simulations using suitable reaction mechanisms from the literature. In this context, suggestions for model improvements were made. The huge dataset obtained can be used for future validation and development of both available and new reaction mechanisms. In addition, the PolyMech reaction mechanism developed in the research unit FOR 1993 was successfully modified. It allows the prediction of fuel-rich natural gas/DME conversion processes under engine-relevant conditions.

## 12.2 Outlook

The results showed that both high pressures and the use of additives can significantly increase the reactivity of natural gas mixtures. In contrast, high amounts of reactive additives can also lead to rapid consumption of oxygen so that the methane conversion decreases. The new experimental setup could be used to investigate methane/additive mixtures at high pressures using only a small amount of additive. Low-temperature oxidation of methane due to radicals provided by the additive could lead to an enhanced formation of low-temperature species at high equivalence ratios, e.g., oxygenated species such as methanol or formaldehyde. Prior to the experiments, the modified PolyMech reaction mechanism could be used to determine the optimum amount of additive with respect to the formation of target species or the reaction onset temperature.

To overcome the challenge of rapid oxygen consumption by carbon-based additives completely, ozone seems to be a promising alternative. A recent study by Schröder et al. [15] already showed that ozone is a suitable additive for fuel-rich HCCI processes. Ozone can be easily produced from oxygen by corona discharge. To allow ozone experiments with the flow reactor it was equipped with an ozone generator. Preliminary results of the partial oxidation of methane/ozone and natural gas/ozone mixtures show that ozone starts to decompose at temperatures around 450 K at a pressure of 4 bar yielding O radicals that react with methane or natural gas. Using the TOF-MS, large signals of hydroperoxides and oxygenated species like methanol

and formaldehyde were found. In this preliminary study, only 350 ppm ozone was introduced into the reactor. It is expected that higher ozone amounts and/or higher pressures will result in higher methane conversion and high yields of methanol and formaldehyde at very low temperatures. The obtained results can further be used for the validation or development of ozone sub-mechanisms. These mechanisms are of great interest in the context of controlling HCCI operation.

In addition, the pyrolysis or partial oxidation of natural gas mixtures at  $\phi > 20$  could be interesting in terms of energy storage. In this thesis, it was shown that considerable yields of ethylene and propene can be produced by the fuel-rich oxidation of ethane and propane, respectively. High yields can be interesting with respect to energy storage as the enthalpies of formation of the unsaturated hydrocarbons are much higher than the enthalpies of the saturated ones. The experimental setup could be used to perform experiments at temperatures of up to 1400 K in combination with pressures of up to 40 bar.

---

# Appendix

## A Supplementary material for chapter 8

### Additional validation with RCM experimental data

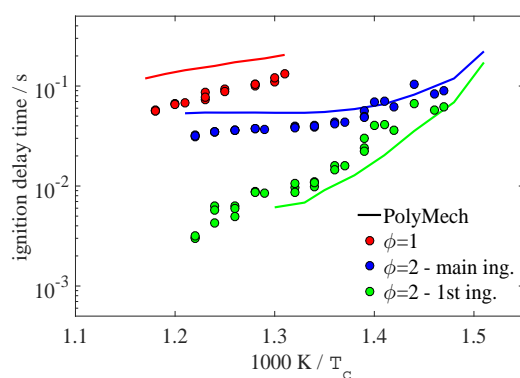


**Figure A-1:** Ignition delay times measured in the RCM (symbols) and simulations (straight lines) for mixtures 1 – 2.

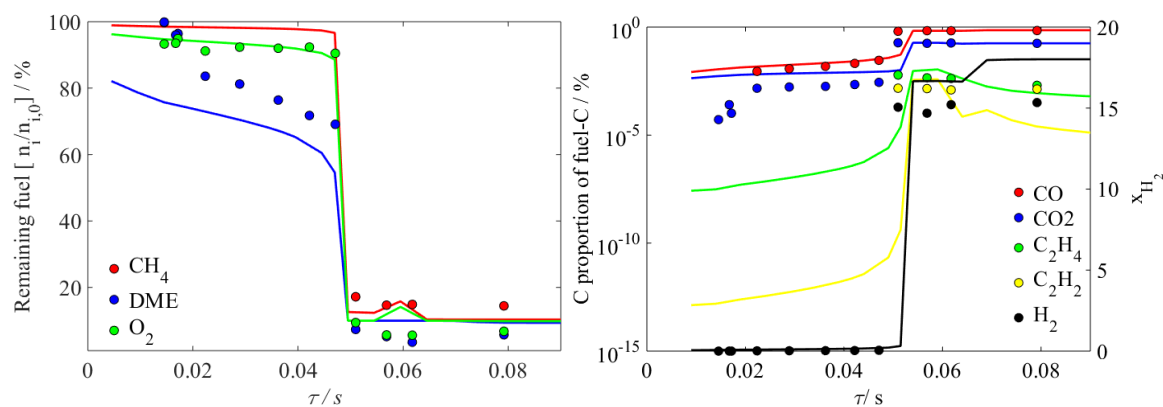


**Figure A-2:** Species time profiles measured in a RCEM (symbols) and simulations (straight lines) for mixture 14.

## Additional validation with shock tube experimental data

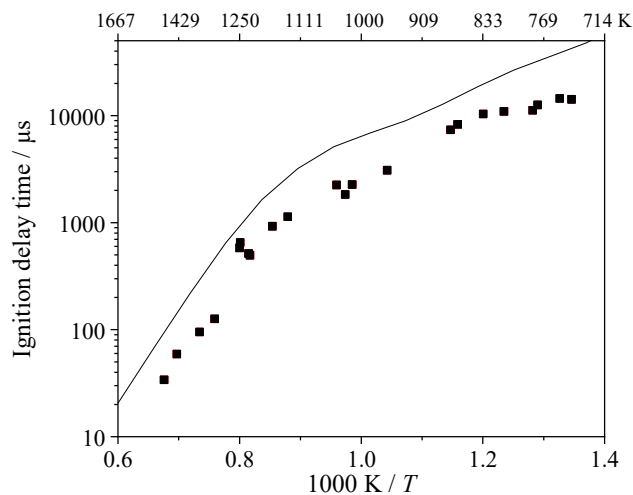


**Figure A-3:** Measured (symbols) and simulated (lines) ignition delay times of a  $\text{CH}_4/\text{DME}/\text{air}$  mixture ( $\phi = 2$ ) at 30 bar with  $[\text{CH}_4]/[\text{DME}] = 19/1$ .

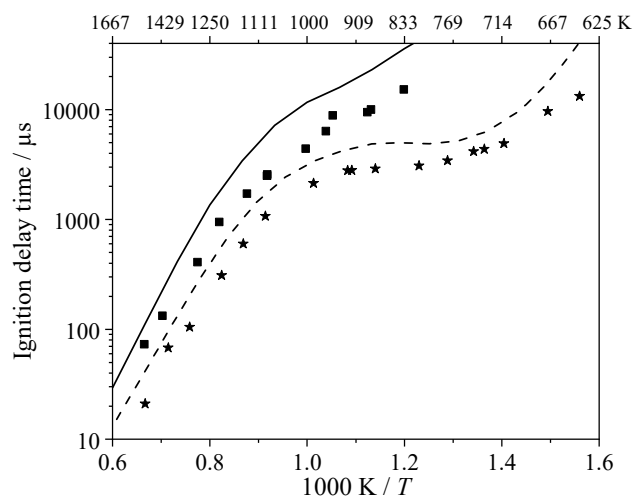


**Figure A-4:** Measured and calculated ignition delay times of  $\text{CH}_4/\text{DME}/\text{air}$  mixtures ( $\phi = 2$ ) at 20 bar. Black squares: Experiments with  $[\text{CH}_4]/[\text{DME}] = 19/1$ , black stars: Experiments with  $[\text{CH}_4]/[\text{DME}] = 4/1$ . Solid lines: Simulations with  $[\text{CH}_4]/[\text{DME}] = 19/1$ , dashed lines: Simulations with  $[\text{CH}_4]/[\text{DME}] = 4/1$ .

Additional validation with flow reactor experimental data

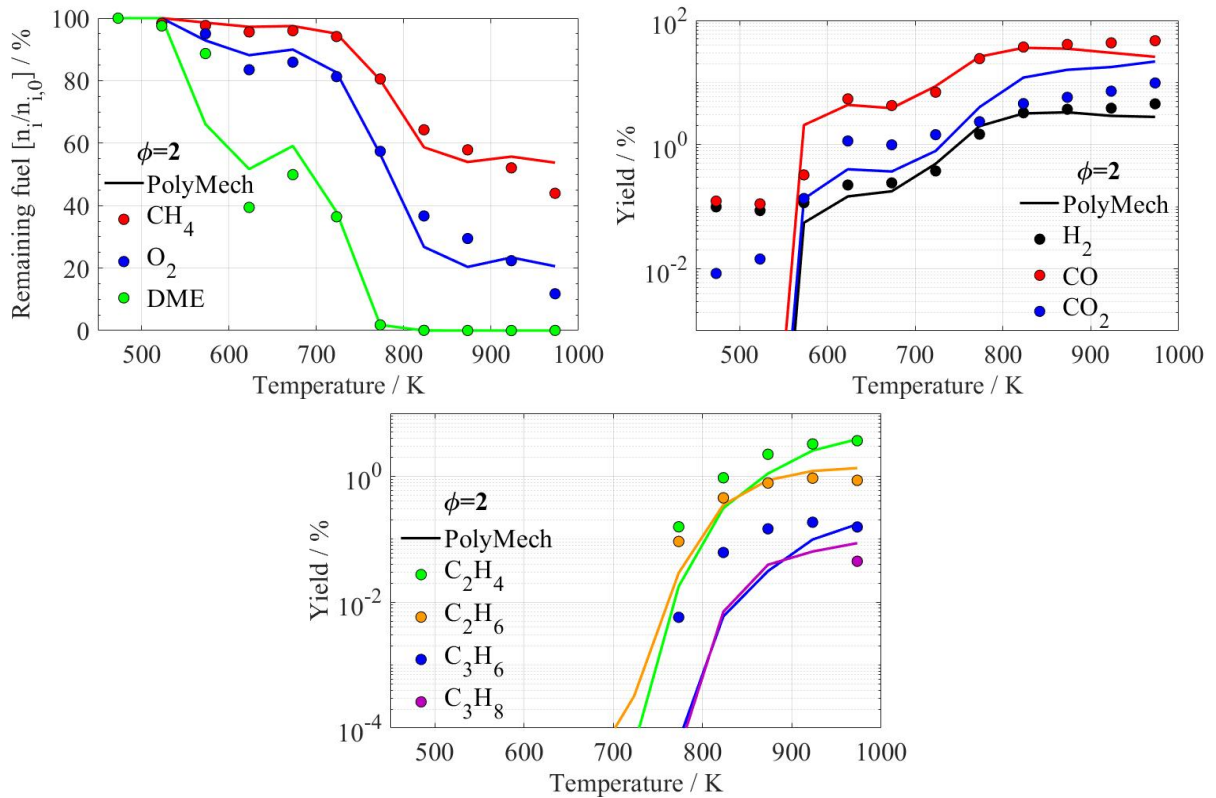


**Figure A-5:** Species profiles measured in a flow reactor for mixtures at  $\phi = 2$  and fuel composition: 10:90 DME/CH<sub>4</sub>.

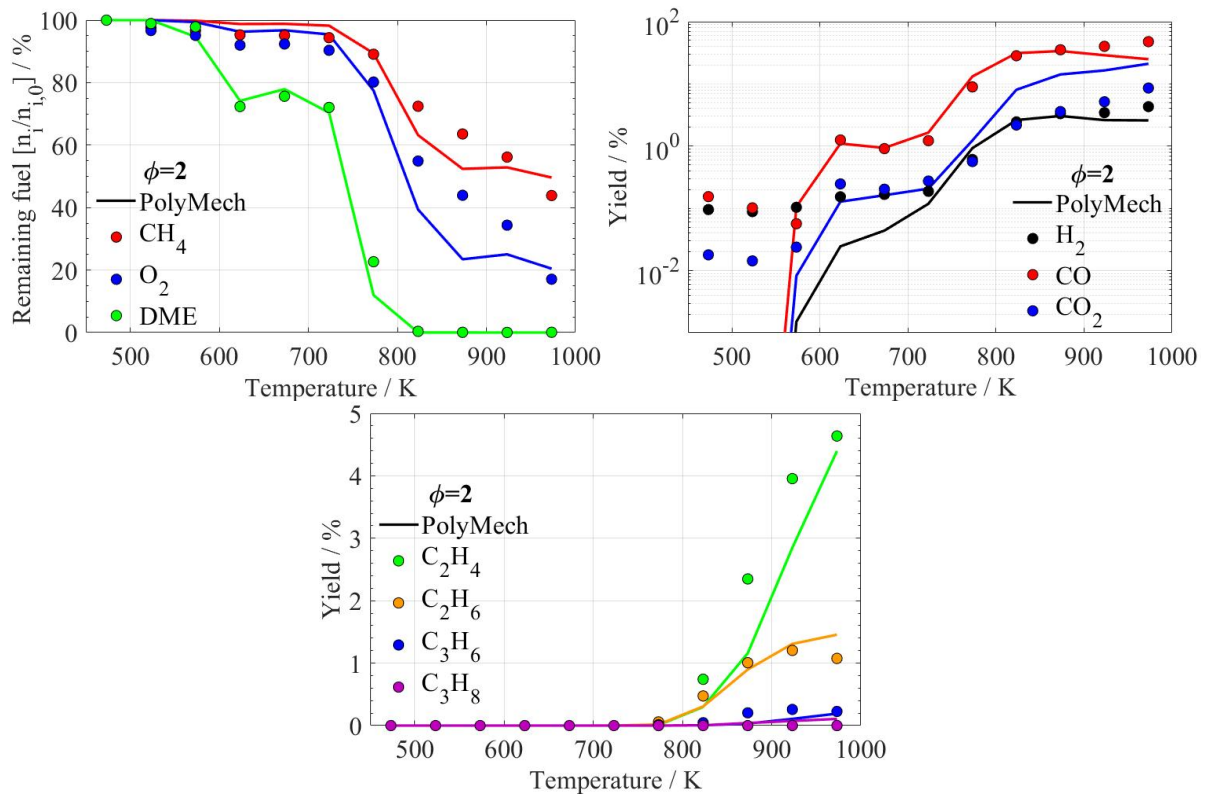


**Figure A-6:** Species profiles measured in a flow reactor for mixtures at  $\phi = 2$  and fuel composition: 5:95 DME/CH<sub>4</sub>.

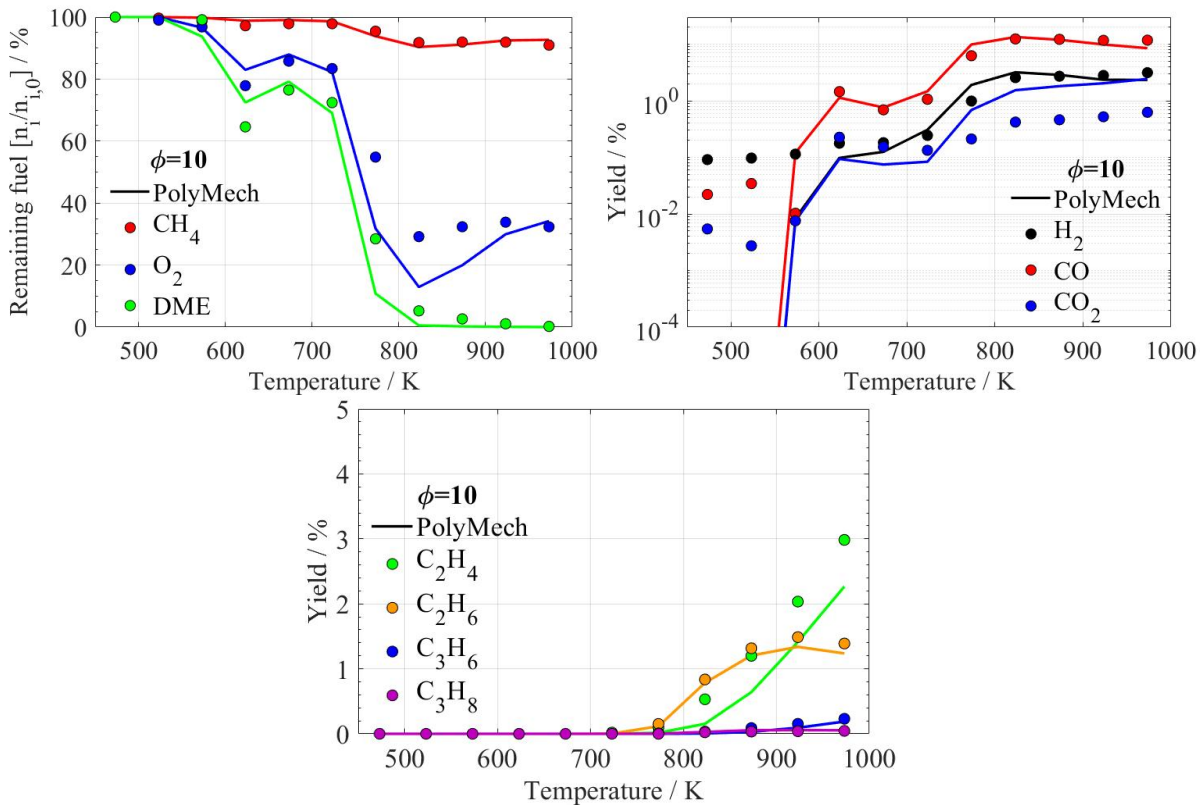


**Figure A-7:** Species profiles measured in a flow reactor for mixtures at  $\phi = 10$  and fuel composition: 5:95 DME/ $\text{CH}_4$ .

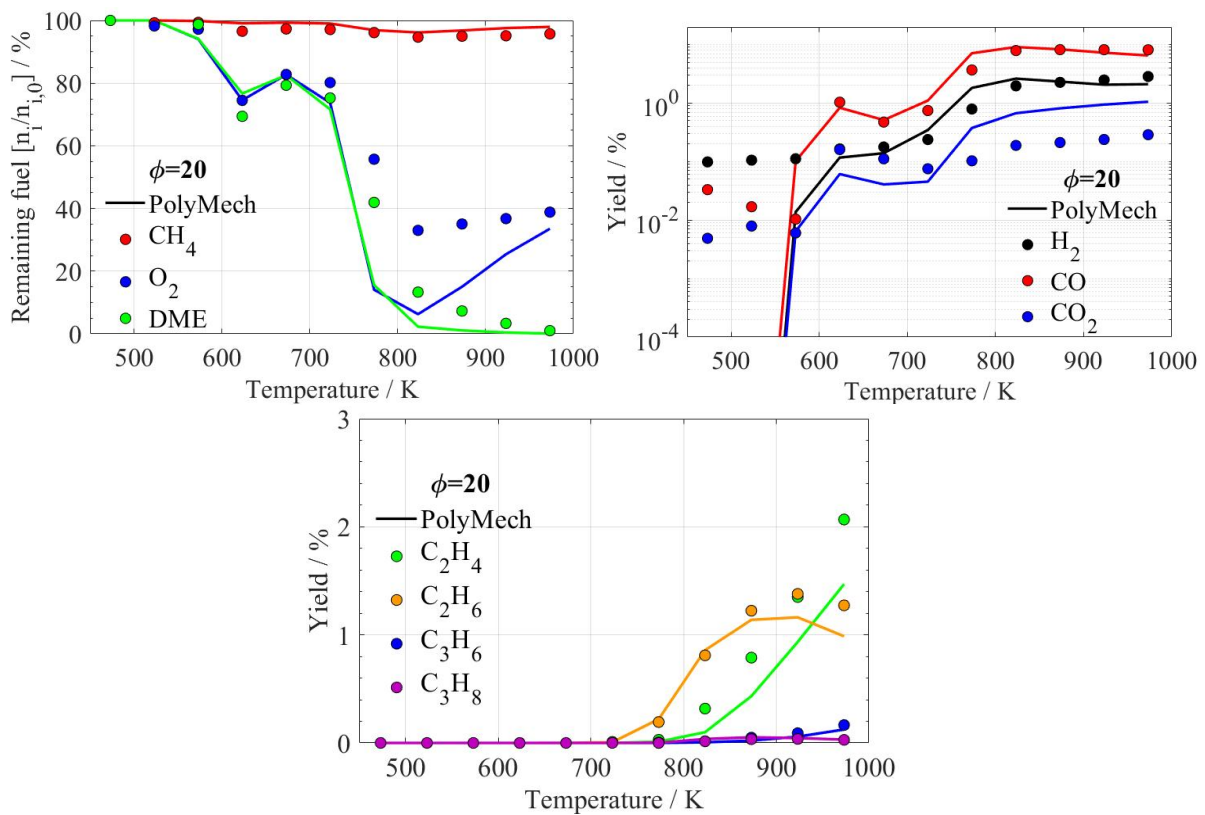


**Figure A-8:** Species profiles measured in a flow reactor for mixtures at  $\phi = 20$  and fuel composition: 5:95 DME/ $\text{CH}_4$ .

## Validation with experimental data from other authors

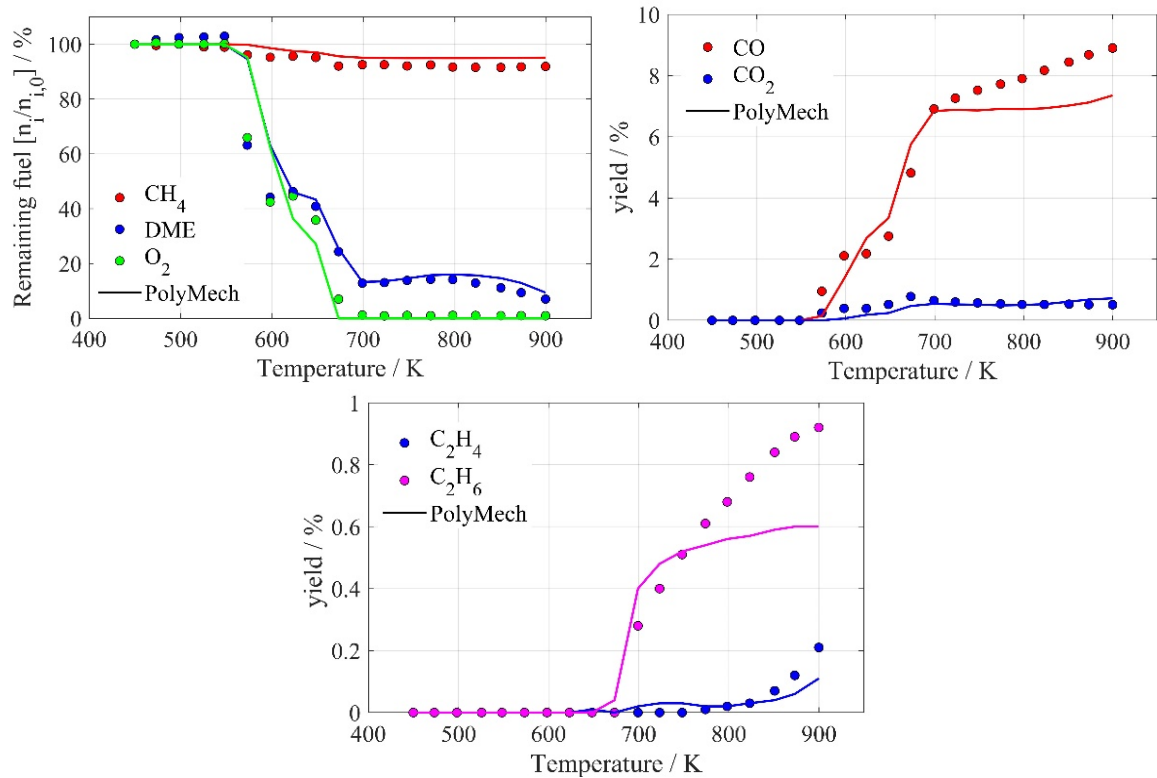


**Figure A-9:** Species profiles measured in a flow reactor for DME/CH<sub>4</sub> mixtures at  $\phi = 20$  and 100 bar. The inlet composition was 16470 ppm methane, 530 ppm DME and 1736 ppm oxygen all diluted in N<sub>2</sub>. Experimental data from Hashemi et al [186].



## B Supplementary material for chapter 9

### B.1 Plug-flow reactor

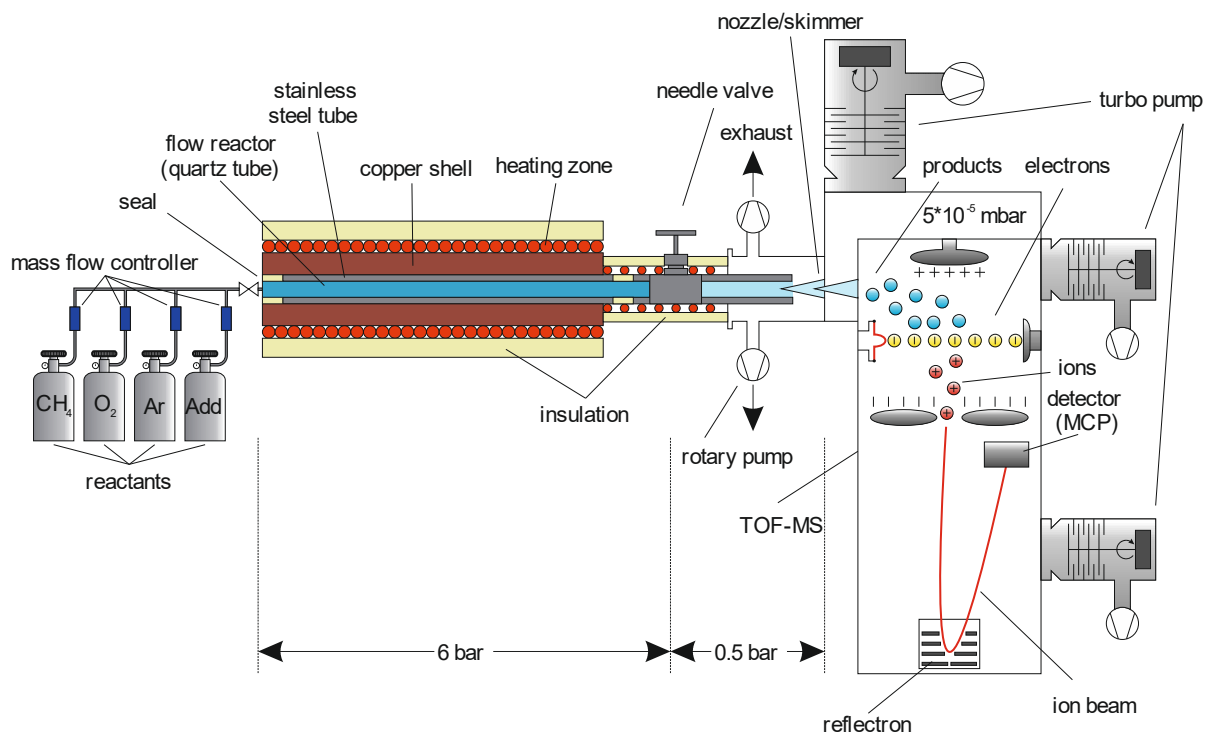


Figure B-1: Plug-flow reactor and time-of-flight mass spectrometer.

### B.2 Shear-flow simulations

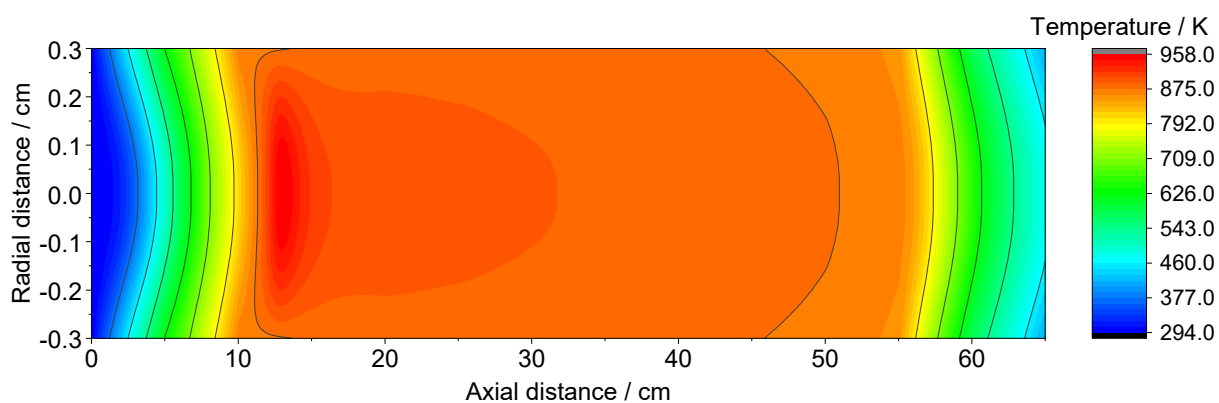
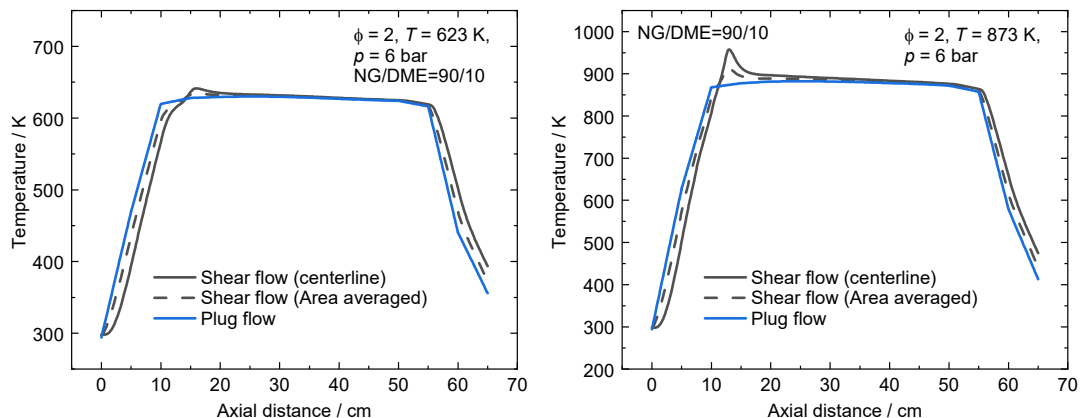
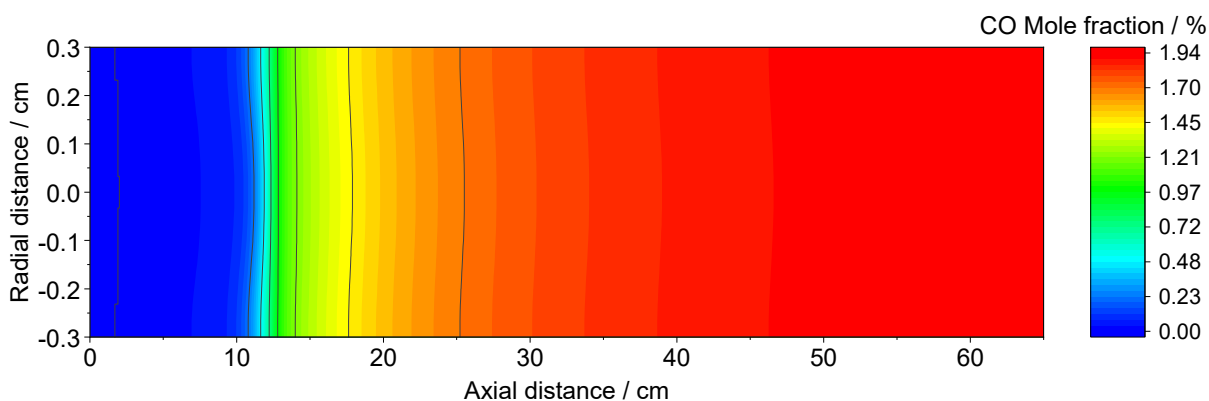


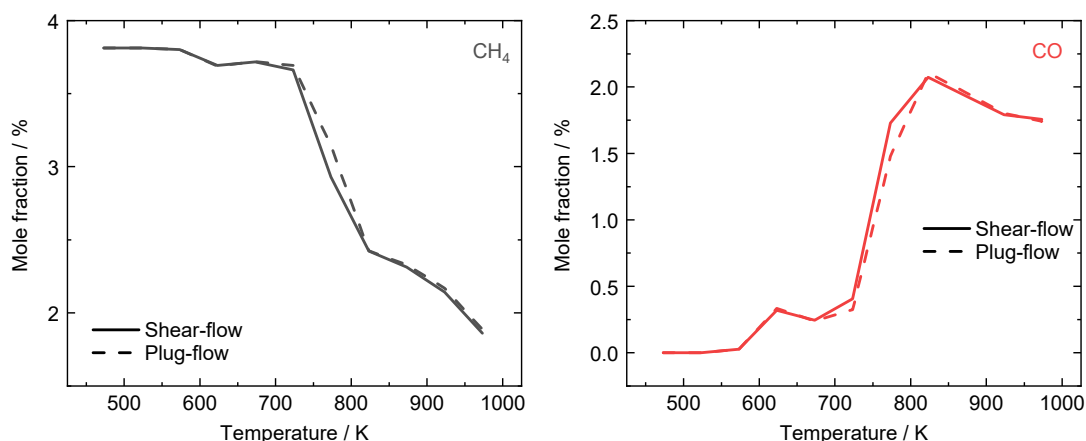
Figure B-2: Temperature distribution as a function of radial and axial distance for the NG/DME=90/10 mixture at  $\phi = 2$ ,  $p = 6$  bar and  $T_{\text{set}} = 873$  K. Simulated using the Poly-Mech1.0 [19].

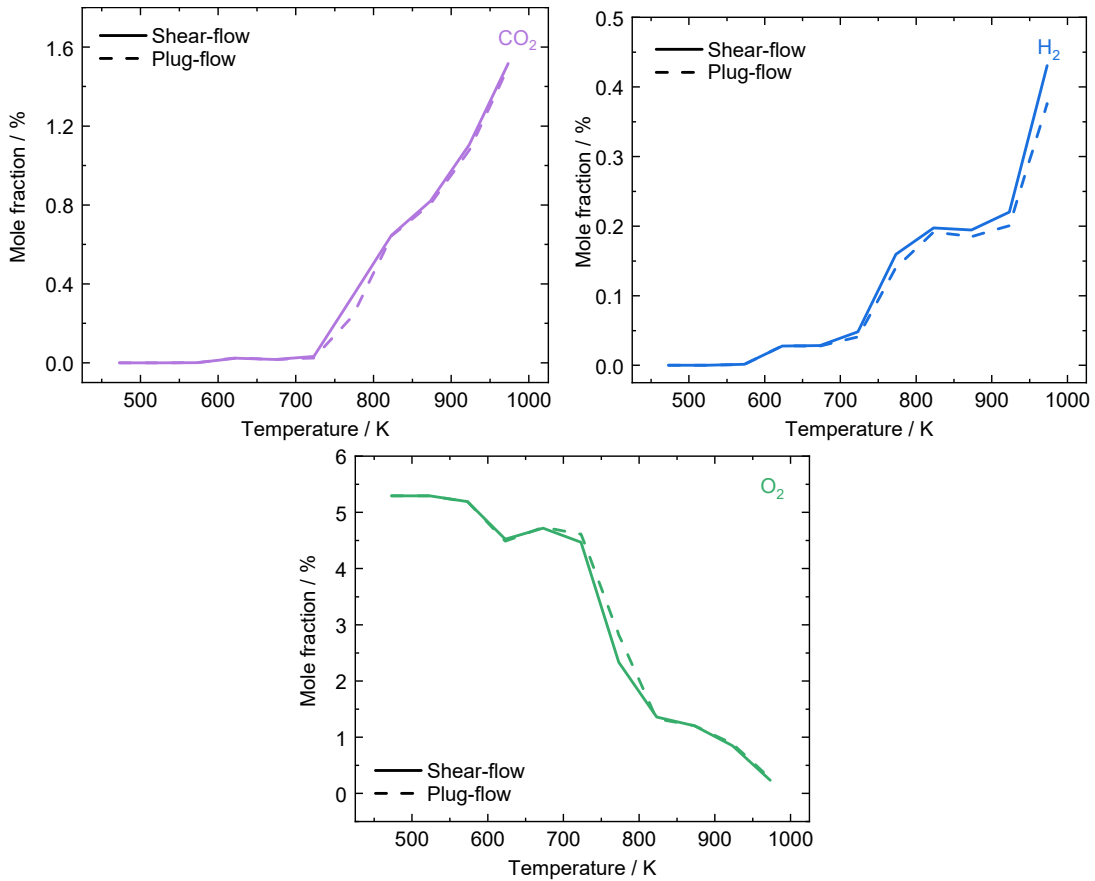


**Figure B-3:** Comparison of simulated temperature profiles using the 1-D plug-flow and 2-D shear-flow approach of ChemKin Pro 19.0 [43] and the PolyMech1.0 [19]. At set temperatures of 623 K and 873 K temperature rises of  $\approx 13$  K and  $\approx 84$  K were found for the NG/DME=90/10 mixture at  $\phi = 2$  and  $p = 6$  bar, respectively.



**Figure B-4:** CO mole fraction as a function of radial and axial distance for the NG/DME=90/10 mixture at  $\phi = 2$  and  $p = 6$  bar and  $T_{\text{set}} = 873$  K. Simulated using the PolyMech1.0 [19]. The CO mole fraction deviates only 1.3 % from the mole fraction obtained in the plug-flow simulation.

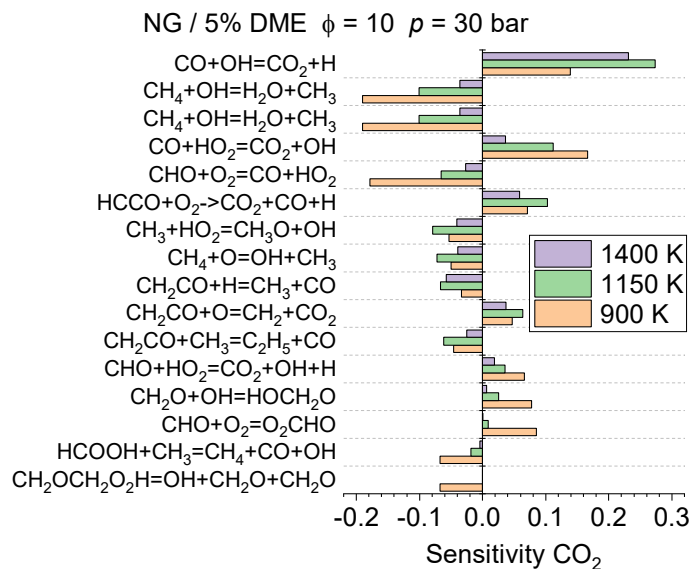




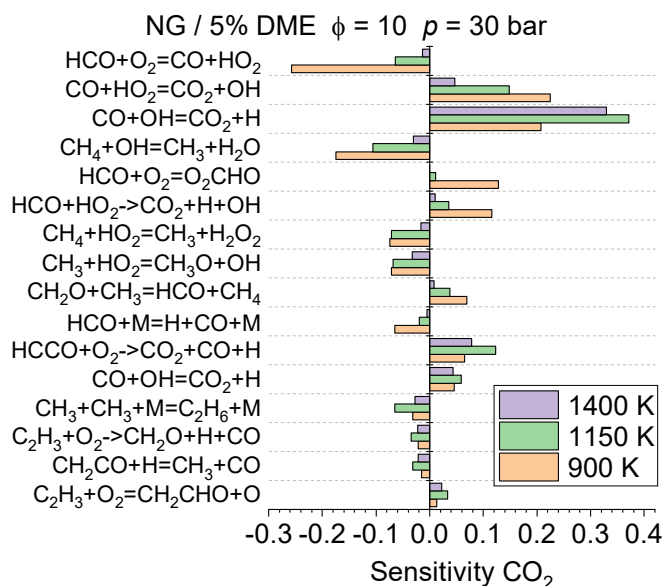
**Figure B-5:** Comparison of simulated mole fractions as a function of temperature for the NG/DME=90/10 mixture at  $\phi = 2$  and  $p = 6$  bar using the 1D plug-flow and 2D shear-flow approach of ChemKin Pro 19.0 [43] and the PolyMech1.0 [19].

### B.3 Additional sensitivity analyses

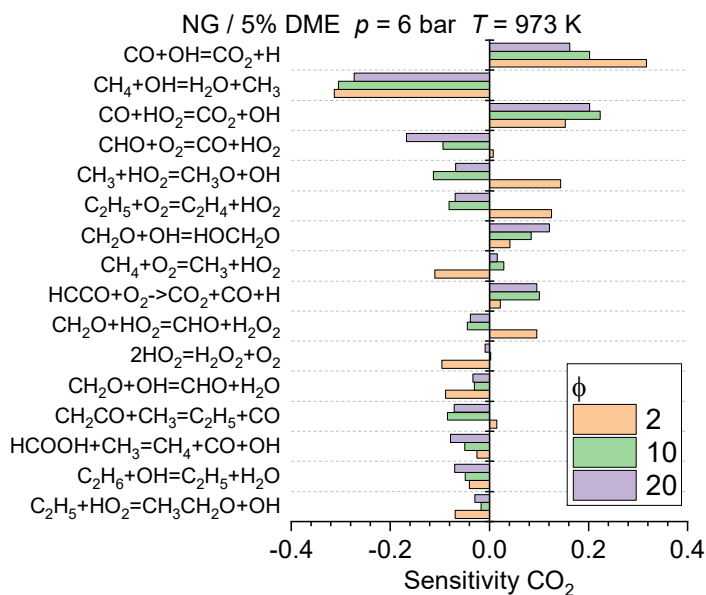
#### B.3.1 CO<sub>2</sub>



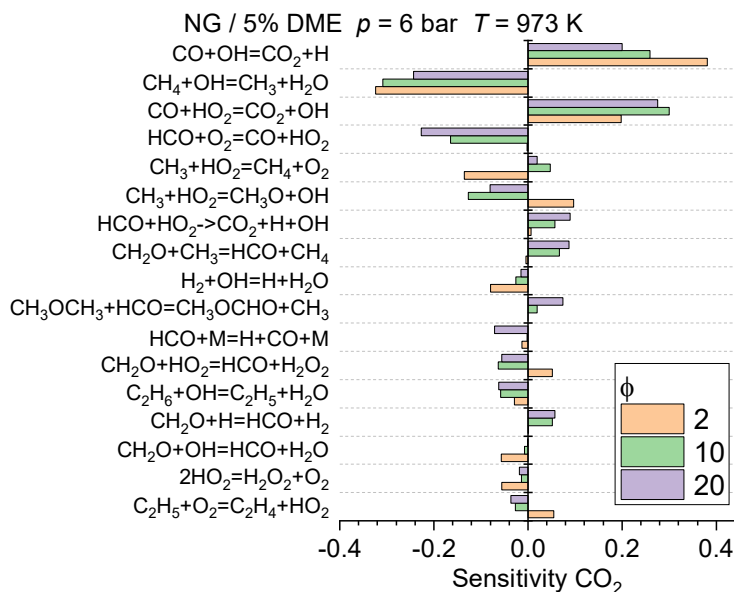
**Figure B-6:** Sensitivity coefficients of CO<sub>2</sub> mole fraction for selected shock-tube conditions (NG/DME=95/5 mixture at  $\phi = 10$  and  $p = 30$  bar) using the PolyMech2.0.



**Figure B-7:** Sensitivity coefficients of CO<sub>2</sub> mole fraction for selected shock-tube conditions (NG/DME=95/5 mixture at  $\phi = 10$  and  $p = 30$  bar) using the AramcoMech3.0 [124].

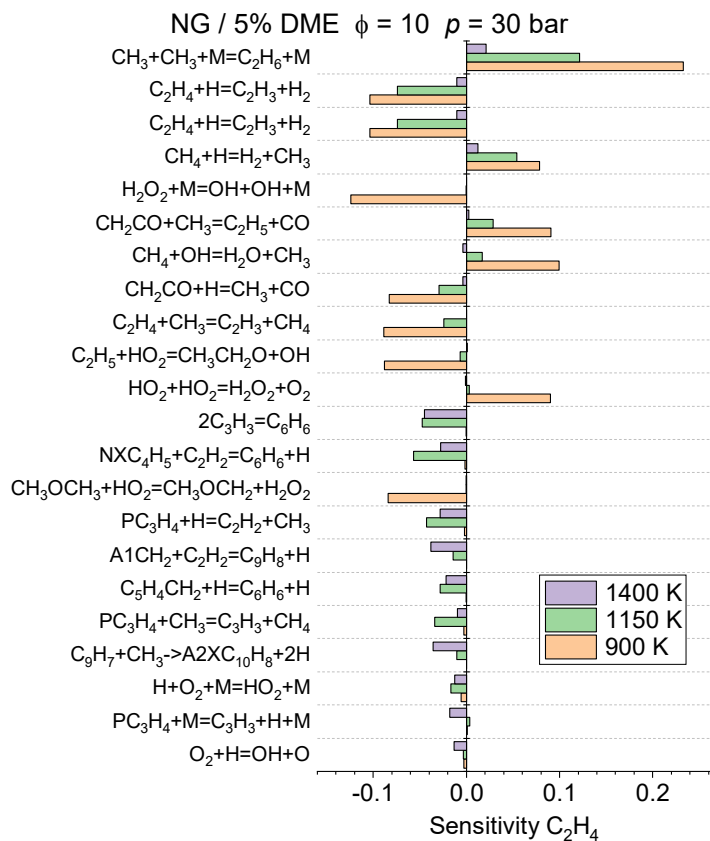


**Figure B-8:** Sensitivity coefficients of CO<sub>2</sub> mole fraction for selected plug-flow conditions (NG/DME=95/5 mixture at  $T = 973$  K and  $p = 6$  bar) using the PolyMech2.0.

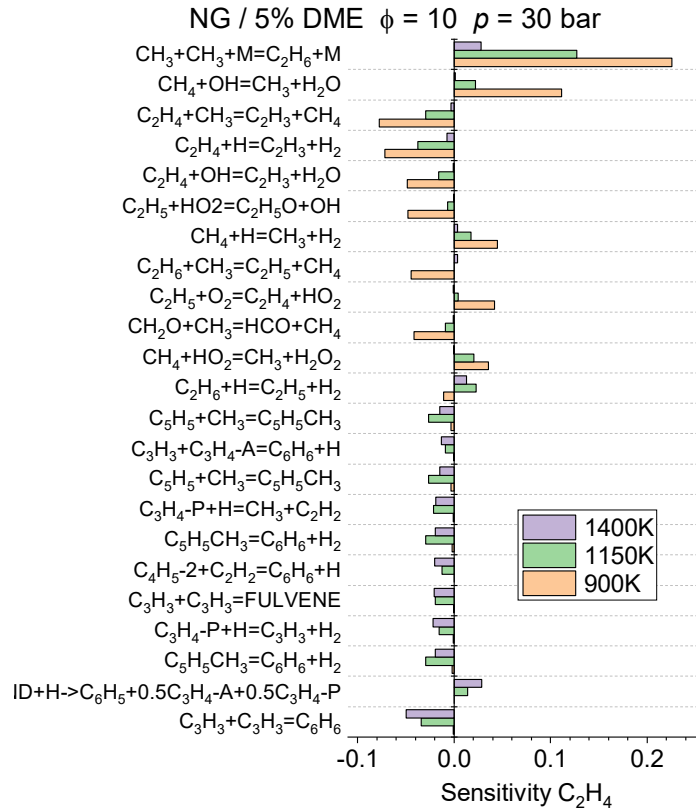


**Figure B-9:** Sensitivity coefficients of CO<sub>2</sub> mole fraction for selected plug-flow conditions (NG/DME=95/5 mixture at  $T = 973$  K and  $p = 6$  bar) using the AramcoMech3.0 [124].

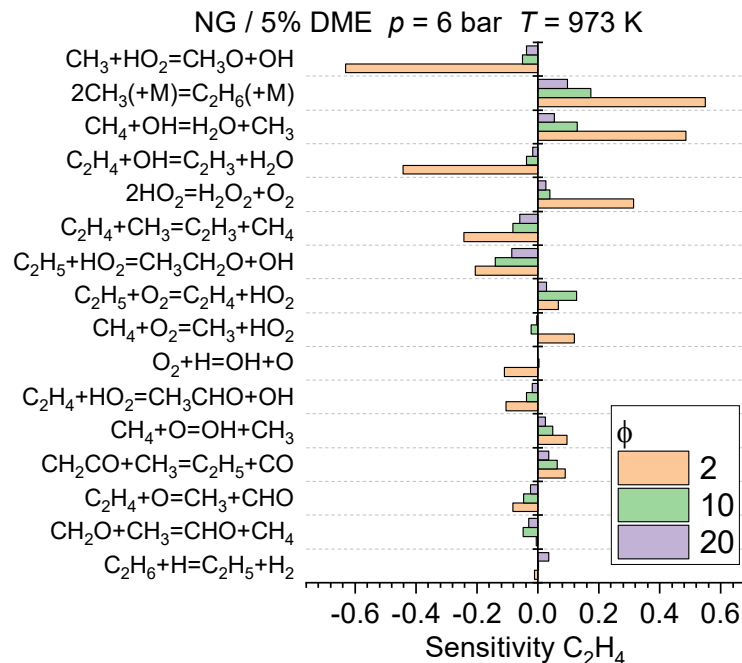
The sensitivities for CO<sub>2</sub> are very similar for both mechanisms (PolyMech2.0 and AramcoMech3.0). This applies for both the shock-tube and the plug-flow conditions. The most sensitive reactions for CO<sub>2</sub> production are  $\text{CO} + \text{OH} \rightleftharpoons \text{CO}_2 + \text{H}$  and  $\text{CO} + \text{HO}_2 \rightleftharpoons \text{CO}_2 + \text{OH}$  whereas  $\text{CH}_4 + \text{OH} \rightleftharpoons \text{CH}_3 + \text{H}_2\text{O}$  and  $\text{CO} + \text{HO}_2 \rightleftharpoons \text{HCO} + \text{O}_2$  decrease CO<sub>2</sub> production. Comparing the sensitivities for the PolyMech2.0 and PolyMech1.0 [19] (Figure 9-1) the much less important influence of the CO<sub>2</sub> production by  $\text{CO} + \text{HO}_2 \rightleftharpoons \text{CO}_2 + \text{OH}$  by the lower rate constant for this reaction is obvious: the CO<sub>2</sub> production by  $\text{CO} + \text{OH} \rightleftharpoons \text{CO}_2 + \text{H}$  is now more sensitive whereas for the PolyMech1.0 the  $\text{CO} + \text{HO}_2 \rightleftharpoons \text{CO}_2 + \text{OH}$  reaction is by far the most sensitive CO<sub>2</sub> production channel.

B.3.2 C<sub>2</sub>H<sub>4</sub>

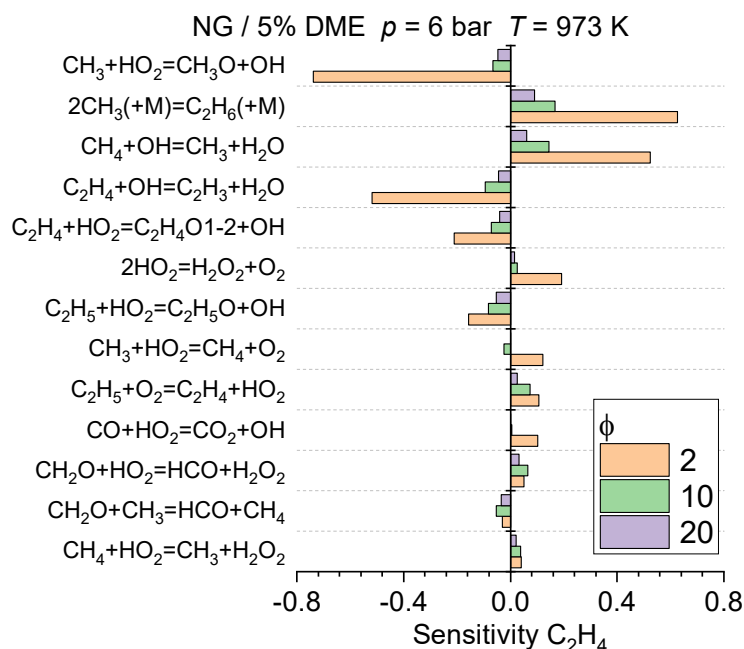
**Figure B-10:** Sensitivity coefficients of C<sub>2</sub>H<sub>4</sub> mole fraction for selected shock-tube conditions (NG/DME=95/5 mixture at  $\phi = 10$  and  $p = 30$  bar) using the PolyMech2.0.



**Figure B-11:** Sensitivity coefficients of  $C_2H_4$  mole fraction for selected shock-tube conditions (NG/DME=95/5 mixture at  $\phi = 10$  and  $p = 30$  bar) using the AramcoMech3.0 [124].

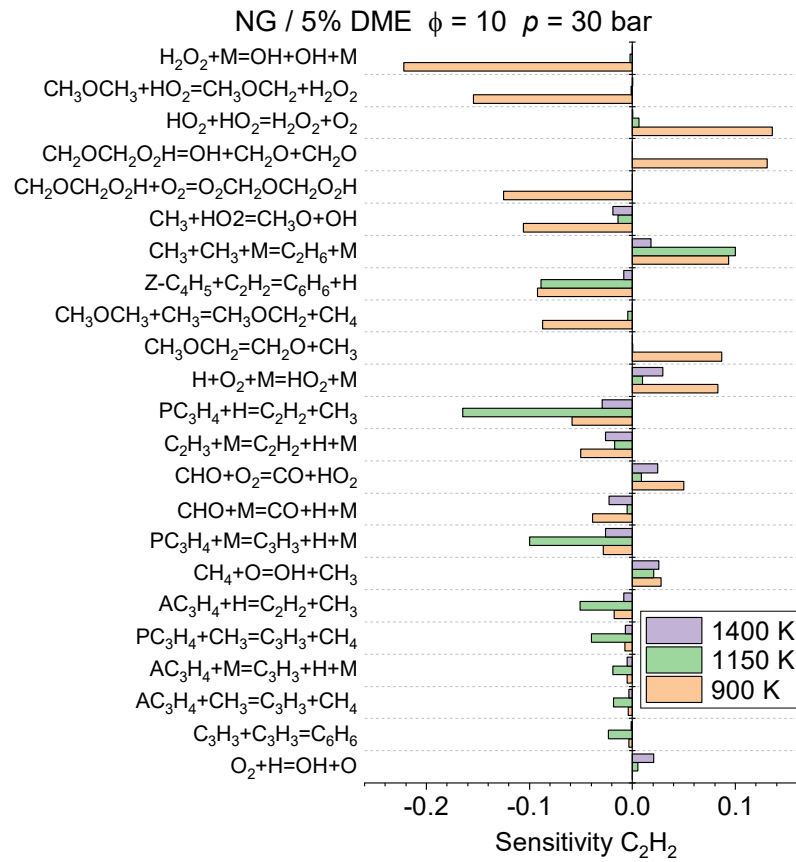


**Figure B-12:** Sensitivity coefficients of  $C_2H_4$  mole fraction for selected plug-flow conditions (NG/DME=95/5 mixture at  $T = 973$  K and  $p = 6$  bar) using the PolyMech2.0.



**Figure B-13:** Sensitivity coefficients of  $\text{C}_2\text{H}_4$  mole fraction for selected plug-flow conditions (NG/DME=95/5 mixture at  $T = 973$  K and  $p = 6$  bar) using the AramcoMech3.0 [124].

The most important reactions for  $\text{C}_2\text{H}_4$  production of all three mechanisms (PolyMech1.0 (Figure 9-3), PolyMech2.0, AramcoMech3.0) are  $\text{CH}_3 + \text{CH}_3 + \text{M} \rightleftharpoons \text{C}_2\text{H}_6$ ,  $\text{CH}_4 + \text{OH} = \text{CH}_3 + \text{H}_2\text{O}$  and  $\text{CH}_4 + \text{H} \rightleftharpoons \text{CH}_3 + \text{H}_2$  and  $2\text{HO}_2 \rightleftharpoons \text{H}_2\text{O}_2 + \text{O}_2$  for shock-tube and plug-flow conditions, respectively. The sensitivities are similar for the three mechanisms. For the shock-tube conditions, reactions leading to benzene precursors, benzene and higher PAHs show negative sensitivities. They are different for the three mechanisms due to their different benzene and PAH chemistry. A difference between the two versions of the PolyMech and the AramcoMech3.0 is that reactions important for ignition like the  $\text{H}_2\text{O}_2$  decomposition are sensitive at 900 K contrary to the AramcoMech3.0. This can be explained with the shorter ignition delay times (IDTs) predicted by the AramcoMech3.0 whereas the IDTs of the two PolyMech versions are close to the reaction time in the shock tube so that there is not enough time to form products. For the plug-flow conditions, the reactions  $\text{C}_2\text{H}_4 + \text{H} \rightleftharpoons \text{C}_2\text{H}_3 + \text{H}_2$  and  $\text{CO} + \text{HO}_2 \rightleftharpoons \text{CO}_2 + \text{OH}$  show high sensitivities for  $\text{C}_2\text{H}_4$  conversion in case of the PolyMech1.0 (Figure 9-3). In contrast, these reactions are not found under the 10 most sensitive reactions for the AramcoMech3.0 and the PolyMech2.0 because of different implemented rate constants and the associated lower reaction rates.

B.3.3 C<sub>2</sub>H<sub>2</sub>

**Figure B-14:** Sensitivity coefficients of C<sub>2</sub>H<sub>2</sub> mole fraction for selected shock-tube conditions (NG/DME=95/5 mixture at  $\phi = 10$  and  $p = 30$  bar) using the PolyMech1.0 [19].

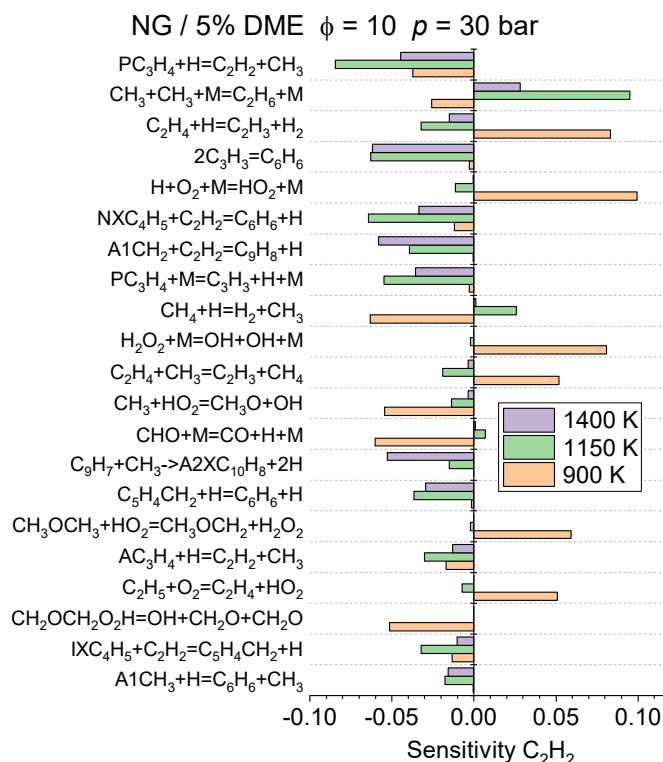


**Figure B-15:** Sensitivity coefficients of  $C_2H_2$  mole fraction for selected shock-tube conditions (NG/DME=95/5 mixture at  $\phi = 10$  and  $p = 30$  bar) using the PolyMech2.0.

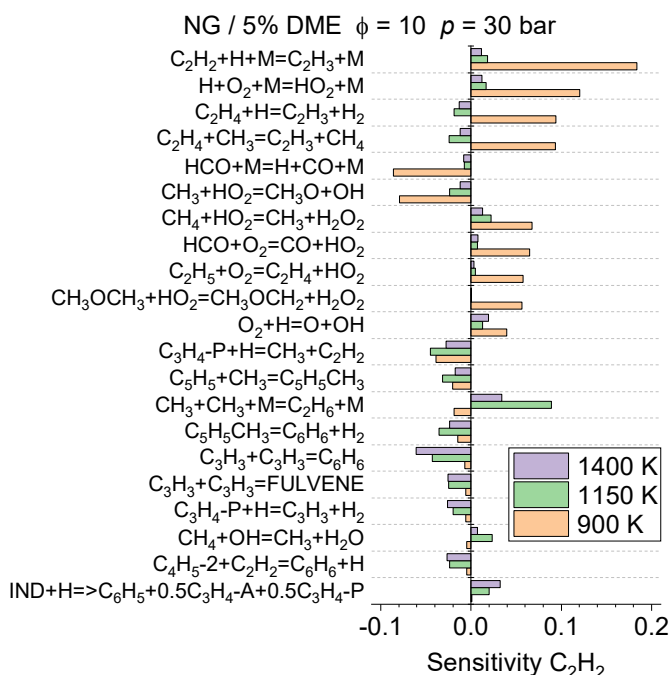
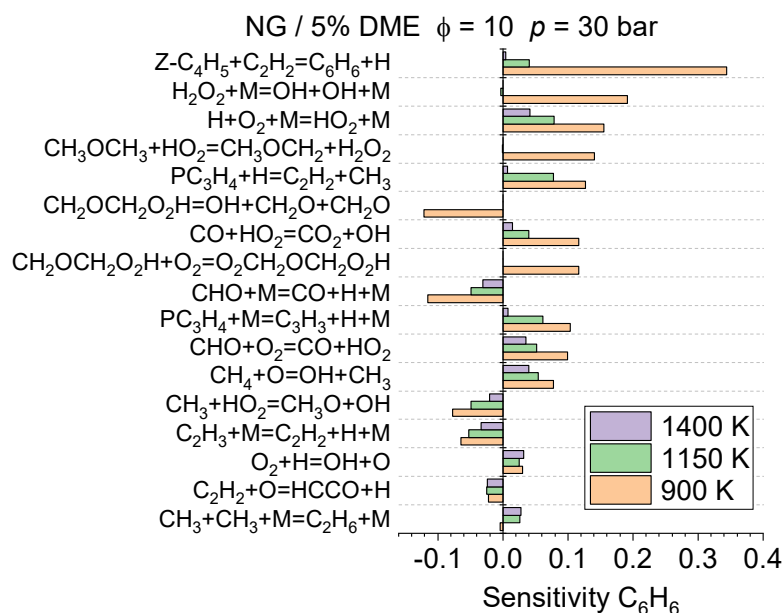


**Figure B-16:** Sensitivity coefficients of  $C_2H_2$  mole fraction for selected shock-tube conditions (NG/DME=95/5 mixture at  $\phi = 10$  and  $p = 30$  bar) using the AramcoMech3.0 [124].

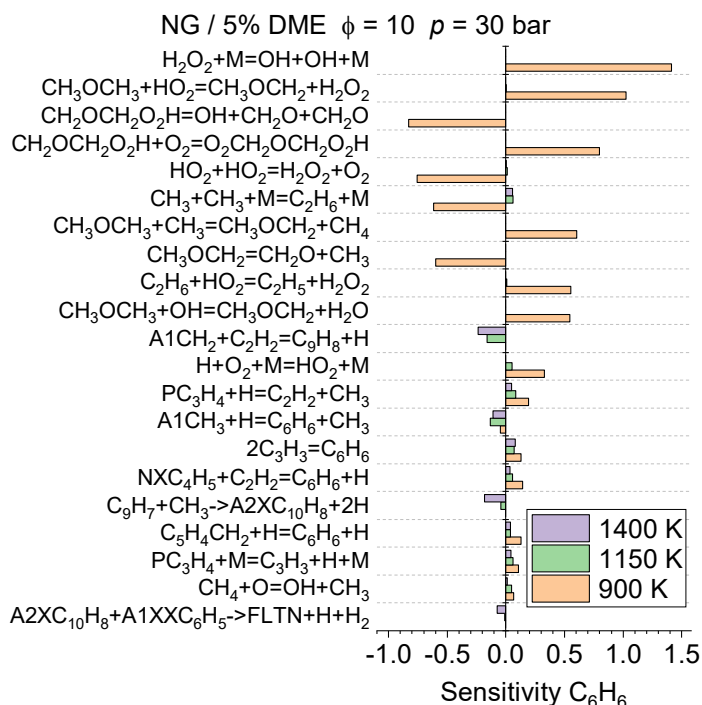
The sensitivities for  $C_2H_2$  show similar low sensitivities for a lot of different reactions. The most sensitive reaction with positive sensitivity is  $CH_3 + CH_3 + M \rightleftharpoons C_2H_6$  whereas benzene precursor forming reactions show a negative sensitivity. At 900 K both PolyMech versions

show again a high sensitivity towards reactions influencing the IDT see explanation above for  $C_2H_4$ .

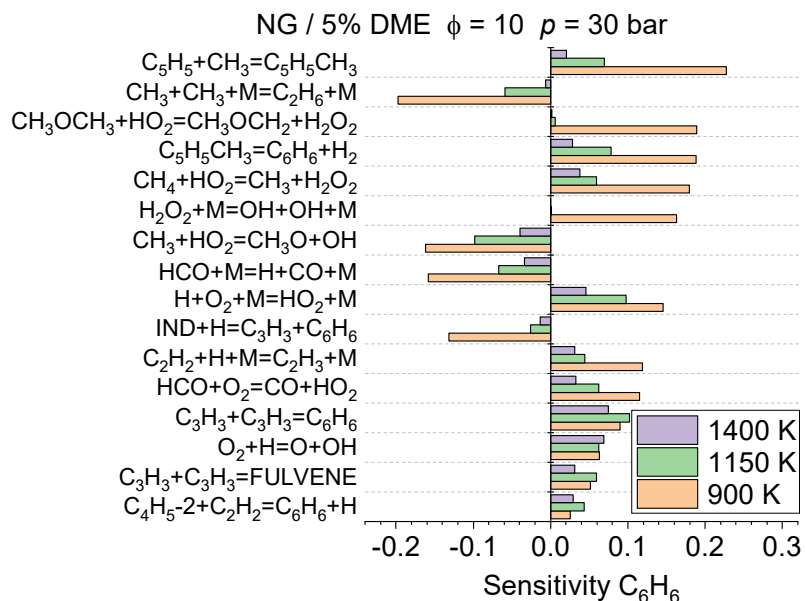
### B.3.4 $C_6H_6$



**Figure B-17:** Sensitivity coefficients of  $C_6H_6$  mole fraction for selected shock-tube conditions (NG/DME=95/5 mixture at  $\phi = 10$  and  $p = 30$  bar) using the PolyMech1.0 [19].

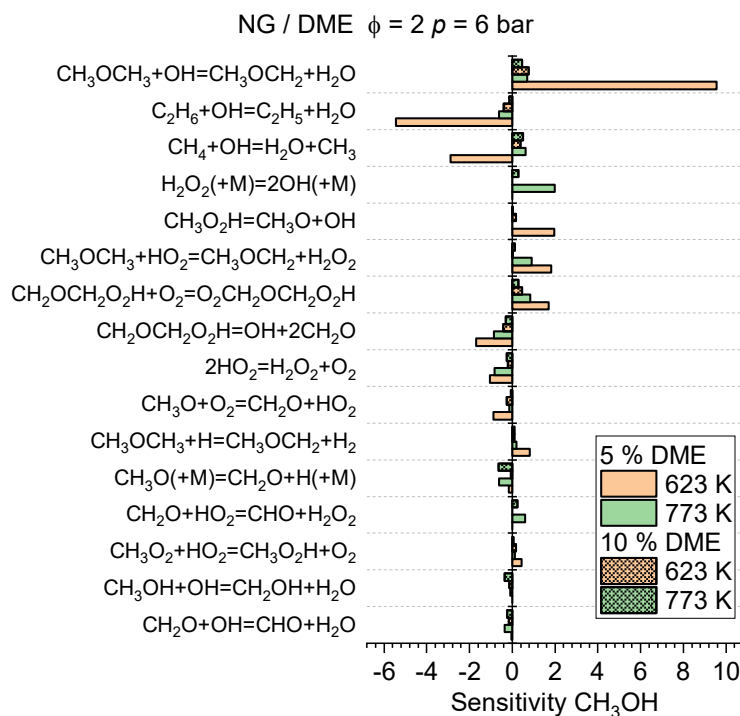


**Figure B-18:** Sensitivity coefficients of  $C_6H_6$  mole fraction for selected shock-tube conditions (NG/DME=95/5 mixture at  $\phi = 10$  and  $p = 30$  bar) using the PolyMech2.0.



**Figure B-19:** Sensitivity coefficients of  $C_6H_6$  mole fraction for selected shock-tube conditions (NG/DME=95/5 mixture at  $\phi = 10$  and  $p = 30$  bar) using the AramcoMech3.0 [124].

The most sensitive benzene forming reactions are  $Z-C_4H_5 + C_2H_2 \rightleftharpoons C_6H_6 + H$  (PolyMech1.0),  $2 CH_3 \rightleftharpoons C_6H_6$ ,  $NX-C_4H_5 + C_2H_2 \rightleftharpoons C_6H_6 + H$ ,  $C_5H_4CH_2 + H \rightleftharpoons C_6H_6 + H$  (PolyMech2.0) and  $C_5H_5CH_3 \rightleftharpoons C_6H_6 + H_2$ ,  $2 CH_3 \rightleftharpoons C_6H_6$ ,  $C_4H_5-2 + C_2H_2 \rightleftharpoons C_6H_6 + H$  (AramcoMech3.0) with similar sensitivities for each reaction. Due to the relative long time necessary for benzene formation reactions important for the IDT are also very sensitive especially at 900 K and for the PolyMech2.0 showing the longest IDTs (IDT close to the reaction time before cooling). The AramcoMech3.0 shows the least sensitivities to reactions influencing the IDTs because it predicts the shortest IDTs.

B.3.5 CH<sub>3</sub>OH

**Figure B-20:** Sensitivity coefficients of CH<sub>3</sub>OH mole fraction for selected plug-flow conditions (NG/DME mixtures at  $\phi = 2$  and  $p = 6$  bar) using PolyMech2.0.

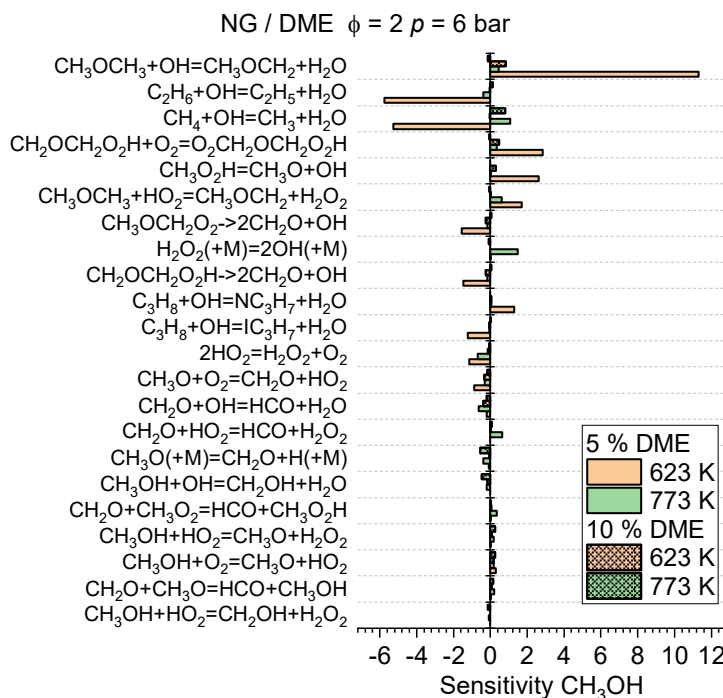
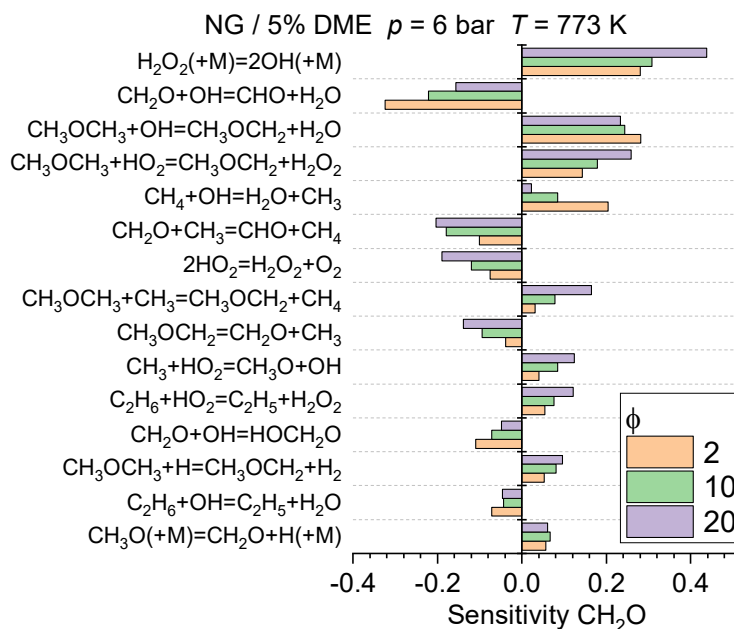


**Figure B-21:** Sensitivity coefficients of CH<sub>3</sub>OH mole fraction for selected plug-flow conditions (NG/DME mixtures at  $\phi = 2$  and  $p = 6$  bar) using the AramcoMech3.0 [124].

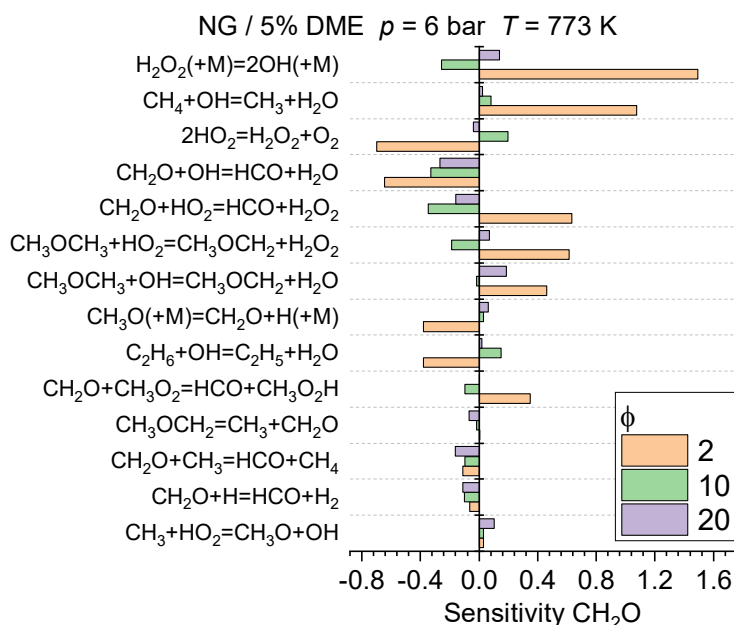
The sensitivities for CH<sub>3</sub>OH are very similar for all three mechanisms. The three most sensitive reactions are the H-abstractions from DME, CH<sub>4</sub> and C<sub>2</sub>H<sub>6</sub> by OH. In addition, DME involved

reactions show high sensitivities at low temperature due to its low-temperature chemistry. A difference between the PolyMech versions and the AramcoMech3.0 is that the H-abstractions from  $C_3H_8$  by OH also show high sensitivities at low temperature. It is assumed that the much more detailed  $C_3$  subset in the AramcoMech3.0 is responsible for this difference.

### B.3.6 $CH_2O$



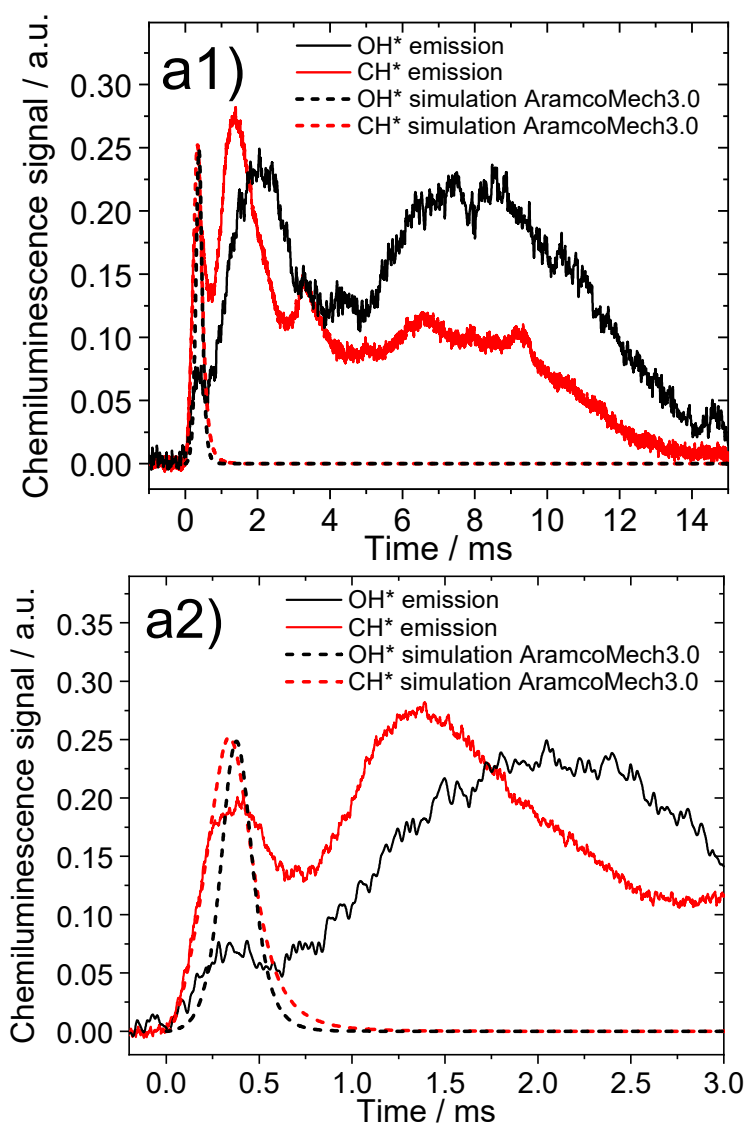
**Figure B-22:** Sensitivity coefficients of  $CH_2O$  mole fraction for selected plug-flow conditions (NG/DME=95/5 mixture at  $T = 973$  K and  $p = 6$  bar) using the PolyMech2.0.



**Figure B-23:** Sensitivity coefficients of  $CH_2O$  mole fraction for selected plug-flow conditions (NG/DME=95/5 mixture at  $T = 973$  K and  $p = 6$  bar) using the AramcoMech3.0 [124].

The sensitivity analysis for CH<sub>2</sub>O is very similar for both PolyMech versions with the difference that the decomposition of H<sub>2</sub>O<sub>2</sub> to OH radicals is the most sensitive reaction for CH<sub>2</sub>O production in case of the PolyMech2.0 compared to CH<sub>2</sub>O + OH ⇌ CHO + H<sub>2</sub>O in case of the PolyMech1.0. This is probably due to the much lower rates resulting from the new rate constant used for CH<sub>2</sub>O + OH ⇌ CHO + H<sub>2</sub>O and other reactions involving OH radicals in the PolyMech2.0. The remaining OH radicals can react with DME to form more CH<sub>2</sub>O. In the study it was shown that most CH<sub>2</sub>O is produced from DME at these conditions, which supports this assumption. This is also shown by the sensitivity analyses of all three mechanisms where DME reactions show a high sensitivity with respect to CH<sub>2</sub>O formation. The sensitivity analysis, performed with the AramcoMech3.0, shows similar reactions as the analyses, performed with the PolyMech. At  $\phi = 2$ , however, the sensitivities of several reactions are much higher compared to those of both PolyMech versions. This corresponds to a higher predicted reactivity of the mixture at these conditions in case of the AramcoMech3.0 compared to the PolyMech (see Figure 9-9 and Figure 9-10 for example).

### B.3.7 Chemiluminescence signals



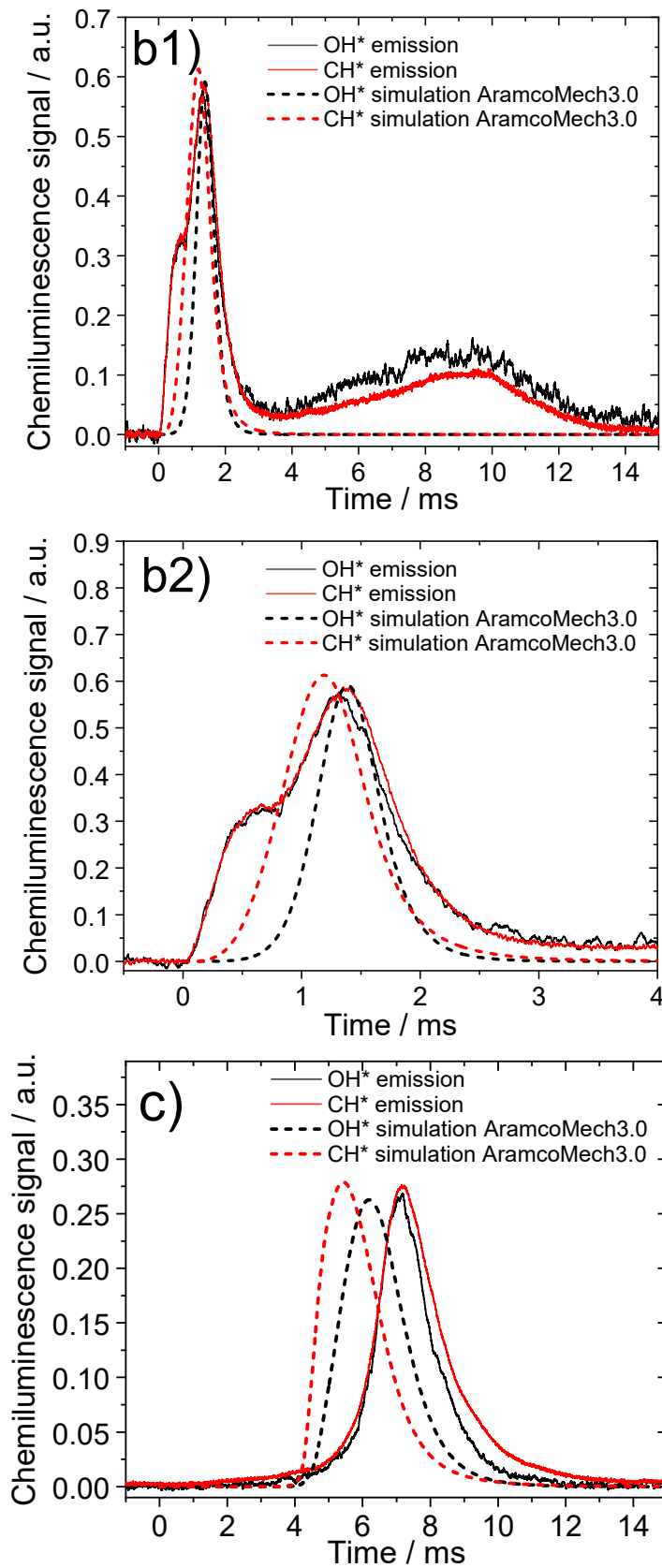


**Figure B-24:** Measured OH\* and CH\*-chemiluminescence signals of a natural gas / air mixture at  $\phi = 10$  compared to simulated OH\* and CH\* concentrations using the AramcoMech3.0 [124].

- a) 1427 K, 26.6 bar
- b) 1204 K, 28.5 bar
- c) 974 K, 31.2 bar

The chemiluminescence signals at high temperatures (e.g. a) and b)) show a complex structure with several peaks or a peak with two distinct increases. This behavior makes it very difficult to determine the experimental ignition delay time. The simulations show only one symmetric peak. At lower temperatures (e.g. c)) and for natural gas with DME only one symmetric peak is observed in the experiments in agreement with the simulations. The width of the experimental peak agrees also very well with the simulations.



## C Supplementary material for chapter 10

### C.1 Calculation of mole fractions

Quantification of reactants, major species and some intermediates is done by comparing the resulting signals with calibration measurements, done with self-mixed binary cold gas mixtures or certified gas mixtures when available, using the same instrument settings as in the experiments. These measurements have to be repeated three to five times for mixtures of different composition, so that a calibration factor  $k$  can be determined according to equation (C-1).  $k$  can then be used, also in conjunction with equation (C-1), to calculate the mole fractions of the calibrated species detected in the mixture.

$$\frac{S_i}{S_{N_2}} = \frac{x_i}{x_{N_2}} \cdot k_i \quad (\text{C-1})$$

$S_{i/N_2}$ : integrated signal intensity of species  $i$  or  $N_2$

$x_{i/N_2}$ : mole fraction of species  $i$  or  $N_2$

$k_i$ : calibration factor of species  $i$

To apply this method, the mole fraction of  $N_2$  must be known. As it is used as a dilution gas in large excess, it is expected that its initial mole fraction remains nearly constant during the whole experiment.

### C.2 Uncertainties

#### C.2.1 Direct calibration

General uncertainties are estimated using the error propagation law, considering uncertainties of all used instruments.

Some errors, such as slight pressure fluctuations in the reactor, can be observed during the measurements. Other measurement uncertainties can be determined by repeated measurements. Error sources are: mass flow controller, gas chromatograph, and syringe pump. The errors that emanate from the slight temperature fluctuations of the evaporator can be neglected due to insignificance. The mass flow controllers from Bronkhorst are factory-provided with tolerances. This causes measurement uncertainties, which are quantified by the manufacturer with a total of 0.5 % of the mass flow rate. Unlike the mass flow controllers, there is no quoted measurement uncertainty for the used syringe pump. This is among other things because components such as capillaries or syringes be individually exchanged or adjusted. In order to keep the error between the set and the actually conveyed flow rate as low as possible, calibration measurements were carried out. Since the calibration is also accompanied by sources of error, this was checked for reproducibility. This procedure resulted in a mean deviation of the calibrations of 0.3 %.

Pressure fluctuations were less than 0.5 % during the experiments.

Reproducibility measurements have been made for the gas chromatograph. These gave a relative error of  $\leq 5\%$ . This error takes into account the uncertainties of the instruments and the manual integration of the signals.

In calculating a total error, the sources of error caused by the syringe pump and the electro-pneumatic pressure regulator are not considered. Only the measurement uncertainties of the gas chromatograph and the mass flow controller are included in the calculation. The Gaussian error propagation law (see equation (C-2)) is used to determine an overall error that applies to the final results.

$$\Delta z = \sqrt{\left(\frac{\partial f}{\partial a} \Delta a\right)^2 + \left(\frac{\partial f}{\partial b} \Delta b\right)^2 + \left(\frac{\partial f}{\partial c} \Delta c\right)^2 + \dots} \quad (\text{C-2})$$

Here,  $z$  represents a function of measured mole fractions and  $\Delta z$  the absolute error in these mole fractions. The single uncertainties are described with  $\Delta a$ ,  $\Delta b$  and  $\Delta c$  and can represent estimated values, calculated uncertainties or manufacturer information.

To determine the total error, the absolute error for the mole fractions used in the calibration measurements is first calculated. This is explained by way of example with reference to the calibration of methane. Since all calibration measurements are carried out using two mass flow controllers, the uncertainties of 0.5 % each must be taken into account. The absolute error in the mole fraction of methane is then calculated according to equation (C-3):

$$\Delta x_{\text{CH}_4} = \sqrt{\left(\frac{\partial x_{\text{CH}_4}}{\partial \dot{V}_{\text{CH}_4}} \Delta \dot{V}_{\text{CH}_4}\right)^2 + \left(\frac{\partial x_{\text{CH}_4}}{\partial \dot{V}_{\text{N}_2}} \Delta \dot{V}_{\text{N}_2}\right)^2} \quad (\text{C-3})$$

Since the species to be calibrated is diluted with nitrogen in each case, the absolute error in the nitrogen mole fraction must also be calculated:

$$\Delta x_{\text{N}_2} = \sqrt{\left(\frac{\partial x_{\text{N}_2}}{\partial \dot{V}_{\text{N}_2}} \Delta \dot{V}_{\text{N}_2}\right)^2 + \left(\frac{\partial x_{\text{N}_2}}{\partial \dot{V}_{\text{CH}_4}} \Delta \dot{V}_{\text{CH}_4}\right)^2} \quad (\text{C-4})$$

The absolute errors in the mole fractions of methane and nitrogen have an influence on the determined calibration factor of methane. Since the respective samples are analyzed with the gas chromatograph or time-of-flight mass spectrometer, their measurement uncertainty of 5 % must be included:

$$\Delta k_{\text{CH}_4} = \sqrt{\left(\frac{\partial k_{\text{CH}_4}}{\partial x_{\text{CH}_4}} \Delta x_{\text{CH}_4}\right)^2 + \left(\frac{\partial k_{\text{CH}_4}}{\partial x_{\text{N}_2}} \Delta x_{\text{N}_2}\right)^2 + \left(\frac{\partial k_{\text{CH}_4}}{\partial S_{\text{CH}_4}} \Delta S_{\text{CH}_4}\right)^2 + \left(\frac{\partial k_{\text{CH}_4}}{\partial S_{\text{N}_2}} \Delta S_{\text{N}_2}\right)^2} \quad (\text{C-5})$$

where  $S$  is used to express the detected signal area. Each particular calibration line consists of several measurement points, so the presented calculations must be performed for each point. Subsequently, the mean value of the absolute errors of the calibration measurements is

determined. Using this average value, the relative error of the methane calibration factor is 5.6 %. In order to calculate the absolute error in the final mole fraction of methane, the flow conditions and the determined signal intensities of the reactants are taken into account. The flow conditions and signal intensities of an equivalence ratio of  $\phi = 2$  at 673 K are used. Unlike the calibration measurements, three mass flow controllers are used in the experiments. So, the absolute error in the volumetric flow rate of oxygen must be included in the calculation:

$$\Delta x_{N_2} = \sqrt{\left(\frac{\partial x_{N_2}}{\partial \dot{V}_{N_2}} \Delta \dot{V}_{N_2}\right)^2 + \left(\frac{\partial x_{N_2}}{\partial \dot{V}_{CH_4}} \Delta \dot{V}_{CH_4}\right)^2 + \left(\frac{\partial x_{N_2}}{\partial \dot{V}_{O_2}} \Delta \dot{V}_{O_2}\right)^2} \quad (C-6)$$

To determine the error in the mole fraction of methane, the following formula is required:

$$\frac{S_{CH_4}}{S_{N_2}} \cdot \frac{x_{N_2}}{k_{CH_4}} = x_{CH_4} \quad (C-7)$$

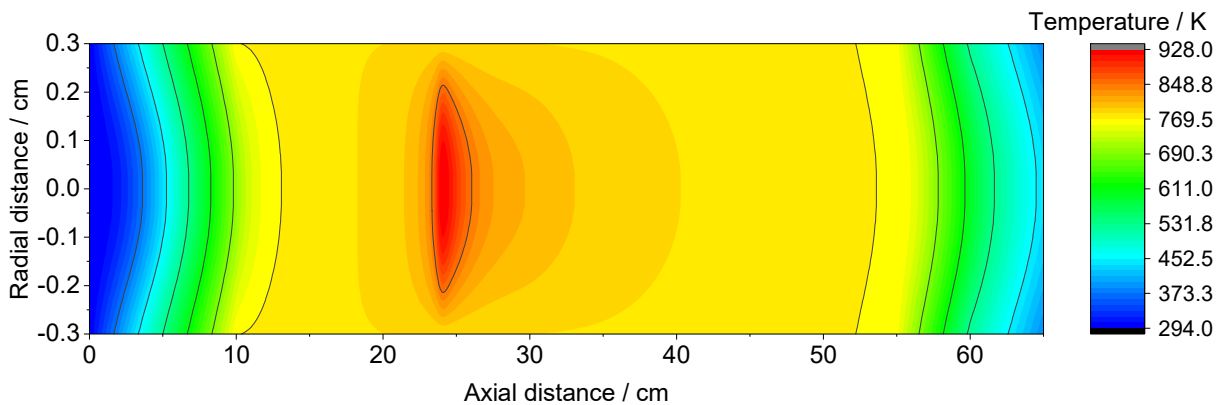
in which all calculated errors must be integrated. Finally, the absolute error in the methane mole fraction is calculated as:

$$\Delta x_{CH_4} = \sqrt{\left(\frac{\partial x_{CH_4}}{\partial k_{CH_4}} \Delta k_{CH_4}\right)^2 + \left(\frac{\partial x_{CH_4}}{\partial x_{N_2}} \Delta x_{N_2}\right)^2 + \left(\frac{\partial x_{CH_4}}{\partial S_{CH_4}} \Delta S_{CH_4}\right)^2 + \left(\frac{\partial x_{CH_4}}{\partial S_{N_2}} \Delta S_{N_2}\right)^2} \quad (C-8)$$

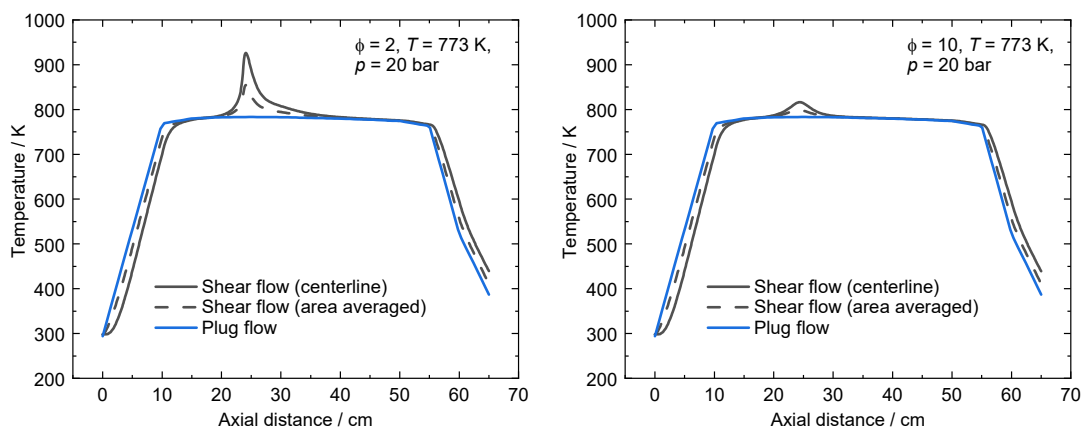
The relative total error in the mole fraction of methane can then be determined, resulting in 7.2 %.

### C.3 Uncertainties

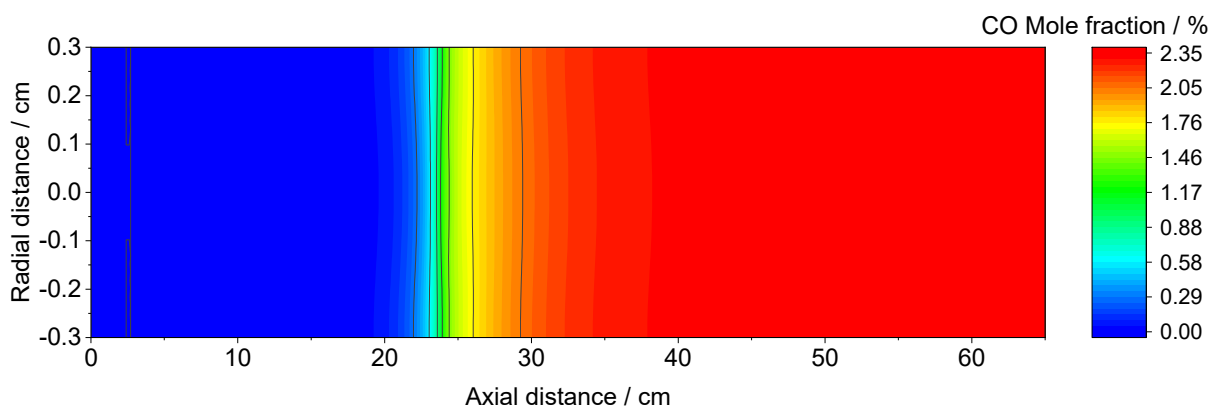
For all 2D shear-flow simulations the temperature profiles, provided in the excel sheet, were used as wall temperature. In addition, a gas inlet temperature of 298 K, a maximum solver step distance of 0.1 cm as well as 10 uniform grid points in the radial direction were used in the simulations.



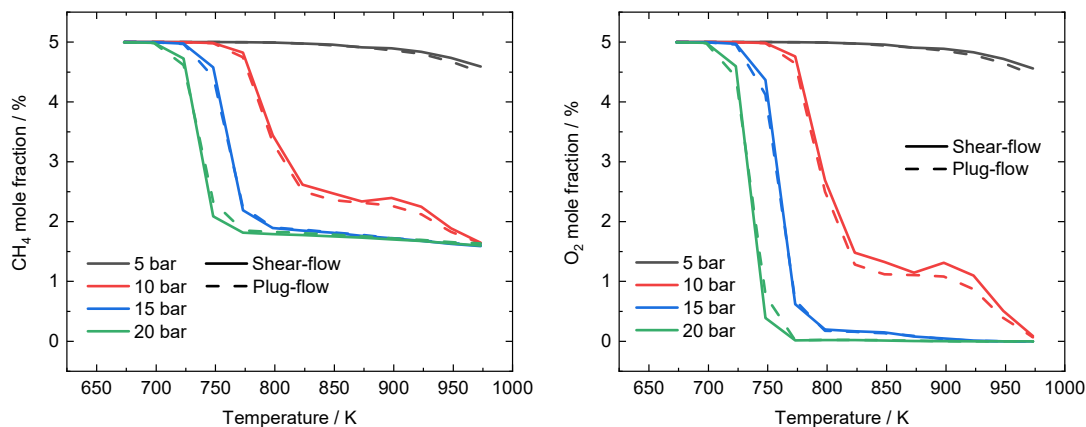
**Figure C-1:** Temperature distribution as a function of radial and axial distance for the  $\phi = 2$  mixture at  $p = 20$  bar and  $T_{set} = 773$  K. Simulated using the modified PolyMech mechanism.



**Figure C-2:** Comparison of simulated temperature profiles using the 1D plug-flow and 2D shear-flow approach of ChemKin Pro 19.2 [310] and the modified PolyMech mechanism.  $T_{\text{set}} = 773 \text{ K}$  was chosen as the highest temperature increase was found at this temperature. Temperature rises of  $\approx 150 \text{ K}$  and  $\approx 40 \text{ K}$  are found for the  $\phi = 2$  and  $\phi = 10$  mixtures at  $p = 20 \text{ bar}$ , respectively.



**Figure C-3:** CO Mole fraction as a function of radial and axial distance for the  $\phi = 2$  mixture at  $p = 20 \text{ bar}$  and  $T_{\text{set}} = 773 \text{ K}$ . Simulated using the modified PolyMech mechanism. The CO mole fraction deviates only 3.5 % from the mole fraction obtained in the plug-flow simulation.



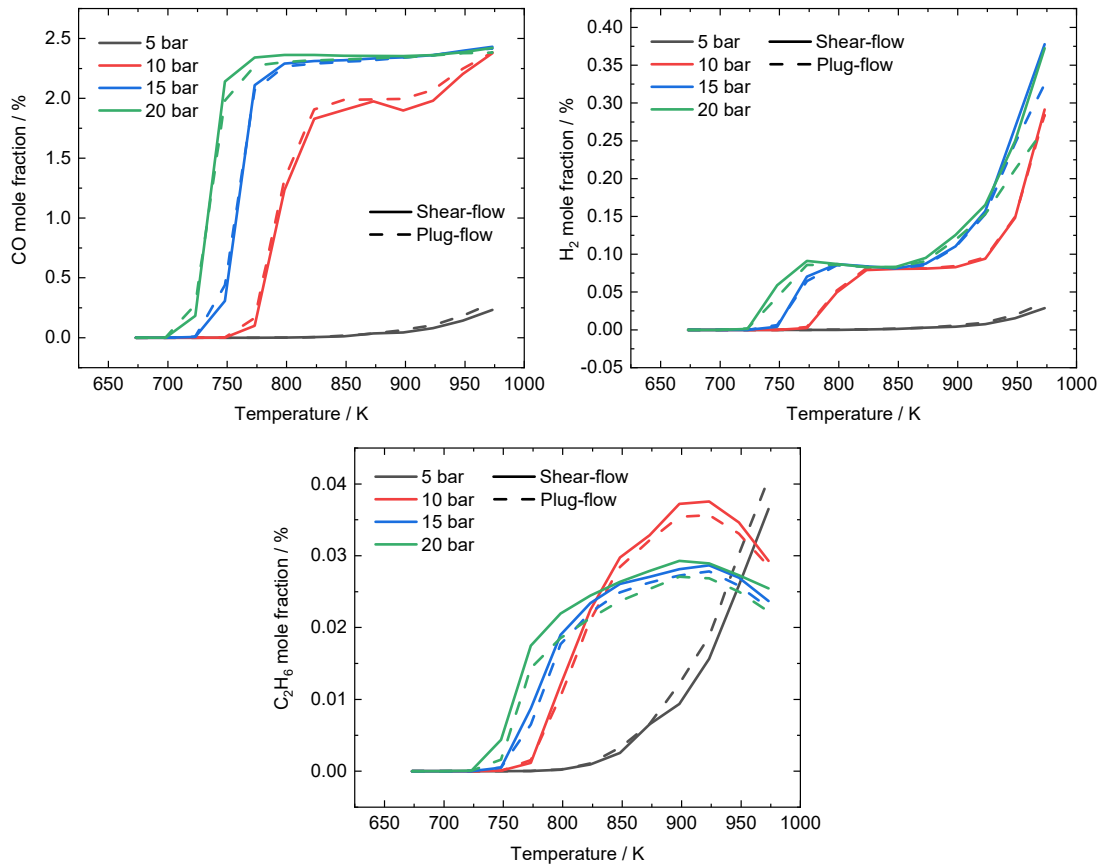


**Figure C-4:** Comparison of simulated mole fractions as a function of temperature using the 1D plug-flow and 2D shear-flow approach of ChemKin Pro 19.2 [310] and the modified Poly-Mech mechanism.

#### C.4 Influence of residence time on the NTC behavior

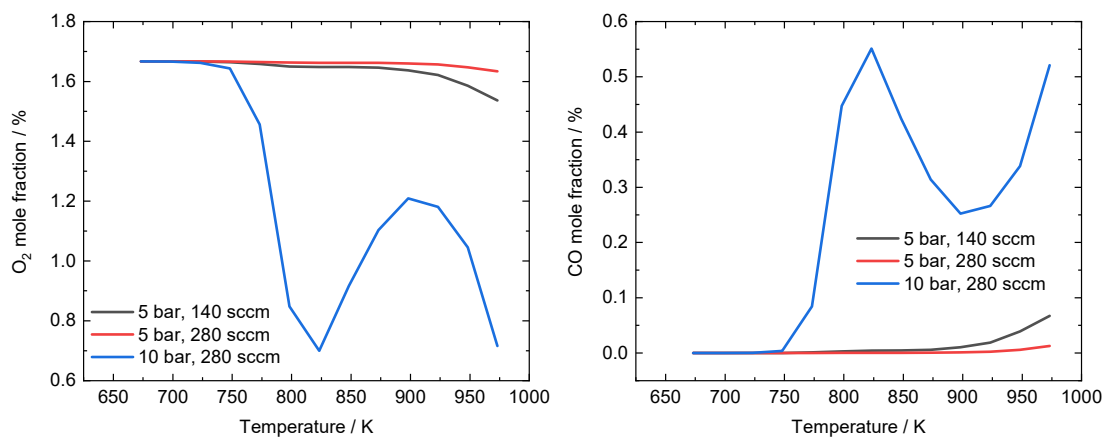


**Figure C-5:** Comparison of model predictions of  $O_2$  and  $CO$  mole fractions at different residence times using the modified PolyMech mechanism ( $p = 5$  and  $10$  bar,  $\phi = 10$  mixture).

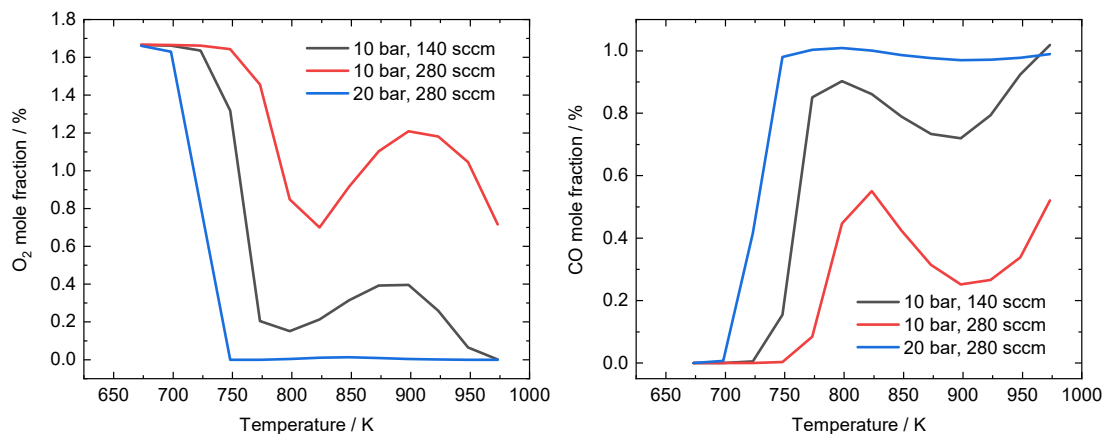


**Figure C-6:** Comparison of model predictions of O<sub>2</sub> and CO mole fractions at different residence times using the modified PolyMech mechanism ( $p = 10$  and  $20$  bar,  $\phi = 10$  mixture).

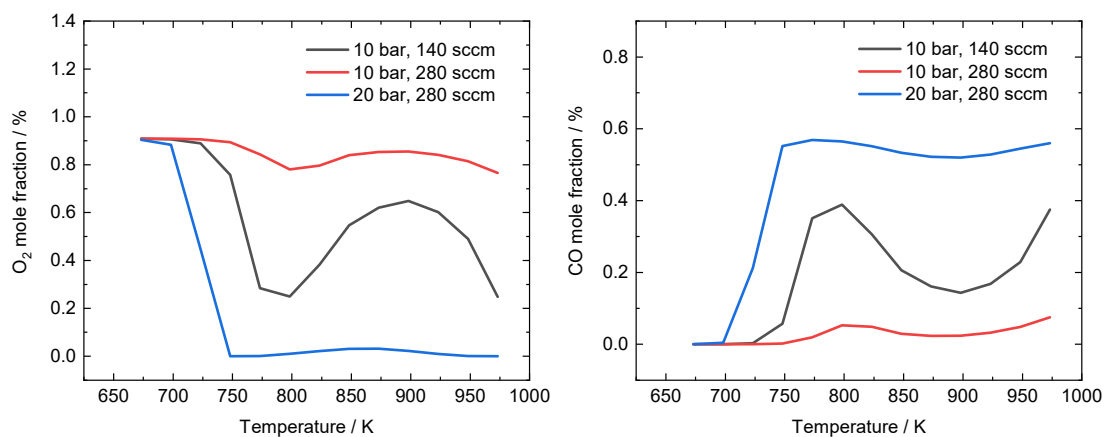


**Figure C-7:** Comparison of model predictions of O<sub>2</sub> and CO mole fractions at different residence times using the modified PolyMech mechanism ( $p = 10$  and  $20$  bar,  $\phi = 20$  mixture).

### C.5 Comparison between experimental and numerical results obtained by the LLNL [314] and Polimi reaction mechanism [144]

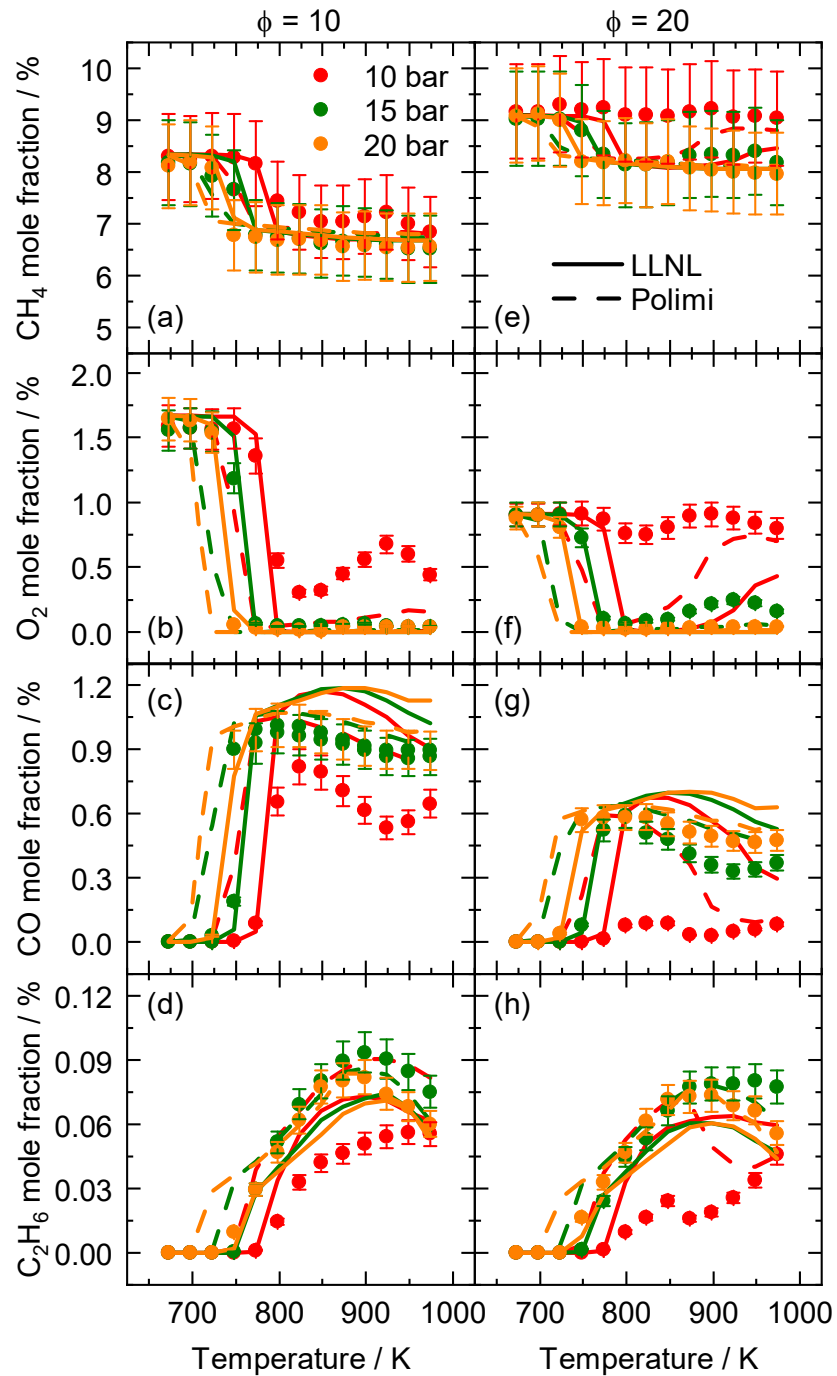


**Figure C-8:** Mole fractions of major species as a function of temperature and equivalence ratio (left:  $\phi = 10$ , right:  $\phi = 20$ ). Symbols: GC/MS experiment, lines: simulations based on the Polimi [144] (dashed lines) and LLNL mechanism [314] (solid lines).

## C.6 Comparison between the reaction pathways predicted by the modified PolyMech and the Aramco3.0 [124] mechanism at $\phi = 10$ , $p = 10$ bar and $T = 823$ K.

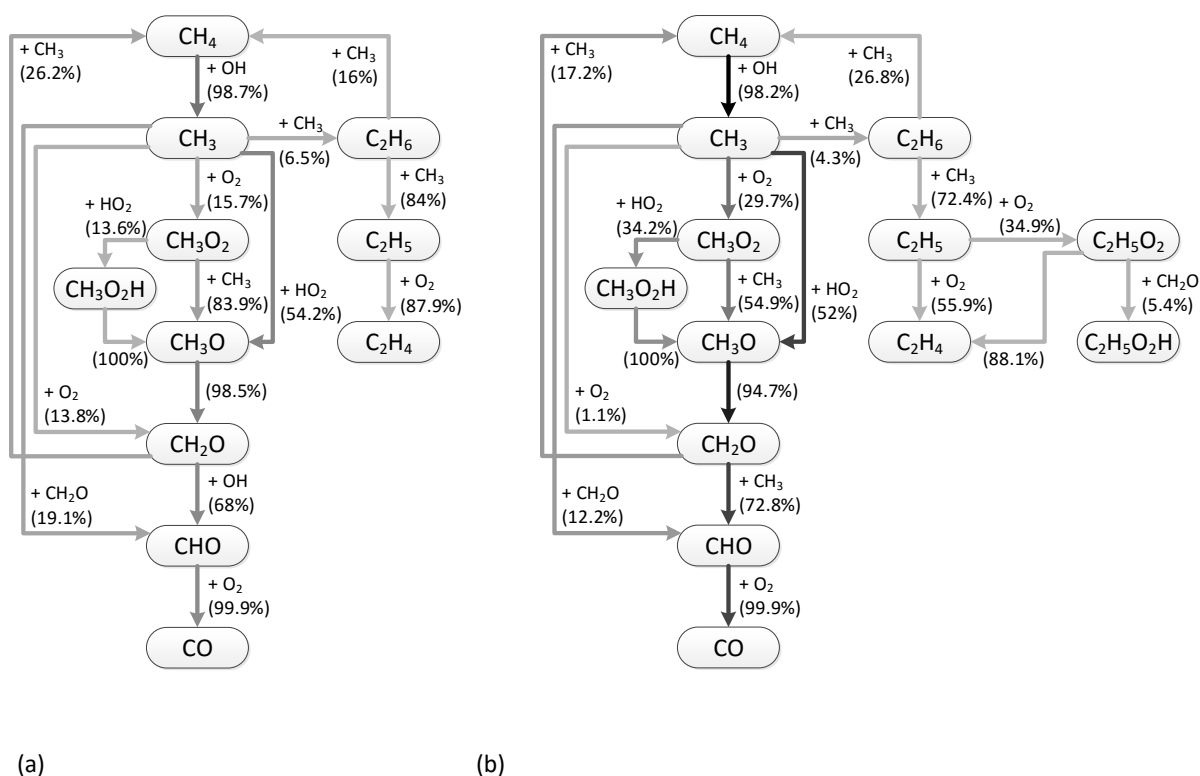


**Figure C-9:** Reaction path analysis using the modified PolyMech (a) and the Aramco 3.0 [124] (b) mechanism for 2 %  $\text{CH}_4$  consumption at 823 K, a pressure of 10 bar and  $\phi = 10$ . The percentages show the relative rate of consumption of the limiting reactant and line darkness represents the percentage of carbon flux, related to the highest carbon flux within the reaction path, which is found between  $\text{CH}_4$  and  $\text{CH}_3$  for the Aramco 3.0 mechanism.

---

## References

- [1] Bundesministerium für Wirtschaft und Energie, *Die Energie der Zukunft*, Berlin, 2018.
- [2] E. Papadis, G. Tsatsaronis, Challenges in the decarbonization of the energy sector, *Energy* 205 (2020) 118025.
- [3] S. Drünert, U. Neuling, T. Zitscher, M. Kaltschmitt, Power-to-Liquid fuels for aviation – Processes, resources and supply potential under German conditions, *Appl. Energy* 277 (2020) 115578.
- [4] C. Panzone, R. Philippe, A. Chappaz, P. Fongarland, A. Bengaouer, Power-to-Liquid catalytic CO<sub>2</sub> valorization into fuels and chemicals, *J. CO<sub>2</sub> Util.* 38 (2020) 314–347.
- [5] M. Thema, F. Bauer, M. Sterner, Power-to-Gas, *Renew. Sust. Energ. Rev.* 112 (2019) 775–787.
- [6] A. Kätelhön, R. Meys, S. Deutz, S. Suh, A. Bardow, Climate change mitigation potential of carbon capture and utilization in the chemical industry, *Proc. Natl. Acad. Sci. USA* 116 (2019) 11187–11194.
- [7] C. Bassano, P. Deiana, G. Vilaridi, N. Verdone, Modeling and economic evaluation of carbon capture and storage technologies integrated into synthetic natural gas and power-to-gas plants, *Appl. Energy* 263 (2020) 114590.
- [8] International Energy Agency (IEA), *World Energy Outlook 2019*, Paris, 2019.
- [9] V. Quaschnig, *Regenerative Energiesysteme: Technologie - Berechnung - Klimaschutz*, 10th ed., Carl Hanser Verlag, München, 2019.
- [10] C. Acar, I. Dincer, Comparative assessment of hydrogen production methods from renewable and non-renewable sources, *Int. J. Hydrog. Energy* 39 (2014) 1–12.
- [11] T. Pregger, D. Graf, W. Krewitt, C. Sattler, M. Roeb, S. Möller, Prospects of solar thermal hydrogen production processes, *Int. J. Hydrog. Energy* 34 (2009) 4256–4267.
- [12] T. Blumberg, T. Morosuk, G. Tsatsaronis, A Comparative Exergoeconomic Evaluation of the Synthesis Routes for Methanol Production from Natural Gas, *Appl. Sci.* 7 (2017) 1213.
- [13] E.G. Lim, E.E. Dames, K.D. Cedrone, A.J. Acocella, T.R. Needham, A. Arce, D.R. Cohn, L. Bromberg, W.K. Cheng, W.H. Green, The engine reformer: Syngas production in an engine for compact gas-to-liquids synthesis, *Can. J. Chem. Eng.* 94 (2016) 623–635.
- [14] M. Yao, Z. Zheng, H. Liu, Progress and recent trends in homogeneous charge compression ignition (HCCI) engines, *Prog. Energy Combust. Sci.* 35 (2009) 398–437.
- [15] D. Schröder, K. Banke, S.A. Kaiser, B. Atakan, The kinetics of methane ignition in fuel-rich HCCI engines: DME replacement by ozone, *Proc. Combust. Inst.* 38 (2021), doi:10.1016/j.proci.2020.05.046.

- [16] B. Atakan, S.A. Kaiser, J. Herzler, S. Porras, K. Banke, O. Deutschmann, T. Kasper, M. Fikri, R. Schießl, D. Schröder, C. Rudolph, D. Kaczmarek, H. Gossler, S. Drost, V. Bykov, U. Maas, C. Schulz, Flexible energy conversion and storage via high-temperature gas-phase reactions: The piston engine as a polygeneration reactor, *Renew. Sust. Energ. Rev.* 133 (2020) 110264.
- [17] F. Sen, B. Shu, T. Kasper, J. Herzler, O. Welz, M. Fikri, B. Atakan, C. Schulz, Shock-tube and plug-flow reactor study of the oxidation of fuel-rich CH<sub>4</sub>/O<sub>2</sub> mixtures enhanced with additives, *Combust. Flame* 169 (2016) 307–320.
- [18] F. Sen, T. Kasper, U. Bergmann, R. Hegner, B. Atakan, Partial Oxidation of Methane at Elevated Pressures and Effects of Propane and Ethane as Additive: Experiment and Simulation, *Z. Phys. Chem.* 229 (2015) 955–976.
- [19] S. Porras, D. Kaczmarek, J. Herzler, S. Drost, M. Werler, T. Kasper, M. Fikri, R. Schießl, B. Atakan, C. Schulz, U. Maas, An experimental and modeling study on the reactivity of extremely fuel-rich methane/dimethyl ether mixtures, *Combust. Flame* 212 (2020) 107–122.
- [20] E. de Hoffmann, V. Stroobant, *Mass spectrometry: Principles and applications*, 3rd ed., John Wiley & Sons, West Sussex, 2007.
- [21] J.H. Gross, *Mass spectrometry: A Textbook*, 3rd ed., Springer, Cham, 2017.
- [22] G. Scoles (Ed.), *Atomic and Molecular Beam Methods: Volume 2*, Oxford University Press, New York, 1992.
- [23] G. Scoles (Ed.), *Atomic and Molecular Beam Methods: Volume 1*, Oxford University Press, New York, 1988.
- [24] D.R. Miller, Free jet sources, in: G. Scoles (Ed.), *Atomic and Molecular Beam Methods: Volume 1*, Oxford University Press, New York, 1988, pp. 14–53.
- [25] H. Ashkenas, F.S. Sherman, The Structure and Utilization of Supersonic Free Jets in Low Density Wind Tunnels, in: J.H. de Leeuw (Ed.), *Rarefied Gas Dynamics, Volume 2*, Academic Press, New York, 1965, pp. 84–105.
- [26] M.D. Morse, Supersonic Beam Sources, in: *Experimental Methods in the Physical Sciences*, Academic Press, San Diego, 1996, pp. 21–47.
- [27] M. Barr, K.M. O'Donnell, Fahy A., W. Allison, P.C. Dastoor, A desktop supersonic free-jet beam source for a scanning helium microscope (SHeM), *Meas. Sci. Technol.* 23 (2012), doi:10.1088/0957-0233/23/10/105901.
- [28] J.B. Fenn, Mass spectrometric implications of high-pressure ion sources, *Int. J. Mass. Spectrom.* 200 (2000) 459–478.
- [29] W.C. Wiley, I.H. McLaren, Time-of-Flight Mass Spectrometer with Improved Resolution, *Rev. Sci. Instrum.* 26 (1955) 1150–1157.
- [30] B.A. Mamyrin, Time-of-flight mass spectrometry (concepts, achievements, and prospects), *Int. J. Mass. Spectrom.* 206 (2001) 251–266.
- [31] W. Paul, H. Steinwedel, Ein neues Massenspektrometer ohne Magnetfeld, *Zeitschrift für Naturforschung A* 8 (1953) 448–450.
- [32] D.C. Harris, *Lehrbuch der quantitativen Analyse*, 8th ed., Springer Spektrum, Berlin, Heidelberg, 2014.
- [33] H.-J. Hubschmann, *Handbook of GC/MS: Fundamentals and applications*, 3rd ed., Wiley-VCH, Weinheim, 2015.

- 
- [34] H.M. McNair, J.M. Miller, N.H. Snow, *Basic gas chromatography*, 2019th ed., Wiley, Hoboken, NJ, 2019.
- [35] D.A. Skoog, F.J. Holler, S.R. Crouch, *Instrumentelle Analytik: Grundlagen - Geräte - Anwendungen*, 6th ed., Springer Spektrum, Berlin, Heidelberg, 2013.
- [36] K. Dettmer-Wilde, M. Adahchour, *Practical gas chromatography: A comprehensive reference*, Springer, Berlin, Heidelberg, 2014.
- [37] W. Demtröder, *Experimentalphysik 3: Atome, Moleküle und Festkörper*, 5th ed., Springer, Berlin Heidelberg, 2016.
- [38] C.F. Poole, *Gas chromatography*, 1st ed., Elsevier, Oxford, 2012.
- [39] J. de Zeeuw, *Chromatography: Gas-Solid Gas Chromatography*, in: I.D. Wilson (Ed.), *Encyclopedia of separation science*, Academic Press, San Diego, 2000, pp. 481–489.
- [40] A.J.P. Martin, R.L.M. Synge, A new form of chromatogram employing two liquid phases, *Biochem. J.* 35 (1941) 1358–1368.
- [41] A.E. Lawson, J.M. Miller, Thermal Conductivity Detectors in Gas Chromatography, *J. Chromatogr. Sci.* 4 (1966) 273–284.
- [42] P.J. Linstrom, W.G. Mallard, NIST Chemistry WebBook, NIST Standard Reference Database Number 69. National Institute of Standards and Technology, 2020, <https://webbook.nist.gov/>.
- [43] CHEMKIN-PRO 19.0, Reaction Design: San Diego, 2017.
- [44] Kintech Laboratory, Chemical WorkBench® 4.1, 2016.
- [45] E. Müller-Erlwein, *Chemische Reaktionstechnik*, 3rd ed., Springer Spektrum, Wiesbaden, 2015.
- [46] C.R. Wilke, A Viscosity Equation for Gas Mixtures, *J. Chem. Phys.* 18 (1950) 517–519.
- [47] M. Kleiber, R. Joh, Berechnungsmethoden für Stoffeigenschaften, in: VDI e.V. (Ed.), *VDI-Wärmeatlas*, Springer, Berlin, Heidelberg, 2013, pp. 139–174.
- [48] B.E. Poling, J.M. Prausnitz, J.P. O'Connell, *The properties of gases and liquids*, 5th ed., McGraw-Hill, New York, 2001.
- [49] F. Durst, *Grundlagen der Strömungsmechanik: Eine Einführung in die Theorie der Strömungen von Fluiden*, Springer, Berlin, Heidelberg, 2006.
- [50] F. Monge, V. Aranda, A. Millera, R. Bilbao, M.U. Alzueta, Tubular Flow Reactors, in: F. Battin-Leclerc, J.M. Simmie, E. Blurock (Eds.), *Cleaner Combustion: Developing Detailed Chemical Kinetic Models*, Springer, London, 2013, pp. 211–230.
- [51] O. Levenspiel, *Chemical Reaction Engineering*, 3rd ed., John Wiley & Sons, New York, 1999.
- [52] G.I. Taylor, Conditions under which dispersion of a solute in a stream of solvent can be used to measure molecular diffusion, *Proc. R. Soc. Lond. A* 225 (1954) 473–477.
- [53] G.I. Taylor, Dispersion of soluble matter in solvent flowing slowly through a tube, *Proc. R. Soc. Lond. A* 219 (1953) 186–203.
- [54] R. Aris, On the dispersion of a solute in a fluid flowing through a tube, *Proc. R. Soc. Lond. A* 235 (1957) 67–77.
- [55] J.O. Hirschfelder, C.F. Curtiss, R.B. Bird, *Molecular theory of gases and liquids*, John Wiley & Sons, New York, 1964.
- [56] J.E. Jones, On the determination of molecular fields. II. From the equation of state of a gas, *Proc. R. Soc. Lond. A* 106 (1924) 463–477.
-

- [57] J.E. Jones, On the determination of molecular fields. I. From the variation of the viscosity of a gas with temperature, *Proc. R. Soc. Lond. A* 106 (1924) 441–462.
- [58] R.B. Bird, W.E. Stewart, E.N. Lightfoot, *Transport phenomena*, 2nd ed., John Wiley & Sons, New York, 2007.
- [59] J.O. Hirschfelder, R.B. Bird, E.L. Spatz, The transport properties of gases and gaseous mixtures. II., *Chem. Rev.* 44 (1949) 205–231.
- [60] M. Klein, F.J. Smith, Tables of collision integrals for the (m,6) potential function for 10 values of m, *J. Res. Natl. Bur. Stan. Sect. A*. 72A (1968) 359.
- [61] S.U. Kim, C.W. Monroe, High-accuracy calculations of sixteen collision integrals for Lennard-Jones (12–6) gases and their interpolation to parameterize neon, argon, and krypton, *Journal of Computational Physics* 273 (2014) 358–373.
- [62] E. Laurien, H. Oertel jr., *Numerische Strömungsmechanik: Grundgleichungen und Modelle - Lösungsmethoden - Qualität und Genauigkeit*, 6th ed., Springer Vieweg, Wiesbaden, 2018.
- [63] H. Schlichting, K. Gersten, *Boundary-Layer Theory*, 9th ed., Springer, Berlin, Heidelberg, 2017.
- [64] R.J. Kee, M.E. Coltrin, P. Glarborg, H. Zhu, *Chemically reacting flow: Theory, modeling, and simulation*, John Wiley & Sons, Hoboken, NJ, 2018.
- [65] L.L. Raja, R.J. Kee, O. Deutschmann, J. Warnatz, L. D. Schmidt, A critical evaluation of Navier–Stokes, boundary-layer, and plug-flow models of the flow and chemistry in a catalytic-combustion monolith, *Catal. Today* 59 (2000) 47–60.
- [66] F.A. Lindemann, S. Arrhenius, I. Langmuir, N.R. Dhar, J. Perrin, W.C. McC. Lewis, Discussion on “the radiation theory of chemical action”, *Trans. Faraday Soc.* 17 (1922) 598–606.
- [67] K.A. Holbrook, M.J. Pilling, S.H. Robertson, *Unimolecular reactions*, 2nd ed., John Wiley & Sons, Chichester, 1996.
- [68] J. Troe, Theory of Thermal Unimolecular Reactions in the Fall-off Range. I. Strong Collision Rate Constants, *Berichte der Bunsengesellschaft für physikalische Chemie* 87 (1983) 161–169.
- [69] R.G. Gilbert, K. Luther, J. Troe, Theory of Thermal Unimolecular Reactions in the Fall-off Range. II. Weak Collision Rate Constants, *Berichte der Bunsengesellschaft für physikalische Chemie* 87 (1983) 169–177.
- [70] P.H. Stewart, C.W. Larson, D.M. Golden, Pressure and temperature dependence of reactions proceeding via a bound complex. 2. Application to  $2\text{CH}_3 \rightarrow \text{C}_2\text{H}_5 + \text{H}$ , *Combust. Flame* 75 (1989) 25–31.
- [71] P.K. Venkatesh, A.M. Dean, M.H. Cohen, R.W. Carr, Chebyshev expansions and sensitivity analysis for approximating the temperature- and pressure-dependence of chemically-activated reactions, *Rev. Chem. Eng.* 13 (1997) 1–67.
- [72] H.J. Curran, Developing detailed chemical kinetic mechanisms for fuel combustion, *Proc. Combust. Inst.* 37 (2019) 57–81.
- [73] S. Gordon, B.J. McBride, *Computer Program for Calculation of Complex Chemical Equilibrium Compositions, Rocket Performance, Incident and Reflected Shocks and Chapman-Jouguet Detonations*, NASA Report SP-273 (1976).

- 
- [74] L. Monchick, E.A. Mason, Transport Properties of Polar Gases, *J. Chem. Phys.* 35 (1961) 1676–1697.
- [75] S. Mathur, P.K. Tondon, S.C. Saxena, Thermal conductivity of binary, ternary and quaternary mixtures of rare gases, *Molecular Physics* 12 (1967) 569–579.
- [76] G. Dixon-Lewis, Flame structure and flame reaction kinetics II. Transport phenomena in multicomponent systems, *Proc. R. Soc. Lond. A* 307 (1968) 111–135.
- [77] J. Warnatz, Influence of Transport Models and Boundary Conditions on Flame Structure, in: N. Peters, J. Warnatz (Eds.), *Numerical Methods in Laminar Flame Propagation*, Springer Fachmedien, Wiesbaden, 1982, pp. 87–111.
- [78] O. Levenspiel, *The Chemical Reactor Omnibook*, OSU Book Stores, Inc., Corvallis, Oregon, 1993.
- [79] H. Schwarz, M. Geske, C. Franklin Goldsmith, R. Schlögl, R. Horn, Fuel-rich methane oxidation in a high-pressure flow reactor studied by optical-fiber laser-induced fluorescence, multi-species sampling profile measurements and detailed kinetic simulations, *Combust. Flame* 161 (2014) 1688–1700.
- [80] D. Kaczmarek, J. Herzler, S. Porras, S. Shaqiri, M. Fikri, C. Schulz, B. Atakan, U. Maas, T. Kasper, Plug-flow reactor and shock-tube study of the oxidation of very fuel-rich natural gas/DME/O<sub>2</sub> mixtures, *Combust. Flame* (2021).
- [81] F. Vietmeyer, Electron transfer rates in coupled semiconductor systems, Diploma thesis, Bielefeld, 2009.
- [82] U. Struckmeier, P. Oßwald, T. Kasper, L. Böhling, M. Heusing, M. Köhler, A. Brockhinke, K. Kohse-Höinghaus, Sampling Probe Influences on Temperature and Species Concentrations in Molecular Beam Mass Spectroscopic Investigations of Flat Premixed Low-pressure Flames, *Z. Phys. Chem.* 223 (2009) 503–537.
- [83] Kim, Y.-K., Irikura, K.K., Rudd, M.E., Ali, M.A., Stone, P.M., Chang, J., Coursey, J.S., Dragoset, R.A., Kishore, A.R., Olsen, K.J., Sansonetti, A.M., Wiersma, G.G., Zucker, D.S., and Zucker, M.A., Electron-Impact Ionization Cross Section for Ionization and Excitation Database (version 3.0). National Institute of Standards and Technology, Gaithersburg, MD, 2004, <http://physics.nist.gov/ionxsec>, accessed 22 September 2020.
- [84] J.C. Biordi, Molecular beam mass spectrometry for studying the fundamental chemistry of flames, *Prog. Energy Combust. Sci.* 3 (1977) 151–173.
- [85] W.L. Fitch, A.D. Sauter, Calculation of relative electron impact total ionization cross sections for organic molecules, *Anal. Chem.* 55 (1983) 832–835.
- [86] C.J. Cowper, A.J. DeRose, *The Analysis of Gases by Chromatography*, Pergamon Press, Oxford, 1983.
- [87] B. Thompson, *Fundamentals of Gas Analysis by Gas Chromatography*, Varian Associates, Palo Alto, 1977.
- [88] W.A. Dietz, Response Factors for Gas Chromatographic Analyses, *J. Chromatogr. Sci.* 5 (1967) 68–71.
- [89] J. Gislason, Wharry S. M., Relative molar response factors for thermal conductivity detectors, *J. Chromatogr. Sci.* 38 (2000) 129–132.
- [90] D. Kaczmarek, S. Shaqiri, B. Atakan, T. Kasper, The influence of pressure and equivalence ratio on the NTC behavior of methane, *Proc. Combust. Inst.* 38 (2021), doi:10.1016/j.proci.2020.06.112.
-

- [91] D. Felsmann, M. Baroncelli, J. Beeckmann, H. Pitsch, Molecular-beam mass spectrometry study of oxy-combustion in a novel coal-plate experiment, *Proc. Combust. Inst.* (2018).
- [92] Z. Lu, J. Cochet, N. Leplat, Y. Yang, M.J. Brear, A high-pressure plug flow reactor for combustion chemistry investigations, *Meas. Sci. Technol.* 28 (2017) 105902.
- [93] S. Wiemann, R. Hegner, B. Atakan, C. Schulz, S.A. Kaiser, Combined production of power and syngas in an internal combustion engine – Experiments and simulations in SI and HCCI mode, *Fuel* 215 (2018) 40–45.
- [94] B. Atakan, Gas turbines for polygeneration? A thermodynamic investigation of a fuel rich gas turbine cycle, *Int. J. Thermodyn.* 14 (2011) 185–192.
- [95] R. Hegner, B. Atakan, A polygeneration process concept for HCCI-engines – Modeling product gas purification and exergy losses, *Int. J. Hydrog. Energy* 42 (2017) 1287–1297.
- [96] R. Hegner, M. Werler, R. Schiessl, U. Maas, B. Atakan, Fuel-rich HCCI-engines as chemical reactors for polygeneration: A modeling and experimental study on product species and thermodynamics, *Energy Fuels* 31 (2017) 14079–14088.
- [97] H. Gossler, O. Deutschmann, Numerical optimization and reaction flow analysis of syngas production via partial oxidation of natural gas in internal combustion engines, *Int. J. Hydrog. Energy* 40 (2015) 11046–11058.
- [98] D.W. Rytz, A. Baiker, Partial Oxidation of Methane to Methanol in a Flow Reactor at Elevated Pressure, *Ind. Eng. Chem. Res.* 30 (1991) 2287–2292.
- [99] C.L. Rasmussen, P. Glarborg, Direct partial oxidation of natural gas to liquid chemicals: Chemical kinetic modeling and global optimization, *Ind. Eng. Chem. Res.* 47 (2008) 6579–6588.
- [100] C.L. Rasmussen, J.G. Jakobsen, P. Glarborg, Experimental Measurements and Kinetic Modeling of CH<sub>4</sub>/O<sub>2</sub> and CH<sub>4</sub>/C<sub>2</sub>H<sub>6</sub>/O<sub>2</sub> Conversion at High Pressure, *Int. J. Chem. Kinet.* 40 (2008) 454–480.
- [101] P. Glarborg, L.L.B. Bentzen, Chemical effects of a high CO<sub>2</sub> concentration in oxy-fuel combustion of methane, *Energy Fuels* 22 (2008) 291–296.
- [102] H. Hashemi, J.M. Christensen, S. Gersen, H. Levinsky, S.J. Klippenstein, P. Glarborg, High-pressure oxidation of methane, *Combust. Flame* 172 (2016) 349–364.
- [103] T.B. Hunter, H. Wang, T.A. Litzinger, M. Frenklach, The oxidation of methane at elevated pressures, *Combust. Flame* 97 (1994) 201–224.
- [104] T. Amano, F.L. Dryer, Effect of dimethyl ether, NO<sub>x</sub>, and ethane on CH<sub>4</sub> oxidation, *Symp. (Int.) Combust.* 27 (1998) 397–404.
- [105] P. Dagaut, J.-C. Boettner, M. Cathonnet, Methane oxidation: Experimental and kinetic modeling study, *Combust. Sci. Technol.* 77 (1991) 127–148.
- [106] D. Healy, H.J. Curran, J.M. Simmie, D.M. Kalitan, C.M. Zinner, A.B. Barrett, E.L. Petersen, G. Bourque, Methane/ethane/propane mixture oxidation at high pressures and at high, intermediate and low temperatures, *Combust. Flame* 155 (2008) 441–448.
- [107] X. Zhou, C. Chen, F. Wang, Modeling of non-catalytic partial oxidation of natural gas under conditions found in industrial reformers, *Chem. Eng. Process.* 49 (2010) 59–64.
- [108] A. El Bakali, P. Dagaut, L. Pillier, P. Desgroux, J.-F. Pauwels, A. Rida, P. Meunier, Experimental and modeling study of the oxidation of natural gas in a premixed flame, shock tube, and jet-stirred reactor, *Combust. Flame* 137 (2004) 109–128.

- 
- [109] C.J. Aul, W.K. Metcalfe, S.M. Burke, H.J. Curran, E.L. Petersen, Ignition and kinetic modeling of methane and ethane fuel blends with oxygen, *Combust. Flame* 160 (2013) 1153–1167.
- [110] E.L. Petersen, D.M. Kalitan, S. Simmons, G. Bourque, H.J. Curran, J.M. Simmie, Methane/propane oxidation at high pressures, *Proc. Combust. Inst.* 31 (2007) 447–454.
- [111] Y. Tan, P. Dagaut, M. Cathonnet, J. Claude Boettner, J. Sylvain Bachman, P. Carlier, Natural gas and blends oxidation and ignition, *Symp. (Int.) Combust.* 25 (1994) 1563–1569.
- [112] N. Donohoe, A. Heufer, W.K. Metcalfe, H.J. Curran, M.L. Davis, O. Mathieu, D. Plichta, A. Morones, E.L. Petersen, F. Güthe, Ignition delay times, laminar flame speeds, and mechanism validation for natural gas/hydrogen blends at elevated pressures, *Combust. Flame* 161 (2014) 1432–1443.
- [113] Z. Li, X. Cheng, W. Wei, L. Qiu, H. Wu, Effects of hydrogen addition on laminar flame speeds of methane, ethane and propane, *Int. J. Hydrog. Energy* 42 (2017) 24055–24066.
- [114] E.J.K. Nilsson, A. van Sprang, J. Larfeldt, A.A. Konnov, The comparative and combined effects of hydrogen addition on the laminar burning velocities of methane and its blends with ethane and propane, *Fuel* 189 (2017) 369–376.
- [115] P. Dagaut, A. Nicolle, Experimental and detailed kinetic modeling study of hydrogen-enriched natural gas blend oxidation over extended temperature and equivalence ratio ranges, *Proc. Combust. Inst.* 30 (2005) 2631–2638.
- [116] P. Dagaut, G. Dayma, Hydrogen-enriched natural gas blend oxidation under high-pressure conditions, *Int. J. Hydrog. Energy* 31 (2006) 505–515.
- [117] U. Burke, K.P. Somers, P. O’Toole, C.M. Zinner, N. Marquet, G. Bourque, E.L. Petersen, W.K. Metcalfe, Z. Serinyel, H.J. Curran, An ignition delay and kinetic modeling study of methane, dimethyl ether, and their mixtures at high pressures, *Combust. Flame* 162 (2015) 315–330.
- [118] R. Burch, G.D. Squire, S.C. Tsang, Direct conversion of methane into methanol, *J. Chem. Soc., Faraday Trans. 1* 85 (1989) 3561–3568.
- [119] V.S. Arutyunov, V.M. Rudakov, V.I. Savchenko, E.V. Sheverdenkin, O.G. Sheverdenkina, A.Y. Zheltyakov, Partial alkane oxidation kinetics at high pressures: Methane oxidation in stainless steel and quartz reactors, *Theor. Found. Chem. Eng.* 36 (2002) 472–476.
- [120] S.M. Gallagher, H.J. Curran, W.K. Metcalfe, D. Healy, J.M. Simmie, G. Bourque, A rapid compression machine study of the oxidation of propane in the negative temperature coefficient regime, *Combust. Flame* 153 (2008) 316–333.
- [121] E.E. Dames, A.S. Rosen, B.W. Weber, C.W. Gao, C.-J. Sung, W.H. Green, A detailed combined experimental and theoretical study on dimethyl ether/propane blended oxidation, *Combust. Flame* 168 (2016) 310–330.
- [122] H. Hashemi, J.M. Christensen, L.B. Harding, S.J. Klippenstein, P. Glarborg, High-pressure oxidation of propane, *Proc. Combust. Inst.* (2018) In Press., DOI: 10.1016/j.proci.2018.07.009.
- [123] F. Battin-Leclerc, Detailed chemical kinetic models for the low-temperature combustion of hydrocarbons with application to gasoline and diesel fuel surrogates, *Prog. Energy Combust. Sci.* 34 (2008) 440–498.
-

- [124] C.-W. Zhou, Y. Li, U. Burke, C. Banyon, K.P. Somers, S. Ding, S. Khan, J.W. Hargis, T. Sikes, O. Mathieu, E.L. Petersen, M. AlAbbad, A. Farooq, Y. Pan, Y. Zhang, Z. Huang, J. Lopez, Z. Loparo, S.S. Vasu, H.J. Curran, An experimental and chemical kinetic modeling study of 1,3-butadiene combustion: Ignition delay time and laminar flame speed measurements, *Combust. Flame* 197 (2018) 423–438.
- [125] S. Gersen, A.V. Mokhov, J.H. Darneveil, H.B. Levinsky, P. Glarborg, Ignition-promoting effect of NO<sub>2</sub> on methane, ethane and methane/ethane mixtures in a rapid compression machine, *Proc. Combust. Inst.* 33 (2011) 433–440.
- [126] C.L. Rasmussen, A.E. Rasmussen, P. Glarborg, Sensitizing effects of NO<sub>x</sub> on CH<sub>4</sub> oxidation at high pressure, *Combust. Flame* 154 (2008) 529–545.
- [127] S. Sato, D. Yamashita, N. Iida, Influence of the fuel compositions on the homogeneous charge compression ignition combustion, *Int. J. Engine Res.* 9 (2008) 123–148.
- [128] J. Herzler, M. Fikri, O. Welz, C. Schulz, High-pressure shock-tube study of the ignition of fuel-rich CH<sub>4</sub>/air and CH<sub>4</sub>/additive/air mixtures over a wide temperature range, 7th European Combustion Meeting, ECM 2015, Budapest, Hungary (2015).
- [129] A. Chakir, M. Bellimam, J.C. Boettner, M. Cathonnet, Kinetic study of *n*-heptane oxidation, *Int. J. Chem. Kinet.* 24 (1992) 385–410.
- [130] A. Cavaliere, A. Ciajolo, A. D'Anna, R. Mercogliano, R. Ragucci, Autoignition of *n*-heptane and *n*-tetradecane in engine-like conditions, *Combust. Flame* 93 (1993) 279–286.
- [131] P. Dagaut, M. Reuillon, M. Cathonnet, High Pressure Oxidation of Liquid Fuels From Low to High Temperature. 1. *n*-Heptane and *iso*-Octane, *Combust. Sci. Technol.* 95 (1993) 233–260.
- [132] P. Dagaut, M. Reuillon, M. Cathonnet, Experimental study of the oxidation of *n*-heptane in a jet stirred reactor from low to high temperature and pressures up to 40 atm, *Combust. Flame* 101 (1995) 132–140.
- [133] O. Herbinet, B. Husson, Z. Serinyel, M. Cord, V. Warth, R. Fournet, P.-A. Glaude, B. Sirjean, F. Battin-Leclerc, Z. Wang, M. Xie, Z. Cheng, F. Qi, Experimental and modeling investigation of the low-temperature oxidation of *n*-heptane, *Combust. Flame* 159 (2012) 3455–3471.
- [134] H.M. Hakka, R.F. Cracknell, A. Pekalski, P.-A. Glaude, F. Battin-Leclerc, Experimental and modeling study of ultra-rich oxidation of *n*-heptane, *Fuel* 144 (2015) 358–368.
- [135] K. Zhang, C. Banyon, J. Bugler, H.J. Curran, A. Rodriguez, O. Herbinet, F. Battin-Leclerc, C. B'Chir, K.A. Heufer, An updated experimental and kinetic modeling study of *n*-heptane oxidation, *Combust. Flame* 172 (2016) 116–135.
- [136] Z. Wang, B. Chen, K. Moshhammer, D.M. Popolan-Vaida, S. Sioud, V.S.B. Shankar, D. Vuilleumier, T. Tao, L. Ruwe, E. Bräuer, N. Hansen, P. Dagaut, K. Kohse-Höinghaus, M.A. Raji, S.M. Sarathy, *n*-Heptane cool flame chemistry, *Combust. Flame* 187 (2018) 199–216.
- [137] C.V. Callahan, T.J. Held, F.L. Dryer, R. Minetti, M. Ribaucour, L.R. Sochet, T. Faravelli, P. Gaffuri, E. Rani, Experimental data and kinetic modeling of primary reference fuel mixtures, *Symp. Int. Combust. Proc.* 26 (1996) 739–746.
- [138] T.J. Held, A.J. Marchese, F.L. Dryer, A Semi-Empirical Reaction Mechanism for *n*-Heptane Oxidation and Pyrolysis, *Combust. Sci. Technol.* 123 (1997) 107–146.

- 
- [139] D.B. Lenhert, D.L. Miller, N.P. Cernansky, K.G. Owens, The oxidation of a gasoline surrogate in the negative temperature coefficient region, *Combust. Flame* 156 (2009) 549–564.
- [140] K. Yasunaga, H. Yamada, H. Oshita, K. Hattori, Y. Hidaka, H. Curran, Pyrolysis of *n*-pentane, *n*-hexane and *n*-heptane in a single pulse shock tube, *Combust. Flame* 185 (2017) 335–345.
- [141] A. Rousso, S. Yang, J. Lefkowitz, W. Sun, Y. Ju, Low temperature oxidation and pyrolysis of *n*-heptane in nanosecond-pulsed plasma discharges, *Proc. Combust. Inst.* 36 (2017) 4105–4112.
- [142] M. Li, X. Liu, T. Zhang, Q. Zheng, A kinetic study on the effects of methane substitution on the ignition of *n*-heptane/air mixture, *Journal of the Energy Institute* (2018) 1–15.
- [143] J. Liang, Z. Zhang, G. Li, Q. Wan, L. Xu, S. Fan, Experimental and kinetic studies of ignition processes of the methane–*n*-heptane mixtures, *Fuel* 235 (2019) 522–529.
- [144] E. Ranzi, A. Frassoldati, R. Grana, A. Cuoci, T. Faravelli, A.P. Kelley, C.K. Law, Hierarchical and comparative kinetic modeling of laminar flame speeds of hydrocarbon and oxygenated fuels, *Prog. Energy Combust. Sci.* 38 (2012) 468–501.
- [145] Y. Li, C.-W. Zhou, K.P. Somers, K. Zhang, H.J. Curran, The oxidation of 2-butene: A high pressure ignition delay, kinetic modeling study and reactivity comparison with isobutene and 1-butene, *Proc. Combust. Inst.* 36 (2017) 403–411.
- [146] I. Glassman, R.A. Yetter, N.G. Glumac, *Combustion*, Elsevier Science, 2014.
- [147] L. Seidel, K. Moshhammer, X. Wang, T. Zeuch, K. Kohse-Höinghaus, F. Mauss, Comprehensive kinetic modeling and experimental study of a fuel-rich, premixed *n*-heptane flame, *Combust. Flame* 162 (2015) 2045–2058.
- [148] L. Cai, H. Pitsch, Optimized chemical mechanism for combustion of gasoline surrogate fuels, *Combust. Flame* 162 (2015) 1623–1637.
- [149] G. Chicco, P. Mancarella, Distributed multi-generation, *Renew. Sust. Energ. Rev.* 13 (2009) 535–551.
- [150] K.J. Hughes, T. Turányi, A.R. Clague, M.J. Pilling, Development and testing of a comprehensive chemical mechanism for the oxidation of methane, *Int. J. Chem. Kinet.* 33 (2001) 513–538.
- [151] E. Petersen, Davidson, D. F., Hanson, R.K., Kinetics modeling of shock-induced ignition in low-dilution CH<sub>4</sub>/O<sub>2</sub> mixtures at high pressures and intermediate temperatures, *Combust. Flame* 117 (1999) 272–290.
- [152] L. Brett, J. Macnamara, P. Musch, J.M. Simmie, Simulation of methane autoignition in a rapid compression machine with creviced pistons, *Combust. Flame* 124 (2001) 326–329.
- [153] S. Gersen, N. Anikin, A. Mokhov, H. Levinsky, Ignition properties of methane/hydrogen mixtures in a rapid compression machine, *Int. J. Hydrog. Energy* 33 (2008) 1957–1964.
- [154] V.P. Zhukov, V.A. Sechenov, A.Y. Starikovskii, Spontaneous Ignition of Methane-Air Mixtures in a Wide Range of Pressures, *Combustion, Explosion, and Shock Waves* 39 (2003) 487–495.
- [155] C.L. Rasmussen, J. Hansen, P. Marshall, P. Glarborg, Experimental measurements and kinetic modeling of CO/H<sub>2</sub>/O<sub>2</sub>/NO<sub>x</sub> conversion at high pressure, *Int. J. Chem. Kinet.* 40 (2008) 454–480.
-

- [156] P. Dagaut, J.-C. Boettner, M. Cathonnet, Methane Oxidation, *Combust. Sci. Technol.* 77 (1991) 127–148.
- [157] F.P. Larkins, A.Z. Khan, Pyrolysis of Methane to Higher Hydrocarbons, *Aust. J. Chem.* 42 (1989) 1655.
- [158] O. Olsvik, O.A. Rokstad, A. Holmen, Pyrolysis of methane in the presence of hydrogen, *Chem. Eng. Technol.* 18 (1995) 349–358.
- [159] C. Keramiotis, G. Vourliotakis, G. Skevis, M.A. Founti, C. Esarte, N.E. Sánchez, A. Millera, R. Bilbao, M.U. Alzueta, Experimental and computational study of methane mixtures pyrolysis in a flow reactor under atmospheric pressure, *Energy* 43 (2012) 103–110.
- [160] H.-s. Kang, D.h. Lee, K.-t. Kim, S. Jo, S. Pyun, Y.-h. Song, S. Yu, Methane to acetylene conversion by employing cost-effective low-temperature arc, *Fuel Process. Technol.* 148 (2016) 209–216.
- [161] N. Muradov, F. Smith, C. Huang, A. T-Raissi, Autothermal catalytic pyrolysis of methane as a new route to hydrogen production with reduced CO<sub>2</sub> emissions, *Catal. Today* 116 (2006) 281–288.
- [162] T.A. Semelsberger, R.L. Borup, H.L. Greene, Dimethyl ether (DME) as an alternative fuel, *Journal of Power Sources* 156 (2006) 497–511.
- [163] P. Dagaut, J.-C. Boettner, M. Cathonnet, Chemical kinetic study of dimethylether oxidation in a jet stirred reactor from 1 to 10 atm, *Symp. (Int.) Combust.* 26 (1996) 627–632.
- [164] S.L. Fischer, F.L. Dryer, H.J. Curran, The reaction kinetics of dimethyl ether. I: High-temperature pyrolysis and oxidation in flow reactors, *Int. J. Chem. Kinet.* 32 (2000) 713–740.
- [165] E.W. Kaiser, T.J. Wallington, M.D. Hurley, J. Platz, H.J. Curran, W.J. Pitz, C.K. Westbrook, Experimental and Modeling Study of Premixed Atmospheric-Pressure Dimethyl Ether–Air Flames, *J. Phys. Chem. A* 104 (2000) 8194–8206.
- [166] H.J. Curran, W.J. Pitz, C.K. Westbrook, P. Dagaut, J.-C. Boettner, M. Cathonnet, A wide range modeling study of dimethyl ether oxidation, *Int. J. Chem. Kinet.* 30 (1998) 229–241.
- [167] M.C. Lee, S.B. Seo, J.H. Chung, Y.J. Joo, D.H. Ahn, Industrial gas turbine combustion performance test of DME to use as an alternative fuel for power generation, *Fuel* 88 (2009) 657–662.
- [168] H.J. Curran, S.L. Fischer, F.L. Dryer, The reaction kinetics of dimethyl ether. II: Low-temperature oxidation in flow reactors, *Int. J. Chem. Kinet.* 32 (2000) 741–759.
- [169] P. Dagaut, C. Daly, J.M. Simmie, M. Cathonnet, The oxidation and ignition of dimethylether from low to high temperature (500–1600 K), *Symp. (Int.) Combust.* 27 (1998) 361–369.
- [170] A. Mcilroy, T.D. Hain, H.A. Michelsen, T.A. Cool, A laser and molecular beam mass spectrometer study of low-pressure dimethyl ether flames, *Proc. Combust. Inst.* 28 (2000) 1647–1653.
- [171] U. Pfahl, K. Fieweger, G. Adomeit, Self-ignition of diesel-relevant hydrocarbon-air mixtures under engine conditions, *Symp. (Int.) Combust.* 26 (1996) 781–789.
- [172] X.L. Zheng, T.F. Lu, C.K. Law, C.K. Westbrook, H.J. Curran, Experimental and computational study of nonpremixed ignition of dimethyl ether in counterflow, *Proc. Combust. Inst.* 30 (2005) 1101–1109.

- [173] C.A. Daly, J.M. Simmie, J. Würmel, N. Djebaïli, C. Paillard, Burning velocities of dimethyl ether and air, *Combust. Flame* 125 (2001) 1329–1340.
- [174] X. Qin, Y. Ju, Measurements of burning velocities of dimethyl ether and air premixed flames at elevated pressures, *Proc. Combust. Inst.* 30 (2005) 233–240.
- [175] A. Andersen, E.A. Carter, A hybrid density functional theory study of the low-temperature dimethyl ether combustion pathways. I, *Isr. J. Chem.* 42 (2002) 245–260.
- [176] A. Andersen, E.A. Carter, Hybrid Density Functional Theory Predictions of Low-Temperature Dimethyl Ether Combustion Pathways. II. Chain-Branching Energetics and Possible Role of the Criegee Intermediate, *J. Phys. Chem. A* 107 (2003) 9463–9478.
- [177] J.J. Nash, J.S. Francisco, Unimolecular Decomposition Pathways of Dimethyl Ether, *J. Phys. Chem. A* 102 (1998) 236–241.
- [178] Z. Zhao, M. Chaos, A. Kazakov, F.L. Dryer, Thermal decomposition reaction and a comprehensive kinetic model of dimethyl ether, *Int. J. Chem. Kinet.* 40 (2008) 1–18.
- [179] R. Sivaramakrishnan, J.V. Michael, A.F. Wagner, R. Dawes, A.W. Jasper, L.B. Harding, Y. Georgievskii, S.J. Klippenstein, Roaming radicals in the thermal decomposition of dimethyl ether, *Combust. Flame* 158 (2011) 618–632.
- [180] Y. Hidaka, K. Sato, M. Yamane, High-temperature pyrolysis of dimethyl ether in shock waves, *Combust. Flame* 123 (2000) 1–22.
- [181] J. de Vries, W.B. Lowry, Z. Serinyel, H.J. Curran, E.L. Petersen, Laminar flame speed measurements of dimethyl ether in air at pressures up to 10 atm, *Fuel* 90 (2011) 331–338.
- [182] Z. Chen, X. Qin, Y. Ju, Z. Zhao, M. Chaos, F.L. Dryer, High temperature ignition and combustion enhancement by dimethyl ether addition to methane–air mixtures, *Proc. Combust. Inst.* 31 (2007) 1215–1222.
- [183] C. Tang, L. Wei, J. Zhang, X. Man, Z. Huang, Shock Tube Measurements and Kinetic Investigation on the Ignition Delay Times of Methane/Dimethyl Ether Mixtures, *Energy Fuels* 26 (2012) 6720–6728.
- [184] W.B. Lowry, Z. Serinyel, M.C. Krejci, H.J. Curran, G. Bourque, E.L. Petersen, Effect of methane-dimethyl ether fuel blends on flame stability, laminar flame speed, and Markstein length, *Proc. Combust. Inst.* 33 (2011) 929–937.
- [185] S.S. Yoon, D.H. Anh, S.H. Chung, Synergistic effect of mixing dimethyl ether with methane, ethane, propane, and ethylene fuels on polycyclic aromatic hydrocarbon and soot formation, *Combust. Flame* 154 (2008) 368–377.
- [186] H. Hashemi, J.M. Christensen, P. Glarborg, High-pressure pyrolysis and oxidation of DME and DME/CH<sub>4</sub>, *Combust. Flame* 205 (2019) 80–92.
- [187] Y. Hidaka, K. Sato, Y. Henmi, H. Tanaka, K. Inami, Shock-tube and modeling study of methane pyrolysis and oxidation, *Combust. Flame* 118 (1999) 340–358.
- [188] C.I. Heghes, C<sub>1</sub>–C<sub>4</sub> Hydrocarbon Oxidation Mechanism, Dissertation, Heidelberg, 2007.
- [189] M. Werler, L.R. Cancino, R. Schiessl, U. Maas, C. Schulz, M. Fikri, Ignition delay times of diethyl ether measured in a high-pressure shock tube and a rapid compression machine, *Proc. Combust. Inst.* 35 (2015) 259–266.
- [190] G. Mittal, C.-J. Sung, A Rapid Compression Machine for Chemical Kinetics Studies at Elevated Pressures and Temperatures, *Combust. Sci. Technol.* 179 (2007) 497–530.

- [191] X. He, S.M. Walton, B.T. Zigler, M.S. Wooldridge, A. Atreya, Experimental investigation of the intermediates of isooctane during ignition, *Int. J. Chem. Kinet.* 39 (2007) 498–517.
- [192] D. Lee, S. Hochgreb, Rapid Compression Machines, *Combust. Flame* 114 (1998) 531–545.
- [193] J. Würmel, J.M. Simmie, CFD studies of a twin-piston rapid compression machine, *Combust. Flame* 141 (2005) 417–430.
- [194] M. Werler, Untersuchungen der Niedertemperaturoxidation von Kohlenwasserstoffen in einer schnellen Kompressions-Expansions-Maschine, Dissertation, Karlsruhe, 2016.
- [195] H. Oertel, Stossrohre: Theorie, Praxis, Anwendungen. Mit einer Einführung in die Physik der Gase. Shock tubes., Springer, Wien, 1966.
- [196] H.B. Palmer, B.E. Knox, Contact surface tailoring in a chemical shock tube, *ARS Journal* (1961) 826–828.
- [197] D. Kaczmarek, B. Atakan, T. Kasper, Plug-Flow Reactor Study of the Partial Oxidation of Methane and Natural Gas at Ultra-Rich Conditions, *Combust. Sci. Technol.* (2019) 1574–1584.
- [198] M. Werler, R. Schießl, U. Maas, A rapid compression expansion machine (RECM) for measuring species histories, in: *Proceedings of 26th International Colloquium in the Dynamics of Explosions and Reactive Systems*, Boston, USA, 2017.
- [199] J. Herzler, Y. Sakai, M. Fikri, C. Schulz, Shock-tube study of the ignition and product formation of fuel-rich CH<sub>4</sub>/air and CH<sub>4</sub>/additive/air mixtures at high pressure, *Proc. Combust. Inst.* 37 (2019) 5705–5713.
- [200] D. Kaczmarek, B. Atakan, T. Kasper, Investigation of the partial oxidation of methane/*n*-heptane-mixtures and the interaction of methane and *n*-heptane under ultra-rich conditions, *Combust. Flame* 205 (2019) 345–357.
- [201] D.L. Baulch, C.T. Bowman, C.J. Cobos, R.A. Cox, T. Just, J.A. Kerr, M.J. Pilling, D. Stocker, J. Troe, W. Tsang, R.W. Walker, J. Warnatz, Evaluated Kinetic Data for Combustion Modeling, *J. Phys. Chem. Ref Data* 34 (2005) 757–1397.
- [202] A. Kéromnès, W.K. Metcalfe, K.A. Heufer, N. Donohoe, A.K. Das, C.-J. Sung, J. Herzler, C. Naumann, P. Griebel, O. Mathieu, M.C. Krejci, E.L. Petersen, W.J. Pitz, H.J. Curran, An experimental and detailed chemical kinetic modeling study of hydrogen and syngas mixture oxidation at elevated pressures, *Combust. Flame* 160 (2013) 995–1011.
- [203] J. A. Manion, R. E. Huie, R. D. Levin, D. R. Burgess Jr., V. L. Orkin, W. Tsang, W. S. McGivern, J. W. Hudgens, V. D. Knyazev, D. B. Atkinson, E. Chai, A. M. Tereza, C.-Y. Lin, T. C. Allison, W. G. Mallard, F. Westley, J. T. Herron, R. F. Hampson, and D. H. Frizzell, NIST Chemical Kinetics Database, NIST Standard Reference Database 17, Version 7.0 (Web Version), Release 1.6.8, Data version 2015.09. National Institute of Standards and Technology, 2020, <https://kinetics.nist.gov/>.
- [204] C. Heghes, Karbach, V., Warnatz, J., Evaluation of new data for hydrocarbon kinetics, in: *Proceedings of the 2nd European Combustion Meeting*, 2005.
- [205] K. Hoyermann, F. Mauß, T. Zeuch, A detailed chemical reaction mechanism for the oxidation of hydrocarbons and its application to the analysis of benzene formation in fuel-rich premixed laminar acetylene and propene flames, *Phys. Chem. Chem. Phys.* 6 (2004) 3824–3835.

- [206] Y. Hidaka, H. Masaoka, H. Oshita, T. Nakamura, K. Tanaka, H. Kawano, Thermal decomposition of vinylacetylene in shock waves, *Int. J. Chem. Kinet.* 24 (1992) 871–885.
- [207] Y. Hidaka, T. Nakamura, A. Miyauchi, T. Shiraishi, H. Kawano, Thermal decomposition of propyne and allene in shock waves, *Int. J. Chem. Kinet.* 21 (1989) 643–666.
- [208] N.M. Marinov, A detailed chemical kinetic model for high temperature ethanol oxidation, *Int. J. Chem. Kinet.* 31 (1999) 183–220.
- [209] M. Scott, R.W. Walker, Addition of toluene and ethylbenzene to mixtures of H<sub>2</sub> and O<sub>2</sub> at 773 K: Part I: Kinetic measurements for H and HO<sub>2</sub> reactions with the additives and a data base for H abstraction by HO<sub>2</sub> from alkanes, aromatics and related compounds, *Combust. Flame* 129 (2002) 365–377.
- [210] C.-J. Chen, J.W. Bozzelli, Thermochemical Property, Pathway and Kinetic Analysis on the Reactions of Allylic Isobutenyl Radical with O<sub>2</sub>: an Elementary Reaction Mechanism for Isobutene Oxidation, *J. Phys. Chem. A* 104 (2000) 9715–9732.
- [211] R.R. Baldwin, P.N. Jones, R.W. Walker, Determination of the rate constant for HO<sub>2</sub> + CH<sub>4</sub> → H<sub>2</sub>O<sub>2</sub> + CH<sub>3</sub> at 443 °C, *Journal of the Chemical Society, Faraday Transactions 2: Molecular and Chemical Physics* (1988) 199–207.
- [212] N. Cohen, The use of transition-state theory to extrapolate rate coefficients for reactions of H atoms with alkanes, *Int. J. Chem. Kinet.* 23 (1991) 683–700.
- [213] J.W. Sutherland, M.-C. Su, J.V. Michael, Rate constants for H + CH<sub>4</sub>, CH<sub>3</sub> + H<sub>2</sub>, and CH<sub>4</sub> dissociation at high temperature, *Int. J. Chem. Kinet.* 33 (2001) 669–684.
- [214] W.K. Metcalfe, S.M. Burke, S.S. Ahmed, H.J. Curran, A Hierarchical and Comparative Kinetic Modeling Study of C<sub>1</sub> – C<sub>2</sub> Hydrocarbon and Oxygenated Fuels, *Int. J. Chem. Kinet.* 45 (2013) 638–675.
- [215] R. Zhu, C. Lin, The CH<sub>3</sub> + HO<sub>2</sub> Reaction, *J. Phys. Chem. A* 105 (2001) 6243–6248.
- [216] I.A.B. Reid, C. Robinson, D.B. Smith, Spontaneous ignition of methane: Measurement and chemical model, *Symp. Int. Combust. Proc.* 20 (1985) 1833–1843.
- [217] K. Glänzer, M. Quack, J. Troe, A spectroscopic determination of the methyl radical recombination rate constant in shock waves, *Chemical Physics Letters* 39 (1976) 304–309.
- [218] H. Hippler, K. Luther, A.R. Ravishankara, J. Troe, High-Pressure Effects in the Recombination Reaction CH<sub>3</sub> + CH<sub>3</sub> → C<sub>2</sub>H<sub>6</sub>, *Z. Phys. Chem.* 142 (1984) 1–12.
- [219] I.R. Slagle, D. Gutman, J.W. Davies, M.J. Pilling, Study of the recombination reaction CH<sub>3</sub> + CH<sub>3</sub> → C<sub>2</sub>H<sub>6</sub>. 1. Experiment, *J. Phys. Chem.* 92 (1988) 2455–2462.
- [220] M.T. Macpherson, M.J. Pilling, M.J.C. Smith, Determination of the absorption cross section for methyl at 216.36 nm and the absolute rate constant for methyl radical recombination over the temperature range 296–577 K, *J. Phys. Chem.* 89 (1985) 2268–2274.
- [221] D. Walter, H.-H. Grotheer, J.W. Davies, M.J. Pilling, A.F. Wagner, Experimental and theoretical study of the recombination reaction CH<sub>3</sub>+CH<sub>3</sub>→C<sub>2</sub>H<sub>6</sub>, *Symp. Int. Combust. Proc.* 23 (1991) 107–114.
- [222] M.A. Blitz, N.J.B. Green, R.J. Shannon, M.J. Pilling, P.W. Seakins, C.M. Western, S.H. Robertson, Reanalysis of Rate Data for the Reaction CH<sub>3</sub> + CH<sub>3</sub> → C<sub>2</sub>H<sub>6</sub> Using Revised Cross Sections and a Linearized Second-Order Master Equation, *J. Phys. Chem. A* 119 (2015) 7668–7682.

- [223] C. Oehlers, H.G. Wagner, H. Ziemer, F. Temps, S. Dóbé, An Investigation of the D/H Addition–Elimination and H Atom Abstraction Channels in the Reaction  $D + H_2CO$  in the Temperature Range  $296\text{ K} \leq T \leq 780\text{ K}$ , *J. Phys. Chem. A* 104 (2000) 10500–10510.
- [224] J. Vandooren, L.O. de Guertechin, P.J. van Tiggelen, Kinetics in a lean formaldehyde flame, *Combust. Flame* 64 (1986) 127–139.
- [225] A.A. Westenberg, N. DeHaas, Measurement of the rate constant for  $H + H_2CO \rightarrow H_2 + HCO$  at 297–652 K, *J. Phys. Chem.* 76 (1972) 2213–2214.
- [226] E.A. Irdam, J.H. Kiefer, L.B. Harding, A.F. Wagner, The formaldehyde decomposition chain mechanism, *Int. J. Chem. Kinet.* 25 (1993) 285–303.
- [227] B. Eiteneer, C.-L. Yu, M. Goldenberg, M. Frenklach, Determination of Rate Coefficients for Reactions of Formaldehyde Pyrolysis and Oxidation in the Gas Phase, *J. Phys. Chem. A* 102 (1998) 5196–5205.
- [228] A.M. Held, K.C. Manthorne, P.D. Pacey, H.P. Reinholdt, Individual rate constants of methyl radical reactions in the pyrolysis of dimethyl ether, *Can. J. Chem.* 55 (1977) 4128–4134.
- [229] C. Anastasi, Reaction of methyl radicals with formaldehyde in the range  $500 \leq T/K \leq 603$ , *J. Chem. Soc., Faraday Trans. 1* 79 (1983) 749.
- [230] T.K. Choudhury, W.A. Sanders, M.C. Lin, A shock tube and modeling study of the methyl + formaldehyde reaction at high temperatures, *J. Phys. Chem.* 93 (1989) 5143–5147.
- [231] J.A. Kerr, M.J. Parsonage, Evaluated Kinetic Data on Gas Phase Hydrogen Transfer Reactions of Methyl Radicals, *Berichte der Bunsengesellschaft für physikalische Chemie* 80 (1976) 825.
- [232] J. Warnatz, Rate Coefficients in the C/H/O System, in: W.C. Gardiner (Ed.), *Combustion Chemistry*, Springer US, New York, NY, 1984, pp. 197–360.
- [233] W. Tsang, R.F. Hampson, Chemical Kinetic Data Base for Combustion Chemistry. Part I. Methane and Related Compounds, *J. Phys. Chem. Ref Data* 15 (1986) 1087–1279.
- [234] J.M. Dyke, A.P. Groves, E.P.F. Lee, M.H. Zamanpour Niavaran, Study of the  $CH_3CHOH$  Radical with Ultraviolet Photoelectron Spectroscopy, *J. Phys. Chem. A* 101 (1997) 373–376.
- [235] Z. Hong, D.F. Davidson, E.A. Barbour, R.K. Hanson, A new shock tube study of the  $H+O_2 \rightarrow OH+O$  reaction rate using tunable diode laser absorption of  $H_2O$  near  $2.5\ \mu m$ , *Proc. Combust. Inst.* 33 (2011) 309–316.
- [236] J.W. Sutherland, J.V. Michael, A.N. Pirraglia, F.L. Nesbitt, R.B. Klemm, Rate constant for the reaction of  $O(3P)$  with  $H_2$  by the flash photolysis—shock tube and flash photolysis—resonance fluorescence techniques;  $504\text{ K} \leq T \leq 2495\text{ K}$ , *Symp. Int. Combust. Proc.* 21 (1988) 929–941.
- [237] D.A. Masten, R.K. Hanson, C.T. Bowman, Shock tube study of the reaction hydrogen atom + oxygen .fwdarw. hydroxyl + oxygen atom using hydroxyl laser absorption, *J. Phys. Chem.* 94 (1990) 7119–7128.
- [238] R.W. Bates, D.M. Golden, R.K. Hanson, C.T. Bowman, Experimental study and modeling of the reaction  $H + O_2 + M \rightarrow HO_2 + M$  ( $M = Ar, N_2, H_2O$ ) at elevated pressures and temperatures between 1050 and 1250 K, *Phys. Chem. Chem. Phys.* 3 (2001) 2337–2342.
- [239] R.X. Fernandes, K. Luther, J. Troe, V.G. Ushakov, Experimental and modelling study of the recombination reaction  $H + O_2 (+M) \rightarrow HO_2 (+M)$  between 300 and 900 K, 1.5 and

- 950 bar, and in the bath gases  $M = \text{He}, \text{Ar}, \text{and } \text{N}_2$ , *Phys. Chem. Chem. Phys.* 10 (2008) 4313.
- [240] J. Troe, The thermal dissociation/recombination reaction of hydrogen peroxide  $\text{H}_2\text{O}_2(+M) \rightleftharpoons 2\text{OH}(+M)$  III.: Analysis and representation of the temperature and pressure dependence over wide ranges, *Combust. Flame* 158 (2011) 594–601.
- [241] H. Hippler, J. Troe, J. Willner, Shock wave study of the reaction  $\text{HO}_2 + \text{HO}_2 \rightarrow \text{H}_2\text{O}_2 + \text{O}_2$ : Confirmation of a rate constant minimum near 700 K, *J. Chem. Phys.* 93 (1990) 1755–1760.
- [242] B.A. Ellingson, D.P. Theis, O. Tishchenko, J. Zheng, D.G. Truhlar, Reactions of Hydrogen Atom with Hydrogen Peroxide, *J. Phys. Chem. A* 111 (2007) 13554–13566.
- [243] J. Mendes, C.-W. Zhou, H.J. Curran, Rate Constant Calculations of H-Atom Abstraction Reactions from Ethers by  $\text{HO}_2$  Radicals, *J. Phys. Chem. A* 118 (2014) 1300–1308.
- [244] H.-H. Carstensen, A.M. Dean, Rate constants for the abstraction reactions  $\text{RO}_2 + \text{C}_2\text{H}_6$ ;  $R = \text{H}, \text{CH}_3$ , and  $\text{C}_2\text{H}_5$ , *Proc. Combust. Inst.* 30 (2005) 995–1003.
- [245] Q.S. Li, Y. Zhang, S. Zhang, Dual Level Direct ab Initio and Density-Functional Theory Dynamics Study on the Unimolecular Decomposition of  $\text{CH}_3\text{OCH}_2$  Radical, *J. Phys. Chem. A* 108 (2004) 2014–2019.
- [246] K. Banke, R. Hegner, D. Schröder, C. Schulz, B. Atakan, S.A. Kaiser, Power and syngas production from partial oxidation of fuel-rich methane/DME mixtures in an HCCI engine, *Fuel* 243 (2019) 97–103.
- [247] F. Herrmann, P. Oßwald, K. Kohse-Höinghaus, Mass spectrometric investigation of the low-temperature dimethyl ether oxidation in an atmospheric pressure laminar flow reactor, *Proc. Combust. Inst.* 34 (2013) 771–778.
- [248] F. Herrmann, B. Jochim, P. Oßwald, L. Cai, H. Pitsch, K. Kohse-Höinghaus, Experimental and numerical low-temperature oxidation study of ethanol and dimethyl ether, *Combust. Flame* 161 (2014) 384–397.
- [249] A. Rodriguez, O. Frottier, O. Herbinet, R. Fournet, R. Bounaceur, C. Fittschen, F. Battin-Leclerc, Experimental and Modeling Investigation of the Low-Temperature Oxidation of Dimethyl Ether, *J. Phys. Chem. A* 119 (2015) 7905–7923.
- [250] N. Kurimoto, B. Brumfield, X. Yang, T. Wada, P. Diévar, G. Wysłocki, Y. Ju, Quantitative measurements of  $\text{HO}_2/\text{H}_2\text{O}_2$  and intermediate species in low and intermediate temperature oxidation of dimethyl ether, *Proc. Combust. Inst.* 35 (2015) 457–464.
- [251] K. Moshhammer, A.W. Jasper, D.M. Popolan-Vaida, A. Lucassen, P. Diévar, H. Selim, A.J. Eskola, C.A. Taatjes, S.R. Leone, S.M. Sarathy, Y. Ju, P. Dagaut, K. Kohse-Höinghaus, N. Hansen, Detection and Identification of the Keto-Hydroperoxide ( $\text{HOCH}_2\text{OCHO}$ ) and Other Intermediates during Low-Temperature Oxidation of Dimethyl Ether, *J. Phys. Chem. A* 119 (2015) 7361–7374.
- [252] E. Hu, Z. Zhang, L. Pan, J. Zhang, Z. Huang, Experimental and Modeling Study on Ignition Delay Times of Dimethyl Ether/Propane/Oxygen/Argon Mixtures at 20 bar, *Energy Fuels* 27 (2013) 4007–4013.
- [253] J. Zhang, E. Hu, L. Pan, Z. Zhang, Z. Huang, Shock-Tube Measurements of Ignition Delay Times for the Ethane/Dimethyl Ether Blends, *Energy Fuels* 27 (2013) 6247–6254.

- [254] R.W. Crossley, E.A. Dorko, K. Scheller, A. Burcat, The effect of higher alkanes on the ignition of methane-oxygen-argon mixtures in shock waves, *Combust. Flame* 19 (1972) 373–378.
- [255] T. Tsuboi, H.G. Wagner, Homogeneous thermal oxidation of methane in reflected shock waves, *Symp. (Int.) Combust.* 15 (1975) 883–890.
- [256] C.S. Eubank, M.J. Rabinowitz, W.C. Gardiner, R.E. Zellner, Shock-initiated ignition of natural gas—Air mixtures, *Symp. (Int.) Combust.* 18 (1981) 1767–1774.
- [257] R. Zellner, Niemitz, K. J., Warnatz, J., Gardiner, W. C., C.S. Eubank, J.M. Simmie, Hydrocarbon Induced Acceleration of Methane-Air Ignition, *Prog. Aeronaut. Astronaut.* (1983) 252–272.
- [258] M. Frenklach, D.E. Bornside, Shock-initiated ignition in methane-propane mixtures, *Combust. Flame* 56 (1984) 1–27.
- [259] L.J. Spadaccini, M.B. Colket, Ignition delay characteristics of methane fuels, *Prog. Energy Combust. Sci.* 20 (1994) 431–460.
- [260] E.L. Petersen, M. Röhrig, D.F. Davidson, R.K. Hanson, C.T. Bowman, High-pressure methane oxidation behind reflected shock waves, *Symp. (Int.) Combust.* 26 (1996) 799–806.
- [261] E.L. Petersen, D.F. Davidson, R.K. Hanson, Ignition Delay Times of Ram Accelerator CH<sub>4</sub>/O<sub>2</sub>/Diluent Mixtures, *J. Propul. Power* 15 (1999) 82–91.
- [262] C.J. Goy, A.J. Moran, G.O. Thomas, Autoignition Characteristics of Gaseous Fuels at Representative Gas Turbine Conditions, in: *Proceedings of the ASME Turbo Expo 2001: Power for Land, Sea, and Air. Volume 2: Coal, Biomass and Alternative Fuels; Combustion and Fuels; Oil and Gas Applications; Cycle Innovations.* New Orleans, Louisiana, USA. June 4–7, 2001, V002T02A018.
- [263] N. Lamoureux, C.-E. Paillard, Natural gas ignition delay times behind reflected shock waves, *Shock Waves* 13 (2003) 57–68.
- [264] J. Huang, P.G. Hill, W.K. Bushe, S.R. Munshi, Shock-tube study of methane ignition under engine-relevant conditions, *Combust. Flame* 136 (2004) 25–42.
- [265] J. Huang, W.K. Bushe, Experimental and kinetic study of autoignition in methane/ethane/air and methane/propane/air mixtures under engine-relevant conditions, *Combust. Flame* 144 (2006) 74–88.
- [266] J. de Vries, E.L. Petersen, Autoignition of methane-based fuel blends under gas turbine conditions, *Proc. Combust. Inst.* 31 (2007) 3163–3171.
- [267] D. Healy, H.J. Curran, S. Dooley, J.M. Simmie, D.M. Kalitan, E.L. Petersen, G. Bourque, Methane/propane mixture oxidation at high pressures and at high, intermediate and low temperatures, *Combust. Flame* 155 (2008) 451–461.
- [268] S. Heyne, A. Roubaud, M. Ribaucour, G. Vanhove, R. Minetti, D. Favrat, Development of a natural gas reaction mechanism for engine simulations based on rapid compression machine experiments using a multi-objective optimisation strategy, *Fuel* 87 (2008) 3046–3054.
- [269] G. Mittal, M. Chaos, C.-J. Sung, F.L. Dryer, Dimethyl ether autoignition in a rapid compression machine, *Fuel Process. Technol.* 89 (2008) 1244–1254.

- [270] J. Herzler, C. Naumann, Shock-tube study of the ignition of methane/ethane/hydrogen mixtures with hydrogen contents from 0% to 100% at different pressures, *Proc. Combust. Inst.* 32 (2009) 213–220.
- [271] R.D. Cook, D.F. Davidson, R.K. Hanson, Shock tube measurements of ignition delay times and OH time-histories in dimethyl ether oxidation, *Proc. Combust. Inst.* 32 (2009) 189–196.
- [272] E. Hu, X. Li, X. Meng, Y. Chen, Y. Cheng, Y. Xie, Z. Huang, Laminar flame speeds and ignition delay times of methane–air mixtures at elevated temperatures and pressures, *Fuel* 158 (2015) 1–10.
- [273] I.N. Kosarev, S.V. Kindysheva, I.V. Kochetov, A.Y. Starikovskiy, N.L. Aleksandrov, Shock-tube study of dimethyl ether ignition by high-voltage nanosecond discharge, *Combust. Flame* 203 (2019) 72–82.
- [274] J. Herzler, L. Jerig, P. Roth, Shock tube study of the ignition of lean *n*-heptane/air mixtures at intermediate temperatures and high pressures, *Proc. Combust. Inst.* 30 (2005) 1147–1153.
- [275] E.L. Petersen, M.J.A. Rickard, M.W. Crofton, E.D. Abbey, M.J. Traum, D.M. Kalitan, A facility for gas- and condensed-phase measurements behind shock waves, *Meas. Sci. Technol.* 16 (2005) 1716–1729.
- [276] X. You, H. Wang, E. Goos, C.-J. Sung, S.J. Klippenstein, Reaction kinetics of  $\text{CO} + \text{HO}_2 \rightarrow$  products: Ab initio transition state theory study with master equation modeling, *J. Phys. Chem. A* 111 (2007) 4031–4042.
- [277] A.W. Jasper, S.J. Klippenstein, L.B. Harding, Theoretical rate coefficients for the reaction of methyl radical with hydroperoxyl radical and for methylhydroperoxide decomposition, *Proc. Combust. Inst.* 32 (2009) 279–286.
- [278] A.V. Joshi, H. Wang, Master equation modeling of wide range temperature and pressure dependence of  $\text{CO} + \text{OH} \rightarrow$  products, *Int. J. Chem. Kinet.* 38 (2006) 57–73.
- [279] S.J. Klippenstein, J.A. Miller, L.B. Harding, Resolving the mystery of prompt  $\text{CO}_2$ : The  $\text{HCCO} + \text{O}_2$  reaction, *Proc. Combust. Inst.* 29 (2002) 1209–1217.
- [280] C. Fittschen, B. Delcroix, N. Gomez, P. Devolder, Rate constants for the reactions of  $\text{CH}_3\text{O}$  with  $\text{CH}_2\text{O}$ ,  $\text{CH}_3\text{CHO}$  and *i*- $\text{C}_4\text{H}_{10}$ , *J. Chim. Phys.* 95 (1998) 2129–2142.
- [281] M. Altarawneh, A.'A.H. Al-Muhtaseb, B.Z. Dlugogorski, E.M. Kennedy, J.C. Mackie, Rate constants for hydrogen abstraction reactions by the hydroperoxyl radical from methanol, ethenol, acetaldehyde, toluene, and phenol, *J. Comput. Chem.* 32 (2011) 1725–1733.
- [282] U. Burke, W.K. Metcalfe, S.M. Burke, K.A. Heufer, P. Dagaut, H.J. Curran, A detailed chemical kinetic modeling, ignition delay time and jet-stirred reactor study of methanol oxidation, *Combust. Flame* 165 (2016) 125–136.
- [283] V. Vasudevan, D.F. Davidson, R.K. Hanson, Direct measurements of the reaction  $\text{OH} + \text{CH}_2\text{O} \rightarrow \text{HCO} + \text{H}_2\text{O}$  at high temperatures, *Int. J. Chem. Kinet.* 37 (2005) 98–109.
- [284] S. Wang, E.E. Dames, D.F. Davidson, R.K. Hanson, Reaction Rate Constant of  $\text{CH}_2\text{O} + \text{H} = \text{HCO} + \text{H}_2$  Revisited, *J. Phys. Chem. A* 118 (2014) 10201–10209.
- [285] G. P. Smith, D. M. Golden, M. Frenklach, N. W. Moriarty, B. Eiteneer, M. Goldenberg, C. T. Bowman, R. K. Hanson, S. Song, W. C. Gardiner, Jr., V. V. Lissianski, Z. Qin, *GRI-Mech 3.0*.

- [286] J.P. Senosiain, S.J. Klippenstein, J.A. Miller, Reaction of Ethylene with Hydroxyl Radicals, *J. Phys. Chem. A* 110 (2006) 6960–6970.
- [287] J.W. Bozzelli, A.M. Dean, Chemical activation analysis of the reaction of ethyl radical with oxygen, *J. Phys. Chem.* 94 (1990) 3313–3317.
- [288] L.K. Huynh, S. Panasewicz, A. Ratkiewicz, T.N. Truong, Ab Initio Study on the Kinetics of Hydrogen Abstraction for the  $H + \text{Alkene} \rightarrow H_2 + \text{Alkenyl}$  Reaction Class, *J. Phys. Chem. A* 111 (2007) 2156–2165.
- [289] S.J. Klippenstein, Y. Georgievskii, L.B. Harding, Predictive theory for the combination kinetics of two alkyl radicals, *Phys. Chem. Chem. Phys.* 8 (2006) 1133.
- [290] B. Wang, H. Hou, L.M. Yoder, J.T. Muckerman, C. Fockenberg, Experimental and Theoretical Investigations on the Methyl–Methyl Recombination Reaction, *J. Phys. Chem. A* 107 (2003) 11414–11426.
- [291] R. Sivaramakrishnan, J.V. Michael, Rate Constants for OH with Selected Large Alkanes, *J. Phys. Chem. A* 113 (2009) 5047–5060.
- [292] B. Wang, H. Hou, Y. Gu, Mechanism and rate constant of the reaction of atomic hydrogen with propyne, *J. Chem. Phys.* 112 (2000) 8458–8465.
- [293] S. Wang, D.F. Davidson, R.K. Hanson, Improved Shock Tube Measurement of the  $CH_4 + Ar = CH_3 + H + Ar$  Rate Constant using UV Cavity-Enhanced Absorption Spectroscopy of  $CH_3$ , *J. Phys. Chem. A* 120 (2016) 5427–5434.
- [294] N.K. Srinivasan, M.-C. Su, J.W. Sutherland, J.V. Michael, Reflected Shock Tube Studies of High-Temperature Rate Constants for  $OH + CH_4 \rightarrow CH_3 + H_2O$  and  $CH_3 + NO_2 \rightarrow CH_3O + NO$ , *J. Phys. Chem. A* 109 (2005) 1857–1863.
- [295] L.N. Krasnoperov, J.V. Michael, Shock Tube Studies Using a Novel Multipass Absorption Cell, *J. Phys. Chem. A* 108 (2004) 5643–5648.
- [296] V. Sivakumaran, D. Hölscher, T.J. Dillon, J.N. Crowley, Reaction between OH and HCHO, *Phys. Chem. Chem. Phys.* 5 (2003) 4821–4827.
- [297] J. Herzler, M. Fikri, C. Schulz, High-pressure shock-tube study of the ignition and product formation of fuel-rich dimethoxymethane (DMM)/air and  $CH_4$ /DMM/air mixtures, *Combust. Flame* 216 (2020) 293–299.
- [298] P. Desgroux, A. Faccinetto, X. Mercier, T. Mouton, D. Aubagnac Karkar, A. El Bakali, Comparative study of the soot formation process in a “nucleation” and a “sooting” low pressure premixed methane flame, *Combust. Flame* 184 (2017) 153–166.
- [299] D. Nativel, B. Shu, J. Herzler, M. Fikri, C. Schulz, Shock-tube study of methane pyrolysis in the context of energy-storage processes, *Proc. Combust. Inst.* 37 (2019) 197–204.
- [300] R.U. Khan, S. Bajohr, D. Buchholz, R. Reimert, H.D. Minh, K. Norinaga, V.M. Jannardhanan, S. Tischer, O. Deutschmann, Pyrolysis of propane under vacuum carburizing conditions, *J. Anal. Appl. Pyrolysis* 81 (2008) 148–156.
- [301] K. Wang, S.M. Villano, A.M. Dean, Fundamentally-based kinetic model for propene pyrolysis, *Combust. Flame* 162 (2015) 4456–4470.
- [302] S.M. Burke, W. Metcalfe, O. Herbinet, F. Battin-Leclerc, F.M. Haas, J. Santner, F.L. Dryer, H.J. Curran, An experimental and modeling study of propene oxidation. Part 1, *Combust. Flame* 161 (2014) 2765–2784.
- [303] H. Gossler, S. Drost, S. Porras, R. Schießl, U. Maas, O. Deutschmann, The internal combustion engine as a  $CO_2$  reformer, *Combust. Flame* 207 (2019) 186–195.

- 
- [304] Sun Oil Co, P. E. Oberdorfer, Partial Oxidation of Methane in a Motored Engine, 1960.
- [305] A. Cavaliere, M. de Joannon, Mild Combustion, *Prog. Energy Combust. Sci.* 30 (2004) 329–366.
- [306] P. Sabia, M.d. Joannon, A. Picarelli, R. Ragucci, Methane auto-ignition delay times and oxidation regimes in MILD combustion at atmospheric pressure, *Combust. Flame* 160 (2013) 47–55.
- [307] P. Sabia, M. de Joannon, A. Picarelli, A. Chinnici, R. Ragucci, Modeling Negative Temperature Coefficient region in methane oxidation, *Fuel* 91 (2012) 238–245.
- [308] T. Tao, S. Kang, W. Sun, J. Wang, H. Liao, K. Moshhammer, N. Hansen, C.K. Law, B. Yang, A further experimental and modeling study of acetaldehyde combustion kinetics, *Combust. Flame* 196 (2018) 337–350.
- [309] O.V. Sokolov, Y.V. Parfenov, V.S. Arutyunov, V.V. Basevich, V.L. Vedeneev, Study of cool-Dame phenomena during self-ignition of methane-oxygen mixtures, *Russ Chem Bull* 45 (1996) 2316–2320.
- [310] CHEMKIN-PRO 19.2, Reaction Design: San Diego, 2017.
- [311] G. P. Smith, D. M. Golden, M. Frenklach, N. W. Moriarty, B. Eiteneer, M. Goldenberg, C. T. Bowman, R. K. Hanson, S. Song, W. C. Gardiner, Jr., V. V. Lissianski, Z. Qin, GRI-Mech 3.0, [http://www.me.berkeley.edu/gri\\_mech/](http://www.me.berkeley.edu/gri_mech/).
- [312] H. Wang, X. You, A. V. Joshi, S. G. Davis, A. Laskin, F. Egolfopoulos, C. K. Law, USC Mech Version II. High-Temperature Combustion Reaction Model of H<sub>2</sub>/CO/C<sub>1</sub>-C<sub>4</sub> Compounds, 2007, [http://ignis.usc.edu/USC\\_Mech\\_II.htm](http://ignis.usc.edu/USC_Mech_II.htm).
- [313] Mechanical and Aerospace Engineering (Combustion Research), University of California at San Diego, Chemical-Kinetic Mechanisms for Combustion Applications, <http://combustion.ucsd.edu>.
- [314] S.M. Sarathy, C.K. Westbrook, M. Mehl, W.J. Pitz, C. Togbe, P. Dagaut, H. Wang, M.A. Oehlschlaeger, U. Niemann, K. Seshadri, P.S. Veloo, C. Ji, F.N. Egolfopoulos, T. Lu, Comprehensive chemical kinetic modeling of the oxidation of 2-methylalkanes from C<sub>7</sub> to C<sub>20</sub>, *Combust. Flame* 158 (2011) 2338–2357.
- [315] acatech – National Academy of Science and Engineering, Coupling the different energy sectors – options for the next phase of the energy transition, 2018.
- [316] A.P. Simpson, A.E. Lutz, Exergy analysis of hydrogen production via steam methane reforming, *Int. J. Hydrog. Energy* 32 (2007) 4811–4820.
- [317] H. Li, H. Hong, H. Jin, R. Cai, Analysis of a feasible polygeneration system for power and methanol production taking natural gas and biomass as materials, *Appl. Energy* 87 (2010) 2846–2853.
- [318] K. Jana, A. Ray, M.M. Majoumerd, M. Assadi, S. De, Polygeneration as a future sustainable energy solution – A comprehensive review, *Appl. Energy* 202 (2017) 88–111.
- [319] G.-j. Liu, Z. Li, M.-h. Wang, W.-d. Ni, Energy savings by co-production, *Appl. Energy* 87 (2010) 2854–2859.
- [320] Y. Khojasteh Salkuyeh, T.A. Adams, Integrated petroleum coke and natural gas polygeneration process with zero carbon emissions, *Energy* 91 (2015) 479–490.
- [321] Y. Khojasteh Salkuyeh, T.A. Adams, A novel polygeneration process to co-produce ethylene and electricity from shale gas with zero CO<sub>2</sub> emissions via methane oxidative coupling, *Energy Convers. Manag.* 92 (2015) 406–420.
-

- [322] Leonid Tartakovsky, Moshe Sheintuch, Fuel reforming in internal combustion engines, *Prog. Energy Combust. Sci.* 67 (2018) 88–114.
- [323] A. Eyal, L. Tartakovsky, Second-law analysis of the reforming-controlled compression ignition, *Appl. Energy* 263 (2020) 114622.
- [324] F. D. F. Chuahy, S.L. Kokjohn, High efficiency dual-fuel combustion through thermochemical recovery and diesel reforming, *Appl. Energy* 195 (2017) 503–522.
- [325] J. Hunicz, M. Mikulski, M.S. Geca, A. Rybak, An applicable approach to mitigate pressure rise rate in an HCCI engine with negative valve overlap, *Appl. Energy* 257 (2020) 114018.
- [326] S. Peucheret, M.L. Wyszynski, R.S. Lehrle, S. Golunski, H. Xu, Use of catalytic reforming to aid natural gas HCCI combustion in engines, *Int. J. Hydrog. Energy* 30 (2005) 1583–1594.
- [327] L. von Szeszich, Herstellung von Synthesegas im Otto-Motor bei gleichzeitiger Arbeitsgewinnung, *Chemie Ing. Techn.* 28 (1956) 190–195.
- [328] M.H. McMillian, S.A. Lawson, Experimental and modeling study of hydrogen/syngas production and particulate emissions from a natural gas-fueled partial oxidation engine, *Int. J. Hydrog. Energy* 31 (2006) 847–860.
- [329] G.A. Karim, N.P.W. Moore, Examination of Rich Mixture Operation of a Dual Fuel Engine SAE Technical Paper 901500, 1990.
- [330] J.C. Prince, F.A. Williams, A short reaction mechanism for the combustion of dimethyl ether, *Combust. Flame* 162 (2015) 3589–3595.
- [331] B.J. McBride, M.J. Zehe, S. Gordon, NASA Glenn Coefficients for Calculating Thermodynamic Properties of Individual Species, 2002.
- [332] S. Drost, R. Schießl, M. Werler, J. Sommerer, U. Maas, Ignition delay times of polyoxymethylene dimethyl ether fuels (OME<sub>2</sub> and OME<sub>3</sub>) and air: Measurements in a rapid compression machine, *Fuel* 258 (2019) 116070.
- [333] W.J. Pitz, C.V. Naik, T.N. Mhaolduin, C.K. Westbrook, H.J. Curran, J.P. Orme, J.M. Simmie, Modeling and experimental investigation of methylcyclohexane ignition in a rapid compression machine, *Proc. Combust. Inst.* 31 (2007) 267–275.
- [334] T. Echekki, E. Mastorakos, *Turbulent Combustion Modeling: Advances, New Trends and Perspectives*, Springer, Dordrecht, 2011.
- [335] T. Turányi, A.S. Tomlin, *Analysis of Kinetic Reaction Mechanisms*, Springer, Berlin, Heidelberg, 2014.
- [336] S. Porras, V. Bykov, V. Gol'dshtein, U. Maas, Joint Characteristic Timescales and Entropy Production Analyses for Model Reduction of Combustion Systems, *Entropy* 19 (2017) 264.
- [337] V. Bykov, V. Gol'dshtein, U. Maas, Scaling Invariant Interpolation for Singularly Perturbed Vector Fields (SPVF), in: A.N. Gorban, D. Roose (Eds.), *Coping with Complexity: Model Reduction and Data Analysis*, Springer, Berlin, Heidelberg, 2011, pp. 91–111.
- [338] S. Porras, C. Yu, V. Bykov, U. Maas, Global Quasi-Linearization (GQL) method for high dimensional detailed reaction mechanisms, in: *9th European Combustion Meeting*, Lisboa, Portugal, 2019.

- [339] S. Porras, V. Bykov, V. Gol'dshtein, U. Maas, Reduction of detailed reaction mechanisms using characteristic time scales: analysis and implementation, in: 8th European Combustion Meeting, Dubrovnik, Croatia, 2017.
- [340] U. Maas, J. Warnatz, Ignition processes in hydrogen–oxygen mixtures, *Combust. Flame* 74 (1988) 53–69.
- [341] S. Drost, R. Schießl, U. Maas, Rapid compression machine (RCM) studies on the production of unsaturated hydrocarbons from methane, in: Proceedings of 27th International Colloquium in the Dynamics of Explosions and Reactive Systems, Peking, China, 2019.
- [342] B. Atakan, Compression–Expansion Processes for Chemical Energy Storage, *Energies* 12 (2019) 3332.
- [343] F.G. Billaud, C.P. Gueret, F. Baronnet, Thermal coupling of methane in a tubular flow reactor, *Ind. Eng. Chem. Res.* 31 (1992) 2748–2753.
- [344] C. Guéret, M. Daroux, F. Billaud, Methane pyrolysis, *Chem. Eng. Sci.* 52 (1997) 815–827.
- [345] S. Drost, R. Schießl, U. Maas, Feasibility of natural gas pyrolysis for production of unsaturated hydrocarbons: an RCM study, in: 9th European Combustion Meeting, Lisboa, Portugal, 2019.
- [346] J. Herzler, D. Nativel, M. Fikri, C. Schulz, Untersuchung des Zerfalls von Methan und Erdgas für die chemische Energiespeicherung, in: 29. Deutscher Flammentag, Bochum, Germany, 2019.
- [347] F. Calise, M. Dentice d'Accadia, A. Piacentino, Exergetic and exergoeconomic analysis of a renewable polygeneration system and viability study for small isolated communities, *Energy* 92 (2015) 290–307.
- [348] F. Calise, M.D. d'Accadia, A. Macaluso, A. Piacentino, L. Vanoli, Exergetic and exergoeconomic analysis of a novel hybrid solar–geothermal polygeneration system producing energy and water, *Energy Convers. Manag.* 115 (2016) 200–220.
- [349] F. Foucher, P. Higelin, C. Mounaïm-Rousselle, P. Dagaut, Influence of ozone on the combustion of *n*-heptane in a HCCI engine, *Proc. Combust. Inst.* 34 (2013) 3005–3012.
- [350] H. Nishida, T. Tachibana, Homogeneous Charge Compression Ignition of Natural Gas/Air Mixture with Ozone Addition, *J. Propul. Power* 22 (2006) 151–157.
- [351] J.-B. Masurier, F. Foucher, G. Dayma, P. Dagaut, Investigation of *iso*-octane combustion in a homogeneous charge compression ignition engine seeded by ozone, nitric oxide and nitrogen dioxide, *Proc. Combust. Inst.* 35 (2015) 3125–3132.
- [352] J.-B. Masurier, F. Foucher, G. Dayma, P. Dagaut, Ozone applied to the homogeneous charge compression ignition engine to control alcohol fuels combustion, *Appl. Energy* 160 (2015) 566–580.
- [353] A. Lazzaretto, G. Tsatsaronis, SPECO: A systematic and general methodology for calculating efficiencies and costs in thermal systems, *Energy* 31 (2006) 1257–1289.
- [354] O. Balli, H. Aras, A. Hepbasli, Exergoeconomic analysis of a combined heat and power (CHP) system, *Int. J. Energy Res.* 32 (2008) 273–289.
- [355] G. Tsatsaronis, Definitions and nomenclature in exergy analysis and exergoeconomics, *Energy* 32 (2007) 249–253.
- [356] G. Tsatsaronis, Thermo-economic analysis and optimization of energy systems, *Prog. Energy Combust. Sci.* 19 (1993) 227–257.

- [357] D. Schröder, R. Hegner, A. Güngör, B. Atakan, Exergoeconomic analysis of an HCCI engine polygeneration process, *Energy Convers. Manag.* 203 (2020) 112085.
- [358] J.M. Sala, L.M. López-González, M. Ruiz de Adana, J.L. Míguez, J. Eguía, I. Flores, Exergetic analysis and thermoeconomic study for a container-housed engine, *Appl. Therm. Eng.* 26 (2006) 1840–1850.
- [359] T. Keipi, H. Tolvanen, J. Konttinen, Economic analysis of hydrogen production by methane thermal decomposition: Comparison to competing technologies, *Energy Convers. Manag.* 159 (2018) 264–273.
- [360] D. Schröder, R. Hegner, A. Güngör, B. Atakan, The influence of uncertainty of economic parameters and upscaling on product costs of an engine polygeneration system, in: 32nd International Conference on Efficiency, Cost, Optimization, Simulation and Environmental Impact of Energy Systems (ECOS), Wroclaw, Poland, 2019.
- [361] A. Saltelli, M. Ratto, T. Andres, F. Campolongo, *Global sensitivity analysis: The primer*, Wiley, Chichester, 2008.
- [362] M.S. Peters, K.D. Timmerhaus, R.E. West, *Plant design and economics for chemical engineers*, 5th ed., McGraw-Hill, Boston, 2004.
- [363] M. Cord, B. Husson, J.C. Lizardo Huerta, O. Herbinet, P.-A. Glaude, R. Fournet, B. Sirjean, F. Battin-Leclerc, M. Ruiz-Lopez, Z. Wang, M. Xie, Z. Cheng, F. Qi, Study of the low temperature oxidation of propane, *J. Phys. Chem. A* 116 (2012) 12214–12228.

---

## Publications

### Submitted journal articles

- T. Bierkandt, P. Oßwald, N. Gaiser, D. Krüger, M. Köhler, M. Hoener, S. Shaqiri, D. Kaczmarek, Y. Karakaya, P. Hemberger, T. Kasper, Observation of low-temperature chemistry products in laminar premixed low-pressure flames by molecular-beam mass spectrometry, *International Journal of Chemical Kinetics*, under review.

### Peer-reviewed journal articles

- D. Kaczmarek, B. Atakan, T. Kasper, Plug-Flow Reactor Study of the Partial Oxidation of Methane and Natural Gas at Ultra-Rich Conditions, *Combustion Science and Technology*, (2019), 1-14.
- D. Kaczmarek, B. Atakan, T. Kasper, Investigation of the partial oxidation of methane/*n*-heptane mixtures and the interaction of methane and *n*-heptane under ultra-rich conditions, *Combustion and Flame* 205, (2019), 345-357.
- S. Porras, D. Kaczmarek, J. Herzler, S. Drost, M. Werler, T. Kasper, M. Fikri, R. Schießl, B. Atakan, C. Schulz, U. Maas, An experimental and modeling study on the reactivity of extremely fuel-rich methane/dimethyl ether mixtures, *Combustion and Flame* 212, (2020), 107-122.
- M. Hoener, D. Kaczmarek, T. Kasper, A. Bodi, P. Hemberger, T. Kasper, A Pressurized Flow Reactor Combustion Experiment Interfaced with Synchrotron Double Imaging Photoelectron Photoion Coincidence Spectroscopy, *Review of Scientific Instruments* 91, (2020), 045115.
- B. Atakan, S. A. Kaiser, J. Herzler, S. Porras, O. Deutschmann, T. Kasper, M. Fikri, R. Schießl, D. Schröder, C. Rudolph, D. Kaczmarek, H. Gossler, S. Drost, V. Bykov, U. Maas, C. Schulz, Flexible energy conversion and storage via high-temperature gas-phase reactions: The piston engine as a polygeneration reactor, *Renewable & Sustainable Energy Reviews* 133, (2020), 110264.
- D. Kaczmarek, S. Shaqiri, B. Atakan, T. Kasper, The Influence of Pressure and Equivalence Ratio on the NTC Behavior of Methane, *Proceedings of the Combustion Institute* 38, (2021).
- C. O. Rogers, D. Kaczmarek, T. Kasper, N. J. Labbe, Probing the Low-Temperature Chemistry of Methyl Hexanoate: Insights from Oxygenate Intermediates, *Proceedings of the Combustion Institute* 38, (2021).

- D. Kaczmarek, J. Herzler, S. Porras, S. Shaqiri, M. Fikri, C. Schulz, B. Atakan, U. Maas, T. Kasper, Plug-flow and shock-tube study of the oxidation of very fuel-rich natural gas/DME/O<sub>2</sub> mixtures, *Combustion and Flame* 225, (2021), 86-103.

#### Conference contributions (oral presentation)

- D. Kaczmarek, T. Kasper, B. Atakan, P. Oßwald, M. Köhler, D. Krüger, Testing a Jet-stirred Reactor Under Atmospheric Pressure for the Ability to Perform Gas-phase Kinetic Studies, 24<sup>th</sup> „Journées d’Etude“ of the Belgian Section of the Combustion Institute, Louvain-La-Neuve, Belgium, May 19-20, 2016.
- D. Kaczmarek, T. Kasper, B. Atakan, Kinetic Investigation of the Homogenous Partial Oxidation of CH<sub>4</sub>/C<sub>2</sub>H<sub>5</sub>OH and CH<sub>4</sub>/*n*-C<sub>7</sub>H<sub>16</sub> Mixtures, SMARTCATS 2<sup>nd</sup> General Meeting & Workshop on Smart Energy Carriers in Industry, Lisbon, Portugal, November 14-16, 2016.
- D. Kaczmarek, S. Porras, F. Sen, T. Kasper, R. Schießl, U. Maas, B. Atakan, Kinetische Untersuchung der partiellen Oxidation von Methan/DME- und Methan/Ethanol-Gemischen, 28. Deutscher Flammentag, Darmstadt, Germany, September 6-7, 2017.
- D. Kaczmarek, T. Kasper, B. Atakan, Plug-Flow Reactor Study of the Partial Oxidation of Methane and Natural Gas at Ultra-Rich Conditions, Joint Meeting of the German and Italian Sections of the Combustion Institute, Sorrento, Italy, May 23-26, 2018.
- D. Kaczmarek, T. Kasper, B. Atakan, Kinetische Untersuchung der partiellen Oxidation von Ozon/Sauerstoff/Erdgas-Gemischen im ultrafetten Bereich, Thermodynamik-Kolloquium, Kassel, Germany, September 26-28, 2018.
- T. Kasper, P. Hemberger, P. Oßwald, M. Köhler, D. Krüger, T. Bierkandt, Y. Karakaya, D. Kaczmarek, Diagnostics for combustion and nanoparticle formation, International Bunsen Discussion Meeting, Bielefeld, Germany, June 21-23, 2017.
- M. Köhler, D. Kaczmarek, M. Höner, P. Hemberger, P. Oßwald, T. Bierkandt, T. Kasper, Investigation of combustion processes in different reactor setups using i2PEP-ICO, Photon Tools for Physical Chemistry, Beatenberg, Switzerland, January 8-11, 2019.
- T. Kasper, M. Höner, D. Kaczmarek, Y. Karakaya, M. Gonchikzhapov, S. Peukert, D. Krüger, T. Bierkandt, P. Oßwald, M. Köhler, P. Hemberger, High-Temperature Reaction Pathways, 11<sup>th</sup> International Conference on Chemical Kinetics, Orléans, France, June 23-27, 2019.
- D. Kaczmarek, B. Atakan, T. Kasper, Experimentelle Untersuchung der partiellen Oxidation von Diethylether/Methan-Gemischen unter brennstoffreichen Bedingungen in einem Strömungsreaktor, 29. Deutscher Flammentag, Bochum, Germany, September 17-18, 2019.

#### Conference contributions (poster presentation)

- D. Kaczmarek, B. Atakan, D. Krüger, P. Oßwald, M. Köhler, T. Kasper, Investigation of the partial oxidation of propane using a jet-stirred reactor and molecular-beam mass spectrometry, 64<sup>th</sup> ASMS Conference on Mass Spectrometry and Allied Topics, San Antonio, USA, June 5-9, 2016.

- 
- D. Kaczmarek, T. Kasper, B. Atakan, Investigation of the Partial Oxidation of Methane and the Effect of Ethanol and *n*-Heptane as Additives Using a Plug-Flow Reactor and Time-of-flight Mass Spectrometry, 36<sup>th</sup> International Symposium on Combustion, Seoul, South Korea, July 31 - August 5, 2016.
  - D. Kaczmarek, T. Kasper, B. Atakan, Kinetische Untersuchung der partiellen Oxidation von Methan/Ethanol und Methan/*n*-Heptan Gemischen, Thermodynamik-Kolloquium, Kaiserslautern, Germany, October 5-7, 2016.
  - D. Kaczmarek, T. Kasper, S. Shaqiri B. Atakan, An Experimental Investigation of the Partial Oxidation of Methane: the Influence of *n*-Heptane Addition, 8<sup>th</sup> European Combustion Meeting, Dubrovnik, Croatia, April 18-21, 2017.
  - D. Kaczmarek, B. Atakan, T. Kasper, Investigation of the Partial Oxidation of CH<sub>4</sub>/C<sub>2</sub>H<sub>5</sub>OH and CH<sub>4</sub>/O<sub>3</sub>-mixtures Using a Plug-Flow Reactor and Time-of-Flight Mass Spectrometry, 65<sup>th</sup> ASMS Conference on Mass Spectrometry and Allied Topics, Indianapolis, USA, June 4-8, 2017.
  - D. Kaczmarek, F. Sen, T. Kasper, B. Atakan, The effect of dimethyl ether and ethanol on the homogenous partial oxidation of methane, International Bunsen Discussion Meeting, Bielefeld, Germany, June 21-23, 2017.
  - D. Kaczmarek, T. Kasper, B. Atakan, Untersuchung des Einflusses von Ozon auf die partielle Oxidation von Methan bei atmosphärischem Druck, Thermodynamik-Kolloquium, Dresden, Germany, September 27-29, 2017.
  - D. Kaczmarek, T. Kasper, B. Atakan, Molecular-Beam Mass Spectrometry Study of the Impact of Hydrogen Addition to Natural Gas Mixtures in Partial Oxidation Reactions, 66<sup>th</sup> ASMS Conference on Mass Spectrometry and Allied Topics, San Diego, USA, June 3-7, 2018.
  - M. Hoener, D. Kaczmarek, T. Kasper, Lean Partial Oxidation of Methane in the Presence of Nitrogen Monoxide as a Model for Exhaust Gas Recirculation, 66<sup>th</sup> ASMS Conference on Mass Spectrometry and Allied Topics, San Diego, USA, June 3-7, 2018.
  - D. Kaczmarek, T. Kasper, B. Atakan, Ultra-rich oxidation of methane and natural gas in a plug-flow reactor, 37<sup>th</sup> International Symposium on Combustion, Dublin, Ireland, July 29 - August 3, 2018.
  - D. Kaczmarek, S. Shaqiri, B. Atakan, T. Kasper, Activation Effect of diethyl ether on the partial oxidation of methane, 9<sup>th</sup> European Combustion Meeting, Lisbon, Portugal, July 14-17, 2019.
  - M. Höner, D. Kaczmarek, P. Oßwald, T. Kasper, Photoelektronen-Photoionen Koinzidenz Spektrometrie in Hochdruckreaktorexperimenten mit NO dotierten mageren und fetten Methangemischen, 29. Deutscher Flammentag, Bochum, Germany, September 17-18, 2019.
  - T. Bierkandt, D. Krüger, P. Oßwald, M. Köhler, D. Kaczmarek, Y. Karakaya, J. Attiah, P. Hemberger, T. Kasper, Observation of alkyl hydroperoxides in laminar premixed alkane- and alkene-doped hydrogen flames at low-pressure, 29. Deutscher Flammentag, Bochum, Germany, September 17-18, 2019.
  - D. Kaczmarek, S. Shaqiri, B. Atakan, T. Kasper, Untersuchung der partiellen Oxidation von Methan unter brennstoffreichen Bedingungen in einem Strömungsreaktor bei

Drücken von 1 – 20 bar, Thermodynamik-Kolloquium, Duisburg, Germany, September 30 - October 02, 2019.

- S. Shaqiri, D. Kaczmarek, B. Atakan, T. Kasper, Additivwirkung von Diethylether auf die partielle Oxidation von Methan, Thermodynamik-Kolloquium, Duisburg, Germany, September 30 - October 02, 2019.

# DuEPublico

Duisburg-Essen Publications online

UNIVERSITÄT  
DUISBURG  
ESSEN

*Offen im Denken*

ub | universitäts  
bibliothek

Diese Dissertation wird via DuEPublico, dem Dokumenten- und Publikationsserver der Universität Duisburg-Essen, zur Verfügung gestellt und liegt auch als Print-Version vor.

**DOI:** 10.17185/duepublico/74072

**URN:** urn:nbn:de:hbz:464-20210226-153502-4

Alle Rechte vorbehalten.